OCEANS FROM SPACE V

Scuola Grande di San Marco, Venezia
24 - 28 October 2022

OCEANS FROM SPACE
Scuola Grande di San Marco, Venezia
24 - 28 October 2022

PROCEEDINGS

OCEANS FROM SPACE V

Extended Abstracts of the contributions presented at the
"Oceans form Space V" Symposium
Scuola Grande di San Marco, Venice (Italy), 24-28 october 2022

V. BARALE, J.F.R. GOWER, L. ALBEROTANZA, ED.S

FORWARD

The "Oceans from Space" Symposium series aims to provide, every ten years, a thorough state-of-the-art outline, an overview of ongoing research and a forum to debate topical issues, in the field of Satellite Oceanography. The present volume of Proceedings refers to the "Oceans from Space" 5th edition, held once again in Venice, Italy, on 24-28 October 2022, after two years of delay imposed by the COVID-19 pandemic. The 2022 edition followed the four previous events held in 1980, 1990, 2000 and 2010, and the very first "Oceanography from Space" workshop, held in Woods Hole, MA (USA), back in 1964.

Venue of "Oceans from Space" V was the *Scuola Grande di San Marco*, in the *Sestiere di Castello*, in the very center of Venice. The edifice, which holds a score of cultural treasures, has been the seat of the Fraternity of Saint Mark since 1260. In 1485, it was destroyed by a fire, and later rebuilt under a new design, with elements of Renaissance classicism, and a masterful front of Byzantine flavor. Following the conquest by Napoleon, and the annexation of the Republic of Venice to the Austro-Hungarian Empire, in 1819 it became a military hospital, and today still provides the entrance of the Venice main hospital.

The present volume collects the Extended Abstracts of all contributions presented in either oral or poster form, grouped according to the thematic criteria of their respective session. The Abstracts' scientific themes cover every facet of oceanographic remote sensing, including missions, satellites, sensors; passive and active techniques; visible, infrared and microwave spectral regions; calibration and validation, algorithms and models. Further, physical parameters and dynamical processes, bio-geo-chemical cycles and ecological status, from local to global scales, as well as socio-economic issues, are also assessed.

The Symposium was organized and managed by international Co-Chair, Scientific and Organizing Committees (see Symposium Governing Bodies composition in the following). The scientific program was complemented by social events that include a visit to the MOSE *(i.e. MOdulo Sperimentale Elettromeccanico)* installation, destined to protect Venice and its Lagoon from the acqua alta flooding events, as well as art exhibits and music recitals. Thanks are due to all Contributors who provided the following scientific material, as well as to the sponsoring Institutions and Agerncies, which made "Oceans from Space V" possible, i.e.

- European Commission, Joint Research Centre (EC JRC),
- European Space Agency (ESA),
- European Organization for the Exploitation of Meteorological Satellites (EUMETSAT),
- National Aeronautics and Space Administration (NASA), USA,
- Tethys Research Institute (TRI),
- NDPI Remote Sensing,
- NSA Group.

Vittorio Barale
Venice, October 2022

SYMPOSIUM GOVERNING BODIES

The composition of the governing bodies of the *"Oceans from Space" V Symposium* comprised a Co-Chair Committee, a Scientific Committee and an Organizing Committee. The active Committee members, subdivided by functional group, have been:

1.   CO-CHAIR COMMITTEE

V. Barale, (Ret.) Joint Research Centre, European Commission, Ispra (I)
J.F.R Gower, (Ret.) Institute for Ocean Sciences, Sidney (CAN)
L. Alberotanza, (Ret.) Consiglio Nazionale delle Ricerche, Venezia (I)

2.   SCIENTIFIC COMMITTEE

Members of the Co-Chair Committee
J. Benveniste, European Space Agency, Frascati (I)
P. Bontempi, University of Rhode Island, Narragansett RI (USA)
E. Boss, School of Marine Sciences, University of Maine, Orono, ME (USA)
V. Brando, Consiglio nazionale della Ricerche, Roma (I)
C. Donlon, European Space Agency, Noordwijk (NL)
M. Gade, Institut für Meereskunde, Universität Hamburg, Hamburg (D)
L. Lorenzoni, National Aeronautics and Space Administration, Washington DC (USA)
F. Melin, Joint Research Centre, European Commission, Ispra (I)
F. Muller-Karger, University of South Florida, St Petersburg FL (USA)
E. Obligis, European Organization Exp Meteorological Satellites, Darmstadt (D)

3.   ORGANIZING COMMITTEE

Members of the Scientific Committee
Representative of the Conference Support Agency, NSA Group srl, Rome (I)

SCUOLA GRANDE DI SAN MARCO

THE SCUOLA GRANDE DI SAN MARCO IN VENICE

Established in 1261 as a confraternity of penitents, the Scuola Grande di San Marco over the centuries became a philanthropic institution that combined acts of devotion with healthcare and assistance for its needy members. The headquarters of the Scuola, completed between the late 15th and mid-16th century, is a celebrated example of early Renaissance Venetian architecture. Until the Napoleonic period, when lay confraternities were suppressed and the Scuola became a civil hospital, its rooms housed three cycles of paintings dedicated to St Mark, the patron saint of Venice: one executed by the Bellini family and other leading practitioners of early 16th-century Venetian painting, and the other two completed by Jacopo Tintoretto and his son Domenico.

SYMPOSIUM PROGRAM

WELCOME TO "OCEANS FROM SPACE" V

SESSION 1
MISSIONS, SATELLITES, SENSORS

SESSION 7
SURFACE PROCESSES, COASTAL ISSUES, EXTREME EVENTS

SESSION 8
SEA LEVEL

SESSION 9
SEA LEVEL RISE & COASTAL CITIES

SESSION 10
CLOSING SESSION

POSTER SESSION

*The Extended Abstract of contributions marked N.A. was Not Available at the time of printing

WELCOME TO
"OCEANS FROM SPACE" V

'Oceans from Space' Venice 2020: Scientific and Technical Themes

V. Barale *

Tethys Research Institute, Milan , Italy

Abstract – The scientific themes of Oceans from Space V, Venice 2022, cover all aspects of oceanographic remote sensing, including both passive and active techniques, in the visible, infrared and microwave spectral regions. Special attention is placed on the fusion of optical, thermal and structural data, and on future perspectives. General themes are space missions, satellites and sensors, calibration and validation, algorithms and models. Applications include marine parameters and processes, bio-geo-chemical cycles and ecological status, from local to global scales. Linkages to management and policy, as well as economic aspects, are also considered, in view to support decision makers and civil society at large.

Keywords: Symposium, Program, Scientific Themes.

1. INTRODUCTION

In the last half century, satellite observations have become a cornerstone of all planetary sciences. No other technology allows to gather the required information, at suitable space and time scales, like satellite remote sensing does, while the list of current or potential applications is virtually endless. Sustainable environmental management, in particular, relies on the provision of both land and sea services, via ad hoc communication and knowledge exchange between the scientific community and the user community at large.

A key role in this interaction is played by specialized conventions, which can focus the awareness of both know-how providers and customers. In the marine sector, the 'Oceans from Space' conference series, held every 10 years since 1980, is one of the most celebrated, and best attended by marine practitioners. The series aims to provide, on a decadal timeframe, a thorough outline of the state-of-the-art in satellite oceanography, an overview of current research on the world scene, and a forum to debate topical issues.

The scientists who attended the 1980 edition were like sea-faring pioneers who opened new trade routes, and whose discoveries, since then, have surpassed many times what was expected in the beginning (Gower 1981). In 1990, they were faced by the hardships of continuing their enterprise, in spite of the extraordinary possibilities hinted by early results. By 2000, the need for new commitments, in funding and programs, became evident to the scientific community and policy-making circles alike (Barale et al. 2000, 2004).

Climate change, and its dear environmental and socio-economic consequences, were taking center stage at the time, and action seemed urgent. It did still in 2010, when the same community got together once again in Venice, the city that represents so well our complex, daring and yet captivating bond with the sea. In spite of the achievements and the knowledge gained over the preceding decades of ocean observations, new trials were brought about in the course of the most recent studies (Barale et al. 2010a, 2010b).

The 2020 edition of 'Oceans from Space', hosted by the *Scuola Grande di San Marco*, in Venice (see Figure 1) – postponed to 2022, due to thew COVID-19 pandemic – is to provide an overview of the path followed so far, the tools available today, and the plans for tomorrow. It highlights the added value of complementary techniques and their combined views, addressing the scientific community that backs present and future missions.

Figure 1. *Scuola Grande di San Marco*, Venice.

2. SCIENTIFIC PROGRAM THEMES

"Oceans from Space" Venice 2020 is the latest in a decadal series of discussions on the past, present and future successes, problems, and requirements in using satellites to study the oceans. Therefore, the scientific program of the Symposium covers new sensing techniques and results, for water color, wind, waves, ice, floating vegetation, salinity and pollution, including effects on coastlines, multi-mission combinations, policy applications, or citizen science. And, in particular, the program includes a special session on global sea level rise and the future of Venice, in the hope that future conferences, in 2030 and later, will continue to be possible.

The main themes of the Symposium's scientific program are listed in Table 1. First and foremost, the program addresses ocean-oriented missions, satellites and sensors. A number of specialized sessions are to be devoted to new technical developments, instruments and sensors, data analyses and synergies. Novel issues and principles, such as polarimetry and lidar applications, sea surface salinity, or acidification assessment are also foreseen. Lastly, this theme includes the use of satellite constellations, multi-mission and multi-sensor approaches, cube-sats and small-sats arrays (e.g. for global climate research).

Models, data assimilation, calibration/validation issues constitute the second theme of the program. This includes modelling and data assimilation at large, as well as assimilation of ocean data into global models; assimilation of

* Corresponding author. Address: Corso Adda 60, 13100 Vercelli (VC), Italia. Email: vittorio.barale@yahoo.it

numerical model data to derive new products from space; uncertainties and validation, *in situ* technologies, and new calibration approaches. The third theme comprises regional and planetary issues: ocean basins, the Arctic Ocean and Antarctica; but also continental waters, marginal/enclosed seas, and local sea level rise; as well as interfacing research on Earth oceans and oceans on exoplanets.

Table 1. Scientific and Technical Themes

1	**Missions, Satellites, Sensors**
	Technical Issues, Instruments, Data Synergies
	Novel Analyses, Sea Surface Salinity, Acidification
	Arrays, Multi-Mission/Sensor, Cube/Small-Sats
2	**Models, Assimilation, Cal/Val**
	Modelling & Data Assimilation (in Global Models)
	Assimilation of Model Data for New Space Products
	Uncertainties, Cal/Val, *In Situ* Technologies
3	**Regional & Planetary Issues**
	Ocean Basins, Arctic Ocean, Antarctica
	Continental Waters, Marginal Basins, Sea Level Rise
	Relating Earth Oceans & Oceans on Exoplanets
4	**Surface Processes, Coastal Issues, Extremes**
	Ocean-Atmosphere Exchange & Coupled Modelling
	Wind & Waves, Total Surface Current Velocity
	Global Coastal Ocean, Near-Coastal Waters, Hazards
5	**Bio-Geo-Chemical Issues, Pollution Processes**
	Aquatic Carbon from Space
	Biodiversity, Floating Vegetation in the Global Ocean
	Pollution (Plastics, Hydrocarbons, Runoff), Debris
6	**Society, Policy, Economics**
	Science & Society, Management & Policy
	Coastal and Marine Ecosystem Services, Economics
	Emerging Countries & Early-Career Researchers
∗	**"Venice Syndrome" (Coastal Areas at Risk)**
∗	**Covid-19 Pandemic: Oceans' Response**
∗	**Coupling Space Science & Citizen Science**
∗	**UN Decade of Ocean Science (2021-2030)**

Surface processes, coastal issues, and extreme events are grouped together in the fourth theme. Ocean-atmosphere exchange and coupled modelling fall into this category, together with ocean surface observations for assessing wind and waves, or monitoring the total surface current velocity (i.e. doppler oceanography). Furthermore, the global coastal ocean, spanning across the land-to-open-ocean boundary, plus coastal waters at large (wetlands, deltas, estuaries, saline intrusions), and coastal hazards and extremes (e.g. near-coastal vs open ocean level rise, surges, erosion, sediment transport) are also included.

Theme five comprises bio-geo-chemical issues, pollution agents and processes. The aquatic carbon from space item links biology to physics of the air-sea interface, while that on biodiversity calls for a vision to assess the diversity of life beyond simple and popular measures of biomass/carbon. Floating vegetation in the global ocean means observations of the changing distribution of Sargassum, its causes and future projections, and observations of other species in other oceans. Marine pollution (including plastics, hydrocarbons, river runoff), marine debris monitoring from high-resolution microwave and optical sensors complete this theme.

Finally, theme six - society, policy, economics - brings about the connection to strategies and management, linking what can be observed, and the next generation of science questions to address (e.g. water quality, HABs, carbon management, water resources), to how it can provide support

to decision makers. Science and society, valuation of coastal and marine ecosystems (ecosystem services), and economic issues are to be considered. Further, this theme focuses on involving in the same processes early-career researchers, new contributors such as satellite sensor engineers/technologists, and scientists from emerging countries.

A set of particular topics concludes the Symposium themes: (a) global sea level changes and the future of Venice, which parallels that of the many other urban areas around the world at risk from analogous hazards; (b) the oceans' response to the Covid-19 Pandemic, as seen from space; (c) the emerging potential of coupling space science and citizen science, for water quality monitoring in particular; (d) the UN Decade for Ocean Science for Sustainable Development (2021-2030), for which 'Oceans from Space' can offer a key opportunity to articulate the space applications' contribution to "ocean science that is fit for purpose".

3. CONCLUSION

Research in Ocean and Earth System Science has become increasingly multidisciplinary, as well as focused on societal benefits. It demands collaboration of experts not only in traditional sciences, but also in social sciences, informational technology, and policy. The 'Oceans from Space' conference series provides a forum to discuss the use of spaceborne measurements, promote interdisciplinary education, stimulate new collaborations, and involve in this process participants with varied background, including the next generation of early-career scientists.

REFERENCES

Barale, V., J.F.R. Gower, and L. Alberotanza, Ed.s (2000). 'Oceans from Space' Venice 2000 Abstracts. European Commission, EUR 19661 EN, pp 282.

Barale, V., J.F.R. Gower, and L. Alberotanza, Guest Ed.s (2004). Special Issue 'Oceans from Space'. International Journal of Remote Sensing, 25 (7-8), pp 1255-1543.

Barale, V., J.F.R. Gower, and L. Alberotanza, Ed.s (2010 a). Oceanography from Space, Revisited. Springer, Dordrecht Heidelberg London New York, pp 374.

Barale, V., J.F.R. Gower, and L. Alberotanza, Ed.s (2010 b). Proceedings (Extended Abstracts Collection) 'Oceans from Space' Venice 2010. EUR 24324 EN, Publication Office of the European Union, Luxemburg, pp 265.

Gower, J.F.R., Ed. (1981). Oceanography from Space. Marine Science Series, Vol. 13, Springer-Verlag, New York, pp 978.

SESSION 1

MISSIONS, SATELLITES, SENSORS

Operational Ocean Colour global and regional products for Essential Ocean Variables within the Copernicus Marine Service

V. E. Brando[1]*, R. Santoleri[1], S.Colella[1], G. Volpe[1], J. A. Concha[1], A. Di Cicco[1], M. Sammartino[1], L . Gozalez-Vilas, M.. Bracaglia[1], M. Benincasa[1], E. Böhm[1], C. Cesarini[1], V. Forneris[1], F. La Padula[1], P. Garnesson[2], A. Mangin[2], O. Hembise Fanton d'Andon[2], M. Bretagnon[2], S. Pardo[3], T. Jackson[3], B. Calton[3], J. Netting[3], B. Howe[3], H. Krasemann[4], M. Hieronymi[4], D. D'Alimonte[5], T. Kajiyama[5], J. Attila ([6]), S. Kaitala ([6]), S. Koponen[6], D. Van der Zande[7], J. F. Cardoso Dos Santos Q. Vanhellemont[7], K. Stelzer[8], M. Böttcher[8], C. Lebreton[8], S. Sterxck[9]

1 CNR ISMAR; 2: ACRI, 3: PML, 4: HEREON, 5: AEQUORA, 6 SYKE, 7 :RBINS, 8 : Brockmann Consult, 9 : VITO

Abstract – The Ocean Colour Thematic Assembly Center (OCTAC) of the Copernicus Marine Service provides high-quality core Ocean Colour products for the global ocean and the European seas based on multiple satellite missions. From 2015, the global and regional higher-level combined OCTAC products provide added-value information not readily available from space agencies, as observations from multiple missions are processed together to ensure homogenized and inter-calibrated datasets with higher spatial coverage than the single-sensor data streams. The OCTAC has continued to improve the accuracy at the basin level of existing Essential Ocean Variables for the global ocean and the European regional seas: Atlantic and Arctic Oceans, Baltic, Mediterranean and Black Seas. New EOVs related to Phytoplankton Functional Groups, community structure and Primary Production were introduced from 2019 onwards. This talk will provide an overview of the evolution of the OCTAC catalogue from 2015 to date, the accuracy of the global and regional products, and the plans for new products in coming years.

Keywords: Ocean Colour, Operational Oceanography, Sentinel-2, Sentinel-3.

1. INTRODUCTION

The Ocean Colour Thematic Assembly Center (OCTAC) of the Copernicus Marine Service (CMEMS) provides high-quality core Ocean Colour products for the global ocean and the European seas based on multiple Ocean Colour missions. The OCTAC serves users across the scientific and operational oceanography communities, commercial providers focused on the use of marine resources, and public agencies focused on environmental monitoring, with interests in data across oceanic, shelf and coastal waters. Depending on their applications, these users require different spatial resolutions (i.e., ~1km in ocean, 300m over the shelf, down to 10's of metres in coastal waters).

To meet these needs, the global and regional higher-level combined OCTAC products provide added-value information not readily available from space agencies. From 2015, the OCTAC has continued to improve the accuracy at the basin level of existing Essential Ocean Variables (EOVs), i.e., Chlorophyll-a concentration (CHL), Inherent Optical Properties (IOPs), as well as the radiometry in itself (GOOS, 2018). Blended CHL datasets are produced for all basins applying the appropriate algorithms across the open ocean the shelf and coastal waters, as well as the bio- optical characteristics of each regional Atlantic and Arctic Oceans, Baltic, Mediterranean and Black Seas). New EOVs related to Phytoplankton Functional Groups, community structure and Primary Production were introduced from 2019 onwards.

2. PRODUCT OVERVIEW

Within the CMEMS operational oceanography framework, data are produced in near-real time (NRT), and as reprocessed Multi-Year (MY) data. They are delivered as daily and monthly datasets (Level 3, L3) and as "gap-free" products (Level 4, L4) to overcome cloud cover in subsequent oceanographic analyses (Le Traon et al., 2017; Le Traon et al., 2019). The L4 "gap-free" products are based on Optimal Interpolation or variants of the DINEOF procedure.

Since 2015, CMEMS has been providing single sensor as well as multi-sensor products at 1km resolution for European seas, and at 4km resolution for the Global Ocean. In May 2021, OLCI datasets at 300m resolution combining Sentinel-3 A and B, as well as the Sentinel-2/MSI datasets at 100m, were added to the catalogue.

During the years, the upstream OC data shifted from science missions (i.e., SeaWiFS, MERIS and MODIS) towards operational missions (i.e., the two OLCI and two VIIRS, as well as the two MSI sensors). In 2015, all NRT regional products were based on single sensors (MODIS and VIIRS), these datasets were replaced by multi-sensor datasets leading to a significant increase of the spatial coverage of daily observations.

3. ALGORITHM IMPROVEMENTS

Algorithms improvements for chlorophyll retrieval were carried out based on optical characteristics of the basin and round-robin procedures. It produced blended Chl-a maps applying appropriate algorithms across the open ocean and coastal waters depending on the occurring water types. The same regional bio-optical algorithms used in NRT production are applied to generate MY chlorophyll in all basins for the OLCI and the multi-sensor datasets.

Within the Copernicus-GlobColour processor, the chlorophyll-a (CHL) multi-sensor daily product merged chlorophyll-a values recomputed using an equivalent scheme for each sensor (Garnesson et al., 2019). For oligotrophic waters, the product relied on the CI algorithm (Hu et al., 2012). For mesotrophic and coastal waters, it relied on the OC5 algorithm (Gohin et al., 2002) tuned for each sensor. The blended OC5 and CI was obtained using the same approach as NASA with a transition between concentration from 0.15 to 0.2mg/m3 to ensure a smooth merging.

In the Arctic and Atlantic Seas the regional chlorophyll algorithm is OC5CCI, a variation of OC5 (Gohin et al., 2002), developed by IFREMER and PML. To this end, an OC5CCI look-up table was generated specifically for application over OC-CCI daily-merged remote sensing

---

reflectances. The resulting OC5CCI algorithm was tested and selected after a calibration exercise and sensibility analysis of the existing algorithms (OC3, OC4, OCI, OC5CI, OC5, OC5CCI) that included a round robin quantitative performance assessment against in situ data.

In the Mediterranean Sea, the blended chlorophyll product are based on two algorithms: 1) the MedOC4, an updated version of the regionally parameterized Maximum Band Ratio (Volpe et al., 2019) for Open Ocean waters, and the ADOC4 algorithm (D'Alimonte and Zibordi, 2003) for optically complex waters. Since 2020, the determination of the water type accounts specifically for waters with high chlorophyll concentration due to phytoplankton blooms (e.g. Gulf of Lions) or mixing (e.g. Alborán Sea) that can be erroneously identified as Case II waters.

In the Black Sea, the retrieval of the Chl concentration is based on a merging scheme (Kajiyama et al., 2018) designed two different regional algorithms exhibiting lower and higher optical complexity: 1) a band-ratio algorithm based on two wavelengths (490 and 555 nm) (Zibordi et al., 2015); and a Multilayer Perceptron (MLP) neural net based on Rrs values at three wavelengths (490, 510 and 555 nm) that features interpolation capabilities helpful to fit data non-linearities.

In the Baltic Sea An ensemble MLP algorithm was introduced in 2021: the CHL is retrieved by combining results from individual MLPs based on different Rrs spectral subsets, weighting their contribution through the corresponding novelty index (Brando et al., 2021). This ensemble approach substituted the regional recalibration of the OC4v6 with in situ data by Pitarch et al. (2016).

The Phytoplankton type variables were introduced in the OCTAC catalogue from 2019 for the global ocean and all regional seas using global and regionally tuned methods (Brewin et al. 2015; Brewin et al., 2017; Di Cicco et al., 2017; Xi et al 2020). The Phytoplankton Size Classes (PSCs) and Phytoplankton Functional Types are expressed as chlorophyll-a concentration (mg m-3). PSCs include Micro-, Nano- and Pico-phytoplankton .

The Sentinel 2 MSI datasets introduced in 2021 are produced for the European coastal waters in a 20km strip from the coastline. Diverse atmospheric conditions and fast changing water types in space and time are addressed by combining different algorithms for Atmospheric Correction and the in-water retrieval for turbidity, suspended matter concentration, backscatter and chlorophyll concentration.

4. CONCLUSION

As of December 2022, the OCTAC catalogue will be composed of 40 OC NRT and MY Products and 210 datasets, across the multi-sensor, the Sentinel3 and the Sentinel2 data-streams. In summary, the catalogue will include:

- NRT and MY multi-sensor datasets (at 1km for regional seas, 4 km for global);
- OLCI Sentinel 3 data streams in multi-sensor datasets;
- OLCI NRT and MY datasets at 300m resolution combining the Sentinel-3 A and B missions.
- MY Interim production for the multi-sensor and the Sentinel3 data-streams.
- Multi-sensor and the Sentinel3 datasets produced with the same processing chain for each basin.
- MSI NRT datasets at 100m resolution combining the Sentinel-2 A and B missions.
- L4 "gap free" NRT and MY datasets for all basins for the multi-sensor and Sentinel-3 datasets, with the exception of the Artic and Baltic Seas

- L4 "gap free" NRT datasets for coastal waters of all basins for the Sentinel-2 datasets
- Blended Chl-a datasets across the open ocean and coastal waters depending on the occurring water types.
- Regional algorithms for chlorophyll retrieval on the basis of optical characteristics of each basin for the multi-sensor and the Sentinel3 data-sets
- Datasets on Phytoplankton Functional Groups and community structure for all basins
- Datasets on Primary Production at Global Scale

REFERENCES

Brando, V.E, et al (2021), J. Phytoplankton bloom dynamics in the Baltic Sea using a consistently reprocessed time series of multi-sensor reflectance and novel Chlorophyll-a retrievals. Remote Sens. 2021, 13, 3071.

Brewin, R.J.W., et al. (2015) Influence of light in the mixed-layer on the parameters of a three-component model of phytoplankton size class, Remote Sensing of Environment 168 (2015)

Brewin, R.J., et al., (2017). Uncertainty in Ocean-Color Estimates of Chlorophyll for Phytoplankton Groups. Frontiers in Marine Science, 4, p.104.

D'Alimonte, D. and Zibordi, G.: Phytoplankton determination in an optically complex coastal region using a multilayer perceptron neural network, IEEE T. Geosci. Remote, 41, 2861–2868,.

Di Cicco, A., et al (2017) Regional Empirical Algorithms for an Improved Identification of Phytoplankton Functional Types and Size Classes in the Mediterranean Sea Using Satellite Data. Front. Mar. Sci. 4:126.

Garnesson, P., et al.: The CMEMS GlobColour chlorophyll a product based on satellite observation: multi-sensor merging and flagging strategies, Ocean Sci., 15, 819-830, 2019.

Gohin, F., et al.,.: Towards a better assessment of the ecological status of coastal waters using satellite-derived chlorophyll-a concentrations, Remote Sensing of Environment, 112, 3329-3340, 2008.

GOOS, 2018. Global Ocean Observing System, Essential Ocean Variables Specification Sheet: Ocean Colour. https://www.goosocean.org/index.php?option=com_oe&task=viewDocumentRecord&docID=19959.

Kajiyama T., et al, "Algorithms merging for the determination of Chlorophyll-a concentration in the Black Sea," IEEE Geoscience and Remote Sensing Letters, 2018. https://-www.doi.org/¬10.1109/¬LGRS.2018.2883539

Le Traon, P. Y., et al. (2017). The copernicus marine environmental monitoring service: main scientific achievements and future prospects. Mercator. Ocn. J. 56, 101.

Le Traon, P. Yet al., (2019) From Observation to Information and Users: The Copernicus Marine Service Perspective. Front. Mar. Sci., 6, 234

Pitarch, J., et al.: Remote sensing of chlorophyll in the Baltic Sea at basin scale from 1997 to 2012 using merged multi-sensor data, Ocean Sci., 12, 379-389, 10.5194/os-12-379-2016, 2016.

Volpe, G., et al. (2019). Mediterranean ocean colour Level 3 operational multi-sensor processing. Ocean Science, 15(1), 127-146.

Xi H., et al (2020) Global retrieval of phytoplankton functional types based on empirical orthogonal functions using CMEMS GlobColour merged products and further extension to OLCI data. Remote Sensing of Environment, 240, 111704

TROPOMI's high spectrally resolved satellite data to fill gaps in ocean color observations

A. Bracher[1,2*], J. Oelker[1,2], L. Alvarado[1], S. Losa[1], H. Xi[1], M. A. Soppa[1], A. Brito[3], V. Brotas[3], M. Costa[4], L. Favareto[3], M. Gomes[3], V. P. Suseelan[4], A. Richter[2]

[1]Alfred-Wegener-Institute, Helmholtz Center for Polar and Marine Research, Bremerhaven, Germany
[2]Institute of Environmental Physics, University of Bremen, Bremen, Germany
[3]MARE, Faculdade de Ciências, Universidade de Lisboa, Lisbon, Portugal
[4]Department of Geography, University of Victoria, Victoria, BC, Canada

Abstract – In this study, we exploited Sentinel-5 Precursor's (S5P) sensor TROPOMI's potential to retrieve globally as novel products, the diffuse attenuation for three bands reaching from the UV-B to the short blue wavelengths range. Additionally, we investigated the potential of TROPOMI to retrieve certain phytoplankton groups. As a baseline, previously developed algorithms applied to similar atmospheric satellite sensors such as SCIAMACHY, GOME-2 and OMI were adapted and extended. Opposed to these precursor sensors, TROPOMI enable data acquisition due to a large swath with spatial and temporal resolution nearly as good as obtained from common ocean color sensor, until today only multispectral. The later sensors do not enable retrievals in the UV spectral region, but also algorithms to obtain cyanobacteria chlorophyll-a conc. (chla) are of minor quality as compared to the retrievals from TROPOMI. In this presentation, we provide detailed insights into the retrieval method, its uncertainty and the application to obtain data in the global ocean in open ocean and coastal regions.

Keywords: Ocean color, phytoplankton groups, diffuse attenuation, high spectrally resolved satellite data.

1. INTRODUCTION

High spectrally resolved satellite data of the top of the atmosphere backscattered radiance offer the opportunity to develop novel algorithms aimed for observations of phytoplankton groups biomass and the spectral composition of the light-lit ocean. Atmospheric sensors such as SCIAMACHY, GOME-2 and OMI have proven in the past to yield valuable information on phytoplankton diversity (Bracher et al. 2009, Sadeghi et al. 2012, Losa et al. 2017), sun-induced marine fluorescence (Wolanin et al. 2015), and the underwater light field (Dinter et al. 2015, Oelker et al. 2019). However, the use of these data sets was limited by their temporal and spatial resolution mostly not meeting requirements for time series studies. Within the ESA Sentinel-5p+Innovation Theme 7 ocean color (S5POC, https://eo4society.esa.int/projects/sentinel-5p-innovation-expro-theme-7-ocean-colour-s5p-i-oc/), we explored Sentinel-5P instrument TROPOMI's potential for deriving the diffuse attenuation coefficient and the quantification of different phytoplankton groups.

2. ALGORITHM, APPLICATION AND INTERCOMPARISON TO INDEPENDENT DATA

As commonly used for the retrieval of atmospheric trace gases, we apply the differential optical absorption spectroscopy (DOAS; Perner and Platt 1979) combined with radiative transfer modeling (RTM) using the SCIATRAN software package (Rozanov et al. 2014, 2017) to infer the diffuse attenuation Kd and phytoplankton groups by exploring TROPOMI bands 3 (310-405 nm) and 4 (405-495 nm; mind: TROPOMI does not provide measurements at 496-674 nm). More details on the algorithms can be found in Oelker et al. (2022a) and Oelker et al. (2022b).
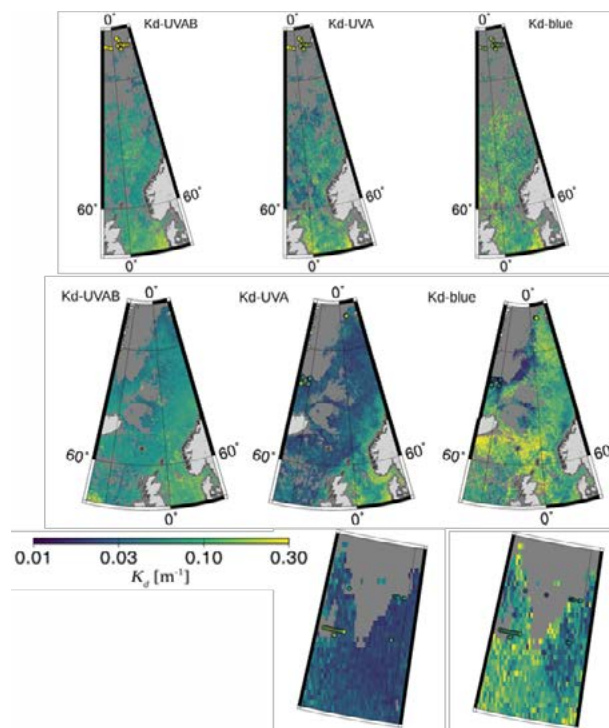
Figure 1. *TROPOMI (left: KdUVAB (312.5-338.5 nm), middle: KdUVA (356.5-390 nm), and right: Kdblue (390-423 nm)) gridded at 0.083° as mean for (upper panel) for the Transect from North Sea to the East Greenland Sea for a) upper panels: 11 Aug to 10 Sep 2019 (the PS121 time period), and b) two lower panels: 27 Jun to 25 Jul 2020 (time period MSM93, only KdUVA and KdUVA for detailed view 70°N-75°N and 10°W-20°W). Accordingly, KdUVAB, KdUVA, and Kdblue measured at stations during expedition PS121 and at Triaxus casts during MSM93 are overlaid as diamonds (match-ups) and circles (unmatched stations).*

The diffuse attenuation coefficient Kd, a measure describing the diminishing of incoming radiation in the ocean with depth, is derived by the retrieval of the vibrational Raman scattering signal in backscattered radiances measured by TROPOMI in the UV and blue spectral range which then is

* Corresponding author. Address: Am Handelshafen 12, 27570 Bremerhaven, Germany. Email: astrid.bracher@awi.de

further converted to the associated KD using RTM. The final TROMPOMI Kd data sets resolved for three spectral regions (UV-B+short wave UV-A, UV-A and short blue) agree well with in-situ data sampled during three expeditions: RV Polarstern expeditions PS113 in the the Atlantic transect from South America to the English Channel (results presented in Oelker et al. 2022a) and two expeditions in the North Sea and East Greenland Sea (RV Polarstern expedition PS121 in 2019 and RV Maria S. Merian MSM93 in 2020), as presented in Figure 1. Further, KD-blue compared to wavelength-converted KD(490 nm) products (OLCI-A and the merged OC-CCI) from common, multispectral, ocean color sensors, show that differences between the three data sets are within uncertainties given for the OC-CCI product (see Oelker et al. 2022a for details).

TROPOMI's potential for retrieving phytoplankton groups using DOAS and RTM calculations for constructing Look-Up-tables and performing sensitivity studies (details see S5POC-ATBD) is explored for the Atlantic open ocean and, additionally, for the Portuguese Coast (Figure 2) and Salish Sea on the shelf of the Pacific Ocean. Comparison to independent phytoplankton groups biomass data derived from in-situ pigment data and similar satellite products (CMEMS global PFT product based on Xi et al. 2021) TROPOMI cyanobacteria and diatom retrievals show reasonable agreement (for details see Bracher et al. 2021).
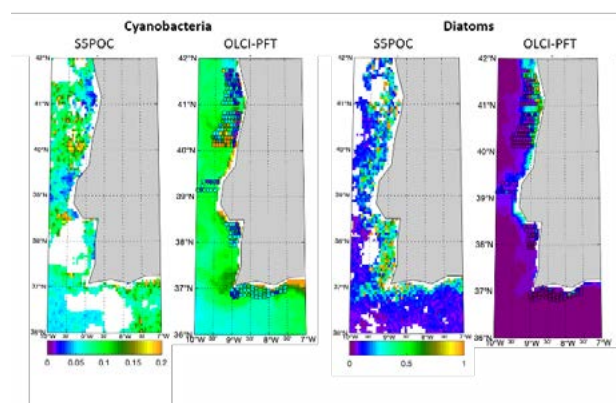
Figure 2. *Monthly mean (1 to 31 Oct 2018) of chlorophyll-a concentration (chla) for cyanobacteria (also named prokaryotes, two left panels) and diatoms (two right panels) for the time of AQUIMAR Oct 2018 campaign in region B for S5POC (left and second right) and OLCI-PFT v2.2 (second left and right). The in-situ cyanobacteria chla from AQUIMAR Oct 2018 is plotted on top of the maps.*

The evaluation of TROPOMI diatom and cyano-bacteria chla data sets with in-situ and intercomparison to other satellite phytoplankton group products (e.g., OLCI-PFT) indicate that retrievals from TROPOMI are feasible. Considering also the assessment of the geographical patterns and short-term variability, these data sets show promising application not only for the open ocean, but also for the coastal waters. TROPOMI cyanobacteria data compared to in-situ show very low bias with no pronounced difference among the different study regions and high short-term stability. However, TROPOMI diatom retrievals show a positive bias in low chla waters. Despite, current validation results indicate that the uncertainty of S5POC diatom data is as good as OLCI-PFT. Although the footprint of TROPOMI is rather large (7 km x 3.5 km), the quality not only of cyanobacteria, but also of diatoms showed a very a good performance by capturing the short term variability in the coastal region of the Salish Sea.

* Corresponding author. Address: Am Handelshafen 12, 27570 Bremerhaven, Germany. Email: astrid.bracher@awi.de

Considering the much lower performance of OLCI-PFT cyanobacteria in coastal waters, results confirm that TROPOMI retrievals, based on fitting the actual spectra and by that retrieving specifically the PFT optical signature, are less dependent on empirical assumptions. This explains that even in the higher turbid coastal waters still valuable information is obtained (for details see Bracher et al. 2021).

3. CONCLUSION

Having established these novel TROPOMI diffuse and phytoplankton group products, the next steps are to investigate global products over the full operating period of TROPOMI to assess the temporal and spatial stability of the products. These data products delivering information on the spectral underwater light and phytoplankton composition can then be used as auxiliary information for modeling marine ecosystem/biogeochemical functioning or photochemical reaction rates of climatically important compounds and inhibition of primary productivity.

In future, we will explore if the information on sources of colored dissolved organic matter and ultraviolet-absorbing phytoplankton pigments can be inferred from these data sets. In addition, we plan to explore the potential of synergy between the two products following previous work of combining SCIAMACHY and OC-CCI phytoplankton group data (Losa et al. 2017), to benefit from the higher spatial resolution of multispectral and the higher accuracy of the physical-based hyperspectral retrievals.

REFERENCES

Bracher A., et al. (2009). Biogeosciences 6: 751-764.
Bracher A. et al. (2021) Sentinel-5P Ocean Colour: Validation Report. S5POC VR Version 3.0. 23 Dec 2021.
Dinter T. et al. (2015) Ocean Science, 11: 373-389.
Losa S. N., et al. (2017) FMARS 4 (203), 1-22.
Oelker J. et al. (2019) Optics Express, 27 (12): A829-A855.
Oelker J. et al. (2022a) Frontiers in Marine Science 9: 787992. doi: 10.3389/fmars.2022.787992.
Oelker J. (2022b) Sentinel-5P Ocean Colour: ATBD. S5POC-ATBD-D04 Version 6.1. 13 May 2022.
Perner D., Platt, U. (1979) GRL 6(12): 917-920.
Sadeghi A. et al. (2012) Ocean Science, 8: 1055-1070.
Rozanov V V et al. (2014) J QSRT 133, 13–71.
Rozanov V V et al. (2017) J QSRT 194, 65–85.
Wolanin et al. (2015) RSE 166, 243–261.

Cloud Aerosol Lidar for Global Scale Observations of the Ocean-Land-Atmosphere System – CALIGOLA

P. Di Girolamo[1]*, D. Dionisi[2], A. Cosentino[3], F. Longo[4], N. Franco[1],
D. Summa[5], S. Lolli[5], E. Suetta[3], A. Perna[3], V. Sacchieri[3], S. Zoffoli[4]

1 School of Engineering, University of Basilicata, Potenza, Italy
2 Institute of Marine Sciences - National Research Council of Italy, Roma, Italy
3 Leonardo S.p.A, Pomezia, Italy
4 Agenzia Spaziale Italiana, Roma, Italy
5 Institute of Methodologies for Environmental Analysis- National Research Council of Italy, Potenza, Italy

Abstract – The space mission CALIGOLA has a primary focus on atmospheric monitoring, but it presents also a strong potential in the characterization and study of the Ocean-Earth-Atmosphere system and the mutual interactions within it. Exploiting the three Nd: YAG laser emissions at 354.7, 532 and 1064 nm and the elastic (Rayleigh-Mie), depolarized and Raman lidar echoes from atmospheric constituents, CALIGOLA will carry out 3 λ profile measurements of the particle backscatter coefficient and depolarization ratio and 2 λ profile measurements of the particle extinction coefficient from aerosols and clouds. These measurements will be used for the purpose of aerosol typing and for determining particle size and microphysical properties. Furthermore, measurements of the elastic and depolarized backscattered echoes from the sea surface and the underlying layers will be exploited to characterize optical properties of the marine surface (ocean color) and of the suspended particulate matter. Two specific measurement channels at 460 and 680 nm will be devoted to measure fluorescent scattering both from marine chlorophyll and atmospheric aerosols for the characterization of the ocean primary production and for the purpose of aerosol typing, respectively. The space mission CALIGOLA is explicitly included the on-going ASI Three-Year Activity Plan (2021-2023), with a scheduled tentative launch window of 2026-2028.

Keywords: Symposium, Program, Scientific Themes.

1. INTRODUCTION

The Italian space industry, and specifically Leonardo S.p.A., has unique skills at international level in the development of space-qualified power laser sources for lidar Earth observation applications (Aeolus, EarthCARE). Moreover, Leonardo S.p.A. and the Italian optical industry, has a consolidated technical-scientific experience in the development of specific lidar receiver sub-systems and the payload thermo-mechanical structure. The Italian Space Agency (ASI) intends to benefit from these knowledges and skills to design and develop a lidar system for Earth observation. A Phase A study focusing on the technological feasibility of the laser source and receiver is on-going, commissioned and funded by ASI to Leonardo S.p.A. Scientific studies in support of the mission are also on-going, with the University of Basilicata being the leading scientific institution.

By exploiting the three wavelengths emitted by a Nd: YAG laser source in the UV, VIS and nIR and the polarized and depolarized elastic lidar (Rayleigh-Mie) and Raman echoes from atmospheric constituents, CALIGOLA will carry out vertical profile measurements of the particle backscatter coefficient at 354.7, 532 and 1064 nm, the extinction coefficient at 354.7, 532 nm, and the depolarization ratio at 354.7, 532 and 1064 nm. Furthermore, by exploiting the elastic polarized and depolarized backscatter echoes from the sea surface and the underlying water layers, CALIGOLA will measure the optical properties of the sea (ocean color) and the suspended particulate matter. This information is fundamental in the characterization of the seasonal and inter-annual dynamics of marine phytoplankton and in the study of its role in the marine biogeochemistry and in the global carbon cycle.

Two specific channels, and this represents an absolute novelty with respect to any previous space lidar mission, will measure fluorescence from atmospheric particles and marine chlorophyll to be used for the purpose of aerosol typing and the quantification of ocean primary production. It is to be underlined that numerous atmospheric aerosol types (biological particles, biomass fuels, sulfates and dust) are fluorescent when excited with UV rays. Most part of the fluorescence spectrum is in the 400–700 nm interval (Pan, 2015). This spectrum varies with the composition of the sounded aerosols and consequently fluorescence measurements represent an effective tool for identifying aerosol typologies (Veselovskii et al., 2020, Veselovskii et al., 2021). Furthermore, since water is not fluorescent, fluorescence measurements from clouds allow obtaining information on aerosols inside clouds, at least on those located near the cloud base or top. CALIGOLA is therefore well suited to study of aerosol-cloud coexistence situations. CALIGOLA will also carry out accurate measurements of the small-scale variability of the earth's surface elevation, associated with changes in the terrain, vegetation and forest canopy.

2. METHODS

The strategy in developing a space mission in a relatively short time (hopefully 4-6 years) consists in the exploitation of sub-systems already developed at national level for space applications, with a high TRL (TRL>7). For this reason, ASI is willing to pursue this mission in a coordinated way with one or more other European or extra-European Space Agencies, with a bilateral or multi-lateral contributed mission approach.
If we consider the current and future space lidar missions, it is evident that one of the important characteristics of this

---

mission is not only the high scientific impact but also the timeliness:

- the NASA-CNE CALIPSO mission, launched in 2006 and still in operation, provided new insight into the role that clouds and atmospheric aerosols play in regulating Earth's weather, climate, and air quality. The mission is scheduled to end in December 2023;
- the ESA mission AEOLUS, launched in 2018, is providing unprecedented high-quality measurements of both wind and aerosol and clouds. However, although AEOLUS is demonstrating enormous longevity, it is unlikely that it will be still operational in in the time frame 2026-2028;
- the ESA mission EarthCARE, hosting the high-spectral resolution lidar ATLID, will be launched in 2023 with a specific focus on the study of the relationship of clouds, aerosols and radiation. EarthCARE has a design lifetime of three years, including a six-month commissioning phase, and therefore its life cycle will likely partially superimpose with CALIGOLA;
- In 2030, NASA will launch the space mission "Aerosol-Cloud-Ecosystem" (ACE), hosting a lidar system operating at two wavelengths (532 and 1064 nm), both with depolarization measurement capability.

The launch of CALIGOLA between 2026-2028 will potentially fill a gap of space-based lidars dedicated to studying the atmosphere. Furthermore, it will be the first space lidar mission with the objective of also observing the ocean. In fact, although the feasibility of deriving ocean optical properties through space lidars was demonstrated by Behrenfeld et al. (2013) with CALIPSO measurements, the previous space-borne lidar missions were not dedicated to ocean observation and there are no planned space-borne lidar dedicated to the ocean in the near-future, to the best of our knowledge. The CALIGOLA technical specifications of the Power-Aperture-Efficiency Product at the different wavelengths are illustrated in Table 1.

Table 1. *Power-Aperture-Efficiency Product at the different wavelengths*

	355	532	1064
Single pulse energy (mJ)	197	47	256
Repetiton rate (Hz)	51	51	51
Telescope aperture (m)	0.7	0.7	0.7
Laser Transmission & Beam expansion (%)	90	90	90
Telescope reflectivity (%)	92.5	85.5	91.5
Interference filters' CWL Tarsmission (%)	90	90	90
Quantum efficiency (%)	30	40	20
Power-Aperture-Efficiency (Wm²)	0.869	0.256	0.745

3. RESULTS

The expected performance of CALIGOLA in observing the atmosphere has been assessed based on the application of an end-to-end lidar simulator (Di Girolamo et al., 2006, Di Girolamo et al., 2018), which includes a forward module and a retrieval module. The forward module simulates the interaction mechanisms of the laser radiation with the atmospheric constituents and the behavior of all the devices present in the experimental system (telescope, optical components, etc…), which allows generating synthetic lidar

signals. The simulated signals are then fed into the retrieval module to obtain vertical profiles of multi-wavelength particle backscatter/extinction/depolarization profiles. The simulator provides statistical (RMS) and systematic (bias) uncertainties. Figure 1 illustrates the simulations of the statistical uncertainty affecting the elastic signals at 355, 532 and 1064 nm. Results refer to clear-sky conditions. Simulations consider a horizontal resolution of 50 km, which corresponds to an averaging over 335 single-shot lidar echoes (with a pulse repetition rate of 50 Hz), and a vertical resolution of 200 m (dwell time = 1.33 usec). The ISS orbit is characterized by a β-angle varying in between ± 75.1º during the year. In the simulations a similar variability of the "sun zenith angle (SZA) of the sub-satellite point was assumed. The simulation of the depth-resolved backscatter (b_{bp}) and the diffuse light attenuation (K_d) coefficients in the ocean is under assessment.
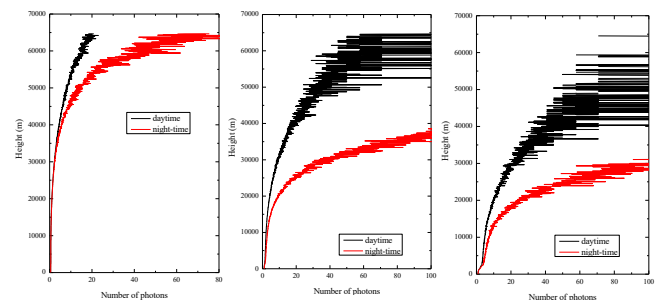
Figure 1. *Simulations of the statistical uncertainty affecting the elastic signals at 355, 532 and 1064 nm.*

REFERENCES

Behrenfeld, M. J., Hu, Y., Hostetler, C. A., Dall'Olmo, G., Rodier, S. D.,Hair, J. W., et al..: Space-based lidar measurements of global ocean carbon stocks. Geophysical Research Letters, 40, 4355–4360. doi: 10.1002/grl.50816, (2013)

Di Girolamo, P., Behrendt, A., Wulfmeyer, V.: Spaceborne profiling of atmospheric temperature and particle extinction with pure rotational Raman Lidar and of relative humidity in combination with differential absorption Lidar: performance simula-tions. Applied Optics, vol. 45, p. 2474-2494, ISSN: 0003-6935, doi: 10.1364/AO.45.002474 (2006).

Di Girolamo, A. Behrendt, and V. Wulfmeyer, Space-borne profiling of atmospheric thermodynamic variables with Raman lidar: Performance simulations, Optics Ex-press, 26(7), 8125-8161, https://doi.org/10.1364/OE.26.008125 (2018).

Pan, Y.-L.: Detection and characterization of biological and other organic-carbon aer-osol particles in atmosphere using fluorescence, J. Quant. Spectrosc. Ra. 150, 12–35 (2015).

Veselovskii, I., Hu, Q., Goloub, P., Podvin, T., Korenskiy, M., Pujol, O., Dubovik, O., and Lopatin, A.: Combined use of Mie–Raman and fluorescence lidar observations for improving aerosol characterization: feasibility experiment, Atmos. Meas. Tech., 13, 6691–6701, https://doi.org/10.5194/amt-13-6691-2020 (2020).

Veselovskii, I., Hu, Q., Goloub, P., Podvin, T., Choël, M., Visez, N., and Korenskiy, M.: Mie–Raman–fluorescence lidar observations of aerosols during pollen season in the north of France. Atmos. Meas. Tech., 14, 4773–4786, https://doi.org/10.5194/amt-14-4773-2021 (2021).

Sensitivity of polarized airborne observations over coastal waters

A. El-Habashi*, J. Bowles, R. Foster, D. Gray

U.S. Naval Research Laboratory, Washington, DC 20375, USA

Abstract – Measurement of the upwelling polarimetric radiance offers the possibility of improving our ability to accurately characterize the aerosol and hydrosol optical properties from space. Airborne polarimeters are developed to verify the space polarimeter concept and validate data processing and algorithm performance. We demonstrate results from an airborne multi-spectral, hyper-angular imaging polarimeter called the Versatile Imager for the Coastal Ocean (VICO). VICO data is used to support the analysis of ocean color polarized observations and their implication for future space-borne polarimetry such as the polarimeters planned to be deployed as part of the NASA Plankton, Aerosol, Cloud, and ocean Ecosystem (PACE) mission. The instrument's measurements show consistent agreements with modeling of both radiance and polarization from the visible to the near-infrared spectrum and at different viewing angles over the open ocean and coastal waters. A vector radiative transfer (VRT) code was used to model the observed scenes based on measured inherent optical properties determined from shipborne instruments and measured atmospheric parameters from nearby Aerosol Robotic Network (AERONET) and a shipborne sunphotometer at different locations. It is shown that the polarized remote sensing reflectance measured at various angles could be used to distinguish between the aerosols' and hydrosols' optical signatures by exploiting the fact that the polarized reflectance is fairly insensitive to hydrosols for some acquisition geometries. This study thus provides an opportunity to investigate various relationships between the microphysical properties of the oceanic and atmospheric particulates such as refractive index and particle size properties that will be retrieved from the forthcoming polarimetric satellite missions.

Keywords: Radiative transfer, Polarization, Ocean Color.

1. INTRODUCTION

Over the last several decades, space-based measurements of the ocean relied on measurements of a single-view multi-spectral radiance. First single-viewed ocean color instrument was the Coastal Zone Color Scanner Experiment (CZCS) launched into space in 1978. Following the CZCS, a fleet of single-view satellite sensors such as SeaWiFS, MODIS, VIIRS, MERIS, OLCI, and GOCI were launched, providing a continuous data record of the global ocean over the past two decades. The Multi-angle Imaging SpectroRadiometer (MISR) was launched in 1999, to observe Earth's climate with cameras pointed at nine different angles. These instruments provided a wealth of ocean information from space; however, the retrieved data accuracy was limited. A higher retrieval accuracy and additional products are needed for better characterization of the aerosol and hydrosol constituents. Recent work on polarimetry has shown that it is capable of providing higher retrieval accuracies and additional information on the micro-physical and macro-physical properties of aerosol and hydrosol particles, which

are difficult to infer from the scalar scattered radiation observed by the current ocean color instruments (Hansen, et al., 1974 and Mishchenko, et al., 2004). Polarization is sensitive to the aerosol and hydrosol particles composition (complex refractive index), size, and shape. The polarized light reflected from the sea surface contains useful information on the sea state. Current and future remote sensing polarimeters can measure the degree of linear polarization to an absolute accuracy < 0.2%. The radiative transfer codes used to analyze these polarimetric measurements can provide an accuracy that exceeds state-of-the-art polarimeters < 0.2%. It is expected that the polarized remote sensing will provide an accurate atmospheric correction that can lead to improved aerosol and hydrosol products (El-Habashi, et al., 2021).

VICO, the presented instrument, is designed to collect hyper-angular linear polarization at four visible and NIR spectral channels in an imaging mode, as done with the HARP2/PACE instrument, but with higher polarimetric accuracy, similar to the SPEXone/PACE instrument. The accuracy level in the measured VICO DoLP is better than 0.25% (Bowles, 2015) with sufficiently small angular resolution (~0.12°). In addition, VICO is a pointable instrument (gimbaled system), which makes it suitable for ocean color applications by allowing the measurement of the polarized light field in and off the principle-viewing plane. VICO design and specification make it a retrieval-capable instrument providing a better characterization of the aerosol and hydrosol properties. The polarimetric dataset acquired by the instrument is expected to be utilized to verify data processing and validate algorithm performance for spaceborne polarimeters such as HARP2 and SPEXone on the forthcoming PACE observatory.

2. METHODOLOGY AND RESULTS

The aircraft-based remote sensing instrument used for this study is the Versatile Imager for the Coastal Ocean (VICO) developed by the Naval Research Laboratory (NRL). Bowles et al. 2015. described the design, fabrication, calibration, and airborne deployment methodologies of VICO in more detail. To briefly summarize, VICO provides multi-spectral radiance and linear polarization images at high spatial resolution with a ground sample distance (GSD) of 22 cm at nadir from a height of 1525 m. Measurement of linear-polarization was obtained using a four-camera system. The cameras are rigidly mounted on an aluminum plate automatically controlled by a rotating stage to allow imaging at different viewing angles. A wire grid polarizer is placed over each camera with orientations at 0°, 45°, 90° and 135° relative to the vertical. The 0° filter is aligned with the forward-to-aft axis of the aircraft. A motorized filter wheel is attached in front of each polarizing filter to provide multi-spectral measurements from the system. The filter wheel contains five-positions; four contain narrow-band spectral filters centered at 435, 550, 625, and 750 nm and the last

---

position was used for the dark current measurements. A combined global positioning system (GPS) with an inertial measurement unit (IMU,)mounted on the same plate as the cameras, was used to record the attitude and position information. The position was also supplied by a more accurate second GSP/INS system installed on the airframe. The attitude and position information from the rotating stage and airframe were both used in the geometric processing to determine the geographical positions and viewing angles of each pixel in the data. The cameras imaged at a rate of about 1.1 Hz, limited by the speed of the filter wheels, to provide radiances measured with the linear polarizers oriented in the 0°, 45°, 90°, and 135° directions. The radiance values recorded from the four cameras are donated by I_0, I_{45}, I_{90}, and I_{135}.

The Ocean Successive Orders with Atmosphere - Advanced (OSOAA) vector radiative transfer (VRT) code was used to model the field measurement. OSOAA allows the computation of the complete radiance field and the polarization state in a coupled ocean-atmosphere system. It calculates the radiative parameters for each component of the environment, assuming a set of plane-parallel homogeneous layers throughout the atmospheric and marine profiles . The code numerically computes the contribution of each scattering order based on the successive orders of scattering method. A detailed description of the code is in Chami, 2015.
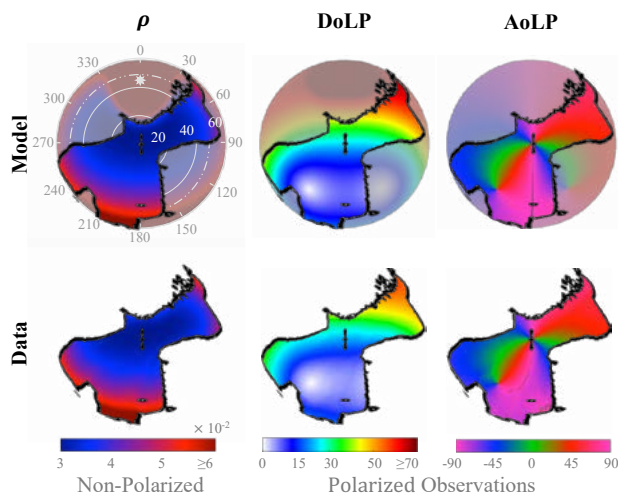
Fig. 1: Non-Polarized vs. Polarized Observations over coastal waters. Figure shows hyper-angular VRT match with aircraft total reflectance ρ (sr^{-1}), Degree of Linear Polarization *DoLP* (%) and Angle of Linear Polarization *AoLP* (°) observations at the blue band (443 nm) , where solar position is at $\theta_0 = 44°$ and $\varphi_0 = 110°$.

In this study, we start with optical closures between the observed polarized radiances by the airborne polarimeter, and the in-situ measured water and aerosol parameters by the shipborne and the ground-based AERONET near each site. The in-situ measurements were used in the VRT forward modeling to reproduce the observed polarized radiances at the aircraft level for the different cases. The use of the shipborne and AERONET measurements in this study is necessary to reach a VRT closure that relies on real-world conditions and not based on adjustments of many optical parameters. We then compute the linear Stokes contributions of the atmosphere and extract the water-leaving total and polarized radiances based on the closure achieved between the VRT model and the VICO observation at each case. Finally, we perform a sensitivity study of the impact of the different seawater conditions on the aircraft level and the TOA total and polarized reflectances.

Figure 1 shows an example of the VICO-VRT match. The second water-type is characterized by high Chla, medium non-algal particles, and medium CDOM concentrations representative of green-like waters typically found in productive phytoplankton waters. The atmospheric condition of the first case is characterized by a lower SSA, indicating more absorbing aerosol compared to the second case. The aerosol optical thickness, at 500nm, is about twice lower (0.046) for Case 2 than for Case 1 (0.084). The results show considerable match quality across hyper-angular spectrum. The achieved closure showed a potential sensitivity to the measured aerosol and in-water optical properties. The substantial matching across wavelengths, and a large portion of angle space, both polarized radiance and radiance is a strong evidence of the utility of these measurements. The results open the possibility to exploit the distinction between hydrosols and aerosols parameters from airborne and space-borne polarized observations.

3. CONCLUSION

We illustrate strong consistency between data taken with an airborne multi-spectral polarimetric imager and VRT simulations over coastal water conditions. The sensitivity of the remotely sensed total and polarized reflectance to the measured in-water optical properties was analyzed at the aircraft altitude and the TOA. Total and polarized values above and below the detection limits were highlighted for both elevations. Overall, the results demonstrated provide strong evidence that measuring remotely sensed polarized reflectance in the lower atmosphere (with further evidence that the utility remains even at the TOA) may be able to provide detailed information about aerosol and water constituents such as particle size and type.

REFERENCES

Bowles J., Korwan D., Montes M., Gray D., Gillis D., Lamela G., Miller W. (2015). 'Airborne system for multispectral, multiangle polarimetric imaging'. Appl Opt., 54:F256-F67.

Chami M., Lafrance B., Fougnie B., Chowdhary J., Harmel T., Waquet F. (2015). 'OSOAA: a vector radiative transfer model of coupled atmosphere-ocean system for a rough sea surface application to the estimates of the directional variations of the water leaving reflectance to better process multi-angular satellite sensors data over the ocean'. Optics Express, 23:27829-52.

El-Habashi A., Bowles J., Foster R., Gray D., Chami M. (2021). 'Polarized observations for advanced atmosphere-ocean algorithms using airborne multi-spectral hyper-angular polarimetric imager'. Journal of Quantitative Spectroscopy and Radiative Transfer JQSRT, 262:107515.

Hansen J., Travis L. (1974). 'Light scattering in planetary atmospheres'. Space science reviews, 16:527-610.

Mishchenko M., Cairns B., Hansen J., Travis L., Burg R., Kaufman Y., Martins V., Shettle E. (2004). 'Monitoring of aerosol forcing of climate from space: analysis of measurement requirements'. Journal of Quantitative Spctroscopy and Radiative Transfer JQSRT, 88:149-61.

Ocean Color Remote Sensing from the L1 Orbit

R. Frouin *[1], J. Tan, J. R. Herman[2]

[1]Scripps Institution of Oceanography, La Jolla, California, United States
[2]University of Maryland, Baltimore County, Baltimore, Maryland, United States

Abstract – The Earth Polychromatic Imaging Camera (EPIC) onboard the DSCOVR observatory in Lagrange-1 (L1) orbit provides imagery of the Earth's surface lit by the Sun at a cadence of 13 to 22 images/day and optical resolution of about 10 km in 10 spectral bands from 317 to 780 nm. The data can be used to estimate surface solar irradiance and water reflectance, basic variables from which a variety of optical and biogeochemical products can be obtained. EPIC-derived global products for ocean biology/biogeochemistry are presented and, whenever possible, evaluated against other satellite estimates. They include surface fluxes (planar and scalar) in the ultraviolet and visible, water reflectance and derived variables (e.g., chlorophyll-a concentration), and the fraction of photosynthetically available radiation absorbed by live algae, a key variable controlling primary production. Space Agencies should consider utilizing the L1 orbit for future satellite ocean-color missions.

Keywords: Ocean Color, L1 Orbit, DSCOVR Mission.

1. INTRODUCTION

At Lagrange points, gravitational pull of large masses (Sun and Earth equals the centripetal force for a small object (satellite) to move with them, i.e., the relative positions of the 3 objects are fixed. The first Lagrange point (L1) is at about 1.5 million km from Earth. From L1, the entire face of the Earth lit by the Sun can be regularly observed. The advantages of observing from L1 for ocean color remote sensing are: 1) The entire Sunlit oceans can be observed simultaneously at high temporal resolution from a single platform, allowing detailed coverage of evolving systems and diurnal (e.g., tidal) phenomena; 2) Spatial coverage is not an issue at low/middle latitudes, unlike with LEO polar orbiters; Sun glint can be mitigated; polar regions partially seen from GEO satellites can be viewed; 3) Atmospheric correction may be facilitated by viewing at the same scattering angle but different zenith angles; 4) Radiometric calibration, pixel-to-pixel uniformity, and long-term instrument stability can be maintained by lunar observations whenever the Earth has a full moon (once a month), i.e., no need for an onboard calibration system (saving a lot of cost and complexity); and 5) The thermal environment (no day-night thermal changes) and particle radiation environment (no southern Atlantic anomaly or polar regions) are quiet; and fuel consumption is reduced to maintain position.

The EPIC camera onboard the DSCOVR observatory in L1 orbit provides imagery of the Earth's surface lit by the Sun at a cadence of 13 to 22 images/day and optical resolution of about 10 km in 10 spectral bands from 317 to 780 nm, i.e., centered on 3.17.5, 325.0, 340.0, 388.0, 443.0, 551.0, 680.0, 687.7, 764.0, and 779.5 nm with FWHMs of 0.8 to 3 nm (Marshak et al., 2018). The data can be used to estimate surface solar irradiance and water reflectance, basic variables

from which a variety of optical and biogeochemical products can be derived. The band at 687.7 nm (FWHM of 0.84) may be used to estimate FLH by quantifying the filling of the O_2-B band by the inelastic chlorophyll fluorescence signal but limited by the relatively low S/N ratio. Measuring at practically the same scattering angle (about 171.5 deg.), a characteristic of the L1 orbit, offers a unique capability to handle atmospheric influence using multi-directional observations. This capability suggests a new instrument concept for ocean color remote sensing from LEO orbits (conical scanning with optical axis aligned with the Sun). In the following, examples of EPIC-derived global products for ocean biology and biogeochemistry are presented. They include surface fluxes (above and below surface, planar and scalar) in the ultraviolet and visible, average cosine for total light, photosynthetically available radiation (PAR), water reflectance, chlorophyll-a concentration, and the fraction of PAR absorbed by live algae, a key variable controlling primary production.

2. EXAMPLES OF OCEAN COLOR PRODUCTS

Figure 1 displays for 3/20/2018 (equinox) daily mean planar PAR and spectral fluxes at 317, 340, and 551 nm and scalar PAR and average cosine for total light just below the surface.
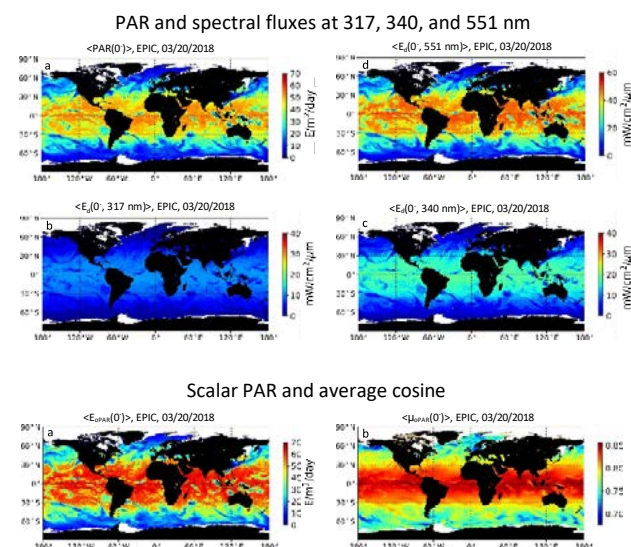
Figure 1. Daily mean ocean surface radiation products obtained from EPIC data. Date is 3/20/2018 (equinox).

Planar PAR values below the surface are lower than those above surface (not shown here –see Frouin et al., 2022 for PAR above surface) by 3 to about 10% depending on latitude and cloudiness. The UV fluxes resemble the flux at 551 nm but have much smaller magnitude and are more modulated by ozone distribution. Scalar PAR and average cosine are obtained from cloud factor (effect of cloudiness on PAR) and clear sky PAR just above surface (Frouin et al., 2018). Scalar

---

PAR below surface follows planar PAR above and below surface, but the values are somewhat higher, as expected. Average cosine for total PAR light has relatively high values of 0.8 to 0.85 at low and tropical latitudes (illumination more vertical), i.e., the average nadir angle of the upwelling and downwelling photons is small (32-37 deg.), but values are as low as 0.70 at high latitudes, especially in clear sky regions (illumination more slanted and less diffuse).

Figure 2 displays retrievals of water reflectance at 443nm and chlorophyll-a concentration from EPIC and MODIS data. Date is 3/19/2020. The water reflectance is obtained using a spectral matching algorithm (Steinmetz et al., 2011). Level 1b EPIC reflectance at 388, 443, 551, 680, and 780 nm is used. Water reflectance is retrieved on source grid for each EPIC observation during the day, normalized, then remapped to 18.4 km grid, and averaged. OC3-type bio-optical algorithm adapted to EPIC bands centered on 443, 488, and 551 nm and developed on NOMAD data is used for chlorophyll-a concentration. Spatial coverage is increased at low/middle latitudes using EPIC (compared with MODIS) data, for example to 40% instead of 10% at the equator. (Figure 3, left). A good agreement is obtained between EPIC and MODIS-A chlorophyll-a concentrations; the histogram of values is similar for both sensors (Figure 3, right).
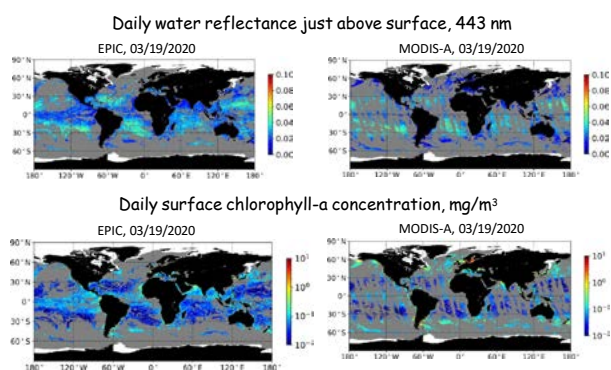
Figure 2. Daily mean water reflectance at 443 nm and chlorophyll-a concentration derived from EPIC and MODIS data for 3/19/2020, left and right, respectively.
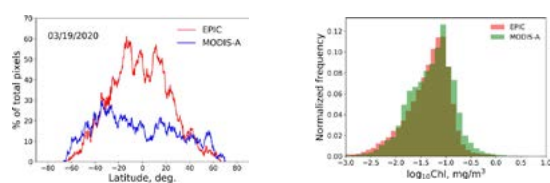
Figure 3. (Left) percentage of retrieved EPIC and MODIS pixels. (Right) Histogram of EPIC and MODIS chlorophyll-a concentration values for 3/19/2020.

3. INSTRUMENT/MISSION CONSIDERATIONS

The spatial resolution of EPIC (about 10 km at nadir) is coarse for ocean-color remote sensing applications, especially in coastal regions. A spatial resolution of 1 km (or less) is desirable. Since the resolving power (angular resolution) of an optical system is $1.22*l/D$ where D is the diameter of the lens' aperture, at the L1 point (1.5 million kilometers from earth), a D of 0.9 m would allow 1 km spatial resolution at 0.5 μm. This would require a large telescope.

Several instrument concepts can be envisioned, e.g.: 1) Full disk imager (same as EPIC), with aggregated CCD arrays in focal plane (e.g., 5x5 2048x2048 arrays to cover Earth's disk edge to edge), rotating filter wheel (with eventually polarizers) for multi-spectral polarimetric measurements. Earth rotation (4 km/s) should not be a problem to achieve acceptable S/R ratio for ocean color (typically 0.1 s exposure time); and 2) Geographic scanning instrument: spectrometer with high dispersion grating for hyper-spectral resolution, mechanical device to achieve spatial sampling, a 30-minute cadence is reasonable, giving 45 measurements per 24 hours, polarization analyzing optics to determine state of polarization. Advantage, compared with full disk imager, is that all wavelengths are obtained at the same time.

Some issues are Image stabilization to compensate for spacecraft jitter (need high quality momentum wheels), correction of straylight, and cost of telescope (e.g., Offner telescope with aspherical optics instead of spherical Cassegrain telescope used by EPIC) and of placing a large instrument in L1 orbit.

4. CONCLUSION

EPIC/DISCOVR has demonstrated the feasibility of ocean color remote sensing from the L1 orbit. Basic quantities for ocean biology/biogeochemistry have been estimated, namely surface solar irradiance (UV, visible, planar, scalar) and diffuse water reflectance, from which a variety of optical and biogeochemical variables can be deduced, e.g., chlorophyll concentration, diffuse attenuation coefficient, and fraction of PAR absorbed by live algae. A major advantage of the L1 orbit compared to LEO and GEO orbits is the possibility, from a single platform, to image the entire sunlit ocean frequently, i.e., to resolve diurnal variability of biological phenomena. This fills a major gap in current satellite ocean color systems. Other advantages include increased spatial coverage at low/middle latitudes, no Sun glint problem, better coverage of polar regions than GEOs, especially during summer solstice, and no need for onboard calibration system. Preliminary calculations and considerations and heritage designs indicate that it is feasible to build a hyper-spectral, polarimetric sensor measuring from UV to NIR with 1 km resolution from L1. Space agencies should consider an ocean color mission from the L1 orbit and initiate pre-phase 0 studies.

REFERENCES

Frouin R, Ramon D, Boss E, Jolivet D, Compiègne M, Tan J, Bouman H, Jackson T, Franz B, Platt T and Sathyendranath S (2018a) Satellite Radiation Products for Ocean Biology and Biogeochemistry: Needs, State-of-the-Art, Gaps, Development Priorities, and Opportunities. Frontiers in Marine Science 5:3. doi: 10.3389/fmars.2018.00003

Frouin R, Tan J, Compiègne M, Ramon D, Sutton M, Murakami H, Antoine D, Send U, Sevadjian J and Vellucci V (2022) The NASA EPIC/ DSCOVR Ocean PAR Product. Frontiers in Remote Sensing 3:833340. doi: 10.3389/ frsen.2022.833340

Marshak, A., Herman, J., Szabo, A., et al. (2018). Earth observations from DSCOVR EPIC instrument. Bull. *Amer. Meteor. Soc.* 99, 1829–1850.

Steinmetz, F., Deschamps, P-Y, and Ramon, D (2011). Atmospheric correction on the presence of sun glint: application to MERIS, *Optics Express* 19, 9783-9800.

Satellite Altimetry for Ocean and Coastal Applications

M. Srinivasan*, V. Tsontos

Jet Propulsion Laboratory California Institute of Technology, Pasadena, California USA

Abstract – **Thirty years of observations from an international suite of satellite altimeter missions continue to provide key data enabling research discoveries and operational, user-driven applications. Time series of precise ocean surface topography (OST) measurements reveal changes in ocean dynamic topography, sea level variations at global to regional scales, and provides key information about ocean trends on climate change. New satellite missions will allow measurements at higher spatial resolutions close to coastlines, where the impacts from sea level rise on coastal communities and infrastructure are manifest. These missions will extend the continuous data record into the next decade. Applications for societal benefit that leverage these valuable, long-term datasets continue to expand beyond the science objectives that drove their initial development. NASA and partners are advancing awareness and growing the user community. Applications benefiting from these altimetry products span weather prediction, coastal impact assessments, fisheries management, marine transport, and disaster risk management. Identifying existing and potential uses of the data in operational, scientific, and other realms validates the significant resources dedicated by international space agencies to these missions. Here we seek to communicate and illustrate this value to decision makers and scientific and operational organizations.**

Keywords: Satellite, Altimetry, Applications, User.

1. INTRODUCTION

For over 30 years, a series of satellite altimeter missions, led by the National Aeronautics and Space Administration (NASA) and partners at the French space agency, Centre National d'Etudes Spatial (CNES), have measured ocean surface topography (OST), producing a continuous time series data. Along the way, other national and international partners have joined the missions, including the National Oceanographic and Atmospheric Administration (NOAA), the European Space Agency, the European Organisation for the Exploitation of Meteorological Satellites, the Canadian Space Agency, and the United Kingdom Space Agency. These partnering organizations continue to enhance science and operational returns on the investments made in these satellite systems. With scheduled launches through 2025 and planned missions beyond, the benefit to research and to applications for societal benefit of these continued missions and partnerships will continue to grow.

The heritage of missions building this long-term record of data began with the launch of the flagship TOPEX/Poseidon in 1992, followed by Jason-1 in 2001, Jason-2 in 2008, Jason-3 in 2016, and Sentinel-6 Michael Freilich (S6MF) in 2020. The Surface Water and Ocean Topography (SWOT) mission, designed with enhanced technologies for significantly higher resolution data, will launch in 2022, followed by Sentinel-6B, scheduled in 2025. These missions measure SSH, surface height on large lakes and rivers, significant ocean wave height, surface wind speed, and sea ice height and thickness.

S6MF ensures continuity of sea level observations by measuring global sea level rise—a key indicator of climate change. It supports operational oceanography by improving forecasts of ocean currents and wind and wave conditions. Due to spectral limitations on heritage nadir altimeters, data in coastal regions is limited to approximately 40 kilometers from the coast (Vignudelli et al. 2011). With new digital altimeter technology and dedicated onboard processing on S6MF, more precise measurements of sea surface height (SSH) are possible, as well as information on coastal ocean dynamics within a few kilometers of the coast.

SWOT, with exciting new Ka band radar interferometer technology and a nadir altimeter, will measure ocean and freshwater regions, resolving lakes of 250 m^2 in size, rivers 100 m wide, and submesoscale ocean features. SWOT will provide the first measurements of high-resolution ocean and surface water features with a single satellite mission.

2. USER COMMUNITIES

These missions were designed to advance technologies and to address scientific questions related to ocean circulation, ocean heat potential, tides, and climate change. They can also address operational needs of oceanographic and meteorological organizations who provide information to fishing and shipping fleets to optimize routes and operations, for disaster management, and to assess tropical cyclone heat potential (Lin et al. 2013) and other applications related to ocean heat content.

S6MF is continuing to chart the rise of sea level more precisely than previously possible, allowing researchers to understand how climate change is reshaping coastlines at an accelerating rate. Understanding trends will allow improved assessments of threats to coastal regions. Hurricanes regularly cause hundreds of billions of dollars in damage and are exacerbated by rising sea levels. Frequent high tide flooding along the Atlantic coast of the U.S. illustrates a troubling trend that is increasingly common due to higher relative sea level in many coastal communities. This "nuisance flooding" is expected to increase in frequency over the coming decades (Sweet et al. 2021).

3. APPLICATIONS

Measuring global water surface topography will enable a wide range of practical applications with tangible societal benefits including planning for the impacts of sea level rise on coastal communities, operational oceanography, improved flood modeling, transboundary water information sharing, weather and climate forecasting, and water resources management. Select applications relevant to coastal issues are highlighted, with examples of user communities engaged in use of the data.

Operational oceanography. Unique capabilities for ocean operations are enabled by the long data record and development of data merging techniques. Near real-time, high resolution global sea level anomaly maps are routinely

---

*Corresponding author. Address: 4800 Oak Grove Dr., MS 264-355, Pasadena CA 91109 USA, Email: mss@jpl.nasa.gov

produced and used in setting initial and boundary conditions for operational circulation models. These forecast conditions for maritime operations support optimization of shipping routes, assessment of risks to offshore infrastructure, and oil spill tracking.

Fisheries management and Biodiversity. Satellite altimetry data has been instrumental in resolving associations of pelagic fish, marine mammal, and turtle species with dynamic seascape features (eg. Belkin 2021). These include mesoscale eddies and fronts that serve as hotspots of biological productivity and are the target of commercial fishing activity (Watson et al. 2018). When applied synergistically with complementary sea surface temperature and satellite ocean color observations, SSH and altimeter-derived current measurements can provide the environmental information necessary to support emerging ecosystem-based fisheries assessment frameworks (eg. Chassot et al. 2011). Together, these can inform decisions on the designation of fisheries closed areas and marine protected areas (Della Penna et al. 2017). Higher spatial resolution OST observations will provide unique insights into the spatial dynamics of marine populations in relation to their environment for improved fisheries management and biodiversity conservation.

Weather & climate forecasting. Altimetry mission data is a critical component of global climate studies, yielding insights on short-term climate events such as the El Niño and La Niña and longer-term events such as the Pacific Decadal Oscillation. The data are used to monitor ocean circulation and improve understanding of the role of the ocean in climate and weather (Salama et al. 2011). Initial and boundary conditions derived from the state of the ocean surface and the hydrologic conditions of catchment areas informs numerical models that dictate the quality of weather and climate forecasting. SWOT will enable more accurate weather and climate forecasting, especially seasonally.

Improved flood modeling. Satellite altimeters demonstrate the ability to observe water level variations of lakes, rivers, and floodplains on land. River discharge from these regions to and across the coastline are estimated from a combination of satellite-based rainfall and hydrologic modeling (Hossain et al. 2014). Satellite altimetry use in data assimilation can improve predictive abilities of models to assess flood risk and impacts to coastal regions (Siddique-E-Akbor et al. 2011). Nuisance flooding, flooding from land, and coastal erosion during extreme events can be assessed using these tools to provide valuable information for coastal planners.

Decision support for environmental risk. Through altered weather patterns and rising sea level, climate change is expected to significantly alter coastal and inland environments for humans, infrastructure, and ecosystems. Coupled with predictions for steady increase in sea level rise and storm frequency and intensity, potential land use changes and population increases present a significant planning challenge for coastal communities. Measurements from land hydrological systems, in situ and other remote sensing assets will support development of information products for evolving user requirements (Intl. Altimetry Team 2021).

3. CONCLUSION

Improved monitoring of coastal zones to mitigate threats posed by sea level rise and climate change will help decision makers better understand impacts to these highly dynamic systems. Threats include sea level rise, local oceanic and atmospheric processes, ground subsidence, and other anthropogenic forcing factors (Benveniste et al. 2019).

Continued monitoring from satellites will help improve our knowledge of Earth's water cycle. As we enhance our observation capacity by collecting unique data on water storage and fluxes, we can promote better understanding of the physics that drives surface water and ocean dynamics. Water resources, natural risks, biodiversity, health (preventing the propagation of water-borne diseases), the agricultural sector, offshore energy, and territorial development are all sectors that will benefit from both continued and new altimetry mission sensor technologies.

REFERENCES

Belkin, I. (2021). Remote Sensing of Ocean Fronts in Marine Ecology and Fisheries. Rem. Sens. 13(5) 883, doi:10.3390/rs13050883.

Benveniste, J., Cazenave, A., et al. (2019). Requirements for a Coastal Hazards Observing System, Front. Mar. Sci., Vol. 6, p.348, doi:10.3389/fmars.2019.00348.

Chassot, E, S. et al. (2011). Satellite remote sensing for an ecosystem approach to fisheries management. ICES Jour, Mar. Sci., 68(4), 651–666, doi:10.1093/icesjms/fsq195.

Della Penna, A. et al. (2017). Lagrangian analysis of multi-satellite data in support of open ocean marine protected area design. Deep Sea Res. Part II, 140, 212-221, doi:10.1016/j.dsr2.2016.12.014.

Hossain, F. et al. (2014). A Promising Radar Altimetry Satellite System for Operational Flood Forecasting in Flood-Prone Bangladesh, IEEE Geosci. Rem. Sens., 2(3), 27-36, doi: 10.1109/MGRS.2014.2345414.

International Altimetry Team (2021). Altimetry for the future: Building on 25 years of progress. Adv. Sp. Res., doi:10.1016/j.asr.2021.01.022.

Lin, II., et al. (2013). Ocean heat content for tropical cyclone intensity forecasting and its impact on storm surge. Nat. Haz., 66, 1481–911 1500, doi:10.1007/s11069-012-0214-5.

Salama A., et al. (2011) Mapping Sea Level from Space. In: Linkov I., Bridges T. (eds) Climate. NATO Science for Peace and Security Series C: Environmental Security. Springer, Dordrecht, doi:10.1007/978-94-007-1770-1_22.

Siddique-E-Akbor, et al. (2011). Inter-comparison study of water level estimates derived from hydrodynamic–hydrologic model and satellite altimetry for a complex deltaic environment. Rem. Sens. Env., 115(6), 1522-1531, doi:10.1016/j.rse.2011.02.011.

Sweet, W., Simon, S., Dusek, G., Marcy, D., Brooks, W., Pendleton, M., & Marra, J., Eds. (2021). The State of High Tide Flooding and Annual Outlook, NOAA Tides & Currents.

Taconet, M., et al. (2019). Global Atlas of AIS-based fishing activity - Challenges and opportunities. Rome, FAO.

Vignudelli, S., A.G. Kostianoy, P. Cipollini and J. Benveniste, Eds. (2011). Coastal altimetry. Springer Science & Business Media.

Watson, J.R., et al. (2018). Fishermen follow fine-scale physical ocean features for finance. Front. Mar. Sci., 5, 46, doi:10.3389/fmars.2018.00046.

Improving SAR Altimetry Processing Over the Coastal Zone - From SAMOSA to HYDROCOASTAL

P.D. Cotton[*1]

M. Roca[2], A. Garcia-Mondejar[2], C. Gommenginger[3], O. B. Andersen[4], L. Fenoglio-Marc[5], M.J.Fernandes[6], C. Lazaro[7], M. Naeije[8], T. Moreau[9], S. Dinardo[9], C. Martin Puig[10], K. Raney[11], M. Cancet[12], A. Egido[13], M. Restano[14], J Benveniste[15]

[1]Satellite Oceanographic Consultants, [2]isardSAT, Spain, [3]National Oceanography Centre, UK, [4]DTU Space, DK, [5]University of Bonn, DE, [6]University of Porto, PT, [7]TU Delft, NL, [8]CLS, FR, [9]EUMETSAT, DE, [10]2kR-LLC, USA, [11]NOVELTIS, FR, [12]ESA-ESTEC, [13]SERCO-ESRIN, [14]ESA-ESRIN

Abstract – The European CryoSat-2, Sentinel-3A and 3B, and most recently Sentinel-6 Michael Freilich, satellites are the first to operate SAR (Delay-Doppler) mode altimeters. These missions have initiated a new era in satellite altimetry over the oceans, in which a step change in improvement in measurements over the open ocean and coastal zone has been achieved in terms of accuracy of measurement, the capability to map features that could not previously be resolved, and to provide measurements closer to the coast than ever before, as well as over difficult terrains such as inland water and sea ice. This presentation looks back through a series of projects initiated by ESA with the aim to develop improved processing of SAR altimeter data over specific targets: SAMOSA, CP4O, SCOOP and HYDROCOASTAL. The development and assessment of new processing schemes for SAR mode altimeter measurements and the performance improvements achieved will be reviewed.

Keywords: Coastal zone, Oceanography, Sea Level, Bathymetry, Tides, Altimeter.

1. SAMOSA

SAMOSA (SAR Altimetry Mode Studies and Applications) was an ESA-funded project initiated in 2007 to investigate the improvements offered by SAR mode altimetry over ocean, coastal and inland water surfaces, developing practical implementation of new theoretical models for the SAR echo waveform as part of this process.

Building on work by Raney (2013). SAMOSA developed physical based models for SAR altimeter ocean waveforms, and applied them to develop re-trackers for SAR mode products, which were further developed and tested on simulated data, airborne data, and then on real satellite data from CryoSat-2. Approaches to reduce SAR mode data to "RDSAR" data were also investigated, to infer the statistical equivalence between SAR mode and the traditional low-resolution altimetry. Subsequent work further developed the "SAMOSA" model, balancing the aim to improve the modelling of the waveform against efficiency of processing to achieve a practical scheme that could be implemented in the Sentinel-3 Ground Segment. Ray et al. (2015) describes the SAMOSA SAR altimeter algorithm developed during this project.

2. CP4O

CP4O (CryoSat Plus for Oceans) was a project supported under the ESA Programme Element coined "Support to Science Element" (STSE) with the objectives to build a sound scientific basis for new scientific and operational applications of CryoSat-2 data, generate and evaluate new methods and products to enable the full exploitation of the CryoSat-2 SIRAL altimeter, extending their application beyond the initial mission objectives, and to ensure that the scientific return of the CryoSat-2 mission is maximised. Within CP4O, processing schemes for CryoSat-2 data were developed and evaluated for SAR and RDSAR products over the open ocean, and SAR and SARin modes data over the coastal ocean. New geophysical correction products and models (Wet Troposphere, Ionosphere, and Regional Tide Models) were developed and assessed, as was specialized processing of SAR mode data to improve Polar Ocean bathymetry and tidal modelling. References include Fenoglio-Marc et al., (2015), Fernandes et al (2013), Garcia et al (2018), Makhoul-Varona et al (2018)

3. SCOOP

SCOOP (SAR Altimetry Coastal & Open Ocean Performance) was funded under the ESA SEOM (Scientific Exploitation of Operational Missions) Programme Element, with the objective to characterise the expected performance of Sentinel-3 SRAL SAR mode altimeter products, and then to develop and evaluate enhancements to the baseline processing scheme. An improved Wet Troposphere correction for Sentinel-3 was also developed and evaluated (Fernandes et al., 2018)

SCOOP provided important recommendations, including:

SAR mode processing
- Modifications to the Sentinel-3 SAR mode processing (Zero-padding and Hamming window) were recommended
- A SAR dedicated Sea State Bias correction is needed for accurate Sea Surface Height.
- Further development and testing of coastal re-trackers for SAR mode is recommended.
- Continue development and evaluation of other processing approaches: Stack characterisation / selection; Amplitude and Dilation Compensation (ACDC); Fully Focussed SAR processing; effect of vertical motion of wave particles

RDSAR processing
- Coastal re-trackers should be applied for coastal data sets.
- Further tests on MLE4 re-tracker on the RDSAR product should be carried out

Wet Troposphere Correction

- The GPD+ correction clearly outperforms the ECMWF operational model-derived correction.
- The composite correction included in Sentinel-3 products was not suitable for use. The GPD+ WTC would provide added value for Sentinel-3A products

References include Abulaitijiang et al (2019), Buchhaupt et al (2018), Cancet et al (2018 and 2019), Fenoglio-Marc et al (2019),

4. HYDROCOASTAL

HYDROCOASTAL is a project funded by ESA with the objective to maximise exploitation of SAR and SARin altimeter measurements in the coastal zone and inland waters, by evaluating and implementing new approaches to process SAR and SARin data from CryoSat-2, and SAR altimeter data from Sentinel-3A and Sentinel-3B. Optical data from Sentinel-2 MSI and Sentinel-3 OLCI instruments will also be used in generating River Discharge products. New SAR and SARin processing algorithms for the coastal zone and inland waters will be developed and implemented and evaluated through an initial Test Data Set for selected regions. From the results of this evaluation a processing scheme will be implemented to generate global coastal zone and river discharge data sets. A series of case studies will assess these products in terms of their scientific impacts. All the produced data sets will be available on request to external researchers, and full descriptions of the processing algorithms will be provided. References so far include Biasio et al (2020), Fernandes et al (2020), Tarpanelli et al (2020).

5. PERSPECTIVES

This series of studies have provided important input to the development of improved operational processing schemes, resulting in improved measurements for SAR altimeters, especially at the coast.

The earlier studies also provided input into recommendations to implement the "interleaved" mode adopted as the "standard" for modern ocean altimetry and now operational on Sentinel-6 / Michael Freilich. A keystone contribution for that major step forward was the report of the study led by C Gommenginger (2013).

The latest project, HYDROCOASTAL, is now addressing the challenge of bringing together coastal zone measurements by SAR altimeter with those over inland waters. We invite the community to access the data products that will be produced and to carry out their own case studies to assess the potential scientific impact of these data. HYDROCOASTAL will also provide a further scientific Road Map with recommendations and guidance for future scientific data exploitation projects, for algorithmic evolutions within baseline processing and for future interferometric altimetry missions.

References

Abulaitijiang, A., O. B. Andersen, D. Sandwell, (2019) Improved Arctic Ocean Bathymetry derived from DTU17 Gravity model. Earth and Space Science, July 2019, https://doi.org/10.1029/2018EA000502.

F. de Biasio, G. Baldin, S. Vignudelli (2020) Revisiting Vertical Land Motion and Sea Level Trends in the Northeastern Adriatic Sea Using Satellite Altimetry and Tide Gauge Data, J. Mar, Sci. Eng. 8, 949 https://doi.org/10.3390/jmse8110949

Buchhaupt C., Fenoglio-Marc L., Dinardo S., Scharroo R., Becker M (2018): "A Fast Convolution Based Waveform Model for Conventional and Unfocused SAR Altimetry", Advances in Space Research, Volume 62, Issue 6, p. 1445-1463. https://doi.org/10.1016/j.asr.2017.11.039

Cancet M., O. B. Andersen, F. Lyard, D. Cotton, J. Benveniste, (2018). Arctide2017, A high-resolution regional tidal model in the Arctic Ocean, Advances in Space Research, Vol 62, Issue 6, 15 September 2018 pp 1324-1343. https://doi.org/10.1016/j.asr.2018.01.007

Cancet, M., Andersen, O., Abulaitijiang, A., Cotton, D., Ben veniste, J. (2019) Improvement of the Arctic Ocean bathymetry and regional tide atlas – First result on evaluating existing Arctic Ocean bathymetric models. *In: Mertikas S., Pail R. (eds) Fiducial Reference Measurements for Altimetry. International Association of Geodesy Symposia, vol 150. Springer, Cham.* https://doi.org/10.1007/1345_2019_85

Fenoglio-Marc, L, S. Dinardo, R. Scharroo, A. Roland, M. Dutour Sikiric, B. Lucas, M. Becker, J. Benveniste, R. Weiss, (2015) The German Bight: A validation of CryoSat-2 altimeter data in SAR mode, Advances in Space Research, Vol 55., issue 11, 1 June 2015, 2641-2656.

Fenoglio-Marc, L., S. Dinardo, B. Uebbing, C. Buchhaupt, J. Kusche, M. Becker (2019). Calibrating CryoSat-2 and Sentinel-3A sea surface heights along the German coast, International Association of Geodesy Symposia, https://doi.org/10.1007/1345_2019_73 Springer Nature Switzerland AG.

Fernandes, M.J.; Nunes, A.L.; Lázaro, C., (2013) Analysis and Inter-Calibration of Wet Path Delay Datasets to Compute the Wet Tropospheric Correction for CryoSat-2 over Ocean. Remote Sens. 5, 4977-5005

Fernandes, M. J. & Lázaro, C. (2018). Independent assessment of Sentinel-3A wet tropospheric correction over the open and coastal ocean. *Remote Sensing 2018, 10(3), 484. doi:10.3390/rs10030484*

Fernandes, M. J., C. Lazaro, T. Vieira (2021) On the role of the troposphere in satellite altimetry, Remote Sensing of Environment 252 112149, https://authors.elsevier.com/sd/article/S0034-4257(20)30522-8

Garcia P., C. Martin-Puig, M. Roca, (2018) SARin Mode, and a window delay approach, for coastal altimetry, Advances in Space Research Vol 62, Issue 6, 15 September 2018, pp 1358-1370. https://doi.org/10.1016/j.asr.2018.03.015

Gommenginger, C. C. Martin-Puig, L. Amarouche, and R. K. Raney, (2013) *Review of State of Knowledge for SAR Altimetry over Ocean,* Version 2.2, EUMETSAT,EUM/RSP/REP/ 14/74930421, November 2013.

Makhoul-Varona, M. Roca, C. Ray, R. Escolà, Evaluation of different Delay-Doppler Processor (DDP) algorithms using CryoSat-2 data over open ocean, (2018) Advances in Space Research, Vol 62, Issue 6, 15 September 2018 pp 1464-1478. https://doi.org/10.1016/j.asr.2018.04.004

Raney, R. K. (2013) "Maximizing the intrinsic precision of radar altimetric measurements," *IEEE Geoscience and Remote Sensing Letters,* Vol. 10, No. 5, pp. 1171-1174, 2013.

Ray, C., Martin-Puig, C., Clarizia, M.P., Ruffini, G., Dinardo, S., Gommenginger, C. and Benveniste, J., (2015) SAR Altimeter Backscattered Waveform Model, Geoscience and Remote Sensing, Vol. 53, Iss. 2., pp 911 – 919, Doi: 10.1109/TGRS.2014.2330423

Tarpanelli, A., F. Iodice, L. Brocca, M. Restano, J. Benveniste, (2020) River flow monitoring by Sentinel-3 OLCI and MODIS: comparison and combination, Remote Sens., 12(23), 3867

Ocean circulation from the synergy of altimeter-derived and oceanic tracers observations

D. Ciani[1,*], M-H. Rio[2], B. Buongiorno Nardelli[3], S. Guinehut[4,5], E. Charles[4], H. Etienne[4], R. Santoleri[1]

1 CNR-Institute of Marine Sciences, 00133, Rome, Italy
2 European Space Agency, ESA-ESRIN, 00044, Frascati, Italy
3 CNR-Institute of Marine Sciences, 80133, Naples, Italy
4 CLS, 31520, Ramonville St-Agne, France
5 Mercator Océan International, 31400, Toulouse France

Abstract – Measuring the ocean surface currents at high spatio-temporal resolutions is crucial for scientific and socio-economic applications. Since the early 1990s, the synoptic and global-scale monitoring of the ocean surface currents has been provided by constellations of Radar Altimeters. The Altimeter observations enable to derive the geostrophic component of the surface currents with effective spatial-temporal resolutions O(100 km) and O(10 days), respectively. Therefore, only the largest mesoscale oceanic features can be accurately resolved. In order to enhance the altimeter system capabilities, we propose a synergistic use of high resolution, satellite-derived Sea Surface Temperature (SST), Chlorophyll concentrations (Chl) and Altimeter-derived currents and show that this approach can improve the performances of the altimeter-derived products.

Keywords: Ocean Currents, Altimetry, Satellite observations synergy.

1. INTRODUCTION

Oceanic currents are a key factor in modulating both the short-term and climatological dynamics of the ocean–atmosphere system. On a large scale, their monitoring is needed to evaluate the meridional transport of heat and salt and better predict ocean thermohaline circulation variability and changes. At smaller spatial-temporal scales, 0.1 to 10 km and hours to days, ocean currents can create significant heterogeneities in both horizontal and vertical velocities, affecting the local 3D transport properties. Since the early 1990s, radar altimeters onboard satellites have been providing indirect measures of the marine surface circulation at global scale. This is achieved by measuring the Sea Surface Height (SSH) relative to an equipotential surface (the so-called geoid) and inferring the surface motion via the geostrophic approximation. This system has intrinsic limitations related to the sampling of SSH and to the approximation considered in the retrieval. Indeed, only larger mesoscale geostrophic processes can be described with this approach. Several methodologies have been developed in recent years to extract 2D fine-scale sea surface currents from satellite imagery. Some techniques rely on the use of Sea Surface Temperature (SST) as a proxy of the sea surface density and derive the surface motion from the surface quasi geostrophic theory. Other methods rely on the recognition of feature displacements from satellite-derived tracer images and infer the marine surface currents from maximum cross correlation algorithms. Rio and Santoleri 2018 (RS18) implemented an optimal combination of altimeter-derived geostrophic currents and higher resolution gap-free (Level 4,

L4 hereinafter) satellite SST data. The main idea is that remotely sensed distributions of ocean tracers are linked to ocean currents' advection, so that improved ocean currents' estimates can be derived by optimally merging high spatio-temporal resolution tracer images with lower resolution altimeter data. This method, based on the theoretical and numerical studies of Piterbarg 2009, also accounts for the source/sink terms of the tracer evolution equation. RS18, combining the global geostrophic currents distributed by the Copernicus Marine Service with global L4 SST satellite data, noted an improved surface current retrieval in most of the global ocean, with the exception of the Southern Ocean, where the reconstruction actually degrades the ocean current retrievals. With the aim of further investigating the optimal combination proposed by RS18, we tested the impact of using different satellite SST data to reconstruct the global surface currents. Then, the synergistic reconstruction is also implemented with surface Chlorophyll concentrations (Chl) data in the Mediterranean Sea, where we tested the method feasibility in an Observing System Simulation Experiment relying on CMEMS physical and biogeochemical model outputs.

2. METHODS AND RESULTS

At global scale, the ocean currents reconstruction is obtained implementing the RS18 method, i.e. from the synergy of the Copernicus Marine Service altimeter-derived currents (daily, 1/4°) and the three following daily satellite SST data: the REMSS SST data (1/10°) (Wentz et al. 2014), the Copernicus OSTIA SST (1/20°) (Good et al. 2020) and the Multiscale Ultra-High resolution (MUR) SST (1/100°) (Chin et al. 2017). While the REMSS SST are uniquely built from Infrared and Microwave Satellite observations, the OSTIA and MUR datasets are optimally interpolated from both satellite and in-situ SST observations. The quality assessment of the synergistic OPtimized Currents (OPC) is carried out via direct comparison with the in-situ measured currents from the Global Drifter Program. The percentage of improvement (PI) with respect to standard Altimetry is given by a ratio of root mean square errors (RMSE) between the OPC and the Altimeter-derived Geostrophic (GEO) currents and is expressed by (1),

$$\mathrm{PI}_{U,V} = 100 \left[1 - \left(\frac{\mathrm{RMSE}_{U,V}^{\mathrm{OPC}}}{\mathrm{RMSE}_{U,V}^{\mathrm{GEO}}} \right)^2 \right] \tag{1}$$

where U,V stand for zonal and meridional currents, respectively. The synergistic reconstruction based on the OSTIA SST yielded the best overall performances. The comparison with in-situ measured currents showed that the OPC can improve the altimeter estimates up to 30% locally,

---

with enhanced improvements in the equatorial band and for the meridional component of the motion. In Fig. 1 the PI has been computed by means of (1) in 20°x20° boxes and accounting for the 2014-2016 period.
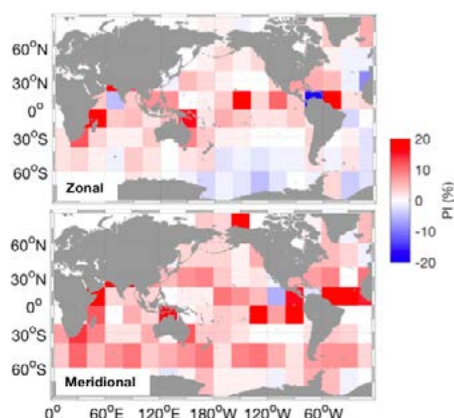
Figure 1. *PI of the optimized currents computed relying on the CMEMS OSTIA L4 SSTs (2014-2016 period).*

Unlike the reconstruction based on the REMSS SSTs, the surface currents computed with the OSTIA dataset enabled to mitigate the degradations obtained in the Southern Ocean, where the satellite SST retrieval is largely affected by cloud cover and persistent high wind regimes. This was partially explained by the use of in-situ SST observations in the OSTIA optimal interpolation algorithm, that can improve the L4 analysis compared to a processing uniquely based on satellite estimates, as for the REMSS case. On the other hand, using the very high resolution MUR dataset yielded degradations (mostly for the zonal component) in both low and high latitude areas. This effect was due to inhomogeneities in the L4 SST effective spatial resolution, generating artefacts in the L4 SST field and preventing to extract useful dynamical information from the satellite SST patterns (Ciani et al 2020). To further push the RS18 methodology, and in the future perspective of exploiting a multivariate synergy (e.g. SST in combination with other tracers) we also tested the RS18 methodology using surface Chl concentration data. We ran an Observing System Simulation Experiment (OSSE) in preparation of the eventual future applications to satellite-derived data. We tackled the problem of the surface currents reconstruction in the Mediterranean Area, where the most energetic signals are found at small spatial-temporal scales (up to 10 km and a few days). We relied on the Copernicus physical and biogeochemical regional forecast models for the Mediterranean Sea. Based on one year of model outputs (2017), we simulated the Synthetic Altimeter-derived Currents (SAC), and we combined them with the surface modelled Chl data in order to get the OPC. In the OSSE approach, the modelled total surface currents were used as a validation benchmark. Fig. 2 shows the RMS of the zonal and meridional SAC and OPC, validated against the model-derived total currents, i.e. our ground truth. When the SAC are analysed, we find RMS always equal to or larger than 5 cm·s^{-1}, with maximum values exceeding 20 cm·s^{-1} in the Western Mediterranean, in the Atlantic Ionian Stream across the Sicily Channel and in many areas of the Levantine Basin. When the information from the surface Chl is introduced within the Altimeter currents, large improvements are observed at the basin-scale. Patches of RMS ≃20 cm·s^{-1} only cover 2 to 3% of the basin and are mostly limited to coastal areas in the Western Mediterranean (Ciani et al. 2021).
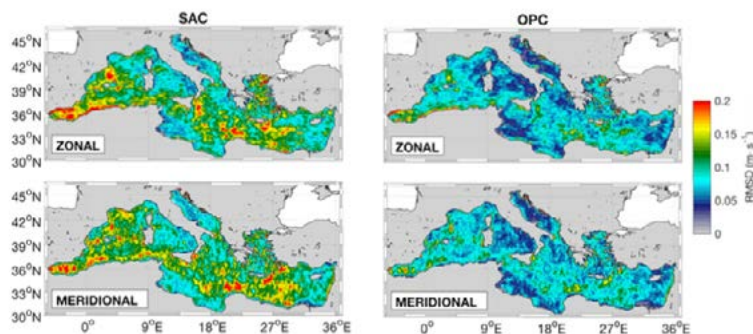
Figure 2. *Left column: RMSDs of the SAC against the model total currents, top and bottom panels show results for the zonal and the meridional currents. Right column: same as the left column, for the OPC.*

3. CONCLUSION

The optimal combination of altimeter-derived currents and high resolution observations of surface oceanic tracers is a promising technique to improve the gridded altimetry products. The study evidenced that, in order to get the improvements, the satellite-derived tracers fields have to be characterized by high and homogeneous effective spatial resolutions. The case of SST and the feasibility of using Chl were analysed. Future studies should tackle the problem of a multivariate (e.g. SST in combination with Chl) reconstruction.

REFERENCES

Chin, T.M.; Vazquez-Cuervo, J.; Armstrong, E.M. A multi-scale high-resolution analysis of global sea surface temperature. Remote. Sens. Environ. 2017, 200, 154–169

Ciani, D., Charles, E., Buongiorno Nardelli, B., Rio, M. H., & Santoleri, R. (2021). Ocean Currents Reconstruction from a Combination of Altimeter and Ocean Colour Data: A Feasibility Study. Remote Sensing, 13(12), 2389.

Ciani, D., Rio, M. H., Nardelli, B. B., Etienne, H., & Santoleri, R. (2020). Improving the altimeter-derived surface currents using sea surface temperature (SST) data: A sensitivity study to SST products. Remote Sens., 12(10), 1601.

Good, S.; Fiedler, E.; Mao, C.; Martin, M.J.; Maycock, A.; Reid, R.; Roberts-Jones, J.; Searle, T.; Waters, J.; While, J.; et al. The Current Configuration of the OSTIA System for Operational Production of Foundation Sea Surface Temperature and Ice Concentration Analyses. Remote. Sens. 2020, 12, 720

Piterbarg, L.I. A simple method for computing velocities from tracer observations and a model output. Appl. Math. Model. 2009, 33, 3693–3704

Rio, M.H.; Santoleri, R. Improved global surface currents from the merging of altimetry and Sea Surface Temperature data. Remote Sens. Environ. 2018, 216, 770–785

Wentz, F.; Meissner, T.; Gentemann, C.; Hilburn, K.; Scott, J. Remote Sensing Systems GCOM-W1 AMSR2 Daily Data, Environmental Suite on 0.25 Degrees Grid, 2014, Version V.8

CFOSAT: a breakthrough to observe and predict ocean surface wind and waves

C. Tourain [1]*, D. Hauser[2]**, L. Aouf[3]

[1] CNES, Toulouse, France
[2] LATMOS, Paris, France
[3] Météo-France, Toulouse, France

Abstract – **CFOSAT is China-France mission dedicated to ocean surface winds and waves measurement. Embarking a wind scattermometer, SCAT, and an innovative wave scatterometer SWIM, it provides simultaneously wind vectors and wave spectral characteristics. After three years in orbit the CFOSAT products have been qualified and scientific works has demonstrated the added value of the new set of data. In this paper we summarize the main performances of SWIM and give examples of scientific results obtained with CFOSAT data.**

Keywords: Oceanography, scatterometer, Scientific Themes.

1. INTRODUCTION

Since October, 29th 2018, the new space-borne system CFOSAT (China France Oceanography Satellite) [1] has been deployed for measuring ocean surface parameters. This mission, developed under the responsibilities of the French and Chinese Space agencies (CNES, CNSA) was designed to monitor at the global scale, ocean surface winds and waves. It is composed of two radar sensors both scanning in azimuth: SCAT, a fan-beam wind scatterometer [2], and SWIM designed for wave measurements [3]. With its collocated measurements of ocean surface wind and waves, CFOSAT aims at better understanding processes at the ocean surface and ocean/atmosphere interactions and at improving atmospheric and oceanographic models and predictions by feeding forecast systems through assimilation. This paper focuses on the SWIM measurements. SWIM is an innovative Ku-band real-aperture wave scatterometer, with 6 low-incidence rotating beams [2].

This new instrument allows for the first time the systematic production of directional spectra of ocean waves with a real-aperture radar system. This usefully complements the existing missions based on SAR systems which also provide spectral information on surface ocean waves but with more limitations [4]. After an important task of CALibration and VALidation (CAL/VAL) on the instrument and products at the beginning of the mission, the expected performances have been demonstrated, as it is recalled in section 2. In section 3, we present the studies performed by the science teams, showing the potential of CFOSAT mission for several Oceanography applications and even more.

2. Products performances

SWIM delivers several types of information: from its nadir beam the significant wave height and wind speed are provided, whereas from its 5 off-nadir beams are produced the ocean wave spectra and also normalized radar cross-section σ0 profiles for incidence from 0 to 10 degrees.

To retrieve the significant wave height, the normalized radar cross-section and wind speed from radar nadir echoes, the Adaptive algorithm was implemented in the SWIM ground segment [6]. From simulations, it has been shown in [6] that nadir parameters are retrieved without bias and with less noise when compared to the classical MLE4 algorithm (noise reduction of 60% for SWH and 11% for σ0).

This ensures the same level of performance over ocean as conventional altimetry missions, in spite of the SWIM instrument lower measurement rate (4.5Hz vs 20Hz). It also improves the relevance of the retrieved parameters on specific areas such as near sea-ice, or bloom or rain impacted surfaces.

The normalized radar cross-section σ0 profiles are provided at level 2 as averaged values per bins of 0.5° in incidence and 15° in azimuth. They are referenced in the geometry of the wave cells, which are boxes of about 70 x 90 km. The mean trend of these profiles is globally consistent with results provided by GPM datasets [7]. The dependence of σ0 with wind speed is very consistent (less than 1 dB difference) with the GPM data mean trend. The smallest sensitivity to wind speed is observed for the 10° and 8° beams (1dB to 1.5 dB difference between 5 and 20 m/s), making them the most valuable incidences for the wave inversion as the dominant effect in the σ0 fluctuations within the footprint will be the tilt of the long waves.
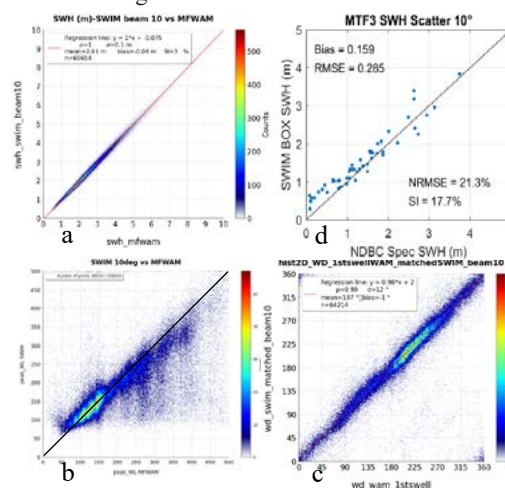
Figure 1. *SWIM wave parameters compared to MFWAM for observations from 26 January 2020 to 5 February 2020, a: SWH, b: dominant wavelength, c: dominant wave direction. d: SWIM wave parameter SWH from the 10° beam compared to NDBC buoys data for observations from 2020, January the 25th to February the 7th.*

Wave slope spectra are determined based on 6°, 8° and 10° beams measurements. 2D spectra are provided at level 2 in the wave cell geometry (boxes of about 70 x 90 km). Impact of speckle noise is mitigated in the processing using an empirical model of the density spectrum of speckle noise. It was shown in [5] that its impact is the most important when then antenna look direction is aligned with the satellite track (at ±15°). In this direction is also varies with latitude and sea state conditions. The modulation transfer function which is used to invert the directional modulation into wave slope spectra is currently estimated by using the nadir SWH as reference. This processing configuration leads to the current wave spectra and wave parameter performances [8]: Waves are identified for wavelength from 50 to 500m and the main wave parameters (significant wave height, dominant wavelength and dominant direction) extracted from spectra are consistent with models as shown in fig. 1a, b, c, . SWH is consistent with buoys outputs as shown in fig. 1d for SWH larger than about 1.8 m. The spectra show consistent shapes in frequency and direction with however some perturbations at low sea-state due to spurious peaks in the wave height spectra.

---

* Corresponding author. Address: 18 av. Edouard Belin, 31401 Cedex 9, France. Email: cedric.tourain@cnes.fr
** Presenting authors: Address : 11 Boulevard d'Alembert 78280 Guyancourt, France. Email: daniele.hauser@latmos.ipsl.fr

3. CFOSAT SWIM data contribution to oceanography and perspectives

Use of the SWIM data by scientific teams has already demonstrated several significant contributions for ocean surface characterization.

It was shown by [9] that in strongly forced situations like in the Southern Ocean, the assimilation of dominant wavelengths and directions from SWIM [9] spectra provide wave fields in better agreement with independent observations from altimeter than when assimilating the SWH. Biases observed when comparing SWH from model runs with and without assimilation against observations from altimeter sensors are reduced from 13cm to 3cm when dominant wavelengths and directions from SWIM spectral partitions are assimilated. This improvement was attributed to a more realistic energy transfer during the wave growth phase in the conditions of very high winds in the Southern hemisphere. This result also reveals that such assimilated observations have an impact on the mixing in the upper layers of the ocean and hence on the sea surface temperature and air/sea exchanges.

Additional useful parameters have also already been derived from SWIM wave spectra. The frequency width of the omni-directional spectra, the directional spread of the dominant waves, and the related Benjamin-Feir index (BFI) have been studied in [10] based on SWIM data. This led to the production for the first time of global statistics and maps of spectral shape parameters and Benjamin-Feir Index from satellite observations. This study also shows systematic differences between model and observations concerning the shape of the frequency spectra, with observed spectra more narrow and peaked than those from the MF-WAM model. This corroborates previous studies which indicate that due to their simplifications in the non-linear interaction term, the numerical model tends to produce spectra which are too broad even if their performance in terms of total energy is excellent. Associated analysis shows that for most of the open ocean conditions, SWIM derived parameters values are consistent. The impact of spurious peaks at low frequency in omnidirectional wave height spectra was also mentioned for low wave height (Hs < 1.8 m) and short dominant wavelength (λp <70m) conditions, and confirmed the importance of on-going work about the filtering of these spurious peaks.
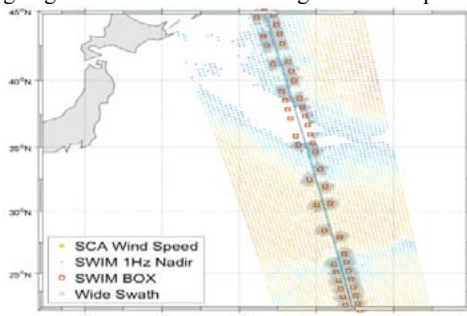
Figure 3. *Geometry used for the wide swath SWH retrieval. SWIM wave boxes and nadir data are marked as red boxes and blue points, respectively. The wind grid points from SCAT are marked as points colored based on wind speed, and the wide swath SWH grid points are indicated as gray circles.*

The CFOSAT mission offers the opportunity to exploit the synergy between SCAT and SWIM data, opening opportunities for oceanography. As shown in [11], the global feature of the wave induced stress was investigated from satellite data for the first time, and the contributions of wind sea and swell in the air-sea momentum flux could be separated thanks to the simultaneous and collocated wind and wave spectra measurements from CFOSAT. A novel method was proposed in [12] for obtaining the SWH over a wide swath (i.e. outside the swath of the SWIM instrument) from the synchronous observations of SWIM and SCAT. Based on a deep neural network (DNN) the method allows to estimate the SWH over SCAT grid points at a swath distance of up to 200 km at a 25km resolution (SCAT wind product spatial resolution), increasing significantly the number of CFOSAT SWH observations. When assimilated in the MFWAM model

these data have an equivalent positive impact to the assimilation of SWIM nadir SWH observations.

4. CONCLUSION

SWIM instrument has fulfilled its objective by providing at the global scale, new observations with directional wave spectra, nadir parameters and NRCS profiles. Performances of SWIM products and coupling with CFOSAT SCAT wind scatterometer or other sensor measurements open the field for improvements in ocean surface characterization and modeling. New perspectives are emerging by exploiting SWIM advanced capacities such as SWH and wind obtained at a 5 Hz sampling along-track for coastal applications, sea ice detection and characterization through the analysis of NRCS [13], wave field studies in the marginal ice zone and in extreme events [14] or global estimation of additional wave-related parameters (like e.g. the Stokes drift). CFOSAT is thus a new and original source of observations for many studies and applications.

REFERENCES

[1] Hauser D. et al., "Overview of the CFOSAT mission", IGARSS' 2016, Beijing (China), July 2016

[2] Liu Jianqiang, et al, « First Results From the Rotating Fan Beam Scatterometer Onboard CFOSAT », *10.1109/TGRS.2020.2990708*, 2020

[3] Hauser D., et al, SWIM: the first spaceborne wave scatterometer, *10.1109/TGRS.2017.2658672*, 2017

[4] W. R. Alpers and C. Brüning, "On the relative importance of motion related contributions to the SAR imaging mechanism of oceansurface waves," IEEE TGRS vol. GE-24, no. 6, pp. 873–885, Nov. 1986

[5] Hauser D. et al, "New observations from The SWIM radar on board CFOSAT; instrument validation and ocean wave measurement assessment", doi 10.1109/TGRS.2020.2994372, 2020

[6] C. Tourain *et al*., "Benefits of the Adaptive Algorithm for Retracking Altimeter Nadir Echoes: Results From Simulations and CFOSAT/SWIM Observations," in *IEEE TGRS*, doi: 10.1109/TGRS.2021.3064236.

[7] Gressani V. et al , "Wave Spectrometer Tilt Modulation Transfer Function Using Near-Nadir Ku-and Ka-Band GPM Radar Measurements", *Proceedings of the 2018 IEEE IGARSS*, Valencia (Spain), 2018

[8] C. Tourain *et al*., "Evolutions and Improvements in CFOSAT SWIM Products," *2021 IEEE IGARSS*, 2021, pp. 7386-7389, doi: 10.1109/IGARSS47720.2021.9553274

[9] Aouf, L. et al. (2021). New directional wave satellite observations: Towards improved wave forecasts and climate description in Southern Ocean. *Geophysical Research Letters*, 48, e2020GL091187. https://doi.org/10.1029/2020GL091187

[10] Le Merle E. et al. (2021). Directional and frequency spread of surface ocean waves from SWIM measurements. *JGR: Oceans*, 126, e2021JC017220. https://doi.org/10.1029/2021JC017220

[11] Chen, S. et al, (2020). On the first observed wave-induced stress over the global ocean. *JGR: Oceans*, 125, e2020JC016623. https://doi.org/10.1029/2020JC016623

[12] Wang, J. et al, (2021). Acquisition of the significant wave height from CFOSAT SWIM spectra through a deep neural network and its impact on wave model assimilation. *JGR : Oceans*, 126, e2020JC016885. https://doi.org/10.1029/2020JC016885

[12] Wang, J. et al, (2021). The wide swath significant wave height: An innovative reconstruction of significant wave heights from CFOSAT's SWIM and scatterometer using deep learning. *Geophysical Research Letters*, 48, e2020GL091276. https://doi.org/10.1029/2020GL091276

[13] Peureux C. et al., Sea-ice detection from near-nadir Ku-band echoes of CFOSAT/SWIM scatterometer. *JGR: Oceans: Submitted*

[14] Shi, Y. et al, (2021). Asymmetric wave distributions of tropical cyclones based on CFOSAT observations. *JGR: Oceans*, 126, e2020JC016829. https://doi.org/10.1029/2020JC016829

ODYSEA: a first global Doppler scatterometer to explore currents, winds, and air-sea interactions

F. Ardhuin*, S. Gille, T. Lee

LOPS, Univ. Brest, CNRS,Ifremer, IRD, Brest, France
Scripps Institution of Oceanography, CA
Jet Propulsion Laboratory, California Institute of Technology, CA

Abstract – ODYSEA simultaneously measures winds and ocean currents at the air–sea interface. With a single satellite, ODYSEA provides the first-ever global measurements of total ocean surface currents, achieves new refinements in spatial resolution of vector winds at the ocean surface, and captures the interplay between two key components of the Earth system. The mission directly addresses an Earth system measurement challenge outlined by the Decadal Survey for Earth Science and Applications from Space (National Academies of Sciences, Engineering, and Medicine, 2018; henceforth ESAS2018), providing global-scale information that is vital to improving our understanding of weather and climate, addressing the underlying ESAS2018 goal to provide new measurements critical to allowing us to thrive on our changing planet.

Keywords: Symposium, Program, Scientific Themes.

1. INTRODUCTION

For more than a century, we have known that winds power the ocean (Ekman, 1905). Winds essentially drive upper-ocean currents, and traditional ocean observing systems—whether based on buoys or satellites—have been designed with the premise that knowing the winds will improve our understanding of ocean circulation. However, close scrutiny of satellite scatterometer wind measurements demonstrated that the exchanges between the wind and ocean are a two-way process. Surface winds feel the effects of ocean currents: the wind stress that powers the ocean depends not on the wind speed relative to the solid Earth but rather on the wind speed relative to the ocean currents (Kelly et al, 2001; 2005). Subsequent modeling studies have shown that ocean currents feedback on the atmosphere, influencing the horizontal and vertical transport of momentum, energy, and moisture in the atmosphere, and thus shaping the nature of weather — and climate (Renault et al. 2016a, 2016b, 2017, 2019, 2022; Shi and Bourassa 2019; Seo et al, 2019, 2021). In other words, at small scales, ocean currents also govern the atmosphere.

In probing the impact of these 'relative' winds, numerical modeling studies have exposed the limits of our knowledge. Competing models predict different forms of interactions between winds and currents. One set of scenarios shows the role of instantaneous exchanges between winds and currents, meaning that wind-current feedbacks are local phenomena (Dewar and Flierl 1987; Dawe and Thompson 2006; Duhaut and Straub 2006; Hughes and Wilson 2008; Eden and Dietze 2009, Renault et al., 2016a,2018,2022, Seo et al., 2016, 2019, Oerder et al., 2016, Jullien et al., 2020). A second group of studies suggests that wind-current feedbacks trigger inertial responses that propagate away from their point of origin, with an identifiable far-field effect (Renault et al., 2016b, 2017, 2019, Seo et al., 2021). The relative importance of these two

categories of responses likely depends on multiple factors, including ocean stratification, ocean mixed-layer depth, and the structure of the atmospheric planetary boundary layer. Unraveling the competing hypotheses will therefore require global measurements, spanning all seasons and all latitude bands.
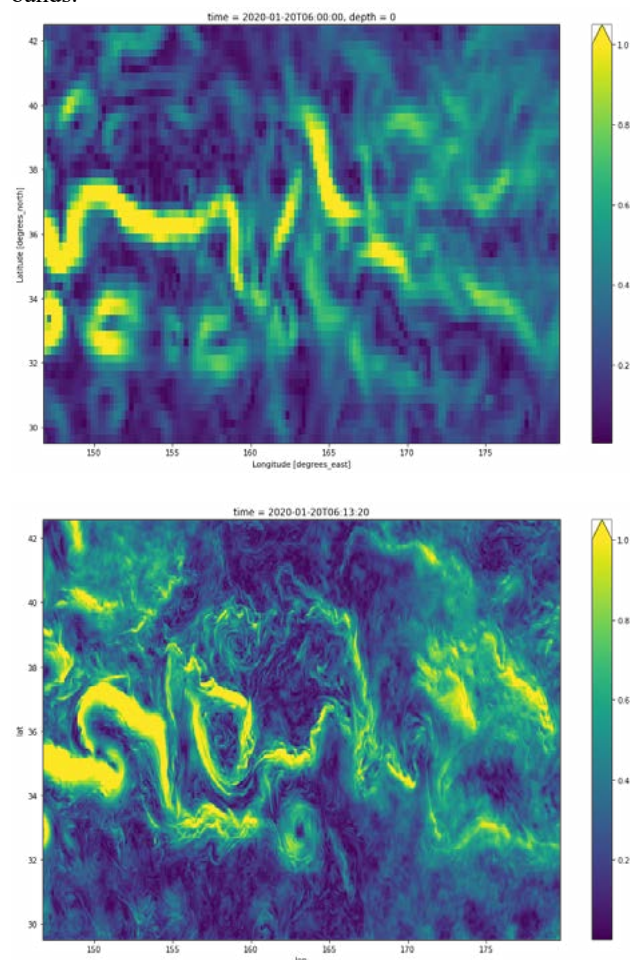
Figure 1. (top) Present-day ocean surface currents from Globcurrent. (bottom) Current resolution expected from ODYSEA, plotted from a 1/24° resolution version of the MITgcm model. Note that ODYSEA will also resolve the associated temporal scales.

Measurements of surface currents will be especially transformative in the tropics, where the near-zero Coriolis parameter makes geostrophic and Ekman currents unreliable. Tropical ocean surface currents can have significant impacts on climate variability (e.g., McPhaden et al. 2006; Zhang et al 2014; Wang et al. 2017). For example, eastward anomalies of surface currents associated with westerly wind bursts can push the edge of the western tropical warm and fresh pool towards the east. The eastward shift of the warm and fresh pool edge can affect atmospheric convection, thereby

* Corresponding author. Address: Corso Adda 60, 13100 Vercelli (VC), Italia. Email: vittorio.barale@yahoo.it

providing feedback to the wind field to influence ENSO development (McPhaden et al. 2020). The response of surface currents to wind events is not well understood, in part because of the lack of knowledge about how near-surface stratification modulates the response of surface currents to intraseasonal wind events (Kessler et al. 2021) . For example, the presence of a shallow freshwater layer near the surface can trap the momentum input from wind stress within a shallow layer, amplifying the response of surface currents to wind stress (Maes et al. 2002; Gasparin and Roemmich et al. 2016). ODYSEA measurements of winds and surface currents allow us to improve the understanding of surface current response to intraseasonal winds (Marin et al, 2009) under a range of wind conditions and rain and stratification climatology as well as the effects of local wind stress versus other forcings (Drushka et al. 2015).

2. MISSION CONTEXT

ODYSEA builds on the scientific understanding of currents contribution to Doppler signals recorded from space and follows a first global Doppler mission proposal "SKIM" for currents and waves that went through a phase A as part of ESA Earth Explorer 11. Unlike SKIM that used a near-nadir observation, which was necessary to resolve waves, ODYSEA uses a pencil beam scatterometer at 55° incidence angle which allows a much wider swath (1700 km), hence a daily revisit, and a stronger sensitivity to wind speed. ODYSEA will be proposed to NASA's Earth System Explorers for simultaneous measurements of ocean-surface winds and currents with 5-km data postings.

The proposal will be submitted in the coming months and it is expected that NASA will eventually implement 2 missions convering different Earth System measurement challenges (ESAS2018). Ongoing activities cover the full range of necessary developments. In particular, the sensor sensitivity to surface currents is being verified with the DopplerScatt airborne demonstrator (Rodriguez et al. 2018) as part of the NASA suborbital S-MODE program (Farrar et al. 2022). Sampling and accuracy trade-offs have been considered in a number of studies (Chelton et al. 2019, Wineteer et al. 2020). Work is also underway to prepare the assimilation of surface current measurements. In this context it is important to separate fast-varying currents, such as near-inertial oscillations (NIOs), from slow-varying motions that are dominated by quasi-geostrophic dynamics. Ubelmann et al. (2020) showed that the 3-day revisit of SKIM was already sufficient to reconstruct most of the NIOs dynamics, and this should be much easier with a daily revisit and the joint measurement of wind and currents.

3. CONCLUSION

Doppler Oceanography from Space (DOfS) has been demonstrated on a number of occasions using either Doppler centroid technique from SAR imagery or SAR Along Track Interferometry. DOfS is now mature enough to allow global monitoring of ocean dynamics at unprecedented spatial and temporal scales. Given the strong coupling of ocean and atmosphere at small scales and the strong connection of wind and currents in the measurement, a Doppler scatterometer is therefore an ideal instrument for probing ocean dynamics and air-sea coupling a the ocean mesoscale.

ACKNOWLEDGEMENTS

REFERENCES

Chelton, D. B., M. G. Schlax, R. M. Samelson, J. T. Farrar , M. J. Molemaker, J. C. McWilliams, J. Gula (2019), Prospects for future satellite estimation of small-scale variability of ocean surface velocity and vorticity, Prog. Oceanogr., https://doi.org/10.1016/j.pocean.2018.10.012

Ekman, V. W. 1905. On the influence of the Earth's rotation on ocean currents. Arch. Math. Astron. Phys., 2, 1-52.

Kelly, K. A., Dickinson S. , McPhaden M. J. , and Johnson G. C. , 2001: Ocean currents evident in satellite wind data. Geophys. Res. Lett., 28 , 2469–2472. https://doi.org/10.1029/2000GL012610

Kelly, Kathryn A., Suzanne Dickinson, and Gregory C. Johnson. "Comparisons of Scatterometer and TAO Winds Reveal Time-Varying Surface Currents for the Tropical Pacific Ocean", Journal of Atmospheric and Oceanic Technology 22, 6 (2005): 735-745, https://doi.org/10.1175/JTECH1738.1

Kessler, W.S., S. Cravatte and Lead Authors, 2021: Final Report of TPOS 2020. GOOS-268, 83 pp. https://tropicalpacific.org/tpos2020-project-archive/reports/

Renault, L., M. J. Molemaker, J. Gula, S. Masson, and J. C. McWilliams, 2016: Control and stabilization of the Gulf Stream by oceanic current interaction with the atmosphere, J. Phys. Oceanogr., 46, 3439–3453, doi:10.1175/JPO-D-16-0115.1.

Seo, Hyodae, Arthur J. Miller, and Joel R. Norris. "Eddy–wind interaction in the California Current System: Dynamics and impacts." Journal of Physical Oceanography 46, no. 2 (2016): 439-459. https://doi.org/10.1175/JPO-D-15-0086.1

Seo, Hyodae, Aneesh C. Subramanian, Hajoon Song, and Jasti S. Chowdary. "Coupled effects of ocean current on wind stress in the Bay of Bengal: Eddy energetics and upper ocean stratification." Deep Sea Research Part II: Topical Studies in Oceanography 168 (2019): 104617. https://doi.org/10.1016/j.dsr2.2019.07.005

Shi, Q. and M. A. Bourassa, 2019: Coupling Ocean Currents and Waves with Wind Stress over the Gulf Stream. Remote Sens. 2019, 11(12), 1476; https://doi.org/10.3390/rs11121476

Ubelmann, C., Dibarboure, G., Gaultier, L., Ponte, A., Ardhuin, F., Ballarotta, M., & Faugère, Y. (2021). Reconstructing ocean surface current combining altimetry and future spaceborne Doppler data. Journal of Geophysical Research: Oceans, 126, e2020JC016560. https://doi.org/10.1029/2020JC016560

SESSION 2

SEA SURFACE SALINITY

A Decade of Advance in Salinity Remote Sensing

T. Lee[1*], J. Boutin[2], N. Reul[3], N. Vinogradova-Shiffer[4]

[1]NASA Jet Propulsion laboratory, California Institute of Technology, Pasadena, California, USA
[2]Sorbonne University, Paris, France
[3]Ifremer, Univ. Brest, CNRS, IRD, Laboratoire d'Oceanographie Physique et Spatiale (LOPS), IUEM, Brest, France
[4]NASA Headquarters, Washington DC, USA

Abstract – Sea surface salinity (SSS), an Essential Climate Variable, is important to research and applications in ocean dynamics, marine biogeochemistry, climate variability, and water cycle. Since 2010, ESA's SMOS and NASA's Aquarius and SMAP missions have pioneered SSS measurements from space. These measurements provide the capabilities to map global SSS on weekly and longer time scales with unprecedented spatial details down to approximately 40-km spatial scale, in complementarity with the in-situ salinity observing system. Satellite SSS have enabled new insights about oceanic physical processes and ocean-water cycle linkages, and advanced research in marine biogeochemistry, ocean state estimation, and climate prediction. Continuity of satellite SSS and improvement of accuracy and spatial resolution, especially for polar oceans, are essential for the integrated salinity observing system.

Keywords: salinity, L-band, passive microwave radiometry

1. INTRODUCTION

Sea surface salinity (SSS) is an Essential Climate Variable of the Global Ocean Climate Observing System and the European Space Agency, and Essential Ocean Variable of the Global Ocean Observing System. SSS is important to oceanic physical processes, marine biogeochemistry, climate variability, and water cycle linkages. Historically, salinity measurements are typically collected from ships and moorings, which are sparse and inhomogeneously distributed in space and time. The development of the Argo array since the mid-2000s is a major advance in salinity observing system. Nevertheless, Argo floats are insufficient to resolve salinity features with spatial scales smaller than hundreds of km and time scales less than a month. The Argo array also has poor coverage in coastal oceans, marginal seas, and polar oceans.

The advent of salinity-measuring satellites since the 2010s has dramatically reduced this observing-system capability gap. Three missions have pioneered SSS measurements from space: the Soil Moisture and Ocean Salinity (SMOS) mission (late 2009 onward) by ESA, the Aquarius/SAC-D mission (2011-2015) by NASA and CONAE, and the Soil Moisture Active Passive (SMAP) mission (2015 onward) by NASA. These satellites use passive microwave radiometry at approximately 1.4-GHz (L-band) frequency to measure sea-surface brightness temperature (T_B) emitted by the upper 1 cm (radiometric depth) layer of the ocean. SSS are retrieved from T_B after corrections for various effects on T_B unrelated to SSS such as those due to sea surface temperature (SST) and wind-induced surface roughness. Aquarius and SMAP have combined Active-Passive sensors that include the integrated L-band radar for surface-roughness measurements, but SMAP's radar ceased operation about 3 months into the mission.

2. SAMPLING AND ACCURACIES

SSS measurements from these satellites cover the global ice-free ocean at approximately weekly intervals. Their spatial resolutions are approximately 35-60 km for SMOS and SMAP and 100-150 km for Aquarius. The spatiotemporal sampling characteristics of SMOS and SMAP allow their SSS measurements to capture the (larger) mesoscale SSS variations in dynamic areas and other transient features such as large river plumes and near-coastal SSS that pose a major challenge for the in-situ observing system.

Much efforts have been made to evaluate the accuracies of gridded (level-3) satellite SSS using gridded in-situ near-surface salinity products typically on monthly, 1° grid. In tropical to mid-latitude oceans, the average discrepancies between monthly, 1° satellite SSS and in-situ near-surface salinity products range from somewhat less than 0.2 pss to approximately 0.3 pss, depending on the product (e.g., Lee et al. 2016, Boutin et al., 2018). The aforementioned estimates of discrepancies are not entirely due to the errors of the gridded satellite SSS because they also include the poorly-documented sampling and mapping errors of the in-situ gridded salinity products on monthly, 1° scales (Lee 2016, Boutin et al., 2016, Vinogradova et al. 2019, Reul et al. 2020). The effect of near-surface salinity stratification on the differences between satellite SSS (for the upper cm of the ocean) and in-situ near-surface salinity, most of which have a shallowest sampling depth of 5 m. If one considers SSS variations only (i.e., excluding time-mean biases), the uncertainties of satellite SSS are smaller, especially for nonseasonal variations (i.e., excluding the seasonal cycles). For example, the averaged upper-bound uncertainty estimate for Aquarius SSS is 0.16 (0.1) pss for temporal (nonseasonal) variations (Lee 2016). The uncertainty also decreases when satellite SSS are averaged over larger scales (Lee 2016, Reul et al. 2020).

The evaluation of along-swath (level-2) satellite SSS measurements using point-wise in-situ salinity measurements has been complicated by the differences in horizontal and vertical samplings between satellite SSS and in-situ salinity measurements as well as the mis-match in sampling time (see Boutin et al 2016 for a comprehensive discussion). NASA's salinity field campaigns SPURS-1 (Lindstrom et al. 2015) and SPURS-2 (Lindstrom et al. 2019) advanced the understanding of small-scale SSS variability and near-surface salinity stratification. The joint ESA-NASA effort on a multi-mission satellite SSS evaluation and exploitation platform (https://www.salinity-pimep.org) aims to further our understanding of satellite SSS accuracies and the effects of sampling differences on the assessment of satellite SSS uncertainties.

3. SCIENTIFIC ACCOMPLISHMENTS

Satellite SSS have enabled new insights about oceanic physical processes and ocean-water cycle linkages, and advanced research in marine biogeochemistry, ocean state estimation and climate prediction. Due to the limited space of this abstract, the following discussion will not include references to the related studies. However, the review articles by Vinogradova et al (2019) and Reul et al. (2020) and the references therein provided comprehensive discussion of the applications of satellite SSS for the aforementioned topics. The presentation in the Ocean From Space 2022 will provide an overview and highlight various examples.

Ocean dynamics. Satellite SSS revealed SSS signatures of many oceanic features that have not been captured or poorly depicted before. For examples, satellite SSS show that the speed of tropical instability waves (TIWs) in the Pacific are different on and off the equator and depends on the phase of El Niño-Southern Oscillation (ENSO), which has significant implication for eddy-mean flow interaction and ocean mixing. SSS variations associated with Atlantic TIWs are found to play a key role in TIW energetics across much of the tropical Atlantic, prompting for further investigation of the relative roles of baroclinic vs. barotropic instabilities that have not been studied adequately due to limited spatiotemporal distribution of SSS observations prior to the L-band satellites. Satellite SSS also revealed haline hurricane wakes and the impact of salt-stratified upper fresh layer on their intensification, providing additional observational evidence for evaluating mixing processes in ocean models and improving hurricane forecasts using coupled models. The spatial resolutions of SMOS and SMAP SSS enabled the tracking of mesoscale SSS features (e.g., associated with Gulf Stream meanders and eddies), opening new area of research in mixed-layer processes and salt/freshwater transport. The possibility of characterizing and quantifying the eddy transport of salt in the ocean surface mixed layer can now rely on the use of satellite observations of SSS. These measurements also greatly facilitated the studies of inter-basin linkages (e.g., between the Pacific and Indian Oceans and between the Bay of Bengal and the Arabian Sea).

Linkages with water cycle and climate variability. Satellite SSS have significantly strengthened the capability to study land-sea linkage and the variability of large river plumes. A prominent example is the discovery of previously unidentified freshwater plume in the Gulf of Mexico as a result of runoff from the Texas-Louisiana shelf caused by severe storms near in that region. The unusually large freshwater plume that rivals the Mississippi River plume has been reported to be devasting to the ecosystem in the northern Gulf. SMAP and SMOS SSS have led to the insight that monsoonal rain and runoff in the Indonesian Seas can substantially weaken the upper-layer transport of the Indonesian throughflow during boreal winter and spring, with significant implications to the transports of heat and other oceanic properties between the Pacific and Indian Ocean. The unprecedented coverage and sampling of satellite SSS have also significantly strengthened our ability to study the linkages of the North Indian Ocean and monsoonal variability. Satellite SSS have the ability to monitor SSS signatures associated with climate variability such as ENSO, Indian Ocean Dipole, and Madden Julian Oscillation, illustrating the interplay of these climate variability with ocean dynamics with potential feedbacks. Satellite SSS have been shown to improve ENSO predictions.

Constraining ocean state estimation. Satellite SSS are being used by increasing numbers of research groups and operational centers to constrain ocean state estimation and to initialize ocean and climate predictions, demonstrating values added in regions where in-situ salinity data are sparse, especially in coastal oceans near river plumes where many ocean models, affected by the use of climatological river discharges and relaxation of SSS to climatology, have poor representations of nonseasonal variation of SSS.

Marine biogeochemistry. Satellite SSS enable global estimation of the spatiotemporal variability of surface-ocean total alkalinity (using linear correlation with SSS), which is important for ocean acidification. Satellite SSS have also been used together with satellite SST, ocean color, and wind measurements to estimate air-sea CO_2 flux.

4. THE WAY FORWARD

The global coverage and unprecedented spatiotemporal sampling of satellite SSS have greatly enhanced the research in ocean, water cycle, climate variability to address societal needs in complementary to in-situ salinity measurements that are more accurate but much sparser. The continuity and enhancement (accuracy and resolution) of satellite SSS are essential to the integrated salinity observing system, especially for polar oceans. The Copernicus Imaging Microwave Radiometer (CIMR) mission (2028) is a necessary next step. Future technology innovation is essential, especially for improving spatial resolution and the accuracy of polar-ocean SSS because of the critical role pf polar-ocean salinity in ocean dynamics and Earth system interactions. NASA's upcoming Arctic Ocean field campaign SASSIE will enhance the understanding of polar-ocean and sea-ice dynamics, thereby gaining insights that will benefit future satellite SSS missions. The SMOS High Resolution concept (in phase A at CNES) looks towards an innovative interferometric concept to reach a 10-km spatial resolution.

REFERENCES

Boutin, J., Y. Chao, W. Asher, et al. (2016). Satellite and in situ salinity: understanding near surface stratification and sub-footprint variability. Bull. Amer. Meteorol. Soc., 97 (8) 1391-1401.

Boutin, J., J.L. Vergely, and S. Marchand, et al. (2018). New SMOS Sea Surface Salinity with reduced systematic errors and improved variability. *Remote Sensing of Envir.*, *214*, 115–134.

Fournier, S., T. Lee, and W. Tang, et al. (2019). Evaluation and intercomparison of SMOS, Aquarius, and SMAP sea surface salinity products in the Arctic Ocean. *Remote Sensing*, *11*(24).

Lee, T. (2016). Consistency of Aquarius sea surface salinity with Argo products on various spatial and temporal scales. *Geophys. Res. Lett.*, *43*(8), 3857–3864.

Lindstrom, E., F. Bryan, and R. Schmitt (2015). SPURS: Salinity Processes in the Upper-ocean Regional Study -The North Atlantic Experiment. Oceanogr. 28(1):14–19.

Lindstrom, E., J.B. Edson, and J.J. Schanze, et al. (2019). SPURS-2: Salinity Processes in the Upper-Ocean Regional Study 2 – The Eastern Equatorial Pacific Experiment. Oceanogr. 32(2): 15-19.

Reul, N., S. Grodsky, and M. Arias, et al. (2020. Sea Surface Salinity estimates from Spaceborne L-band radiometers: an overview of the first decade of observation (2010-2019). Remote Sensing of Env., 242, 111769, https://doi.org/10.1016/j.rse.2020.111769.

Vinogradova, N., Lee, T., and J. Boutin, et al. (2019). Satellite Salinity Observing System: Recent Discoveries and the Way Forward. *Frontiers in Marine Science*, *6*. https://doi.org/10.3389/fmars.2019.00243.

The Copernicus Imaging Microwave Radiometer (CIMR) mission: Benefits for the present-day Copernicus Marine Service L4 Sea Surface Salinity products

D. Ciani[1,*], R. Santoleri[1], G.L. Liberti[1], C. Donlon[2], C. Prigent[3],
A. Pisano[1], A. Storto[1], C. Yang[1], B. Buongiorno Nardelli[4]

1 CNR-Institute of Marine Sciences, 00133, Rome, Italy
2 European Space Agency, ESA-ESTEC, 2201 AZ, Noordwijk, The Netherlands
3 Laboratoire d'Études du Rayonnement et de la Matière en Astrophysique et Atmosphères (LERMA), 75014 Paris, France
4 CNR-Institute of Marine Sciences, 80133, Naples, Italy

Abstract – Sea Surface Salinity (SSS) has been identified as an Essential Climate Variable by the Global Climate Observing System. It is a key element to understand the hydrological cycle, ocean dynamics and marine biogeochemistry at all scales. SSS observations are presently provided by in-situ and satellite sensors, the latter guaranteeing a large scale and synoptic monitoring. The Copernicus Imaging Microwave Radiometer (CIMR) is a future single payload satellite mission of the European Copernicus Expansion program (2027+ timeframe). We tested the potential of the future CIMR SSS observations within the framework of the Copernicus Marine Service SSS operational production. Our results showed that CIMR will guarantee the accuracy and the effective mesoscale resolution of the L4 SSS routinely produced within the Copernicus Marine Service.

Keywords: CIMR, Sea-Surface Salinity, Copernicus Marine Service.

1. INTRODUCTION

The salinity of the ocean is a crucial parameter to investigate the water cycle, ocean dynamics and the marine biogeochemistry from global to regional scales. In the framework of the Global Climate Observing System (GCOS) programme it has been classified an Essential Climate Variable. Salinity affects both the sea water density and the marine carbonate chemistry, making its monitoring crucial to investigate the thermohaline global circulation, the surface and deep circulation, the water mass transformation and the ocean carbon uptake.

In the past, salinity has suffered from poor observational coverage, being uniquely sampled via point-wise in situ observations, impacting the accurate assessment of its spatial variability and dynamics, in particular for the construction of gap-free optimally interpolated fields, e.g., the in situ-based Reanalysis of the Global Ocean Temperature and Salinity (ISAS) (Gaillard et al. 2009). Recently, the characterization of the sea-surface salinity (SSS) has benefited from satellite observations and on their synergy with in situ measurements.

In the framework of the Copernicus Marine Service, a daily, mesoscale resolving SSS multi-year gap-free Level-4 analysis (L4 hereinafter) product was developed by Buongiorno Nardelli et al. 2016 and Droghei et al. 2018. This product is distributed operationally in near real time since late 2018 and relies on a multivariate optimal interpolation (OI) algorithm combining satellite and in-situ SSS with high-resolution satellite L4 SST measurements. The success of this product depends on the continuity of satellite SSS measurements after the SMOS (Soil Moisture and Ocean Salinity) and SMAP (Soil Moisture Active Passive) missions. The Copernicus Imaging Microwave Radiometer (CIMR) measurements, scheduled for the 2028+ timeframe, will be made over a forward scan arc followed ~260 s later by a second measurement over a backward scan arc. Polarised (H and V) channels centered at 1.414, 6.925, 10.65, 18.7 and 36.5 GHz are included in the mission design under study. The real-aperture resolution of the 6.925/10.65 GHz channels is <15 km and 5/4 km for the 18.7/36.5 GHz channels, respectively. The 1.414 GHz channel will have a real-aperture resolution of ~60 km (fundamentally limited by the size of the ~8 m deployable mesh reflector). However, all channels will be oversampled allowing gridded products to be generated at much better spatial resolution. Channel NEdT is 0.2–0.8 K with a goal absolute radiometric accuracy of ~0.5 K. CIMR will fly in a dawn-dusk orbit providing ~95% global all weather coverage every day with one satellite and complete (no hole-at-the-pole) sub-daily coverage of the polar regions (Fig. 1).
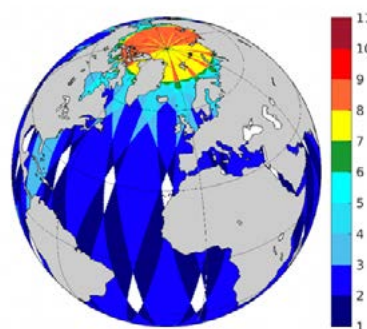
Figure 1. *CIMR – number of daily passes*

CIMR is thus designed to provide global, all-weather, mesoscale-to-submesoscale resolving observations of sea-surface temperature, sea-surface salinity and sea-ice concentration. The availability of the CIMR SSSs with global coverage would represent an opportunity to continue ingesting satellite SSS measurements in the Copernicus multivariate OI, potentially allowing to improve the interpolated product effective spatial resolution and accuracy with respect to L4 analyses built from in situ observations alone. The present study is thus focused at demonstrating this potential.

2. METHODS AND RESULTS

The Copernicus L4 SSS processing chain relies on a multi-dimensional (multivariate) OI technique that combines satellite and in situ retrievals of SSS with higher-resolution

---

satellite sea-surface temperature (SST) information. The algorithm is based on the assumption that SSS and SST covary at spatial scales smaller than those characterizing atmospheric fluxes. This allows us to extract useful dynamical information from the high-pass filtered satellite L4 SSTs for use with the SSS fields, thus guaranteeing the accuracy and effective resolution of the L4 SSS fields (Droghei et al. 2018).

Based on the Copernicus MERCATOR global operational model (Nouel et al. 2019) we implemented an Observing System Simulation Experiment (OSSE) to quantify the CIMR expected impact within the Copernicus Marine Service SSS global L4 products. The MERCATOR model provides 1/12°, daily outputs of 3D temperature, salinity and currents. A one year long (2016) time series of surface outputs was extracted. The MERCATOR SSSs were used to generate synthetic, in situ and CIMR SSS and, at the same time, they provided a reference ground-truth SSS to validate the output of the study. The synthetic SSS were used to run the multi-dimensional OI algorithm in combination with sea-surface temperature information, the latter also extracted from the MERCATOR model. The L4 SSS processing chain is run in two different configurations: once ingesting the synthetic in situ SSS alone and, in a second run, the in situ plus the CIMR observations. In both cases, the result of the processing, i.e., the multivariate OI algorithm, is a L4 SSS global map. Finally, the SSS maps obtained in the two configurations are compared with the original MERCATOR SSS fields, i.e. the ground-truth. The metrics of the comparison are the root mean square error (RMSE) and the power spectral density (PSD).

Looking at case studies in dynamically active regions as the Gulf Stream, we found that if the CIMR observations are not included in the processing chain, the resulting L4 SSSs misrepresent the salinity values as well as the mesoscale activity found in the ground-truth salinity field. Indeed, the optimal interpolation yields smooth fields exhibiting features close to a climatological estimate. The mesoscale activity is only retrieved in proximity of the in situ measurement locations, where the multivariate algorithm can account for the high resolution spatial and temporal information contained in the SST field (Fig. 2). The ground-truth meso- to sub-mesoscale features are well retrieved when the CIMR observations are ingested, yielding improvements in the L4 analysis both in coastal areas and in the open ocean.
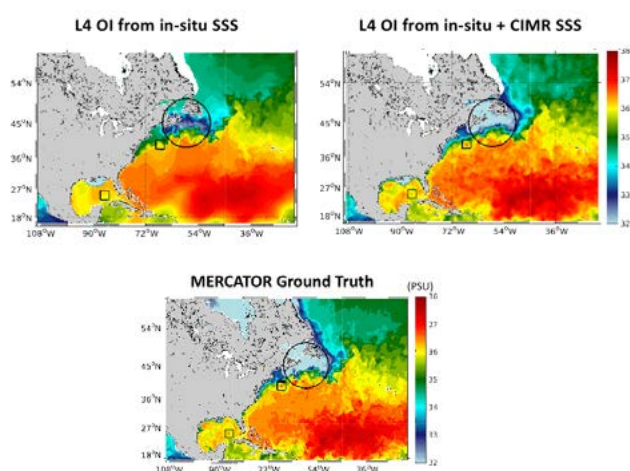
Figure 2. *Top) L4 SSS built without/with CIMR SSS, respectively. Bottom) MERCATOR ground - truth (Jan, 1st 2016).*

The impact of CIMR was also quantified computing the one year long time series of RMSE and mean PSD between the MERCATOR (benchmark) SSS and the L4 SSS computed with/without the CIMR synthetic measurements, respectively. We obtained that, including CIMR in the L4 processing, enabled to systematically reduce the RMSE throughout the year in the 45°S to 90°N latitudinal band, showing improvements up to 50% compared to reconstructions uniquely based on in-situ SSS. Moreover, the PSD analysis confirmed that the CIMR measurements will be crucial to maintain the mesoscale-resolving capability of the Copernicus Marine Service global SSS maps. Similar results were obtained for the retrieval of the surface SSS gradients (Ciani et al. 2019)

3. CONCLUSION

These results indicate that the future SSS observations from CIMR will be crucial for the Copernicus Marine Service global SSS monitoring. Furthermore, the CIMR potential will go even beyond the operational requirements within Copernicus Marine. The application of the CIMR SSS to scientific and societal studies will be wide. The global L4 SSS obtained with CIMR will enable capturing the signatures of the major mesoscale dynamical features, e.g., the main Gulf Stream or Agulhas Rings (Carton, 2001), guaranteeing the monitoring of their spatial distribution and migration pathways. This will contribute to evaluating the global scale SSS distribution and budget. The monitoring of the global SSS is also a key element in studies of water cycle, oceanic water formation and ocean-atmosphere coupled dynamics. The future loss of the SMOS and SMAP missions fully justifies the high priority of the CIMR mission development within the framework of Copernicus.

ACKNOWLEDGEMENTS

REFERENCES

Buongiorno Nardelli, B.; Droghei, R.; Santoleri, R. Multi-dimensional interpolation of SMOS sea surface salinity with surface temperature and in situ salinity data. Remote Sens. Environ. 2016, 180, 392–40

Carton, X. Hydrodynamical Modeling of Oceanic Vortices. Surv. Geophys. 2001, 22, 179–263

Ciani, D., Santoleri, R., Liberti, G. L., Prigent, C., Donlon, C., & Buongiorno Nardelli, B. (2019). Copernicus Imaging Microwave Radiometer (CIMR) Benefits for the Copernicus Level 4 Sea-Surface Salinity Processing Chain. Remote Sensing, 11(15), 1818.

Droghei, R.; Buongiorno Nardelli, B.; Santoleri, R. A New Global Sea Surface Salinity and Density Dataset From Multivariate Observations (1993–2016). Front. Mar. Sci. 2018, 5, 84

Gaillard, F.; Brion, E.; Charraudeau, R. ISAS–V5: Description of the method and user manual. In IFREMER Rapport LPO; LPO: Brest, France, 2009; Volume 9, p. 34

Nouel, L. Global Ocean 1/12 of a Degree Physics Analysis and Forecast Updated Daily—Product User Manual (CMEMS-GLO-PUM-001-024); Issue 1.4; E.U. Copernicus: Brussels, Belgium, 2019

The Climate Change Initiative (CCI) Sea Surface Salinity: Achievements and future perspectives

J. Boutin [1]*, N. Reul[2], A. Martin[3], J. Jouanno[4], R. Catany[5], F. Rouffi[6], R. Sabia[7] and the CCI+SSS consortium

[1]LOCEAN-IPSL laboratory, Paris, France;
[2]LOPS laboratory, Toulon, France;
[3] NOCS, Southampton, UK;
[4] LEGOS laboratory, Toulouse, France;
[5] ARGANS Ltd, Plymouth, UK;
[6] ACRI-st, Sophia Antipolis, France;
[7]Telespazio-UK for ESA, ESRIN, Frascati, Italy

Abstract – **The Climate Change Initiative Salinity project (CCI+SSS) aims to produce a Sea Surface Salinity (SSS) Climate Data Record (CDR) that addresses well-established user needs based on satellite salinity measurements from various spaceborne missions. A ten-year time series (2010-2020) of weekly and monthly global SSS fields at ~50km resolution has been produced. Once representativity errors between punctual in situ SSS and satellite SSS are taken into account, mean uncertainty of weekly CCI+SSS fields is estimated to be 0.14, while the uncertainty of monthly fields is about 0.10. A variety of case studies illustrate several climate-related processes, ranging from large mesoscale SSS variability, e.g. related to the transport of freshwater near river plumes by surface currents, to regional scale variability related to climate events such as El Niño Southern Oscillation or Indian Ocean Dipole. Perspectives for the extension and improvements of the CCI+SSS time series will also be discussed.**

Keywords: Salinity, Climate, Multi-Mission, Uncertainties.

1. INTRODUCTION

Sea Surface Salinity (SSS) is an increasingly-used Essential Ocean and Climate Variable. The Soil Moisture and Ocean Salinity (SMOS), Aquarius, and Soil Moisture Active Passive (SMAP) satellite missions all provide SSS measurements, with very different instrumental features leading to specific measurement characteristics (Reul et al., 2020). The Climate Change Initiative Salinity project (CCI+SSS) aims to produce a SSS Climate Data Record (CDR) that addresses well-established user needs based on those satellite measurements. In this presentation, we will review the user requirements, the methodology followed to merge the various satellite mission datasets, and the performance of the CCI+SSS product as assessed with independent in situ information. Besides, we will provide an inventory of climate-related case studies, and discuss limitations of the present CCI+SSS product and future perspectives for salinity remotely sensed products.

2. USER NEEDS

The community of users of CCI+SSS products is increasingly broad and involves among others climate scientists interested in monitoring evolutions of the water cycle, ocean and climate modelers using SSS to validate or constrain their models, physical oceanographers interested in the dynamical functioning of the ocean at regional and global scale, and more recently developers of operational applications preparing the assimilation of SSS in reanalyses or forecast applications.

Such diversity of users is reflected in a variety of requirements that shaped the development of 1/4° products at 50km, monthly and weekly spatio-temporal resolution with target accuracy of 0.1 (goal) to 0.2 (threshold) for monthly-100km resolution fields. Users are also advocating for uncertainty quantification, long term stability, consistent documentation and easy data access.

3. DATA AND METHODS

To generate a homogeneous CDR, instrumental differences are carefully adjusted based on in-depth analysis of the measurements themselves, together with some limited use of independent reference data (Boutin et al., 2021). An Optimal Interpolation in the time domain without temporal relaxation to reference data or spatial smoothing is applied. This allows preserving the original datasets variability. SSS CCI fields are well-suited for monitoring weekly to interannual signals, at spatial scales ranging from 50 km to the basin scale (Stammer et al., 2021). Each SSS measurement is provided with its corresponding uncertainty.

4. VALIDATION

CCI SSS and their uncertainties have been validated using colocations between CCI+SSS datasets and independent in situ measurements performed at the ESA-NASA Salinity Pilot-Mission Exploitation Platform (Pi-MEP; https://www.salinity-pimep.org/; Guimbard et al. 2021).
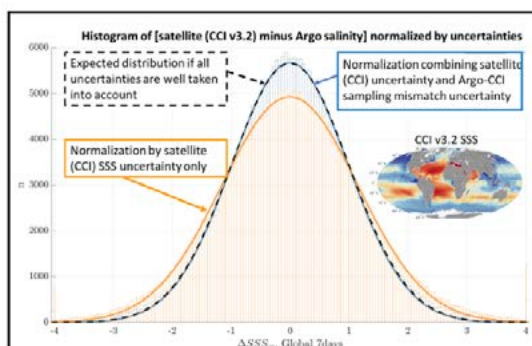
Figure 1. *Distribution of differences between CCI and Argo SSS normalized with uncertainties considering (orange) only CCI+SSS uncertainties, (blue) CCI+SSS uncertainties and sampling mismatch uncertainties over the global ocean. The black line depicts the theoretical Gaussian distribution with standard deviation of 1 which is expected if all uncertainties are correctly estimated (Thouvenin-Masson et al., 2022).*

* Corresponding author. Address: LOCEAN, Sorbonne Universite, Paris, France. Email: jb@locean.ipsl.fr

A particular emphasis has been put in taking into account the sampling mismatch between in situ and satellite SSS (Thouvenin-Masson et al., 2022) (Figure 1). The mean uncertainty of weekly CCI+SSS fields is estimated to be 0.14, the one of monthly fields 0.10.

5. CASE STUDIES

We then show a sample collection of case studies demonstrating the strength of satellite SSS for monitoring SSS variability over the 2010-2020 period. The length of the record allows to identify mechanisms driving the interannual variability of the SSS in the tropical oceans, but also the impacts on other ECVs. In the tropical Pacific Ocean, a co-variability between SSS, Sea Surface Temperature and Chlorophyll is identified and related to ENSO events. In the Bay of Bengal, the Indian Ocean Dipole and associated anomalous coastal currents are shown to influence the fate of the freshwaters originating from river plumes (Akhil et al., 2020). In the tropical western Atlantic Ocean, the processes controlling the spread and extent of the Amazon river outflow are investigated (Reverdin et al., 2021, Gevaudan et al. 2022) and an important impact of the Amazon plume on the air-sea CO_2 fluxes in winter is identified (Figure 2, Olivier et al., 2022).
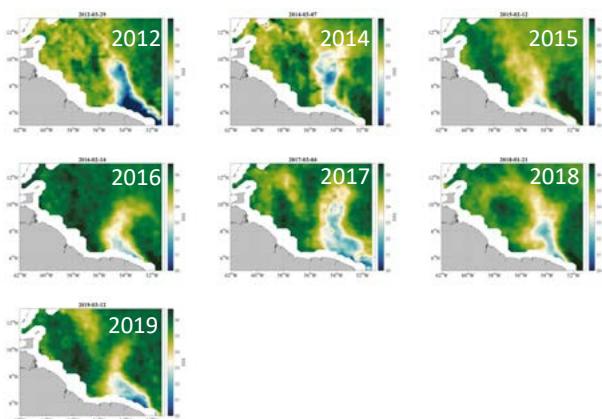
Figure 2. *Fresh plumes originating from the Amazon river in the northwestern tropical Atlantic Ocean during February months. While the Amazon outflow is very small during this period of the year, CCI+SSS fields evidence that fresh water was exported from the plateau to the open ocean in 7 out of 10 years (Reverdin et al. 2021).*

6. DISCUSSION AND PERSPECTIVES

During the CCI+SSS phase 2 (2022-2024), specific efforts will be devoted to reducing SSS uncertainties in polar regions, mitigating radio frequency interferences and extending the time series backward to 2002 in tropical river plumes areas using C/X band radiometer data. The continuation of the climate time series beyond 2022 will rely on the availability of satellite SSS measurements, SMOS is 12.5 years old, SMAP is 7.5 years old. New satellite missions dedicated to SSS measurements are therefore urgently needed.

The ESA CCI+SSS phase 2 consortium gathers scientists and engineers from various European research institutes and companies (LOCEAN/IPSL, LOPS, LEGOS, Mercator-Ocean, Metoffice, NOC, ARGANS, ACRI-st, Adwaiseo) and is conducted in collaboration with US colleagues from NASA and Remote Sensing System.

REFERENCES

Akhil, V. P., J. Vialard, M. Lengaigne, M. G. Keerthi, J. Boutin, J. L. Vergely, and F. Papa (2020), Bay of Bengal Sea surface salinity variability using a decade of improved SMOS re-processing, *Remote Sensing of Environment*, *248*, 111964, doi:https://doi.org/10.1016/j.rse.2020.111964.

Boutin, J., et al. (2021), Satellite-Based Sea Surface Salinity Designed for Ocean and Climate Studies, *Journal of Geophysical Research: Oceans*, *126*(11), e2021JC017676, doi:https://doi.org/10.1029/2021JC017676.

Gévaudan, M., Durand, F., & Jouanno, J. (2022). Influence of the Amazon-Orinoco Discharge Interannual Variability on the Western Tropical Atlantic Salinity and Temperature. Journal of Geophysical Research: Oceans, e2022JC018495.

Guimbard, S., et al. (2021), The Salinity Pilot-Mission Exploitation Platform (Pi-MEP): A Hub for Validation and Exploitation of Satellite Sea Surface Salinity Data, *Remote Sensing*, *13*(22), 4600.

Olivier, L., et al. (2022), Wintertime process study of the North Brazil Current rings reveals the region as a larger sink for CO2 than expected, *Biogeosciences, accepted*, *2022*, 1-30, doi:10.5194/bg-2021-269.

Reul, N., et al. (2020), Sea surface salinity estimates from spaceborne L-band radiometers: An overview of the first decade of observation (2010–2019), *Remote Sensing of Environment*, *242*, 111769, doi:https://doi.org/10.1016/j.rse.2020.111769.

Reverdin, G., et al. (2021), Formation and Evolution of a Freshwater Plume in the Northwestern Tropical Atlantic in February 2020, *Journal of Geophysical Research: Oceans*, *126*(4), e2020JC016981, doi:10.1029/2020jc016981.

Stammer, D., M. S. Martins, J. Köhler, and A. Köhl (2021), How well do we know ocean salinity and its changes?, *Progress in Oceanography*, *190*, 102478, doi:https://doi.org/10.1016/j.pocean.2020.102478.

Thouvenin-Masson, C., J. Boutin, J.-L. Vergely, G. Reverdin, A. C. H. Martin, S. Guimbard, N. Reul, R. Sabia, R. Catany, and O. Hembise Fanton-d'Andon (2022), Satellite and In Situ Sampling Mismatches: Consequences for the Estimation of Satellite Sea Surface Salinity Uncertainties, *Remote Sensing*, *14(8):1878*, doi:https://doi.org/10.3390/rs14081878.

Challenges and Opportunities for Future SSS Remote Sensing from Space

A. Akins*, S. Yueh, S. Brown, T. Lee, S. Misra, A. Fore, W. Tang

Jet Propulsion Laboratory, California Institute of Technology, Pasadena, US

Abstract – While SMOS, Aquarius, and SMAP have opened new doors in the study of sea surface salinity (SSS) in the last decade, these missions have also brought attention to several challenges in SSS remote sensing via microwave radiometry, particularly in regions with colder waters and high near-surface wind speeds. We discuss these challenges and their potential solutions in the context of future planned missions and ongoing developments in microwave radiometer instrumentation. Future missions should prioritize the use of multi-frequency, wide bandwidth radiometers, active/passive instruments, and higher spatial resolution to improve upon available SSS measurements. Lower-cost missions can also be designed to ensure operational continuity.

Keywords: Sea surface salinity, microwave remote sensing.

1. INTRODUCTION

Global measurements of sea surface salinity (SSS) are important for the study of the ocean circulation and consequently for improving climate predictions. Over the past decade, the data from satellites flying with L-band (1.4 GHz) microwave radiometers have been used to produce global SSS records. Among them, the Soil Moisture and Ocean Salinity (SMOS) mission (2009-Present; Font et al., 2009; Boutin et al., 2012), features a synthetic aperture radiometer, the Aquarius/SAC-D mission (2011-2015; Lagerloef et al., 2008) include both a radiometer and scatterometer, and the Soil Moisture Active Passive (SMAP) mission (2015-Present; Entekhabi et al. 2010) includes a conical scanning radiometer and radar (2015 only). Given the success of these missions, ESA has prioritized L-band radiometry as a component of the Copernicus Imaging Microwave Radiometer (CIMR), which is currently under development. CIMR is a multifrequency radiometer (including channels between 1.4-36 GHz), permitting coincident SSS, wind speed and sea surface temperature (SST) measurements which may provide significant insight into air-sea interaction processes.

The principle of SSS remote sensing is based on the response of the L-band brightness temperatures over the ocean to SSS (Yueh et al., 2001; Reul et al., 2020). To achieve high accuracy, the impact of sea surface roughness, galactic radiation, Faraday rotation, and atmospheric gases/aerosols on the observed brightness temperature must be corrected to better than a few tenths of a degree Kelvin. For SMOS and SMAP passive observations, ancillary ocean wind speed and direction products are required to account for ocean surface roughness and the resulting accuracy of their SSS products is about 0.2 practical salinity unit (psu) monthly (Tang et al., 2017; Reul et al., 2020). Taking advantage of radar data, JPL has developed a Combined Active-Passive (CAP) algorithm for simultaneous retrieval of SSS and ocean wind speed (Yueh et al., 2014; Tang et al. 2015). The CAP SSS has an accuracy of about 0.1-0.2 psu in tropics and mid-latitudes (monthly average), superior to other passive-only

products. The future CIMR spacecraft are expected to produce results comparable or superior to Aquarius due to their multifrequency capability (Kilic et al. 2018).

The crucial remaining issues for current SMOS and SMAP SSS products are their poor accuracy at high latitudes (Tang et al., 2018), near sea ice edges (sea ice contamination), and over high wind regions. CIMR's multifrequency approach should permit mitigation of sea ice and high wind effects. However, further enhancement to the CIMR design might be needed to allow more sensitive detection of salinity changes at high latitudes. Both NASA and ESA-funded study teams are working to refine concepts that could enable SSS remote sensing at higher resolution (such as SMOS-HR, Rodriguez-Fernandez et al. 2020) and with greater sensitivity (such as UWBRAD, Demir et al. 2018). While these studies have provided encouraging results, there remains no solid path forward for SSS remote sensing from space beyond CIMR. It may also be necessary to design lower-cost missions with heritage technology that are capable of maintaining continuity in SSS measurements. Such continuity is necessary to ensure continued integration of SSS into climate forecasts.

To assess how different trades in mission design impact the ability of a satellite mission to measure SSS, we have developed a mission simulator capable of generating L1 and L2 equivalent data products for arbitrary mission geometries and instrument characteristics. In this paper, we apply this mission simulator to case studies of SSS remote sensing in challenging environments. We confirm that concurrent observations at higher frequencies and use of wide bandwidth instrumentation are more capable of SSS retreivals in these environments.

2. SSS REMOTE SENSING MISSION SIMULATIONS

Our mission simulator (see Akins et al. 2022) takes inputs of spacecraft orbital information, instrument characteristics, and time-referenced ancillary data to generate forward model brightness temperatures (L1 equivalent) and retrievals of SSS (L2 equivalent). The inputs that most directly affect the quality of retrieved interval-averaged SSS are instrument noise (NEΔT, related to bandwidth and integration time), incidence angle, revisit time, and the accuracy of ancillary data sources. In all simulation cases discussed here, we use the HYCOM model as ancillary data for ocean state parameters and NCEP data products for atmosphere state parameters.

First, we simulate 2 weeks worth of radiometer measurements over the southern pole. SSS measurements in this region are complicated by both the high wind speeds and the weaker sensitivity at L band to SSS changes over colder waters. Bias in the retrieval input ancillary wind data is introduced by shifting the ancillary values by 1 timestep (6 hr. for NCEP data). The results of the averaged SSS retrieval with corrupted winds for different sensor configurations are shown in Figure 1. While, the SMAP-like sensor (top right) suffers significantly in the quality of the retrieved SSS, the CIMR-like sensor exhibits improved performance. This can

* Corresponding author. Address: 4800 Oak Grove Dr., Pasadena, CA, US. Email: alexander.akins@jpl.nasa.gov
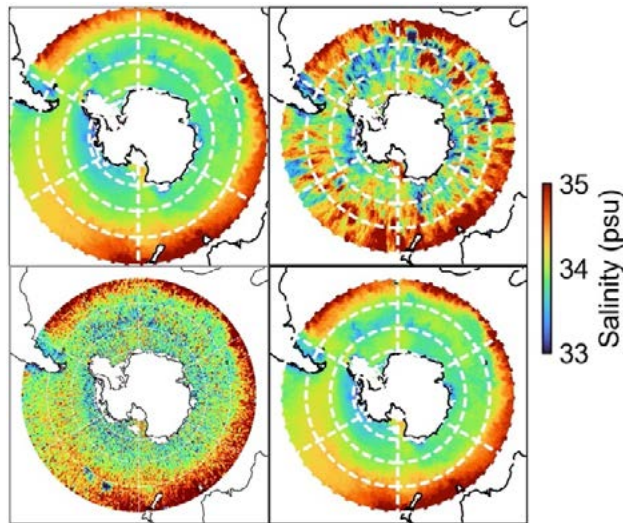
Figure 1. 14 day-averaged SSS over the South Pole from (top left) the HYCOM model, (top right), simulated SMAP SSS retrievals, (bottom left) simulated CIMR SSS retrievals, and (bottom right) simulated CIMR+ SSS retrievals (see text).

Figure 2. 2 day-averaged SSS over the Gulf Stream from (top) the HYCOM model, (middle), simulated SMAP SSS retrievals, and (bottom) simulated constellation SSS retrievals (see text)

be attributed to CIMR's co-boresighted receivers at higher frequencies (6.9-36.5 GHz) which are capable of measuring vector winds, compensating for the ancillary data corruption. While the retrieved SSS is improved, it remains significantly noisier than the model due to the poor cold water SSS sensitivity. In the final simulation (bottom right), the CIMR L band receiver has been replaced with a wideband receiver (1.1-1.7 GHz, denoted CIMR+). The addition of a wideband L band receiver significantly improves the quality of the retrieved SSS relative to the narrowband sensors.

Our second simulation illustrates the capability of different mission geometries to capture phenomena which vary rapidly in time. A SMAP-like architecture is compared against a 3-element, varying-inclination small satellite constellation with high revisit over the Gulf Stream region. While the constellation includes a wideband receiver backend, the frontend of each element consists of a fixed-pointing antenna with both significantly poorer spatial resolution and poorer spatial coverage per track (compensated via use of multiple satellites). Over the chosen date range of HYCOM model output, an eddy with a high salinity core propagates across the stream boundary and dissipates over the course of two days. Figure 2 shows the results of the retrieved SSS averaged over 2 days for each sensor. The constellation average is able to capture the signature of the salty eddy, whereas this feature exists below the noise floor for the SMAP-like observations. While the swath coverage of fixed pointing instruments is inherently poorer, this simulation demonstrates that time-variable phenomenon can still be captured using the improved snapshot accuracy of a wideband L-band receiver (significantly cheaper to implement as a fixed pointing instrument when compared to a conical scanner with a large antenna reflector like SMAP or CIMR).

While not illustrated via simulation here, improvements in spatial resolution for L band radiometers would be of significant value in the observations of fine mesoscale features and in pushing the SSS observing limits closer to the coast. Such higher spatial resolution can be accomplished via large real aperture antennas or via interferometric aperture synthesis.
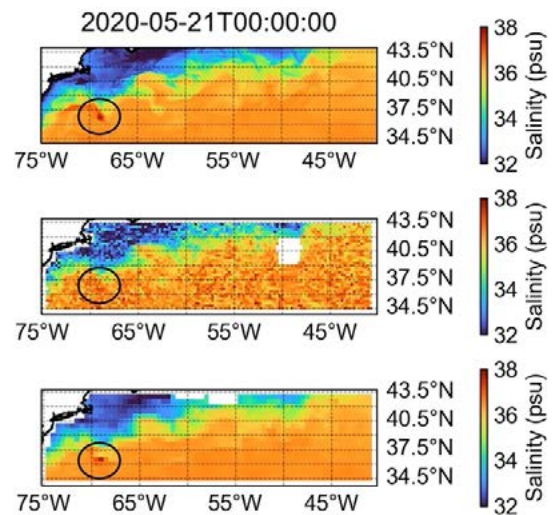
3. CONCLUSION

After over 10 years of measurements, the discipline of SSS remote sensing from space has matured significantly. Still, obstacles remain in retrievals of SSS with high accuracy, temporal, and spatial resolution, particularly in challenging environments such as the polar oceans. While the CIMR mission shows promise for improved retrieval accuracy in high wind speed environments, it is crucial to advance research into observing technologies with greater sensitivity over colder waters (wideband instruments) and higher spatial resolution (interferometers) to improve future spaceborne measurements. We have illustrated here how different outstanding challenges in spaceborne SSS remote sensing can be addressed with such improvements in radiometer technology. Lower cost missions, such as small satellite concepts, can also maintain continuity of SSS observations.

REFERENCES

A. Akins et al., (2022) IEEE International Geoscience and Remote Sensing Symposium.
J. Boutin, et al., (2012) IEEE TGRS, Vol. 50, 5, 1662-1675.
O. Demir, et al., (2018) IEEE International Geoscience and Remote Sensing Symposium.
D. Entekhabi, et al., (2010) Proc. IEEE, Vol. 98, 5, pp. 704-716.
J. Font, et al., (2009) Proc. IEEE, Vol. 98, 5.
A. G. Fore, et al., (2016) IEEE TGR., Vol. 54, 12, 7396-7404.
L. Kilic, et al., (2018) JGR: Oceans, Vol. 123.
G. Lagerloef, et al., (2008) Oceanography, Vol. 21, 1.
N. Reul, et al., (2020) Remote Sens. Environ, Vol. 242, 1.
N. J. Rodriguez-Fernandez, et al., (2020) IEEE International Geoscience and Remote Sensing Symposium.
W. Tang, et al., (2017) Remote Sens. Environ. Vol. 200.
W. Tang, et al., (2018) Remote Sensing, Vol. 10, 6.
S. H. Yueh, et al., (2001) IEEE TGRS, Vol. 39, 1049-1060.
S. H. Yueh, et al., (2013) IEEE TGRS, Vol. 51, 9, 4619-4632.

'Validation and Application of Satellite Derived Sea Surface Salinity (SSS) and Sea Surface Temperature (SST) Gradients in Coastal Regions: Use of the Saildrone Uncrewed Vehicle

J. Vazquez-Cuervo, W. Tang*, M. García-Reyes, J. Gómez-Valdés

Jet Propulsion Laboratory, California Institute of Technology, Pasadena, California, Untied States

Abstract – Coastal regimes are one of the most productive regions of the World's Oceans. Additionally, along with Western Boundary Currents, they are also one of the most dynamic, dominated by submesoscale and mesoscale variability. Here we will present an overview on how the Saildrone uncrewed vehicle has provided a unique opportunity for validating satellite observations – a conjunctive analysis joining in situ and remote sensing to fill the gap of coastal observation. We present the validation of remote sensing derived sea surface temperature and sea surface salinity in coastal areas associated with Baja California and the Arctic. Focus will also be on validating SST gradients in Baja California. An assessment of the results in relation to using satellite derived SST and SSS to monitor critical changes in these regions will be given. The assessment will focus on the need for continued validation and application of gradients to monitor the changes in these regions. We also demonstrate how saildrone data collected along the North American West Coast help to identify issues to improve the land correction algorithm to retrieve satellite SSS closer to land.

Keywords: Symposium, Program, Scientific Themes.

1. INTRODUCTION

The California coast is embedded in one of the world's oceans major Eastern Boundary Currents (Chavez and Messié, 2009), where, in addition to a cool equatorward current, coastal upwelling fuels a productive marine ecosystem. Coastal upwelling, driven by strong alongshore equatorward winds during spring and summer, brings cool, salty and nutrient-rich deep water to the surface, where it is transported offshore by plumes, eddies and other mesoscale and sub-mesoscale activity. At the edges of these features, the fronts, seen as strong gradients on ocean characteristics and convergence of surface flows, are found which result in high concentrations of primary biological productivity (Castelao et al., 2006), that attracts marine life of all trophic levels. Satellite sea surface temperature (SST) and chlorophyll concentration (Chlo) fronts have been largely studied given their importance and relation to the ecosystem but also due to the availability and resolution of remote sense data (Kahru et al., 2012).

Less common is the study of density gradients, given that salinity data has a shorter time span and has a lower resolution. However, a study on fronts using glider data showed (powell and ohman 2015; Olaya et al. (2021)) clear fronts. Also, In a study by Mauzole et al. (2020) results were shown examining the relationship of density gradients to frontal structures. The frontal structures included both upwelling, as well as those associated with mesoscale to submesoscale activity. Using a numerical simulation from the high resolution MIT General Ocean Circulation Model LLC4320 (Adcroft et al., 2004; Forget et al., 2015) they also compared the density fronts due to both SST and SSS to vertical velocity and the location of coastal upwelling. Overall they found density gradients and fronts associated with the coastal upwelling along the Central California Coast, but significantly reduced density gradients along the Baja Coast. The density gradients along the Central California Coast were also associated with stronger vertical velocities. One overall conclusion was that frontal activity along the Baja Coast was driven by possible advection due to the California Current. The research showed explicitly how important the application of satellite derived SST and SSS is to fully understanding coastal dynamics and the relationship to density gradients. This is a crtical finding for understanding the application of both SST and SSS fronts to monitoring critical changes in the coast regions. The derivation of gradients becomes a critical component for such monitoring.

Belkin (2021) reviewed the different methodologies for detecting fronts. A significant number of the methods were based on application of gradients. Thus we will attempt to validate both the SST and SSS gradients using the Saildrone uncrewed vehicle. Additionally, we will apply wavelets to identify the possible fronts associated with those gradients. The goal here is not to develop a new methodology for detecting fronts, but to use the wavelet approach to compare the possible locations of SST and SSS fronts and how they compare to previously derived locations of fronts and upwelling along the California Coast. The validation of both SST and SSS fronts is crucial for applications to understand the role density plays in the dynamics of these coastal regions, specifically tied into the vertical velocities. Thus, a major objective of this work will be to validate the SST and SSS gradients derived from satellites and analyze how well they are reproducing documented areas of coastal upwelling and frontal activity along the California and Baja Coasts, as well as other coastal areas and the Arctic. A secondary objective of the paper will be to build on the results of Vazquez-Cuervo et al (2020) compared SST and SSS gradients with those derived from the Saildrone uncrewed vehicle. A major conclusion from that paper was that even though correlations between SST and SSS collocated values with Saildrone are high, gradient correlations are significantly reduced. This presentation will add to the original study by extending beyond the validation to examine how well the remote sensed SST and SSS products are defining known fronts in the region. For example, are the gradients showing the same fronts as those derived using the Coastal Upwelling Transport Index (Coastal Upwelling Transport Index (CUTI) .index(Jacox, et al., 2018) ?. used in Vazquez-Cuervo et al. (2020) will be applied to this work.

2. RESULTS

The figure below shows the a) mean SST gradients from the Multi-Scale Ultra-High Resolution for June-September 2018.. b) for January 2018 c) mean SSS gradients derived

from NASA's Soil Moisture Active Passive Mission (JPL) for June to September 2018 d) same as c) except for the Remote Sensing Systems Product.
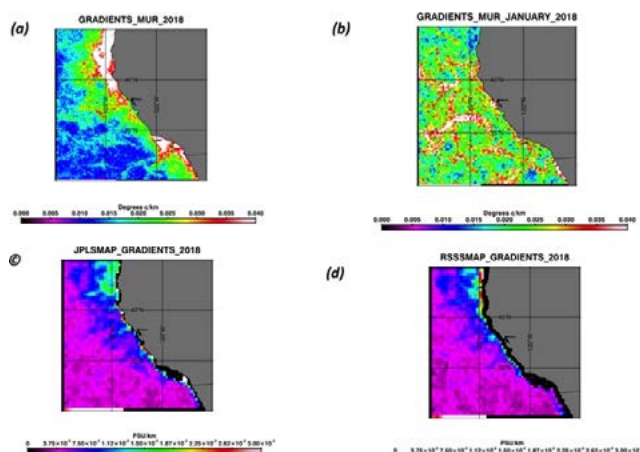
Figure 1 (a,b,c,d): Example Mean sea surface salinity and mean sea surface temperature gradients off the Califonnia Coast for 2018. a) mean SST for June-September 2018 b) Mean for January 2018, c) Mean SSS gradients from SMAP JPL product d) Mean SSS for RSS SMAP product

2. CONCLUSION

Application of remote sensing derived Sea Surface Temperature and Sea Surface Salinity to derive gradients for monitoring changes in coastal upwelling and submesocale dynamics looks very promising based on comparisons with the Saildrone uncrewed vehicle. Comparisons in the Arctic h look promising for possible monitoring of impacts of river discharge, specifically along the Alaskan Coast.

Parameter	Correlation	Bias (Degrees Kelvin/km PSU/km)	RMSD (Degrees Kelvin/km PSU/km)
MUR SST	0.81	0.05	0.21
JPL SSS	0.28	-0.004	0.17
RSS SSS	0.65	-0.01	0.11

ACKNOWLEDGEMENTS

REFERENCES

Adcroft, A.; Hill, C.; Campin, J.-M.; Marshall, J.; Heimbach, P. Overview of the formulation and numerics of the MIT GCM, Proceedings of the ECMWF seminar series on numerical methods, recent *developments in numerical methods for atmosphere and ocean modelling, 2004,* 139– 149.

Belkin, I.M. Remote Sensing of Ocean Fronts in Marine Ecology and Fisheries. *Remote Sen*s. **2021**, 13, 883. https://doi.org/10.3390/rs13050883

Castelao, R.M.; Barth, J.A. Upwelling around Cabo Frio, Brazil: The importance of wind stress curl. *Geophys. Res. Lett.* **2006**, 33, 33. [CrossRef]

Chavez, F, P.; Messié, M. A comparison of Eastern Boundary Upwelling *Ecosystems,Progress in Oceanography*, **2009**, 83 (1-4), 80-96, https://doi.org/10.1016/j.pocean.2009.07.032.

Jacox, M. G.; Edwards, C. A.; Hazen, E. L.; Bograd, S. J. (2018). Coastal upwelling revisited: Ekman, Bakun, and improved upwelling indices for the U.S. West Coast. *Journal of Geophysical Research: Oceans,* **2018**, 123, https://doi.org/10.1029/ 2018JC014187.

Olaya, F.C.; Durazo, R.; Oerder, V.; Pallàs-Sanz, E.; Bento, J.P. Ocean Front Detection with Glider and Satellite-Derived SST Data in the Southern California Current System. *Remote Sens.* **2021**, *13*, 5032. https://doi.org/10.3390/rs13245032

Powell J. R.; Ohman, M. D. Covariability of zooplankton gradients with glider-detected density fronts in the Southern California Current System, *Deep Sea Research Part II: Topical Studies in Oceanography*, **2015**, 112, 79-90, https://doi.org/10.1016/j.dsr2.2014.04.002.

Vazquez-Cuervo, J.; Gomez-Valdes, J.; Bouali, M. Comparison of Satellite-Derived Sea Surface Temperature and Sea Surface Salinity Gradients Using the Saildrone California/Baja and North Atlantic Gulf Stream Deployments. *Remote Sens.* **2020,** 12, 1839. https://doi.org/10.3390/rs12111839

Large mesoscale salinity features detected by SMOS and perspectives for next generation mission

J. Boutin [1]*, G. Alory[2], V. Echevin[1], N. Kolodziejczyk[3], L. Olivier[1], E. Remy[4], N. Reul[3], G. Reverdin[1], A. Supply[3], C. Thouvenin-Masson[1], J. Vialard[1], F. Vivier[1], J.-L. Vergely[5], Y. H. Kerr[6], N. Rodriguez-Fernandez[6]

[1]LOCEAN-IPSL laboratory, Paris, France; [2]LEGOS, Toulouse, FRANCE; [3]LOPS laboratory, Plouzane, France; [4]Mercator-Ocean, Toulouse, France; [5]ACRI-st, Guyancourt, France; [6]CESBIO, Toulouse, France

Abstract – The Soil Moisture and Ocean Salinity (SMOS) mission provides the longest satellite sea surface salinity (SSS) time series (2010-ongoing). Its averaged spatial resolution of ~45km allows to detect large mesoscale structures, density-compensated structures, the influence of freshwater fluxes (rainfall, river plumes) on salinity and, by extension, on the density of sea water. We illustrate them with SMOS results which show the scientific interest of increasing the spatial resolution of satellite salinity measurements. This supports the development of the new SMOS high resolution (SMOS-HR) concept (~10km resolution) under study at CNES (Centre National d'Etudes Spatiales).

Keywords: Salinity, Surface Processes, Freshwater fluxes.

1. INTRODUCTION

The Soil Moisture and Ocean Salinity (SMOS) mission has been launched in November 2009 and is still in operation. It is an Earth Explorer mission of the European Space Agency. It was innovative in two respects: it carried MIRAS (Microwave Imaging Radiometer using Aperture Synthesis), the first L-band radiometer, and the first synthetic aperture radiometer dedicated to observing the earth from space.

The SMOS retrieved sea surface salinity (SSS) represents the longest satellite salinity time series allowing the detection of SSS interannual variations with a better synopticity than that obtained from in situ measurements, and over a longer time periods than that obtained with Aquarius and SMAP missions. Main results obtained with SMOS salinities concern the detection of large mesoscale structures with a spatial resolution (~45km) at least twice better than that obtained with Aquarius measurements and comparable to that obtained with SMAP measurements, the identification of density-compensated structures, the detection of the influence of freshwater fluxes (rainfall, river plumes) on salinity and, by extension, on the density of sea water.

We review some of the main achievements concerning the small-scale features detected with SMOS SSS and we show the scientific value of increasing the spatial resolution of satellite salinity measurements. This supports the development of the new SMOS High Resolution (SMOS-HR) concept studied at CNES (Centre National d'Etudes Spatiales). The SMOS-HR interferometric system aims at providing a spatial resolution of 10km while maintaining an uncertainty on the individual measurement at this resolution of the same order as the one of SMOS measurements at ~45km resolution (~0.5 to 1pss on punctual retrievals, ~0.3pss on 10day averages).

2. SMALL-SCALE FEATURES

SMOS SSS have been used to assess ocean circulation and salt transport in the ocean by eddies [*Delcroix et al.*, 2019; *Hasson et al.*, 2019; *Melnichenko et al.*, 2021]. Indeed, this transport is one of the processes contributing to salinity variations that needs to be taken into account to link salinity and freshwater fluxes, to better characterize water exchanges between upper and deep ocean, and between coastal and open ocean regions. Improved spatial resolution would allow better characterization of mid-latitude mesoscale and sub-mesoscale variability, improve the signal-to-noise ratio and extend these capabilities to the polar oceans.

The assimilation of SMOS and SMAP SSSs in ocean models [*Martin et al.*, 2019; *Tranchant et al.*, 2019] has been shown to improve the accuracy of simulated SSSs by 7 to 12% depending on the models used and the regions, but these authors also point that improving the spatial resolution down to the order of 10 km would represent an even more significant breakthrough [*Martin et al.*, 2020].

In the Gulf of Guinea, [*Alory et al.*, 2021] have shown, by coupling model simulations and satellite measurements, that changes in geostrophic currents and vertical stratification are generated by the Niger River plume and that they warm the coastal upwelling region by up to 1°C near the mouth of the Niger River. This phenomenon has important consequences for fisheries resources, as the upwellings generate nutrient inputs at the surface. At low resolution, ocean model SSS and SMOS SSS are in good agreement. Nevertheless, the spatial resolution of SMOS does not allow a detailed description of the structure of the near-shore SSS, while very strong gradients are present and ocean model simulations remain subject to uncertainties related to river discharge, parameterizations of coastal processes, such as mixing, internal tide...

In the northwestern tropical Atlantic, during the Eurec4A in situ campaign in February 2020, SMOS measurements allowed the identification of a plume of desalinated water from the Amazon and showed that a significant part of this water was transported offshore, with a volume equivalent to the discharge from the Amazon River in January [Reverdin et al., 2021]. There, the small scale features structure the spatial distribution of the air-sea CO_2 fluxes [Olivier et al., 2022]. An improved spatial resolution would allow a detailed description of the processes responsible for the complex circulation (coastal current influenced by bathymetry, filaments, eddies...) of coastal water masses, as shown by a comparison of ocean colour maps (kilometre resolution) and SSS (the spatial structures of Chla and SSS are very often qualitatively coherent in this area) (Figure 1).

At high latitudes, SMOS allows to detect spatial variability of salinity in the Arctic Ocean, in particular related to river plumes [Olmedo et al., 2018; Supply et al., 2020; Tarasenko et al., 2021] (Figure 2). The need for increased resolution is even stronger. It is driven by a description of mesoscale phenomena (in the Arctic Ocean, the synoptic scales are

---

* Corresponding author. Address: LOCEAN, Sorbonne Univierste, Paris, France. Email: jb@locean.ipsl.fr

naturally small of the order of 1-10km); a better monitoring of desalination related to ice melts, by allowing to approach to ~10km of the ice edge against ~50km with SMOS and SMAP satellite measurements; a better filtering of small-scale ice that strongly contaminates the satellite SSS; a better monitoring of desalination from river discharges, as much of the freshwater in the Arctic flows along the coast. These plumes are very poorly reproduced by the models due, among other things, to the lack of knowledge of river flows.
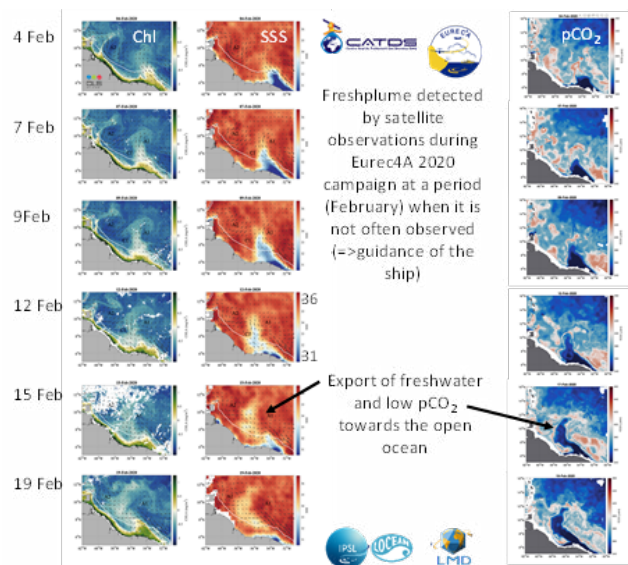
Figure 1. *Left) Satellite Chla, middle) SMOS+SMAP SSS, Right) CO_2 partial pressure. NW tropical Atlantic Ocean (Amazone plume region).*
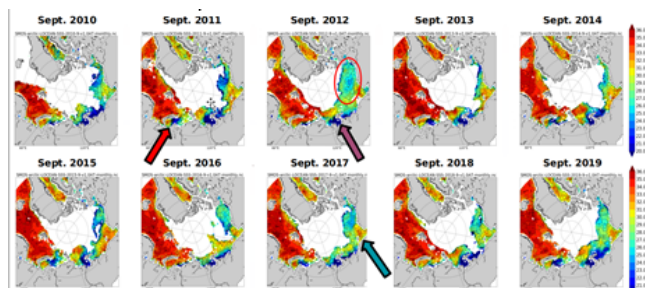
Figure 2. *Interannual variability of SMOS SSS in the Arctic Ocean (Supply et al. 2020) illustrating large variability in the Beaufort Gyre during ice free periods (red circle), related to river runoff in the Laptev Sea and the Lena river plume (purple arrow), in the Kara Sea and Ob and Yenisei river plumes (red arrow), related to the entry of the Pacific waters in the Chukchi and East Siberian Sea (blue arrow).*

Last, a higher resolution would also ease satellite SSS validations as it would reduce sampling mismatch between in situ punctual measurements and satellite spatially integrated SSS.

3. CONCLUSION

Satellite SSS have provided a new mean to monitor SSS at large mesoscale at low to middle latitudes. At high latitude, remotely sensed SSS are very valuable as very few other sources of measurements exist and as these regions are experiencing very large salinity changes related to ice melt and to new freshwater sources. Apart from the potential offered by L-Band radiometry, the SMOS mission has demonstrated the great capability offered by interferometry

to access high spatial resolution with a much lighter antenna than a conventional radiometer. The SMOS-HR concept would allow to monitor smaller SSS features and get closer to the land and ice.

REFERENCES

Alory, G., C. Y. Da-Allada, S. Djakouré, I. Dadou, J. Jouanno, and D. P. Loemba (2021), Coastal Upwelling Limitation by Onshore Geostrophic Flow in the Gulf of Guinea Around the Niger River Plume, *Frontiers in Marine Science*, 7(1116), doi:10.3389/fmars.2020.607216.

Delcroix, T., A. Chaigneau, D. Soviadan, J. Boutin, and C. Pegliasco (2019), Eddy-Induced Salinity Changes in the Tropical Pacific, *Journal of Geophysical Research: Oceans*, 124(1), 374-389, doi:https://doi.org/10.1029/2018JC014394.

Hasson, A., J. T. Farrar, J. Boutin, F. Bingham, and T. Lee (2019), Intraseasonal Variability of Surface Salinity in the Eastern Tropical Pacific Associated With Mesoscale Eddies, *Journal of Geophysical Research: Oceans*, 124(4), 2861-2875, doi:https://doi.org/10.1029/2018JC014175.

Martin, M. J., R. R. King, J. While, and A. B. Aguiar (2019), Assimilating satellite sea-surface salinity data from SMOS, Aquarius and SMAP into a global ocean forecasting system, *Quarterly Journal of the Royal Meteorological Society*, 145(719), 705-726, doi:https://doi.org/10.1002/qj.3461.

Martin, M. J., E. Remy, B. Tranchant, R. R. King, E. Greiner, and C. Donlon (2020), Observation impact statement on satellite sea surface salinity data from two operational global ocean forecasting systems, *Journal of Operational Oceanography*, 1-17, doi:10.1080/1755876X.2020.1771815.

Melnichenko, O., P. Hacker, and V. Müller (2021), Observations of Mesoscale Eddies in Satellite SSS and Inferred Eddy Salt Transport, *Remote Sensing*, 13(2), 315.

Olivier, L., et al. (2022), Wintertime process study of the North Brazil Current rings reveals the region as a larger sink for CO2 than expected, Biogeosciences, 19(12), 2969-2988, doi:10.5194/bg-19-2969-2022.

Olmedo, E., C. Gabarró, V. González-Gambau, J. Martínez, J. Ballabrera-Poy, A. Turiel, M. Portabella, S. Fournier, and T. Lee (2018), Seven Years of SMOS Sea Surface Salinity at High Latitudes: Variability in Arctic and Sub-Arctic Regions, *Remote Sensing*, 10(11), 1772.

Reverdin, G., et al. (2021), Formation and Evolution of a Freshwater Plume in the Northwestern Tropical Atlantic in February 2020, *Journal of Geophysical Research: Oceans*, 126(4), e2020JC016981, doi:10.1029/2020jc016981.

Supply, A., J. Boutin, J.-L. Vergely, N. Kolodziejczyk, G. Reverdin, N. Reul, and A. Tarasenko (2020), New insights into SMOS sea surface salinity retrievals in the Arctic Ocean, *Remote Sensing of Environment*, 249, 112027, doi:https://doi.org/10.1016/j.rse.2020.112027.

Tarasenko, A., A. Supply, N. Kusse-Tiuz, V. Ivanov, M. Makhotin, J. Tournadre, B. Chapron, J. Boutin, N. Kolodziejczyk, and G. Reverdin (2021), Properties of surface water masses in the Laptev and the East Siberian seas in summer 2018 from in situ and satellite data, *Ocean Sci*, 17(1), 221-247, doi:10.5194/os-17-221-2021.

Tranchant, B., E. Remy, E. Greiner, and O. Legalloudec (2019), Data assimilation of Soil Moisture and Ocean Salinity (SMOS) observations into the Mercator Ocean operational system: focus on the El Niño 2015 event, *Ocean Sci.*, 15(3), 543-563, doi:10.5194/os-15-543-2019.

Key drivers of interannual variability in the Laptev Sea from satellite based sea surface salinity

P. Hudson[1,2], A. Martin[2], A. Angeloudis[1], S. Josey[2], A. Marzocchi[2]

1. University of Edinburgh, Edinburgh UK
2. National Oceanography Center, Southampton, UK

Abstract – Laptev Sea processes play a key role in controlling both freshwater distribution around the Arctic and Arctic-wide sea ice state. Understanding variability in the transport of freshwater will be crucial in order to predict changes in the future Arctic system. A number of SMOS and SMAP satellite sea surface salinity (SSS) products are compared with the GLORYS reanalysis over the Laptev Sea. These products are then used to investigate the drivers of interannual variability in Laptev SSS. Zonal wind forcing was found to be the dominant driver of interannual variability and good consensus found between all products; highlighting the potential of satellite SSS for Arctic process studies.

Keywords: Arctic, sea surface salinity (SSS), interannual variability.

1. INTRODUCTION

The Arctic Ocean is relatively small, containing only 1% of total ocean volume, but receives 10% of global river runoff. This river runoff is a key component of the Arctic hydrological cycle, providing significant freshwater exchange between land and ocean. Of this runoff, Russian rivers contribute around half of the total river discharge, or a quarter of the total freshwater to the Arctic Ocean, predominantly to the Kara and Laptev Seas[1]. In these seas, riverine water remains at the surface, helping to form the cold, fresh layer that sits above inflowing warm and salty Atlantic Water. This creates the halocline that governs Eurasian shelf sea, and wider Arctic Ocean, stratification. This fresh surface layer prevents heat exchange between the underlying Atlantic Water and the overlying sea ice, limiting melt and strengthening the existing sea ice barrier to atmosphere-ocean momentum transfer. However, the processes that govern variability in riverine freshwater runoff and its interactions with sea ice are poorly understood and are key to predicting the future state of the Arctic Ocean. Understanding these processes is particularly important in the Laptev Sea as a source region of the Transpolar Drift and a key region of sea ice production and deep water formation[2].

Over most of the globe, L-band satellite acquisitions of sea surface salinity (SSS), such as from Aquarius (2011–2015), SMOS (2010- present), and SMAP (2015-present), provide a new tool to study freshwater storage and transport. However, the low sensitivity of L-band signal in cold water and the presence of sea ice makes retrievals at high latitudes a challenge. Nevertheless, retreating Arctic sea ice cover and continuous progress in satellite product development make the satellite based SSS measurements of great value in the Arctic. This is particularly evident in the Laptev Sea, where gradients in SSS are strong and in situ measurements are sparse. Previous work has demonstrated good consistency of satellite based SSS data against in situ measurements, enabling greater confidence in acquisitions and making satellite SSS data a truly viable potential in the Arctic[3,4].
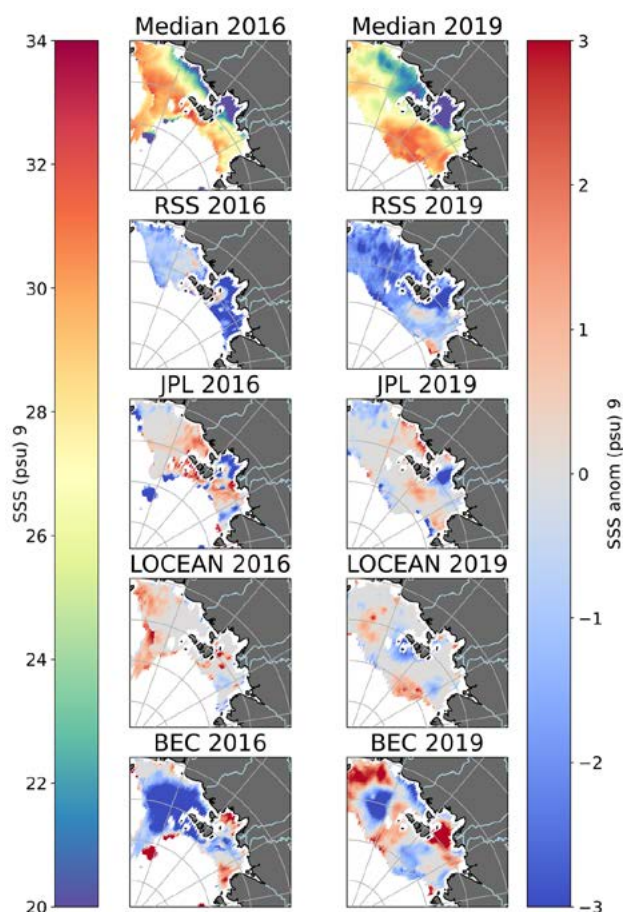
Figure 1. *SSS field in September (9) for the median of 4 products shown over the Laptev Sea with the difference from this median for JPL and RSS SMAP sea surface salinity, and for LOCEAN Artic and BEC Arctic+ SMOS sea surface salinity for (top) 2016 and (bottom) 2019*

2. METHODS

This study combined satellite based SSS data, in-situ observations and reanalysis products to study the roles of Lena river discharge, ocean circulation, vertical mixing and sea ice cover on interannual variability in Laptev Sea dynamics. Comparison of two SMOS products, SMOS LOCEAN CEC L3 Arctic v1.1 and SMOS BEC Arctic L3 v3.1, and two SMAP SSS products, SMAP JPL L3 v5.04.2 and SMAP RSS L3 v4.03 were considered.

Years were identified as being particularly eastward or westward based on the mean ERA5 turbulent surface stress over June-September over the Laptev Sea near the mouth of the Lena River (70-80°N, 120-160°E). A composite analysis of SSS was then conducted using the JPL SMAP, LOCEAN SMOS and GLORYS products. The eastward and westward composites were calculated from the three most eastward and westward years over the relevant satellite period (2011-2020 for SMOS and 2015-2022 for SMAP).
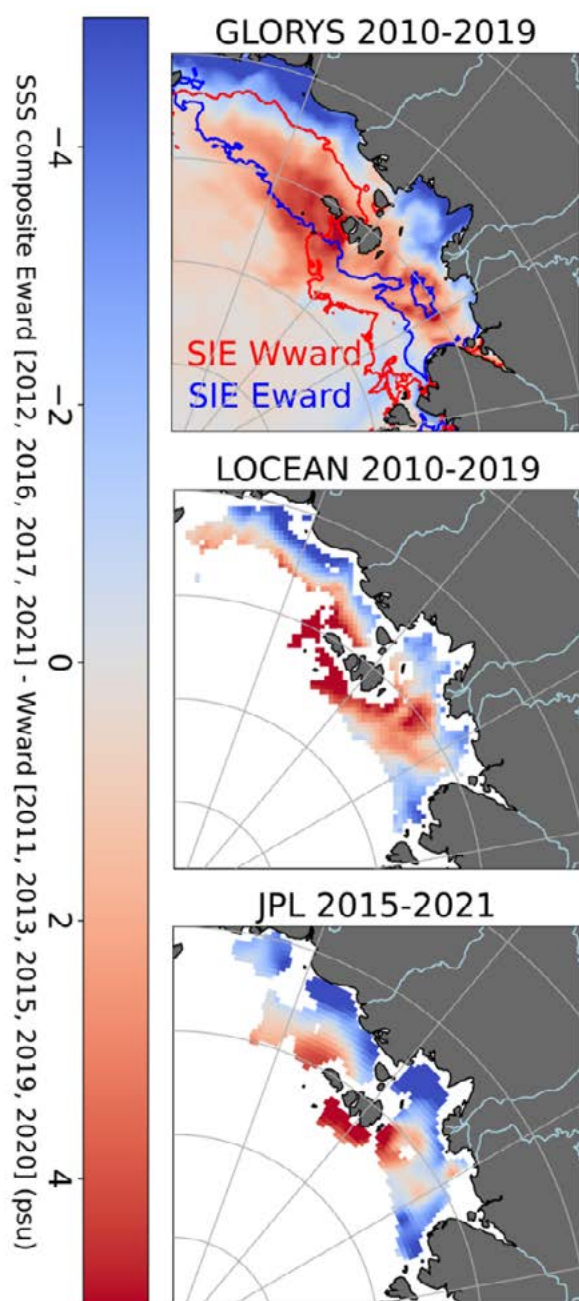
Figure 2. *Composite difference between eastward (2012, 2016, 2017, 2021) and westward (2011, 2013, 2019, 2020) years for GLORYS12 (no 2020, 2021), LOCEAN Arctic (no 2020, 2021) and for JPL SMAP (no 2011, 2012, 2013). The GLORYS mean 1% sea ice contour for eastward (red) and westward (blue) years is overlaid on the GLORYS composite difference.*

3. RESULTS / DISCUSSION

The general patterns of salinity are broadly similar in all products, but their patterns differ interannualy, with particular discrepancies in magnitude. Interannual variability in the LOCEAN SMOS SSS closely resembles that in both SMAP products, most notably in the magnitude and direction of Lena river plume propagation. However, the mean state of SMAP RSS SSS is much fresher than the other products. Comparison against GLORYS reanalysis highlights similar interannual pattern with both SMAP products and SMOS LOCEAN, but with lower amplitude. The close resemblance of the SMOS LOCEAN and the SMAP products gives confidence in using the full SMOS LOCEAN timeseries (2012-present) to study interannual variability on a 10-year time scale.

LOCEAN SMOS and JPL SMAP both indicate that the Lena river plume alternates between several dominant modes of variability. Whilst some years (notably 2018 and 2019) stand out as having a particularly larger, fresher river plume, others have a particularly small, coastally confined plume. These modes of variability have been suggested to control the fate of this fresh water and whether it enters and remains in the Beaufort Gyre or if it enters the Transpolar Drift and transported out of the Arctic[5]. It is hence crucial to understand the drivers of plume variability to understand how the distribution of freshwater in the Arctic might change in future. Here, we show that the spatial distribution of the Lena plume does not appear to be caused by variability in Lena river runoff. Numerical model output and satellite products are used to show that the zonal wind component is the dominant cause of this variability.

4. CONCLUSION

The strong agreement found between GLORYS SSS and all satellite products demonstrates the considerable potential of satellite SSS for Arctic based process studies. This finding is further highlighted by the strong agreement between eastward and westward SSS composites for GLORYS, LOCEAN SMOS and JPL SMAP. SSS composites also reaffirm the dominant role of the zonal wind component in controlling the spatial pattern of the Lena river plume as well as wider Laptev SSS dynamics. Similar composite analysis of Laptev SST and SIC support the dominant role of the zonal wind component and suggest it is also a primary control on heat transport around the Laptev Sea and of September Laptev sea ice extent. This finding highlights that it will be vital to understand and quantify changes in Arctic-wide atmospheric circulation to predict future Arctic sea ice state and future freshwater transport.

REFERENCES

1. Osadchiev, A. A., Pisareva, M. N., Spivak, E. A., Shchuka, S. A. & Semiletov, I. P. Freshwater transport between the Kara, Laptev, and East-Siberian seas. Sci. Rep. 10, 13041 (2020).

2. Reimnitz, E., Dethleff, D. & Nürnberg, D. Contrasts in Arctic shelf sea-ice regimes and some implications: Beaufort Sea versus Laptev Sea. Mar. Geol. 119, 215–225 (1994).

3. Fournier, S., Lee, T., Tang, W., Steele, M. & Olmedo, E. Evaluation and Intercomparison of SMOS, Aquarius, and SMAP Sea Surface Salinity Products in the Arctic Ocean. Remote Sens. 11, 3043 (2019).

4. Supply, A. et al. New insights into SMOS sea surface salinity retrievals in the Arctic Ocean. Remote Sens. Environ. 249, 112027 (2020).

5. Wang, Q., Danilov, S., Sidorenko, D. & Wang, X. Circulation Pathways and Exports of Arctic River Runoff Influenced by Atmospheric Circulation Regimes. Front. Mar. Sci. 8, (2021).

Update of JPL's SMAP Sea Surface Salinity Product – Retrieval with Sea Ice Correction and Validation with in situ Measurements in the Arctic Ocean

W. Tang [1]*, S. Yueh[1], A. Fore[1], A. Hayashi[1], M. Steele[2], and A. Akins[1]

[1]Jet Propulsion Laboratory/California Institute of Technology, Pasadena, California, USA
[2]Applied Physics Laboratory, University of Washington, Seattle, Washington, USA

Abstract – The Combined Active Passive (CAP) algorithm developed at JPL has been used to retrieve sea surface salinity (SSS) over global oceans from measurements of NASA's Aquarius and SMAP missions. In the Arctic Ocean, one of the major challenges of SSS remote sensing is the presence of sea ice. We developed a data-driven ice correction (IC) algorithm which extracts TB representing emission from the water portion of the footprint mixed with water and sea ice, based on estimation of the ice fraction (f_{ice}) and TB of ice derived from adjacent pixels surrounding the footprint under consideration. The IC algorithm is applied to SMAP TB data to obtain TB with ice correction (TB_{IC}), which are used for SSS retrieval using the standard JPL SMAP CAP processing system. We show that the algorithm is most effective near the ice edge, thereby increasing the f_{ice} threshold for possible SSS retrieval to 15% from the current 3% without IC. SMAP SSS are validated using in situ salinity collected in various field campaigns in the Arctic Seas. The next JPL product release (pre-V6.0) will include SMAP SSS with and without IC, and use the most updated dielectric constant model [Boutin et al., 2020].

Keywords: SMAP, sea surface salinity, sea ice, Arctic Ocean.

1. INTRODUCTION

Arctic sea ice has dramatically changed over the last few decades. Areas covered by perennial ice shrank from covering more than two-thirds of the surface area of the Arctic Basin in the late 1970s to about one-third now. In seawater, opened up after seasonal ice melt, low sea surface salinity (SSS) can be a tracer for freshwater changes associated with sea ice melt, river discharge, net precipitation less evaporation, and the advection of relatively low (high) salinity waters from the south from the North Pacific Ocean (North Atlantic Ocean).

SSS fields over global oceans have been observed by three satellite missions based on L-band microwave radiometry: ESA's SMOS, NASA's Aquarius and SMAP. Although L-band sensitivity to oceanic salinity decreases in cold water (especially < 5°C), satellite SSS remains valuable in monitoring Arctic SSS, supported by the finding that the variability of SSS observed in the Arctic largely exceeds the satellite SSS uncertainty (~1 psu) forced by (among other things) sea ice and river discharges variability [Tang et al., 2018; Fournier et al., 2019].

One of the open questions challenging SSS remote sensing in the Arctic is how to isolate and remove the effect of sea ice. We know that at L-band, emissivity or radiometer measured brightness temperature (TB) from the sea ice surface (TB^{ice}) is significantly higher than from the water surface (TB^{water}). Therefore, TB received from a footprint consisting of both ice and water ($TB^{meas.}$) largely exceeds TB^{water}, resulting in false low SSS estimation if a retrieval algorithm designed for homogeneous seawater is used. To avoid this kind of false low signature, a rather strict ice mask or equivalent filter is applied in the current SSS retrieval algorithms, which commonly leave a large data gap near the ice edge.

This study explores the feasibility to retrieve SMAP SSS in the presence of sea ice, in response to the community's desire that SSS information be retrieved as close to the ice edge as possible, to facilitate understanding the linkages between oceanic processes and sea ice changes. Here we present an ice correction (IC) algorithm for SSS retrieval which mitigates the ice effect in measured TB where the measurement consists of emission from both ice and water surfaces [Tang et al., 2021]. SMAP SSS was retrieved in parallel with or without IC using the standard JPL SMAP CAP processing system. Validation was conducted in comparison with in situ salinity data collected in the Arctic Ocean.

2. ICE CORRECTION ALGORITHM

Our data-driven approach aims to obtain TB with ice correction (TB_{IC}) which represents emission from the water portion of in a scene mixed with water and ice. The approach extracts information needed for separating water/ice features from adjacent measurements based on single pixel correction (SPC), which was introduced to improve SSM/I retrieval near the coast [Bennartz, 1999] and recently adopted to improve SMAP soil moisture retrieval [Chaubell et al., 2019].

The IC algorithm is briefly summarized below. Under the assumption that in a footprint mixed with sea ice and water, radiometer measured TB ($TB^{meas.}$) represents the sum of emission from ice and water portion, which is proportional to ice fraction (f_{ice}) and water fraction ($f_{water}=1-f_{ice}$) respectively, we have,

$$TB^{meas.} = (1 - f_{ice})TB^{water} + f_{ice}TB^{ice} \quad (1)$$

where the two unknowns, TB^{ice} and TB^{water}, are assumed to be constant over their respective portion within the footprint. Our approach is to obtain an estimation of TB^{ice} and TB^{water} for each pixel using SMAP measurements in the adjacent area surrounding the pixel under consideration.

The IC algorithm is implemented in a two-pass correction scheme and summarized in **Fig. 1**. For a given $F_{ice}^{thred.}$ (a threshold of sea ice fraction, which is the maximum ice fraction of a TB pixel on which the sea ice correction is applied before SSS retrieval), the TB measurements collected in one satellite orbit are divided into two sets: the "ice" set ($f_{ice} > F_{ice}^{thred.}$), and the "water" set ($f_{ice} < F_{ice}^{thred.}$). In the first

---

* Corresponding author. Address: 4800 Oak Grove Drive, Mail Stop 300/323, Pasadena, California 91109, USA. Email: Wenqing.Tang@jpl.nasa.gov
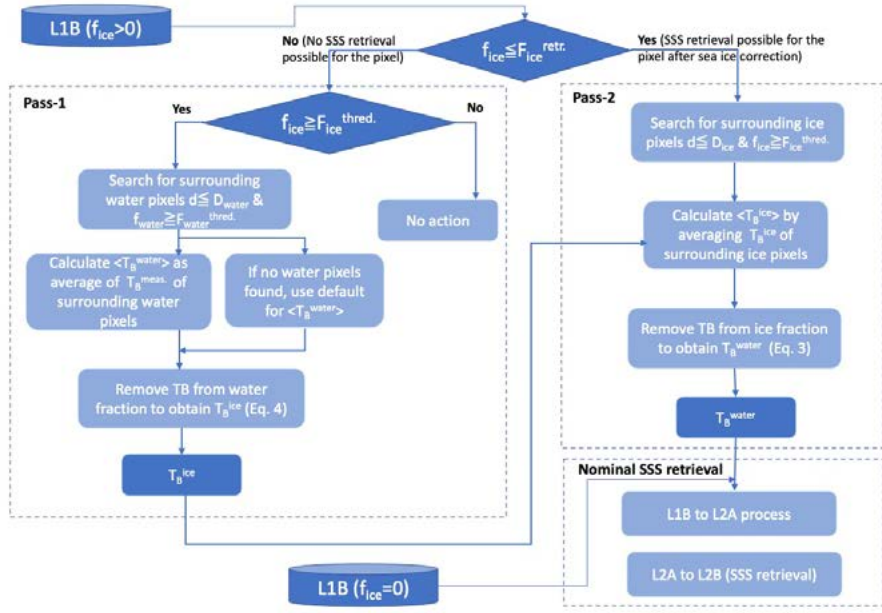
Fig.1. Flowchart of the sea ice correction algorithm.

pass, the process removes the emission from the water portion of each footprint in the "ice" set to obtain TB^{ice}. In the second pass, TB^{ice} obtained in pass-1 are used to calculate TB^{water} for each pixel with $f_{ice} < F_{ice}^{thred.}$. Additional quality controls are implemented to eliminate unrealistic corrections. The output from pass-2 (TB^{water}) is then used for SSS retrieval.

3. VALIDATION

In situ salinity measurements composed from various field campaigns were used to validate SMAP SSS retrieved with or without IC. Here we show one example using data of NASA's Ocean Melting Greenland (OMG) mission from 2016 to 2020 along the Greenland coast. There are a total of 1140 OMG/AXCTD temperature/salinity profiles with OMG data quality control. We use AXCTD salinity measured at a depth closest to surface (i.e. ~0.72 m, denoted as SSS$_{OMG}$). The number of collocations between OMG and SMAP daily gridded salinity increased by more than 30% with IC. The statistical analysis shows a similar retrieval accuracy with or without IC, with the standard deviation of the difference between matchups of OMG and SMAP of 1.41 psu (with IC) and 1.42 psu (without IC). The bias adjusted SMAP SSS (Fig.2) depicts salinity patterns and gradients around Greenland consistent with OMG measurements. We see that SMAP not only depicted the large contrast between the east and west coasts of Greenland consistent with OMG, but also captured small scale salinity features as well as the sharp salinity gradient away from the coast. The fresh area observed in 2018 northwest of Greenland is likely a sampling of the relatively fresh East Greenland Current outflow from the Arctic Ocean, possibly enhanced by Greenland glacial melt.

4. CONCLUSION

With the proposed sea ice correction algorithm, we can obtain SMAP L-band sea surface salinity with improved coverage near the sea ice edge (up to 15% of sea ice fraction) which is significant increase from the current 3% or less for facilitating the understanding of ice melt/formation processes and their impact on the ocean.

Fig. 2. SMAP SSS (with sea ice correction) maps averaged over the period of OMG campaign for each year from 2016 to 2020 (background color), and solid dots are OMG/AXCTD salinity at depth of 0.72m from surface.

REFERENCES

Bennartz, R. (1999). On the use of SSM/I measurements in coastal regions. *J. Atmos. Ocean. Technol.,* vol. 16, no. 4, pp. 417–431, Apr. 1999.

Boutin, J., et al. (2020), Correcting Sea Surface Temperature Spurious Effects in Salinity Retrieved From Spaceborne L-Band Radiometer Measurements, IEEE Transactions on Geoscience and Remote Sensing, 1-14, doi:10.1109/tgrs.2020.3030488.

Chaubell, J. *et al.,* (2019). Improving Brightness Temperature Measurements near Coastal Areas for SMAP. *JSTARS*, 12(11), Nov. 2019, DOI 10.1109/JSTARS.2019.2951323.

Fournier, S., Lee T., Tang W., Steele M. and Olmedo E. (2019). Evaluation and Intercomparison of SMOS, Aquarius, and SMAP Sea Surface Salinity Products in the Arctic Ocean. *Remote Sens.*, 2019, 11, 3043.

Tang, W., Yueh S., Yang D., Fore A., Hayashi A., Lee T., Fournier S., and Holt B. (2018). The potential and challenges of using SMAP SSS to monitor Arctic Ocean freshwater changes. *Remote Sens.,* 2018, 10, 869.

Tang, W., Yueh S., Fore A., Hayashi A., and Steele M. (2021). An Empirical Algorithm for Mitigating the Sea Ice Effect in SMAP Radiometer for Sea Surface Salinity Retrieval in the Arctic Seas. *JSTARS*, VOL. 14, 2021. DOI 10.1109/JSTARS.2021.3127470.

SESSION 3

MODELS, CAL-VAL, ASSIMILATION

Uncertainties in retrieval of remote sensing reflectance from OLCI satellite sensors

A. Gilerson[1,2]*, E. Herrera-Estrella[1,2], J. Agagliate[1], S. Ahmed[1], R. Foster[3], J. I. Gossn[4], D. Dessailly[4] and E. Kwiatkowska[4]

[1]Optical Remote Sensing Laboratory, The City College of New York, New York, NY, USA
[2]Earth and Environmental Sciences, The Graduate Center, New York, NY, USA
[3]Remote Sensing Division, Naval Research Laboratory, Washington, DC, USA
[4]EUMETSAT, Darmstadt, Germany

Abstract – Spectral composition of total remote sensing reflectance R_{rs} uncertainties in Sentinel 3A and 3B OLCI level 2 products is analyzed, taking advantage of the spectral differences between the uncertainty components. Uncertainties were examined at multiple scenes in the open ocean and coastal waters by comparing the retrieved R_{rs} to in-situ measurements made at several AERONET-OC sites and at the MOBY site. It is shown that uncertainties associated with the Rayleigh-type components (molecular scattering and surface effects) as well as water variability proportional to R_{rs}, play the most significant role, while the contributions of other components are usually smaller. Total uncertainties for OLCI have spectral shapes similar to the ones for SNPP VIIRS for the same area but are typically higher at the coastal sites. As previously found for VIIRS, the uncertainties are at least partially attributed to the variability of the Rayleigh optical thickness (ROT) in the atmosphere.

Keywords: Remote sensing reflectance, uncertainties, atmospheric correction.

1. INTRODUCTION

The color of a water body is determined by scattering and absorption of pure water and its natural constituents, which are estimated from the spectra of remote sensing reflectance $R_{rs}(\lambda)$ retrieved in the atmospheric correction process from satellite sensors. This retrieval is strongly affected by the accuracy of modeling of radiances in the atmosphere, sun glint and surface effects (Gordon and Wang, 1992, 1994). It is of paramount importance to accurately estimate radiances at the surface level from these at the top of the atmosphere (TOA), since any uncertainties will propagate into the retrieval of water parameters, characteristics of in-water particulates, concentrations of chlorophyll-a and detection of algal blooms (IOCCG, 2019).

Atmospheric correction uncertainties stem at least partially from the estimation of aerosol models, and from air-water interface effects due to sky and Sun light reflections at the wind-roughened air-water interface.

The estimation of uncertainties can be carried out by comparison of the parameters determined from satellite imagery with the "true" values, which include *in situ* measurements from autonomous systems on offshore platforms such as the AERONET-OC Network (Zibordi et al., 2009), buoys like Marine Optical BuoY (MOBY) and from ships (Moore et al., 2015). Specifically, in Moore et al., 2015 it was found that R_{rs} uncertainties are generally highest in the blue part of the spectrum in both clear and coastal waters with some spectral features visible in the green part of the spectra at coastal sites. Recently, R_{rs} uncertainties determined from the comparison of data from SNPP VIIRS sensor and *in situ* (MOBY and AERONET-OC) were decomposed into their spectral components based on the differences in spectral shapes of these components (Gilerson,

et al, 2022). It was shown that the main uncertainties come from the Rayleigh-shaped component. It was also noticed that the shape of Rayleigh uncertainties is similar to the uncertainties due to the standard deviations of gains in the process of sensor vicarious calibration. In this work, a similar approach is applied to the analysis of the uncertainties from Sentinel 3A and 3B OLCI sensors. Total uncertainties for these sensors were recently analyzed in a very rigorous manner (Zibordi, et al, 2022). The focus of this work is the identification of their main spectral components.

2. SPECTRAL COMPOSITION OF UNCERTAINTIES

Uncertainties for $R_{rs}(\lambda)$ were calculated from the comparison of Sentinel 3A and 3B OLCI Collection 3 data with the data from MOBY and six AERONET-OC stations, which include USC, WaveCIS, LISCO in the US and Venise, Gloria and Helsinki Lighthouse in Europe. OLCI data had only a subset of the recommended flags applied to increase the matchup numbers (EUMETSAT, 2022). Satellite bands were 412, 443, 490, 560, and 665 nm and AERONET-OC bands were 412, 443, 490, 551, and 667 nm. Due to the strong $R_{rs}(\lambda)$ gradient around 560 nm, R_{rs} (551) was multiplied by 1.1 in coastal waters and divided by 1.1 at MOBY and USC. The standard deviation, which characterized uncertainty in remote sensing reflectance retrieval $\sigma(\lambda)$ in sr^{-1}, was assumed to be equal to the root mean square difference (RMSD) from all matchups for each station. Taking into account the main components of the total radiance at the top of the atmosphere (TOA) $L_t(\lambda)$, the variance of $\sigma(\lambda)$ for $R_{rs}(\lambda)$ in sr^{-1} was considered as

$$\sigma^2 = (\sigma_t^2 + \sigma_R^2 + \sigma_a^2 + \sigma_g^2)/t^2 + \sigma_{surf}^2 + \sigma_{water}^2$$

where corresponding variances on the right-hand side are due to vicarious calibration (VC) in σ_t, Rayleigh scattering, aerosols, glint, surface reflectance and water variability respectively and t is the diffuse transmission. VC variances were determined as $\sigma_{vc}(\lambda) = \sigma_{gains}(\lambda)L_t(\lambda)/E_d(\lambda)$, where $\sigma_{gains}(\lambda)$ is the standard deviation of gains (unitless) for S3A and S3B OLCI from EUMETSAT processing. While surface effects are usually simulated as a part of the Rayleigh component, in this model these two components were separated because they have slightly different spectra. The main assumption of the model was that the spectra of standard deviations of the above components are proportional to the spectra of the corresponding radiance components normalized by the downwelling irradiance $E_d(\lambda)$, and that σ_{water} was proportional to $R_{rs}(\lambda)$. Radiance components themselves were determined at each site as the mean of radiances at the available illumination-viewing parameters, aerosol optical thicknesses and Angstrom coefficients. Proportionality coefficients for each component at each site were determined through a MATLAB optimization

procedure of the sum of spectral variances into the total variance, thus determining the contribution of each component to the total variance. In the first run, the VC component was not considered, and it was considered in the second run. For more robust fitting, the procedure was carried out on the normalized spectra.

Examples of the spectral decomposition of uncertainties for two stations, MOBY and Venise, when VC were not considered, are shown in Figure 1. This demonstrates that main contributions to uncertainties are different between the two sites and come from surface effects and water variability for MOBY and from Rayleigh, water and aerosol components for Venice. When VC were included in the fitting procedure, due to their spectral similarity to the Rayleigh-type components (this includes Rrs spectrum at MOBY), spectra related to standard deviations of gains converted into R_{rs} uncertainties became the dominant components in all total uncertainties' spectra, with examples shown in Figure 2. It should be noted that the number of matchups for OLCI is about 10 times smaller than for VIIRS, which affects the quality of matchups and decomposition procedures. The spatial resolution of both sensors is also different, i.e. OLCI is 300 m and VIIRS is 750 m.

Comparison of uncertainties spectra at selected stations for OLCI and for VIIRS (Gilerson et al, 2022) showed that OLCI and VIIRS uncertainties were similar spectrally. At the same time, OLCI uncertainties for both 3A and 3B satellites were typically higher than those for VIIRS at Venise and other coastal sites.
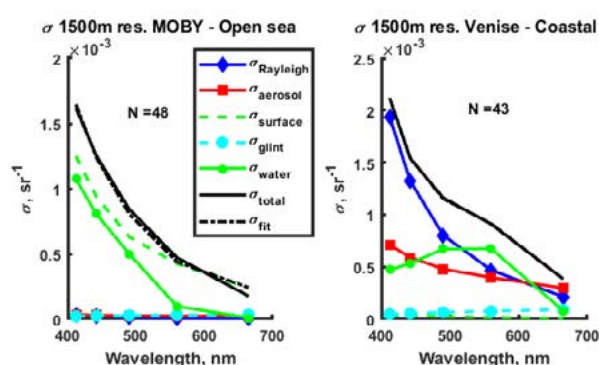
Figure 1. Spectral composition of R_{rs} uncertainties retrieved from OLCI S3B at the MOBY and Venise AERONET-OC sites.
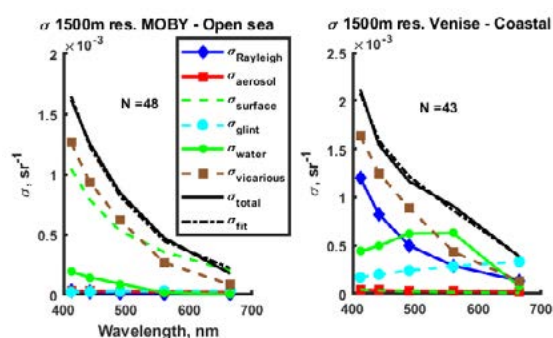
Figure 2. Spectral composition of Rrs uncertainties retrieved from OLCI S3B at the MOBY and Venise AERONET-OC sites with VC uncertainties included into the model.

It can be assumed that, as in VIIRS, main uncertainties are related to the variability of surface effects and the Rayleigh optical thickness. These uncertainties are further slightly amplified by OLCI sensor-specific effects at the oastal sites due probably to either design features and/or differences in processing schemes: these effects should be studied further.

The contribution of water variability to total uncertainty at the Venise site is responsible for the spectral feature at 550 nm, it is typical for coastal areas and is non-negligible. It is also possible that the model applied in this analysis underestimates the contribution of uncertainties related to the effects of inaccurate aerosol models, especially in the presence of absorbing aerosols. However, effects of absorbing aerosols were determined to be present in small or non-existent quantities at all stations considered in this study.

3. CONCLUSION

The recently developed model for estimating of the spectral composition of R_{rs} uncertainties from satellite sensors is applied to the analysis of uncertainties from OLCI S3A and S3B sensors, showing that as in the case of VIIRS, the main component in uncertainties are surface effects and Rayleigh-like shapes associated with molecular scattering, with additional features coming from water variability. The contribution of other components is found to be typically much smaller.

REFERENCES

EUMETSAT, https://www.eumetsat.int/media/48139, 2022.

Gilerson, A., E. Herrera-Estrella, R. Foster, J. Agagliate, C. Hu, A. Ibrahim, and B. Franz (2022). Determining the Primary Sources of Uncertainty in Retrieval of Marine Remote Sensing Reflectance from Satellite Ocean Color Sensors. Frontiers in Remote Sensing.

Gordon, H. R. and Wang, M. (1992). Surface-roughness considerations for atmospheric correction of ocean color sensors. I: The Rayleigh-scattering component. Appl. Opt. 31(21), pp. 4247–4260.

Gordon, H. R., and Wang, M. (1994). Retrieval of water-leaving radiance and aerosol optical thickness over the oceans with SeaWiFS: a preliminary algorithm. Appl. Opt. 3, pp. 443–452.

IOCCG (2019). Uncertainties in Ocean Colour Remote Sensing," in Reports No. 18 of the International Ocean-Colour Coordinating Group, ed F. Mélin (Dartmouth, NS: IOCCG).

Moore, T.S., Campbell, J.W., and Feng, H. (2015). Characterizing the uncertainties in spectral remote sensing reflectance for SeaWiFS and MODIS-Aqua based on global in situ matchup data sets. Remote Sens. Environ. 159, pp. 14-27.

Zibordi, G., Mélin, F., Berthon, J.F., Holben, B., Slutsker, I., Giles, D., D'Alimonte, D., Vandemark, D., Feng, H., Schuster, G., et al. (2009). AERONET-OC: A Network for the Validation of Ocean Color Primary Products. J. Atmos. Ocean Technol. 26(8), pp. 1634-1651

G. Zibordi, E. Kwiatkowska, F. Melin, M. Talone, I. Cazzaniga, D. Dessailly, J. I. Gossn, "Assessment of OLCI-A and OLCI-B radiometric data products across European seas," Rem. Sens. of Environm. 272 (2022).

On the AERONET-OC L_{WN} uncertainties: a re-evaluation

I. Cazzaniga*, G. Zibordi

European Commission, Joint Research Centre (JRC), Ispra, Italy

Abstract – The Ocean Color component of the Aerosol Robotic Network (AERONET-OC) aims at supporting the assessment of satellite ocean color radiometric products with *in situ* reference data derived from automated above-water measurements. This study, benefitting of recent network advances, revisited the uncertainty estimates formerly provided for the normalized water-leaving radiance L_{WN}. Relative and absolute uncertainty values were determined for various sites together with contributions from each source of uncertainty affecting measurements. Results show uncertainties generally increasing with the optical complexity of water and wind speed.

Keywords: *In situ* data, uncertainties.

1. INTRODUCTION

Primary ocean color radiometric product is the spectral normalized water-leaving radiance L_{WN}. Satellite-derived L_{WN} are matter of extensive validation programs aiming at verifying the compliance of their uncertainties with mission requirements. The assessment implies accessing to highly accurate *in situ* reference data exhibiting uncertainties quantified in agreement with metrology principles. The Ocean Color component of the Aerosol Robotic Network (AERONET-OC) was specifically conceived to support the assessment of satellite L_{WN} products through automated *in situ* measurements performed from offshore fixed structures in a variety of water types (Zibordi et al., 2021, 2009).

Benefitting of advances in AERONET-OC data measurements and data processing, this work aims at revisiting the AERONET-OC L_{WN} uncertainties formerly quantified by Gergely and Zibordi (2014) following the *Guide to the Expression of Uncertainty in Measurement* (GUM, JCGM, 2008). Relevant advances are: i. the availability of time-series produced with CE-318T 12-band instruments exhibiting higher measurement frequency when compared to those performed with the former CE-318 9-band instruments; ii. a recent rigorous quantification of uncertainties affecting absolute radiometric calibrations; iii. the potential for a more accurate estimate of the uncertainties affecting corrections for the in water bidirectional effects; iv. the determination of uncertainties affecting the sea surface reflectance factor on a measurement-by-measurement basis (Zibordi et al., 2021). This work additionally investigates the potential for relationships to statistically estimate uncertainties for L_{WN} regardless of site and ideally of wavelength, as already proposed by Zibordi et al. (2022).

2. MATERIALS AND METHODS

Version 3 Level 2.0 L_{WN} data from CE-318T instruments were considered from AERONET-OC sites representative of a variety of water types: Casablanca Platform (CPL) exhibiting frequent occurrence of Case-1 waters; the Acqua Alta Oceanographic Tower (AAOT), the Galata Platform (GLT) and the Section-7 Platform (ST7) characterized by

optically complex waters with varying concentrations of sediments and chromophoric dissolved organic matter (*CDOM*); finally, the Gustaf Dalen Lighthouse Tower (GDLT) and Irbe Lighthouse (ILT), characterized by very high concentrations of *CDOM*.

AERONET-OC instruments allows for the determination of the spectral water-leaving radiance L_W from *in situ* measurements of the total radiance from the sea L_T and of the sky radiance L_i, according to

$$L_W(\lambda, \theta, \varphi, \theta', \theta_0) = L_T(\lambda, \theta, \varphi, \theta_0) - \rho(\theta, \varphi, \theta_0, W)\, L_i(\lambda, \theta', \varphi, \theta_0)$$

where θ (set to 40°) is the sensor sea-viewing angle, θ' (with $\theta' = 180° - \theta$) the sensor sky-viewing angle, φ the sensor relative azimuth angle with respect to the sun (set to 90°), and θ_0 the sun zenith angle. The term ρ is the sea surface reflectance factor that quantifies the sky radiance reflected by the sea surface into the field of view of the sensor. Its value is a function of the viewing and illumination geometries, and of the sea state conveniently expressed through the wind speed W (Mobley, 1999). In the current AERONET-OC processing, W is extracted from the *National Centers for Environmental Prediction* (*NCEP*) data products.

The normalized water leaving radiance L_{WN} is thus determined from

$$L_{WN}(\lambda) = L_W(\lambda, \theta, \varphi, \theta', \theta_0)\, C_Q(\lambda, \theta, \varphi, \theta_0, W, \tau_a, IOP) C_A(\lambda, \theta_0, \tau_a, D)$$

where C_Q is the correction applied to normalize L_W for the in-water bidirectional effects as a function of the viewing and illumination geometries, wind speed, atmospheric and marine optical properties expressed through the aerosol optical depth τ_a and the water inherent optical properties IOP, respectively. Finally, the term C_A is used to minimize the dependence on illumination conditions.

The methodology applied in this study for the quantification of L_{WN} uncertainties relies on GUM guidelines and is equivalent to that implemented by Gergely and Zibordi (2014). The combined uncertainty $u_c(L_W)$ for the spectral values of L_W were determined from the quadrature sum of the uncertainties affecting L_T, L_i and ρ (hereafter indicated by $u(L_T)$, $u(L_i)$ and $u(\rho)$). The value of $u_c(L_{WN})$ was instead determined considering the additional uncertainties affecting C_Q and C_A, hereafter defined as $u(C_Q)$ and $u(C_A)$, respectively.

$u(L_T)$ and $u(L_i)$ were determined from the uncertainties estimated for absolute radiometric calibrations and sensitivity decay (both site-independent), and environmental perturbations. These latter are due to sea surface roughness and on a lesser extent by changes in in-water optical properties or illumination conditions during measurement sequences. They were quantified through the median of coefficients of variation (*CV*s) calculated with triplicates (triplets) of spectral L_T and L_i determined within a time interval typically shorter than 10 minutes. This solution,

* Corresponding author. Address: Via E. Fermi, 2749, Ispra (VA), Italy. Email: Ilaria.Cazzaniga@ec.europa.eu

allowed by CE-318T instruments, led to a more accurate quantification of the impact of environmental perturbations occurring during measurement sequences and consequently of those perturbations strictly related to the measurement methodology itself. The effects of correlations on combined uncertainty values were introduced considering only the correlation between L_i and L_T, which show correlations generally higher than those exhibited by other quantities.

$u(\rho)$ was quantified as the quadrature sum of two contributions: the uncertainty associated with *NCEP* estimates of W (assessed through the comparison with *in situ* measurements at AAOT) and the one associated with the L_T data reduction method. This consists in averaging the lowest 2 out of 11 measurements of the total radiance from the sea from each measurement sequence. This processing implies that the computed L_T may not be statistically represented by the associated W value, but rather by a lower one. The impact of such a data reduction process was defined by the median of the *CV*s between ρ calculated with $W = W_{NCEP}$ and alternatively with $W = 0$.

$u(C_A)$ largely depends on that assigned to the diffuse atmospheric transmittance. Its relative value was tentatively set to 1.5% (which is probably underestimated). Conversely, the relative value of $u(C_Q)$ varies depending on the wavelengths and the type of water according to Talone et al. (2018). Uncertainties were determined for both the Chlorophyll-a (*Chla*) based and Inherent Optical Properties (IOP) based corrections for in-water bi-directional effects included in the AERONET-OC data products. Corresponding L_{WN} values are indicated as L_{WN}^{Chla} and L_{WN}^{IOP}, respectively.

Finally, site-dependent temporal variabilities were estimated benefitting of the enhanced measurement frequency of CE-318T instruments. The variability was quantified by determining *CVs* from pairs of $\bar{L}_{WN}$ for 1, 2 or 3 hours delay, where $\bar{L}_{WN}$ indicates values of L_{WN} averaged across existing triplets performed within a ± 4 hours interval centered at local noon.

3. RESULTS

Overall, the revisited uncertainties determined for L_{WN}^{Chla} do not significantly differ from the previous proposed by Gergely and Zibordi (2014). This is largely explained by compensations enacted in their quantification by the increase or decrease of diverse contributions. The quantified uncertainties exhibit values varying from above 3% at 490 nm for CPL, and up to approximately 25% at 400 nm in *CDOM*-dominated waters.

The largest contribution to combined uncertainties is the sea surface reflectance factor ρ explained by the uncertainties in wind speed and in the data reduction method leading to the determination of L_T. This is particularly evident at those sites characterized by larger median values of wind speed. For the remaining sites such as CPL and AAOT, a large fraction of the total uncertainty is explained by the contributions due to correction factors for bidirectional effects determined with the *Chla*-based method. The data reduction analysis shows that restricting the dataset to measurements characterized by $W<3$ m s^{-1}, or $\theta_0<45°$ or *Chla*<0.7 mg m^{-3} leads to a reduction of the uncertainties.

The analysis of potential relationship between L_{WN} and associated uncertainties confirmed the solution formerly proposed by Zibordi et al. (2022), still at the expense of applying two different linear relationships, to accommodate an increased spectral dispersion between radiances and uncertainties as shown in Figure 1. Nevertheless, a single linear relationship is instead applicable for measurement

conditions characterized by $W<3$ m s^{-1}, due to a reduction of the dispersion between median spectral radiances and related uncertainties.

Regarding the impact of temporal variability, simply considering a time difference $\Delta_t=1$ hour between satellite and *in situ* data, the combined values accounting for L_{WN} uncertainties and contributions due to temporal variability are generally confined below 5% in Case-1 and moderately optically complex waters (i.e., at CPL and AAOT) in the blue-green center-wavelengths. Conversely, they exceed 5% at the other AERONET-OC sites considered in the study, or for larger Δ_t.
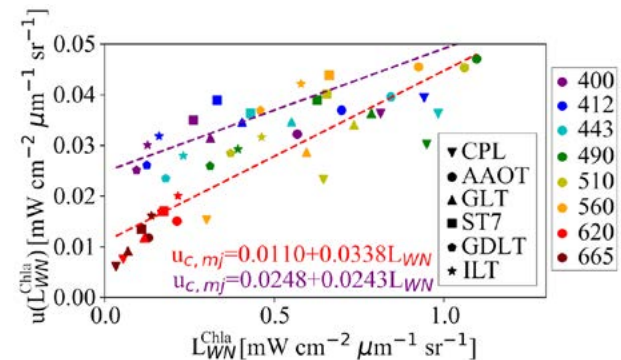
Figure 1. Scatterplot of median L_{WN} values (normalized through *Chla*-based method, L_{WN}^{Chla}) versus corresponding uncertainties $u_c(L_{WN}^{Chla})$. The purple and red dashed lines indicate robust linear regressions determined solely using the Black and Baltic seas "blue-bands" and, alternatively, all the remaining data.

REFERENCES

Gergely, M., Zibordi, G. (2014). Assessment of AERONET-OC LWN uncertainties. Metrologia 51, 40–47.

JCGM (2008). 'Evaluation of measurement data — Guide to the expression of uncertainty in measurement'. Int. Organ. Stand. Geneva ISBN 50, 134.

Mobley, C.D. (1999). 'Estimation of the remote-sensing reflectance from above-surface measurements'. Appl. Opt. 38, 7442.

Talone, M. et al. (2018). Correction for the non-nadir viewing geometry of AERONET-OC above water radiometry data: an estimate of uncertainties. Opt. Express 26, A541.

Zibordi, G. et al. (2009). AERONET-OC: A Network for the Validation of Ocean Color Primary Products. J. Atmos. Ocean. Technol. 26, 1634–1651.

Zibordi, G. et al. (2021). Advances in the Ocean Color Component of the Aerosol Robotic Network (AERONET-OC). J. Atmos. Ocean. Technol. 38, 725–746.

Zibordi, G. et al. (2022). 'Uncertainty Estimate of Satellite-Derived Normalized Water-Leaving Radiance'. IEEE Geosci. Remote Sens. Lett. 19, 1–5.

WATERHYPERNET: Automated in situ measurements of hyperspectral water reflectance for satellite validation ... and more

Kevin Ruddick[1]*, Matthew Beck[1], Agnieszka Bialek[2], Vittorio Brando[3], André Cattrijsse[4], Javier Concha[3], Alexandre Corizzi[5], Pieter de Vis[2], Ana Dogliotti[6], David Doxaran[5], Anabel Gammaru[1], Claudia Giardino[7], Luis Gonzales Vilas[3], Clémence Goyens[1], Sam Hunt[2], Joel Kuusk[8], Kaspars Laizans[8], Edouard Leymarie[5], Francesca Ortenzio[1], Pablo Perna[6], Estefania Piegari[6], Lucas Rubinstein[6], Quinten Vanhellemont[1], Dieter Vansteenwegen[4]

1. Royal Belgian Institute for Natural Sciences (RBINS), Brussels, Belgium
2. National Physical Laboratory (NPL), Teddington, United Kingdom
3. Consiglio Nazionale delle Ricerche (CNR-ISMAR), Rome, Italy
4. Flanders Marine Institute (VLIZ), Oostende, Belgium
5. Laboratoire Océanographique de Villefranche, Sorbonne Université (SU/LOV), Villefranche-sur-mer, France
6. Instituto de Astronomía y Física del Espacio, Consejo Nacional de Investigaciones Científicas y Técnicas (IAFE, CONICET/UBA), Buenos Aires, Argentina
7. Consiglio Nazionale delle Ricerche (CNR-IREA), Milan, Italy
8. Tartu University (TU), Tartu, Estonia

Abstract – Spaceborne optical remote sensing is routinely used for monitoring of water quality in coastal and inland waters via parameters such as phytoplankton pigments (chlorophyll a, phycocyanin, etc.) and suspended particulate matter. The quality of end-user products depends strongly on intermediate processing, particularly atmospheric correction and associated sunglint and adjacency corrections. In situ measurements of water reflectance are needed to validate the satellite data products. Building on experience gained from the multispectral AERONET-OC network, the WATERHYPERNET is being set up as an international network of sites running automated systems of pointable hyperspectral radiometers. An overview is presented of the WATERHYPERNET network, including a summary of hardware, data acquisition and processing and validation sites. Examples are provided of satellite validation applications. While satellite validation has been the primary motivation for development of this network, the availability of high frequency and long-term hyperspectral reflectance data is also stimulating spin-off applications, such as phytoplankton monitoring.

Keywords: ocean colour, satellite validation, phytoplankton, hyperspectral reflectance.

1. INTRODUCTION

Spaceborne optical remote sensing from daily 100-1000m resolution "ocean colour" missions such as MODIS, VIIRS and Sentinel-3/OLCI provides operational data to end-users for applications such as coastal water quality management (eutrophication, sediment transport, etc.). 10-100m resolution missions such as Landsat-8 and Sentinel-2 have also become popular tools for coastal and inland water monitoring. 1-10m resolution missions, including cubesat constellations such as Planetscope Doves, are now emerging (Vanhellemont, 2019) and offering new opportunities for applications inside ports and small lakes and for monitoring coastal operations (construction, dredging/disposal)

To ensure that the products from all these satellite missions can be trusted by end-users, and particularly to identify any atmospheric correction errors, in situ measurements of water reflectance are needed to validate the satellite data products. Building on experience from the multispectral AERONET-

OC network (Zibordi et al, 2009), WATERHYPERNET is setting up an international network of sites running automated systems of pointable hyperspectral radiometers. WATERHYPERNET will thus provide water reflectance validation data at hyperspectral resolution every day for sites with diverse aquatic and atmospheric conditions.

2. HARDWARE and DATA PROCESSING

WATERHYPERNET hardware currently consists of two systems: a) the PANTHYR system based on the mature TRIOS/RAMSES radiometer, and b) the HYPSTAR® system based on a newly-designed radiometer.

The PANTHYR system, shown in Figure 1a, is described in detail by (Vansteenwegen et al, 2019) and consists of two TRIOS/RAMSES radiometers (one irradiance, one radiance; 400-900nm at 10nm FWHM) with an external camera mounted on a FLIR PTU-48E pan-tilt unit controlled by a single-board Beaglebone Black computer and associated custom-built electronics.

The HYPSTAR® system, shown in Figure 1b, consists of a newly-designed hyperspectral radiometer (380-1020nm at 3nm FWHM) with integrated radiance and irradiance fore-optics and embedded RGB camera, mounted on a Bowler Rx pan-tilt unit and controlled by a rugged PC.

Both systems include auxiliary sensors and site-dependent power supplies (grid, solar panels, batteries, etc.) and data transmission hardware (cabled Internet, wifi, 4G, etc.).

Both systems acquire data typically every 20 minutes during daylight following an abovewater radiometry acquisition protocol based on (Mobley et al, 1999). Measurements are acquired at both 90° and 135° relative azimuth to sun and potentially both left and right of sun, when permitted by the local mounting structure and its shadows/reflections. Data is transmitted to land in near real time for automated, centralised processing and quality control. Extension of the processing to generate uncertainty estimates for each data value is in progress following the work of the FRM4SOC project (Banks et al, 2020; Ruddick et al 2019). A data portal is under development to distribute data publicly to users such as satellite mission validation entities and developers of atmospheric correction algorithms.

---

* Corresponding author. Address: 29 Rue Vautierstraat, 1000 Brussels, Belgium. Email: kruddick@naturalsciences.be

Figure 1. (a-top) PANTHYR radiometer system, (b-bottom) HYPSTAR® radiometer system. Cable tie spikes are used for bird avoidance.

3. VALIDATION SITES

PANTHYR and/or HYPSTAR® systems are currently running at 7 locations and are planned for 5 further locations in 2022 – see Table 1.

Table 1. WATERHYPERNET sites running (top 7) or planned in late 2022/early 2023 (bottom 5). System: P=PANTHYR, H=HYPSTAR; PI= Principal Investigator.

System	Location	PI
P,H	Aqua Alta, near Venice, Adriatic Sea, IT	CNR
P,H	Blankaart Reservoir, BE	RBINS
P	RT1, near Oostende, North Sea, BE	VLIZ
H	Etang de Berre, FR	LOV
H	Le Verdun, Gironde Estuary, FR	LOV
H	Near Buenos Aires, La Plata Estuary, ARG	IAFE
H	Lake Garda, IT	CNR
2022/23: P+H	Thornton Bank, North Sea, BE	RBINS
2022/23: P+H	Near Zeebrugge, North Sea, BE	RBINS
2022/23: H	Chascomus Lake, ARG	IAFE
2022/23: H	Lampedusa, Mediterranean, IT	CNR
2022/23: H	MESURO, Rhône plume, FR	LOV

4. CONCLUSIONS

Hyperspectral reflectance data from the PANTHYR system has already proven useful for validation of Sentinel-3/OLCI (Vanhellemont and Ruddick, 2021), Sentinel-2, Landsat-8 and Planetscope Doves (Vanhellemont, 2020) and PRISMA (Giardino et al, 2020). High quality data is now emerging also from the HYPSTAR® systems and the first matchups with satellite data are being analysed. The user need for hyperspectral water reflectance data is clear and growing stronger every year, with the existing satellite missions being joined by the new generations of cubesat constellations and hyperspectral satellite missions. The WATERHYPERNET has been developed to meet this need and the PANTHYR and HYPSTAR® systems and associated processing chains are now approaching maturity for routine operations to start in 2022 and 2023 respectively.

However, the utility of these systems is not limited to the application of satellite validation. A first application for phytoplankton species monitoring has also been demonstrated (Lavigne et al, 2022).

REFERENCES

Banks, A. C. et al. Fiducial Reference Measurements for Satellite Ocean Colour (FRM4SOC). Remote Sens. 12, 1322 (2020).

Giardino, C. et al. First Evaluation of PRISMA Level 1 Data for Water Applications. Sensors 20, 4553 (2020).

Lavigne, H. et al. Monitoring of high biomass Phaeocystis globosa blooms in the Southern North Sea by in situ and future spaceborne hyperspectral radiometry. Rem Sens Env, 282, p.113270. DOI: https://doi.org/10.1016/j.rse.2022.113270 (2022).

Mobley, C. D. Estimation of the remote-sensing reflectance from above-surface measurements. Appl. Opt. 38, 7442–7455 (1999).

Ruddick, K. et al. A Review of Protocols for Fiducial Reference Measurements of Water-Leaving Radiance for Validation of Satellite Remote-Sensing Data over Water. Remote Sens. 11, 2198 (2019).

Vansteenwegen, D. et al. The pan-and-tilt hyperspectral radiometer system (PANTHYR) for autonomous satellite validation measurements. Remote Sens. 11, 1360 (2019).

Vanhellemont Q. Daily metre-scale mapping of water turbidity using CubeSat imagery. Optics Express, Vol. Vol. 27 Issue 20 pp. A1372–A1399 (2019).

Vanhellemont, Q. Sensitivity analysis of the dark spectrum fitting atmospheric correction for metre- and decametre-scale satellite imagery using autonomous hyperspectral radiometry. Opt. Express 28, 29948–29965 (2020).

Vanhellemont Q. & Ruddick K. Atmospheric correction of Sentinel-3/OLCI data. Rem Sens Env, 256, p. 112284. DOI: https://doi.org/10.1016/j.rse.2021.112284 (2021).

Zibordi, G. et al. AERONET-OC: A network for the validation of ocean color primary product. J. Atmos. Ocean. Techn. 26, 1634–1651 (2009).

Automated hyperspectral validation site in the Río de la Plata (Argentina): first match-up results

A. I. Dogliotti[1]*, E. Piégari[1], P. Perna[1], L. Rubisntein[1,2]

[1]Instituto de Astronomía y Física del Espacio (CONICET/UBA), Argentina
[2]Laboratorio de Acústica y Electroacústica (LACEAC), FIUBA, Argentina

Abstract – A new generation hyperspectral radiometer, the HYPSTAR® instrument, with a pointing system and auxiliary sensors, has been designed within H2020/HYPERNETS project and has been recently deployed in the turbid waters of Río de la Plata estuary (Argentina). *In situ* data collected autonomously during the first ten days of deployment have been compared with surface water reflectance data from various satellites, like Landsat-8, Sentinel-2 & Sentinel-3. Results show the great potential of this automated system to provide high quality and quantity of data for validation of satellite data at all wavelengths in a multi-mission perspective.

Keywords: HYPSTAR, Hyperspectral, Automated, Validation, Río de la Plata.

1. INTRODUCTION

Validation of satellite-derived products, in particular water reflectance, using *in situ* data is essential to ensure the quality of derived parameters useful for water quality monitoring, like turbidity and chlorophyll-a concentration. The use of autonomous systems has shown to be effective for increasing the number of validation match-ups compared to oceanographic cruises. Within H2020/HYPERNETS project, a new generation hyperspectral radiometer, the HYPSTAR® (HYperspectral Pointable System for Terrestrial and Aquatic Radiometry) instrument, with a pointing system and auxiliary sensors has been designed and is being tested in different test sites around the world. On water sites, HYPSTAR-SR (Standard Range) provides water reflectance at fine spectral resolution (3nm FWHM) in the 350-1100nm region with high quality at a lower cost and is integrated into the WATERHYPERNETS, a federated Network of Hyperspectral Radiometers on zenith- and azimuth- pointing systems (https://waterhypernets.org).

Since mid-December 2021, this autonomous system has been installed in the turbid waters of Río de la Plata upper estuary, 60 km south of the city of Buenos Aires (Fig.1). The Río de la Plata (RdP) is a large and shallow funnel shaped estuary with high values of suspended particulate matter, ranging from 100 to 300 g m^{-3} (Framiñan et la. 2006) and reaching 940 g m^{-3} in the maximum turbidity zone, being an ideal site to test atmospheric correction algorithm performance.

Figure 1. *Location of the HYPERNETS site in the Río de la Plata, Argentina.*

2. DATA AND METHODS

In situ radiometric data have been collected using the autonomous system installed at the end of a 1.10 Km long jetty located 60 Km south of Buenos Aires city (34°49'04.8" S, 57°53'45.3" W). The HYPSTAR-SR (https://hypstar.eu/) radiance (FOV 2°) and irradiance (FOV 180°) optical entrances are optically multiplexed to one VNIR (Visible and NIR) spectrometer module. Since the same spectrometer is used for both radiance and irradiance measurements, these can't be made simultaneously. Therefore the downwelling sky radiance (L_{sky}), upwelling radiance from the water (L_u) and downwelling irradiance (E_d) measurements, needed to derive water reflectance (ρ_w), are measured sequentially. The zenith angles of the sea- and sky-viewing radiance sensors are 40° and the relative azimuth angle respect to the sun is 90°. This geometry is kept constant all through the day thanks to the automated pan/tilt mechanism that rotates the radiometer. Data is collected and sent in near-real time to WATERHYPERNET's server where it is processed and quality controlled and re-distributed to the project's partners as Level 2 water reflectance (ρ_w).

Cloud-free satellite images from Landsat-8/OLI (L8), Sentinel-2/MSI (S2), and Sentinel-3/OLCI (S3) systems covering the site have been selected. Level 1T data have been downloaded from USGS Earth Explorer (http://earthexplorer.usgs.gov/) for L8 (225/084), and Level 1C from Sentinel Scientific Data Hub (https://scihub.copernicus.eu/) for S2-A/B (21HVB), and Copernicus Open Data Access (https://coda.eumetsat.int/), for S3-A/B images. All images have been processed using ACOLITE (v20211124), applying the DSF (Dark Spectrum Fitting) atmospheric correction (Vanhellemont & Ruddick 2018, 2021; Vanhellemont 2019), and using default options but applying sun glint correction to L8 and S2 imagery. Surface reflectance (ρ_s) values have been extracted at a 3 x 3 pixel window centered at the site location at all VIS/NIR bands at 10 m (S2), 30 m (L8) and 700 m (S3). The median and standard deviation were calculated from the valid pixels of the window by removing the outliers (*i.e.* when the pixel value was lower/higher than the mean minus/plus 1.5 standard deviation of the window). The time difference between *in situ* and satellite overpass was always within 10 min (Table 1).

Table 1. Satellite images used for the match-up analysis

Sat	Satellite date (yyyy-mm-dd)	Satellite time (hh:mm:ss)	In situ time (hh:mm:ss)
S2A	2021-12-16	13:52:15	13:42:02
S3B	2021-12-18	13:17:27	13:22:06
S3B	2021-12-19	13:01:06	13:02:06
S3B	2021-12-22	13:23:33	13:22:03
L8	2021-12-22	13:44:56	13:42:07
S3B	2021-12-23	12:57:22	13:02:04
S3A	2021-12-24	13:10:31	13:02:02
S2B	2021-12-24	14:02:06	14:02:03
S3B	2021-12-26	13:19:48	13:22:04
S2A	2021-12-26	13:52:16	13:41:50

3. RESULTS

During a preliminary one-day field campaign on March 30 2021, simultaneous measurements using the HYPSTAR® and TriOS/RAMSES radiometers have been collected from a pier located in the city of Buenos Aires. This first

---

* Corresponding author. Address: Av. Güiraldes s/n, 1428 Buenos Aires, Argentina. Email: adogliotti@conicet.gov.ar

comparison showed a very good agreement between both sensors (Fig. 2).
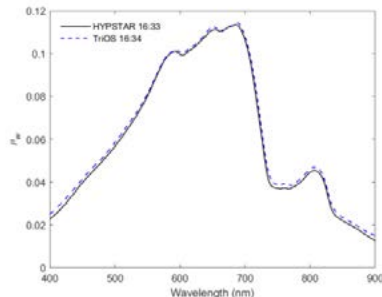
Figure 2. *Simultaneous reflectance spectra measured with HYPSTAR® and TriOS/RAMSES radiometers.*

A total of 10 match-ups (N_{L8}=1, N_{S2}=3, N_{S3}=6) was attained within 15 and 26 Dec 2021. They showed a good performance of DSF approach, especially for L8 and S2 (Fig. 3 upper frame) while some underestimation for S3 for all bands is clearly observed (Fig. 3 lower frame).
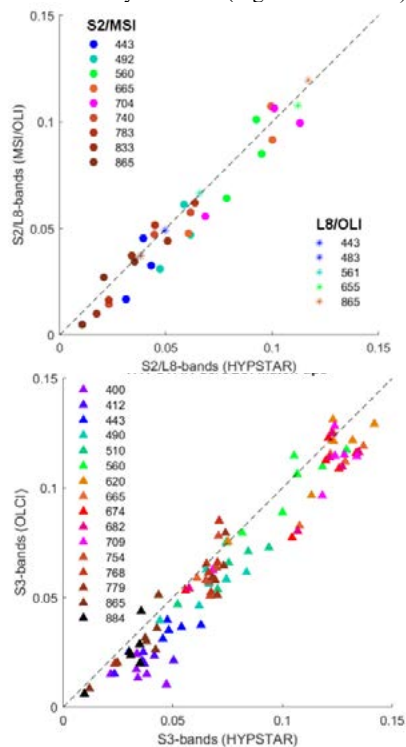
Figure 3. *Match-up analysis for S2/MSI and L8/OLI (upper) and S3/OLCI (lower) systems.*

Within 10 days the system collected a varied set of measurements showing different optical conditions of the water. Two quite different conditions are shown in Fig.4. The spectra collected on 26 Dec show lower reflectance in the red part of the spectra, probably associated to higher chlorophyl-*a* absorption (generally associated with higher phytoplankton biomass), and also around 620 nm, possibly related to the presence of phycocyanin, a characteristic pigment present in cyanobacteria cells. Their presence is highly probable, since cyanobacteria-dominated blooms have been frequently recorded in the estuary at this time of the year (Dogliotti et al. 2021), but their presence still needs to be confirmed from water samples.
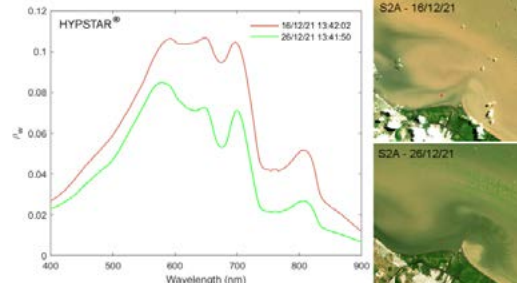
Figure 4. *Two hyperspectral spectra (HYPSTAR) collected on 16 and 26 Dec 2021 and corresponding S2A images. Location of the site is indicated (red dot).*

4. CONCLUSION

The HYPSTAR-SR system has been successfully deployed in the turbid waters of Río de la Plata estuary on December 14, 2021. Since then, the autonomous system has been collecting data every 20 min from 8 am to 6 pm every day. Within the first ten days after deployment, a total of 10 match-ups have already been collected and used to test the DSF atmospheric correction applied to L8, S2-A/B and S3-A/B imagery. Results show the great potential of this automated system to provide high quality and quantity of data for validation of satellite data at all wavelengths in a multi-mission perspective, including hyper-spectral missions, like PRISMA (Hyperspectral Precursor of the Application Mission) and the upcoming EnMAP (Environmental Mapping and Analysis Program) and CHIME (Copernicus Hyperspectral Imaging Mission for the Environment). Moreover, it has been shown its potential use for monitoring water quality (detecting cyanobateria bloom) in near real time.

REFERENCES

Dogliotti, A.I., Gossn, J. I., Gonzalez, C, Yema, L., Sanchez, L., L. O'Farrell, I. (2021). Evaluation of multi- and hyper- spectral Chl-*a* algorithms in the Río de la Plata turbid waters during a cyanobacteria bloom. *IEEE Int. Geoscience and Rem. Sens. Symposium IGARSS* 2021, p7442-7445.
Framiñan, M., and O. Brown (1996), Study of the Río de la Plata turbidity front, Part 1: Spatial and temporal distribution, *Cont. Shelf Res.*, 16, p1259–1282.
Vanhellemont, Q., Ruddick, K. (2018). Atmospheric correction of metre-scale optical satellite data for inland and coastal water applications. *Rem. Sens. Env.*. 216, p586-597.
Vanhellemont, Q. (2019). Adaptation of the dark spectrum fitting atmospheric correction for aquatic applications of the Landsat and Sentinel-2 archives. *Rem.Sens.Env.* 225, p175.
Vanhellemont Q., Ruddick K. (2021). Atmospheric correction of Sentinel-3/OLCI data for mapping of suspended particulate matter and chlorophyll-a concentration in Belgian turbid coastal waters. *Rem. Sens. Env.* 256, 112284.

SMOS sea surface high wind speed validation and data performances assessment

R. Crapolicchio[1] *, N. Reul[2], J. Piolle[2], C. Prevost[2], D. Briand[2], E. Bodéré[2], J. Tenerelli[3]

[1]Serco Italia S.p.A. for ESA-ESRIN, Frascati, Italy
[2]IFREMER, Brest, France
[3]OceanDataLab, Brest, France

Abstract – L-Band measurements from passive sensors (e.g. SMOS, SMAP) have shown good sensitivity to high surface wind speed over ocean as confirmed by validation results presented during the International Workshop On Measuring High Wind Speeds Over The Ocean at Met Office (November 2016) and in following peer reviewed papers. Based on those results, the user community has expressed its interest for a systematic data near real time generation of such innovative product. Considering the above mentioned interest, ESA has decided to implement the generation of a pre-operational product from SMOS brightness temperature measurements since 2018 (V100). The paper presents the result of the validation of the new V300 SMOS sea surface high wind product performed by comparison with satellite and airborne radiometers (e.g. SMAP, SFMR), and SAR (e.g. Sentinel-1, Radarsat-2) sea surface wind speed products, as well as product timeliness and completeness performances during the operational phase since August 2021 till present.

Keywords: SMOS, High Sea Surface Winds, Validation, Near Real Time.

1. INTRODUCTION

Since 2012, ESA has been funding a project called SMOS+ STORM (as part of its Support To Science Element program) which aimed to explore these capabilities in more depth. In November 2016 the main science outcome of the SMOS+ STORM project were presented during the "International Workshop on Measuring High Wind Speeds over the Ocean" that was held at the UK MetOffice in Exeter (UK). At the end of the workshop, in the executive report (Organising Committee, 2016) the user community has expressed its interest for a systematic data generation of sea surface winds (SSW) derived from L-band measurements in near real time for Tropical Cyclone and Extra Tropical Cyclone prediction and monitoring systems in the context of maritime applications and Numerical Weather Prediction operational centres activities. Considering the above mentioned interest from the users community for L-band SSW over ocean, ESA has decided to implement an operational service.
The service was in pre-operational phase since summer 2018 delivering V100 of the SMOS high SSW product to selected users and became fully operational since beginning of 2020. In August 2021 the service has been upgraded to product version V300 with a Bayesian method for the wind speed retrieval and to use as input the latest L1B SMOS product baseline v724 (ESA Earth online news, 2021). In June 2022 the entire SMOS archive has been reprocessed and delivered to the users (ESA Earth online news, 2022).
The SMOS high winds products delivered with 4-6 hours from sensing time are: the level 2 high winds based on satellite swath with a spatial sampling of 1/4°x 1/4°, and the level 4 wind radii fixes which contains: the SMOS 10-min

maximum-sustained winds (in knots) and wind radii (in nautical miles) for the 34 kt (17 m/s), 50 kt (25 m/s), and 64 kt (33 m/s) winds per geographical storm quadrants and for each SMOS pass intercepting a Tropical Cyclone in all the active ocean basins.
Figure-1 provides an example of such product in case of the Tropical Cyclone Larry which was active in the Atlantic Ocean in September 2021. SMOS high winds products are accessible form the ESA SMOS dissemination server (https://smos-diss.eo.esa.int/oads/access/).
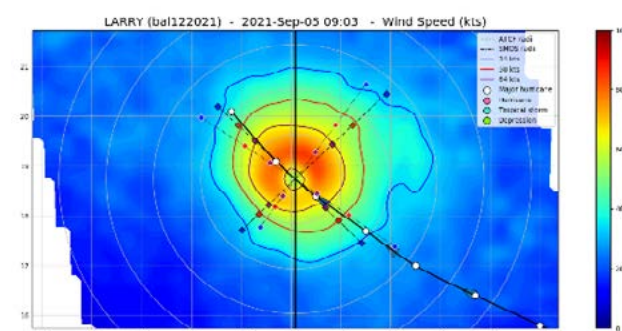
Figure 1. *Tropical Cyclone Larry as sensed by SMOS on 5th September 2021.* Wind speed and Wind Radii are shown. *NOAA Automated Tropical Cyclone Forecast (ATCF) system "Best-Track" estimates are also include.*

2. VALIDATION RESULTS

To validated the SMOS high wind speed, the SMOS Near Real Time (NRT) products and SMAP surface wind speed products were co-located for the period from the beginning of V300 product generation in August 2021 to June 2022. The number of co-localized SMOS/SMAP match-up points within a spatial radius of Δx=25 km and temporal window of Δt=±1 hour and for the full period is ~ 1.9×10^7 points.
SMOS NRT Surface Wind Speeds (SWS) match the SMAP winds in the full wind speed range with a Mean of ΔSWS(SMOS-SMAP) of 0.1 m/s and a STD difference of 2.2 m/s as shown in Figure 2. In term of wind speed regime statists were computed for low to intermediate winds (SWS<12 m/s), below Tropical Storm Force (12<SWS < 17 m/s), above Tropical Storm Force (17.5 <SWS<32.5 m/s), above Hurricane strength (SWS>32.5 m/s).The RMSD between SMOS and SMAP is minimum (~1.7 m/s) for 12<SWS < 32 (m/s). It slightly increases to 2.0 m/s for low to moderate winds (<12 m/s) and to ~3.7 m/s above hurricane force.
SMOS is on average ~3 m/s lower than SMAP in the hurricane conditions as reported below on Table 1. An example of co-localized fields between SMOS SWS and SAR/S1A over hurricane Larry is given in Figure 3.

* Corresponding author. Address: Largo Galileo Galilei,1, 00044 Frascati (Roma), Italia. Email: raffaele.crapolicchio@esa.int
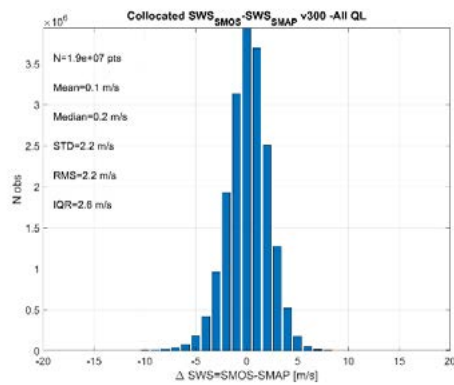
Figure 2. *Histogram of the differences between SMOS and SMAP NRT Sea Surface Wind Speed (SWS) at co-localized match-up points for the complete period (Aug 2021-June 2022).*

Table 1. Statistics of the differences between the SMOS NRT and SMAP co-localized SWS for different wind speed regimes

SWS range [m/s]	Number of points	Mean [m/s]	STD [m/s]	RMSD [m/s]
SWS≤ 12	9.8 x 10^6	0.3	1.9	1.9
12<SWS≤17	9.8 x 10^5	-0.5	1.7	1.8
17<SWS≤32	1.3 x 10^5	0.1	2.1	2.1
SWS>32	3.0 x 10^3	-3.9	8.0	8.9
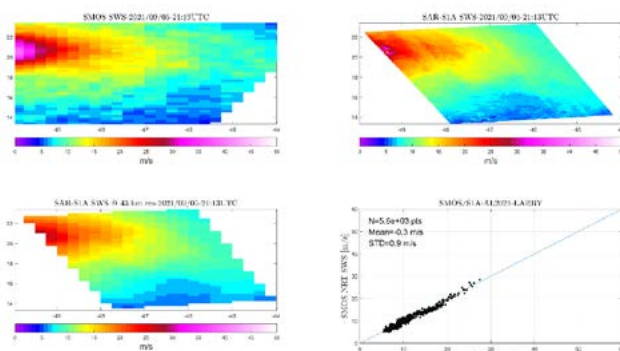
Figure 3 *SMOS SWS (upper left) vs Sentinel-1A SWS (upper right). Sentinel-1A SWS averaged at SMOS resolution (lower left) and associated SWS scatter-plot (lower right)*

We evaluated the SAR SWS at a similar spatial resolution than SMOS SWS. The original SAR data at 1 km resolution were spatially averaged with a Gaussian running mean windows with half-width of 22 km. The spatially smoothed wind field given on the original lat/lon grid of the SAR was then interpolated on the SMOS SWS grid using a nearest neighbor method. Considering that only 9 occurred during the operation period of the V300 NRT processor we show here the overall statistics for the ensemble of the V300 data (106 intercepts since 2010 for both Sentinel-1 and Radarsat missions). The results are provided in Figure 4. As found, SMOS SWS well match the low-resolution co-localized SAR surface winds with a mean bias of -0.6 m/s and an STDs of 2.1 m/s, respectively.
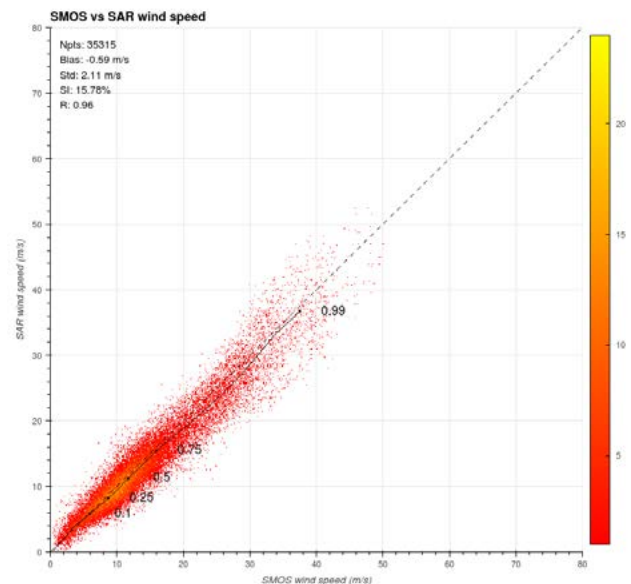
Figure 4 *SMOS SWS (x-axis) comparison with SAR SWS (y-axis) over 2012-2021. The dashed curve is the x=y line. The thin black line is showing the mean SAR SWS per bins (1 m/s width) of SMOS SWS*

2. PPRODUCT PERFORMANCES RESULTS

In term of data performances the daily number of files delivered in less than 4 hours is computed since the operational deployment of the V300 products in August 2021. The percentage of files delivered within 4 hours (light green and green) had continuous improved from about 92.9% in 2021 to 98.7% in June 2022 (excluding delay due to sensor anomaly or late receiving of input L1B dataset).

3. CONCLUSION

SMOS Sea SWS V300 and SMAP Sea SWS shows a difference of 0.1 m/s and an STD difference of 2.2 m/s globally. Comparison with SAR dataset shows a mean bias of -0.6 m/s and an STD of 2.1 m/s. About 98% of data is delivered within 4 hours from sensing.

REFERENCES

ESA Earth online news, 4th August 2021, New SMOS Near Real Time Sea Surface Wind Speed new baseline is released - Earth Online (esa.int)

ESA Earth online news, 1st June 2022, SMOS reprocessed Sea Surface Wind Speed dataset is now available - Earth Online (esa.int)

Organising Committee, Proceedings of the "International Workshop on Measuring High Wind Speeds over the Ocean", 15-17 November 2016, Met Office, Exeter (UK) 48845.pdf (ifremer.fr)

Waves attenuation in the Marginal Ice Zone : thanks to directional wave satellite observations

L. Aouf [1*], D. Hauser [2], F. Collard [3], B. Chapron [4], C. Tourain [5]

[1*] Météo France, CNRM, Université de Toulouse, Toulouse, France
[2] IPSL/LATMOS [3] Ocean Data Lab. [4] IFREMER [5] CNES

Abstract – Waves in the Marginal Ice Zone (MIZ) change rapidly and induce a strong impact on the mixing at upper ocean layers. Until now the directional properties of waves in such regions were not explored in detail because of lack of satellite observations. This work uses directional wave spectra from CFOSAT to examine the variability of wave regime in the MIZ, particularly during summer (austral and boreal). The methodology is based on the assimilation of wave spectra of CFOSAT in the wave model MFWAM. The model runs uses free ice flag to examine the impact of the assimilation in region with thick sea ice conditions. The results show the attenuation of the energy of waves in presence of ice floes during a storm from 17 to 19 january 2020 which affected strongly the Weddell sea. Wave heights after the ice floes from the assimilation run is consistent with Sentinel-3 significant wave heights recorded nearby the studied positions.

Keywords: CFOSAT, wave spectrum, directional, damping, ice floe.

1. INTRODUCTION

Since April 2020 directional wave spectra provided by the SWIM instrument of CFOSAT mission shows the capacity of well capturing both wind-wave and swell with wavelengths from 60 to 500 m. The assimilation of such directional wave observations improves significantly the scaling of wind-wave growth during storms and the transition to swell regime, for instance in the Southern Ocean (Aouf et al. 2021). The objective of this work is to investigate the assimilation of directional wave spectra in the marginal ice zone for arctic ocean and antarctic seas particularly the Weddell Sea. The use of restrictive ice flag provided by the atmospheric system removes wave propagation in the Marginal Ice Zone (MIZ) and result with strong bias of Significant Wave Height (SWH) induced by the estimate of fetch conditions near ice zone.

Moreover, the uncertainties on wind forcing increase significantly in critical ocean regions where sea ice evolves rapidly during the seasonal variability related to transition from summer to fall season. Figure 1 shows the impact of the assimilation of directional wave spectra from CFOSAT on the dominant wave direction in the Southern Ocean during austral summer. This clearly reveals significant correction and the strong variability of wave direction in critical seas such as the one observed in the Weddell Sea.

2. METHODOLOGY AND RESULTS

In this study we have selected several tracks of CFOSAT passing in free ice zone in the Antarctic (weddell sea) and Arctic (east siberian and Beaufort) seas. The methodology consists in selecting a more accurate sea ice concentration from AMSR2 processed by Univ. of Bremen, and then performing wave model runs with release of sea ice fraction input. Storm events are investigated and we examined the impact of the assimilation of directional wave spectra of following the wave propagation in the MIZ.
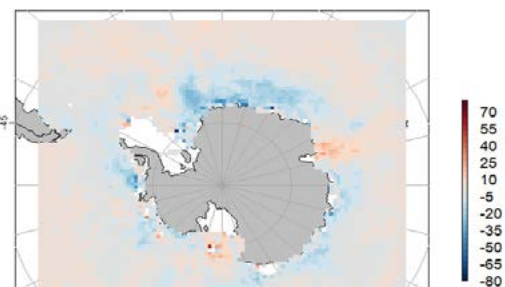
Figure 1. Mean difference (in degrees) of dominant wave direction with and without assimilation of SWIM directional wave spectra during January and February 2020. Positive and negative values stand for clockwise increase and anticlockwise decrease of the dominant wave direction, respectively.

Figure 2 indicates the sea ice concentration during the storm event of 18 January, which induces a strong swell propagating to the south-west direction in the eastern part of Weddell sea. Figure 2 also indicates Sentinel-3 tracks in this zone, where it was recorded SWH greater than 5 m before the thick ice zone. Three positions illustrated in figure 2, namely before (31.8°W-71°S position 1), after (31.8°W-73°S position 2) and far (35°W-75°S position 3) positions from the big ice zone have been selected to investigate the wave propagation. Before entering the thick sea ice conditions the wave regime at position 1 illustrated in figure 3 is composed by a dominant short swell propagating to south-west and growing wind sea moving to west and north-west direction. We can also observe a third wave system of southward long swell with less energy.

Figure 4 show the wave spectrum at positions 3, 6 hours later after the passage of thick sea conditions. The comparison between figures 3 and 4 illustrates clearly the wave energy damping of southward swell and the increase of frequency spreading (propagating westward and to south-west) induced by the ice floes. It is most striking to see the attenuation of wave energy in the 1D wave spectra at different positions 1, 2 and 3, as illustrated in figure 5.

SWH computed from wave spectrum at position 3 is estimated at 0.71 m, which fits well SWH from Sentinel-3 roughly 0.75 passing nearby this position. The comparison of SWH at position 1 also indicates good consistency between model with data assimilation (2.41 m) and S3A (2.6 m).
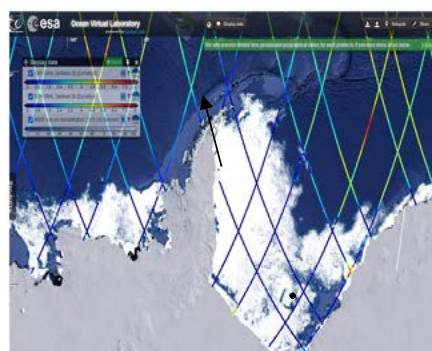
Figure 2. Sea ice fraction from AMSR2 processed by Univ. Bremen (Melsheimer et al. 2020) and Sentinel-3 SWH

tracks during storm event on 18 January 2020 at Weddell Sea. Purple and gray squares stand for position before and after ice floe, respectively. While black diamond stand for far position.
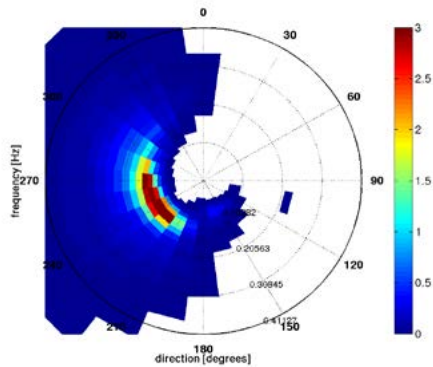
Figure 3. variation of Spectral density of energy of waves in direction and frequency at position 31.8°W-71°S (before ice floe) on 18 january 2020, 03:00 (UTC). 0 indicates the north direction.

3. CONCLUSION

For the first time directional wave spectra from satellite have been used to track the wave propagation in the MIZ under thick sea ice conditions at Weddell Sea for instance. The results show the damping of swell energy after the passage of big ice floe zone. We clearly observed the increase frequency spreading induced by wave-ice interaction. The use of SWIM wave spectra opens excellent perspective to implement a wave-ice interaction term that can be added in wave models in order to improve the wave forecasts in Arctic ocean and Antarctica seas. This will also have a better understanding of waves-ice-ocean coupling in critical ocean regions, where changes of climate projections need to be investigated.
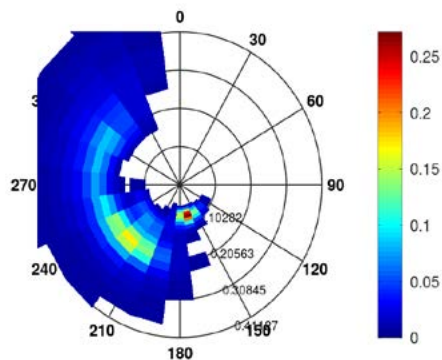
Figure 4. variation of Spectral density of energy of waves in direction and frequency at position 35°W-75°S (far after ice floe) on 18 january 2020, 09:00 (UTC). 0 indicates the north direction.
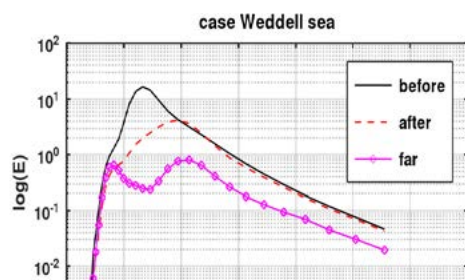
Figure 5. 1-D wave spectra depending on frequency at position 1,2 and 3 represented by black, dashed and circles lines, respectively.

REFERENCES

Aouf, L., D. Hauser, B. Chapron, A. Toffoli, C. Tourain, C. Peureux, (2021). 'New directional wave satellite observations : Towards improved wave forecasts and climate description in Southern Ocean', Geophysical Research Letters, Vol. 48 , N. 5 , 10.1029/2020GL091187
Melsheimer, C., Spreen, G., (2020): AMSR-E ASI sea ice concentration data, Antarctic, version 5.4 (NetCDF) (June 2002 - September 2011). *PANGAEA*, https://doi.pangaea.de/10.1594/PANGAEA.919778

Towards the coupled assimilation of satellite radiances: Assimilating CIMR brightness temperatures in an atmosphere-ocean coupled variational analysis system

A. Storto[1,*], G. Liberti[1], D. Ciani[1], A. Pisano[1], C. Yang[1], A. Lewinschal[2], R. Santoleri[1]

[1] Institute of Marine Sciences (ISMAR), National Research Council of Italy (CNR), Rome, Italy

[2] University of Stockholm, Stockholm, Sweden

Abstract – It is expected that coupled air-sea data assimilation algorithms may enhance the exploitation of satellite observations whose measured brightness temperatures depend upon both the atmospheric and oceanic states, thus improving the resulting numerical forecasts. To demonstrate in practice the advantages of the fully coupled assimilation scheme, the assimilation of brightness temperatures from a forthcoming microwave sensor (the Copernicus Imaging Microwave Radiometer, CIMR) is evaluated within idealized assimilation and forecast experiments. The forecast model used here is the single-column version of a state-of-the-art Earth system model (EC-Earth), while a variational scheme, complemented with ensemble-derived background-error covariances, is adopted for the data assimilation problem. Benefits from the assimilation of brightness temperatures from CIMR – compared to the assimilation of geophysical retrievals – are found significant for both wind and oceanic variables.

Keywords: CIMR, Coupled assimilation, 3DVAR.

1. INTRODUCTION

During recent years, the science of numerical weather, ocean and climate predictions has rapidly evolved thanks, among other factors, to the observing capabilities offered by new sensors and the methodological challenges that these inevitably pose.

Satellite instruments capable to sense both the sea-surface ocean and the low-troposphere foster consequently the re-thinking of most assimilation schemes, which are traditionally uncoupled. Even in many Earth system prediction systems, the assimilation schemes are kept independent for simplicity, due to the difficulty of modeling cross-medium errors and balances. On the contrary, strongly coupled data assimilation (SCDA) schemes, where an observation in one medium can impact variables in another medium at analysis time, are subject of intense development and investigations both at academic level and in operational centers. SCDA schemes (e.g. Storto et al., 2018) are expected to attenuate imbalances of the initial conditions between different media and maximize the exploitation of the informative content of the observations, especially for remotely sensed observation types.

The problem of assimilating satellite data is particularly relevant for oceanographic applications. Most operational analysis system do indeed assimilate geophysical retrievals (for instance sea surface temperature, SST, and sea surface salinity, SSS) calculated from a variety of sensors. Figure 1 sketches a typical processing chain of satellite observations for oceanographic forecasts. Long-standing experience in Numerical Weather Prediction has proved that the retrieval

approach is rather suboptimal (see e.g. Joyner and Dee, 2000), because retrieval algorithms i) use several assumptions and require an additional step prior to the assimilation; ii) introduce error cross-covariances between the background fields - used within the retrieval algorithm - and retrievals, and iii) have difficulty in estimating retrieval uncertainty, for further use in the data assimilation step.

The above arguments foster the rethinking of satellite data assimilation in the context of coupled air-sea predictions, which is the subject of the present work. In order to assess the potential benefits of assimilating brightness temperatures in a coupled ocean-atmosphere assimilation system, we focus our investigations on the use of a forthcoming microwave sensor, the Copernicus Imaging Microwave Radiometer (CIMR).

CIMR is scheduled for the 2027+ timeframe, and is a high priority mission of the Copernicus Expansion Missions Programme. Polarised (H and V) channels centered at 1.414, 6.925, 10.65, 18.7 and 36.5 GHz are included in the mission design under study. CIMR is thus designed to provide global, all-weather, mesoscale-to-submesoscale resolving observations of sea-surface temperature, sea-surface salinity and sea-ice concentration. The coupled observation operator is derived as polynomial regression from the application of the Radiative Transfer for TOVS (RTTOV) model, and we perform Observing System Simulation Experiments (OSSE) to assess the benefits of different assimilation methods and observations in the forecasts.
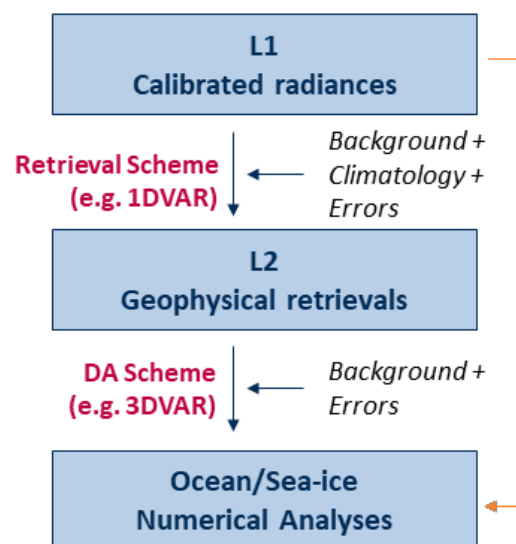
Figure 1. A typical processing chain of satellite observations in numerical ocean predictions, consisting of separate retrieval and assimilation steps. The orange connector indicates the approach proposed here, where calibrated radiances are assimilated directly in the analysis/forecast system.

---

* Corresponding author. Address: via del Fosso del Cavaliere 100, I-00133 Roma (Italy). Email: andrea.storto@cnr.it

2. THE ANALYSIS SYSTEM

The analysis system used in this study includes a single-column version of an Earth system model, and a variational data assimilation scheme, both detailed below.

The one-dimensional coupled AOGCM used in this study is the single-column model (SCM) version of EC-Earth (Hartung et al., 2018). This single-column coupled model includes the same modeling components of EC-Earth, developed and maintained by the homonymous consortium, which are the NEMO ocean model, the OpenIFS atmospheric model, the LIM3 multi-category sea-ice model, and uses OASIS3-MCT for coupling OpenIFS and NEMO-LIM3. Both oceanic and atmospheric models are configured to be used in the one-dimensional configuration. In our experiments, the SCM is located in correspondence of the PAPA station (50.1°N, 144.9°W), which is a sea-ice free location, so that the sea-ice model is in practice inactive.

Variational data assimilation is widely used in meteorology and oceanography for research, climate and operational applications. The variational algorithm iteratively minimizes a cost function, whose terms measure the distance between the analysis and the background, and the analysis and the observations, weighed by the respective error covariances. The actual implementation allows for hybrid ensemble-variational covariances that thus embed a flavor of flow-dependence of the background errors (Storto et al., 2018b).

In order to obtain a dataset of ensemble anomalies for use within the background-error covariance estimation and the observation operator, we run a large number of ensemble simulations for the 1-month simulation period. In particular, oceanic and atmospheric initial conditions and oceanic and atmospheric physics parametrizations were perturbed to form a dataset of 990 ensemble members.

Data assimilation experiments have been run following the Observing system simulation experiments (OSSE) methodology: a nature run with perturbed physics and initial conditions was used as ground truth, from which different types of observations were extracted – adding as usual a perturbation drawn from the Gaussian distribution, with variance equal to the nominal observational error variance. In particular, we extracted oceanic in-situ observations from Argo floats and atmospheric in-situ observations from radiosondes, with uncertainty given as in state-of-the-art reanalysis systems. Additionally, we extracted geophysical retrievals in accordance with CIMR mission specification (sea surface temperature and salinity and 10m marine winds) and brightness temperature observations corresponding to the CIMR channels.

For CIMR brightness temperatures, the observation operator includes a simplified version of the Radiative Transfer for TOVS (RTTOV) model (Saunders et al., 2018). From the dataset of ensemble anomalies, we run the RTTOV forward model corresponding to the SMOS and AMSR-2 sensors (which together provide a similar spectral portfolio as CIMR), and then we applied polynomial regression in order to ease the inclusion of the adjoint operators in the variational code. The regression provided an accuracy comparable to the original RTTOV, with normalized errors smaller than 1% within all CIMR channels.

Next we run several experiments to assess the benefits of strongly coupled versus weakly coupled data assimilation, the impact of background-error covariances and their hybridization in the coupled assimilation context, and the assessment of brightness temperature data assimilation compared to the assimilation of geophysical retrievals.

3. RESULTS

Results show that the strongly coupled assimilation formulation outperforms the weakly coupled one in both experiments assimilating atmospheric data and verified against oceanic observations and experiments assimilating oceanic observations verified against atmospheric observations. The sensitivity of the analysis system to the choice of the coupled background-error covariances is found significant and discussed in detail.

Finally, the assimilation of microwave brightness temperature observations is compared to the assimilation of the corresponding geophysical retrievals (sea surface temperature and salinity and marine winds), in the coupled analysis system. We found that assimilating microwave brightness temperatures significantly increases the short-range forecast accuracy of the oceanic variables and near-surface wind vectors, while it is neutral for the atmospheric mass variables. This suggests that adopting radiance observation operators in oceanic and coupled applications will be beneficial for operational forecasts.

3. CONCLUSION

The potential benefits of assimilating directly brightness temperature observations in a coupled atmosphere-ocean variational analysis system is investigated in this study. Although the modelling component is a single-column version of a state-of-the-science Earth system model, results foster the re-thinking of satellite data assimilation, especially for brightness temperature observations sensitive to both the atmospheric and oceanic states.

ACKNOWLEDGEMENTS

REFERENCES

Hartung, K., Svensson, G., Struthers, H., Deppenmeier, A.-L., and Hazeleger, W.: An EC-Earth coupled atmosphere–ocean single-column model (AOSCM.v1_EC-Earth3) for studying coupled marine and polar processes, Geosci. Model Dev., 11, 4117–4137, https://doi.org/10.5194/gmd-11-4117-2018, 2018.

Joiner, J. and Dee, D.P. (2000), An error analysis of radiance and suboptimal retrieval assimilation. Q.J.R. Meteorol. Soc., 126: 1495-1514. https://doi.org/10.1002/qj.49712656514

Saunders, R., Hocking, J., Turner, E., Rayer, P., Rundle, D., Brunel, P., Vidot, J., Roquet, P., Matricardi, M., Geer, A., Bormann, N., and Lupu, C., 2018: An update on the RTTOV fast radiative transfer model (currently at version 12), Geosci. Model Dev., 11, 2717-2737, https://doi.org/10.5194/gmd-11-2717-2018

Storto, A., Martin, M. J., Deremble, B., & Masina, S. (2018a). Strongly Coupled Data Assimilation Experiments with Linearized Ocean–Atmosphere Balance Relationships, Monthly Weather Review, 146(4), 1233-1257.

Storto, A., Oddo, P., Cipollone, A., Mirouze, I. and Lemieux-Dudon, B. (2018b) Extending an oceanographic variational scheme to allow for affordable hybrid and four-dimensional data assimilation. Ocean Modelling, 128, 67– 86. https://doi.org/10.1016/j.ocemod.2018.06.005.

Global Seafloor Mapping from Ships, Satellites, and Geological Information for High Resolution Ocean Models: SYNBATH

D. T. Sandwell*[1], J. A. Goff[2], J. Gevorgian[1], H. Harper[1], S. S. Kim[3], Y. Yu, B. Tozer[4], P. Wessel[5], and W. H. F. Smith[6]

[1]Scripps Institution of Oceanography, La Jolla, California, USA
[2]University of Texas at Austin, Austin, Texas, USA
[3]Chungnam National University, Daejeon, Korea
[4]GNS Science, Wellington, New Zealand
[5]University of Hawaii at Manoa, Honolulu, HI, USA
[6]Laboratory for Satellite Altimetry, NOAA, College Park, MD, USA

Abstract – To date, 23% of the ocean floor has been surveyed by ships at a spatial resolution of 400 m or better. The remaining 77% has depth predicted from satellite altimeter-derived gravity measurements at a relatively low resolution. This study is focused on the development of synthetic bathymetry to fill the gaps. There are two types of seafloor features that are not typically well resolved by satellite gravity: abyssal hills and small seamounts (< 2.5 km tall). We generate synthetic realizations of abyssal hills by combining the measured statistical properties of mapped abyssal hills with regional geology including fossil spreading rate/orientation, rms height from satellite gravity, and sediment thickness. With recent improvements in accuracy and resolution, it is now possible to detect all seamounts taller than about 800 m in satellite-derived gravity. However, the width of the gravity anomaly is much greater than the actual width of the seamount so the seamount predicted from gravity will underestimate the true seamount height and overestimate its base dimension. In this study we use the amplitude of the vertical gravity gradient (VGG) to estimate the mass of the seamount and then use their characteristic shape, based on well surveyed seamounts, to replace the smooth predicted seamount with a seamount having a more realistic shape. Applications to ocean dynamic models will be discussed at the meeting. This paper is an update of our recent work [Sandwell et al., 2022; Gevorgian et al., 2022].

Keywords: global bathymetry, satellite gravity, seafloor characterization.

1. INTRODUCTION

Bathymetry is foundational data, providing basic infrastructure for scientific, economic, educational, military, and political work. High resolution, deep ocean bathymetry is critical for: (1) understanding the geologic processes responsible for creating ocean floor features unexplained by simple plate tectonics, such as abyssal hills, seamounts, microplates, propagating rifts, and intraplate deformation; (2) determining the effects of bathymetry and seafloor roughness on ocean circulation, ocean mixing, and climate; and (3) understanding how marine life is influenced by seafloor depth, roughness, and interactions of currents with the seafloor. The Seabed 2030 project [https://seabed2030.org] "aims to bring together all available bathymetric data to produce the definitive map of the world ocean floor by 2030 and make it available to all." The Seabed 2030 global compilation will be based on swath mapping using multibeam sonar which has a spatial resolution of about 400 m at a typical ocean depth of 4 km [Mayer et al., 2018].

The Seabed 2030 project has made considerable progress over the past few years by increasing the multibeam coverage in public compilations from 11% [e.g., GEBCO 2020; Tozer et al., 2019] to more than 20% today [GEBCO 2020]. Much of this data has been made available by the international community with nearly complete coverage of several exclusive economic zones as well as dense coverage of areas of high scientific interest. The remaining seafloor has depth predicted from a combination of spatially dense satellite altimeter gravity measurements and sparse soundings to provide the large-scale shape of the ocean basins as well as to calibrate the local ratio of bathymetry-to-gravity [e.g., Smith and Sandwell, 1997]. However, the best satellite gravity models available today can only resolve ½ wavelength of 6 km when the regional depth is 4 km [Tozer et al., 2019]. **Thus, the resolution of gravity-predicted depth is more than 10 times worse than the Seabed 2030 objective.**

There are many remote ocean areas in the southern hemisphere that will probably not be completely mapped at 400 m resolution during this decade and well beyond. This study is focused on the development of SYNthetic BATHymetry (SYNBATH) to fill the gaps. The synthetic bathymetry has the geostatistical properties of real seafloor bathymetry but it is not as accurate as ship soundings. While the synthetic data will be replaced with real soundings as they become available in the future, in the interim such realistic realizations can provide key inputs for several important scientific applications [Table 1].

Table 1. Applications of Synthetic Bathymetry

Appropriate Applications
hydrodynamic tide models and tidal friction
ocean circulation models
tidal role in ocean mixing
plate tectonics
planning shipboard surveys
education and outreach
Marginal Applications
tsunami propagation and hazard models
fisheries management
Inappropriate Applications
seafloor geography and feature names
navigation
law of the sea
fiber optic cable route planning

---

* Corresponding author. Address: 1102 IGPP, La Jolla, CA, USA, 92093-0225. Email: dsandwell@ucsd.edu

2. MODELING ABYSSAL HILLS

We use the model of Goff and Arbic [2010] to generate synthetic abyssal hills. The resulting synthetic bathymetry (e.g., Figure 1) is added to a previous iteration of global depth to make a new synthetic bathymetry data set. The final result matches the real soundings where they exist and blends smoothly into the updated predicted depth in the data voids.
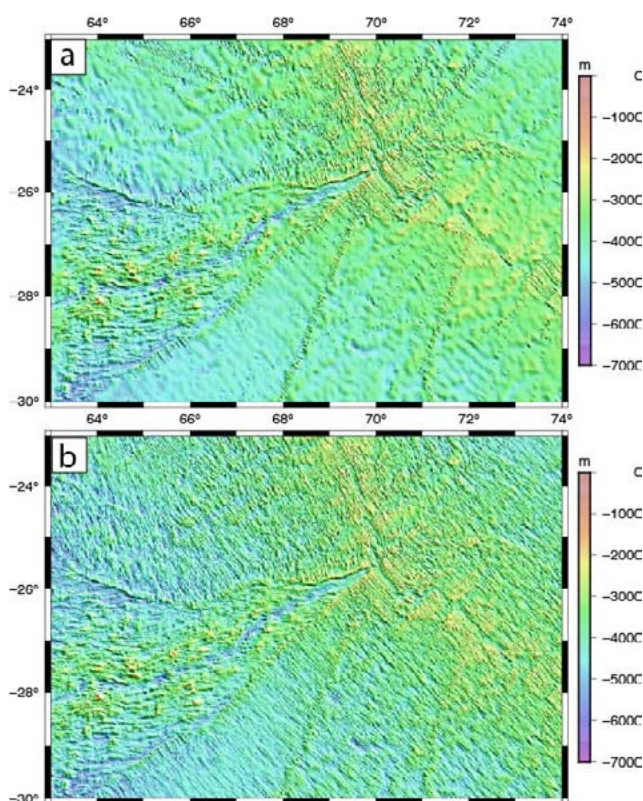
Figure 1. Example of synthetic abyssal hills around the Indian Ocean Triple Junction illustrate their variation with spreading direction and rate. (a) Gravity-predicted bathymetry to fill the gaps. (b) Synthetic abyssal hills superimposed on gravity-predicted bathymetry to fill the gaps.

3. MODELING SEAMOUNTS

Seamounts are isolated elevations in the seafloor with circular or elliptical plan, comparatively steep slopes, and relatively small summit area [Menard, 1964]. The vertical gravity gradient (VGG), which is the curvature of the ocean surface topography derived from satellite altimeter measurements, has been used to map the global distribution of seamounts [Kim and Wessel, 2011; 2015]. We used the latest grid of VGG to update and refine the global seamount catalog; we identified 10,796 new seamounts, expanding the seamount catalog by 1/3. 739 well-surveyed seamounts, having heights ranging from 421 m to 2500 m, were then used to estimate the typical radially-symmetric seamount morphology.

4. CONCLUSION

• Bathymetry predicted from satellite gravity cannot resolve the small-scale fabric of the deep ocean associated with abyssal hills and seamounts.
• We extend two methods to fill these gaps with higher resolution synthetic bathymetry.

• Synthetic abyssal hills are generated using an anisotropic statistical model based on high resolution multibeam surveys in a variety of tectonic settings.
• Small seamounts > 700 m tall can be accurately located in satellite gravity but their shape cannot be resolved. We use ~800 well-surveyed small seamounts to calibrate the expected shapes of and create synthetic bathymetry for all seamounts in the 800-2500 m height range.
• We generate two global bathymetry/topography products at 15 arcseconds using identical ship soundings. The SRTM15+ product has gaps filled with smooth predicted bathymetry and serves as the base layer for the 15 arcsecond GEBCO grid. The SYNBATH product has gaps filled with synthetic bathymetry from abyssal hills and seamounts superimposed on the smooth predicted bathymetry. The global grids, the characteristics of the 35,000 seamounts, and Google Earth overlays are all available at https://topex.ucsd.edu/pub/ .
• Ka-band altimeters such as SARAL/AltiKa and SWOT promise a dramatic improvement in marine gravity/bathymetry accuracy and resolution.

ACKNOWLEDGEMENTS

REFERENCES

GEBCO Bathymetric Compilation Group. (2020). The GEBCO_2020 Grid - a continuous terrain model of the global oceans and land. British Oceanographic Data Centre, National Oceanography Centre.

Gevorgian, J., Sandwell, D.T., Yu, Y., Kim, S.S. and Wessel, P., 2022. Global Distribution and Morphology of Small Seamounts. Submitted to Earth and Space Science.

Goff, J. A., & Arbic, B. K. (2010). Global prediction of abyssal hill roughness statistics for use in ocean models from digital maps of paleo-spreading rate, paleo-ridge orientation, and sediment thickness. Ocean Modelling, 32(1–2), 36–43. h

Kim, S., & Wessel, P. (2011). New global seamount census from altimetry-derived gravity data. Geophysical Journal International, 186, 615– 631.

Kim, S. S., & Wessel, P. (2015). October. Finding seamounts with altimetry-derived gravity data. In OCEANS 2015-MTS/IEEE Washington (pp. 1–6). IEEE.

Mayer, L., Jakobsson, M., Allen, G., Dorschel, B., Falconer, R., Ferrini, V., Lamarche, G., Snaith, H. and Weatherall, P., 2018. The Nippon Foundation—GEBCO seabed 2030 project: The quest to see the world's oceans completely mapped by 2030. Geosciences, 8(2), p.63.

Menard H. W. (1964) Marine Geology of the Pacific. McGraw Hill, New York

Sandwell, D.T., Goff, J.A., Gevorgian, J., Harper, H., Kim, S.S., Yu, Y., Tozer, B., Wessel, P. and Smith, W.H., 2022. Improved Bathymetric Prediction using Geological Information: SYNBATH. Earth and Space Science, 9(2), p.e2021EA002069.

Smith, W.H.F. and Sandwell, D.T. (1997) Global seafloor topography from satellite altimetry and ship depth soundings. Science, 277, 1956–62.

Tozer, B., Sandwell, D.T., Smith, W.H., Olson, C., Beale, J.R. and Wessel, P. (2019) Global bathymetry and topography at 15 arc sec: SRTM15+. Earth and Space Science, 6(10), pp.1847-1864.

Wessel, P., Luis, J. F., Uieda, L., Scharroo, R., Wobbe, F., Smith, W. H. F., & Tian, D. (2019). The generic mapping tools version 6. Geochemistry, Geophysics, Geosystems, 20(11), 5556–5564.

SESSION 4

BIO-GEO-CHEMICAL ISSUES, POLLUTION AGENTS & PROCESSES

Turbulent characteristics of the satellite-sensed submesoscale surface chlorophyll concentrations

Eun Ae Lee and Sung Yong Kim *

Environmental Fluid Mechanics Laboratory, Department of Mechanical Engineering,
Korea Advanced Institute of Science and Technology (KAIST)

Abstract – Turbulent characteristics of submesoscale surface chlorophyll concentrations are examined with hourly maps of geostationary ocean color imagery-derived chlorophyll concentration maps at a 0.5-km resolution for a period of five years off the East/Japan Sea. The wavenumber domain energy spectra of the chlorophyll concentrations exhibit anisotropy reflecting bathymetric effects and regional circulation, and their decay slopes change from $k^{-5/3}$ to k^{-1} at $O(10)$ km scales and from k^{-1} to k^{-3} at $O(1)$ km scales and have weak seasonality, which is consistent with the two-dimensional quasi-geostrophic turbulence theory and can be interpreted with the baroclinic instability in the weak seasonal mixed layer and non-seasonal regional circulations.

Keywords: Submesoscale, Energy Spectra, Geostrophic Turbulence, Geostationary Ocean Color Imager

1. INTRODUCTION

In the study of geostrophic turbulence, the spectral decay slopes of the one-dimensional wavenumber domain (k) kinetic energy (KE) spectra of dynamic variables (e.g., currents or density) have been used to identify the theoretical classifications of oceanic turbulent flows (e.g., Armi & Flament, 1985; Soh & Kim, 2018). The KE spectra of the currents in the quasi-geostrophic (QG), surface QG (sQG), and semi-QG (SG) theories show spectral decay slopes of k^{-3}; $k^{-5/3}$, and $k^{-8/3}$ at the highest wavenumbers, respectively (e.g., Blumen, 1978; Hoskins, 1975). In contrast, the wavenumber domain energy spectra of passive tracers exhibit theoretical slopes of $k^{-5/3}$ for inverse cascades and k^{-1} for forward cascades under the QG theory (e.g., Vallis, 2006).
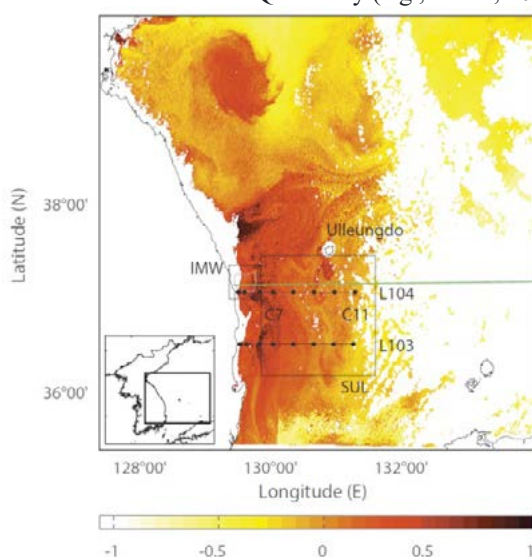
Figure 1. An example of the GOCI-derived chlorophyll concentrations ($\log_{10}$; μg L^{-1}) off the East/Japan Sea (EJS),

Specifically, the wavenumber domain energy spectra of chlorophyll concentrations have been described with spectral

decay slopes of k^{-1} for the two-dimensional turbulence, k^{-2} at a spatial scale of $O(1)$ km, and between k^{-1} and k^{-2} based on numerical simulations and the theory of growing phytoplankton in two-dimensional turbulent flows. These spectral slopes are valid up to the $O(1)$ km scale and become steeper below that scale (k^{-3}). On a large scale, the tracer-variance spectrum asymptotically approaches a decay slope of $k^{-5/3}$ (e.g., Vallis, 2006). In addition, Holloway (1986) reported the cross-shore variations of turbulent characteristics with the spectral decay slopes of k^{-2} in the offshore region and ranging from $k^{-1.5}$ to k^{-2} in the nearshore coastal area as a result of the increased energy inputs at shorter length scales near the coast associated with tidal mixing, interactions with bathymetry, and the rapid growth of phytoplankton in the coastal region.
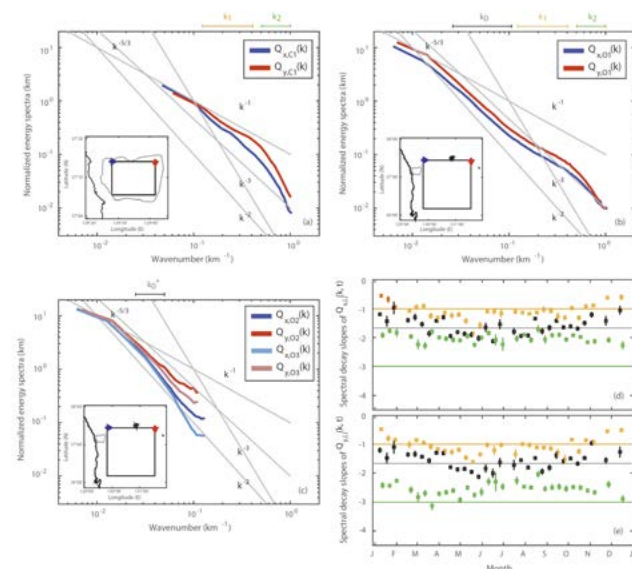
Figure 2. (a) and (b): Wavenumber domain energy spectra of GOCI-derived normalized chlorophyll concentrations (CHLs) for a period of 5 years (2011–2015) in the coast region [IMW] and open ocean area [Q; SUL]. (c) GOCI-derived chlorophyll concentrations [Q_{O1}], MODIS-derived chlorophyll concentrations [Q_{O2}], and VIIRS-derived chlorophyll concentrations [Q_{O3}]. The energy spectra of the chlorophyll concentrations sampled on multiple one-dimensional cross-shore lines (x) are averaged in the along-shore direction (y) to estimate the wavenumber domain energy spectrum (Q_x) in the cross-shore direction. Four gray auxiliary lines of k^{-1}, $k^{-5/3}$, k^{-2}, and k^{-3} spectral decay slopes are overlaid. (d) and (e): Time series of spectral decay slopes in the cross-shore and along-shore directions.

2. RESULTS

The spectral decay slopes of the wavenumber domain energy spectra become steeper and flatter depending on the characteristics of the turbulent flows and relevant theories. For instance, the spectral decay slopes of the energy spectra of the currents [E(k)] and concentrations [Q(k)] are described

---

* Corresponding author. Address: N7-6111, KAIST 291 Daehak-ro, Daejeon, 34141 Republic of Korea. Email: syongkim@kaist.ac.kr

with k^{-n} and $k^{(n-5)/2}$, respectively (e.g.,Vallis, 2006). Two length scales can be defined wherein the spectral decay slopes are changed corresponding to the transition of turbulent characteristics: an injection scale (λ_I) to delineate the inverse and forward cascades and a dissipation scale (λ_D) to divide the forward cascades and surface dissipation (e.g., Soh & Kim, 2018; Vallis, 2006).

The wavenumber domain energy spectra [Q(k)] of the chlorophyll concentrations sampled in the coastal region (IMW) show consistent spectral decay slopes of k^{-1} ($\lambda > \lambda_D$; $\lambda_D = 3$ km) and $k^{<-3}$ ($\lambda < \lambda_D$) in both cross-shore and along-shore directions (Figure 2a). In the same region, the KE spectra of the (surface) currents have spectral decay slopes between k^{-2} and k^{-3} at a scale of 2 km (e.g., Yoo et al., 2018).

These two submesoscale observations of the chlorophyll concentrations and surface currents can be explained by either QG theory or turbulent flows under geostrophic bathymetric effects, which have spectral decay slopes of k^{-3} and $k^{-2.5}$ at a scale of $O(1)$ km, respectively (e.g., Vallis, 2006). The energy spectra of the chlorophyll concentrations in the cross-shore and along-shore directions are consistent, but not identical (Figure 2a). The spatial anisotropy in this region has been reported in the surface current observations as a result of the circulation bounded by the coastal boundaries (e.g., Yoo et al., 2018).

The time series of the spectral decay slopes in the forward cascade region ($\lambda > \lambda_D$) exhibits seasonality and fluctuations at seasonal superharmonic frequencies, shown as k^{-2} for the summer and k^{-1} for the winter. These spectral decay slopes may be explained with the regional baroclinic instabilities within the moderate seasonal MLDs associated with the submesoscale eddies and circulations influenced by coastal boundaries (e.g., Yoo et al., 2018). Conversely, the spectral decay slopes below the dissipation scale ($\lambda < \lambda_D$) appear to be nearly out of phase those in the forward cascade region and have weak seasonality.

The GOCI-derived chlorophyll concentrations sampled in the open ocean (SUL) exhibit spectral decay slopes of $k^{-5/3}$ ($\lambda > \lambda_I$; $\lambda_I = 10$ km), k^{-1} ($\lambda_D < \lambda < \lambda_I$), and k^{-3} ($\lambda_I < \lambda_D$) based on their wavenumber domain energy spectra [$Q_o(k)$] in both the cross-shore and along-shore directions (Figure 2b). These spectral decay slopes can be interpreted as (1) the forward cascades of enstrophy (the integral of the square of the vorticity) and inverse cascades of energy appear at the injection scale [$\lambda_I = O(10)$ km], where the baroclinic instability in the mixed layer plays a more dominant role as the driver of the submesoscale processes rather than the mesoscale eddy-derived surface frontogenesis does at a scale of $O(100)$ km (e.g., Ferrari & Wunsch, 2009) and (2) the surface dissipation scale appears near $O(1)$ km. Note that the KE spectra of the HFR-derived surface currents do not clearly show the dissipation scale due to limited spatial scale of the observations ($\lambda > 2$ km) (Yoo et al., 2018). Similarly, the MODIS and VIIRS-derived chlorophyll concentrations sampled in the same region have nearly consistent variance of their energy spectra and spectral decay slopes at spatial scales greater than 30 km in the forward cascade region (Figures 2b and 2c). Note that the spectral decay slopes in both directions are nearly identical and differ at length scales of less than 5 km (Figure 2b), which shows the length scale that characterizes the anisotropy.

Similarly, based on the energy spectra of the open ocean chlorophyll concentrations, the spectral decay slopes in the forward cascade ($\lambda > \lambda_I$; k_0 and k_0^*) and inverse cascade ($\lambda_D < \lambda < \lambda_I$; k_1) show seasonality (Figures 2d and 2e). The spectral decay slopes below the dissipation scale ($\lambda < \lambda_D$; k_2) are slightly out of phase with those within the two wavenumber ranges (k_0, k_0^*, and k_1) (Figures 2d and 2e).

In three-dimensional turbulence, the dissipation scale appears at $O(1)$ cm, which can be associated with molecular dissipation. In contrast, in two-dimensional turbulent flows, the dissipation scale is related to the scales at which the gravity waves start to break; three-dimensional effects become important at scales of $O(1-100)$ m (e.g., Nikurashin et al., 2013). Thus, the surface dissipation scale appears near $O(1)$ km, which can be an upper bound of the observations analyzed in this paper (Figure 6 in Ferrari & Wunsch, 2009).

3. CONCLUSION

The wavenumber domain energy spectra of the chlorophyll concentrations exhibit anisotropy reflecting bathymetric effects and regional circulation, and their decay slopes change from $k^{-5/3}$ to k^{-1} at $O(10)$ km scales and from k^{-1} to k^{-3} at $O(1)$ km scales and have weak seasonality, which is consistent with the two-dimensional quasi-geostrophic turbulence theory.

REFERENCES

Armi, L., & Flament, P. (1985). Cautionary remarks on the spectral interpretation of turbulent flows. Journal of Geophysical Research, 90(C6), 11779–11782.

Blumen, W. (1978). Uniform potential vorticity flow: Part I. Theory of wave interactions and two-dimensional turbulence. Journal of the Atmospheric Sciences, 35(5), 774–783.

Ferrari, R., & Wunsch, C. (2009). Ocean circulation kinetic energy: Reservoirs, sources, and sinks. Annual Review of Fluid Mechanics, 41, 253–282

Hoskins, B. J. (1975). The geostrophic momentum approximation and the semi-geostrophic equations. Journal of the Atmospheric Sciences, 32(2), 233–242.

Nikurashin, M., Vallis, G., & Adcroft, A. (2013). Routes to energy dissipation for geostrophic flows in the Southern Ocean. Nature Geoscience, 6(1), 48–51.

Soh, H. S., & Kim, S. Y. (2018). Diagnostic characteristics of submesoscale coastal surface currents. Journal of Geophysical Research: Oceans, 123, 1838–1859.

Vallis, G. K. (2006). Atmospheric and oceanic fluid dynamics (745. pp.). Cambridge, UK: Cambridge University Press.

Yoo, J. G., Kim, S. Y., & Kim, H. S. (2018). Spectral descriptions of submesoscale surface circulation in a coastal region. Journal of Geophysical Research: Oceans, 123, 4224–4249.

Assessment of the phytoplankton bloom variability in the NW Mediterranean Sea by the Robust Satellite Techniques (RST)

E. Ciancia[1] *, T. Lacava[1], N. Pergola[1], V. Vellucci[2], D. Antoine[3,4], V. Satriano[5] and V. Tramutoli[5]

[1] Institute of Methodologies for Environmental Analysis, Italian National Research Council, C.da Santa Loja, Tito Scalo, 85050, Potenza, Italy

[2] Sorbonne Université, CNRS, Institut de la Mer de Villefranche, LOV, F-06230 Villefranche-sur-Mer, France

[3] Remote Sensing and Satellite Research Group, School of Earth and Planetary Sciences, Curtin University, Perth, WA 6845, Australia

[4] Sorbonne Université, CNRS, Laboratoired'Océanographie de Villefranche, IMEV, F-06230 Villefranche-sur-Mer, France

[5] School of Engineering, University of Basilicata, Via dell'Ateneo Lucano 10 Potenza 85100, Italy

Abstract – Investigating the variability of phytoplankton phenology plays a key role in regions characterized by cyclonic circulation regimes or convective events. The main goal of this study is to evaluate the potential of the Robust Satellite Techniques (RST) in identifying anomalous phytoplankton blooms in the NWM by using 9 years (2008-2017) of multi-sensor chlorophyll-a (chl-a) products from the OC-CCI dataset. Further implementation of the RST approach on a corresponding time-series of in situ chl-a measurements acquired at the BOUSSOLE site allows assessing the accuracy of the satellite-based change detection index. The integration of the achieved results has ensured to characterize an anomalous chl-a bloom that occurred in March 2012 at regional scale. Results show positive chl-a anomalies between the BOUSSOLE site and the Center of Convection Zone (CCZ).

Keywords: phytoplankton phenology; multi-sensor ocean colour data; long-term analysis.

1. INTRODUCTION

Satellite Ocean Colour Radiometry (OCR) is a powerful tool to study phytoplankton phenology, as it ensures synoptic and long-term observations of the sea-surface chlorophyll-a concentration (chl-a), a proxy of phytoplankton biomass. Although the chl-a seasonality is well documented at basin scale of analysis, the assessment of its inter-annual variability deserves to be deeply investigated. Irregular (i.e. non-seasonal) inter-annual chl-a variations can be found in areas affected by intense wind forcing or winter deep water convection (WDWC) events such as the North Western Mediterranean Sea. Although WDWC is an annual feature in the NWM, its inter-annual fluctuations determine a high variability in terms of magnitude and spatial extension of the spring bloom. In this context, it is worth implementing tools

capable of identifying the non-seasonal chl-a variations. The Robust Satellite Technique (RST) (Tramutoli et al. 2007) is a general change detection scheme based on the analysis of long-term datasets homogeneous in the spatiotemporal domain. The inherent rationale for the RST approach is to discard any cyclical fluctuations (daily or seasonal) of a geophysical variable in order to identify only its statistically infrequent variations and therefore are defined as anomalies (Ciancia et al. 2021). The homogenized and inter-calibrated time series of multi-sensor OCR products provided by the European Space Agency (ESA) Ocean Colour Climate Change Initiative Program (OC-CCI) are suitable for the RST implementation. This work aims at testing the RST approach on a new study area (i.e. NWM) by such multi-sensor merged data, thus requiring a preliminary assessment through sea-truth data. The in situ measurements acquired by a permanent optical mooring, namely BOUée pour l'acquiSitiond'une Série Optique à Long termE (BOUSSOLE), located in the Ligurian Sea, can be profitably exploited for this purpose as it provides collections of quasi-continuous data since 2003 (Antoine et al. 2011). Our twofold objective is (1) to validate results of the RST methodology applied to 9 years (2008-2017) of multi-sensor merged chl-a products from the OC-CCI (version 4.2) against corresponding in situ data; (2) move from a local to a regional scale analysis (i.e. NWM) in order to characterize the chl-a anomalies in the spatio-temporal domain.

2. DATA AND METHODS

2.1 In situ chl-a data

In this work we considered Chl-a fluorescence (Fluo) data acquired at the BOUSSOLE site on the optical mooring by the deployment of two sets of WetLabs (now Sea-Bird Scientific) ECOFLNTUs fluorometers. For each day, average Fluo data acquired before dawn, and after sunset are averaged to obtain the daily Fluo value (i.e., approximately the interpolated value at about 11h30' UTC local time) and the corresponding daily chl-a (mg m-3) (Ciancia et al. 2021). In detail, we exploited such in situ chl-a data for the 2008-2017 period to implement the RST approach.

2.2 Satellite chl-a data

Based on the OC-CCI dataset, we used the Level 3 daily chl-a product at 4 km spatial resolution, hereafter OC-CCI chl-a. This is a multi-sensor merged product based on a blended algorithm for chl-a retrievals. The OC-CCI chl-a products were downloaded for the same period of in situ chl-a measurements (2008-2017).

2.3 The Robust Satellite Techniques

RST is a statistical method developed to analyse multi-annual series of satellite data. RST requires the computation, at pixel level, of the climatological mean and standard deviation (called reference fields) of the investigated variable observed within homogenous conditions (i.e., same location, month and acquisition time) (Tramutoli et al. 2007).

After calculation of reference fields, the Absolutely Local Index of Change of the Environment for chl-a, namely chl-a ALICE index (Ciancia et al. 2021), is computed as:

$$\otimes_{chl-a}(x,y,t) = \frac{chl-a\,(x,y,t) - \mu_{chl-a}\,(x,y)}{\sigma_{chl-a}\,(x,y)} \qquad (1)$$

* Corresponding author. Address: C. da Santa Loja, 85050 Tito Scalo (PZ), Italy. Email: emanuele.ciancia@imaa.cnr.it

where *chl-a(x,y,t)* is the chl-a value at longitude *x*, latitude *y* and time *t*, $\mu_{chl-a}(x,y)$ and $\sigma_{chl-a}(x,y)$ are the climatological monthly mean and standard deviation computed at the same location. These parameters are computed for the two 2008-2017 datasets considered here (i.e., OC-CCI and in situ), and we refer alternatively to each of them using the same symbols in the following. A positive/negative chl-a ALICE value indicates an increase/decrease of chl-a respect to its climatological value. For construction, the chl-a ALICE index is a standardized variable, which tends to have a Gaussian distribution. The occurrence probability of values above/below ±1, ±2 and ±3 is about 16%, 2.5% and 0.13%, respectively (Ciancia et al. 2021).

3. RESULTS

3.1 Validation of the satellite chl-a ALICE

One of the main goals of this work is to evaluate the RST suitability to detect anomalous phytoplankton blooms at the BOUSSOLE site and within the NWM area. For this reason, we evaluated the temporal variability of the two chl-a ALICE indices considered for each blooming period (i.e., November – May) of the 2008-2017 time series. In particular, the two chl-a ALICE indices are able to concurrently detect statistically significant anomalies (i.e., chl-a ALICE Index > 2) at the BOUSSOLE site as for example in March and May 2012, as shown in Fig.2.
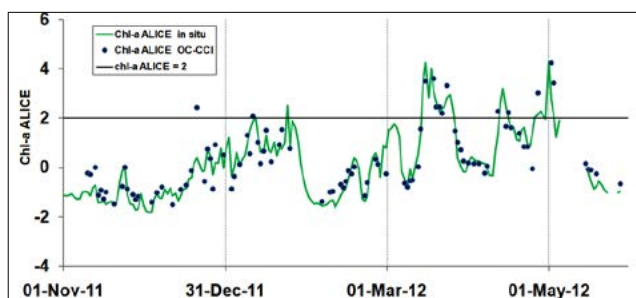
Figure 2. *Temporal variability of the two chl-a ALICE indices at the BOUSSOLE site for the November 2011 - May 2012 period.*

The two chl-a ALICE indices show a good agreement thus inherently proving the effectiveness of the RST approach in detecting relative variations of the investigated signal regardless the different source of data (satellite vs in situ). The accuracy of the satellite-based chl-a ALICE index has been confirmed by a match-up analysis with the corresponding in situ values for the whole investigated period (i.e., 2008-2017). The chl-a ALICE OC-CCI exhibits a good performance when compared to in situ data with R^2 and RMSE values of 0.75 and 0.48, respectively.

3.2 Regional scale analysis: the March 2012 case study

The statistically significant anomalies (i.e., chl-a ALICE values > 2) recorded in March 2012 at the BOUSSOLE site indicate the occurrence of a phytoplankton bloom deserving to be in-depth investigated. Both the chl-a ALICE indices identify persistent chl-a anomalies at the BOUSSOLE site on 6 days (i.e. 16, 19, 20, 21, 22, 24 of March 2012). To characterize the spatial extension of the chl-a anomalies we computed the daily OC-CCI chl-a ALICE maps over the whole NWM area within the 16-30 March 2012 period (Fig.3).
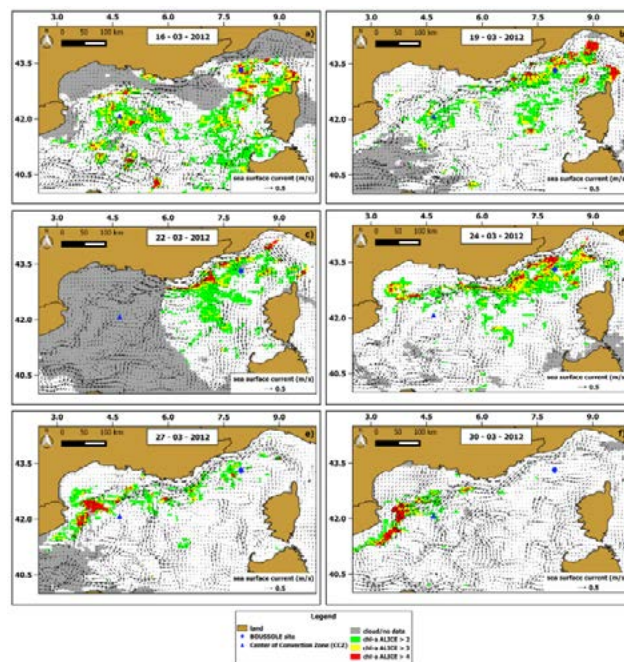
Figure 3. *Chl-a ALICE OC-CCI maps of 6 days between 16 – 30 March 2012. The superimposed black arrows are the corresponding daily data of sea surface current (speed and direction). Adapted by Ciancia et al. 2021.*

Chl-a anomalies were mostly detected within the first four days (i.e., 16, 19, 22, 24 March 2012), especially between the BOUSSOLE site and the Center of Convection Zone.

4. CONCLUSION

In this work, we assessed the potential of the RST approach in identifying anomalous phytoplankton blooms in the NWM by using 9 years (2008-2017) of multi-sensor merged chl-a products from the OC-CCI dataset. The application of RST on a corresponding time series of in situ chl-a measurements at the BOUSSOLE site allowed evaluating the accuracy of the satellite-based chl-a ALICE, that exhibited a good performance with R^2 and RMSE values of 0.75 and 0.48, respectively. Furthermore the implementation of the chl-a ALICE OC-CCI allowed at characterizing the anomalous phytoplankton bloom of mid-March 2012. The area roughly encompassed between the BOUSSOLE site and the CCZ showed the highest persistence of positive chl-a anomalies (i.e., $\otimes_{chl-a}(x,y,t) > 2$), probably due to the cyclonic circulation regime characterizing the area.

REFERENCES

Tramutoli, V. (2007). Robust Satellite Techniques (RST) for Natural and Environmental Hazards Monitoring and Mitigation: Theory and Applications. In Proceedings of the Fourth International Workshop on the Analysis of Multitemporal Remote Sensing Images, Louven, Belgium.

Ciancia, E., Lacava, T., Pergola, N., Vellucci, V., Antoine, D., Satriano, V., Tramutoli, V. (2021). Quantifying the Variability of Phytoplankton Blooms in the NW Mediterranean Sea with the Robust Satellite Techniques (RST). Remote Sens. 13, 5151.

Antoine, D., Siegel, D.A., Kostadinov, T., Maritorena, S., Nelson, N.B., Gentili, B., Vellucci, V., Guillocheau, N. (2011). Variability in optical particle backscattering in contrasting bio-optical oceanic regimes. Limnol. Oceanogr. 56(3), 955-973.

The Use of Ocean Colour in New Caledonia, Vanuatu, Fiji, and Tonga Archipelagos: From large *Trichodesmium* oceanic blooms to chlorophyll in shallow coral lagoons

C. Dupouy [a, b,]*, A. Whiteside [a,b] A. Singh [b], J. Lefèvre [c], G. Wattelez [d], H. Murakami [e], R. Frouin [f]

[a] Aix Marseille U., Toulon U., CNRS, IRD, Mediterranean Institute of Oceanography, Marseille, France
[b] PaCE-SD, University of the South Pacific, awnesh.sing@usp.ac.fj, andra.whiteside@gmail.com
[c] ENTROPIE Centre IRD de Noumea, New Caledonia, Jerome.lefevre@ird.fr
[d] University of New Caledonia, New Caledonia, guillaume.wattelez@univ-nc.nc
[e] Japan Agency for Exploration of Space, Japan, murakami.hiroshi.eo@jaxa.jp
[f] Scripps Institution of Oceanography, USA, frouin@ucsd.edu

Abstract – The Southwest Tropical Pacific oceanic waters at 15°S are mostly oligotrophic. Still, these large ocean areas are subject to large dendritic phytoplankton blooms, developing within archipelagos, sometimes in connection with lagoons surrounding islands. The variety of spectral signatures of these blooms has been measured during research cruises, in open oceans as well as in lagoons. In lagoons, the seabed reflectance effect is predominant and must be minimized or at least determined in order to be able to use high resolution ocean color imagery and to assess lagoon chlorophyll (Chla).

Keywords: archipelagos, phytoplankton, *Trichodesmium*, lagoons, climate change.
.

1. INTRODUCTION

Southwest Tropical Pacific ecological status of seas of archipelagos is vital for the economy of Pacific Islands Countries. Oceanic waters at 15°S are dominated by oligotrophic conditions. Still, large ocean areas are subject to large dendritic phytoplankton blooms, developing between archipelagos, mostly in connection with islands or lagoons surrounding them (Figure 1).
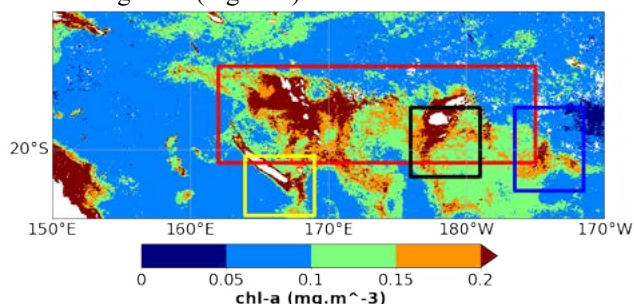
Figure 1. *Chlorophyll a blooms in the Southwest Tropical Pacific Ocean with New Caledonia, Vanuatu, Fiji, Tonga archipelagos (MODIS composite for April 2016). Boxes indicate where different algorithms have been developed.*

The satellite imagery can be used to understand what governs the chlorophyll variability in this tropical region, characterized by highly stratified and warm waters, as well as in shallow coral lagoons.

2. CHLA IN OPEN SEAS

Satellite and aerial observations show the presence of surface *Trichodesmium* blooms over 3000 km, mainly around islands of Vanuatu, New Caledonia, and as far east as the Tongan Trench (Dupouy et al., 2011; Figure 2). *Trichodesmium* represents 60% of total chlorophyll during open sea summer blooms while it represents only 10% during winter in the open sea (Tenorio et al., 2018; Dupouy et al, 2018). It represents also a few percent in more coastal and lagoon waters (Dupouy et al., 2020). In summer, microscopic observations show that the cyanobacterial diazotrophs community dominates while picoplankton is present during winter periods (Tenorio et al., 2018).
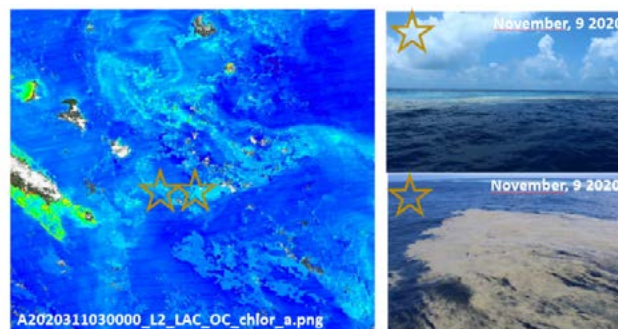
Figure 2. *Large Trichodesmium surface accumulation, linked to a large dendritic chlorophyll bloom at the east of Loyalty Islands (New Caledonia archipelago). MODIS image of 9 November 2020 coincided with a cruise observation.*

Cyanobacteria are responsible for a large percentage of global oceanic N_2 fixation. Developed algorithms for discrimination of surface blooms (McKinna, 2015; Dupouy et al., 2018) are successful when atmospheric corrections are appropriately used above surface mats (keeping the near-infra red reflectance) or when *Trichodesmium* is dominant vs other species (Rousset et al., 2018). The succession between *Trichodesmium* and other phytoplankton fueled by them is yet to be analyzed and satellite imagery will be the only tool available.

In the Tongan region, Chla blooms may be mixed with special volcanic eruptive signatures such as discolored waters, consolidated and fragmented pumice rafts, and do not appear to be necessarily linked to eruptions. However, such events may result in a lag in Chla enrichment from the release of nutrients (Whiteside et al. 2021).

3. CHLA IN SHALLOW CORAL LAGOONS

Southwest Tropical lagoons are classified as Case 2 waters with influence of shallow bathymetry, high turbidity and where the estimation of surface chlorophyll requires

---

* Corresponding author. Address: PaCE-SD, Suva, Fiji, cecile.dupouy@ird.fr

algorithm adjustments (Minghelli-Roman and Dupouy, 2014). Chlorophyll a are often underestimated when applied to bio-optical data and satellite reflectance (Favareto et al., 2018; Dupouy et al., 2020). Algorithms could be successfully adapted to New Caledonia waters for Chla (Wattelez et al., 2016) and turbidity (Wattelez et al., 2017). Recently, seabed reflectance could be inverted from high resolution imagery (Wattelez et al., 2022) and such a method could be applied to all lagoons, provided that bathymetry is known for the whole area. Indeed, lagoons are a major source of nutrients useful for phytoplankton and satellite imagery can be used to explain the processes at the interface between coastal lagoons and surrounding shallow ocean (Figure 3).
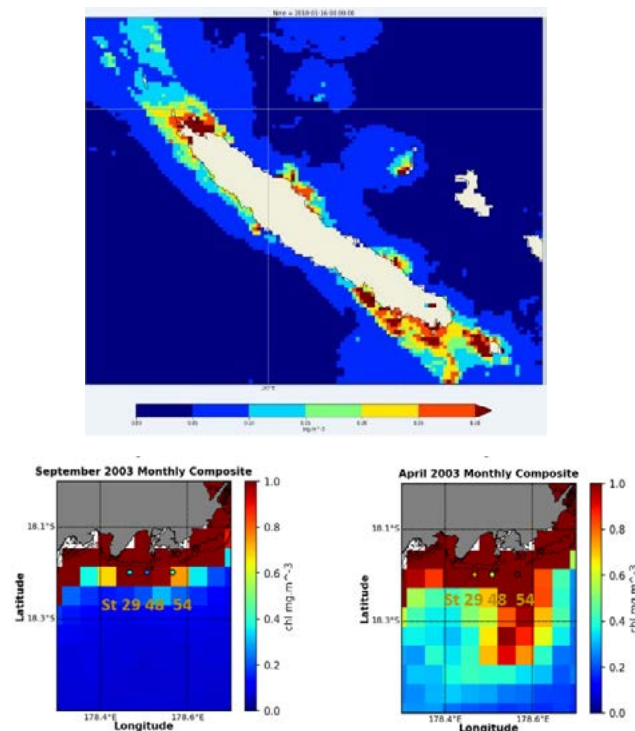
Figure 3. *Maps of the New Caledonia lagoon and South Fijian coastal area indicating in brown, waters where regional algorithms for Chla must be applied.*

4- CONCLUSION

What governs the chlorophyll variability in the Southwest tropical archipelagos and lagoons? It is necessary to look at variability and trends of Chla issued from ocean colour time series as a function of environmental parameters and climatic indices. These analyses require discriminating *Trichodesmium*, the major nitrogen fixing species from other phytoplankton, and the application of regionally adapted algorithms for coastal ocean and coral lagoons. Both oceanic and coastal oceans are vital for the economy of Small Island Developing states and multivariate correlative analysis will help to quantify ecosystem changes over spatial and temporal scales relevant to human activity and how they respond to (natural and anthropogenic) disturbance.

ACKNOWLEDGEMENTS

REFERENCES

Dupouy, C., Benielli-Gary, D., Neveux, J., Dandonneau, Y, and T. Westberry, (2011). An algorithm for detecting *Trichodesmium* surface blooms in the South Western Tropical Pacific, Biogeosciences, 8, 3631–3647.

Dupouy, C., Frouin, R, Tedetti, M., Maillard, M., Rodier, M., Duhamel, S., Guidi, L., Lombard, F., Picheral, M., Neveux, J., Charrière, B., and R. Sempéré (2018). Diazotrophic *Trichodesmium* impact on UV VIS radiance and pigment composition in the South West Tropical Pacific, Biogeosciences, 15, 5249–5269.

Dupouy C., Röttgers, R., Tedetti M., Frouin R., Rodier, M., Martias, C., and M. Goutx (2020). Influence of meteorological conditions on the distribution of CDOM and biogeochemical parameters in the Eastern lagoon of New Caledonia, Front. Earth. Sci., 8.

Favareto, L., De Moraes Rudorff, N., Kampel M., Frouin, R., Röttgers, R., Doxaran, D., Murakami H., and C. Dupouy (2018). Bio-optical properties of the Eastern lagoon of New Caledonia, South Trop. Pacific, Remote Sens., 10(7), 1043.

Ganachaud, A., von Schuckmann, K., Whiteside, A., C. Dupouy et al. (2022). CMEMS SST and Chl-a indicators for two Pacific Islands: a co-construction monitoring framework for an integrated, transdisciplinary, multi-scale approach. Journal of Operational Oceanography 16, 1-15.

McKinna, 2015 Three decades of ocean-color remote-sensing *Trichodesmium* spp. in the World's oceans: A review Progress in Oceanography, 131, 177-199.

Minghelli-Roman A., and C. Dupouy (2014). Seabed mapping in the lagoon of New Caledonia with MeRIS images, IEEE JSTAR Remote Sens, 7, 6, 2619-2629.

Murakami, H., and C. Dupouy (2013). Atmospheric correction and inherent optical property estimation in the southwest New Caledonia lagoon using AVNIR-2 high-resolution data, Applied Optics, 52, 2, 182–198.

Rousset G., De Boissieu F., Lefèvre J., Rodier M., Laran S., Ridoux V., Roudault G., Gardes L., Frouin, R., C. Menkes, S. Bonnet, and C. Dupouy (2018). Remote Sensing of *Trichodesmium* spp. mats in the Western Tropical South Pacific. Biogeosciences, 15, 5203–5219.

Tenório, M., Dupouy C., Rodier, M., and J. Neveux (2018). *Trichodesmium* and other Filamentous Cyanobacteria in New Caledonian waters (South West Tropical Pacific) during an El Niño Episode. Aquat. Microb. Ecol. 81, 219-241.

Wattelez, G., Dupouy, C., Mangeas, M., Lefèvre, J., Touraivane, and R. Frouin (2016). A statistical algorithm for estimating chlorophyll concentration in the New Caledonian lagoon, Remote Sens. 8(1), 45.

Wattelez, G., Dupouy, C., Juillot, F., Fernandez, J.M., Lefèvre, J., and S. Ouillon (2017). Remotely-sensed assessment of turbidity with MODIS in the oligotrophic lagoon of Voh-Koné-Pouembout area, Water, 9, 737.

Wattelez, G., Dupouy, C., and F. Juillot (2022). Unsupervised Optical Classification of the Seabed Color in Shallow Oligotrophic Waters from Sentinel-2 Images: A Case Study in the Voh-Koné-Pouembout Lagoon (New Caledonia), Remote Sens. 2022, 14(4), 836.

Whiteside A., Dupouy, C., Singh A., Frouin R., Menkes C., and J. Lefèvre (2021). Automatic Detection of Optical Signatures within and around Floating Tonga-Fiji Pumice Rafts Using MODIS, VIIRS, and OLCI Satellite Sensors, Remote Sensing, 13(3), 501.

'COLOR: CDOM-proxy retrieval from aeOLus ObseRvations

D. Dionisi[1]*, S. Bucci[2], C. Cesarini[1], S. Colella[1], D. D'Alimonte[3], L. Di Ciolo[2], P. Di Girolamo[4], G. Giuliano[1], M. Di Paolantonio[1], N. Franco[4], G. Gostinicchi[2], T. Kajiyama[3], G. L. Liberti[1], E. Organelli[1], R. Santoleri[1]

(1) Institute of Marine Sciences, Italian National Research Council, Rome, Italy
(2) Serco Italia S.p.A., Frascati, Italy
(3) AEQUORA, Lisbon, Portugal
(4) School of Engineering, University of Basilicata, Potenza, Italy

Abstract – During the last decade, new applications exploiting data from satellite borne lidar measurements demonstrated that the potential information that these sensors can provide to the ocean color studies. Within this framework, COLOR (CDOM-proxy retrieval from aeOLus ObseRvations), which is an on-going 18-month study approved by ESA within the Aeolus+ Innovation program, has the objective is to evaluate and document the feasibility of deriving an in-water prototype product from AEOLUS observations at 355 nm. In particular, COLOR project focuses on the AEOLUS potential retrieval of: 1) Diffuse attenuation coefficient for downwelling irradiance (K_d [m^{-1}]); 2) Subsurface hemispheric particulate backscatter coefficient (b_{bp} [m^{-1}]). The preliminary results of the project will be here presented.

Keywords: AEOLUS, ocean color, satellite borne lidar.

1. INTRODUCTION

Recently, new applications using CALIOP (Cloud-Aerosol Lidar with Orthogonal Polarization) instrument onboard CALIPSO (Cloud-Aerosol Lidar and Infrared Pathfinder Satellite Observation) demonstrated that satellite-borne lidar can give valuable information about ocean optical properties (Behrenfeld et al., 2019; Dionisi et al., 2020).

The ESA Earth Explorer Wind Mission ADM-Aeolus (Atmospheric Dynamics Mission, ESA, 2008), launched on 22 August 2018, has the goal to provide global observations of wind profiles, demonstrating the impact of wind profile data on operational weather forecasting and on climate research. Furthermore, although Aeolus's mission primary objectives and subsequent instrumental and sampling characteristics are not ideal for monitoring ocean sub-surface properties, the potential application of AEOLUS observations to ocean color studies could bring benefits to the oceanographic community. Indeed, being the first HSRL (High Spectral Resolution Lidar) launched in space, ALADIN (Atmospheric LAser Doppler INstrument) of ADM-Aeolus gives an unprecedented new opportunity to investigate the information content of the 355 nm signal backscattered by the ocean sub-surface components.

Based on the above considerations, COLOR (CDOM-proxy retrieval from aeOLus ObseRvations), a selected Aeolus+ Innovation ITT project, aims to evaluate and document the feasibility of deriving an in-water AEOLUS prototype product from the analysis of the ocean sub-surface backscattered component of the 355 nm signal acquired by the ALADIN. An overview of the project and some preliminary results are presented.
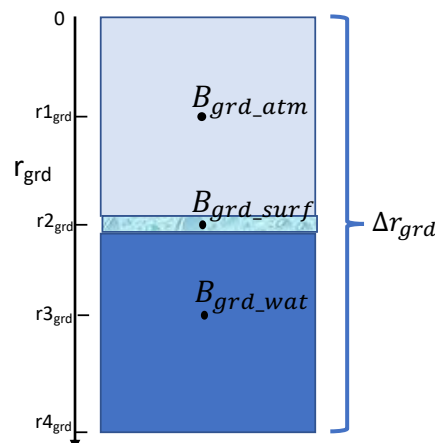
Figure 1. *Schematic geometry description of the AEOLUS ground bin.*

2. METHODS

The objective of the COLOR project is to assess the feasibility and document the AEOLUS potential retrieval of the ocean optical properties at 355 nm: diffuse attenuation coefficient for downwelling irradiance, K_d [m^{-1}], and sub-surface hemispheric particulate backscatter coefficient, b_{bp} [m^{-1}]. Being dominated by the absorption due to CDOM (Chromophoric Dissolved Organic Matter), K_d coefficient at 355 nm, $K_d(355)$, can be used as a proxy to describe spatial and temporal variability of this variable, which contributes to regulating the Earth's climate.

To reach COLOR objectives, the core activity of the project is the characterization of the signal from the AEOLUS ground bin (Δr_{grd}). In principle, the ground bin backscattered radiation signal is generated by the interaction of the emitted laser pulse radiation with two media (atmosphere and ocean, B_{grd_atm} and B_{grd_wat}, respectively) and their interface (B_{grd_surf}, see Figure 1).

To characterize the AEOLUS ground bin signal and then develop an ocean color AEOLUS retrieval algorithm, two parallel and strongly interacting activities were developed:

a) Radiative transfer numerical modelling. This tool is essential to simulate the relevant radiative processes expected to be responsible for the generation of AEOLUS surface bin signal.

---

* Corresponding author. Address: Via Fosso del Cavaliere 100, 00133 Roma Tor Vergata (RM), Italia. Email: davide.dionisi@cnr.it

b) AEOLUS data analysis. The objective of this activity is to verify the information content of the AEOLUS ground bin signals and the assumptions for data product retrieval.

The preliminary results about the above-mentioned activities will be here presented.

3. RESULTS

A Monte Carlo based radiative transfer numerical model was developed and validated to simulate AEOLUS signal propagation in ocean. In particular, numerical simula-tions were used to estimate: 1) the fraction of radiant power back-scattered by the sea surface as a function of the wind speed; 2) the fraction of radiant power back-transmitted from seawater to air at varying Chl-a values and different CDOM added contributions; 3) and the fraction of back-transmitted radiant power specifically origi-nated from the sea-bottom reflection.
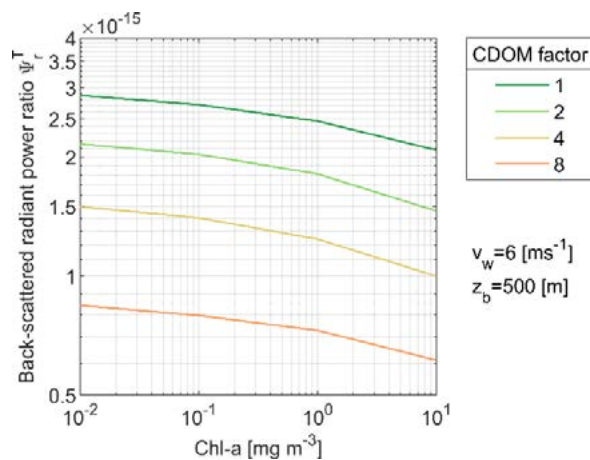
Figure 2. *Backscattered radiant power ratio Ψ^T for Chl-a=0.01, 0.1, 1, 10 $mg\ m^{-3}$. Different lines correspond to added CDOM for factors from 2 to 8 (the case labeled as 1 indicates Case-1 water conditions). The wind speed is $v_w = 6\ ms^{-1}$. The depth of the sea bottom is $z_b = 500\ m$.*

As an example of RTMT simulation results, Figure 2 shows the contribution of the water bin to the received signal, which is expressed as the back-transmitted radiant power ratio Ψ^T (i.e., the ratio of the total received radiant power over the emitted radiant power) as a function of Chl-a at varying CDOM contributions. Simulations are performed considering z_b=500 m for the sea bottom and v_w=6 ms^{-1} for the wind speed. The reference Case-1 water corresponds to a CDOM factor α_{CDOM}=1. Optically complex waters where the CDOM contribution is n times that of Case-1 waters correspond to α_{CDOM}=n (a geometrical progression from 2 to 8 is considered). Results show a Ψ^T decrease as Chl-a and the α_{CDOM} factor increase.

The second step was the design of an inversion algorithm to evaluate a potential AEOLUS ocean color product. This algorithm, which used only Mie channel observa-tion, is capable to obtain analytically the term B_{grd_wat} under several assumption. In order to have a very preliminary evaluation of the validity of the proposed model, the algorithm was applied to a set of AEOLUS data (i.e. from December 2019 to May 2021) extracted for the ocean test areas selected within COLOR project. Figure 3 depicts the probability density functions of the computed B_{grd_wat} for different test areas with different ocean optical properties. This figure seems to

confirm the results obtained by the model: for oligotrophic regions B_{grd_wat} is higher whereas for high absorption regions B_{grd_wat} decreases. Further studies and assessment will be conducted in the last phase of COLOR project.
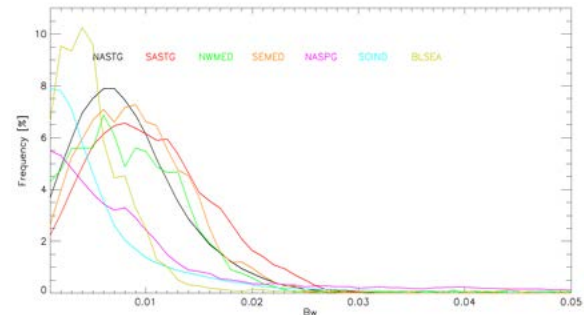
Figure 3. *Histogram plots for the B_{grd_wat} derived using the developed AEOLUS ocean color algorithm for the Mie channel. The AEOLUS dataset from December 2019 to May 2021 have been used for the different test areas.*

ACKNOWLEDGEMENTS

REFERENCES

Behrenfeld M., et al.: Global satellite-observed daily vertical migrations of ocean animals, Nature, vol. 576, n. 7786, Art. n. 7786, doi: 10.1038/s41586-019-1796-9, 2019.
Dionisi D. et al.: Seasonal distributions of ocean particulate optical properties from spaceborne lidar measurements in Mediterranean and Black sea, Remote Sens. Envi-ron., vol. 247, pag. 111889, doi: 10.1016/j.rse.2020.111889, 2020.
European Space Agency: ADM-Aeolus Science Report, ESA SP-1311, 2008.

Ocean fronts observed using multiscale satellite and model data provide a proxy for marine litter aggregation

P.I. Miller [1], J. Clark [1], A. Kurekin [1], L. Biermann [1], M. Al Azhar [1], F. Gibert [2], M. Cole [1], V. Martinez Vicente [1]

1: Plymouth Marine Laboratory, Prospect Place, The Hoe, PL1 3DH, Plymouth, UK
2: Lobelia/isardSAT, Barcelona, Spain

Abstract: Fronts – the boundaries between water masses, in coastal and oceanic regions – are hotspots for rich and diverse marine life, and are also where floating marine debris tends to accumulate. The goal of this research is to develop effective satellite and model proxies for marine litter aggregation, which can be used to identify frontal areas where interventions would be most effective.

Keywords: oceanic fronts, marine litter aggregation, SST, ocean colour, remote sensing, hydrographic modelling, FVCOM.

1. SUMMARY

We have considered the most appropriate spatial scale of ocean fronts as a proxy of marine litter, through automated detection of ocean fronts on various satellite datasets: sea-surface temperature (SST) at 1km resolution, and ocean colour at 300m and 30m resolution. These fronts are then compared against floating debris both observed using very high resolution satellite images, and modelled as particles with a detailed hydrographic model. The FVCOM model can predict where floating debris will aggregate, and also reveal coherent structures in the surface current fields which attract particles. We have trialed this satellite and modelling approach in a case study area near Da Nang Bay in Vietnam, which is exposed to significant marine litter. Results for the case study will be presented, together with recommendations for application of these satellite and model techniques to address the growing environmental crisis of marine litter.

2. FRONT DETECTION USING DIFFERENT SATELLITE SENSORS

2.1. Thermal front detection

2.1.1   Data

Daily NASA Multi-Sensor Merged Ultra-High Resolution (MUR) Sea Surface Temperature (SST) imagery for 2018 was mapped to the study area at 1 km resolution. The strength of MUR is that it combines cloud-free data from multiple infrared sensors, and merges this with coarser passive microwave data to produce a gap-free daily SST map. However, the interpolated map is not a perfect basis for detecting fronts, as the inclusion of coarser passive microwave SST is unhelpful when there is persistent cloud obscuring the infrared data, causing overly smoothed patches in the SST map on which fronts cannot be precisely located.

We have considered the pixels without recent infrared observations as 'missing' rather than relying on the coarse microwave data gap filling, such that when a front is not detected at a specific location it is clearer whether this is because there is no front present, or there is insufficient good quality SST data in order to detect a front.

2.1.2   Method

Composite front maps were prepared for the study area by detecting fronts on each daily MUR SST map using a histogram statistical approach, and then combining the partial front observations according to their gradient magnitude, persistence and proximity (Miller, 2009). Multiple SST maps within the 2018 period are processed using the SIED algorithm to detect front locations using statistics on a local window of 32x32 pixels. The minimum SST step allowed across a front was 0.6°C.

2.1.3   Results

The front detection algorithms worked effectively on the merged MUR SST daily fields, visualising a range of frontal features within the region of interest. To facilitate comparison with marine litter locations and other types of ocean front data, a time-series of the simplified KML version of the front maps was studied using the time slider in Google Earth (Figure 1).
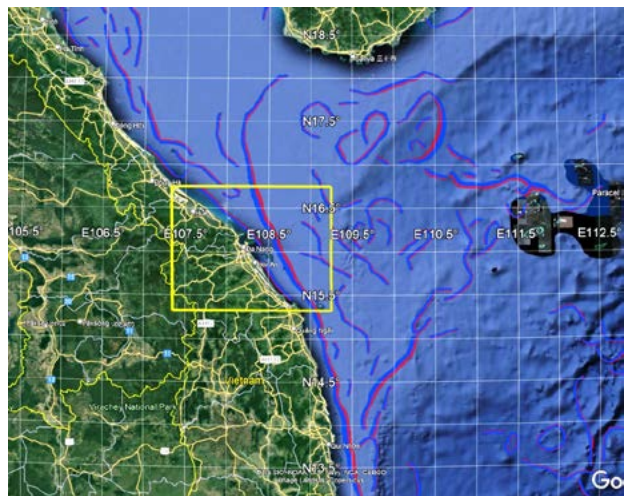
Figure 1. Sample weekly thermal front map derived from 1km MUR SST for 25-31 Mar. 2018, simplified contours where red/blue indicates warm/cold side of front, and ribbon width indicates strength of front.

Sample original and improved thermal front maps are shown in Figure 2, each derived from the same 7 day period. Figure 2a depicts unrealistic circular features in the centre of area due to interpolation artefacts caused by coarse passive microwave data, whereas in Figure 2b these features have been suppressed by masking areas on the daily SST fields which have no recent infrared data.

2.2   Optical front detection

2.2.1   Data

For this project we acquired Sentinel-3A OLCI data for the whole year of 2018, processed using the standard ESA calibrations and atmospheric correction, and mapped at 300m
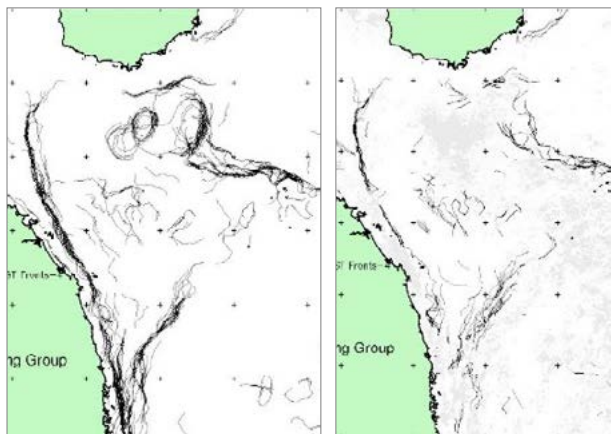
Figure 2. Example 7-day thermal front map for 25-31 Mar. 2018 comparing methods: (a) Original method derived from daily MUR gap-filled SST data including coarse passive microwave data; (b) Improved method derived from daily MUR SST data, masked if no recent infrared data; grey areas indicate persistent cloud-cover.

resolution. We selected the current standard open-water chlorophyll-a algorithm: the OC4ME maximum band ratio semi-analytical algorithm, which was log-transformed before storing as an integer array for input into the front detection (interval 0.015 log Chl-a m^{-3}).

2.2.2   Method

The composite front map algorithm described above for SST data was applied identically to the daily Chl-a scenes (Miller et al., 2015). The only difference is the constraint that the minimum step size across a front is 0.06 log Chl-a m^{-3}.

2.2.3   Results

Analysing a weekly front map highlights the chaotic patterns of mesoscale (and possibly submesoscale) fronts that can be detected using the higher 300m resolution of the OLCI ocean colour data (Figure 4). Monthly chl-a front maps allow us to perceive the broad seasonal changes in frontal distribution within the wider Vietnam area of interest during 2018 (Figure 3). It is noticeable that the main clusters of fronts are visible throughout the year, whereas the thermal front maps were impeded by persistent cloud cover during certain months of this year. This improvement could be because the fronts are detected directly on the cloud-free patches of the OLCI scenes; whereas the MUR SST dataset is daily merged from multiple partially cloud-covered satellite sources, and the interpolation may not adequately preserve the visibility of frontal features when there is insufficient cloud-free data.

3. CONCLUSIONS

Further results on the detection of fronts on FVCOM model data, and high-resolution Sentinel-2 optical data, will be presented during the conference, together with comparisons of multi-scale front contours with the location of marine litter. Satellite front detection represents an effective proxy for marine litter aggregation, and will be applied to design optimal strategies for preventing and removing marine litter.

ACKNOWLEDGEMENTS
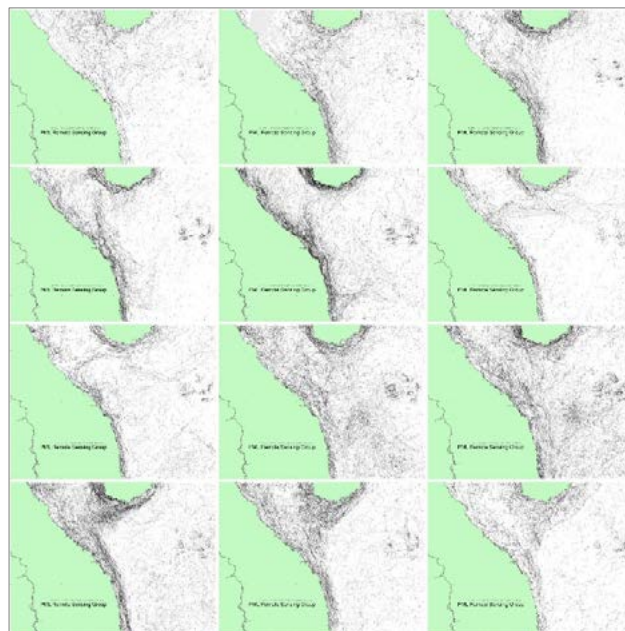
Figure 3. Sequence of monthly chlorophyll-a front maps from the 300m resolution Sentinel-3A OLCI ocean colour data for 2018, across then down from Jan. to Dec.

Figure 4. Example Sentinel-3A 7-day chl-a front map. Green/blue ribbons show the high/low chl-a side of each front, the width indicates the front gradient magnitude, and grey indicates persistent cloud .

REFERENCES

Miller, P.I. (2009) Composite front maps for improved visibility of dynamic sea-surface features on cloudy SeaWiFS and AVHRR data. *Journal of Marine Systems,* 78(3), 327-336. doi: 10.1016/j.jmarsys.2008.11.019

Miller, P.I. (in preparation) A line clustering algorithm with application to simplifying ocean front maps derived from satellite data. *Remote Sensing of Environment.*

Miller, P.I., Xu, W. & Carruthers, M. (2015) Seasonal shelf-sea front mapping using satellite ocean colour and temperature to support development of a marine protected area network. *Deep Sea Research Part II: Topical Studies in Oceanography,* 119, 3-19.

SESSION 5

SOCIETY, POLICY, ECONOMICS

Satellite Oceanography: NOAA's Center for Satellite Applications and Research (STAR)

E. Bayler *

NOAA NESDIS Center for Satellite Applications and Research, College Park, MD, USA

Abstract – The National Oceanic and Atmospheric Administration (NOAA) Center for Satellite Applications and Research (STAR) broadly enables the Oceans From Space themes, supporting operational satellite missions, developing new and enhancing existing ocean observing capabilities, exploiting satellite ocean observations to support informed decision-making, and engaging users to develop fit-for-purpose data, applications, and tools.

Keywords: Satellite, Oceanography, NOAA

1. INTRODUCTION

The National Oceanic and Atmospheric Administration's (NOAA) Center for Satellite Applications and Research (STAR) performs satellite oceanography, spanning research innovation, development needs, transitions to use, and operations, directly enabling informed decision-making for societal benefit. STAR directly engages with diverse users and their applications to provide fit-for-purpose satellite ocean data. With NOAA being an operational agency, STAR's contributions encompass the satellite ocean observation value chain: identifying user needs, developing observing capabilities, exploiting observations, and disseminating ocean observations and derived knowledge for societal benefit. STAR actively contributes to domestic and international fora aimed at addressing critical societal issues to which satellite ocean observations potentially can contribute.

2. SATELLITE OCEANOGRAPHY CONTRIBUTIONS

MISSIONS, SATELLITES, SENSORS

Addressing ocean-observing satellite missions, satellites, and sensors is core to STAR's role within NOAA and NESDIS. STAR provides the research and development for implementing NOAA's operational satellite missions, as well as for leveraging partner satellite observations. Specifically, STAR develops the operational algorithms for the GOES-R series Imager, the JPSS-series Visual Infrared Imaging Radiometer Suite (VIIRS), and the Jason-series altimeters, enabling accurate visual, infrared, altimeter ocean observations. STAR's science efforts develop and refine the science and algorithms for retrieving ocean measurements extracted from active and passive (visual, infrared, microwave) satellite sensors, spanning both physical and ecosystem parameters.

Supporting NOAA's geostationary and polar-orbiting missions, STAR provides the foundational development and algorithms for deriving visual and infrared ocean parameters, notably sea-surface temperature (SST) and derived "ocean color" parameters, such as chlorophyll concentration and suspended particulate matter, factors in the food chain and water quality. These SST data broadly enable NOAA and the broader community to assess the ocean state, inform ocean and weather predictions, assess ecosystem/habitat conditions and associated implications on living marine resources.

STAR's ocean surface topography efforts benefit: hurricane intensity forecasting through improved representation of ocean heat content; enhanced high wave warnings; ENSO forecasting and subsequent global water cycle implications; ocean surface current assessments that inform fisheries management, fishing services, energy siting, habitat health, search and rescue, offshore operations, and incident responses; as well as understanding and mitigating global and regional sea-level rise. STAR's development of advanced altimetry measurement techniques includes altimetric bathymetry, inland water levels, and the cryosphere, focusing on sea-ice thickness (freeboard). In conjunction with NASA, STAR supports research and development of altimetry applications through the international Ocean Surface Topography Science Team. STAR, in conjunction with EUMETSAT and the Delft University of Technology, maintains the Radar Altimeter Database System (RADS), which provides multi-mission consistent sea-level anomalies, waves, and ocean surface wind speed products, which are operationally employed for modeling and prediction.

Beyond NOAA's satellite ocean observations, STAR leverages non-NOAA partner satellite observations for operational robustness, greater coverage and resolution, and developing capabilities not available from NOAA's satellites. Examples include passive microwave observations from GCOM-W1 (AMSR2) and SMAP, scatterometry from METOP (ASCAT), and synthetic aperture radar (SAR) from the RADARSAT Constellation Mission and the Sentinel-1 mission. Leveraged capabilities include sea-surface salinity, ocean surface winds, sea-ice detection and characteristics, oil spill detection, and illegal fishing monitoring.

MODELS, ASSIMILATION, CAL/VAL

The assimilation of satellite ocean observations into predictive modeling, namely NOAA's operational Unified Forecasting System, is the principal use, by volume and parameter type, of STAR's satellite ocean observations. Operational assimilation of satellite ocean observation data requires careful calibration and validation to minimize inserting excess uncertainty into NOAA's operational forecasts. At the most basic level, STAR provides calibration and validation for NOAA's operational ocean sensors, specifically SST, ocean color, and altimetry. Supporting NOAA ocean color sensor calibration, STAR operates the in situ Marine Optical Buoy (MOBY) calibration site. STAR coordinates Office of Marine and Aviation Operations underflights of altimeters to provide calibration and validation for sea-ice observations.

STAR's passive retrieval algorithms support the ongoing evolution of the NOAA Unified Forecast System to radiance-based assimilation. These retrieval algorithms are represented in the Community Surface Emissivity Model (CSEM) and Community Radiative Transfer Model

---

* Corresponding author. Address: 5830 University Research Ct., College Park, MD, USA. Email: Eric.Bayler@noaa.gov

(CRTM), both of which are operational components of the NOAA Unified Forecasting System data assimilation system. Through the CSEM/CRTM, STAR's passive retrieval algorithm developments enable the Joint Effort for Data assimilation Integration (JEDI), comprising U.S. agencies and the UK Met Office, that is evolving the NOAA Unified Forecast System to radiance-based assimilation, where feasible. STAR recently brought satellite ocean data assimilation to the U.S. National Ocean Service for operational regional/coastal ocean modeling, specifically the West Coast Operational Forecast System. For weather and climate applications, SST, ocean-surface winds, SSH, sea-surface roughness, and ocean color contribute to improved representation of ocean heat content and ocean-atmosphere fluxes of heat, moisture, and momentum for improved forecasts and outlooks. In addition to the expected assimilation of SST, SSH, and SSS, satellite ocean color informs predictive modeling on the absorption of solar radiance in the near-surface ocean, which has a bio-physical feedback to ocean-atmosphere heat and moisture fluxes. Satellite sea-surface roughness is employed to identify sea-ice extent to inform weather forecasting and subseasonal-seasonal outlooks on ocean-atmosphere-sea ice fluxes of heat, moisture, and momentum.

REGIONAL & PLANETARY ISSUES

STAR addresses the global oceans, as well as focused regional and coastal ocean domains, including ocean cryosphere regions, creating satellite-based ocean products, analyses, tools, and applications for situational awareness and providing broad access to these items via NOAA's CoastWatch/OceanWatch, and PolarWatch programs, which STAR leads. STAR's Oceanwatch Monitor provides user-selected current and past analyses and visualizations of global and regional satellite ocean observations, including across parameters.

CoastWatch/OceanWatch data applications include: fisheries and aquaculture, water quality assessment, ecosystem monitoring, ocean and coastal dynamics, transportation and safety, and climate and weather. Fisheries and aquaculture applications (SST, ocean color, currents, sea-surface height (SSH)) include nutrient assessments, bycatch minimization, favorable conditions for commercial fisheries, and ocean acidification. Water quality applications exploit SST, ocean color, and SAR data to assess estuary conditions, harmful algal blooms, ocean acidification, and oil spills. Ecosystem monitoring applications employ SST, SSH, ocean color, and SSS data for assessing habitats of temperature-sensitive species and marine heat waves, currents, upwelling, distributions of ecologically important ecosystems, sediment plumes, freshwater influences in estuaries, and sea-level rise impacts. Satellite SST, SSH, SSS, currents, and ocean color observations provide a basis for assessing ocean and coastal dynamics, including upwelling and mesoscale dynamic features, contributing to optimizing marine transportation and fishing efforts. Satellite ocean-surface winds, sea-surface roughness, and SSH data provide the marine transportation and safety sector information on dangerous conditions, surf and swell conditions, ice type and thickness, and improve tide and wave height forecasting for greater efficiency and safety. SAR observations of coastal inundation are employed for public safety and recovery. Extended consistent satellite ocean observation data sets are created to address climate-scale questions and issues.

SURFACE PROCESSES, COASTAL ISSUES, EXTREME EVENTS

STAR efforts enhance understanding and representation of the ocean state, ocean dynamics, surface conditions (SST, SSS, SSH, roughness, sea ice, etc.), spanning near-real-time to climate temporal scales. STAR employs active (scatterometry and SAR) and passive technologies and techniques to measure and interpret ocean surface roughness, producing developmental and operational products that extract routine and extreme ocean surface winds, e.g., tropical cyclones, as well as uses SAR to assess inundation impact from storm surge. STAR also applies SAR observations to characterizing sea ice, aiming for new parameters and higher resolution assessments to support higher-resolution modeling and assimilation. Surface roughness is critical to assessing and representing ocean-atmosphere and ocean-atmosphere-sea ice fluxes, critical components for improving coupled Earth-system predictions. STAR has an explicit focus on the coastal ocean, co-leading the UN Ocean Decade Action *The Committee on Earth Observation Satellites – Coastal Observations, Applications, Services, AND Tools (CEOS COAST)*. As the lead for NOAA CoastWatch/OceanWatch, STAR enables the development of satellite ocean and coast observations and applications, including addressing coastal hazards, e.g., inundation, sea-level rise, wave heights, and coastal and estuarine water quality.

BIO-GEO-CHEMICAL ISSUES, POLLUTION AGENTS & PROCESSES

STAR actively works satellite ocean data approaches to address marine ecosystem biogeochemical challenges. Recently, STAR is supporting development of ocean color data assimilation into NOAA's Global Real-Time Ocean Forecast System (RTOFS) for ecosystem applications and boundary conditions for nested regional modeling applications. STAR pursues enhancing and applying satellite ocean color measurements of chlorophyll, detritus, colored dissolved organic material (CDOM), and sediment to water-quality applications and harmful algal bloom assessments and prediction. STAR also leads NOAA's Coral Reef Watch, which employs SST observations to assess global SST anomalies, trends, hot spots, degree heating weeks, and bleaching alert areas, providing email alerts and critical decision support for coral reef ecosystem management efforts. Additional relevant satellite-derived products address marine heat waves, coral disease outbreak risk, and light stress damage. Research efforts target projections of bleaching and ocean acidification for coral reef areas.

SOCIETY, POLICY, ECONOMICS

Through leadership and satellite ocean observations, STAR works to address societal issues and develop relevant policies. Examples include co-leading the UN Ocean Decade Action CEOS-COAST, as well as the Group on Earth Observations' Blue Planet Initiative, which focuses on ocean and coastal observations for policy and decision making, aiming to bridge the gap between ocean and coastal observational data and societal needs to deliver actionable information.

3. CONCLUSION

The NOAA Center for Satellite Applications and Research (STAR) broadly engages in research, development, and operations to address ocean observations and issues from space.

Expanding the use of Copernicus marine satellite data: EUMETSAT's user support and training activities.

Vittorio Brando[1*], Benjamin Loveday[2,3], Christine Träger-Chatterjee[3], Hayley Evers-King[3], Sally Wannop[3], Vinca Rosmorduc[4], Ana Ruescas[5,6], and Aida Alvera-Azcárate[7]

1. CNR ISMAR, Rome, Italy; 2. Innoflair UG, Germany; 3. EUMETSAT, Eumetsat Allee 1, Darmstadt, Germany; 4. CLS, Ramonville, Saint-Agne, France; 5. Brockmann Consult GmbH, Hamburg, Germany; 6. Universitat de València, Spain; 7. GHER, University of Liege, Belgium

Abstract – Following the successes of the first phase of the European Commission Copernicus programme, EUMETSAT is continuing and expanding its offer of data access services, marine data products, as well as marine training activities and user support services, under phase two.

EUMETSAT operates the Sentinel-3, Sentinel-6 and Jason-3 satellites, and provides level-1 and level-2 marine data products for ocean colour, sea surface temperature, and altimetry science and applications. User support services include data access, customisation, and visualisation platforms, web-based technical information about products, as well as a helpdesk available to answer a full range of user queries on the products and their use.

Interactive training activities are designed to accommodate a diverse range of audiences, both research and operational, putting trainee needs and interests at the centre of learning objectives. A focus on co-development of resources and participant-led learning interventions allows participants to tailor their own experiences towards development of the skills and knowledge that will help them in their own applications and work tasks. Building on four years of successful general courses, EUMETSAT now seeks to develop further specialised training and advanced courses for the marine community.

This presentation will showcase existing services and resources, and provide information on planned training events for 2022 and beyond. It will expand on our training approaches and provide further information on opportunities for collaboration with the wider marine community, during the UN ocean decade.

Keywords: EUMETSAT, Copernicus, ocean, training, user support

Baltic Sea from Space – from Ocean Colour science to management applications

Susanne Kratzer *, Krista Alikas, Jenni Attila, Therese Harvey, Sampsa Koponen and Tiit Kutser

Abstract –Remote Sensing of Baltic Sea waters and other regional seas was only an emerging technology in the late 1980[ties]. Generally, the optical properties of coastal waters and atmospheric correction above optical case 2 waters were regarded as being too complex to be solved. However, tremendous progress has been done in the past decades. The talk addresses relevant Ocean Colour (OC) missions, the use of band-ratio algorithms, inversion methods, Neural Network (NN) approaches, atmospheric correction, specific inherent optical properties (sIOP's) of the Baltic Sea, validation, Baltic Sea management as well as current and future operational systems and management applications.

Keywords: Baltic Sea as a regional Sea, high CDOM absorption, moderate SPM concentrations, HELCOM assessments, future products and services.

1. INTRODUCTION

The Baltic Sea is surrounded by 9 different countries, and thus, remote sensing is one of the key approaches allowing to provide consistent water quality data not limited by national or political boundaries, nor varying methods and protocols.

In this talk we will provide a historical recap of the key remote sensing missions over the last 25 years and also provide a firm look into the future. Furthermore, we will also discuss the progress in our understanding of the IOPs of the Baltic Sea, i.e. the absorption and scattering properties of the main optical components contributing to improved knowledge of the Baltic Sea basin and ecology. Table 1 gives an overview of the ranges of the three main optical components of various Baltic Sea basins: Chlorophyll-a (Chl-a) which is usually used as a proxy of phytoplankton biomass, and may also indicate the trophic status of the water body; coloured dissolved organic matter (CDOM), indicated by the absorption coefficient at 440 nm, a_{CDOM} and being the key determinant of spectral light attenuation; as well as suspended particulate matter (SPM), which is highly correlated with turbidity. Additionally, the Secchi Depth (SD) is also included. It is a rough parameter, indicating the general water quality as it is influenced by all of the previously mentioned optical components. Although more accurate methods for measuring transparency of the water exist, SD has a long history of recordings and a key role in ecological status assessment (e.g. HELCOM indicator).

OC remote sensing started with the launch of the Coastal Zone Color Scanner (CZCS) aboard Nimbus-7 satellite. This prove-of-concept mission was operational over many years (1978-86). Its value was tremendous in oceanic waters; phytoplankton productivity in the world oceans was shown to be in the same range as the primary productivity of terrestrial systems (Longhurst et al, 1995). The shortcomings of CZCS were clearly evident in optically-complex coastal waters; improvements were needed in spectral resolution at visible and near infrared wavelengths to achieve adequate atmospheric correction and derivation of the main optical components.

It took many years before the launch of the next key OC mission - SeaWiFS in 1997. Meanwhile it became apparent that data from the Advanced Very High Resolution Radiometer (AVHRR) instrument onboard the NOAA satellites could be used for monitoring cyanobacteria surface blooms in the Baltic Sea (Kahru et al. 1995). This was possible due to the scatter caused by the gas vacuoles in filamentous cyanobacteria, which causes a specific albedo which differs from that of cloud, land and haze. The method was implemented by various operational systems that allowed for the monitoring of filamentous cyanobacteria blooms in the Baltic Sea.

Table 1. Ranges of optical properties in different Baltic Sea basins (from Kratzer and Moore, 2018 and references cited there within).

Baltic Sea area	[Chl a]	[SPM]	a_{CDOM}	SD
	$\mu g\ l^{-1}$	$g\ m^{-3}$	m^{-1}	m
Arkona Sea	0.3-7	0.7-9	0.2-0.4	5.0-9.5
Bornholm Sea	0.4-4	0.4-5	0.2-0.3	2.0-10.5
Gotland Sea	0.2-4	3.0-6	0.2-0.4	3.0-10
Pomeranian Bight, Germany	0.4-13	0.5-20	0.2-0.9	3.0-7
Gulf of Gdansk Poland	0.4-73	0.4-16	0.4-4.4	4.5-7
Lithuanian coast	0.6-116	1.1-32	0.01-2.0	4.0-6
Pärnu Bay, Estonia	0.7-11	5.0-24	0.6-3.7	0.5-4.3
Gulf of Riga, Estonia	2.0-46	10.0-24	1.5-13	3.1-6.9
Gulf of Finland	1.2-130	0.8-20	0.6-1.2	1.8-4
NW Baltic proper	0.4-52	0.5-22	0.3 - 4.1	0.7-12.8
Öre Estuary, Bothnian Sea	0.5-96	0.2-21	0.75-8.8	0.5 -6

At the turn of the century accelerating progress took place in OC remote sensing due to the NASA SeaWiFS and the MODIS missions, although both were not ideal for the optically-complex waters of the Baltic Sea, due to their relatively low spectral resolution. Nevertheless, Darecki et al. (2004) showed that regionally tuning of OC4v4 allowed for a reliable retrieval of Chl-a (within 30%) and K_d490 (within 5%), although the sensors did not work in inner coastal areas. The validation of MODIS and SeaWiFS water-leaving radiance have shown good results for 551 nm band, but overestimation for blue and underestimation in the red (Zibordi et al., 2009).

Owing to ESA's MERIS and OLCI instruments and the developed processors the current progress in OC remote sensing of optical case 2 waters is accelerating. The improved radiometric and spectral resolution of the ESA MERIS/ENVISAT mission compared to previous OC sensors allowed for the development of various bio-optical models capable to derive water quality parameters from atmospherically corrected Level 2 data (Doerffer & Schiller, 2007) and top of atmosphere Level 1 data (Schreoder 2007). This has shifted the focus from using empirical band ratio methods to more advanced NN approaches (Attila et al, 2013; Beltrán-Abaunza et al. 2014) and indicated the need to have regionally adapted algorithms as recently also shown for OLCI (Ligi et al., 2017; Kratzer and Plowey, 2021).

The constellation of satellites by *Copernicus*, the Earth Observation Programme of the European Commission, allows now to monitor the water quality from small estuaries

* Corresponding author. Address: Email: Susanne.Kratzer@su.se

(Sentinel-2, S2) to the whole Baltic Sea basin (Sentinel-3, S3) almost on a daily basis with continuation of missions foreseen until 2034. The standard radiometric product of the OLCI sensor onboard S3 tends to have systematic underestimation of blue and red wavelengths over the Baltic Sea, possibly due to systematic overestimate of atmospheric effects (Zibordi et al., 2018). This in turn inhibits the use of these wavelengths in bio-optical models and has led to applying alternative locally-adaptable AC approaches, which have improved the accuracy for deriving water products in near-coastal waters (Kratzer and Plowey, 2020). The current algorithms show better sensitivity to specific concentration ranges or to certain periods, e.g. during summer phytoplankton minimum (during May/early June) and during the cyanobacteria season (Kutser et al., 2018). The large seasonal and spatial ranges of IOP's typical for the Baltic Sea should be better adopted in remote sensing methods, also emphasizing the need for regional algorithms and processors (Simis et al. 2017, Ligi et al. 2017).

With the continuous development of operational OC sensors over the past decades, also regional water quality parameters have been derived based on the specific IOP's, e.g. inorganic suspended matter (Figure 1), which can be used as an indicator of terrestrial influence in Baltic Sea coastal areas (Kratzer et al., 2020).
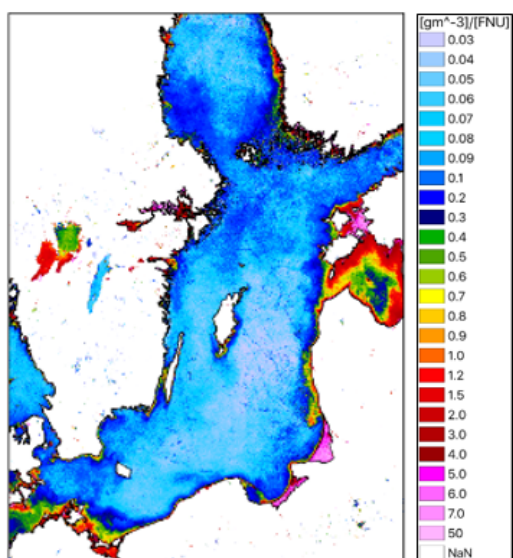
Figure 1. *Inorganic SPM in the Baltic Sea (April 2018 composite) derived from Sentinel-3 OLCI C2RCC reflectance data and applying a regional algorithm (from Kratzer et al, 2020).*

2. APPLICATIONS AND MANAGEMENT

Operational services combined with modelling provide reliable Earth Observation-based information on water quality. These services have evolved over the years from early services providing mostly information on summer blooms and surface temperature which are important for informing water authorities and citizens. Over the years these systems have been improved through the various OC missions described above, and some of the latest operational services aimed specifically for the Baltic Sea also include quantitative information about the Chl-a concentration and turbidity. The Satbaltyk-service provided by IOPAN (Poland) combines modelling and daily EO-based information. SYKE's TARKKA-interface (Finland) derives water quality parameters (turbidity, Chl-a and a_{CDOM}) from multi-resolution Earth Observation (EO) data with focus on the northern Baltic Sea and the coastal waters of Finland. The initial systems based on AVHRR data were hampered by the limited temporal information (i.e. covering only the summer

blooms) and the limited quantitative information (e.g. only providing statistics about the spread of surface accumulations). Due to the improved data quality of the products also in optically-complex waters, OC data and bio-optical parameters are becoming more and more part of the national monitoring programs and are also used for the periodical ecological status assessments performed by the Helsinki Commission (HELCOM) and the Water Framework Directive. The Finnish coastal and lake monitoring programs use EO observations along with other types of monitoring. The HELCOM Holistic Assessment (HOLAS) has been accepting EO/remote sensing as one source of information on Chl-a within the previous assessment (HOLAS II) for most of its open sea areas, and preparations are currently underway to use EO as an information source for Chl-a and cyanobacteria blooms within the next HOLAS III. User requirements for the long-term status assessment are now focusing on providing holistic information on the transparency and brownification of the water. Both can be linked to following the changes of the water not only with respect to eutrophication, but also climate change.

3. CONCLUSIONS

Initially, remote sensing was generally not accepted as a scientific discipline in itself. With regards to OC some of the misunderstandings were mostly caused by the lack of understanding of radiative transfer theory science and its application to optically-complex waters. A breakthrough has been made along with the development of dedicated OC missions and improvements in spectral, spatial and radiometric resolution. Enhanced technology combined with ever more expanding data processing facilities as well as improved atmospheric correction capabilities (e.g. AERONET) and characterization of the IOPs have enabled the use of remote sensing even in optically-complex waters. This process is still ongoing, especially in relation to accounting for the effects of high CDOM absorption and low SPM concentrations. The main bottle neck in remote sensing of the Baltic Sea still seems to be an adequate understanding and characterization of the specific IOPs and their implementation into dedicated regional algorithms.

Baltic Sea remote sensing is likely to be further enhanced by current (e.g. Italian Space Agency PRISMA) and future Earth Observation missions both planned by NASA (e.g. PACE) and ESA (e.g. FLEX, CHIME, Sentinel Next Generation).

REFERENCES

Attila *et al.* 2013. *RSE*, 128. 138–149.
Beltrán-Abaunza *et al.* 2014. *Ocean Science* 10.3, 377-396.
Darecki & Stramski, 2004. *RSE*, 89, 326–350.
Doerffer and Schiller, 2007. *IJRS*. 28:3-4, 517-535.
Kahru *et al.* 1995. *Cont Shelf Res*, 15(6), 663-679.
Kratzer and Moore, 2018. *RS, 10(3), p.418.*
Kratzer *et al.* 2020. *RSE*, 237, 111609.
Kratzer and Plowey, 2021. *IJ-AEOG* 94,102212.
Kutser *et al*., 2018. *IEEE/OES BIS (BALTIC)*, 1-6.
Ligi et al., 2017. *Oceanol*, 59(1), 57-68.
Longhurst, A. *et al.* 1995. *JPRes,*17, 1245–1271.
Schroeder *et al.* 2007. *IJRS*, 28(24), 5627-5632.
Simis et al, 2017. *PloS one*, 12(4), p.e0173357.
Zibordi, G. *et al.* 2018. *IEEE GRSL*, 15 (10) 1490-1494.
Zibordi, G. *et al.* 2009. *RSE,* 113(12), 2574–2591.

Integrated monitoring service for Norwegian coastal waters- examples from the Oslofjord and the Skagerrak

E. T. Harvey*[1,2], Jaccard P. F.[2], King A. L.[2], Knaeps E.[3], Kristiansen T.[2], Staalstrøm A.[2], Sørensen K.[2]

1NIVA Denmark Water Research, Copenhagen, Denmark, **2**Norwegian Institute of Water-NIVA, Oslo, Norway, **3**VITO, Brussels, Belgium

Abstract – Coastal ecosystems are under pressure from well-known anthropogenic impacts, such as nutrient inputs that lead to eutrophication, but also from newer pressures such as coastal darkening, which may lead to a change in the coastal light environment. The pressures affect the pelagic ecosystems at several levels and the need to follow the changes and to understand the impacts is increasing. By an integrated monitoring system of in-situ sampling, continuous sampling with FerryBox sensors and ocean colour remote sensing (RS) observations, the spatial and temporal variability of bio-geo chemical parameters can be followed. Combining data from multiple sources provides increased knowledge and understanding of the coastal ecosystems, which is important for management.

Keywords: Climate change, Monitoring, FerryBox, Ocean colour, EODataBee service

1. INTRODUCTION

The Norwegian coastline is very long with many fjords and inlets as well as remote and inaccessible areas, making the monitoring of the coastal waters difficult and expensive. With new threats, such as climate change, the need for robust data-driven decisions is increasing. Therefore, the use of integrated methods using different types of techniques is becoming more and more important and improved automated sensors as well as ocean colour satellites, such as Sentinel-2 and Sentinel-3, from the European Commission's Copernicus programme, now provide an even better opportunity for this to become the new standard for the monitoring of our oceans.

The Oslofjord in Southern Norway and the Skagerrak are affected by anthropogenic impacts from contamination of hazardous substances[1] as well as eutrophication[2]. Measurements of nutrients started in 1930ties and the routine coastal monitoring program, ØKOKYST, by the Norwegian Environment Agency (NEA) was established 1990 and has been collecting in situ data on a regular basis since then[3]. Nutrient inputs decreased from around 1960 in the inner part of the fjord with implementation of wastewater treatment but have, unfortunately, increased with the increased population the past 20 years. For the Skagerrak area the nutrient levels have increased by 30% since 1993[2] due to increased inputs from wastewater treatments, agriculture and run-off from land. Additionally, has an increase of nutrients and dissolved organic matter (DOM) and the colored fraction (Coloured DOM, CDOM) been observed from land to the coast[4], changes that are attributed to climate change with increased precipitation and changes in run-off from land. An increase in CDOM leads to a reduction of the light availability and an increase in the light attenuation coefficient, K_d, so-called "coastal darkening"[5] . A decrease in Secchi depth has been observed in coastal waters[6] and fjords[5], associated with coastal darkening.

The FerryBox monitoring system is mounted on ships operating along the Norwegian coast as part of the national infrastructure; NorSOOP (www.norsoop.com) and has been implemented in the Oslofjord and Skagerrak waters for 20 years (Fig. 1). The standard measurements include oxygen, temperature, salinity, chlorophyll-a fluorescence (fChl-a), CDOM fluorescence (fCDOM) and turbidity. These are measures at about four meters depth every minute along the ships' routes. It is also possible to carry out automatic sampling of water samples of e.g. dissolved organic carbon, chlorophyll-a concentration (Chl-a) and plankton samples for further analysis in the laboratory. Samples are collected by the autosamplers at fixed stations along the track in e.g. the ØKOKYST FerryBox project as part of the NEA´s ocean acidification programme and as regular monitoring stations within the fjord. Some of the FerryBox systems are equipped with RAMSES TRIOS sensors for measurements of E_d, L_d and L_u to derive remote sensing reflectance and light attenuation. FerryBox data has been used for satellite product validation for many years e.g. back to the MERIS period.

Fig.1 *The Color Line ferry 'MS Color Fantasy' equipped with sensors on deck for light, ocean colour and temperature. Inside the ship is the FerryBox system with sensors installed.*

Ocean colour data from satellites provides a unique opportunity to collect a variety of important water quality parameters, such as $K_d(\lambda)$, Chl-a, CDOM, total suspended particles (TSM) and Secchi depth. With the Copernicus program from the European Commission, the possibilities to include these types of data within monitoring programmes have increased greatly. The use of satellite-based water quality monitoring is now well developed and ready to be implemented in more operational monitoring solutions. A step in this direction has been made by the European Horizon2020 project Data Cube Service for Copernicus (DCS4COP), run between 2018-2021[7]. This project was a collaboration between eight European partners, where systems and services for handling large data volumes, integrating processing data schemes from different sources, validation and generating high-quality data from the Sentinel satellite series was developed into the satellite-based service; EODataBee (https://eodatabee.eu/). EODataBee is a service providing state-of-the-art water quality products and services to customers, including training, scientific consultancy and data cube generation, operation, and visualization.

---

* Corresponding author. Address: Njalsgade 76, DK-2300 Copenhagen S, Denmark. Email: therese.harvey@niva-dk.dk

2. INTEGRATED MONITORING SERVICE

By combining several monitoring platforms, the information available for data-driven decisions within management increases (Fig. 2). Agencies like the NEA demands ever more data in terms of frequency and spatial coverage for management, but this needs to be weighed against the costs. More data means better opportunities to understand the systems and the changes within as well as for developments of e.g. a) remote sensing algorithms to retrieve high-quality water information and b) for development of bio-chemical models. Data for RS are usually only fulfilled through dedicated scientific cruises or satellite match-up campaigns. Thus, strong collaborations with national and regional monitoring programs and the research community provides good opportunities, which has been a reality for the Oslofjord and the Skagerrak areas.
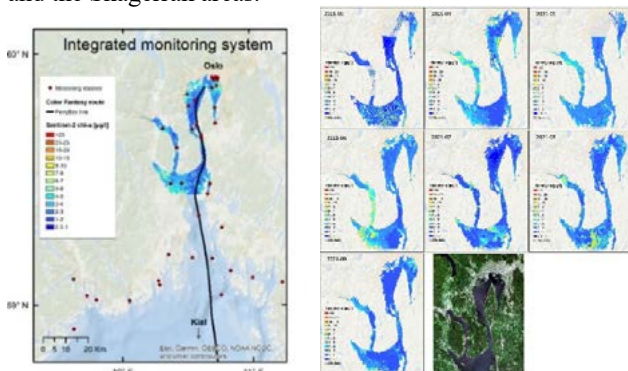
Fig. 2 *L: Integrated monitoring in Oslofjord and Skagerrak by 3 systems; in situ sampling sites; FerryBox measurements; Sentinel-2 Chl-a. R: Sentinel-2 monthly means in 2021.*

The in-situ monitoring programming in the Oslofjord and the Skagerrak runs regularly every month for the whole year with more intense sampling during spring and summer. Water quality parameters from different depths are collected.

FerryBox sensors provide data with high temporal resolution, covering a similar route all year (Fig. 3), and in-situ sampling at certain stations along the route, collected at higher frequency and with much lower costs than dedicated monitoring cruises. The collected data can also be used for remote sensing validation and algorithm development.
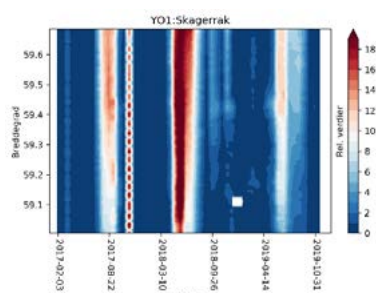
Fig. 3. *FerryBox sensor data for fDOM (rel. values) for 2017-2019 from Vestfjord to Oslo harbor between 59,72-59,90° N. The temporal and spatial variability is clearly seen with higher fDOM in the inner part of the fjord (M. Norli).*

NIVA has led and worked in several projects for ocean colour and RS in Norwegian waters over the last 30 years including studies of the Oslofjord[8] and most recently the H2020 project DCS4COP[7]. It is a challenge to retrieve satellite derived Chl-a concentrations from high CDOM waters, such as the Norwegian coastal and fjord waters, because the reflectance reaching the satellite sensor is low which results in a high signal-to-noise ratio. However,

evaluation of the iCOR atm processor with different Chl-a algorithms applied in the inner Oslo fjord shows that RS data retrieved from Sentinel-2 performs well with observations in the same range as the in-situ data for 2 out of 3 algorithms (Fig. 4). For other parameters such as TSM and $K_d(\lambda)$ performance is generally better than for Chl-a in high CDOM waters. Changes in optical parameters and the remote sensing reflectance retrieved from satellites can be used to study possible changes in the light field due to coastal darkening.
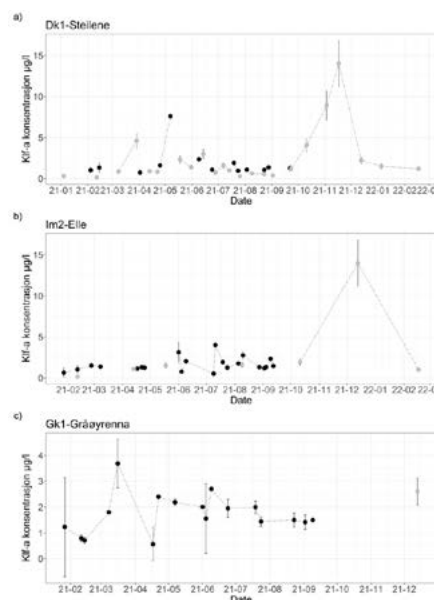
Fig. 4. *Time-series graph of Sentinel-2 Chl-a data [µg/l] for three stations in the inner part of the Oslofjord 2021.*

3. CONCLUSION

End-users are today asking for more holistic information and solutions linked to both known human impacts such as eutrophication but also impacts from climate change, such as coastal darkening, where ocean colour data is adding an extra dimension. In terms of monitoring, the unique temporal and spatial variability that RS images provide and the high temporal variability that can be detected with FerryBox systems needs to be emphasized. The data is useful for evaluation of the representativeness of monitoring stations, as well as for the overall long-term variability and water quality status assessments reported within the European Water Framework Directive. Integrated monitoring systems like the EODataBee Service in connection with FerryBox sensor will therefore become more important in the future.

REFERENCES

1 Green, N. W. et al. *NIVA report* (2020). **2** Staalstrøm, A. et al. *NIVA report* (2021). **3** NEA. Overvåkning av økosystem i kystområder (ØKOKYST)-*Norwegian Environment Agency* (2021). **4** Frigstad, H. et al. *Front. Mar. Sci.* 7, (2020). **5** Aksnes, D. L. et al. *Mar. Eco. Prog. Series* 387, (2009). **6** Capuzzo, E. et al. *Glob Change Biol* 21, (2015). **7** DCS4COP. DataCube Service for Copernicus, *DCS4COP H2020 Project, European Commission*. DCS4COP H2020 (2021). **8** Sørensen, K. & Lindell, T. *NIVA report* (1990).

Oceanographic data and information system for Polish NODC

M .Wichorowski[1] [*], M. Ostrowska[1], J. Stoń-Egiert[1], U. Pączek[2], L. Szymanek[3], M. Wójcik[4], W. Paciura[2]

[1]Institute of Oceanology Polish Academy of Sciences, Sopot , Poland
[2]Polish Geological Institute, National Research Institute, Warsaw, Poland
[3]National Marine Fisheries Research Institute, Gdynia, Poland
[4]Maritime Institute Gdynia Maritime University, Gdańsk, Poland

Abstract – The growth of data volume managed by organizations involved in research in Environmental and Earth Sciences turned exponential within last years. Data covering domain of one's interest are distributed across variety of infrastructures, data centers, collections, and formats. This makes discovery of all available sources of data and their harmonization extremely challenging, and rising the assurance of FAIRness of data as the most emerging problem for data managers.

Consortium of organizations engaged in research and exploitation of marine resources, established as POLMAR, together with Scientific Consortium SatBałtyk, consisting of 7 organizations engaged in research and exploitation of marine resources, for many years has led actions targeting harmonization, integration and coordinated provisioning of environmental data resources. This initiative merges the most of the organizations involved in marine research and continuous acquisition of oceanographic data in Poland to conduct activities towards the deployment of operational state of the system delivering demanded oceanographic data and products to the users and is heading to establish Polish Oceanographic Data Committee.

Keywords: ODIS, Data management, Data stewardship, eCUDO.pl.

1. INTRODUCTION

Polish scientific consortium consisting of Institute of Oceanology Polish Academy of Sciences, Polish Geological Institute National Research Institute, National Marine Fisheries Research Institute, University of Gdańsk, Maritime Institute of Maritime University in Gdynia, Pomeranian Academy in Słupsk and University of Szczecin, being involved in marine research for a long time have consolidated efforts and undertook actions to make Polish oceanographic scientific data resources accessible for public from one national repository.

These organizations established good international cooperation, being members of international projects, organizations, and initiatives provide data to international data and information centers and systems so far. In order to increase Polish contribution to pan European oceanographic data resources they work together to establish the structure of the Polish National Oceanographic Data Committee and ODIS infrastructure for the future cooperation.

Consortium has successfully submitted project proposal in the frame of the Digital Agenda Poland program and has been awarded for the project eCUDO.pl (Oceanographic Data and Information System). This project aims to harmonize Polish oceanographic data, make them interoperable through implementation of committed

standards for information structure and communication protocols. The project is developing and deploying ODIS as distributed infrastructure for data management, and providing open access to oceanographic data resources.

Present activities encompass harmonization of environmental data collection and its preservation in accordance with INSPIRE requirements and SeaDataNet standards, securing resources for data management and stewardship, as well as digitalization of hardcopy data archives. The most significant results as expected, are better data discovery findability, accessibility, interoperability and finally higher potential for reuse of data collected during the years of research activity. Design of the system according to the program requirements is user oriented and driven by development of services demanded by users. This ODIS is open for all stakeholders and ready to accommodate other organizations and data resources. System is designed to provide valuable services for scientists, fostering sustainability of oceanographic sciences, but also for all bodies using oceanographic data for further processing, administration, decision makers, ngo's, and citizens. Most of preselected data objects can be previewed using built in mechanisms, as shown on Figure 1.
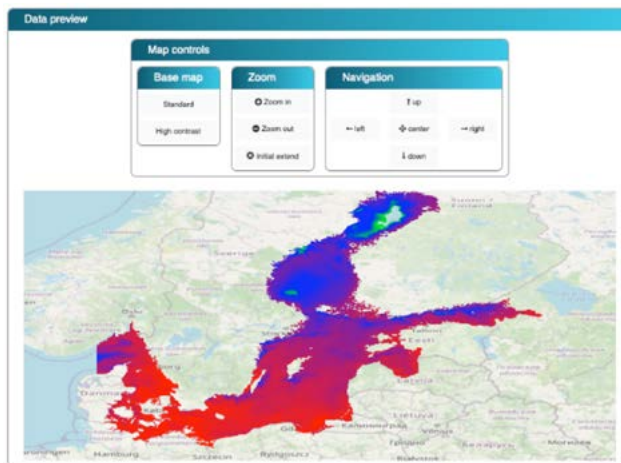
Figure 1. Data preview of selected data object.

2. SYSTEM DESIGN

The central element of the platform is infrastructure based on a virtualization server connected to the data storage system. The use of such a solution allows for easy implementation of individual modules, as well as their replacement in the event of a need to conduct a complex software update or to remove errors in the operation of the system.

The platform's infrastructure consists of a main server that provides required functionalities to external users, a single-sign-on server allowing one-time login to the platform

---

and use of all its resources, spatial data server performing WMS, WFS and CSW services and a server processing data from non-federated external systems.

The platform's environment (users, federated systems and non-federated external systems) can be distributed to any geographical location with communication via the Internet. For the sake of simplifying the model, it is assumed that each external system (both federated and un-federated) will consist of a server providing data, combined with a data warehouse.

Users can access the system via any device (computer, laptop, tablet, mobile phone) with installed software supporting the display of websites using the http protocol or supporting WFS, WMS and CSW type services.

Table 1. Standards deployed into the system

Metadata
Geographic Information – Metadata (ISO 19115-3-.2018)
Geographic Information – Metadata (ISO 19139:2007)(ISO 19139)
ISO 19139 Metadata – SeaDataNet CDI Profile INSPIRE COMPLIANT
Dublin Core
Geographic Information – Methodology for feature cataloguing (ISO 19110)
Vocabularies
NERC Vocabulary Server 2.0
GCMD Keywords
CF Conventions
Data formats
NetCDF / CF
ODV
SHP
GeoTiff
WMS
WFS

For the time being https://eCUDO.pl is providing over 4M oceanographic data objects, covering marine physics, atmosphere, hydrology, biology, geology, coastal areas from Baltic Sea, Atlantic and European Arctic areas. Due to the domain extent, variety of themes and huge volume of data this system is perspective platform for development and utilization of DL algorithms for analysis and management of oceanographic data.

3. CONCLUSION

Deployment of unified system providing access to data resources managed by key scientific organizations in Poland will trigger and added value for national economy through increase of data availability for all levels of administration, with concurrent decrease of the total cost of data acquisition, management and exchange.

Unified data formats and protocols will boost development of the services based on environmental data.

Advanced services provided for clients (including data analysis services) extend availability of oceanographic data both to Polish and European organizations.

System is open for all stakeholders and ready to aggregate other organizations and data sources. Further integration of operations on infrastructural and organizational level will provide solid basis for Polish Oceanographic Data Committee

ACKNOWLEDGEMENTS

REFERENCES

R. Boehnke, M. Wichorowski, E. Trudnowska, K. Balazy, D. Jakubas, A. Wold, K. Wojczulanis-Jakubas, S. Falk-Petersen, D. Kidawa, H. Hop, K. Błachowiak-Samołyk, (2022). Limnology and Oceanography Methods, 20: 159-171. https://doi.org/10.1002/lom3.10478.

M. Wichorowski, J. Ston -Egiert, K. Rutkowski, W. Krzymiński, M. Piotrowski, M. Wójcik, (2021). Bollettino di Geofisica teorica ed applicata, pp 315-316.

SESSION 6

REGIONAL & PLANETARY ISSUES

The Value of Regional & Planetary Information for Earth's Blue Economy

P. Bontempi *

University of Rhode Island, Narragansett RI, USA

Abstract – The ocean covers 71% of Earth's surface, interfaces with the coast, sediments, and atmosphere, and is essential to life on this planet. The ocean also fosters an extensive global economy, and the term "blue economy" refers to the sustainable use of resources and economic activities related to oceans, seas, and coasts. A blue economy prioritizes global economic growth, livelihoods, and jobs while preserving the health of the global ocean ecosystem and its resources. According to the United Nations (UN) 2022 fact sheet, around 680 million people live in low-lying coastal zones and marine fisheries alone provide 57 million jobs. Globally, the ocean economy is estimated at US$3 trillion/year, and the recent NOAA Blue Economy Strategic Plan indicates that, in 2018 alone, the American blue economy supported 2.3 million jobs and contributed approximately $373 billion to the nation's gross domestic product through tourism and recreation, transportation and shipping, fishing, power generation, research, and related goods and services.

Beyond its direct economic worth, Earth's ocean supports life on our home planet in more profound, if less visible, ways. The ocean is the largest heat sink in the climate system, transporting this heat deep into the ocean interior. The ocean is also the most important sink for carbon dioxide (CO_2), absorbing and sequestering 20% to 30% of annual human-induced CO_2 emissions. Ocean currents regulate pole-to-pole nutrient and heat distributions, thereby dictating regional patterns in ecosystem productivity and weather. At high latitudes, the ocean locks up methane (in hydrates) in sediments and shallow seas and, currently, stores about 70 meters of potential sea level rise in its polar ice sheets.

Climate change threatens the ocean and the blue economy nationally and globally through associated sea level rise, marine heatwaves, ocean acidification, hypoxia, (harmful) algal blooms, and coastal flooding. This should not be news. But these impacts cause and will continue to cause substantial damage to our economically vital coastal and oceanic ecosystems, with cascading impacts to human life and livelihood and must be observed, understood, and made predictable on policy-relevant scales before tipping points are behind us.

---

* Corresponding author. Address: Ocean Science Exploration Center, Narragansett RI, USA. Email: paulabontempi@uri.edu

Observation of Arctic Ocean meltwater lenses from space and synergy with in-situ measurements.

A. Supply[1,2*], J. Boutin[3], N. Kolodziejczyk[1], G. Reverdin[3], C. Lique[1], J.-L. Vergely[4] and X. Perrot[5]

[1]Univ. Brest, CNRS, IRD, Ifremer, Laboratoire d'Océanographie Physique et Spatiale (LOPS), IUEM, Brest 29280, France, [2]CNES, Paris, France, [3]Sorbonne University, LOCEAN Laboratory - IPSL, CNRS–IRD–MNHM, Paris, France, [4]ACRI-ST, Guyancourt, France, [5]LMD / IPSL, CNRS, ENS, PSL, Paris, France

Abstract –For the first time, thanks to in-situ measurements recorded by two saildrones deployed during summer 2019 in the Beaufort and Chukchi Sea, we demonstrate the ability of satellite observations by SMOS and SMAP to capture Sea Surface Salinity (SSS) freshening induced by sea ice melt, referred to as meltwater lenses (MWL). MWL induced low SSS pattern which generated strong stratification and restricted the transfer of air-sea momentum to the upper ocean, as illustrated by measured wind speed and vertical profiles of currents. Using sea ice concentration and estimated Ekman transport, we analyze the spatial variability of sea surface properties after the sea ice edge retreat over the Chukchi and the Beaufort seas. The two MWL captured by both, the saildrones and the satellite measurements, result from different dynamics. Over the Beaufort Sea, the MWL evolution follows the meridional sea ice retreat, whereas in the Chukchi Sea, a large persisting MWL is generated by advection of a sea ice filament.

Keywords: Salinity, Arctic Ocean, Meltwater lenses.

1. INTRODUCTION

The Soil Moisture and Ocean Salinity (SMOS; 2010-present, Kerr et al., 2010, Font et al., 2010) and the Soil Moisture Active and Passive (SMAP; 2015-present, Piepmeier et al., 2017) satellites both monitor SSS at a resolution close to 43 km with a repetitivity close to 1 day at very high latitude (Vinogradova et al., 2019; Reul et al., 2020). The low Sea Surface Temperature (SST) characteristic of the Arctic Ocean results in a poor sensitivity of L-Band radiometric measurements to SSS (Meissner et al., 2016). Despite this poor sensitivity, that is somewhat compensated by the very large SSS contrasts in the Arctic (ranging from 35 pss for the Atlantic water to 0 pss for river plumes; Carmack et al., 2016), satellite SSS data have been used to characterize surface water masses in the Arctic Ocean (Olmedo et al., 2018; Tang et al., 2018; Tarasenko et al., 2021).

Nevertheless, numerous challenges remain regarding satellite derived SSS estimates in the Arctic Ocean. Due to sparse in-situ measurements, corrections of regional biases using in-situ derived SSS and an optimal interpolation method, remains difficult (Kolodziejczyk et al., 2021). An additional limitation comes from the sea ice heterogeneity and instrument resolution, limiting the measurements closer than ~43 km from the ice edge, with difficulties in detecting and filtering small ice-covered regions. Furthermore, sea ice presence in a satellite pixel has the potential to significantly contaminate the retrieved satellite SSS: the brightness temperature of sea ice is about twice the one of sea water, so that a coverage of 0.2% of the surface of a considered pixel by sea ice would lead to a SSS underestimate of ~1pss.

2. VALIDATION

During their journey, both saildrones cross various water masses at the sea surface (Supply et al, 2022). Satellite and saildrones measurements are collocated. We demonstrate the ability of SMOS+SMAP SSS to realistically capture SSS synoptic variability and to monitor different surface water masses (Figure 1).
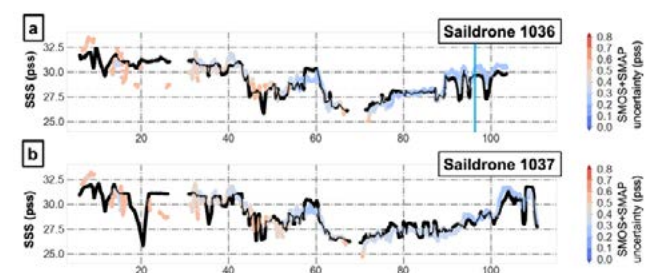
Figure 1. a) S1036 SSS measurement time series (black) and SMOS+SMAP collocated SSS in color (color for SSS uncertainty); b) S1037 SSS measurement time series (black) and SMOS+SMAP collocated SSS in color (color for SSS uncertainty)

3. A LARGE PERSISTENT MELWATER LENS

The largest MWL, captured far away from the sea ice edge, is associated with low SSS and SST (the decrease in SSS reaches 5 pss and the decrease in SST reaches 6°C). We show that saildrone measurements of ocean currents and wind further reveal that the increase in vertical shear driven by an increase in WS remains trapped close to the surface, in the presence of low SSS associated with the MWL. This is likely due to an increase in stratification in the MWL resulting from the SSS decrease.

4. SEA SURFACE VARIABILITY FOLLOWING SEA ICE RETREAT

We found that the MWL can be associated with two different types of dynamics: over the Beaufort Sea, MWL evolution follows the meridional sea ice retreat while in the Chukchi Sea, a large persisting MWL is generated by the advection of a sea ice filament. However, regardless of the type of MWL, regions of low SSS induced by sea ice melting occupied a significant part of the Beaufort and the Chukchi Sea during summer 2019 (figure 2).

---

* Corresponding author. Address: rue Dumont Durville IUEM 29280 Plouzané. Email: alexandre.supply@univ-brest.fr
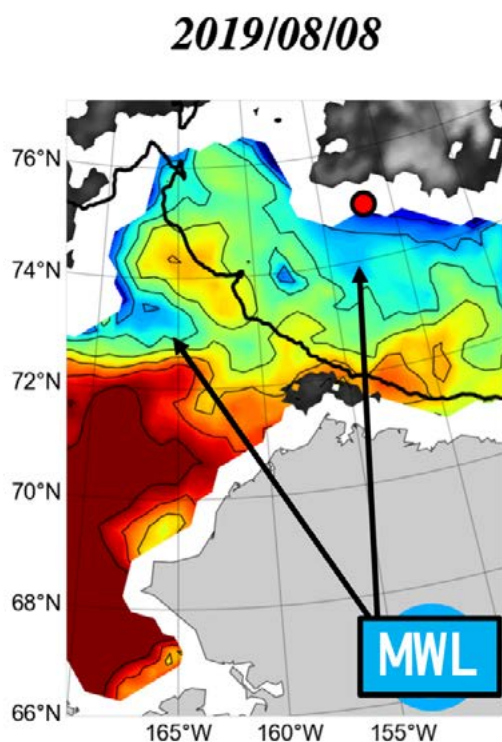
Figure 2. SMOS+SMAP SSS and OSI-SAF in the Chukchi and Beaufort Sea for 2019/08/08. Black bold line for isobath 500m.MWL are indicated with arrows. Red dots indicate the saildrone positions on that day.

5. DISCUSSION AND PERSPECTIVES

The ability of L-Band radiometric SSS to detect sea ice melt effects is particularly encouraging in the changing Arctic Ocean. The synergy between satellite and in-situ measurements is also fundamental to understand the full dynamics of the MWL, and in particular the influence of vertical processes for their evolution. Our study highlights the need for improvement in SSS retrievals from future satellite missions. A mission such as the proposed SMOS-HR project (Rodríguez-Fernández et al., 2019), that aims to estimate SSS with L-band interferometric radiometer measurements with a 10 km resolution, would allow for a better identification of sea ice contaminated measurements and detection of thin sea ice filaments or sea ice patches extracted by ocean currents from these filaments. An improved resolution would also allow for a retrieval of SSS closer to the sea ice edge and thus to capture more accurately MWL.

ACKNOWLEDGEMENTS

REFERENCES

Carmack, E.C., et al., (2016). Freshwater and its role in the Arctic marine system: sources, disposition, storage, export, and physical and biogeochemical consequences in the Arctic and global oceans. J. Geophys. Res. Biogeosci. 121, 675–717. https://doi.org/10.1002/2015JG003140.

Kerr, Y.H., et al., (2010). The SMOS Mission: new tool for monitoring key elements of the global water cycle. Proc. IEEE 98 (5), 666–687. DOI: 10.1109/JPROC.2010.2043032

Kolodziejczyk, N., Hamon, M., Boutin, J., Vergely, J. L., Reverdin, G., Supply, A., & Reul, N. (2021). Objective Analysis of SMOS and SMAP Sea Surface Salinity to Reduce Large-Scale and Time-Dependent Biases from Low to High Latitudes. Journal of Atmospheric and Oceanic Technology, 38(3), 405-421. https://doi.org/10.1175/JTECH-D-20-0093.1

Font, J., Camps, A., Borges, A., Martin-Neira, M., Boutin, J., Reul, N., Kerr, Y.H., Hahne, A., Mecklenburg, S., (2010). SMOS: the Challenging Sea surface salinity measurement from space. Proc. IEEE 98 (5), 649–665. https://doi.org/10.1109/jproc.2009.2033096.

Piepmeier, J.R., et al., (2017). SMAP L-band microwave radiometer: instrument design and first year on orbit. IEEE Trans. Geosci. Remote Sens. 55 (4), 1954–1966. https://doi.org/10.1109/TGRS.2016.2631978.

Olmedo, E., Gabarró, C., González-Gambau, V., Martínez, J., Ballabrera-Poy, J., Turiel, A., Portabella, M., Fournier, S., Lee, T., (2018.) Seven years of SMOS Sea surface salinity at high latitudes: variability in Arctic and sub-Arctic regions. Remote Sens. 10, 1772. https://doi.org/10.3390/rs10111772.

Reul, N., Grodsky, S.A., Arias, M., Boutin, J., Catany, R., Chapron, B., D'Amico, F., Dinnat, E., Donlon, C., Fore, A., Fournier, S., Guimbard, S., Hasson, A., Kolodziejczyk, N., Lagerloef, G., Lee, T., Le Vine, D.M., Lindstrom, E., Maes, C., Mecklenburg, S., Meissner, T., Olmedo, E., Sabia, R., Tenerelli, J., Thouvenin-Masson, C., Turiel, A., Vergely, J.L., Vinogradova, N., Wentz, F., Yueh, S., (2020). Sea surface salinity estimates from spaceborne L-band radiometers: an overview of the first decade of observation (2010–2019). Remote Sens. Environ. 242, 111769. ISSN 0034–4257. https://doi.org/10.1016/j.rse.2020.111769.

Rodríguez-Fernández, Anterrieu, et al., (2019). SMOS-HR: a high-resolution L-band passive radiometer for earth science and applications. IEEE Symp. Geosci. Remote Sens. 2019, 8392–8395. DOI: 10.1109/IGARSS.2019.8897815

A. Supply J. Boutin N. Kolodziejczyk, G. Reverdin, C. Lique J.-L. Vergely X. Perrot (2022). Meltwater lenses over the Chukchi and the Beaufort seas during summer 2019: from in-situ to synoptic view. doi : https://doi.org/10.1002/essoar.10509996.2 Y2 - 2022/7/28

Tang W., Yueh S., Fore A., Hayashi A., Steele M. (2021). An Empirical Algorithm for Mitigating the Sea Ice Effect in SMAP Radiometer for Sea Surface Salinity Retrieval in the Arctic Seas. IEEE Journal of Selected Topics in Applied Earth Observations and Remote Sensing. PP. 1-1. 10.1109/JSTARS.2021.3127470.

Tarasenko, A. and Supply, A. and Kusse-Tiuz, N. and Ivanov, V. and Makhotin, M. and Tournadre, J. and Chapron, B. and Boutin, J. and Kolodziejczyk, N. and Reverdin, G., (2021), Properties of surface water masses in the Laptev and the East Siberian seas in summer 2018 from in situ and satellite data, Ocean Science, 221-247, 10.5194/os-17-221-2021

Vinogradova, N., Lee, T., Boutin, J., Drushka, K., Fournier, S., Sabia, R., Stammer, D., Bayler, E., Reul, N., Gordon, A., Melnichenko, O., Li, L., Hackert, E., Martin, M., Kolodziejczyk, N., Hasson, A., Brown, S., Misra, S., Lindstrom, E., (2019). Satellite salinity observing system: recent discoveries and the way forward. Front. Mar. Sci. 6, 243. https://doi.org/10.3389/fmars.2019.00243.

Lagrangian tracking of meso and submesoscale features on the Southwestern Atlantic

M. Saraceno*[1,2,3], N. Bodnariuk[1,2,3], L.A. Ruiz-Etcheverry[1,2,3], J. Olascoaga[4], F.J. Beron-Vera[5] and C.G. Simionato[1,2,3]

(1) Departamento de Ciencias de la Atmósfera y los Océanos, FCEN-UBA, Buenos Aires, Argentina.
(2) Centro de Investigaciones del Mar y la Atmósfera, CONICET-UBA, Buenos Aires, Argentina.
(3) Instituto Franco-Argentino para el Estudio del Clima y sus Impactos, CNRS-IRD-CONICET-UBA, Buenos Aires, Argentina.
(4) Department of Ocean Sciences, Rosenstiel School of Marine and Atmospheric Science, University of Miami, Miami Florida 33149, USA
(5) Department of Atmospheric Sciences, Rosenstiel School of Marine and Atmospheric Science, University of Miami, Miami Florida 33149, USA

Abstract – The objective of this work is to characterize the Malvinas Current (MC) and its interaction with meso and submesoscale features using the trajectories of 62 surface drifters that have been deployed at the same time across the Patagonian shelf and shelf-break and different satellite missions. Thanks to the large number of drifters deployed within the MC, we show that the MC horizontal structure is very rich, presenting large differences in speed (up to 0.25 m/s) in short distances (2 km), it is affected by tides and it is largely affected by mesoscale features that propagate in the eastern side of the current. The analysis of Lagrangian Coherent Structures (LCSs) and Finite Time Lyapunov Exponents (FTLE) based on satellite altimetry data indicates that the MC is structured along two Lagrangian jets south of 46°S and that water exchanges between the outer-shelf and the shelf-break region are enhanced at 47°S. The lack of satellite altimetry data at given dates might explain a few inconsistencies observed between satellite altimetry data and drifters' trajectories.

Keywords: Malvinas Current, Lagrangian measurements, ocean drifters, LCSs

1. INTRODUCTION

The Malvinas Current (MC) is a branch of the Antarctic Circumpolar Current that flows equatorward along the Argentinean continental shelf-break. It presents an approximately barotropic structure (Paniagua et *al*., 2018) and its flow is strongly constrained by potential vorticity (Matano et *al*., 2010). The MC transports cold, nutrient-rich subantarctic waters to the Confluence Region, where it encounters the warm and salty Brazil Current, which flows poleward and advects subtropical waters (Saraceno et *al*., 2004). The encounter of the two currents generates large meanders and a complex flow (Chelton et al., 1990) that spans across a very rich variety of spatio-temporal scales that affect biological activity in the surface of the ocean and the transport of properties across different regions, contributing to the global meridional heat overturning circulation (e.g. Marshall and Speer, 2012). Such diversity is well documented with satellite images, according to the spatial resolution of the different satellite missions. The study of the MC transport variability has been addressed in the literature based on altimetry data, in-situ measurements and ocean reanalysis. Among these studies, Beron-Vera et *al*. (2020) employed non-linear dynamics techniques and statistical methods to unveil the organization of the MC flow. The authors employed Lagrangian Coherent Structures (LCS) analysis based on satellite altimetry data

and a subset of the Global Drifter Program dataset to assess whether the core of the MC acted as a transport barrier. The analysis of the drifter trajectories for the 1990-2021 time period shows that a reduced number of buoys cover the MC region. In this sense, the present study constitutes the first effort to sample de MC with a dense drifter array (N = 62). The drifters were deployed across the current at two transects (47°S and 47.25°) between the 8th and the 9th of September 2021 (Fig. 1). The particular deployment design of the drifters allowed for the study of different flow features characteristic of the MC. Drifters were set to deliver their position between 10 and 60 minutes, providing accurate Lagrangian trajectories that provide information on a large range of space and time scales.
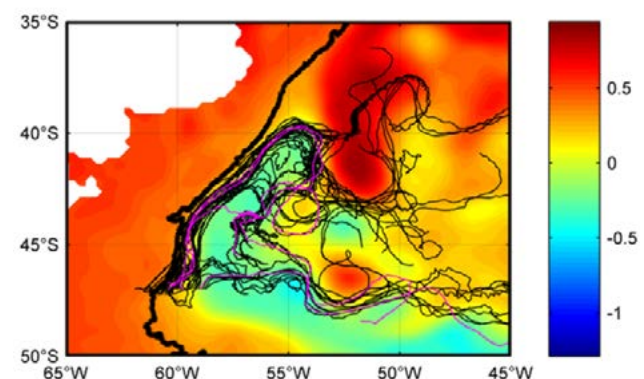
Figure 1. *Drifter trajectories from 08/09/2021 to 06/11/2022. The magenta and black lines indicate the drifters with a temporal frequency of 60 and 10 minutes respectively. The mean ADT (m) field for the time period is displayed in colors. Black solid thick line represents the 200 meters isobath (shelf-break).*

2. RESULTS

The comparison of the drifters trajectories with satellite images shows that, in general, drifters follow mesoscale features that are detectable in satellite altimetry maps. A few non-cloudy high-resolution color images show very good correspondence with sub-mesoscale (1 to 10km) features that are not observable in satellite altimetry data. For example, three drifters were trapped simultaneously for 4 weeks by an eddy of 12 km of diameter that was clearly visible in color images but not in satellite altimeter data. Discrepancies were also observed between datasets. For example, during the first two days of the Lagrangian experiment, the easternmost drifters deployed revealed trajectories that clearly indicate the presence of an eastward flow. However, satellite altimetry data suggest a northward flow for the same region and time.

We show that the discrepancy might be related to a poor coverage of the satellite missions during that time period in that particular area. This eastward flow is very likely generated by a strong mesoscale eddy which core is located further east and is well described by altimetry sea level anomaly.

The high frequency rate of transmission of the drifters allowed to clearly distinguish the different forcings that affect the surface currents in the region. In particular, the semidiurnal tide, characteristic of the Patagonian shelf, is also detected in the strong MC. In the Brazil-Malvinas Confluence region and along the northern branch of the Subantarctic Front, drifters exceed 1.8 m/s, while satellite altimetry velocities do not exceed 80 cm/s. These results reflect the large ageostrophic component that dominates the dynamics of the frontal regions. Satellite altimetry images are also employed to compute Lagrangian Coherent Structures (LCSs) that organize the flow of the along the Patagonian shelf-break as in Beron-vera et al (2020). It is found that the current is structured along two lagrangian jets that act as transport barriers between 46°S and 47°S (Fig. 2). This result is consistent with observations, as drifter trajectories approximately follow both meandering jets and present higher velocities near the cores. Further analysis of both attracting LCS and Finite Time Lyapunov Exponents (FTLE) suggests that water exchanges between the outer-shelf and the shelf-break region are enhanced at 47°S. At this latitude, the FTLE field presents a relative maximum and the attracting LCSs are oriented across the 200 m isobath, which suggest that the shelf-break is permeable to transport. This is consistent with the trajectories of the drifters that were deployed in the outer-shelf region. Generally, the mesoscale organization of the flow as revealed by the LCS analysis is coherent with the coarse features of the satellite color images. For example, the lagrangian jets are readily observable in chlorophyll-a concentration maps as well as in mesoscale filaments that are structured along attracting LCSs.
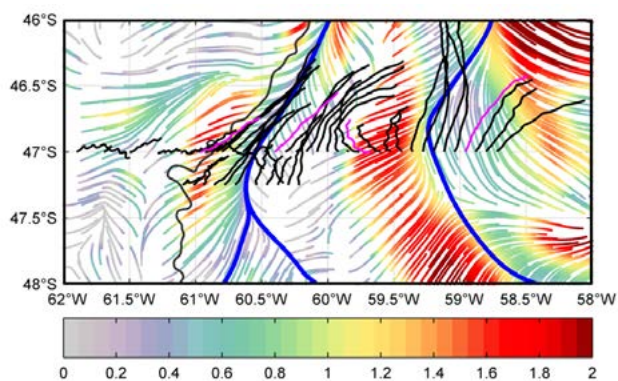
Figure 2. *Drifter trajectories for the first 72 hs since deployment (colors were assigned as in Figure 1). The blue curves constitute the Lagrangian jets of the Malvinas Current for the deployment date (08/09/2021), which were unveiled based on a LCS analysis for this time period. The black thick curve represents the shelf-break. The colored curves constitute altimetric attracting LCS for the same date. The palette was assigned to the logarithm of the FTLE field.*

3. CONCLUSION

The trajectories of 62 drifters deployed within the Patagonian Continental shelf and MC bore a strong resemblance with mean features displayed by satellite altimetry in the MC. For instance, drifters trajectories are largely organized by LCS derived from altimetry data. The drifters closely follow two

Lagrangian jets of the MC detected by the parabolic LCS analysis between 46°S and 47°S. In addition, drifters deployed in the external Patagonian Continental Shelf deviate to the east and enter the Malvinas flow domain, as suggested by the joint analysis of hyperbolic LCS and Finite Time Lyapunov Exponents (FTLE). However, two major discrepancies were observed between datasets: i) the drifters deployed at the eastern side of the current deflect eastward, whereas the altimetry field does not present a large zonal velocity component; ii) the drifters exhibit small-scale features that are not resolved by altimetry data. With regard to the first point, the analysis of the satellite tracks in the region suggests an undersampling of the Malvinas flow at the eastern edge of the current during the first 2 days, which may result in a poor local interpolation for the L4 multi-satellite altimetry product. With regard to submesoscale features, drifter trajectories exhibit a general consistency with submesoscale features of ocean color products but not with satellite altimetry data. We conclude that the analysis of the trajectories produced by a dense array of drifters provide valuable information of the flow that cannot be attained solely on the basis of satellite data.

REFERENCES

Beron-Vera, F. J.; Bodnariuk, N.; Saraceno, M.; Olascoaga, M. J.; Simionato, C. (2020). Stability of the Malvinas Current. Chaos: An interdisciplinary Journal of Nonlinear Science, vol.30. doi.org/10.1063/1.5129441

Chelton, D. B., Schlax, M. G., Witter, D. L., & Richman, J. G. (1990). Geosat altimeter observations of the surface circulation of the Southern Ocean. Journal of Geophysical Research, 95(C10). doi.org/10.1029/jc095ic10p17877

Marshall, J., & Speer, K. (2012). Closure of the meridional overturning circulation through Southern Ocean upwelling. Nature Geoscience. https://doi.org/10.1038/ngeo1391

Matano, R. P., Palma, E. D., & Piola, A. R. (2010). The influence of the Brazil and Malvinas Currents on the Southwestern Atlantic Shelf circulation. Ocean Science. doi.org/10.5194/os-6-983-2010

Paniagua, G. F., Saraceno, M., Piola, A. R., Guerrero, R., Provost, C., Ferrari, R., et al. (2018). Malvinas Current at 40°S–41°S: First assessment of temperature and salinity temporal variability. Journal of Geophysical Research: Oceans, 123, 5323–5340. doi. org/10.1029/2017JC013666

Saraceno, M., Provost, C., Piola, A. R., Bava, J., & Gagliardini, A. (2004). Brazil Malvinas Frontal System as seen from 9 years of advanced very high resolution radiometer data. Journal of Geophysical Research C: Oceans. https://doi.org/10.1029/2003JC002127

Bioregionalization of the coastal oceans of British Columbia and Southeast Alaska based on Sentinel-3A retrievals of phytoplankton biomass patterns

C. Marchese[1,2,3*], B. Hunt[2,3], F. Giannini[4], M. Ehrler[1], and M. Costa[1]

[1]University of Victoria, Victoria, BC, Canada
[2]University of British Columbia, Vancouver, BC, Canada.
[3]Hakai Institute, Heriot Bay, BC, Canada
[4]Federal University of Rio Grande, Rio Grande, Rio Grande do Sul, Brazil

Abstract – We developed a two-step classification procedure (i.e., using a Self-Organizing Maps analysis followed by the affinity propagation clustering method) to define bioregions based on the seasonal climatology of high-resolution (300 m) Sentinel-3A surface chlorophyll-a data for the coastal and open oceans of British Columbia (BC) and Southeast Alaska (SEA). The technique allowed high precision in delineating ten bioregions, broadly divided between off-shelf bioregions and those in neritic waters. Consistent with the high-nutrient, low-chlorophyll regime, relatively low values of phytoplankton biomass (< 1 mg/m3) distinguished off-shelf bioregions, which also displayed, on average, more prominent autumn biomass peaks. In sharp contrast, neritic bioregions were highly productive (>> 1 mg/m3) and characterized by different phytoplankton dynamics. The spring phytoplankton bloom onset varied spatially and inter-annually, with substantial differences among bioregions.

Keywords: Sentinel-3A, Phytoplankton, Bioregionalization.

1. INTRODUCTION

The designation of provinces (also called ecological regions or bioregions) identifies coherent and relatively homogeneous biogeochemical regions with observable boundaries. Overall, regionalization is a valuable strategy for characterizing surface ocean variability, testing ecological hypotheses, contextualizing observations, and implementing relevant management and conservation programs. High-resolution satellite-derived products provide valuable data to address this task.

The coastal and open oceans of BC and SEA host rich assemblages of higher trophic level communities, including iconic marine mammals and productive fisheries with high cultural and economic value, while supporting a growing aquaculture industry (Barth et al. 2019). Across this heterogeneous marine domain, phytoplankton are subject to ocean circulation patterns and atmosphere-ocean-land interactions, and their variability, in turn, influences marine food web structure and function (O'Neel et al., 2015). Phytoplankton biomass is a powerful indicator of productivity and ecosystem functioning on global and regional scales (Racault et al., 2014). Regionalization based on satellite-derived chlorophyll-a (a proxy for phytoplankton biomass) patterns along BC and SEA's coastal and open oceans can be valuable in improving our knowledge of phytoplankton dynamics and representing a baseline for assessing forthcoming changes.

In this regard, the goal of this work was to provide a regional biogeochemical partitioning that minimizes subjectivity and can be refined and continuously updated as more Sentinel-3A satellite data becomes available. Specifically, the main objectives of this study were to (1) delineate a biotic-based (i.e., using Sentinel-3A satellite-derived chlorophyll-a; Gianinni et al., 2021) partition of the BC and SEA coastal oceans into bioregions; (2) assess the resulting bioregions in the context of current knowledge of the basin's oceanographic properties; and (3) evaluate their biological relevance in terms of variability of spring blooms onset. Finally, a workflow (Figure 1) using the Microsoft Azure platform and docker containers was developed to optimize the data processing and create an automated tool to facilitate future analyses.
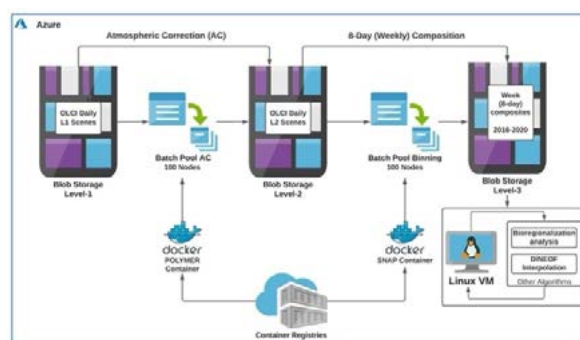
Figure 1. *Workflow showing the main steps made on the cloud computing platform to obtain the Level-3 time series.*

2. DISCUSSION

The ten bioregions (Figure 2) identified by the two-step classification over the research domain were separated based on their chlorophyll-a seasonal cycle. Oligotrophic bioregions, showing low mean values of chlorophyll-a concentrations, matched bioregions #2, 4, 5, and 7. Bioregions #2 and #4, located immediately west of the continental shelf-break, defined a transition zone that marks the boundary between the more productive bioregions (i.e., #1, 3, 6, 8, 9, 10) on the continental shelf and the more oligotrophic deep basin (i.e., west of ~128 °W). The shelf break/slope area thus defines a transition zone between iron-rich, nitrate-poor shelf waters to iron-poor, nitrate-rich offshore waters (Ribalet et al., 2010).

Off-shelf bioregions (i.e., #5 and #7) together with the two bioregions of the transition zone (i.e., #2 and #4) occupied an area extending from the continental shelf-break (~1000 m) to the deep basin (> 3000 m). These bioregions occurred in waters characterized by iron-poor and nitrate-rich conditions. Off-shelf iron limitation restrains phytoplankton growth in spring and early summer, while phytoplankton biomass accumulates in late summer/fall due to reduced zooplankton grazing. These bioregions were therefore characterized by a seasonal pattern with a small peak in spring and a more prominent autumn peak. Low temporal variability in upper-layer chlorophyll-a concentrations has been previously reported at Ocean Station Papa (OSP; 50°N, 145°W), along the offshore section of Line P (Peña et al., 2019), and using observations from a biogeochemical-Argo float (Zhang et al. 2021). Across off-shelf bioregions, spring

bloom initiation dates may vary, on average, from early March to the beginning of April. It is triggered mainly due to the shoaling of the mixed layer depth (Henson, 2007).
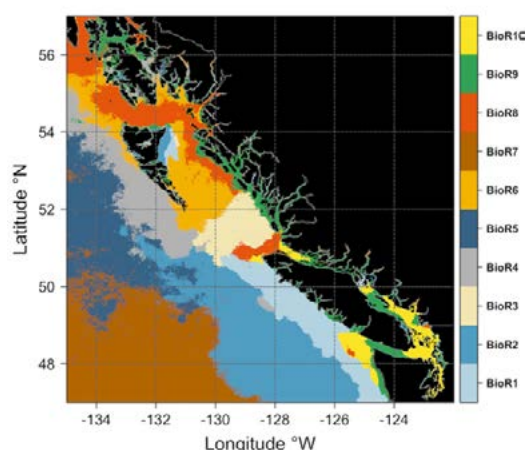
Figure 2. *Maps showing the spatial distribution of the ten bioregions obtained from the two-step classification procedure.*

The neritic bioregions (#1, 3, 6, 8, 9, and 10) were more productive than off-shelf bioregions and characterized by either unimodal (a spring bloom peak) and bimodal (spring and autumn bloom peaks) seasonal cycles. Overall, the on-shelf phytoplankton assemblages are usually dominated by large phytoplankton cells, and nitrate availability may limit productivity (Peña and Varela, 2007). Localized dynamics may strongly influence neritic bioregions. For instance, Bioregion #9, which included the Fraser River mouth, inner coast waters, and most of the complex fjord systems across the study area, was the only bioregion that did not show a clear seasonal cycle. We speculate that this was likely due to runoff-driven estuarine circulation resupplying nutrients, which keeps chlorophyll-a concentrations relatively high and stable under an adequate light regime. The interplay of different oceanographic features on the shelf can also cause notable shifts in bloom initiation times over short distances. For instance, across these bioregions, the balance between mixing (i.e., tide and wind) and buoyancy (i.e., heat and freshwater) processes appears to be crucial in triggering the bloom onset (Henson 2007). Given the dynamical differences in environmental conditions, the spring bloom initiation dates varied, on average, between the end of March and the beginning of May, with the northern continental shelf (i.e., north of ~51°N) characterized by a later bloom.

3. CONCLUSION

The findings of this study strengthen the view that the coastal oceans of BC and SEA cannot be considered homogeneous entities. The 300 m spatial resolution imagery of the Sentinel-3 OLCI sensor and the proposed methodology allowed delineation of bioregion boundaries with high precision and definition of distinctive phytoplankton bloom dynamics, including spring bloom timing for each bioregion.

Looking to the future, when more high-resolution data will be available, the application of the method should consider variability (stability) in the spatial distribution of bioregions. Specifically, temporal changes in the bioregion boundaries should be assessed. Tracking such changes will inform the phenological analysis of phytoplankton and zooplankton, which are essential information in fisheries management (Suchy et al., 2022). In this connection, the recent Sentinel-3 (2016 – ongoing) mission will ensure continuity and consistency of observations, supporting operational applications and monitoring purposes across the target area.

REFERENCES

Barth, J.A., Allen, S.E., Dever, E.P., Dewey, R.K., Evans, W., Feely, R. A., et al. (2019). Better Regional Ocean Observing Through Cross-National Cooperation: A Case Study From the Northeast Pacific. Front. Mar. Sci. 6, 93.

Giannini, F., Hunt, B. P. V., Jacoby, D., and Costa, M. (2021). Performance of OLCI Sentinel-3A satellite in the Northeast Pacific coastal waters. Remote Sensing of Environment 256, 112317. doi: 10.1016/j.rse.2021.112317.

Henson, S.A. (2007). Water column stability and spring bloom dynamics in the Gulf of Alaska. J Mar Res 65, 715–736.

O'Neel, S., Hood, E., Bidlack, A.L., Fleming, S.W., Arimitsu, M.L., Arendt, A., et al. (2015). Icefield-to-Ocean Linkages across the Northern Pacific Coastal Temperate Rainforest Ecosystem. BioScience 65, 499–512.

Peña, M.A., and Varela, D.E. (2007). Seasonal and interannual variability in phytoplankton and nutrient dynamics along Line P in the NE subarctic Pacific. Progress in Oceanography 75, 200–222.

Peña, M.A., Fine, I., and Callendar, W. (2019). Interannual variability in primary production and shelf-offshore transport of nutrients along the northeast Pacific Ocean margin. Deep Sea Research Part II: Topical Studies in Oceanography 169–170, 104637.

Racault, M.F., Platt, T., Sathyendranath, S., Airba, E., Martinez Vicente, V., and Brewin, R. (2014). Plankton indicators and ocean observing systems: support to the marine ecosystem state assessment. Journal of Plankton Research 36, 621–629.

Ribalet, F., Marchetti, A., Hubbard, K. A., Brown, K., Durkin, C.A., Morales, R., et al. (2010). Unveiling a phytoplankton hotspot at a narrow boundary between coastal and offshore waters. Proceedings of the National Academy of Sciences 107, 16571–16576.

Suchy, K.D., Young, K., Galbraith, M., Perry, R.I., and Costa, M. (2022). Match/Mismatch Between Phytoplankton and Crustacean Zooplankton Phenology in the Strait of Georgia, Canada. Front. Mar. Sci. 9, 832684.

Zhang, H., Wang, Y., Xiu, P., and Chai, F. (2021a). Modeling the seasonal variability of phytoplankton in the subarctic northeast Pacific Ocean. Mar. Ecol. Prog. Ser. 680, 33–50.

A satellite-based product for SST Diurnal Variability in the North and Baltic Seas

I. Karagali [*], Jacob L. Hoeyer, Magnus Barfod Suhr, Wiebke M. Kolbe

National Centre for Climate Research, Danish Meteorological Institute, Copenhagen, Denmark

Abstract – SST diurnal variability is a key process occurring during day-time under favourable conditions of moderately low winds and solar heating; it impacts air-sea interaction processes, resulting in erroneous modelled heat budget estimates, thus demised model accuracies. Furthermore, it complicates merging of SSTs from different satellite sensors with direct impact on efforts to create climate records. Finally, misrepresenting diurnal variability of the upper ocean temperature may result in large errors when modelling harmful algal blooms. In this study, we present a new, level-4, optimally interpolated, gap-free, hourly product from satellite SST retrievals, specifically developed for the Baltic Sea and North Sea area, distributed through the Copernicus Marine Service.

Keywords: SST, diurnal variability.

1. INTRODUCTION

Diurnal variability of the sea surface temperature has been observed in the Atlantic Ocean and European Seas (Karagali and Høyer 2014) and at higher latitudes (Karagali et al. 2012). Although some of the important diurnal variability and cool skin effects (Fairall et al. 1996) have been shown to be reproducible (Fallman et al. 2017), SST diurnal variability is not fully resolved by ocean and coupled ocean-atmosphere models; regional Copernicus Marine Service ocean forecasting systems only assimilate a single SST field per day, representative of night-time conditions when the water column is well mixed and thus, no diurnal signal is present. Such simplification of the SST is reported to cause biases in the estimated surface fluxes (Ward 2006). In addition, strong SST diurnal signals can complicate the assimilation of SST fields in ocean and atmospheric models, the derivation of atmospheric correction algorithms for satellite radiometers and the merging of satellite SST from different sensors (Donlon et al. 2007). Not accounting for the daily SST variability can cause biases in the prediction and modelling of algal blooms, especially as cyanobacteria blooms, e.g. in the Baltic Sea, are promoted by high SST values (Lips et al. 2008) - and the estimated net flux of CO_2, as the outflux of oceanic CO_2 is positively correlated with the increase of SST (Takahasi et al. 2002).

This study describes the development and validation of a new Copernicus Marine Service product based on satellite SST retrievals, with an hourly temporal resolution and using optimal interpolation to fill gaps due to missing data. This product, developed by the Danish Meteorological Institute (DMI) within the SST Thematic Assembly Centre (SST TAC) will be distributed daily through the Copernicus Marine Service, starting in November 2022. It aims to improve analyses and understanding of ocean processes occurring at the surface layer which develop and evolve at sub-daily scales, and thus will be relevant for various applications such as monitoring of algal blooms and offshore wind energy.

2. DATA AND METHODS

The L4 Near-Real-Time Diurnal SST product SST-BAL-PHY-SUBSKIN_L4-NRT-010-034 is a gap free satellite sub-skin SST analysis created by the DMI optimal interpolation (DMIOI) system (Høyer and She, 2007; Høyer et al. 2014). The product will be distributed in November 2022 and available from May 2022 onwards, on a regular latitude/longitude grid at 0.02° resolution, providing an estimate of the hourly sub-skin SST with uncertainty estimates, which is the SST including diurnal variability. Input data include infra-red SST observations from polar orbiting platforms such as AVHRR on Metop-A, VIIRS_NPP, NOAA 20, SLSTR SST from Sentinel 3A/B and geostationary platforms, such as SEVIRI on MSG. SST products are currently adjusted to the VIIRS_NPP SST observations in a dynamical way. The Operational Sea Surface Temperature and Ice Analysis (DMIOI) system uses upstream L2 and L3 satellite data along with ice concentration information for the generation of a suite of L3S and L4 SST products at daily near-real-time and as multi-year datasets (Figure 1).
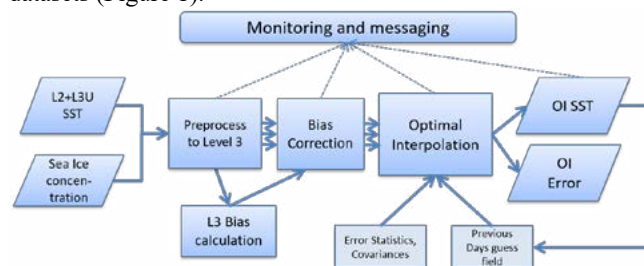
Figure 1. Schematic representation of Optimal Interpolation system at DMI (DMIOI).

The system uses a persistence-based approach utilising the previous analysis field as a first guess. SST observations from the current day are interpreted as anomalies with respect to the first guess field. The errors on the guess field are derived from the data. Pre-processing collates all different products on the analysis grid, creating the L3S products. The time scale for the aggregations is the analysis date +/-12 hours (Copernicus Marine Service, 2021a). For the diurnal product, all satellite data valid for a particular day and hour, within 24 hours from the analysis are considered. The input L2/L3U SST data undergo various QC and processing steps to generate separate level 3 products and single-sensor hourly files are bias-corrected to ensure consistency. Hourly anomalies, dSST, from the SST foundation temperature of the   same   day (SST_BAL_SST_L4_NRT_OBSERVATIONS_010_007_b, Copernicus Marine Service 2021a) are estimated as SST_{hour} minus $SST_{foundation}$. The OI is then applied to the hourly anomaly field, to produce gap-free hourly dSST and the $SST_{foundation}$ is subsequently added to the hourly dSST.

For the validation of the derived diurnal product, daily in situ SST from the shallowest depth level of drifting buoys in the North and Baltic Sea, were obtained from the Copernicus

---

***** Corresponding author. Address: Lyngbyvej 100, 2100 Copenhagen Ø, Denmark. Email: ika@dmi.dk

Marine Service, see products INSITU_GLO_NRT_OBSERVATIONS_013_030 and INSITU_BAL_NRT_OBSERVATIONS_013_032 (Copernicus Marine Service, 2021b).

3. RESULTS

An example of an hourly SST L4 gap-free field for June 01, 2021 16:00 (Figure 2, middle panel) along with the night-time foundation SST field (Figure 3, left panel), computed as the mean SST during 00:00-04:00. The right panel, shows dSST, i.e. the difference $SST_{16:00}$-$SST_{foundation}$, where differences of higher than 0.6°C are found in large parts of the Baltic Sea basin. Higher anomalies, exceeding 1.4°C are concentrated in patches found in the northern Bay of Bothnia, in coastal areas of the south-east Baltic basin and offshore Norway.
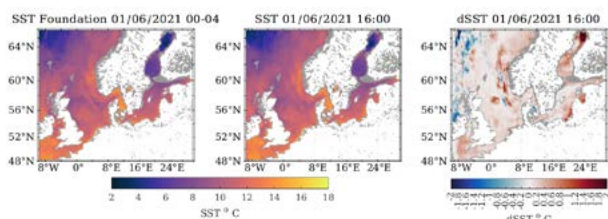
Figure 2. Foundation SST temperature (left), SST at 16:00 (middle), dSST (right).

To assess the variability of the product itself during the test period from May to August 2021, hourly differences were estimated for each time-step h, defined as SST_h-SST_{h-1}. The standard deviation σ, along with the maximum and minimum differences at each grid point are shown in Figure 3. While the standard deviation between hourly SST fields is generally low, not exceeding 0.2°C, differences between the North Sea and the Baltic Sea are found along with isolated areas of the North Atlantic where σ values were higher than the surrounding areas. This suggests that overall, no large variability occurs in the hourly OI SST fields from hour to hour. Maximum and minimum differences can be associated to diurnal variability events, indicating that in most areas at least 2°C of hourly differences were found and in certain regions of both basins, differences could reach up to 5°C, consistent with findings from previous studies (e.g. Karagali and Høyer, 2014) using only hourly satellite SST observations.
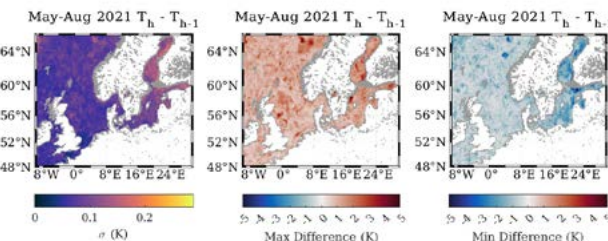
Figure 3. Standard deviation σ (left), maximum (middle) and minimum (right) of hourly differences SST_h-SST_{h-1}, for the period May-August 2021.

Validation of the diurnal product during the test period from May to August 2021, using in situ drifting and moored buoys in the North Sea and Baltic Sea (Table 1) indicated very low biases and standard deviations similar to what is found for other operational L4 SST products (Copernicus Marine Service, 2021a).

Table 1. Validation statistics of the diurnal product.

L4 DIU	Mean	σ	RMS	N.
All	-0.174	0.549	0.576	34690
Day 06:00-19:00	-0.203	0.553	0.589	19869
Night 19:00-06:00	-0.136	0.541	0.558	14821

4. CONCLUSION

My conclusions should be related to the results presented here and also state the importance of such a product and how should it be used.

REFERENCES

Karagali, I., J.L. Høyer, and C.B. Hasager (2012). SST diurnal variability in the North Sea and the Baltic Sea. Rem. Sens. Env., 121, pp 159-170.

Karagali, I., and J.L. Høyer (2014). Characterisation and quantification of regional diurnal SST cycles from SEVIRI. Ocean Sci. Discuss., 11, pp 1093-1128.

Fairall, C.W., E.F. Bradley, J.S. Godfrey, G.A. Wick, J.B. Edson, and G.S. Young (1996). Cool-skin and warm-layer effects on sea surface temperature, J. Geophys. Res. C Oceans, 101 (1), pp 1295-1308.

Fallmann, J., H. Lewis, J.M. Castillo, A. Arnold, and S. Ramsdale (2017). Impact of sea surface temperature on stratiform cloud formation over the North Sea, Geophys. Res. Lett., 44, pp 4296-4303.

Donlon, C., I. Robinson, K.S. Casey, J. Vazquez-Cuervo, et al. (2007). The Global Ocean Data Assimilation Experiment High-resolution Sea Surface Temperature Pilot Project. Bull. Am. Met. Soc., 88 (8), pp 1197-1213.

Lips, I., and U. Lips (2008). Abiotic factors influencing cyanobacterial bloom development in the Gulf of Finland (Baltic Sea). Hydrobiologia, 641 (1), pp 133-140.

Takahashi, T., S.C. Sutherland, C. Sweeney, et al. (2002). Global sea-air CO_2 flux based on climatological surface ocean pCO2 and seasonal biological and temperature effects. Deep-Sea Research Part II-Topical Studies in Oceanography, 49, pp 1601.

Høyer, J.L. and J. She (2007). Optimal interpolation of sea surface temperature for the North Sea and Baltic Sea, J. Mar. Sys. 65, pp 1-4.

Høyer, J.L., P. Le Borgne and S. Eastwood (2014). A bias correction method for Arctic satellite sea surface temperature observations, Rem. Sens. Environ. 146, pp 201-213.

Copernicus Marine Service (2021a). Quality information document for SST TAC products SST_BAL_SST_L4_NRT_OBSERVATIONS_010_007_b and SST_BAL_SST_L3S_NRT_OBSERVATIONS_010_032. Issue 2.1, https://catalogue.marine.copernicus.eu/documents/QUID/CMEMS-SST-QUID-010-007-032.pdf

Copernicus Marine Service (2021b). Product user manual for in situ products. Issue 1.13, http://dx.doi.org/10.13155/43494, https://catalogue.marine.copernicus.eu/documents/PUM/CMEMS-INS-PUM-013.pdf

SESSION 7

SURFACE PROCESSES, COASTAL ISSUES, EXTREME EVENTS

Global coastal attenuation of wind-waves observed with radar altimetry

M. Passaro *[1], M.A. Hemer[2], G.D. Quartly[3], C. Schwatke[1], D. Dettmering[1], F. Seitz[1]

[1] Deutsches Geodätisches Forschungsinstitut, Technischen Universität München (DGFI-TUM), Germany
[2] Commonwealth Scientific and Industrial Research Organisation Oceans and Atmosphere, Hobart, Tasmania, Australia
[3] Plymouth Marine Laboratory (PML), Plymouth, UK

Abstract – Coastal studies of wave climate and evaluations of wave energy resources are mainly regional and based on the use of computationally very expensive models or a network of in-situ data. Considering the significant wave height, satellite radar altimetry provides an established global and relatively long-term source, whose coastal data are nevertheless typically flagged as unreliable within 30 km of the coast. This study, recently published in Nature Communications (Passaro et al., 2021), exploits the reprocessing of the radar altimetry signals with a dedicated fitting algorithm to retrieve several years of significant wave height records in the coastal zone. We show significant variations in annual cycle amplitudes and mean state in the last 30 km from the coastline compared to offshore, in areas that were up to now not observable with standard radar altimetry. Consequently, a decrease in the average wave energy flux is observed. Globally, we found that the mean significant wave height at 3 km off the coast is on average 22% smaller than offshore, the amplitude of the annual cycle is reduced on average by 14% and the mean energy flux loses 38% of its offshore value.

Keywords: Significant Wave Height, Coast, Radar Altimetry, Wave Energy Flux

1. INTRODUCTION

The height of the wind waves in the ocean, together with their period, direction, and speed, is a fundamental parameter to describe the sea state and more generally to study the ocean climate and interactions with the atmosphere (Cavaleri et al., 2012). The significant wave height (SWH), defined as four times the standard deviation (std) of the surface elevation (Ardhuin et al., 2019), is an integral parameter that is extensively used as reference to quantify both extremes and mean sea states. In particular, the relevance of a SWH climatology is manifold, from the optimisation of shipping routes to the quantification of the impact of sea level rise at the coast. Such a climatology is also fundamental to assess the wave energy resources of a particular area and planning the exploitation of a potential source of renewable energy.

Despite the overwhelming importance of measuring waves in the coastal zone, our knowledge of coastal wave climate and coastal wave energy resources is limited in data availability, accuracy, and resolution. In-situ data are collected by buoys, whose records are sparse in time and space. Ocean models work very well in the open ocean, but a nested high resolution model needs to be used in order to correctly simulate the coastal features that modify wave parameters.

Satellite altimeter measurements of SWH, collected along repeating ground tracks, extend from 1985 through to present. The principle is based on the shape of the returned radar echo and in particular on its stretch being proportional to the wave height. Such estimation has the advantage of being independent of atmospheric corrections that are needed to estimate the range (distance between the satellite centre of mass and the sea level). This technique has been used to quantify global open ocean mean wave climate, seasonality, energy flux resources, and global historical trends (e.g. Young and Ribal, 2019). Nevertheless, these studies cannot see small scale variability of coastal processes, given the large grid-points of over 1-degree spacing in latitude and longitude. Other studies identified the potential of using along-track measurements to locally observe variations in the sea state, but efforts have been restricted to specific regions and were limited by the unreliability of standard altimetry data in the coastal strip. This is due to the influence of land and areas with different backscattering characteristics within the satellite footprint, which can negatively affect SWH measurements within about 20 km of the coast (Passaro et al., 2015).

In recent years, coastal altimetry has been the focus of several improvements (Cipollini et al., 2017). In particular, specific algorithms (retrackers) have been designed to fit the returned echo while avoiding spurious coastal reflections that degrade the quality of the estimated parameters. This, coupled with a conservative strategy to detect outliers, has brought strong improvements to the quality and the quantity of SWH retrievals.

Here, we exploit these improvements to provide, based on reprocessed along-track satellite altimetry data, an assessment of the average global coastal wave climate in the coastal zone in terms of SWH, and to highlight the differences with respect to the climatology of previously presented offshore conditions (Stopa, 2019). The results presented are based on the reprocessing of satellite altimetry data from Jason-1 and Jason-2 missions, from July 2001 to January 2016. We are able to quantify the progressive attenuation of the average wave climate towards the coast, even focusing on the differences in the last 30 km. These differences are finally quantified in terms of wave energy flux. The coastal proximity and resolution, as well as the global character of these observations is unprecedented and verified by comparison with buoys and a regional high-resolution nested wave model.

---

* Corresponding author. Address: Arcisstrasse 21, 80333 München, Germany. Email: marcello.passaro@tum.de
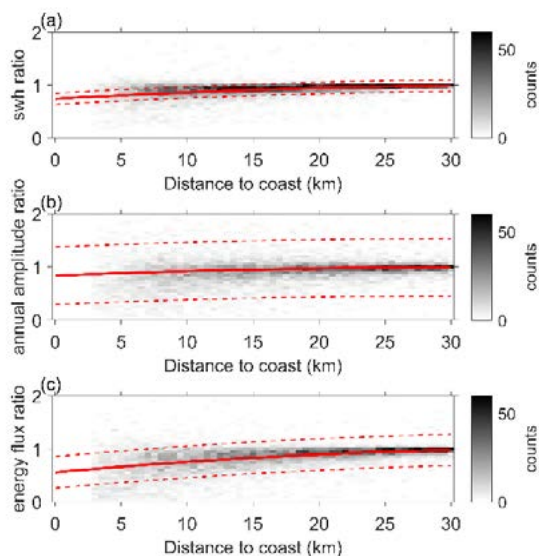
Figure 1. *Density plots of the ratios between wave parameters computed in the coastal zone over the globe and the corresponding parameter computed offshore. The parameters considered are the mean Significant Wave Height (SWH) (a), the amplitude of the annual cycle (b), and the average wave energy flux (c). A second-degree polynomial is fitted to the data and plotted in red. The 95% confidence interval of the fit is shown with red dashed lines.*

2. DISCUSSION

The use of reprocessed time series of coastal altimetry data provide the chance to observe the interaction between waves, bathymetry, and coastlines in terms of SWH. Besides the common understanding that SWH is decreased in the coastal zone, the study quantifies the attenuation of mean state, seasonality, and wave energy flux at an unprecedented resolution that could so far only been achieved using dedicated high-resolution models for regional and local downscalings.

The results are summarised in their global statistics in Fig. 1, where the parameters are shown as a ratio against the value at 30 km from the coast (defined as offshore in this study). The polynomial fit indicates that the mean SWH at 3 km from the coast is on average 22% smaller than offshore, the amplitude of the annual cycle is reduced in the same distance on average by 14% and the average energy flux loses 38% of its offshore value. The global coastal attenuation is verified with a confidence level of 95% for both mean SWH and average energy flux. This is not true for the amplitude of the annual cycle, whose difference between coastal and offshore values has a wider spread.

While dedicated regional high-resolution models are able to take into account the attenuation seen with satellite altimetry, studies of global wave power up to now, including the assessment of the World Energy Council have typically been defined using models or reanalysis with validation relative to offshore satellite altimetry data. The resolution of these models may be high for regional applications (e.g., of order hundreds of metres). At global scale, the resolution of

these models is typically in the range of 0.25° to 0.5° (e.g. Perez et al., 2017). The wave energy generation systems are typically planned to be placed near the shore or in depth ranges of 30–50 m in the offshore cases (Hemer et al., 2010). Given the global observational representation of the coastal attenuation provided in this study, studies of global wave power shall be therefore updated using the latest models at higher resolution.

Finally, this study shows the level of accuracy that reprocessed satellite altimetry offers to describe the coastal wave climate in terms of SWH. Our dataset is unprecedented in presenting altimeter wave height data near to the coast at a global scale. This opens possibilities for future global analyses seeking to quantify near coastal wave transformations across a full distribution of shelf environments. The short time series with respect to the variability of this quantity still hampers the estimation of significant trends. Future efforts in this sense, which are planned for example in the framework of the European Space Agency's Sea State Climate Change Initiative, shall focus on a dedicated irregular coastal gridding in order to increase the sampling while avoiding rough interpolation with offshore data.

REFERENCES

Passaro, M., Hemer, M.A., Quartly, G.D. et al. Global coastal attenuation of wind-waves observed with radar altimetry. Nat Commun 12, 3812 (2021). https://doi.org/10.1038/s41467-021-23982-4

Cavaleri, L., Fox-Kemper, B. & Hemer, M. Wind waves in the coupled climate system. Bull. Am. Meteorol. Soc. 93, 1651–1661, https://doi.org/10.1175/BAMS-D-11-00170.1 (2012).

Ardhuin, F. et al. Observing sea states. Front. Mar. Sci. 6, 124, https://doi.org/10.3389/fmars.2019.00124 (2019).

Young, I. R. & Ribal, A. Multiplatform evaluation of global trends in wind speed and wave height. Science 364, 548–552, https://doi.org/10.1126/science.aav9527 (2019).

Passaro, M., Fenoglio-Marc, L. & Cipollini, P. Validation of significant wave height from improved satellite altimetry in the German Bight. IEEE Trans. Geosci. Remote Sens. 53, 2146–2156, https://doi.org/10.1109/TGRS.2014.2356331 (2015).

Cipollini, P. et al. Satellite Altimetry in Coastal Regions (CRC Press: New York, 2017).

Stopa, J. E. Seasonality of wind speeds and wave heights from 30 years of satellite altimetry. Adv. Space Res. https://doi.org/10.1016/j.asr.2019.09.057 (2019).

Perez, J., Menendez, M. & Losada, I. J. GOW2: A global wave hindcast for coastal applications. Coast. Eng. 124, 1–11, https://doi.org/10.1016/j.coastaleng.2017.03.005 (2017).

Towards SeaWinds-derived coastal winds improvement

G. Grieco[*1], A. Stoffelen[2], J. Vogelzang[2], A. Verhoef[2], M. Portabella[3]

1. Istituto di Scienze Marine (ISMAR) – Consiglio Nazionale della Ricerca (CNR), Napoli , Italy
2. Koninklijk Nederlands Meteorologisch Instituut (KNMI), De Bilt, The Netherlands
3. Institut de Ciencies del Mar (ICM-CSIC) Barcelona, Spain

Abstract – This paper presents a new methodology to correct the land-contaminated normalized radar cross-section (σ_0) measurements acquired by the scatterometer SeaWinds, which flew aboard the QuikSCAT satellite platform from 1999 to 2009, operated by the National Aeronautics and Space Administration (NASA). This method is based on the hypothesis that contaminated σ_0s are linearly dependent on the Land Contribution Ratio (LCR) index, which is defined as the ratio of the footprint area contaminated by the presence of land to the total footprint area. Furthermore, the σ_0 deviations from the expected contaminated σ_0 values are "regularized" by homogenizing their distribution, making them independent of land contamination. The preliminary results show that this methodology is effective up to few kilometers to the coast. In addition, it prevents the presence of negative corrected σ_0s.

Keywords: Ocean vector wind, scatterometer, SeaWinds.

1. INTRODUCTION

Most humans live in coastal areas. Therefore, their lives are heavily affected by local phenomena that are strictly correlated to winds, such as breezes, katabatic winds, pollution dispersion in both atmosphere and sea, and "Acqua Alta" in the Venice lagoon. For these and many other reasons not listed here, accurate coastal winds are of paramount importance to modern societies. Scatterometer-derived winds represent the gold standard for open-ocean vector winds. In coastal areas, their use is strongly limited by land contamination. In fact, the typical linear dimension of the scatterometer footprints is on the order of tens of kilometers, and land contamination may degrade wind retrievals up to 20-30 km to the coastline. In the last two decades, several studies have been published showing how to limit land contamination and improve both the sampling and accuracy of coastal winds. (Owen et al. 2009) shows how to assess land contamination by defining the Land Contribution Ratio (LCR) for SeaWinds measurements, which flew aboard the QuikSCAT satellite platform, operated by NASA. LCR is defined as the ratio of the land-contaminated area of the footprint to the total footprint area. Excessively contaminated footprints are discarded, and consequently, coastal wind retrievals are improved both in sampling and accuracy. (Lindsley et al. 2016) shows how to evaluate LCR for normalized radar cross section (σ_0) acquisitions of the Advanced Scatterometer (ASCAT), operated by EUMETSAT aboard the Meteorological Operational (MetOp) satellite platform, and (Vogelzang et al. 2017) shows how it is implemented to improve coastal winds. This approach is effective, but the number of discarded σ_0s is very high. Therefore, the accuracy of the integrated σ_0s used for wind retrievals is degraded. (Vogelzang & Stoffelen 2017)

shows how to overcome this problem by correcting the ASCAT contaminated σ_0s. In this study, an LCR-based σ_0 correction scheme is applied, based on the hypothesis that σ_0 is linearly dependent on LCR, that the level of σ_0 noise does not depend on σ_0 and that the variability of σ_0 in sea and land is locally negligible. These hypotheses may seem too strong and probably are in some cases, but the methodology proves to be effective for ASCAT. In this study, a similar methodology is applied to SeaWinds coastal measurements. However, the hypothesis that the noise level does not depend on σ_0 is too strong for SeaWinds, as shown in (Grieco et al. 2021). Therefore, σ_0 deviations from the expected linear trend are "regularized" to make their distribution independent of land contamination. This regularization has a damping effect on deviations and prevents negative σ_0s.

Section 2 shows the dataset that has been used in this study. Section 3 describes the methodology, while the preliminary results are shown in Section 4. Finally, Section 5 shows the preliminary conclusions and some tips for future work.

2. DATASET

In this study, all fourteen Full Resolution Level 1B QuikSCAT files (FR) dated 10th of April 2007 are used. They can be freely downloaded from the PODAAC web site. These files contain, among other, all the information relating to slices (footprints), i.e., σ_0 , specific noise level (Kp), position, satellite position and velocity, and quality flags. All acquisitions are quality flagged (QCed) with criteria that can be summarized as follows: a) acquisitions are usable according to the user's manual; b) absence of any problems in the communications with the spacecraft.

There are no requirements for 1) the signal-to-noise ratio (SNR); 2) the sign of σ_0 ; 3) if σ_0 is in the expected range of values. For more information on quality flags, the reader can refer to the QuikSCAT FR-files manual.

3. METHODOLOGY

The LCR-based σ_0 correction scheme implemented in this study is based on the hypotheses that the expected σ_0 depends linearly on LCR. Furthermore, the variation of σ_0 in sea and land is considered negligible. Therefore, the σ_0 model writes as follows:

$$\sigma_0^{pvk} = a^{pv}f^{pvk} + b^{pv} + \epsilon^{pvk} \quad (1)$$

where σ_0^{pvk} is the contaminated measurement, f^{pvk} stands for LCR, a^{pv} and b^{pv} are the slope and the offset of the fitting curve, respectively, and ϵ^{pvk} is the deviation of σ_0^{pvk} from the fitting curve (expected contaminated $\bar{\sigma}_0^{pv}$). The indices p and v stand for {H-Pol, V-Pol} and v for {fore, aft} respectively, while k is the slice index (k $\in$ [0, . . . , 7]). This is to stress that the fitting curve is regressed for each of the four *pol-view* flavors. Before fitting the curves, the FR σ_0s are mapped onto a wind vector cell (WVC) grid with a spacing of 12.5 km. If

---

* **Corresponding author. Address: Calata Porta di Massa, Napoli, Italia. Email: giuseppe.grieco@cnr.it

the σ_0s falling in a given WVC have LCR values lower than 0.02 (2% of contamination), the correction procedure is not applied. Otherwise, all σ_0s that fall in the 5x5 WVC matrix surrounding the given WVC are used to fit the curve. Regression of a^{pv} and b^{pv} is performed with the least-squares method, and the regression error $\sigma_e^{2,pv}$ is also provided [6]. Finally, the correction is applied only to those acquisitions with LCR within 2% and 50%, while those with LCR greater than 50% are discarded. Then, contaminated ϵ^{pvk} are regularized by imposing the same expected value and standard deviation of σ_0 in sea. Note that ϵ^{pvk} are distributed as a normalized χ^2 with degrees of freedom depending on the noise level, which increases with σ_0.

4. RESULTS

The results shown in this section refer to an area test offshore western Sicily. The FR file is that with ID 40653.

Figure 1 shows the map of the FR slice σ_0s before any correction is applied, in LU. Acquisitions with LCR greater than 0.5 are not shown. It is apparent that coastal acquisitions are heavily contaminated by land. Note the change of color towards dark red also around the island of Ustica, in the northern part of the box, proving the efficacy of the method to compute LCR.
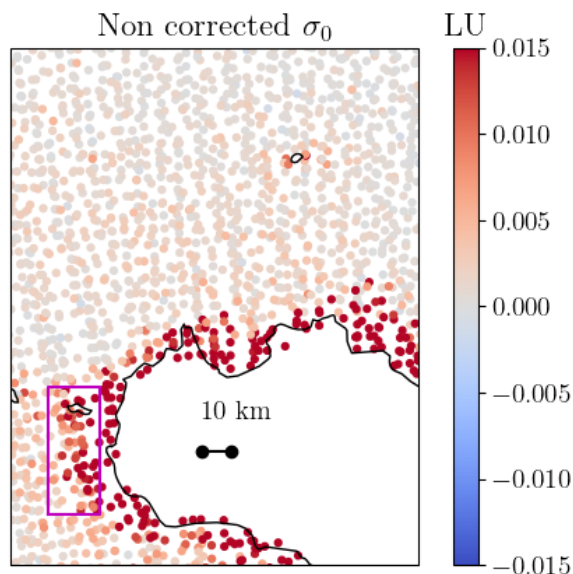
Figure 1: σ_0 before correction.

Figure 2 shows the map of corrected σ_0s . It is apparent that coastal σ_0s are much more similar to those in the open ocean. However, it is important to stress that the distribution of σ_0s near the coast must not necessarily be identical to that in the open ocean. In fact, coastal dynamics is very complex, as it is influenced by many factors, such as local orography, land roughness, currents, and where diurnal variability plays a key role. Coastal validation and even the methodology to validate coastal measurements and retrieved winds are still open and challenging questions.

5. CONCLUSION

This paper presents a new methodology for correcting the SeaWinds acquisitions near the coast, with the final aim of improving the retrieved winds.
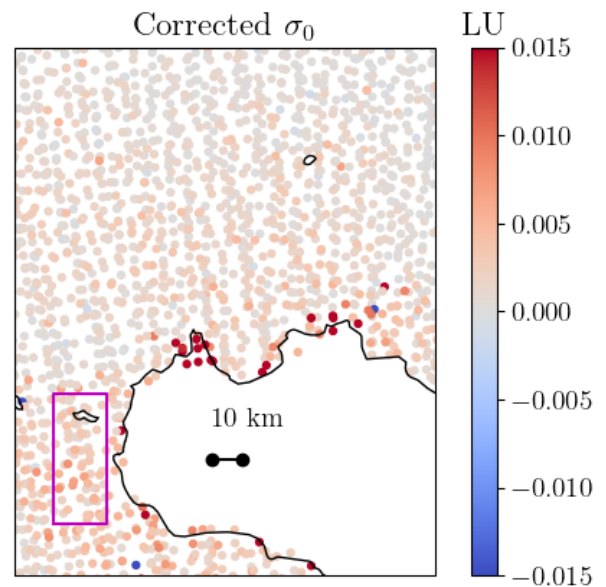
Figure 2: σ_0 after correction.

It consists of de-trending the contaminated cross sections and on a "regularization" of the noise. The last step is useful to homogenize the deviations of the cross sections from their expected value at different levels of contamination. The methodology proves to be effective. Next steps are the wind field retrievals and their validation.

REFERENCES

M. P. Owen and D. G. Long, "Land-contamination compensation for quikscat near-coastal wind retrieval," IEEE Transactions on Geoscience and Remote Sensing, vol. 47, no. 3, pp. 839–850, 2009.
R. D. Lindsley, C. Anderson, J. Figa-Saldaña, and D. G. Long, "A parameterized ascat measurement spatial response function," IEEE Transactions on Geoscience and Remote Sensing, vol. 54, no. 8, pp. 4570–4579, 2016.
J. Vogelzang and A. Stoffelen, "Ascat ultrahigh-resolution wind products on optimized grids," IEEE Journal of Selected Topics in Applied Earth Observations and Remote Sensing, vol. 10, no. 5, pp. 2332–2339, 2017.
J. Vogelzang and A. Stoffelen, "Ascat land correction, report for the eumetsat ocean and sea ice saf," Tech. Rep., Koninklijk Nederlands Meteorologisch Instituut, 2020, SAF/OSI/CDOP3/KNMI/TEC/TN/384.
G. Grieco, M. Portabella, J. Vogelzang, A. Verhoef, and A. Stoffelen, "Quikscat normalized radar cross section noise characterization for coastal wind field retrieval," Tech. Rep., Institute of Marine Sciences (ISMAR-CNR), 2021, OSI-SAF Technical Report # VSA 20 03.

On the improvement of satellite-derived extreme sea surface wind capabilities

M. Portabella[1]*, A.S. Rabaneda[2], G. Grieco[3], F. Polverari[4], A. Stoffelen[5], J. Sapp[6,7], Z. Jelenak[6], P. Chang[6], F. Cossu[1]

[1] Barcelona Expert Centre (BEC), Institut de Ciències del Mar (ICM-CSIC), Barcelona, Spain
[2] Norwegian Meteorological Institute, Oslo, Norway
[3] Institute of Marine Sciences (ISMAR-CNR), Naples, Italy
[4] Jet Propulsion Laboratory (NASA-JPL), Pasadena, USA
[5] Royal Netherlands Meteorological Institute (KNMI), De Bilt, Netherlands
[6] National Oceanic and Atmospheric Administration (NOAA-NESDIS), College Park, MD, USA
[7] Global Science & Technology, Inc., Greenbelt, MD, USA

Abstract – Accurate high and extreme sea surface wind observations are essential for meteorological, ocean, and climate applications. A method to inter-calibrate spaceborne scatterometer and radiometer derived high and extreme winds using NOAA hurricane "hunter" data is presented. The proposed method is effective, providing highly consistent satellite-derived extreme wind datasets in the period 2009-2020. Further work is needed though to consolidate an in-situ reference for extreme wind calibration purposes.

Keywords: Ocean extreme winds, scatterometers, radiometers, inter-calibration.

1. INTRODUCTION

GLOBAL information on the motion near the ocean surface is generally lacking, limiting the physical modelling capabilities of the forcing of the world's water surfaces by the atmosphere (*Belmonte & Stoffelen, 2019*). This also limits our knowledge of the exchange of momentum across the ocean-atmosphere interface, affecting meteorological and ocean applications (*Trindade et al., 2020*). A particularly pressing requirement in the Ocean Surface Vector Wind (OSVW) community is to obtain reliable extreme winds in hurricanes (> 30 m/s) from satellite wind scatterometers and radiometers, since extreme wind, storm surge and wave forecasts for societal warning are a high priority in nowcasting as well as in Numerical Weather Prediction (NWP).

The US National Oceanic and Atmospheric Administration (NOAA) and US Air Force Reserve Command (AFRC) routinely operate "hurricane hunter" flights in the North Atlantic and North-East Pacific. Each flight is equipped with a Stepped Frequency Microwave Radiometer (SFMR) and GPS dropsondes for measuring surface winds, rain rate, sea surface temperature and vertical profiles of wind, pressure and temperature. Data from these in-situ measurements are freely available and can be used for a satellite multi-sensor wind data inter-calibration procedure. This study is carried out in the framework of the ESA OCEAN+EXTREMES MAXSS project, and its goal is to obtain a consistent extreme wind data record for scatterometers and radiometers over the period 2009-2020. In particular, the aims are to adjust scatterometer- and radiometer-derived high and extreme winds using collocated SFMR winds as reference, and to ensure a good inter-calibration of all the mentioned satellite wind sources. This study also serves as preparatory work for the future scatterometer SCA onboard Metop-SG, which will have enhanced extreme wind capabilities.
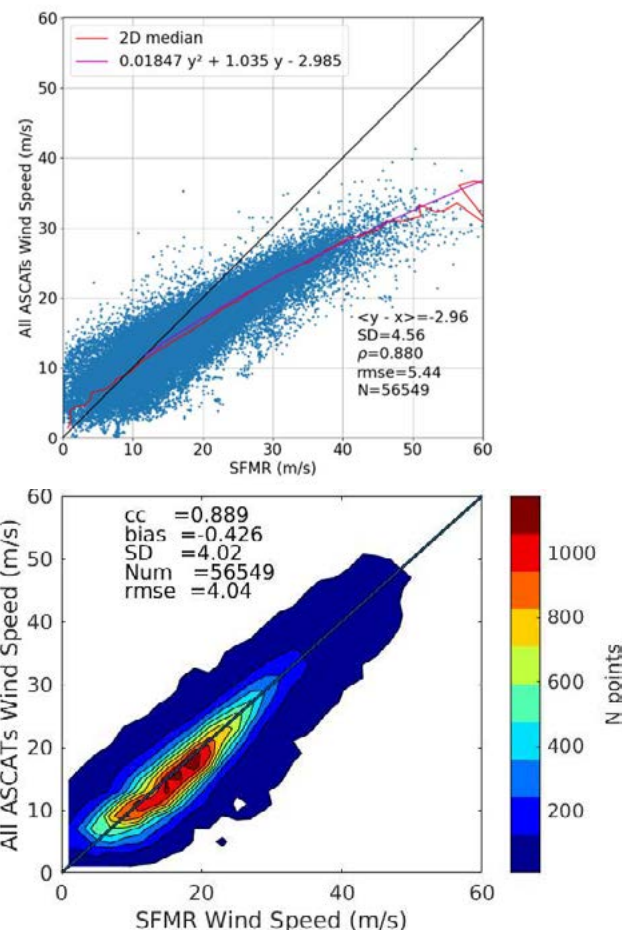
Figure 1. *(Top) Scatterplot of ASCAT-A/B/C winds versus collocated SFMR 40-km averaged winds, for the period 2009-2020, together with the median curve and the polynomial function fit derived from the scatterplot. (Bottom) Contourplot of adjusted ASCAT-A/B/C versus collocated SFMR 40-km averaged winds for the same period.*

2. DATA

Over the mentioned period, there is a varying constellation of satellite scatterometers and radiometers. In particular, the Advanced Scatterometers onboard the Metop series (i.e., ASCAT-A, -B, and -C), the scatterometers onboard Oceansat-2 (OSCAT) and ScatSat-1 (OSCAT-2), and onboard the HY-2 series (HSCAT-A, -B); the Advanced Microwave Scanning Radiometer 2 onboard GCOM-W1 (AMSR-2), the multi-frequency polarimetric radiometer

* Corresponding author. Address: Pg. Marítim Barceloneta 37-49, 08003 Barcelona, Spain. Email: portabella@icm.csic.es

(Windsat), and the L-band radiometers onboard the Soil Moisture and Ocean Salinity (SMOS) and the Soil Moisture Active Passive (SMAP) missions. The scatterometer wind products used are the EUMETSAT Ocean & Sea Ice Satellite Application Facility (OSI-SAF) Level 2 12.5-km and 25-km winds, while the radiometer wind products are the Remote Sensing Systems Level 3 daily 0.25° All Weather (AW) AMSR-2 version 8.2, AW Windsat version 7.0.1, and SMAP version 1.0 near-surface wind products, and the Ifremer Level 2 0.25° SMOS wind product version 2.0.

Collocated SFMR winds and the tropical cyclone (TC) "Best Track" data obtained from the WMO International Best Track Archive for Climate Stewardship (IBTrACS) are used as reference.

3. METHODOLOGY & RESULTS

A two-step strategy has been followed to inter-calibrate the high and extreme wind speeds derived scatterometers and low-frequency radiometers. First, the C-band ASCATs have been adjusted against collocated SFMR wind data in storm-motion centric coordinates (see Fig. 1). The results reveal a substantial underestimation of the ASCAT winds at wind speeds higher than 15 m/s. Despite such disagreement, ASCAT is well correlated with SFMR winds at high winds, with a correlation coefficient of about 0.88, and he adjustment function is effective in further improving ASCAT/SFMR statistical scores. Second, both SFMR winds and ASCAT adjusted winds have been used to adjust all the other satellite wind systems (see, e.g., Fig. 2 for AMSR-2 wind adjustment). In doing so, a good inter-calibration between all the systems is ensured not only under TC conditions, but also elsewhere. Small residual biases are present in the 15-20 m/s range of SMAP and SMOS adjusted winds (not shown), under nominal (non-TC) conditions. Both AMSR-2 and Windsat winds show an anomalous behaviour in the range 10-20 m/s under TC conditions that deserves further investigation (not shown). Finally, it is found that Ku-band extreme winds (i.e., close to the hurricane eyewall region) are substantially impacted by rain contamination, leading to underestimation of such winds. It is therefore recommended to use the quality control flags to filter out such Wind Vector Cells.

3. OUTLOOK

The scatterometer/SFMR analysis reveals an ASCAT wind underestimation for winds above 15 m/s. SFMR measurements are calibrated with dropsondes and averaged along-track to represent satellite spatial scales. On the other hand, *Polverari et al.* (2022) show that scatterometer and buoy winds are in good agreement up to 25 m/s. The buoy high-wind quality has been confirmed using a triple collocation approach. In comparing these results, both SFMR and buoy winds appear to be highly correlated with scatterometer at the high wind regime, however, they show a very different wind speed scaling. The SFMR-based adjustment of scatterometer and radiometer winds proposed here is for use by the extreme wind operational community. However, further work is required to reconcile dropsonde (thus SFMR) and buoy wind measurements under high wind conditions.

Finally, triple collocation analyses (SFMR-satellite-NWP) should be carried out to characterize the errors of the different satellite-derived extreme wind sources.

REFERENCES

Belmonte Rivas, M., and A. Stoffelen, "Characterizing ERA-Interim and ERA5 surface wind biases using ASCAT", *Ocean Sci.,* no. 15, pp. 831-852, 2019.

Trindade, A., M. Portabella, A. Stoffelen, W. Lin and A. Verhoef, "ERAstar: A High-Resolution Ocean Forcing Product", *IEEE Transactions on Geoscience and Remote Sensing,* vol. 58, no. 2, pp. 1337-1347, 2020.

Polverari, F., M. Portabella, W. Lin, J.W. Sapp, A. Stoffelen, Z. Jelenak, and P.S. Chang, "On High and Extreme Wind Calibration Using ASCAT," *IEEE Trans. Geosci. Rem. Sens.*, vol. 60, 2022.
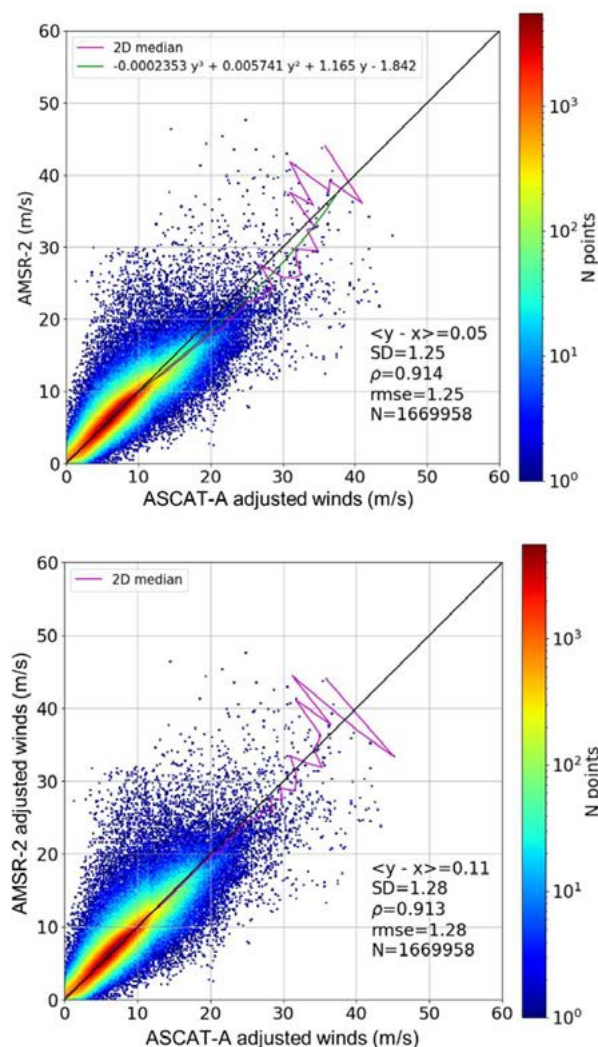
Figure 2. *(Top) Contourplot of collocated AMSR-2 winds versus ASCAT-A adjusted winds, together with the median curve (pink) and the polynomial function fit (green) superimposed. (Bottom) Contourplot of AMSR-2 adjusted winds versus ASCAT-A adjusted winds, together with the median curve (pink). Only collocations within a 3-hour distance are considered.*

When Scatterometers and Altimeters Provide the Wrong Wind Data on the Oceans

L. Cavaleri[1]*, A. Benetazzo[1], L.Bertotti[1], S. Langodan[2], I. Hoteit[2]

1 Institute of Oceanographic Sciences, C.N.R., Venice Italy
2 King Abdullah University of Sciences and Technology, Thuwal, Saudi Arabia

Abstract – We focus on the conditions (rain on the oceans, sand storms on the Arabian/Persian Gulf) when the remotely sensed wind values are strongly underestimated. Granted the previous ocean scale evidence (Cavaleri and Bertotti, 2018), dtailed and extensive data in this respect are provided by the long and accurate hindcast of wind and wave conditions on the Gulf. The physical reason is found on the smoothing of the sea surface (by rain or sand), hence on the misled interpretation of the reduced roughness of the sea surface by the satellite instruments.

Keywords Altimeter, Scatterometer, wind speed, rain on the oceans..

1. INTRODUCTION

A few years ago, some of us analysed the effect of heavy rain on wind wave generation. Using both direct experience on the sea (from the ISMAR oceanographic tower), laboratory tests with an oily surface, and analysis of model vs altimeter data in rainy conditions, we showed how in these conditions the wind information provided by satellite remote sensing is substantially underestimated. The situation is complex because, practically ignored in daily applications, it also leads to an overestimate of the significant wave height by the models. Our interpretation is that the smoothing by rain (if strong enough) of the shortest waves (ideally 10 cm long or less) leads to a "smooth" surface where the wind is literally "sliding upon" with a much reduced interaction. On the tower the practical absence of breakers during the local shower was macroscopic.

Here we explore a similar process with a different origin or cause: we analyse the effect of a sand storm propagating over the sea. The area of interest is the Arabian/Persian Gulf (henceforth the Gulf). Sand storms are possible from various directions and different sources. The most remarkable and frequent ones are associated to the North-West coming Shamal wind, entering the Gulf from Irak at the Tigri-Eufrate delta. Similarly to heavy rain, we hypothesize that suspended sand hitting the surface can suppress or disrupt the (structure of the) basic ripples associated the shear instability when wind blows on a water surface. As for rain, this leads to a smooth surface, hence to reduced generation. No local (buoys or visual) data are directly available. We verify the implications using remote sensing data: altimeter significant wave heights H_s and wind speed U_{10}, and scatterometer for U_{10}. These are compared to a 40 year period of highly accurate wind and wave model data for the 1979-2019 period. The related ERA-5 data have been directionally calibrated using multiple scatterometer data (directionally to take into account the coast distance along the various directions the wind is blowing from). The calibrated wind fields have then been used to drive the WW3 wave model obtaining 40 years of Gulf wave fields. Compared to independent altimeter data, the error has turned out smaller than 0.5%.

The scientists who attended the 1980 edition were like sea-faring pioneers who opened new trade routes, and whose discoveries, since then, have surpassed many times what was expected in the beginning (Gower 1981). In 1990, they were faced by the hardships of continuing their enterprise, in spite of the extraordinary possibilities hinted by early results. By 2000, the need for new commitments, in funding and programs, became evident to the scientific community and policy-making circles alike (Barale et al. 2000, 2004).

Climate change, and its dear environmental and socio-economic consequences, were taking center stage at the time, and action seemed urgent. It did still in 2010, when the same community got together once again in Venice, the city that represents so well our complex, daring and yet captivating bond with the sea. In spite of the achievements and the knowledge gained over the preceding decades of ocean observations, new trials were brought about in the course of the most recent studies (Barale et al. 2010a, 2010b).

The 2020 edition of 'Oceans from Space', hosted by the *Scuola Grande di San Marco*, in Venice (see Figure 1), but postponed to 2021, is to provide an overview of the path followed so far, the tools available today, and the plans for tomorrow. It highlights the added value of complementary techniques and their combined views, addressing the scientific community that backs present and future missions.

Figure 1. Wind sea under heavy rain. No breakers on the surface.

2. HOW EXTENSIVE RESULTS ON THE GULF PROVIDE EVIDENCE OF UNDERESTIMATED REMOTELY SENSED WIND SPEEDS WHEN WIND OR SAND AFFECT THE SURFACE

If our hypothesis (of a reduced generation) is correct, which are the expected results? We analyse in order the three mentioned remote data. H_s (altimeter): a reduced generation leads to lower wave heights, hence the model (as for rain, the

---

model ignores the discussed sand effect) should be in excess. U_{10} (altimeter): a smooth surface is remotely interpreted as a lack of (or the presence of reduced) wind speeds. The model will be in excess. U_{10} (scatterometer): for different reasons (physics is different) with respect to altimeter, here too the instrument will judge lower wind speeds. Therefore the model data will be always in excess. However, for H_s the model will be in excess and the altimeter correct, while for

U_{10} the model is expected to be correct with underestimated remote data. This has been verified with an extended analysis of the 100 major local sand storms in the period 2003-2016. The results fully confirm the above expected results. A typical example is shown in Figure 2.
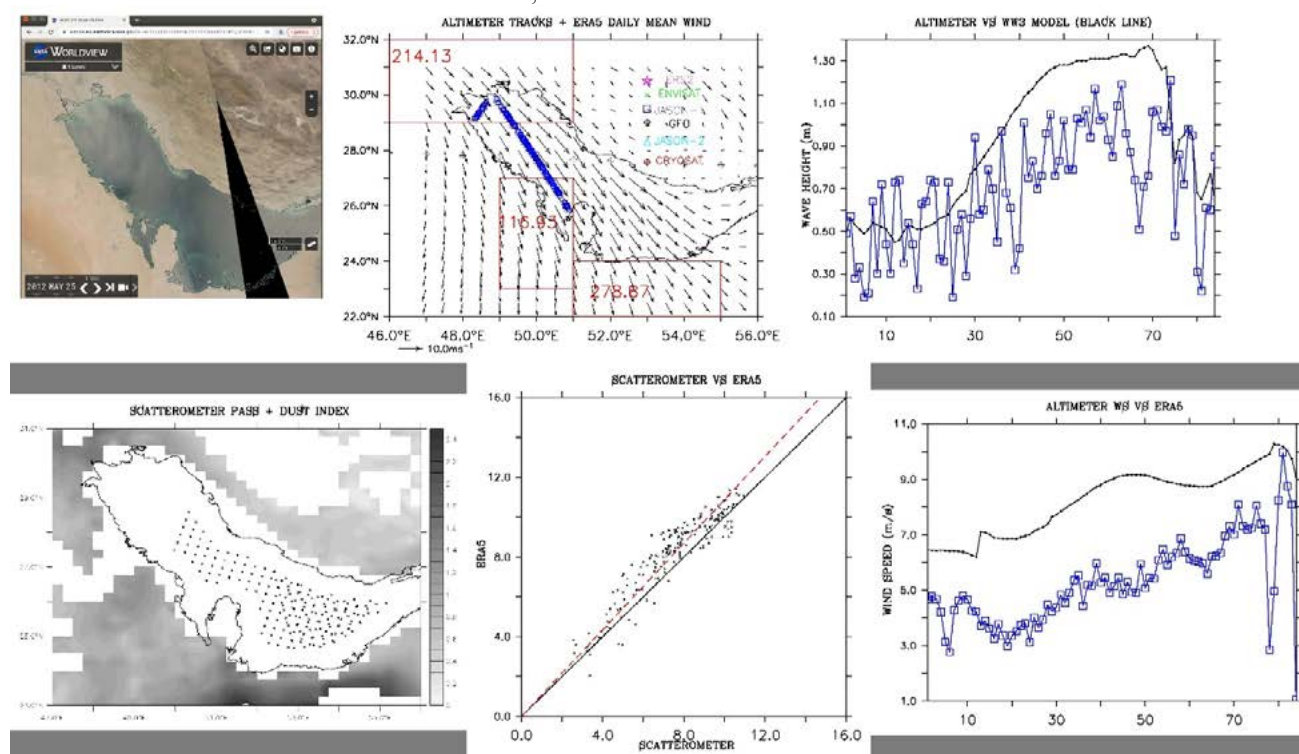
Figure 2 – Situation on the Gulf on 25 May 2012. Panels (horizontally and up/down) show in order: 1) sand storm over the Gulf; 2) the model wind field and the altimeter passes; 3) altimeter and model H_s along the tracks; 4) the scatterometer field; 5) model vs scatterometer U_{10}; 6) model and altimeter U_{10} along the tracks

.

Here we represent a strong Shamal case with a substantial sand storm. Both altimeter (upper center) and scatterometer (lower left) data are available. While in all the non-sand storm cases there is a better than 99% agreement between model and remotely sensed data, the lower-center panel shows how the scatterometer underestimates wind speeds with respect to the model. A similar result (lower-right) appears for altimeter wind data, these too substantially underestimated when compared to the model.

The evidence of a smoothed surface (because of the deposited sand effects) is manifest in the wrong model results for the significant wave height. The H_s altimeter data are not affected by the surface smoothing because this leaves unaffected the crest-to-trough difference. So we know these data are correct. However, as shown by Cavaleri and Bertotti (2018), a smooth surface, where the ripples are much reduced (hence no spectral tail), implies a much reduced momentum and energy input by wind to waves, hence a reduced wave height that the altimeter correctly picks up. However, this know-how is not embedded in the standard wave models (as WW3, SWAN or WAM), and the model, assuming standard conditions, overestimates the energy transfer from atmosphere to ocean, hence the resulting H_s.

3. CONCLUSIONS

While sand can be a rather local effect characteristic of a specific area, rain is a rather distributed feature of the ocean meteorology. We suggest this should be taken into account, also in the practical daily applications. This holds both for the long-term statistics as for data assimilation and daily forecast.

REFERENCES

Cavaleri, L., and L.Bertotti (2018). Rain on generative seas, Geoph. Res. Let., Vol.45, Issue 14, pp 7049-7056, DOI:10.1029/2018GL078006.

Direct Ocean Surface Current Measurements From Space: Achievements of the Last 20 Years and Expectations for the Next 20 Years

R. Romeiser *

Rosenstiel School of Marine, Atmospheric, and Earth Science, University of Miami, Florida, USA

Abstract – At the time of "Oceans From Space" 2010, first SAR along-track interferometry (ATI) results from the Shuttle Radar Topography Mission and TerraSAR-X and promising Doppler centroid anomaly analysis examples from ERS-1/2 and ENVISAT inspired us to give an overview presentation on the potential of Doppler-based direct surface current measurements from space. In the decade since then, further experience has been gained with data from new satellite systems such as TanDEM-X and from various airborne SAR experiments, and a proposal for a dedicated ATI satellite mission for surface current observations has been submitted to ESA. Added Doppler capabilities have also been proposed for future wind scatterometer missions, which will be capable of providing global wind and current vector fields together. As an alternative to the Doppler analysis of radar signals, a new methodology based on spotlight-mode SAR data has emerged, which uses subaperture processing to make moving wave patterns visible and extract currents and coastal water depths via the theoretical dispersion relation. This paper for "Oceans From Space" 2020 reviews these latest achievements and gives an outlook to expected further developments within the next 10-20 years.

Keywords: SAR, Doppler, interferometry, ocean currents.

1. INTRODUCTION

When the previous "Oceans From Space" symposium took place in 2010, the concept of surface current measurements by SAR along-track interferometry (ATI) had already been known for about 25 years, but the use of spaceborne ATI systems was still in an early experimental stage. Our conference paper (Romeiser et al. 2010) discussed the state of the art in this field, including theoretical findings about optimal instrument parameters and the achievable data quality, first spaceborne ATI results from the Shuttle Radar Topography Mission (SRTM) and from TerraSAR-X in divided-antenna mode, as well as promising applications for high-resolution current fields from spaceborne sensors. We also discussed the potential of Doppler centroid anomaly (DCA) analysis, a method for lower-resolution surface current retrievals from single-antenna SAR data that had been discussed in the literature for a while and demonstrated successfully with ERS-1/2 and ENVISAT SAR data since the early 2000s.

In the years since then, a lot of further progress has been made. The two-satellite formation TanDEM-X has given us opportunities to test ATI at near-optimal interferometric baselines (distances between the two receiving antennas) and confirm our theoretical predictions. Dedicated field experiments and analyses of vast amounts of DCA products have resulted in improved models and algorithms for correcting Doppler data for contributions of wave motions. A concept for a dedicated spaceborne ATI system for vector current measurements and an increasing user demand have led to a proposal to ESA that is being evaluated as an Earth Explorer

11 candidate. The wind scatterometer community is planning an addition of Doppler capabilities to the next generation of wind scatterometer systems. As another method for current retrievals, the extraction of short "wave videos" from spotlight-mode SAR data and analysis of Doppler-shifted ocean wave velocities has been demonstrated.

"Oceans From Space" 2020 is a perfect venue to review these achievements of the last decade and attempt another outlook to the next 10-20 years. The following sections of this extended abstract will discuss the developments in several subtopics a little more and provide key references. The conference presentation and the full version of this paper can be expected to include a number of figures and other materials from coauthors, very similar to our aforementioned contributions to "Oceans From Space" 2010.

2. TANDEM-X EXPERIMENTS

With the launch of a second TerraSAR-X type satellite in 2010, flying in close formation with the original one for the land topography mission TanDEM-X, we got opportunities to acquire InSAR data with along-track baselines near the theoretical optimum of about 20 m (for X band). Romeiser et al. (2014) compared TanDEM-X data acquired at the Orkney Islands, Scotland, with divided antenna mode and DCA analysis results from TerraSAR-X. Consistent with theoretical expectations, the effective spatial resolution of the TanDEM-X derived current fields was found to be on the order of 30 m, about 30 times better than that of the two single-satellite products. Romeiser & Runge (2014) and Suchandt & Romeiser (2017) used TanDEM-X data to examine the dependence of the interferometric coherence on the InSAR time lag, determined by the along-track baseline. Other authors, e.g. Elyouncha et al. (2020), studied the dependence of TanDEM-X derived Doppler velocities on the wind vector and other relationships, whose improved understanding is essential for deriving reliable surface current products from Doppler data.

3. DOPPLER CENTROID ANOMALY ANALYSIS

In the field of DCA analysis of conventional SAR data, unexpected difficulties with data from the two Sentinel-1 delayed a wide operational use, but some authors continued to make progress with the development of current retrieval algorithms. As an example, we recommend the paper by Moiseev et al. (2020).

4. WAVEMILL / SEASTAR PROPOSAL

As early as 2005, Buck (2005) proposed to complement future oceanographic altimeter missions with a dedicated ATI system for higher-resolution surface current measurements. Due to the use of four separate beams for full vector current field retrievals on both sides of the satellite, with a beam pattern resembling the look of a windmill, the concept was promoted as "Wavemill" mission.

---

* Corresponding author. Address: 4600 Rickenbacker Causeway, Miami FL 33149, USA. E-Mail: rromeiser@miami.edu

Recognizing the value of such a system for the oceanographic community, the European Space Agency (ESA) funded further studies of the concept, including field experiments with an airborne Wavemill demonstrator, as presented, for example, by Martin et al. (2016). Ultimately, these efforts led to the submission of a full Earth Explorer proposal to ESA, now named SEASTAR (Gommenginger et al., 2019). In 2021, SEASTAR was selected as one of four candidates for Earth Explorer 11, to be launched in the early 2030s.

5. DOPPLER SCATTEROMETER PROPOSALS

The wind scatterometer community has proposed the addition of Doppler capabilities for next-generation wind scatterometer missions. Comprehensive studies by a European team (Fois et al., 2015) and an American team (Rodríguez et al., 2018) discussed technical possibilities and potential data products. A simultaneous measurement of backscattered power and Doppler in multiple look directions would be beneficial for obtaining more accurate vector wind fields together with surface current fields at the same spatial resolution, both of which could be corrected for each other's contributions. The resolution of the current fields would be on the order of 10 km, more than an order of magnitude worse than that of along-track InSAR products. However, unlike a SAR, a wind scatterometer is always on and provides almost full global coverage within just one day. Rodríguez et al. (2019) presented a proposal for a Doppler scatterometer mission named "Winds and Currents Mission" (WaCM), which may become reality within the next decade.

6. WAVE MOTIONS FROM SPOTLIGHT DATA

As an alternative to the interpretation of Doppler shifts of radar signals, Romeiser & Graber (2018, 2021) demonstrated the reprocessing of spotlight-mode SAR data into short "videos" of moving surface wave patterns. A SAR in spotlight mode steers its beam in azimuth to dwell on the same spot for several seconds. This long integration time enables a very high spatial resolution over land. However, due to the motions of ocean waves and currents across several pixels, spotlight-mode images of ocean scenes tend to look blurrier than conventional stripmap-mode images, which initially makes them them less useful for wave retrievals. This effect can be reversed by reprocessing the data into a series of subaperture images with short integration times, which resolves the temporal evolution of the radar signatures of the surface like a short video. From this point on, the data can be analyzed like time series of marine radar images or wave videos from optical cameras, with an extraction of ocean wave spectra, coastal water depths, and current vectors from the shape of the dispersion shell in the wavenumber-frequency domain. Among several pros and cons of the method that will have to be evaluated carefully, an obvious shortcoming is the limitation to relatively small images, e.g. 2800 m × 7600 m in the case of TerraSAR-X Staring Spotlight mode.

7. CONCLUSIONS

We think the above examples illustrate well how much progress has been made in the field of current measurements from space in the last decade. "Oceans From Space" 2020 is a perfect venue to review the state of the art once again and discuss where we expect the proposed new instruments and data analysis techniques to take the ocean remote sensing community within the next 10-20 years.

REFERENCES

Buck, C., (2005). An extension to the wide swath ocean altimeter concept. Proc. 2005 International Geoscience and Remote Sensing Symposium (IGARSS 2005). Inst. of Elec. and Electron. Eng., Piscataway, N.J., USA, pp. 5436-5439.

Elyouncha, A., L.E.B. Eriksson, R. Romeiser, and L.M.H. Ulander (2022). Empirical relationship between the Doppler centroid derived from X-band spaceborne InSAR data and wind vectors. IEEE Trans. Geosci. Remote Sens., 60, 20 pp.

Fois, F., P. Hoogeboom, F. Le Chevalier, A. Stoffelen, and A. Mouche (2015). DopSCAT: A mission concept for simultaneous measurements of marine winds and surface currents. J. Geophys. Res. Oceans, 120, pp. 7857-7879.

Gommenginger, C., et al. (2019). SEASTAR: A mission to study ocean submesoscale dynamics and small-scale atmosphere-ocean processes in coastal, shelf and polar seas. Front. Mar. Sci., 6, pp. 267-273.

Martin, A.C.H., C. Gommenginger, J. Marquez, S. Doody, V. Navarro, and C. Buck (2016). Wind-wave-induced velocity in ATI SAR ocean surface currents: First experimental evidence from an airborne campaign. J. Geophys. Res. Oceans, 121, pp. 1640-1653.

Moiseev, A., H. Johnsen, J.A. Johannessen, F. Collard, and G. Guitton, (2020). On removal of sea state contribution to Sentinel-1 Doppler shift for retrieving Reliable Ocean surface current. J. Geophys. Res. Oceans, 125, 13 pp.

Rodríguez, E., A. Wineteer, D. Perkovic-Martin, T. Gál, B.W. Stiles, N. Niamsuwan, and R. Rodriguez Monje (2018). Estimating ocean vector winds and currents using a Ka-Band pencil-beam Doppler scatterometer. Remote Sensing, 10, pp. 576-634.

Rodríguez, E., M. Bourassa, D. Chelton, J.T. Farrar, D. Long, D. Perkovic-Martin, and R. Samelson (2019). The Winds and Currents Mission concept. Front. Mar. Sci., 6, pp. 438-445.

Romeiser, R., J. Johannessen, B. Chapron, F. Collard, V. Kudryavtsev, H. Runge, and S. Suchandt (2010). Direct surface current field imaging from space by along-track InSAR and conventional SAR. Oceanography From Space, Revisited, V. Barale, J.F.R. Gower, and L. Alberotanza (eds.), Springer Science+Business Media, pp. 73-91.

Romeiser, R., H. Runge, S. Suchandt, R. Kahle, C. Rossi, and P.S. Bell (2014). Quality assessment of surface current fields from TerraSAR-X and TanDEM-X along-track interferometry and Doppler centroid analysis. IEEE Trans. Geosci. Remote Sens., 52, pp. 2759-2772.

Romeiser, R., and H. Runge (2014). Measuring the temporal autocorrelation function of backscattered X-band signals from the ocean with TanDEM-X. Proc. 10th European Conference on Synthetic Aperture Radar (EUSAR 2014), VDE Verlag, Berlin / Offenbach, Germany, pp. 1299-1301.

Romeiser, R., and H.C. Graber (2018). A new technique for phase-resolving ocean wave observations by spaceborne spotlight-mode synthetic aperture radar. Proc. 2018 International Geoscience and Remote Sensing Symposium (IGARSS 2018). Inst. of Elec. and Electron. Eng., Piscataway, N.J., USA, pp. 146-148.

Romeiser, R., and H.C. Graber (2021). Advanced coastal bathymetry retrieval from moving wave patterns in reprocessed spotlight SAR data. Proc. 13th European Conference on Synthetic Aperture Radar (EUSAR 2021). VDE Verlag, Berlin / Offenbach, Germany, pp. 185-187.

Suchandt, S., and R. Romeiser (2017). X band sea surface coherence time inferred from bi-static SAR interferometry. IEEE Trans. Geosci. Remote Sens., 55, pp. 3941-3948.

Ocean Surface Current Airborne Radar (OSCAR): a new instrument to measure ocean surface dynamics at the sub-mesoscale

A. Martin [1]*, D. McCann[1], K. Macedo[2], A. Meta[2], C. Gommenginger[1], M. Portabella[3], L. Marié[4], J. Horstmann[5], J.F. Filipot[6], J. Marquez[7], P. Martín-Iglesias[8], T. Casal[8]

[1]National Oceanography Centre, Southampton, UK
[2]MetaSensing, Milano, Italy
[3]ICM-CSIC, Barcelona, Spain
[4]Ifremer, Brest, France
[5]Hereon, Hamburg, Germany
[6]France Energy Marine, Brest, France
[7]Radarmetrics, Spain
[8]ESA-ESTEC, Netherlands

Abstract – The ocean interacts with the atmosphere, land and ice on multiple spatial scales including fine sub-mesoscales that are often observed in high resolution optical images. Little is known about their dynamics however. SeaSTAR is an innovative satellite mission concept that proposes to address this gap by mapping ocean current and wind vectors at 1 km resolution. In this paper, we present the OSCAR instrument - an airborne demonstrator of the SeaSTAR concept - and the first results from a scientific campaign over the Iroise Sea in May 2022. The capabilities of OSCAR are demonstrated against ground truth data with very promising first results. These results open the door to using OSCAR as a scientific tool to provide unique 2D synoptic views of ocean and atmosphere dynamics at km-scales.

Keywords: Doppler Oceanography, Total Surface Current, Wind

1. INTRODUCTION

Monitoring ocean surface dynamics at high resolution in space and time is of paramount importance for understanding and modelling ocean-atmosphere interactions and other climate mechanisms, especially in coastal and polar areas. Measuring small-scale ocean currents and winds is critical to drive scientific understanding of the exchanges of gas, heat, and momentum between the atmosphere and the ocean, and to support the validation and development of improved forecasting models and climate projections.

SeaSTAR (Gommenginger et al., 2019) has been selected for Phase 0 study for the Earth Explorer 11 program of the European Space Agency (ESA). SeaSTAR aims to observe ocean submesoscale dynamics and small-scale atmosphere-ocean processes in coastal, shelf and polar seas by providing simultaneous measurements of current and wind vectors at 1 km resolution with accuracy of 0.1 m/s and 2 m/s respectively. If finally selected as EE11 mission, SeaSTAR would fly in the 2031 timeframe. OSCAR (Ocean Surface Current Airborne Radar) is the ESA airborne demonstrator of the SeaSTAR mission that was flown over the Iroise Sea (West of French Brittany) in May 2022. The OSCAR operations and products are representative of the spaceborne concept, with geophysical parameters and accuracies that directly relate those of the SeaSTAR satellite mission. In itself, OSCAR provides a new observing capability that will improve our understanding of ocean Doppler sensing thanks to its unique three-look Doppler capability, and can provide

unique 2D synoptic view of ocean and atmosphere dynamics at km-scales to support and complement scientific investigations based on in situ, satellite and model data.

2. THE OSCAR INSTRUMENT

OSCAR is a Ku-band (13.5 GHz) Synthetic Aperture Radar (SAR) system with Along-Track Interferometric (ATI) and scatterometric capabilities in three azimuth directions. It has up to 150MHz bandwidth with 30W average power. In the baseline configuration, the instrument achieves a swath over 2 km wide for wind speeds of 3 m/s and greater. The Noise Equivalent Sigma Zero (NESZ) is between -30dB and -45dB and the radiometric resolution is better than 0.1dB.

The antenna system is stabilized using a 3-axes gimbal with a given accuracy of (0.3° see Speziali et al., 2018) and the antenna motion and attitude are recorded by an AP60 navigation unit and an Inertial Motion Unit (IMU), which are both rigidly mounted onto the antenna frame (Figure 1) with a residual error of 0.005° in yaw and 0.0025° in pitch and roll. Fully polarimetric observations are possible (up to 6 channels available). The instrument has been designed to be flexible in terms of operational parameters and configurations, including an adjustable length of the ATI baseline, to be fully representative of spaceborne scenarios (Figure 2).

OSCAR is tailored to measure 2D ocean surface current and wind vectors. The system features an ATI baseline for two fields of view squinted 45° fore and aft from the broadside direction. Interferometric measurements are obtained in two squinted line-of-sights angularly separated by 90 degrees. This ensures two independent measurements of the ocean surface motion in two lines of sight from which the ocean surface current vector can be derived.

Figure 1. OSCAR system inside the aircraft, showing the mounted gimbal, radio-frequency unit and analog-to-digital converter on the bottom right.

* Corresponding author. Address: European Way, SO14 3ZH Southampton, UK. Email: admartin@noc.ac.uk

Figure 2. OSCAR system mounted on the belly of the aircraft. The mounted antenna frame shows one single broadside antenna in the middle and two squinted antennas pairs on either side looking 45° fore and aft of the broadside direction.

After correcting the interferometric measurements for Doppler effects linked to navigation and geometry, the ocean surface motion sensed by the microwave radar in two lines-of-sight need to be corrected for a bias caused by ocean surface waves. Indeed, the ocean motion has two components: the total ocean surface current – consisting of all currents contributing to actual horizontal transport of water – and an unwanted measurement bias associated with wind-waves, known as wind-wave induced artifact surface velocity (WASV; see Martin et al., 2016). The WASV is understood to be mainly caused by the phase velocity of the surface scatterers responsible for the microwave backscatter (e.g. Bragg waves) modulated by the orbital motion of longer ocean waves. To first order, the WASV is a function of wind direction and wind speed.

3. AIRBORNE CAMPAIGN PRELIMINARY RESULTS

The airborne campaign in French Brittany consisted of four flights on the 17, 22, 25 and 27 May 2022. The first three flights focused over the Iroise Sea, west of Brest (France), where the site is well instrumented. Ground truth measurements of total ocean surface current vector (TSCV) were obtained from a WERA HF radar, supported by data from an X-band marine radar, stereo-video and a down-looking ADCP. For each flight, the aircraft flight path described a star pattern to sample different azimuth directions over an area of homogeneous currents, with additional acquisitions close to Ouessant Island characterized by strong current gradients. Preliminary results focus on this specific area.

Figure 3 presents first results from OSCAR for the ATI antenna pairs squinted fore (left panel) and aft (right panel). The aircraft is heading North with the antennas looking on the left side. Colors from green to brown represents the OSCAR radial velocity for each fore and aft direction (without WASV correction). The middle panel in Figure 3 shows the total velocity (color) and direction (black arrows) measured by the X-band marine radar. The figure shows a general pattern of current flowing to the North-West. The black arrows from the X-band marine radar have been superimposed over the OSCAR data. The fore antenna pair (Fig. 3 left) is aligned with the current and senses strong patterns and gradients (brown to green), which agree well with gradients observed by the X-band marine radar. The aft antenna pair (Fig. 3 right) look perpendicular to the main current, and do not sense any strong gradients (uniform field in brown). These first results are very promising for this long-awaited instrument.
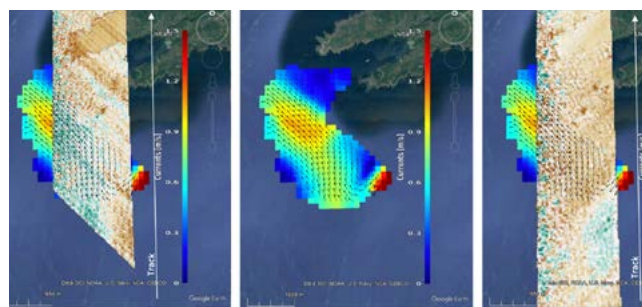

Figure 3. Preliminary OSCAR results for 17 May 2022 over la Jument lighthouse on Ouessant Island. (left) OSCAR 45° squint fore; (right) OSCAR 45° squint aft; (middle) X-band ground-based marine radar.

4. OUTLOOK

OSCAR is a new airborne instrument that offers new high-resolution imaging of current and wind vectors at ~100 meters resolution with high-accuracy (0.10 m/s for current) over a swath 2 to 3 km wide. With a ground speed of ~80 m/s and an autonomy of 5 hours, OSCAR is well suited to supporting process and modelling studies. Bringing unique 2D synoptic views of ocean and atmosphere dynamic properties at km-scale, OSCAR can complement in-situ observations and models to help better understand processes and horizontal and vertical exchanges in the upper ocean and the atmospheric boundary layer.

OSCAR will also improve our understanding of ocean Doppler remote sensing thanks to its distinctive ability to acquire high-resolution backscatter and Doppler data in multiple azimuth directions for the same environmental conditions over well instrumented sites. The knowledge derived from OSCAR will benefit existing Sentinel-1 Doppler and Radial velocity data (Martin et al., 2022), the forthcoming ESA Earth Explorer 10 Harmony mission and the ESA Earth Explorer 11 SeaSTAR mission candidate.

REFERENCES

C. Gommenginger, and the SeaSTAR international Team, "SEASTAR: A Mission to Study Ocean Submesoscale Dynamics and Small-Scale Atmosphere-Ocean Processes in Coastal, Shelf and Polar Seas", Frontiers in Marine Science , 2019 https://doi.org/10.3389/fmars.2019.00457.

A. C. H. Martin, C. Gommenginger, J. Marquez, S. Doody, V. Navarro, and C. Buck, "Wind-Wave induced velocity in ATI SAR Ocean Surface Currents: First experimental evidence from an airborne campaign", Journal of Geophysical Research: Oceans , 2016, http://dx.doi.org/10.1002/2015JC011459.

A. C. H. Martin, C. P. Gommenginger, B. Jacob, and J. Staneva, "First multi-year assessment of Sentinel-1 radial velocity products using HF radar currents in a coastal environment", Remote Sensing of Environment , 2022, https://doi.org/10.1016/j.rse.2021.112758.

F. Speziali, V. Navarro, and S. Placidi, "Ocean Surface Current Airborne Radar Demonstrator (OSCAR) Instrument Performance Report [DD-3]" , 2018. ESA/ESTEC Contract No. 4000116410/16/NL/BJ.

Total ocean surface current radial velocity monitoring from the Sentinel-1 SAR Doppler shift observations

A. Moiseev[1]*, F. Collard[2], J. A. Johannessen[1], B. Chapron[3]

[1]Nansen Environmental and Remote Sensing Center, Bergen, Norway; [2]OceanDataLab, Plouzane, France; [3]IFREMER, Laboratoire d'Ocanographie Physique et Spatiale, Plouzane, France

Abstract – The Sentinel-1 SAR Doppler shift observations can be used to obtain estimates of the total ocean surface current, in the radar line-of-sight direction down to 1 km spatial resolution. Using an advanced calibration and a new algorithm to estimate the contribution from detected sea state motions, the accuracy of retrieved surface current from Sentinel-1 largely improved. In the greater Agulhas Current region, large swath maps of SAR-derived surface current radial velocity appear fully consistent with the satellite-based daily grided geostrophic velocity and SST fields.

Keywords: Total Ocean Surface Current, SAR, Doppler shift, Agulhas current.

1. 1. INTRODUCTION

The Sentinel-1 mission is an operational constellation of two C-band Synthetic Aperture Radar (SAR) instruments (A and B) launched by ESA in 2014 and 2016 to support the CMEMS program. Challenging calibration has prevented their usage for retrieving surface currents. Recent developments on the calibration based on the telemetry from the gyroscope operating onboard the satellite (OceanDataLab 2019) significantly improved the accuracy of the signal over the ocean. The development of a new empirical Geophysical Model Function (GMF) based on a combination of the wind and wave information from collocated models (Moiseev et al 2020b) further improves the accuracy of the contribution of sea state motion to yield more accurate surface current retrievals.

Here, we thus use re-calibrated Sentinel-1A/B Interferometric Wide (IW) observations over the coast of South Africa to further derive and validate these newly SAR-derived radial velocity fields. Systematic case-by-case comparisons with collocated gridded geostrophic velocities from the satellite altimetry and Sea Surface Temperature (SST) fields confirm these improvements.

2. DATA AND METHODS

We used 898 Sentinel-1A/B IW L2 Ocean RVL products acquired in May 2019 - April 2020 of the coast of South Africa (Agulhas current). Each product covers an area of 200x250 km with a pixel size of 1x1 km. The Doppler shift from the standard Sentinel-1 IW RVL products over the ocean contains non-geophysical contributions due to antenna electronic miss pointing and unstable platform attitude (Johnsen et al. 2016). We removed these non-geophysical contributions following the methodology developed by OceanDataLab (2019). The residual signal is a measure of the total surface motion (f_{rvl}), interpreted as a sum of the surface current (f_{osc}) and the sea state (f_{osc}) (Chapron et al., 2005, Johannessen et al. 2008). To estimate the sea state

contribution, we used an empirical GMF called CDOPSiX (Moiseev et al., 2020a, b):

$$f_{ss} = CDOPSiX(x_{10}, \theta, p)$$

where x_{10} is range directed component of the wind speed at 10 m from the ECMWF, and θ is the incidence angle, and p is polarization. We derived f_{osc} by subtracting f_{ss} from f_{rvl} and then converted it to ground-range surface current RVL:

$$u_{osc} = \frac{\pi(f_{rvl}^{SAR} - f_{ss}^{CDOPSiX})}{k_e \sin\theta}$$

We collocated SAR-derived RVL fields with daily grided geostrophic velocity fields from the altimetry and daily satellite-derived SST fields provided by CMEMS

3. RESULTS

Figure 1 shows the Sentinel-1A scene acquired in the ascending pass on 7 July 2019 at 16:36:36 of the east coast of South Africa. Given that the SAR detects only the range component of the motion, the negative RVLs in Figure 1a, b indicates the southwestward oriented surface velocity of the Agulhas Current core. Moreover, analysis of the gradients in the SAR-derived u_{rvl} field (Figure 1a) reveals the boundary of the Agulhas Current core as well as the presence of mesoscale anticyclonic (ACE) and cyclonic (CE) eddies. The positions of these surface current features are consistent with the location in the geostrophic velocity field (Figure 1e) and the SST field (Figure 1f) from the same day.

The u_{rvl} includes the sea state contribution, that, in the first order, is related to the local wind field at 10 m height (Figure 1d). Based on estimates from the CDOPSiX, this sea state contribution yields RVLs from 0.4 m/s in the southern part of the scene to over 1.0 m/s in the near-coastal zone. The different sea state signal is related to the wind direction with respect to SAR antenna, i.e., along-track wind yields a smaller contribution than crosswind. The u_{osc} field (Figure 1b, derived after removal of the sea state) therefore provides a clearer representation of the surface current features compared to the u_{rvl}. Note that the SAR-derived u_{osc} in the Agulhas Current core are up to 2 times stronger than detected in the geostrophic velocity field. This can be related to the fact that the SAR provides instantaneous total surface current estimates, while altimetry products are averaged in space and time to solely provide the geostrophic component of the surface current velocity. Inaccurate estimation of the sea state motions due to errors in the model wind field and CDOPSiX can also yield intensification/reduction of the SAR-derived surface currents.

4. CONCLUSIONS

We can confirm that the ocean surface current RVL fields derived from Sentinel-1 IW SAR Doppler shift can now be

---

* Corresponding author. Address: Jahnebakken 3, N-5007, Bergen, Norway. Email: artem.moiseev@nersc.no
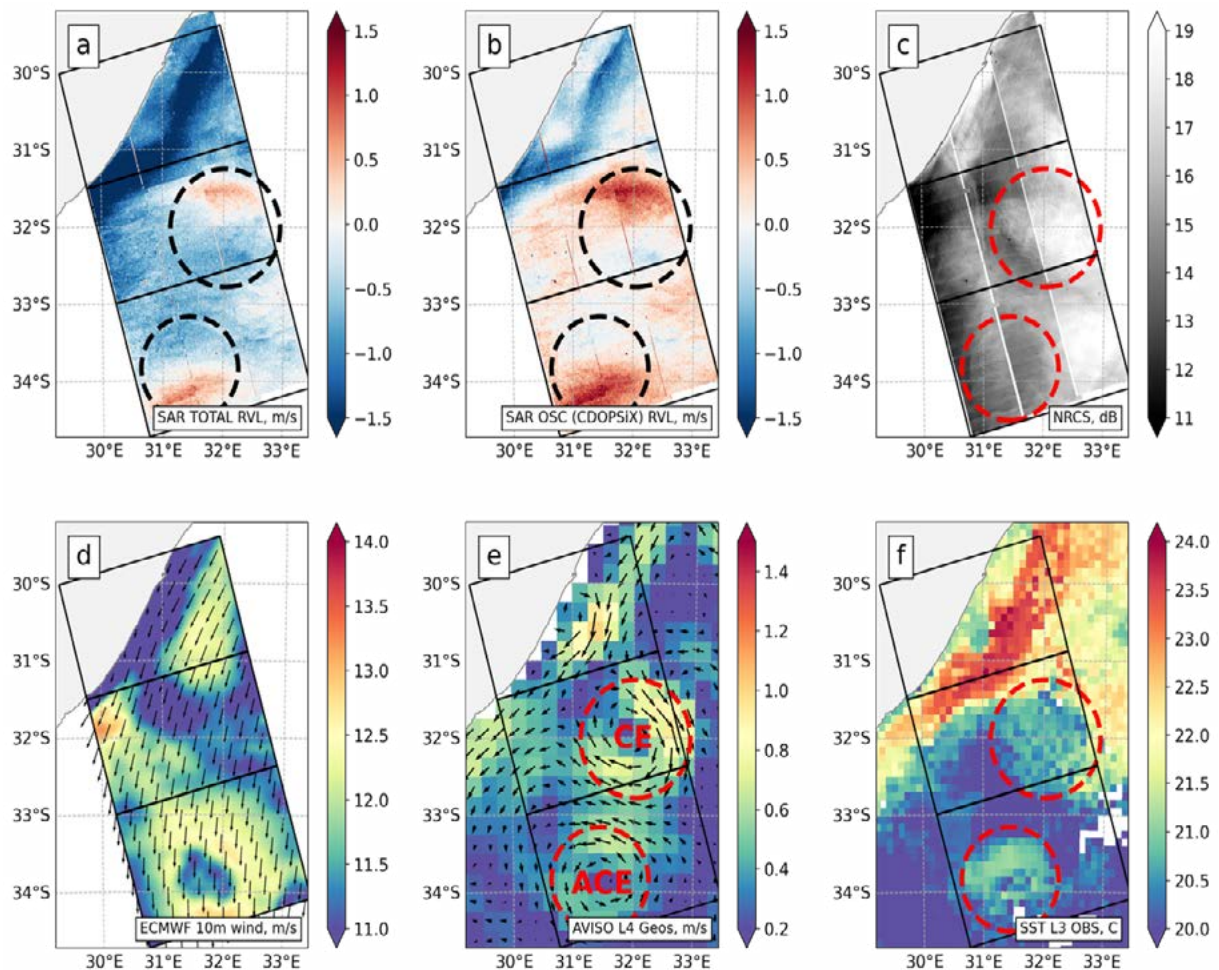
Figure 1. *The Sentinel-1A SAR scene acquired in ascending pass on 7 July 2019 at 16:36:36: (a) Total surface radial velocity (i.e., wave- and surface-current-induced signal) from the Doppler shift; (b) Ocean surface current radial velocity (i.e., after removal of the sea-state-induced signal) from the Doppler shift; (c) Normalized radar cross section. The blue/red color in a, b indicates south-westward/north-eastward velocity. The SAR scene is collocated with: (d) Wind speed (color) and direction (arrows) at 10m height from the ECMFW; (e) Geostrophic velocity from altimetry observations; (f) Satellite derived Sea Surface Temperature field. The black frames indicate footprint of the SAR acquisition frames. The dashed contours in subplots b, c, e, f represent position of the cyclonic (CE) and anticyclonic (ACE) eddies detected in the geostrophic velocity field.*

used to monitor the Agulhas Current with 1 km spatial resolution, based on one year of experimental acquisitions. The SAR estimates indicate maximum surface currents reaching nearly 2 m/s. The spatial distribution is well consistent with the daily grided altimetry observations and SST fields from infrared sensors. These findings are also consistent with previous results acquired over the equatorial current (Moiseev et al 2020a) and Norwegian Coastal Current (Moiseev et al 2020b). Although the study is constrained by the availability of experimental calibration for the Sentinel-1, the methodology shows promising results for studying the upper ocean dynamics with high spatial resolution. Hence, processing of the full archive of the Sentinel-1A/B acquisition since 2014/2016 is strongly recommended for future improvement of the retrieval algorithms and systematic validation. Development of the self-sufficient estimation of the sea state contribution, based on the wind and wave information (e.g., Li et al. 2019) extracted from the SAR observations, shall further improve the accuracy of surface current retrievals from Sentinel-1 (sustained operations until 2030) and future candidate satellite missions designed for monitoring of the upper ocean circulation (e.g., Harmony and SEASTAR concepts).

ACKNOWLEDGEMENTS

REFERENCES

Moiseev, A., H. Johnsen, J.A. Johannessen, F. Collard, G. Guitton. (2020a). On removal of sea state contribution to Sentinel-1 Doppler shift for retrieving Reliable Ocean surface current. Journal of Geophysical Research: Oceans, 125.

Moiseev, A., H. Johnsen, M.W. Hansen, J.A. Johannessen. (2020b). Evaluation of radial ocean surface currents derived from Sentinel-1 IW Doppler shift using coastal radar and Lagrangian surface drifter observations. Journal of Geophysical Research: Oceans, 125.

OceanDataLab. (2019). S-1 RVL DIL4: Algorithm description document. ESRIN: ESA.

Johannessen, J. A., B. Chapron, F. Collard, V. Kudryavtsev. (2008). Direct ocean surface velocity measurements from space: Improved quantitative interpretation of Envisat ASAR observations. Geophysical Research Letters, 35(22), 1-6.

Li, H., Chapron, B., Mouche, A. A., & Stopa, J. E. (2019). A new ocean SAR cross-spectral parameter: Definition and directional property using the global Sentinel-1 measurements. Journal of Geophysical Research: Oceans, 124, 1566–1577.

Chapron, B., Collard, F., and Ardhuin, F. (2005), Direct measurements of ocean surface velocity from space: Interpretation and validation, J. Geophys. Res., 110, C07008, doi:10.1029/2004JC002809

Joint reconstruction of ocean surface temperature and currents through deep learning algorithms

Daniele Ciani, Claudia Fanelli, Bruno Buongiorno Nardelli

Consiglio Nazionale delle Ricerche (CNR), Istituto di Scienze Marine, Italy

Abstract – **Satellite-based data-driven techniques represent an efficient strategy to obtain synoptic observations of oceanic variables to be used for scientific and socio-economic applications. Here we develop and test purely data-driven and physically-informed deep learning models based on Convolutional Neural Networks (CNNs) to jointly improve the reconstruction of Absolute Dynamic Topography (ADT) and Sea Surface Temperature (SST). This approach constitutes a promising way to improve ocean surface monitoring for both scientific studies and operational services.**

Keywords: Sea Surface Temperature, Ocean Dynamics, Deep Learning, Remote Sensing.

1. INTRODUCTION

In the last decade, technological progress has opened new prospects for the application of deep-learning techniques in a wide range of fields. This change originated from the concurrent increase of computational power at widely affordable costs and impressive growth of openly available data. Computer vision is one specific branch of artificial intelligence that is driving significant improvements thanks to the possibility to design and implement complex model architectures based on deep convolutional neural networks (CNN). Computer vision originally aimed to emulate the human capability to immediately discriminate objects and features in a picture or video, as well as to extrapolate/predict relevant information from partial or degraded input, either for recreational, medical, security or other commercial uses, e.g., for automated focusing on specific subjects in consumer and professional cameras, for semantic/instance segmentation and anomaly detection in medical imagery or in support of self-driving automated vehicles.

Within our study, the use of deep networks based on CNN is aimed at optimizing Absolute Dynamic Topography (ADT) and Sea Surface Temperature (SST) L4 observations, such as those routinely distributed within the European Copernicus programme. ADT and SST are strongly interconnected and both contribute to our knowledge of physical and biogeochemical processes occurring at the ocean surface/interior and at the air-sea interface. The space-based retrieval of such variables is affected by both intrinsic/instrumental/sampling limitations and, eventually, by degradations introduced by the algorithms used to interpolate the data up to the level 4 (L4, namely gap-free field) (Ballarotta et al. 2019, Ciani et al. 2020).

Here, we describe two Observing System Simulation Experiments (OSSEs), where the outputs of an ocean general circulation model is used to simulate the satellite observing geometries: i) in a first exercise, we derive high-resolution sea surface dynamical features by combining low-resolution L4 ocean ADTs based on satellite altimetry (resolving $O(100$ km) wavelengths) and high-resolution "perfectly known" SST L4 (whose effective scales range between $O(1$ km) and $O(10$ km) depending on the sensor). This represents a different problem with respect to simple model output downscaling or single variable super-resolution, as we want to combine the information provided by channels at both original and degraded resolution in a multi-channel image, taking advantage of the physical relations among the variables as learned from the model physics and of prior knowledge of the observation geometry; ii) in a second experiment, , we also introduce the SST L4 processing errors and modify the network to predict simultaneously high resolution SST and ADT from the simulated L4 products, in order to assess the extent to which both the SST and ADT can be improved, also introducing dynamical constraints through custom loss functions. All models are trained with OSSE data but successively tested on real satellite-based products. Our study area is the Mediterranean Sea, whose dynamics is dominated by relatively small scales (down to 10 km).

2. METHODS AND RESULTS

The OSSE is based on SST and Sea Surface Height (SSH) model outputs freely available through the Copernicus Marine Service web portal (MEDSEA-ANALYSIS-FORECASTPHY-006-013).
Satellite-equivalent ADTs were computed from the model SSH outputs for the year 2017, simulating an observing system of 4 Altimeters. Improved ADT maps were obtained through CNNs and finally compared with the original modeled ADT. The CNN architecture adopted here (sketched in Figure 1) is the dilated Adaptive Deep Residual Network for Super-Resolution (dADR-SR) developed by Buongiorno Nardelli et al. 2022 (BBN22 hereafter) which was inspired by the findings of Liu et al. 2019.
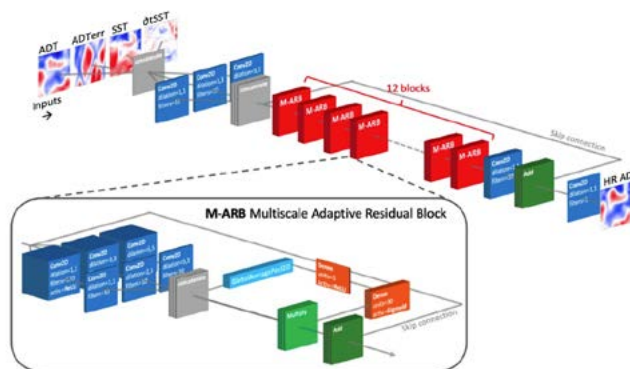
Figure 1. *Adaptive Super‑Resolution (ADR‑SR) baseline model tested for the reconstruction of high resolution ADT from multiple channel inputs. (A) ADR‑SR network. ADR-SR is based on the inclusion of a squeeze‑and‑excitation module within its residual block design (adapted after BBN22).*

In the first experiment, the dADR-SR input dataset is constituted by tiles of low resolution (LR) ADT, the ADT formal mapping error, the SST and its temporal derivative (∂tSST), all shown in the top-left area of Figure 1. The input dataset then passes through three convolutional layers with

different dilation factors that extract information at different scales. After this first stage, the network includes a series of Multiscale Adaptive Residual Blocks (M-ARB), each comprising two sets of convolutional layers and a Squeeze-and-Excitation module. This structure is conceived to maximize the exploitation of multi-scale information and efficiently combine features to produce the final high resolution output. The network is trained using an early stopping rule: we randomly split our training dataset (made of 325 days) into a proper training set (85% of data) and a validation set (15%). Based on this, we carry out the training (hindcast) and validation losses are updated during the network optimization. The validation loss, in particular, is used as an estimate of the generalization error, and early stopping consists in terminating the iterative learning as soon as its values start to increase. The remaining 40 days of our 1 year long time series (2017) are finally used as independent test data. The results sketched in Figure 2 A,B respectively show the Root Mean Squared Differences (RMSD) between the ADT obtained through standard OI and CNN reconstruction using the originally modeled ADT as ground truth. A marked reduction of the RMSD is observed over the entire basin with only extremely few and small extent spots showing minimal degradation. The red areas in Figure 2C express the benefits brought by the CNN approach.
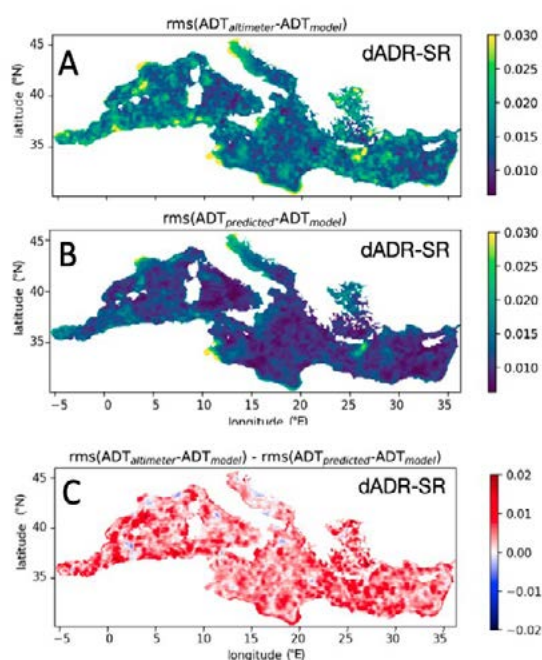

Figure 2. *A) RMSD between the altimeter-like and original model output, B) RMSD between the super-resolved absolute dynamic topography (ADT) obtained with dADR‑SR . C) RMSD differences of the quantities shown in A,B: red areas indicate an improvement brought by the CNN reconstruction (adapted after BBN22).*

The CNN-based prediction model (obtained via the OSSE) was then applied to altimeter-derived ADT observations in the period 2008-2019 (Copernicus product ID: SEALEVEL_EUR_PHY_L4_MY_008_068). The 11 years time series of ADT was reconstructed extracting feature information from satellite SSTs (Product ID: SST_MED_SST_L4_NRT_OBSERVATIONS_010_004_c_V2) and was finally compared with the original ADT estimates. The validation was carried out by means of eddy detection algorithms as well as inter-comparison of surface

geostrophic currents respectively obtained from standard and CNN-derived ADTs. The validation evidenced that the CNN approach allows us to enhance the potential of standard ADT products to detect eddy features often smeared out in the present-day ADT Copernicus products and captured by the high resolution SST. Taking advantage of drifter-derived surface currents measurements, we also found that locally, the CNN approach can improve the geostrophic currents estimate derived from standard Altimetry. The application to satellite data also evidenced that satellite-derived SST errors cannot be neglected within our approach.

Considering this, more recently we worked on a new OSSE in which a satellite-equivalent SST was also derived. We introduced synthetic clouds (replicating true data voids in daily multi-sensor SST products) in the model-derived SSTs and set up an OI procedure to obtain an SST L4 product. In addition, we updated the CNN architecture depicted in Figure 1 and introduced the SST and ∂tSST error fields as predictors leading to a simultaneous reconstruction of "super-resolved" ADT and SST. The preliminary OSSE results show that both ADT and SST can be improved via this approach. In addition, fine tunings of the CNN iterative learning are underway and will allow us to determine how far we can push the network to improve ADT and SST simultaneously, also introducing custom loss functions constraining the SST small scale evolution to be driven by surface currents advection.

3. CONCLUSIONS AND PERSPECTIVES

In the last decades, the combined use of satellite-derived observations has fostered the development of several algorithms for the generation of added-value products for ocean state monitoring. Here we showed the potential of deep neural networks based on computer vision architectures for optimizing ADT and SST observations in the Mediterranean area, based on both numerical experiments and application to state-of-the-art satellite-derived observations. Such an application can potentially be extended to other areas of the ocean as well as to three-way sinergy problems (including e.g. ocean color). The strong operational potential within operational services (such as the European Copernicus Marine Service) is also envisageable.

REFERENCES

-Buongiorno Nardelli, B., Cavaliere, D., Charles, E., & Ciani, D. (2022). Super-Resolving Ocean Dynamics from Space with Computer Vision Algorithms. *Remote Sensing*, *14*(5), 1159.
-Ciani, D., Rio, M. H., Nardelli, B. B., Etienne, H., & Santoleri, R. (2020). Improving the altimeter-derived surface currents using sea surface temperature (SST) data: A sensitivity study to SST products. *Remote Sensing*, *12*(10), 1601.
-Ballarotta, M., Ubelmann, C., Pujol, M. I., Taburet, G., Fournier, F., Legeais, J. F., ... & Picot, N. (2019). On the resolutions of ocean altimetry maps. *Ocean Science*, *15*(4), 1091-1109.
-Liu, S., Gang, R., Li, C., & Song, R. (2019). Adaptive deep residual network for single image super-resolution. *Computational Visual Media*, *5*(4), 391-401.

Imaging small-scale ocean dynamics at interfaces of the Earth System with the SEASTAR Earth Explorer 11 mission candidate

C. Gommenginger[1,*], A.C.H. Martin[1], A. Egido[2], K. Hall[2], P. Martin-Iglesias[2], T. Casal[2], the SEASTAR Mission Advisory Group[3] and the SEASTAR International Science Team[3]

[1] National Oceanography Centre, Southampton, United Kingdom
[2] European Space Agency
[3] International

Abstract – SEASTAR is a satellite mission candidate for ESA Earth Explorer 11 that proposes to measure small-scale ocean dynamics below 10 km at ocean/atmosphere/land/ice interfaces of the Earth System. SEASTAR products consist of high-resolution images of total surface current vectors and wind vectors of unprecedented resolution (1 km) and accuracy over a wide swath. A key objective of SEASTAR is to characterize, for the first time, the magnitude, spatial structure, regional distribution and temporal variability of upper ocean dynamics on daily, seasonal and multi-annual time scales, with particular focus on coastal seas, shelf seas and Marginal Ice Zone boundaries. The mission addresses an urgent need for new measurements of small-scale ocean processes to help understand and model their impacts on air-sea interactions, horizontal water pathways, vertical mixing and marine productivity. High-resolution imaging of total currents with collocated wind and waves data would bring new means of validating and developing models to improve operational forecasts and climate projections.

Keywords: New satellite mission, currents, winds, waves, submesoscale, air-sea interactions, coastal, polar, marine productivity, SAR interferometry, Earth Explorer.

1. INTRODUCTION

The ocean interacts with the atmosphere, land, the cryosphere and the biosphere across a wide variety of spatial and temporal scales. High-resolution satellite images reveal ubiquitous small-scale ocean dynamic features at scales below 10km that permeate the global ocean, but are particularly frequent near current jets and mesoscale eddies, in coastal seas and close to sea ice margins. Numerous publications in recent years indicate that these small-scale ocean surface processes (submesoscales) play an important role in the global Earth System through their impact on vertical exchanges of heat, gases and freshwater between the surface layer and the ocean interior, horizontal transport and dispersion pathways and interactions between the atmosphere, ocean, land and cryosphere (e.g. Lapeyre & Klein, 2006; Levy et al., 2018; D'Asaro et al., 2020). By modulating the availability of nutrients in the euphotic zone, small scale ocean dynamics impact marine biogeochemistry, the growth of phytoplankton and the marine food chain.

In coastal seas, ocean circulation is dominated by dynamic processes on short spatial and temporal scales. As interactions with the sea floor and the coastline become stronger, currents and winds become more complex, intense and spatially variable. Wind/wave/current interactions are particularly important in coastal regions, with direct relevance to air-sea exchanges, safety at sea, marine conservation and coastal management.

Interactions between the atmosphere, waves, sea ice and the ocean are at their strongest in the Marginal Ice Zone, a band of sea ice cover about 150 km wide on average that borders the open ocean. Here too, physical and biological dynamics are conditioned by a multitude of coexisting complex processes associated, for example, with differential wind stress over water and ice, lateral buoyancy gradients linked to variable heat fluxes and melting and the mechanical action of waves and currents changing ice pack rheology and freezing/melting. At present, these fine-scale interactions are not well represented in Earth System Models, even though changes affecting the Marginal Ice Zone bear directly on Arctic sea ice loss projections, deep water formation, marine productivity and the global Earth System.

Figure 1. *Small-scale water turbidity patterns in Venice lagoon and Adriatic Sea in Copernicus Sentinel-2 image on 04 November 2021 (Credits: ESA/Copernicus).*

2. THE NEED FOR NEW HIGH-RESOLUTION CURRENTS AND WINDS MEASUREMENTS

State-of-the-art numerical models predict that ocean dynamics change dramatically when scales reach 1 km, with enhanced air-sea coupling, ageostrophic wind/wave/current interactions and intensified vertical ocean velocities. To date, our knowledge of small-scale ocean dynamics and their large-scale impacts stems mainly from theoretical studies and numerical models. Direct measurements of ocean dynamics at small scales are challenging, expensive and scarce.

Until now, no existing or planned satellite offer the necessary 2D imaging capability with the spatial resolution, precision and sampling needed to observe and characterise these processes. There is an urgent need for new high-quality high-resolution imaging of surface current and wind fields to confront models, validate recent findings and support research on submesoscale dynamics, vertical processes and wind-current-wave interactions in coastal, shelf- and ice-covered seas. Used in synergy with other satellite data, new high-resolution surface dynamics measurements would also

---

* Corresponding author. Address: European Way, Southampton, SO14 3ZH, United Kingdom. Email: cg1@noc.ac.uk

enable downscaling of low-resolution data and facilitate the interpretation of observations from other high-resolution sensors. The strong variability, seasonality and regionality of small-scale phenomena call for a dedicated mission able to systematically assess their magnitude, temporal and spatial characteristics, on daily to multi-annual scales, across all key areas of the globe.

3. THE SEASTAR EE11 MISSION CANDIDATE

SEASTAR is a satellite mission candidate for ESA Earth Explorer 11 that proposes to measure small-scale ocean dynamics below 10 km at ocean/atmosphere/land/ice interfaces of the Earth System. SEASTAR products consist of high-resolution images of total surface current vectors and wind vectors of unprecedented resolution (1 km) and accuracy over a wide swath. A key objective of SEASTAR is to characterize, for the first time, the magnitude, spatial structure, regional distribution and temporal variability of upper ocean dynamics on daily, seasonal and multi-annual time scales, with particular focus on coastal seas, shelf seas and Marginal Ice Zone boundaries. The mission addresses an urgent need for new measurements of small-scale ocean processes to help understand and model their impacts on air-sea interactions, horizontal water pathways, vertical mixing and marine productivity. High-resolution imaging of total currents with collocated wind and waves data would bring new means of validating and developing high-resolution and coupled models to improve operational forecasts and reduce uncertainties in climate projections.

SEASTAR is currently being studied as part of EE11 Phase 0 science and industrial activities. SEASTAR consists of a single instrument on a single satellite flying in sun-synchronous Low-Earth Orbit. SEASTAR is the first single-platform Ku-band SAR system dedicated to squinted along-track ocean interferometry from space. The payload features two squinted SAR beams pointing ±45° in azimuth fore and aft of the satellite (Figure 2) and a standard SAR beam broadside with multi-polarisation capability (VV/VH, HH/HV). This innovative approach makes it possible to retrieve both components of the ocean surface current vector and the wind vector simultaneously in a single pass, with fine resolution and high accuracy. The squinted ATI measurement principle has been validated with airborne data (Martin et al., 2016) that confirmed the excellent performance achieved with this concept to image total surface current vectors at high resolution (Martin & Gommenginger, 2017; Martin et al., 2018)
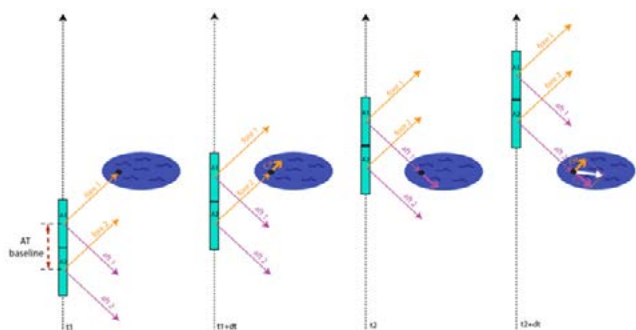

Figure 2. *Measuring principle of squinted along-track interferometry used by SEASTAR. The third beam in the broadside direction is not shown for clarity.*

4. CONCLUSION

The paper outlines the key elements of the SEASTAR mission and the latest status of the mission concept evolution, with the technical solutions and trade-offs that are being considered. We will report on ESA science activities to consolidate user requirements and the current assessment of the Scientific Readiness Level of the mission. Other planned activities, including first results from flight campaigns with the OSCAR airborne demonstrator and numerical end-to-end simulator developments will provide a comprehensive assessment of the suitability and benefits of the mission in preparation for the selection by ACEO and ESA in late 2023 of two of the four EE11 candidates to enter Phase A.

REFERENCES

D'Asaro, E.A., Carlson, D.F., Chamecki, M., Harcourt, R.R., Haus, B.K., Fox-Kemper, B., Molemaker, M.J., Poje, A.C. and Yang, D. (2020). 'Advances in observing and understanding small-scale open ocean circulation during the Gulf of Mexico Research Initiative Era'. Frontiers in Marine Science, 7, 349.

Gommenginger, C., B. Chapron, A. Hogg, C. Buckingham, B. Fox-Kemper, L. Eriksson, F. Soulat, M.-H. Rio, C. Ubelmann, F. Ocampo-Torres, B. Buongiorno Nardelli, D. Griffin, P. Lopez-Dekker, P. Knudsen, O. Andersen, L. Stenseng, N. Stapleton, W. Perrie, N. Violante-Carvalho, J. Schulz-Stellenfleth, D. Woolf, J. Isern-Fontanet, F. Ardhuin, P. Klein, A. Mouche, A. Pascual, X. Capet, D. Hauser, A. Stoffelen, R. Morrow, L. Aouf, O. Breivik, L.-L. Fu, J. Johannessen, Y. Aksenov, L. M. Bricheno, J. Hirschi, A. C. H. Martin, A. P. Martin, G. Nurser, J. Polton, J. Wolf, H. Johnsen, A. Soloviev, G. Jacobs, F. Collard, S. Groom, V. Kudryavstev , J. Wilkin, V. Navarro, A. Babanin, M. Martin, J. Siddorn, A. Saulter, T. Rippeth, B. Emery, N. Maximenko, R. Romeiser, H. Graber, A. Alvera Azcarate, C. Hughes, D. Vandemark, J. da Silva, P.-J. van Leeuwen, A. Naveira-Gabarato, J. Gemmrich, A. Mahadevan, J. Marquez, Y. Munro, S. Doody, and G. Burbidge (2019). 'Developing new spaceborne observations of submesoscale ocean dynamics and small-scale atmosphere-ocean processes in coastal, shelf and polar seas'. OceanObs'2019, Frontiers in Marine Science, 6, 457.

Lapeyre, G. and P. Klein (2006). 'Impact of the small-scale elongated filaments on the oceanic vertical pump'. Journal of marine research, 64(6), 835-851.

Lévy, M., P.J. Franks, and K.S. Smith (2018). 'The role of submesoscale currents in structuring marine ecosystems.' Nature communications, 9(1), 1-16.

Martin, A., and C. Gommenginger (2017). 'Towards wide-swath high-resolution mapping of Total Ocean Surface Current Vectors from Space: airborne proof-of-concept and validation'. Remote Sensing of the Environment, 197, 58-71.

Martin, A. C. H., C. Gommenginger, and Y. Quilfen (2018). 'Simultaneous ocean surface current and wind vectors retrieval with squinted SAR interferometry: geophysical inversion and performance assessment'. Remote Sensing of the Environment, 216, 798-808.

Martin, A. C. H., C. P. Gommenginger, J. Marquez, S. Doody, V. Navarro, and C. Buck (2016). 'Wind-wave-induced velocity in ATI SAR ocean surface currents: First experimental evidence from an airborne campaign'. Journal of Geophysical Research Oceans, 121.

Directional ocean wave spectrum properties from the SWIM instrument under tropical cyclone conditions

E. Le Merle[1]*, D. Hauser[2], R. Santoleri[1], C. Yang[1]

[1]ISMAR (CNR), Roma, Italy
[2]LATMOS (CNRS, Université Saint Quentin en Yvelines, Paris Sorbonne Université), Guyancourt, France

Abstract – The SWIM instrument on-board the CFOSAT mission provides directional ocean wave spectra every 70 km along-track with detailed information about waves with dominant wavelengths between 70 and 500 m. It is a strategic dataset to investigate the properties of the waves in the vicinity of tropical cyclones. Here we show that the asymmetry of the wave field detected with the significant wave height is also visible in the dominant wavelength and spectral shape signature. Such information is very unique to validate or improve the parametric models of wave growth in severe storms which have been proposed in the recent years, and to provide parameters which impact the air-sea interactions (e.g., the Stokes drift, the probability of wave breaking).

Keywords: directional ocean wave spectrum, tropical cyclone, real aperture radar observations.

1. INTRODUCTION

Tropical cyclones (TCs) are characterized by strong rotational winds with high spatial and temporal variability (in speed and direction). As this kind of event generates extreme waves that impact maritime navigation, coastal areas and heighten the ocean-atmosphere interactions, the detailed description of directional wave spectra under TC conditions is a topic of great relevance to oceanographic research and engineering applications. However, as mentioned by Kudryavstev et al., (2015), a classical wave modeling often fails to correctly represent the wave field under TC conditions because the classical wave growth laws established for quasi-stationary or homogeneous situations are no longer valid under these fast-moving systems. Several studies have shown that the wave fields generated by TCs are asymmetric with higher significant wave height (Hs) in the right front quadrant (with respect to the TC track) (Young, 2006; Kudryavstev et al., 2015, 2021). Simulation studies have shown that this asymmetry increases with the TC displacement speed (Kudryavstev et al., 2015, 2021). Correlatively, in the right forward quadrant of the storm the wave spectra look like typical spectra of fetch limited conditions with a unimodal shape (Young, 2006; Hu and Chen, 2011). However, in other quadrants, and at distant regions of the TC center, the wave spectra tend to become bi- and tri-modal in direction (Young 2006; Hu and Chen, 2011; Esquivel-Trava et al., 2014; Hwang & Walsh 2018). Young (2006) suggested that in TCs, the nonlinear interactions are the dominant process that controls the shape of the omni-directional spectra even if the wave energy is contained in several wave components with different directions. However, it is known that these nonlinear interactions are approximately represented in the wave models (Hasselman et al.,1985).

TCs are relatively local events in time and space and their observations from satellite or in-situ devices are rather scarce. Recently (October 2018), the Surface Waves Investigation and Monitoring (SWIM) instrument, on-board the China-France Oceanography Satellite (CFOSAT) mission, was launched in space and allow us to better observe these extreme events. Indeed, SWIM provides directional ocean wave spectra every 90 km with detailed information about the waves with dominant wavelength between 70 and 500 m (Hauser et al, 2021). The high quality of SWIM has been demonstrated by a study on the assimilation of SWIM spectra in a wave model, showing significant improvements of the model results in the Southern Ocean (Aouf et al., 2021). Therefore, SWIM data are useful to analyze the directional properties of the waves but also the probability of extreme waves at the global scale (Le Merle et al., 2021).

One objective of our study is to characterize the shape of the wave spectra in TCs by analyzing several spectral shape parameters, such as the directional spreading of the directional spectra (σ_ϕ) and the "Peakedness" parameter of the omni-directional spectra (noted Qp here after). Preliminary results are presented in section 2. Section 3 presents some conclusions and the perspectives.

2. RESULTS

In this abstract we illustrate a subset of results obtained from the SWIM observations obtained between May 2019 and August 2021. Fig. 1 shows the variation of the wave parameters along one example of a SWIM track crossing over the hurricane Douglas (July 2020) whose characteristics (according to the IBTRACS data base from NCAR) are maximum wind speed 60 m/s, radius of maximum wind 28 km and translation speed 16 m/s. Higher values of Hs are observed on the right side of the TC indicating that higher sea state occurs in this area. This result is consistent with previous studies. In addition, we show in Fig. 1 that the dominant wavelengths (noted λ_p after) are longer and that σ_ϕ is lower on the right side of the TC.
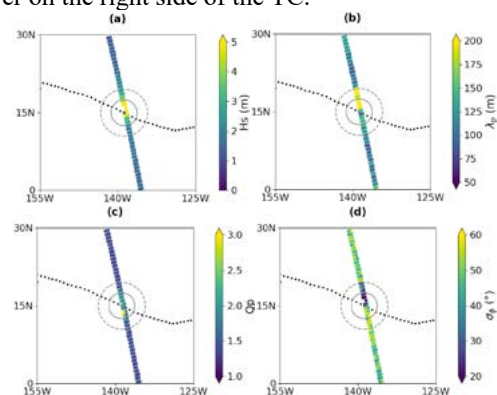

Figure 1. *Variation along the SWIM track of (a) Hs, (b) λ_p, (c) Qp and (d) σ_ϕ. Black points indicate the Douglas hurricane track. The solid circle indicates the radius of ten times the maximum sustained wind radius and the dashed-line circle represents the hurricane radius of 500 km.*

* Corresponding author. Address: Via del Fosso del Cavaliere 100, 00133 Roma (RM), Italia. Email: eva.lemerle@artov.ismar.cnr.it

This indicates that, in this case, the right side of the storm is characterized by more mature waves although these waves remain under influence of the wind. However, even though Qp is higher in the vicinity of the hurricane, the asymmetry is not that obvious for this parameter.
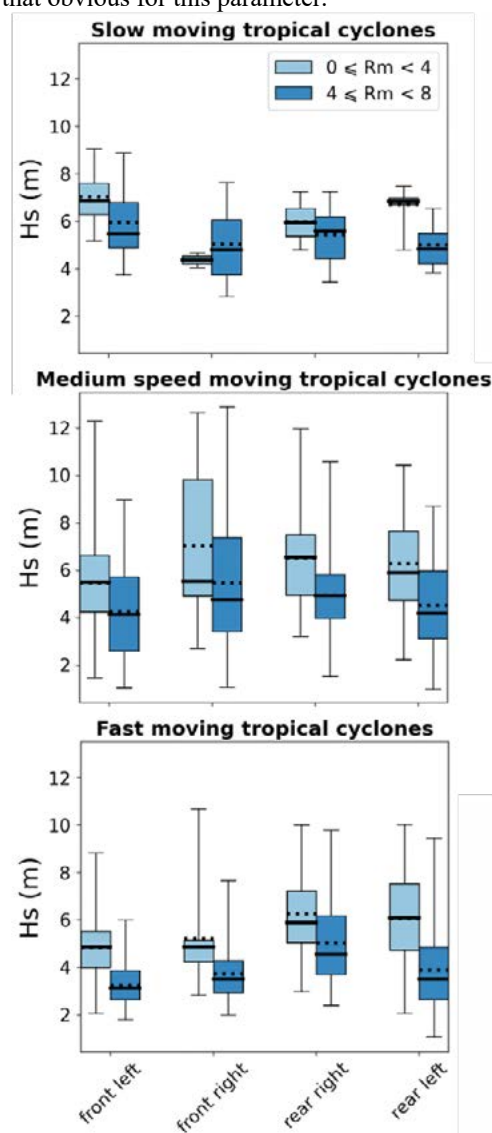

Figure 2. Statistics of the significant wave height for each quadrant of the TCs for (top) slow, (middle) medium speed and (bottom) fast moving events. Light (resp. dark) blue boxes indicate observations close to (resp. far from) the TCs center. The vertical size of the boxplot corresponds to the first to third interquartile interval of the distribution. Error bars indicate the min. and max. value of the data subset. Solid and dotted lines indicate the median and the mean, respectively.

Fig. 2 shows the statistics of the Hs in each quadrant for the 46 events observed in the Northern hemisphere. For this study we have classified TCs in three different categories: slow, medium and fast moving TCs according to the ratio of the maximum wind speed to the translation speed of the TC. In average, close to the center of the TC, Hs are higher than far from the TC center which sounds logical since the wind speed decreases when the distance from the center of the TC increases. Highest values of Hs occur in the front left quadrant for slow moving TC whereas they occur in the front right quadrant for medium speed moving TC. For fast moving TC, highest average values of Hs are visible in the rear quadrants.

Conclusions about the Hs are different according to the relative speed of the TC which indicate that the asymmetry

of the wave field described by several studies may also depend on TC characteristics. These conclusions are in agreement with the simulations made by Kudryavtsev et al. (2021).

3. CONCLUSIONS AND PERSPECTIVES

SWIM observations are very useful and complementary to other space observations (e.g., altimeters, SARs) to study the ocean wave fields under TC conditions. We have presented our results in one hurricane which show that the asymmetry of the wave field is present not only in the significant wave height but also in the dominant wavelength and in the spectral shape parameters such as the directional spread. We also show that TC characteristics have an impact on this asymmetry.

During the conference we will present more results about the evolution of the shape parameters in TCs. We will also show the relationships between the wave parameters and the wave age estimated using the wind data provided by the scatterometer onboard the CFOSAT mission.

REFERENCES

Aouf, L., Hauser, D., Chapron, B., et al. (2021). New directional wave satellite observations: Toward improved wave forecasts and climate description in Southern Ocean. Geophysical Research Letters, 48, doi:10.1029/2020GL091187

Esquivel-Trava, B., Ocampo-Torres, F. J., and Osuna, P., (2014). Spatial structure of directional wave spectra in hurricanes. Ocean Dynamics, doi:10.1007/s10236-014-0791-9

Hasselmann, S., Hasselmann, K., Allender, J.H., and Barnett, T.P. (1985). Computations and parameterizations of the nonlinear energy transfer in a gravity-wave spectrum, Part II: Parameterizations of the nonlinear energy transfer for application in wave models. J. Phys. Oc., 15, pp. 1378-1391

Hauser, C. Tourain, L. Hermozo, et al. (2021), New observations from the SWIM radar on board CFOSAT: instrument validation and ocean wave measurement assessment, IEEE Transaction on Geoscience and Remote Sensing, 59 (1), pp.5-26., doi: 10.1109/TGRS.2020.2994372

Hu, K., and Chen, Q. (2011). Directional spectra of hurricane-generated waves in the Gulf of Mexico, Geophys. Res. Lett., 38, L19608, doi:10.1029/2011GL049145

Hwang P. A. and E. J. Walsh (2018), Propagation Directions of Ocean Surface Waves inside Tropical Cyclones, Journal of Physical Oceanography, 2018, p 1495–1511, doi: https://doi.org/10.1175/JPO-D-18-0015.1

Kudryavtsev, V., Golubkin, P., and Chapron, B., (2015), A simplified wave enhancement criterion for moving extreme events, J. Geophys. Res. Oceans, 120, 7538–7558, doi:10.1002/2015JC011284.

Kudryavtsev, V., Yurovskaya, M., and Chapron, B., (2021) Self-similarity of Surface Wave Developments Under Tropical Cyclones, J. of Geoph. Research: Oceans, 126, doi:10.1029/2021JC016916

Le Merle, E., Hauser, D., Peureux, C., et al. (2021). Directional and frequency spread of surface ocean waves from SWIM measurements, J. of Geoph. Research: Oceans, 126, doi:10.1029/2021JC017220

Moon, I.-J., Ginis, I., and Hara, Y., (2008). Impact of the reduced drag coefficient on ocean wave modeling under hurricane conditions, Mon. Weather Rev., 136, 1217–1223, doi:10.1175/2007MWR2131.1

Young, I. R. (2006). Directional spectra of hurricane wind waves, J. of Geophys. Res, vol 111, C08020, doi:10.1029/2006JC003540

Monitoring the complex and dynamic Amazon-influenced muddy coast (from the Amazon to the Orinoco) with the Sentinel 2 satellites

R. Abileah *

jOmegak, San Carlos, California, USA

Abstract – The muddy coasts of northeast South America are from sediment discharged by the Amazon River, then transported by wave action and currents as far as Orinoco (Venezuela). The mud zone morphology is pockets of mud banks and interbank zones. The mud banks are continuously moving westward. Mapping and monitoring this highly dynamic bathymetry is of interest for Marine geology studies, tide-modeling, coastal management, and navigation. Echo-sounding surveys only provide occasional small area coverage. This paper shows bathymetry derived from wave kinematics measured by the Sentinel 2 satellites. The bathymetry for the entire 1500 km extent of the muddy coast can be updated annually.

Keywords: Sentinel 2, bathymetry, Amazon discharge, muddy coast

1. INTRODUCTION

Sediment discharge of the Amazon River congregates into mud banks, which are then migrated by forces of waves and currents westward along the northeast South America coastline, reaching as far as the Orinoco (Venezuela). The term *Amazon-influenced muddy coast* is suggested in (Anthony et al. 2010), which is also an excellent review on this topic; (Orseau et al. 2019) is another.

Figure 1 (from Allison et al. 2004) illustrates the migration mechanics. Waves, predominantly from NE, liquefy the mud on the East (trailing edges). The alongshore current advects the liquefied mud to settle on the leading edge. The erosion/accretion process continues ad infinitum. The westward movement is 1-5 km/year (Zorrilla, 2018).

Thus, the entire 1500 km coast from the Amazon to the Orinoco is an ever-changing bathymetry up to 40 km offshore. Mapping this dynamic bathymetry is relevant to marine geology researchers, tide modeling and prediction, coastal management, and navigation. Up to now, there have been only occasional and small area echo-sounding surveys. E.g., 310 km^2 in French Guiana (Orseau et al., 2019). The entire Amazonian mud banks area is ~20,000 km^2 and is impractical to survey by echo-sounding, repeating every few years to monitor the movement of mud banks.

The Sentinel 2 satellites have been game-changers for remote sensing coastal phenomena such as wave dynamics, currents, shorelines, and bathymetry. Both academia and commercial efforts favor the Sentinel 2s because of their excellent radiometric accuracy, the worldwide 5-day revisit, pixel resolution (10m), and price competitiveness (Sentinel 2 images are free as compared to ~$10/km^2 from other satellite platforms,)

Here we describe how the Sentinel 2s can map the bathymetry of the entire Amazon-influenced mud coast, repeated regularly.

Satellite-derived bathymetry (SDB) is now a familiar tool for coastal benthic and bathymetry mapping. However, it should be explained that while this paper is about 'satellite-derived' bathymetry, it is not the SDB as commonly understood. SDB is the inversion of bottom reflected sunlight. SDB works well in clear waters (e.g., Bahamas) but is very limited in turbid waters. Most of the world's coasts are moderately turbid [Shi and Wang, 2010], and SDB is limited to a few meters. On the Amazonian mud coast, there is constant sediment transport –very high turbidity, and SDB is even more limited.

The method in this paper is independent of water turbidity. The depth is derived from images of the surface waves. Wave celerity and wavelength transform as the waves shoal and "feel the bottom." The celerity is lower, and wavelengths shorten. Wave displacements are measured within a small time interval. Two near-infrared bands, B08 (842μ) and B8A (865μ), with a 1.79 s separation, are most suitable for this approach. Depth estimates are discretized in 200 m pixels (similar to averaging echo-sounding over a 200 x200 m area). For further explanation of the theory, algorithms, and Sentinel 2-specific implementation, refer to (Abileah and Blot, 2021) and the references cited therein.
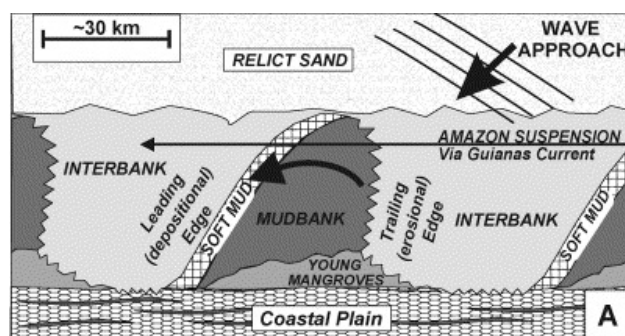
FIGURE 1. A SCHEMATIC EXPLANATION OF MUD BANK EVOLUTION. (COPIED FROM ALLISON AND LEE, 2004.)

2. SENTINEL 2 BATHYMETRY FOR THE SURINAME COASTLINE

Trial runs have been done on several locations along the 1500 km coastline. Here we present results on a 350 km stretch of the Suriname coastline where we have corroborating echo-sounding bathymetry. We downloaded four years (600 images) from the ESA Copernicus portal. The top panel in Figure 2 is the Sentinel 2 derived bathymetry from two years centered on 2018.7. There are seven distinct mud banks. The bathymetry in the following two years, centered on 2020.7, is similar, but all mud banks had shifted west. (A 'two frame movie' to be shown in the conference presentation will make the motion apparent.) Differencing the two periods provides the volume of mud shifted from the East to West edges. The bottom panel of Figure 2 is the 2016 echo-sounding survey by the Suriname authorities [MAS, 2021, private communications]. The MAS survey was conducted two

---

* Corresponding author. Address: 20 Tulip Ln, San Carlos, California, 94070 USA. Email: abileah@jOmegak.com

years earlier, and on close examination with the Sentinel bathymetry, one can see a slight westward migration. The main point is that satellite data produces the same result as echo-sounding surveys.
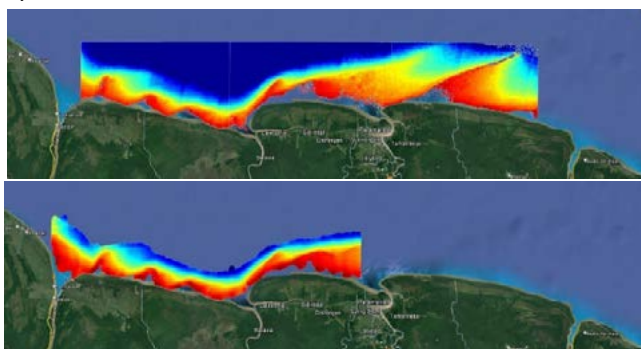
.

FIGURE 2 COLOR CODED DEPTH SUPPERIMPOSED ON GOOGLE EARTH IMAGE OF THE SURINAME COASTLINE (APPROXIMATELY 400 KM). (TOP) SENTINAL 2 BATHYMETERY. (BOTTOM) ECO-SOUNDING BATHYMETRY FROM MAS. THE COLOR SCALE IS 20 M DEPTH (DARK BLUE) TO 0 M (DARK RED). DEPTHS ARE REFERENCED TO LOWER ASTRONOMICAL TIDE (LAT).

The MAS survey stopped at Paramaribo. The Sentinel 2 bathymetry continues 120 km further East to reveal two features. These are 70 km long diagonally, extending at least 40 km from the shoreline. Unlike the rounded mud banks closer to shore, these features narrow to 1 km broad ridges and are very shallow (<3m) at the furthest reach from the coast. The hydrological forces are also different from the standard model (Fig. 1). Waves impact the eastern edge as elsewhere but are also sharply refracted onto the western edge.

Nautical charts do not show these ridges. However, a sailing blog [The Yarmouth23 Sailing Blog, 2012] recommends circumnavigating the area at the 20 m isobath. (The rationale is that the 20 m isobath is stable.) Sailors know well enough to avoid them.

3. CONCLUSION

The Sentinel 2A archive began in 2016. Since 2017 there has been continuous image acquisition with two satellites, 2A and 2B, with 60 images added each year. After culling cloudy images, there are still at least 20 revisits per year, which is adequate for an accurate and complete bathymetry of the mud banks. An annual update with new images of the prior year is feasible with a modest multi-core server. The ESA policy of free distribution of Sentinel data is another factor making this and many other satellite data exploitations possible.

The Suriname example is scalable to the entire muddy coast. The image data is accessed and processed in 100 x 100 km tiles. Three tiles cover Suriname. Seventeen more tiles complete coverage of the entire mud coast.

Three critically important considerations for success with the waves-derived bathymetry are (1) wave energy, (2) sun zenith angle in an optimum range, and (3) cloud-free surface view. The coastline must be exposed to waves from oceanic basin storms for adequate wave energy. A fully-developed wind waves spectrum (peak wavelength of 100 m) is a minimum requirement; swell waves (200-300 m) are even better. There is year-round exposure to N Atlantic wave systems from the Amazon to Trinidad. (Conversely, wave systems are blocked west of Trinidad.)

The optimum sun zenith angle for wave imaging is in a range of 20-40 degrees. In the tropics, this condition is met almost year round. (Conversely, there are no good times for imaging waves on the UK coastline!)

And as far as clouds are concerned, this coast is average – cloudy 50% of the time. But with 5-day repeat visits, there are plenty of opportunities to fill cloud gaps.

All three considerations are met on the northeastern South American coastline. There is one additional consideration specific to mud coasts. Wave energy dissipates as much as 85% while transversing the mud bank (Winterwertp et al., 2007). Often waves are not detected in the shallowest areas. However, there is a 2.5 m tide range. So a handful of high tide dates will fill in the shallow depths. In Figure 2, the minimum LAT depth is 2-3 m. Those shallow depth points came from high tide days.

Byproducts of bathymetry processing include wave direction and wave energy.

In summary, the method described in this paper enables a cost-effective annual bathymetric mapping of the Amazon-influenced muddy coast. The bathymetric 'soundings' are at 200 m resolution, covering a depth range of 3 – 20 m, and can be updated annually to keep track of the mud banks' movements.

.

REFERENCES

Abileah, R., and J. -Y. Blot, (2021) "Bathymetry of the Golfe d'Arguin, Mauritania, derived with the moderate resolution Sentinel-2 satellites," OCEANS 2021: San Diego – Porto

Allison, M. A., and M. T. Lee, (2004) "Sediment exchange between Amazon mud-banks and shore-fringing mangroves in French Guiana," Marine Geology, Volume 208, Issues 2–4

Anthony, E.J., Gardel, A., Gratiot, N., Proisy, C., Allison, M.A., Dolique, F., Fromard, F., (2010), "The Amazon-influenced muddy coast of South America: A review of mud-bank–shoreline interactions." Earth-Sci. Rev. 103, 99–121.

Orseau, S., N. A. Zorrilla, N. Huybrechts, S. Lesourd, and A. Gardel (2020), "Decadal-scale morphological evolution of a muddy open coast," Marine Geology Volume 420

Shi, W., and M. Wang, (2010) "Characterization of global ocean turbidity from Moderate Resolution Imaging Spectroradiometer ocean color observations," J. of Geophysical Research, vol. 115, C11

Winterwerp, C., R.F. de Graaff, J. Groeneweg, NS A.P. Luijendijk, (2007) "Modelling of wave damping at Guyana mud coast," Coastal Engineering, Volume 54, Issue 3

Zorrilla, N., Vincent Vantrepotte, Erwan Gensac, Nicolas Huybrechts, and A. Gardel, (2018) "The Advantages of Landsat 8-OLI-Derived Suspended Particulate Matter Maps for Monitoring the Subtidal Extension of Amazonian Coastal Mud Banks (French Guiana)," Remote Sens. 2018, 10, 1733;

The Yarmouth23 Sailing Blog: Sailing to Paramaribo Suriname, posted August 20, 2012

ENVIRONMENTAL STRAIN ON BEACH ENVIRONMENTS RETRIEVED AND MONITORED BY SPACE-BORNE SYNTHETIC APERTURE RADAR

V. Di Biase[1], R. Hanssen[2]

[1]Technische Universiteit Delft - Faculty of Civil Engineering and Geosciences; 2628 CN Delft / 2600 GA Delft, The Netherlands; v.dibiase@tudelft.nl;

[2]Technische Universiteit Delft - Faculty of Civil Engineering and Geosciences; 2628 CN Delft / 2600 GA Delft, The Netherlands; r.f.hanssen@tudelft.nl;

Abstract – Anthropogenic activities and climate change impose a significant risk on coastal environments, with severe ecological, economical and societal consequences. But how exactly do more intense storms, precipitation, or environmental phenomena affect beaches? Currently, there is a lack of knowledge on causal empirical relationships between these phenomena, due to a lack of observations and models. In the present study, we explore the potential of new satellite radar observations to monitor coastal environments in order to understand mechanisms, prevent damages and improve safety and security. If successful, this could be applied for any coasts in the world.

Keywords: Synthetic aperture radar, Coastal environment, Weather phenomena.

1. INTRODUCTION

How exactly do more intense storms, precipitation and tidal condition affect beaches? The aim of this work, which is part of a collaboration between the Technische Universiteit Delft and Mitsubishi Electric Corporation, is -for the first time- answering to this question by performing an extensive analysis of coastal areas at a high spatiotemporal resolution using remote sensing (RS) instruments.

Continuous monitoring of the coastal area, including its topographic and morphological state, is of great importance for a better understanding and to implement protection strategies able to adapt to climate change (Benveniste et al., 2019). RS provides a unique ability to monitor and map coastal areas with complete, repeated, and frequent coverage of the Earth's surface. The innovative aspect of the presented study is the exploitation of RS data on a beach environment.

2. SCIENTIFIC BACKGROUND

Among the newest satellite remote sensing systems, Synthetic Aperture Radar (SAR) provides continuous and all-weather monitoring (independent of cloud cover) over the entire world with daily repetition. In recent years, many studies demonstrated the advantage of using SAR for the estimation of soil surface characteristics, such as surface roughness and soil moisture (Gorrab et al., 2015). A further advantage of the use of SAR systems for understanding of the beach environment and aeolian transport, is the possibility to provide knowledge of the characteristics of wind fields over both the ocean and the littoral zones with high spatial resolution (Huang et al., 2017).

3. OBJECTIVES

We intend to gain insight into the potential of SAR data for the retrieval and monitoring of soil properties over a sandy area, to establish a causal empirical relationship between the SAR amplitude and wind, precipitation, tidal condition.

4. METHODOLOGY

The present study has been performed on the beach of Noordwijk, located on the central Dutch coastline, and it has been carried out by using Sentinel-1 images. The dataset, provided in Interferometric Wide (IW) swath mode, consists in Level-1 Single-Look Complex (SLC) products, VH and VV polarization, with six-days temporal resolution. The selected acquisition orbit was descending, parallel to the coastline, to ensure good coverage of the interested area (Figure 1). Information regarding wind condition (speed and direction), precipitation accumulation and tide level at the time of the satellite pass during the 2-years corresponding to the SAR dataset were collected. Three masks have been selected on the study area: (i) the city area, which has been particularly relevant for the analysis of the sensor noise; (ii) the beach area, affected by tidal and weather phenomena; (iii) the shallow sea area, which has been particularly relevant for the analysis of the wind conditions. SAR data have been pre-processed and co-registered, then compared to ancillary data as local weather and environmental conditions. Dedicated codes have been implemented in order to understand the relationship between the SAR backscatter (in terms of amplitude) and the considered phenomena in the three different masks. The obtained results have been validated on the beach of Yokoshiba-Hikari, located in the Chiba Prefecture on the Japanese coastline.
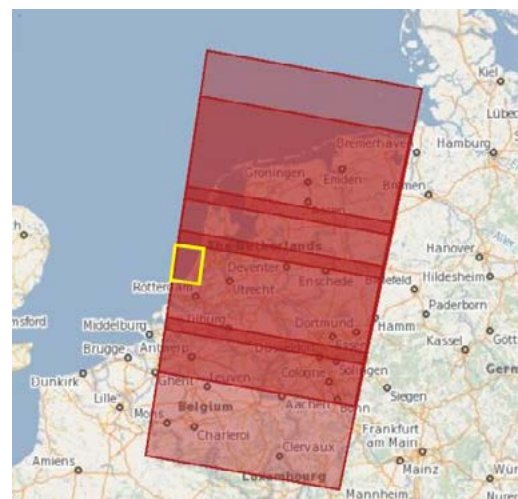

Figure 1: *Sentinel-1 descending orbit track over the Netherlands*

5. RESULTS

The most relevant result is an existing correlation between the amplitude evaluated on the sandy area and wind intensity. Polarizations VH and VV show a significant correlation with the wind intensity on the beach area, where the correlation

factors are $r = 0.51$ and $r = 0.59$ respectively. In general, high wind intensity is associated with high amplitude values. The distribution of wind intensity is associated to low or high amplitude depending on the wind direction (Figure 2). It is interesting to notice how the correlation factor increases or decreases when focusing the analysis to specific wind direction. Figure 3 shows how the correlation factor has the highest value of 0.75 for wind direction −45°- 45°and the minimum value of 0.24 for wind direction 45°-135°.

This correlation, particularly relevant for the beach mask, is more evident in the sea mask where the highest correlation occurs for both polarizations (correlation factor $r = 0.62$ for VH and $r = 0.72$ for VV). As expected, in the city area there is no correlation between the wind (both speed and intensity) and the SAR amplitude.

The rain conditions were also taken into consideration, considering the precipitation accumulation on the beach of Noordwijk at the moment of the satellite pass over the 2-years, and no particular correlation or trend of the amplitude could be noticed in this analysis.

The sensitivity analysis of the amplitude signal to the tidal condition, which is connected to the sensitivity of the amplitude to the soil moisture, has been carried out considering transects of the beach parallel to the coastline in the intertidal area. Both polarizations show a decreasing trend of the amplitude along the transects, moving from the dry area of the beach towards the sea. The correlation coefficient between the amplitude and the tide level gets negative with the increase of the water content along the transects. The results of the validation study performed on the Japanese beach, are consistent with the study performed in the Netherlands.

This analysis can be further investigated in order to find whether it is possible to retrieve a calibration between the amplitude and the wind speed, depending on the wind direction, the beach orientation and the satellite orbit characteristics.
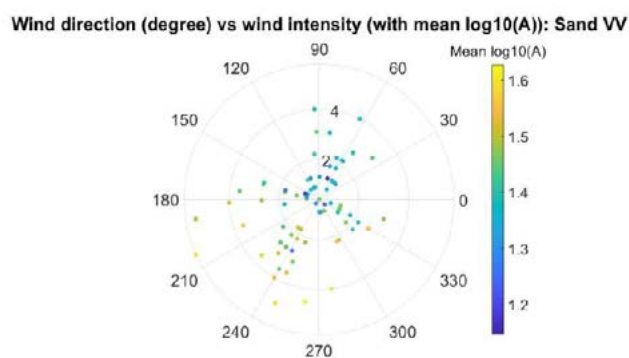

Figure 2. *Scatter plot of the wind direction (degree, 0° = Nord; 90° = East) versus wind intensity (m/s) at the time of the satellite acquisitions on the beach of Noordwijk (NL). SAR amplitude (VV polarization), in logarithmic scale, retrieved on the study area in the sand mask is represented in the colorbar. The distribution of wind intensity is associated to low or high amplitude depending on the wind direction. For some wind angles (eg. 210°–240°), the dependence of the amplitude on the wind is more considerable.*
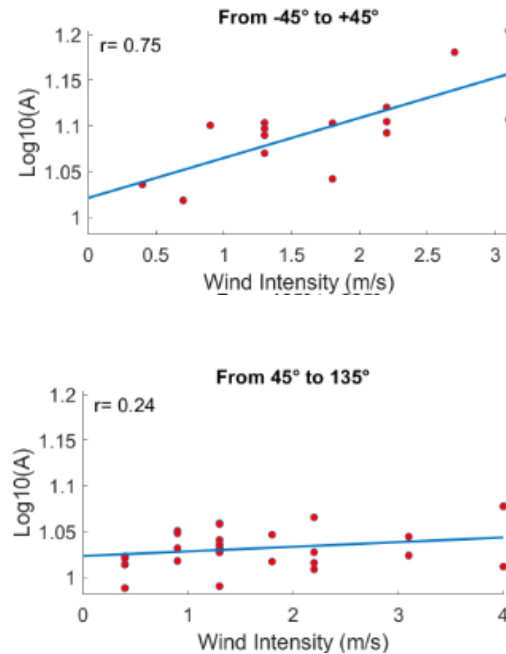

Figure 3: *Noordwijk beach (NL), analysis of the relation between local wind intensity and SAR amplitude in VH polarization. Top: for wind direction (-45° - 45°) the analysis shows an high correlation factor (r = 0.75); Bottom: for wind direction (45°- 135°), the correlation factor results lower (r = 0.22).*

6. CONCLUSION

The present study shows the potential of SAR data to monitor coastal environments, with the main purpose of understanding to what extent can SAR data detect its characteristics in terms of weather and environmental conditions. The results of this innovative study, conducted on a controlled environment, can be deeply investigated and world-wide extended, thanks to the global coverage of SAR dataset. This will ensure a real time monitoring of beach areas, including remote locations or areas not easily accessible to man, in order to prevent damages and improve safety and security.

REFERENCES

Benveniste, J., Cazenave, A., Vignudelli, S., Fenoglio-Marc, L., Shah, R., Almar, R., Andersen, O.B., Birol, F., Bonnefond, P., Bouffard, J., et al. 2019. Requirements for a coastal hazards observing system. Frontiersin Marine Science 6, 348.

Gorrab, A., Zribi, M., Baghdadi, N., Mougenot, B., Chabaane, Z.L. 2015. Potential of X-band TerraSAR-X and COSMO-SkyMed SAR data for the assessment of physical soil parameters. Remote Sensing, 7(1), 747-766.

Huang, L., Liu, B., Li, X., Zhang, Z., Yu, W. 2017. Technical evaluation of Sentinel-1 IW mode cross-pol radar backscattering from the ocean surface in moderate wind condition. Remote Sensing, 9(8), 854.

SESSION 8

SEA LEVEL

'Contemporary sea level rise from global to local scales'

Anny Cazenave

Laboratoire d'Etudes en Géophysique et Océanographie Spatiales, Toulouse, France

Abstract – Sea-level variations spread over a very broad spectrum of spatial and temporal scales as a result of complex processes occurring in the Earth System in response to natural climate variability, as well as to external forcing due to natural phenomena and anthropogenic factors. Here we address contemporary sea-level changes, focusing on the satellite altimetry era (since the early 1990s) for which various observing system from space and in situ allow precise monitoring of sea level variations as well as improved understanding of the sea level components. We summarize the most recent results on observed global and regional sea level changes and on associated causes, and briefly address new challenges encountered in measuring coastal sea level variations using satellite altimetry.

Keywords: Sea Level, Satellite Altimetry, Climate, Global Warming.

1. INTRODUCTION

Sea level is one of the best indicators of current climate change. Indeed, sea level variations result from changes in the different compartments of the Earth's climate system in response to internal climate variability, as well as natural and anthropogenic forcings. These include the contribution of ocean warming, melting of land ice, and changes in water storage in continental river basins.

During the 20th century, tide gauges were the only technique allowing direct observations of sea level variations. Tide gauges measure the relative variations of sea level with respect to the crust, thus vertical movements of the crust are also recorded by tide gauges. Although, coverage of in situ measurements is limited to continental coasts and islands, tide gauge records are highly valuable for estimating the evolution of the mean sea level over the past decades. The most recent studies indicate that between 1900 and 1990, sea level rose by about 15 cm on average. For nearly 30 years, climate -related sea level variations are routinely measured at global and regional scales by the constellation of high-precision satellite altimetry missions: Topex/Poseidon, Janson-1, 2 and 3, Saral/AltiKa, ERS-1 &2, Envisat and Sentinel-3A & B and Sentinel-6. Unlike tide gauges that also record crustal motions, satellite altimetry only measures absolute sea level variations.

2. GLOBAL MEAN SEA LEVEL RISE

Since January 1993 the altimetry-based global mean sea level has risen on average at a rate of 3.3 +/- 0.4 mm per year. This corresponds to an average elevation of 10 cm over the last 30 years (Cazenave and Moreira, 2022; Fig.1). What is most striking is the marked acceleration of the phenomenon. Between 1993 and 2002, sea level rise was around 2.1 mm per year. Since 2013, the rate of rise has exceeded 4 mm per year.
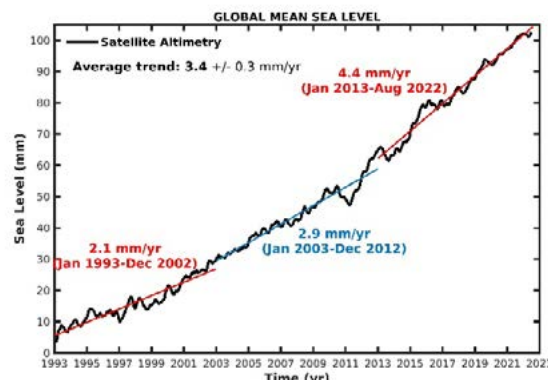

Fig.1: Global mean sea level measured by high precision altimeter satellites between January 1993 and August 2022 (adapted from Cazenave and Moreira, 2022).

The two main causes of present-day global mean sea level rise are ocean warming via thermal expansion of seawater, and melting of continental ice (glaciers, Greenland and Antarctica), in response to anthropogenic greenhouse gas emissions. We now have at our disposal different observing systems allowing us to quantify these different contributions (e.g., Horwath et al., 2022). The international Argo network of about 4000 automatic floats provides ocean temperature and salinity measurements down to 2000 m depth, with near global coverage. In addition, the GRACE space gravimetry mission launched in 2002 measures mass changes in the Earth system, including the loss of ice mass in Greenland and Antarctica. Other space techniques such as radar interferometry and radar and laser altimetry are also used to estimate ice mass losses from the polar ice sheets. Fig. 2 shows the different contributions to the global mean sea level rise and compares their sum to the observed sea level since 2005 (Barnoud et al., 2021). W can note that the global mean sea level budget is almost closed within the data uncertainties.

Fig.2: Global mean sea level budget over 2005-2018 (adapted from Barnoud et al., 2021).

3. REGIONAL AND LOCAL SEA LEVEL CHANGES

The global coverage of altimeter satellites allows estimating the rate of sea level change everywhere over the oceanic domain. This is illustrated in Fig.3 that shows regional trends in sea level over 1993-2021. Fig.3 indicates that the rate of sea level change is not uniform. In some regions, sea level rose about twice as fast as the global mean (e.g., in the western tropical Pacific). This mostly results from the non-uniform thermal expansion of seawater, some regions storing more heat than others in response to redistributions of heat by the ocean circulation and direct exchanges with the atmosphere. In some regions (e.g., in the Arctic), variations in salinity also play an important role.
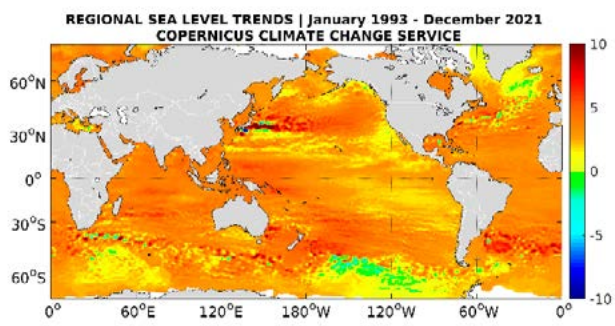

Fig.3: Regional sea level trends over 1993-2021 based on multi-satellite altimetry missions (data from the Copernicus Climate Change Service)

At local scales, particularly in coastal areas, small-scale processes superimpose the components of global mean sea level and its regional variability. These phenomena include small-scale coastal currents, as well as the influx of fresh water in river estuaries which modifies the sea water density, and therefore sea level near the coast. Changes in wind and wave intensity, depth of the continental shelf, and sediment stocks along the coasts can also modify sea level variations in nearshore areas relative to the open ocean. Unlike the global and regional sea level measured by altimetry missions, sea level variations in coastal areas are still poorly known and thus understood. Coastal areas are in fact heavily under-sampled by tide gauges and conventional altimetry missions poorly perform in a band on 15 km around the world coastlines due to the contamination of land surfaces in the radar signal. However, recent dedicated reprocessing of classical altimetry data in the world coastal zones now makes it possible to estimate the sea level variations very close to the coast (Benveniste et al., 2020, Cazenave et al., 2022). Fig. 4 shows three examples of coastal sea level trends expressed as a function of distance to the coast, as a result of such reprocessing We note it is now possible to retrieve valid sea level data very close to the coast. Different situations are observed in Fig.4, i.e., coastal sea level trend can be similar, faster or slower than in the open ocean, depending on site location.
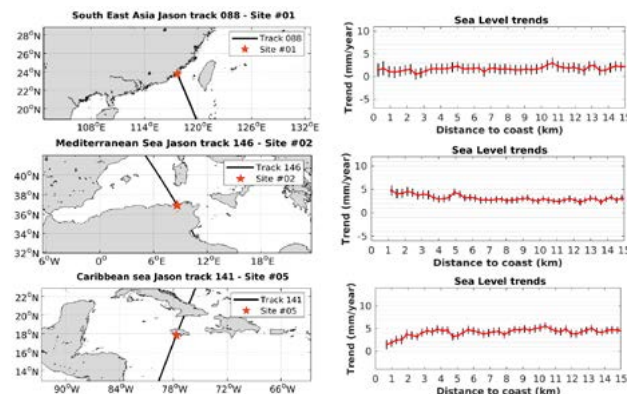

Fig.4: Examples of coastal sea level trends computed over 2002-2020 expressed as a function of distance to the coast along the Jason satellite tracks (adapted from Cazenave et al., 2022).

4. CONCLUSION

Sea level is a major indicator of current climate change. For that purpose, it needs to be accurately monitored on the long term by satellite altimetry. Besides, new altimetry technologies implemented on recent ESA missions (e.g., Sentinel-3A-B) and on Sentinel-6, as well as on the future SWOT mission scheduled for launch end 2022, will make it possible to systematically estimate changes in sea level as close as possible to the coast, with quasi global coverage. Such observations will be of major interest for adaptation to sea level rise, in particular in low-lying coastal regions of the planet where more than 10% of the world's population currently lives.

REFERENCES

Cazenave A. and Moreira L., Contemporary sea level changes from global to local scales: a review, Proc. Royal Society, 478: 20220049. https://doi.org/10.1098/rspa.2022.0049, 2022.

Cazenave A. et al., Sea level along the world's coastlines can be measured by a network of virtual altimetry stations, Nature Communitations, Earth & Environment, 3, 117, https://doi.org/10.1038/s43247-022-00448-z2022, 2022.

Horwath M., et al., Global sea level budget and ocean mass budget, with focus on advanced data products and uncertainty characterization. Earth System Science Data, 14, 411–447, 2022 https://doi.org/10.5194/essd-14-411-2022, 2022.

Barnoud A. et al., including Cazenave A., Contributions of altimetry and Argo to non-closure of the global mean sea level budget since 2016, published online 26 June 2021, Geophys. Res. Lett., https://doi.org/10.1029/2021GL092824, 2021.

Benveniste J. et al., Coastal sea level anomalies and associated trends 2 from Jason satellite altimetry over 2002-2018, *Nature Scientific Data*, 7, 357, https://doi.org/10.1038/s41597-020-00694-w, 2020.

Sea level change in estuarine and coastal water level from high resolution altimetry

L. Fenoglio *

University of Bonn, Bonn, Germany

Abstract

The dynamics of estuaries and coastal zone is affected by a strong variability of the water level at various temporal and spatial scales due to the interaction of different water bodies, be river, tributaries, groundwater and sea, and phenomena, like river discharge, tide, waves, surges and sea level rise. The freshwater discharge to the coast is a fundamental component of global water cycle and impacts sea level on a broad range of spatial and temporal scales. Here, both long-term and extremes water level and discharge are investigated over the years 2010-2022 in the Elbe tidal river. Hamburg city, estuary and coast are covered by the analysis, which uses enhanced quality SAR altimeter data, model simulations and in-situ data. Links to management and policy, as well as economic aspects, are also considered,

Keywords: Symposium, Program, Scientific Themes.

1. INTRODUCTION

Regional models for coastal sea and estuaries reproduce hydrodynamics, mixing, sediment dynamics, morphodynamics, water quality, and nutrient and contaminant transport (Staneva et al., 2009, 2018; Klingbeil et al., 2018, Stanev et al., 2016, Pein et al., 2018). Dynamic effects of salt intrusion on sediments are investigated with semi-analytical models (Wei et al., 2017) and high-resolution unstructured grid (Stanev et al., 2019) three-dimensional models, including impacts of climate change in the last. While models can be quite accurate even on small estuarine scales, in-situ data are missing at global scale to validate and constrain the models. Today the key physical and biogeochemical processes are understood, but not their interplay and gross effect under changing climate and anthropogenic pressure conditions. Of greatest interest are the interactions between tide and streamflow, and the spatial distribution of the hydrodynamic variations, salinity fronts and water mixing and, over long time scales, the effect of coastal sea level rise on the estuary.

This study aims at bringing together remote sensing, oceanography and hydrology topics in the estuary region to disentangle estuarine and coastal processes and their interaction. Our hypothesis is that new altimetry remote sensing observations from the Delay Doppler and wide-swath technique have the potential to make an unprecedented progress at (1) monitoring the river-to-ocean continuum and (2) understanding estuarine and coastal hydrodynamic processes.

The first novelty lies in the Delay Doppler, available since 2010. This new technique of processing altimeter data is also called also SAR altimetry. The second novelty is the wide-swath altimetry sensors, firstly on-board the SWOT mission in late 2022. The challenge is to combine space-base, in-situ and model observations of surface water elevation (SWE)

with a double goal: first to by assess the reliability of space-based new SWE and then to merge the SWE and derive and interpret the space-time variability of the denser field. SWOT swath data at 2 km resolution is on a fixed lat-lon grid, so can be used for time series analysis directly. The "expert" product at 250 m resolution is on the native grid that can vary by +/- 1 km around the nominal groundtrack position.

Our first scientific goal is to study processes of tidal mixing, storm surges and salt water intrusions and the interaction of tide and discharge in the sea/estuary/river environments. Second goal is to understand the observed signals and their errors for an optimal synergy of data and models. We aim at a high-grade analysis of coastal and estuarine dynamics based on superior level of information from space combined with in-situ coastal observations and greater wealth of processes in the coastal and estuarine models that consider explicitly the land boundary condition (including, thus, the linkage to the emerged coast).

Overall goal is the detection of long-term and extreme variation in water level and discharge occurring in the interval 2010-2022 in estuarine and coastal zone by using enhanced space altimeter data. Secondary goal is the understanding of the possible limitations of both nadir and swath altimeter data with implication towards future altimeter mission planning.
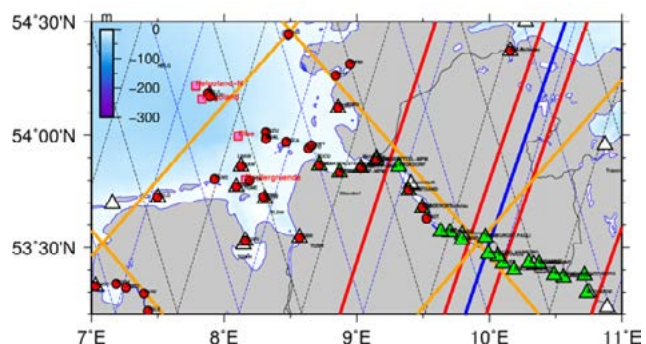

Figure 1. Region of study with S3, S6 and SWOT 1-day track and tide gauges

2. DATA AND METHODOLOGY

Water level and wave heights, physical and water quality parameters are measured in in-situ campaigns and simulated in models with regular and unstructured grids, like the BSHmodel, NEMO-WAM, the Geesthacht Coupled Ocean Model System 3D (GCOAST-SCHISM). Hourly simulations include strong variabilities in river discharge. Fig. 2 shows results from SCHISM. Shorter scenario runs of coastal sea level are considered. For the observational part, a multi-mission along-Track altimeter database in SAR mode for German Bight and Estuaries has been built for the missions CryoSat-2, Sentinel-3 and Sentinel-6. The data are from both unfocused SAR, SARin, Migration Correction (RMC-SAR) and Fully Focused SAR (FF-SAR) processing. Most of the processors are running at the ESA Network of Resources,

included the in-house TUDaBo SAR processor. The STARS processor, developed within the HYDROCOASTAL ESA funded project, is running at the University of Bonn. The quality of geophysical parameters range, wave height and wind are evaluated against in-situ and model data provided by the model runs. New in this study is the use of Delay Doppler altimetry Fully Focus processing and the preparation for the exploitation of the future SWOT altimeter data.
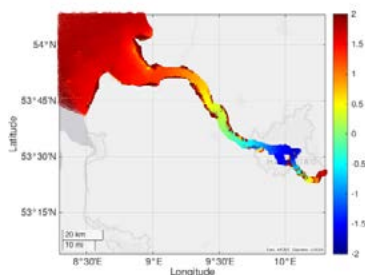

Fig. 2: The High resolution (10 m to 400 m) GCOAST SCHISM 3D baroclinic unstructured grid model

3. RESULTS

The statistics of the difference between altimetry and in-situ includes standard deviation differences (STDD) and correlation. The water level estimated by five retrackers is compared to 19 in-situ stations along the German Bight and South-eastern Baltic coasts. The median of the STDD is smaller than 20 cm for most retrackers, with best agreement with SAMOSA+ on Sentinel-3 data, the second best with STARS on CryoSat-2. Fig. 2 gives the results in a boxplot.
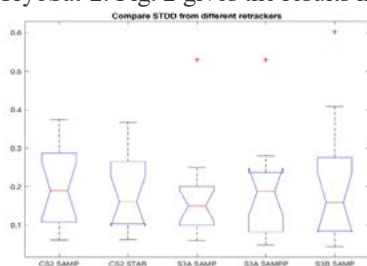

Fig. 3 : Costal Zone, Boxplot od STDD at 19 TG stations and altimetry on coasts of German Bight and South-eastern Baltic

In the estuarine region, the statistics of the difference between time-series is in terms of standard deviation differences (STDD) and correlation. Firstly in-situ and models and after simulated SWOT data and model are compared. In Table 1 the STDD between in-situ and model is larger than 40 cm. The difference arises partly from the error simulated. SWOT observations were simulated using the JPL ocean simulator for the 1-day cal/val phase with input the HR SCHISM model, the error of the observation was simulated and added to the model. The output was in a 2 km by 2 km grid. Fig.4 show the STDD, with larger errors at the edge of the swath.
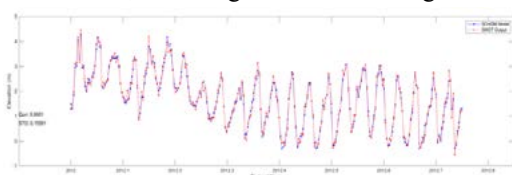

Fig. 4: SWOT simulated and model data at the upstream station Geerstacht Wehr, tide is affected by discharge
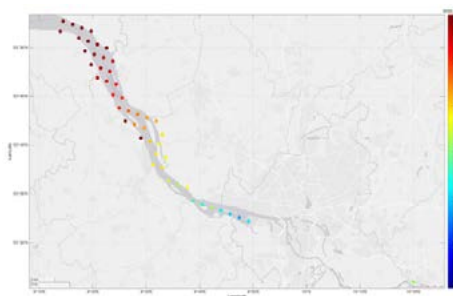

Fig. 5: SWOT observations simulated by JPL ocean simulator for 1-day cal/val and SWOT error added to model.

Table 1. Statistics difference between in-situ data SCHISM

	Dist (LR)	Corr (LR)	Stdd (LR)	Dist (HR)	Corr (HR)	Stdd (HR)
Blankenese	0.089	0.957	0.611	0.027	0.834	0.710
Brünsbüttel	0.120	0.934	0.464	0.100	0.861	0.545
Cuxhaven	0.105	0.950	0.397	0.171	0.884	0.535
Glückstadt	0.136	0.950	0.498	0.110	0.867	0.535
Nok_Brünsbüttel	1.017	-0.01	1.291	1.022	-0.145	1.054
Ottendorf	0.045	0.947	0.409	-	-	-
Schulau	0.102	0.962	0.560	0.015	0.834	0.681
GeestWehr	-	-	-	0.0345	0.813	0.663
Geesthacht				2.425	0.413	1.039

.4. DISCUSSION

First results show large differences between in-situ and model data. This could be due to diffences between water level along the estuary, in addition to the contamination of altimeters. This need to be studied using other models.

5. CONCLUSION

The aim of coupled coastal modelling systems is to monitor and forecast the ocean dynamics in coastal areas. The potential of wide-swath altimetry for ocean analysis and forecasting is under investigation considering synthetic observations for both along-track altimeters and SWOT. A set of Observing System Simulation Experiments (OSSEs) can investigate the contribution of SWOT data to the GCOAST ocean analysis and forecasting. A fundamental step of the experimental design is the characterization of the wide-swath measurements errors to improve the definition of the error covariance required to combine SWOT data and the ocean modelling system. Another aspect is the development of improved SWOT product (water level and discharge)

REFERENCES

Klingbeil, K., Lemarié, F., Debreu, L., & Burchard, H. (2018). The numerics of hydrostatic structured-grid coastal ocean models: State of the art and future perspectives. Ocean Modelling, 125, 80–105.

Laignel, B., N. Ayoub, F. Birol, S. Brown, Y. Chao, B. Cornuelle, S. Costa, P. De Mey, C. Estournel, F. Feddersen, S. Giddings, S. Gille, A. Kurapov, F. Lyard, R. Morrow, M. Simard, T. Strub, I. Turki (2015). Issues and SWOT contribution in the coastal zones and estuaries. White Paper, Science Definition Team SWOT

Stanev, E. V., Schulz-Stellenfleth, J., **Staneva, J**., Grayek, S., Grashorn, S., Behrens, A., Koch, W., and Pein, J. (2016): Ocean forecasting for the German Bight: from regional to coastal scales, Ocean Sci., 12, 1105-1136. doi.org/10.5194/os-12-1105-2016

Sea level variability on interannual, decadal and longer time scales along the Tropical Atlantic

Franck Eitel Kemgang Ghomsi[1,2], Roshin P. Raj[3], Mathieu Rouault[1], Issufo Halo[4]

[1]Nansen Tutu Center for Marine Environmental research, Department of Oceanography, University of Cape Town, 7701, South Africa.
[2]Geodesy Research Laboratory, National Institute of Cartography, P.O. Domain 157, Yaoundé, Cameroon.
[3]Nansen Environmental and Remote Sensing Center, and Bjerknes Center for Climate Research, Bergen, Norway.
[4]Oceans and Coasts Research, Department of Forestry, Fisheries and the Environment, Private Bag X4390, Cape Town 8000, South Africa.

Abstract – Sea Level Variability in the eastern equatorial Atlantic are subject to variability on interannual timescales. During the last 20 years, this variability has shown comparatively high activity along coastal areas. In late 2010, the warmest event in the satellite observation period developed leading to a continuous increase in sea level along the Gulf of Guinea. Analysis suggests that the thermosteric in the western equatorial Atlantic is dominating the steric contribution.

Keywords: Gulf of Guinea, Sea level, Decadal.

1. INTRODUCTION

The tropical Atlantic Ocean is a key area for the advection of heat from the warm water sphere into the North Atlantic Ocean. Through the Atlantic Meridional Overturning Circulation (AMOC) (Buckley and Marshall, 2016), upper ocean heat is transferred from both hemispheres into the North Atlantic Ocean (Chen and Tung, 2018; Zhang et al., 2019). Before entering the northern subtropics, heat advection is impacted by the complex recirculation system and climate variability of the tropical Atlantic Ocean (Zebiak, 1993; Stramma et al., 2005; Chang et al., 2008). This, in turn, is known to trigger regional to large-scale weather and climate patterns (Rodwell and Folland, 2002), and can induce variations in water mass characteristics, and regional sea level patterns at various timescales from sub-seasonal to multi-decadal periods (Dieng et al., 2015). Regional changes in sea level differ significantly from global mean changes. The global mean clearly shows the imprint of anthropogenic effects, whereas regional patterns appear to be largely caused by natural variability (Stammer et al. 2013). As a result, variability conceals the trend contribution made by both anthropogenic and natural factors at interannual to decadal scales. Regional sea level changes on interannual timescales are mostly driven by the steric component (Cazenave and Llovel 2010), except for some shallow or semi-enclosed and deep extratropical areas (Piecuch et al. 2013) where the bottom signal pressure acts. To gain insight into sea level variability and distinguish between anthropogenic and natural processes, it is critical to detect related processes. Steric (thermosteric, halosteric) sea level relates to heat and freshwater changes, circulation and wave-driven redistribution, and freshwater intake from land ice melt and river runoff and plays a substantial role in the overall trend and variability (Llovel et al., 2010). Despite major advances in science for the tropical Atlantic, there remain major gaps in the knowledge of origins of regional sea level patterns, particularly for the Gulf of Guinea. In this analysis, we have used the synergy of remote sensing and in-situ observations as well as data from an ocean reanalysis to further shed light on contemporary regional sea-level changes in the tropical Atlantic Ocean.

2. Data and Methods

The study area encompasses the entire tropical Atlantic Ocean since the tropical Atlantic area is an interconnected system via the subtropical cells (Fig. 1).
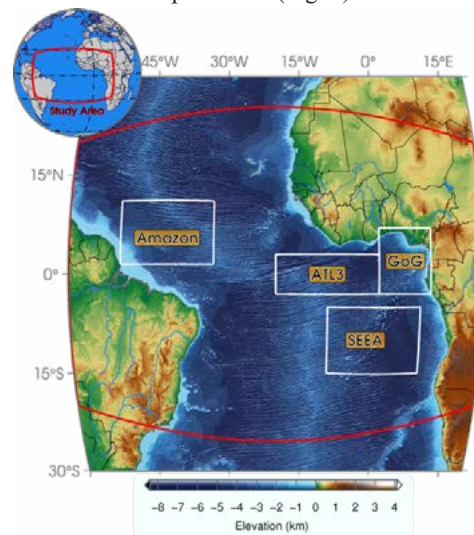

Figure 1. Study area for the analysis of interannual sea-level variations in the tropical Atlantic Ocean. The main study area encompasses the entire tropical Atlantic from between 15°S-15°N and 60°W-20°E. Four subdivisions (white domain lines) have been defined to specifically analyze the impact of know climate variations, i.e. Atlantic 3 Domain (ATL3, 20°W–0°, 3°S–3°N), the South Eastern Equatorial Atlantic domain (SEEA, 15°S–5°S, 10°W–8°E); "GoG" domain (0°-10°, 3°S-7°N) and "Amazon" domain (50°W–32°W, 1.5°N-11°N).

We have further subdivided the area into four domains (see Fig. 1 for more details) to attribute changes to regional (river outflow, regional air-sea interaction) and large-scale patterns (tropical Atlantic climate variability, climate change, long-term circulation changes). The "Amazon" domain is chosen to analyze the impact of the Amazon River inflow and a major pathway of the upper limb of the AMOC (e.g., Foltz et al. 2019), while the location of the domains ATL3 and SEEA is based on the specific track of the impact of tropical Atlantic climate variability modes on sea level variations (e.g., Brandt et al., 2011, Goiveia et al., 2019). The domain "GoG" is chosen to study regional aspects in the Gulf of Guinea. The methodology used followed a two-step analysis. The first step build on a comparison of detrended interannual sea level to major climate modes. We have chosen four climatic modes: the Tropical Northern Atlantic (TNA); the Tropical Southern Atlantic (TSA); the Atlantic Multidecadal Oscillation (AMO) and the North Atlantic Tropical (NAT) indexes (Enfield et al., 1997; Chang et al., 1997; Enfield et al., 2001). These indexes have been downloaded through the Ocean Observations Panel for Climate web portal (OOPC, https://stateoftheocean.osmc.noaa.gov/). In the second step,

regional sea level change has been further analyzed for the entire study area, as well as for the different domain subdivisions (see Fig. 1). The time series of average sea level estimates across the tropical Atlantic for the period from January 2005 to December 2016 was estimated after eliminating the annual and semiannual cycles. In addition, as we are seeking an assessment of the interannual variations in our estimate, in order to mitigate high-frequency (short-term) fluctuations, a three-month moving window is applied to the resulting curve.

3. Results and Discussion

The analysis involved making use of two major approaches, such as the impact of major tropical Atlantic climate variability modes, and in-depth analysis of interannual variations of steric regional sea level in the study area. For the first task, we have compared the area averaged sea level variations in the four domain subdivisions. The glacial isostatic adjustment correction of -0.3mm/yr has been applied to the sea level observations, and the annual, and semi-annual signals have been removed (Peltier, 2004; Spada, 2017).

An increase in sea level has been observed in the Atl3 (3.02 mm/yr), the Gulf of Guinea (3.82 mm/yr), and the SEEA (3.49 mm/yr) regions with an overall sea level trend in the tropical Atlantic of 2.95 mm/year (Fig. 2).
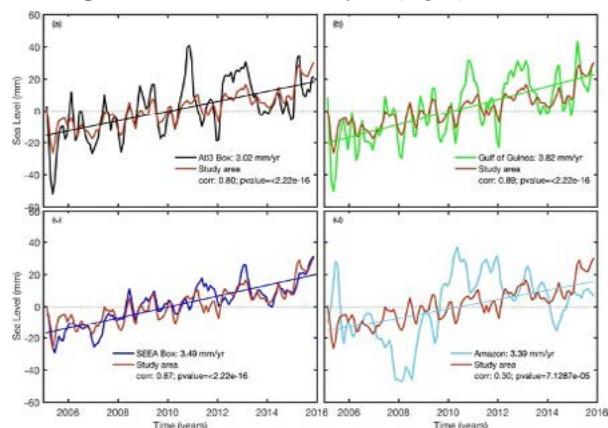

Figure 2: Mean Sea level trend from satellite altimetry for a) Atl3, b) GoG, c) SEEA, d) Amazon domain overlain by Tropical Atlantic trend.

Without a representative slope (positive or negative), the Amazon basin has a trend of 3.39 mm/yr, thus highlighting a possible air-sea interaction process related to a basin-wide mode, mainly the Atlantic Niño mode. The sea level of the Amazon domain shows potentially high variability due to the freshwater influx from the Amazon basin. Visually the trend of the Amazon domain seems lower than of the ATL3 area due to the high variability within the Amazon domain. This observation seems to be contradictory in both cases, but in one case (the west), we have an increase in density, and in the east, we have a compensation of density.

In the second part of our analysis, we have addressed the impact of halosteric and thermosteric changes on regional sea level patterns. Contemporary regional sea level trends in our study area can reach up to 3.39 and 3.82 mm/yr in the Amazon and Gulf of Guinea regions, respectively (Fig. 2). To further evaluate the regional sea level patterns, we have evaluated the thermosteric and halosteric contributions in the different domain subdivisions (see Fig. 1 on details for the domain subdivisions). An example of the area-averaged thermosteric and halosteric sea level variations are shown in Fig. 3, respectively for the Gulf of Guinea domain. The

results show that interannual variations dominate the time series. Since the year 2012 however, there is a steady increase observed in both the thermosteric and halosteric component and reaches values of up 3.04 mm/yr in the year 2016. All products used for the evaluation show similar results, as indicated in the narrow-spread values in Fig. 3.

Figure 3. Time series of components of the sea-level budget (mm) for the upper 700 m, over the Gulf of Guinea.

Our results for the other domain subdivisions show that in the interior northern equatorial Atlantic, a similar pattern
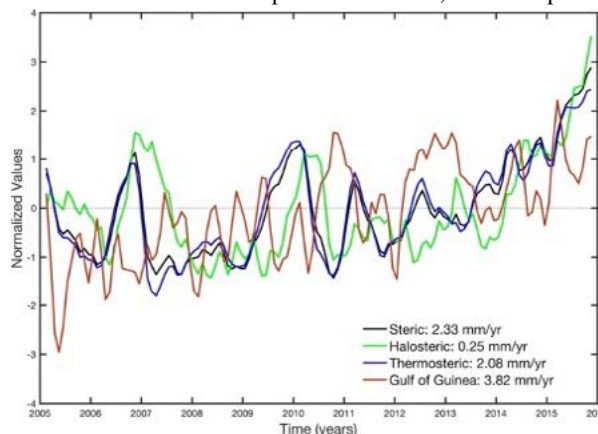
can be observed for both thermosteric and halosteric sea level (not shown), indicating that this regional sea-level variation might be connected to a large-scale pattern of change. However, further evaluations are needed to understand the forcing of this change, and whether this variation can be attributed to climate variability or an emerging long-term trend from climate change. The various contributors to the budget of sea-level change in the Gulf of Guinea from CMEMS data are shown in Fig. 3. Time-series of mean sea-level (red curve) anomalies in the Gulf of Guinea closely follow the steric sea-level (SSL) (black curve). We observed that the sea- level rise in the Gulf of Guinea trend is dominated by the SSL, which is a combination of thermosteric and halosteric components. Further, the time series of sea level and SSL show an acceleration since 2013 along with the acceleration of both thermosteric and halosteric components (Fig. 3). This instigates us to verify possible contributions from thermosteric and halosteric components for the long-term period 2005–2016 and the recent period 2011–2016.

3. CONCLUSION

The sea level variability in the GoG coast is likely to be affected by several small-scale processes arising from the presence of a river estuary, the depth of the continental shelf, and its morphology. As a result, coastal sea levels can be significantly different from open sea level on a wide range of time scales. An overall increase of steric component is well observed with the 2010 Atlantic Zonal Mode anomalous peak recorded.

REFERENCES

Abraham, J.P., Baringer, M., Bindoff, N.L., Boyer, T., Cheng, L.J., Church, J.A., Conroy, J.L., Domingues, C.M., Fasullo, J.T., Gilson, J. and Goni, G., 2013. A review of global ocean temperature observations: Implications for ocean heat content estimates and climate change. Reviews of Geophysics, 51(3), 450-483.

Chen, X. and Tung, K.K., 2018. Global surface warming enhanced by weak Atlantic overturning circulation. Nature, 559(7714), 387-391.

ESA Cryo-TEMPO project: Arctic Sea level variability during the past decade

R. P. Raj [1,*], O. B. Andersen[2], S. K. Rose[2], H. Regan[1], A. Bonaduce[1] S. Hendricks[3], D. Brockley[4], J. Xie[1]

[1]Nansen Environmental and Remote Sensing Center and Bjerknes Center for Climate Research, Bergen, Norway
[2]DTU Space - National Space Institute. Geodesy and Earth Observation (GEO), Denmark
[3]Alfred-Wegener-Institut, Bremerhaven, Germany
[4]University College London, London, England

Abstract – The Arctic Ocean (AO) has experienced rapid climate change in recent decades in comparison to the rest of the globe. Monitoring the sea level of the AO, a key climate change indicator is thus very important, even though the retrieval of precise satellite derived sea level measurements in the region is challenging. The Cryo-TEMPO project of the European Space Agency (ESA) brings together a team of radar altimetry scientific experts and software engineers, to generate state-of-the-art thematic data products. In here, we report the preliminary findings obtained from the reprocessed Arctic sea level data from the CryoSat mission.

Keywords: Arctic Ocean, sea level rise, CryoSat, Beaufort Gyre, CMIP6

1. INTRODUCTION

Sea level rise (SLR), that has a wide range of economic and social consequences is also a key climate indicator which integrates the response of different components of the earth's system to natural and anthropogenic forcing. A recent study (Horwath et al., 2021) has shown a rapid increase in the global mean sea level (GMSL; 3.05 ± 0.24 mm/yr) during 1993-2016, the trend contributed mainly by the mass (57%) and steric changes (38%). Notably, the GMSL rise is faster during the recent decade (2003-2016; 3.64 ± 0.26 mm/yr) and is attributed due to the increase in the mass contribution (61%), the largest contribution from Greenland Ice melt.

In addition to monitoring GMSL, it is also important to investigate and understand regional sea level variability. Regional sea level changes important for coastal ecosystems, infrastructure, and coastal population, differ from GMSL both in terms of magnitude as well as governing mechanisms. Understanding the relevant underlying mechanisms related to regional sea level change is the key to reduce uncertainties and skillfully project SLR. However, since several processes relevant for sea level are not properly represented in climate models (Church et al., 2013), it is a challenge for making accurate regional sea level projections. Here, we focus on the Arctic Sea level variability since the region has experienced the most rapid climate change impacts in the entire globe during the recent decades. The warming of the Arctic has been three times faster than the rest of the globe, and the thermal expansion associated with it together with the accelerated glacier and ice sheet melting influence the sea level. Our study using the state-of-the-art altimeter data and TOPAZ ocean reanalysis aims to investigate the sea level variability of the Arctic Ocean during the past decade.

2. Newly reprocessed Cryosat altimeter data

ESA's Cryo-TEMPO project brings together a team of radar altimetry scientific experts and software engineers, to generate agile and state-of-the-art thematic data products. In this study, we use data from the Phase 1 Polar Ocean (PO) Theme. This data set contains CryoSat data from

the SAR and SARIn modes, and it is processed with a Threshold First Maximum Retracker Algorithm (TFMRA), adjusted to the polar ocean studies. The Cryo-TEMPO-oriented TFMRA retracker is implemented after Ricker et al. (2014). The output from Cryo-TEMPO PO Theme is the along-track sea level anomalies w.r.t. DTU15 Mean Sea Surface and the dynamic ocean topography (Figure 1) w.r.t. the OCMOG geoid.
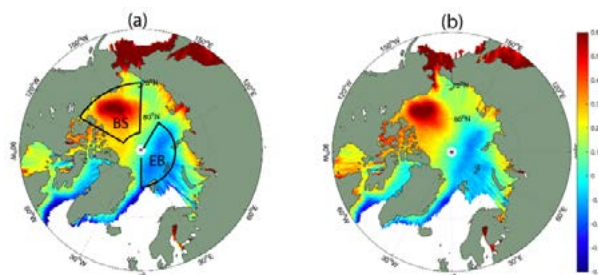

Figure 1. *Mean (bin average) absolute dynamic topography (in meter) in every 1-degree longitude and 0.5-degree latitude bins in the Arctic Ocean during: (a) 2016; (b) 2019. The black frames represent the Beaufort Sea (BS) and the Eurasian Basin (EB) domains.*
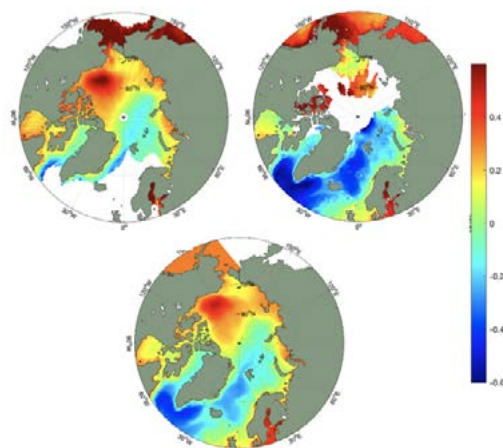
3. TOPAZ ocean reanalysis data

Figure 2. Winter (DJF) *Climatology (2010-2021) of absolute dynamic topography (m): (upper left) Cryo-Tempo data; (upper right) CMEMS data; (bottom panel) TOPAZ*

The new version of the TOPAZ4 reanalysis is based on the HYbrid Coordinate Ocean Model (HYCOM), with 50 hybrid z-isopycnal layers at a horizontal resolution of 12 to 16 km in the Arctic and ensemble Kalman filter data assimilation. TOPAZ4 represents the Arctic component of the Copernicus Marine Environment Monitoring Service (CMEMS) and is forced by ERA5 reanalysis. It assimilates observations such as including along-track altimetry data, sea surface temperatures, sea ice concentrations and sea ice drift from satellites along with in situ temperature and salinity profiles. The good comparison of the TOPAZ reanalysis data with the

* Corresponding author. Address: Jahnebakken 3, N-5007, Bergen, Norway. Email: roshin.raj@nersc.no

CryoTempo data is shown in Figure 2. TOPAZ reanalysis is further used to study the thermosteric and halosteric variability of the Arctic during the CryoSat time-period (2010-2021).

4. Sea level variability in the Arctic

The newly reprocessed CryoSat altimeter data reproduces all main circulation features of the Arctic (Figure 1). The Beaufort Sea (BS) and the Eurasian Basin (EB) are characterized respectively by high and low sea level, difference between them reaching up to 1.0 m. The spatial pattern and ADT gradients also indicate precise positioning of the transpolar drift stream in the Arctic. A main noticeable improvement in the new Cryo-TEMPO data in comparison to other altimeter data (e.g., CMEMS data; Figure 2) is the significant improvement in the retrieval of altimeter data in the central Arctic, thereby reducing the "polar gap", a well-known issue associated with the estimation of altimeter derived sea level in the Arctic. The gradient in sea level between the BS and EB is also found to be less in the Cryo-Tempo data and is much closer to the TOPAZ ocean reanalysis (Figure 2). Further analysis of the monthly and interannual variability of the sea level variability of the BS and EB shows an increasing trend during the past decade (2011-2020), the trend more prominent after 2017.
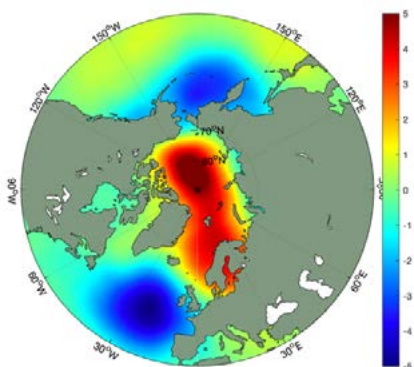

Figure 3. *Regression of mean sea level pressure anomalies on the sea level variability in the Beaufort Sea. The regression relates SLP anomalies in hpa to BS sea level anomalies in cm (location shown in Figure 1).*

The regression analysis shows the prevalence of high-pressure system over the BS in association with high sea level of the region (Figure 3). The composite analysis of the extreme (± 1 STD of the mean) high and low sea level anomalies over the BS also found respectively extreme high and low SLP anomalies over the BS during the two extreme conditions. This is in line with the finding that during an anticyclonic circulation regime, i.e., when high SLP prevails, the Beaufort Gyre (BG) located in the BS accumulates fresh water (FW) through: the increase of ice thickness and area; ice accumulation due to convergence and ridging; and increased river runoff (Proshutinsky et al., 2002), all of which also result in an increase in dynamic height of the region.

Next, we analyze the interannual variability in the spatial extent of the BG (Figure 4), that has been known to significantly regulate the Arctic climate variability. In a previous study, Regan et al. (2019) showed a northwestward expansion of the gyre during the time-period 2003-2014. Our analysis during the CryoSat era (2011-2020) using the methodology detailed in Regan et al. (2019), showed that the westward expansion is no longer evident after 2016. On the contrary, the spatial extent of the gyre during the past decade is the lowest in 2020.
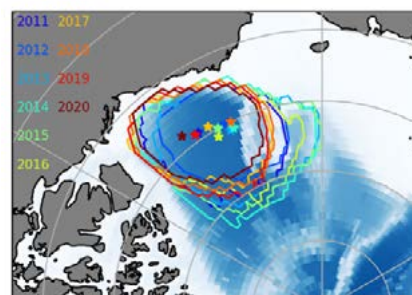

Figure 4. *Interannual variability in the spatial extent of the Beaufort Gyre. The star symbol indicates the center location of the BG.*

The Cryo-TEMPO data is also used for assessing the performance of climate models in reproducing the AO sea level. The 10 climate models selected are ACCESS-CM2, ACCESS-ESM, CMCC-CM2-HR4, CMCC-CM2-SR5, EC-Earth3-Veg-LR, MPI-ESM-1-2-HAM, MPI-ESM-1-2-HR, NorESM2-LM, NorESM2-MM, and IPSL-CM6A-LR. Preliminary analysis found that in comparison to individual model results, their ensemble-mean better reproduce the spatial circulation features of the Arctic.

5. Summary

The Arctic Ocean has experienced rapid climate during the recent decades and thus monitoring its sea level change, a key climate change indicator, is a priority. The Cryo-TEMPO is a recent initiative of ESA, one of its aims is to retrieve state-of-the-art sea level data in the Arctic. Preliminary results showed improved spatial data coverage in the central Arctic thereby significantly reducing the polar gap. The new data reproduced all main circulation features of the Arctic. Notably the sea level gradient between the BS and EB is found to be consistent with that estimated from TOPAZ ocean reanalysis data. Our analysis reiterates the role of large-scale atmospheric circulation on BS sea level variability. Further analysis also found distinct interannual variability in the spatial extent of the BG. Cryo-TEMPO data is also used to assess the performance of climate models in reproducing the AO sea level change.

REFERENCES

Church, J. A., et al. (2013). Sea level change. In T. F. Stocker, et al. (Eds.), In: *Climate change 2013: The physical science basis. Contribution of working group I to the fifth assessment Report of the intergov- ernmental Panel on climate change'*. Cambridge University Press, Cambridge, United Kingdom.

Horwath, M. et al., (2021). 'Global sea-level budget and ocean-mass budget, with focus on advanced data products and uncertainty characterisation', Earth Syst. Sci. Data.

Proshutinsky, A., et al. (2002). 'The role of the Beaufort Gyre in Arctic climate variability: Seasonal to decadal climate scales'. *Geophys. Res. Lett.*, **29**(23), 2100.

Ricker, R et al. (2014). 'Sensitivity of CryoSat-2 Arctic sea-ice freeboard and thickness on radar-waveform interpretation'. Cryosphere, 8, 1607–1622.

Regan, H. et al. (2019) 'The Beaufort Gyre extent, shape, and location between 2003 and 2014 from satellite observations'. J. Geophys. Res. Oceans, 124, 844–862.

Sea Level Change in the Mediterranean Sea from Satellite Altimetry and Tide Gauge

F. De Biasio[1] [*] and S. Vignudelli[2]

National Research Council of Italy, [1] Institute of Polar Sciences, Venice, Italy, [2] Institute of Biophysics, Pisa, Italy

Abstract – We present a refined method to obtain optimal estimates (in the Ordinary Least Squares OLS sense) of linear sea level change rates at selected coastal locations by the synergistic use of satellite altimetry and tide gauge observations. The method, successfully tested in the Northern Adriatic Sea (De Biasio et al., 2020), is now applied to the Mediterranean Sea. Based on previous works of Kuo et al. (2008) and Wöppelmann and Marcos (2012), it extends the observation periods to almost three decades, thanks to the gridded satellite altimetry dataset made available by the Copernicus Climate Change Service of the European Union, and tries to overcome a technical limitation of their method which mined its application to the most general case.

Keywords: Sea Level Rise, Satellite Altimetry, Tide Gauge, Mediterranean Sea, Linear Inverse Problem.
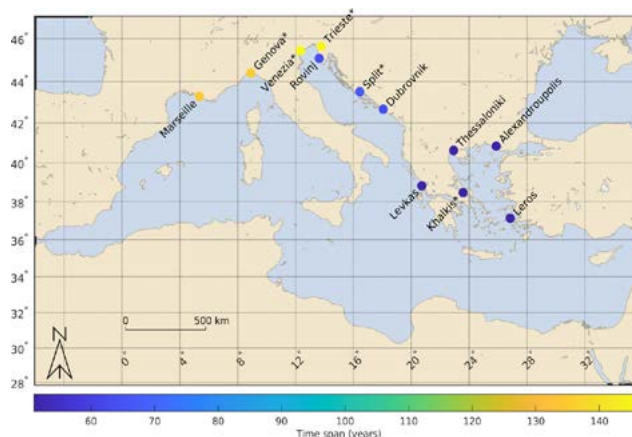
Figure 1. *Geographical position of the tide gauges used in this study. Colors indicate the time extension, in years, of the monthly mean time series of relative sea level height at the corresponding tide gauge.*

1. INTRODUCTION

Estimating sea level change in coastal regions has become an essential step in intercepting potential problems for coastal settlements exposed to flooding and to project sea level along the coasts into a short- or medium-term sea level rise scenario. Investigation of this topic requires high quality absolute and relative sea level height data. The difference of absolute sea level height observations, provided by satellite altimetry, and relative sea level height measurements, traditionally offered by tide gauges, gives the vertical land motion (VLM), i.e. the absolute vertical movement of the ground beneath the tide gauges with respect to the terrestrial reference frame. Such a movements are directly observed by global positioning system (GPS) devices.

The relationship between satellite-derived absolute sea level change rates and tide gauge observations of relative sea level change with respect to direct vertical land motion observations was first investigated by Cazenave et al. (1999). An improved method of deriving vertical land motion from satellite altimetry and tide gauges, based on the linear inverse problem approach, was proposed by Kuo et al., (2004), and refined by Wöppelmann and Marcos (2012).

Other studies made use also of GPS measurements of vertical land motion in addition to tide gauge and satellite altimetry data, highlighting the difficulty of deriving spatially consistent information on the sea level rates at regional scale.

Recently, De Biasio et al., (2020) applied the approach to a few tide gauges in the Adriatic Sea. The novelty of the study is the attempt to overcome the limitation of the Kuo method to extend it to the general case. The approach, tested in the Adriatic Sea, has been extended to the Mediterranean Sea, and major findings will be presented at the "Oceans From Space 2020" conference. Figure 1 shows the geographical position of the tide gauges used in this study, as well as the extension, in years, of their time series, as derived from the Permanent Service of Mean Sea Level (PSMSL), National Oceanographic Centre, Liverpool, UK, https://www.psmsl.org/).

The motivation of this study is that industrial areas are widely spread along the littoral zone of the southern Europe, and residential settlements are densely scattered along the coasts of the Mediterranean Sea. Not least, a strongly rooted seaside tourism is one of the main economic resources of the region, which is particularly exposed to the sea level variability of both natural and anthropogenic origin. A well-known example of such a exposition is Venice (northern Italy) which has been recently hit by the second-highest tide in recorded history (November 2019), and is now protected against storm surges by the MOSE barrier, almost fully operational since October 2020. Therefore, a re-analysis of the actual sea level rates with novel methodologies that take into account a better usage of all available observations is key to understand the future coastal sea level changes and their relative importance.

2. METHODS

Consistent long-term satellite-based datasets of absolute sea level height exist nowadays to study sea level variability, globally and at regional scales. Among them, that released by the European Copernicus Climate Change Service (C3S) is suitable for climate-related studies. The regional dataset for the Mediterranean Sea consists of daily gridded sea level anomaly observations updated to the present time with spatial resolution of 0.125° x 0.125° and is obtained by merging data from all the available satellite altimetry missions but relying only on a simultaneous couple of them at a time, to provide stable long-term variability estimates of sea level.

Relative sea level height observations are traditionally provided by tide gauges. A vast collection of monthly mean time series of tide gauge observations is maintained at PSMSL (Holgate et al., 2013). Other tide gauge observations have been obtained by the Centro Previsioni e Segnalazioni Maree (CPSM) of the Venice Municipality, as well as from

---

the Italian Institute for Environmental Protection and Research (ISPRA), for checking and integrating the Venice Lagoon tide gauge data.

VLM trends have been acquired from the Système d'Observation du Niveau des Eaux Littorales (SONEL) Data Centre and the Nevada Geodetic Laboratory (NGL). In some cases, mainly the Venice Lagoon region, direct observations of GPS devices have been processed and used in this study.

The rate of absolute vertical land motion $\dot{u}$ at tide gauge i is given by the difference between the absolute and relative sea level change rates at the same place, respectively $\dot{g}$ and $\dot{s}$, as estimated by satellite altimetry and tide gauge observations:

$$\dot{u_\imath} = \dot{g_\imath} - \dot{s_\imath}$$

The formula for N of such tide gauges is easily put in matrix form, but the N unknown VLM rates remain mutually independent, and are affected by large errors due to the interannual and decadal sea level variability. Kuo et al. (2004) proposed a more elaborate linear system, in which constraints formed by the differenced time series of TGs over longer time periods (>40 yr) pose strong limits to the magnitude of the final errors. Such constraints are introduced in matrix form with a series of Lagrange multipliers. The resultant linear system is easily inverted, and the unknown VLMs determined. Such methodology is known as the solution of the linear inverse problem (Menke, 1989).

However, the method proposed by Kuo et al. and Wöppelmann and Marcos is inherently affected by the mandatory requirement that the absolute sea level changes are the same at each tide gauge: such a requirement undermines the applicability of the method when different absolute sea level trends are observed in different regions. In our treatment, it is bypassed with a change of variable, leading to the possibility of applying the method to the general case. This study focuses on the Mediterranean Sea.

3. RESULTS

The usefulness of the Kuo's method is the significant reduction of VLM trend errors, due to the introduction of specific constraints on the sea levels observed by pairs of tide gauges. These constraints on the one hand limit the final errors, thanks to the relationship between the sea levels observed by pairs of tide gauges over much longer periods, on the other hand they constrain the errors themselves to be the smallest, as a result of a OLS procedure, namely the inversion of the linear inverse problem. As an example, the VLM rates measured by direct subtraction of the absolute and relative sea level change rates (second column) at each tide gauge considered here (first column), as well as VLM calculated with the refined method proposed in this study (third column), are shown in Table 1.

4. CONCLUSION

As can be seen in Table 1, the estimation of the errors on the VLM rates with the method proposed here are significantly lower than those calculated by subtracting the relative sea level change rates from the absolute ones in the traditional way. VLM rates estimated with this method can be used to infer the absolute sea level change rates at the selected tide gauges, over a longer period than the satellite altimetry era (1993-2020), and with lower inherent errors. The results of this study, as well as the comparison with direct observations of VLM performed by GPS stations near some of the selected tide gauges will be shown at the conference.

Table 1. Comparison of VLM rates calculated with the traditional procedure and the method proposed in this study

TG	VLM (difference)	VLM (this study)
Marseille	-2.31±0.76	-1.77±0.54
Genova	+0.35±0.69	-0.19±0.54
Venezia	-3.47±0.93	-2.54±0.59
Trieste	-1.46±0.73	-1.36±0.57
Rovinj	+0.99±0.91	-0.53±0.55
Split	-0.76±1.34	-1.04±0.55
Dubrovnik	-3.05±2.14	-3.01±0.56
Levkas	-4.30±0.74	-3.57±0.67
Khalkis	+0.86±1.42	+1.73±0.69
Thessaloniki	-0.05±0.67	-0.42±0.59
Alexandroupolis	+0.63±0.95	+0.94±0.59
Leros	+3.16±0.93	+2.35±0.64

REFERENCES

De Biasio, F., Baldin, G. and Vignudelli. S., (2020). Revisiting Vertical Land Motion and Sea Level Trends in the Northeastern Adriatic Sea Using Satellite Altimetry and Tide Gauge Data. Journal of Marine Science and Engineering 8, no. 11: 949. doi:10.3390/jmse8110949.

Kuo, C.Y., Shum, C.K., Braun, A. and Mitrovica, J.X. (2004). Vertical crustal motion determined by satellite altimetry and tide gauge data in Fennoscandia. Geophys. Res. Lett., 31, doi:10.1029/2003GL019106.

Wöppelmann, G. and Marcos, M. (2012). Coastal sea level rise in southern Europe and the nonclimate contribution of vertical land motion. J. Geophys. Res. Ocean. 117, doi:10.1029/2011JC007469.

Cazenave, A., Dominh, K., Ponchaut, F., Soudarin, L., Cretaux, J.F. and Le Provost, C. (1999). Sea level changes from Topex-Poseidon altimetry and tide gauges, and vertical crustal motions from DORIS. Geophys. Res. Lett., 26, 2077–2080, doi:10.1029/1999GL900472.

Holgate, S.J., Matthews, A., Woodworth, P.L., Rickards, L.J., Tamisiea, M.E., Bradshaw, E., Foden, P.R., Gordon, K.M., Jevrejeva, S. and Pugh, J. (2013). New Data Systems and Products at the Permanent Service for Mean Sea Level. J. Coast. Res. 2013, 29, 493–504, doi:10.2112/JCOASTRES-D-12-00175.1.

Menke, W. (1989). Geophysical Data Analysis: Discrete Inverse Theory (1st ed., Vol. 45). Academic Press, Inc.

SESSION 9

SEA LEVEL RISE & COASTAL CITIES

Climate change, sea level rise, and the future of Venice

J. Gower*

Institute of Ocean Sciences, North Saanich, B.C., Canada

Abstract – A dam at the Strait of Gibraltar, together with much smaller construction at Suez, could stabilize Mediterranean and Black Sea level for all projected global sea level rise. The dam could be a loose rock structure, built by dumping rock from specially-designed ships. The volume of rock would be large (1.5 to 2 cubic km), but less than the annual volume of coal production, for example. Benefits would include preservation of all Mediterranean and Black Sea coasts and a land link between Europe and Africa.

Keywords: Sea level, Mediterranean, Venice.

1. INTRODUCTION

This paper aims to promote discussion of the idea of damming the Strait of Gibraltar, and controlling water inflow there and at Suez in such a way as to stabilize sea level in the Mediterranean and Black Seas. Technical details are given in Gower (2015). Venice appears doomed within 50 to 100 years unless the dam is built. The MOSE flood gates provide only short term protection for the city and will not protect against a long-term rise.

2. REACTION TO THE DAM IDEA

Of course, the Gibraltar dam would protect many thousands of km of Mediterranean and Black Sea coastline, and many cities. It is certainly feasible. It would lead to an increase in Mediterranean salinity, but this would be slow, at a rate of about 1psu per 100 years. Clearly this is one of the serious impacts which need to be evaluated in detail, but the numbers suggest that we should have about 500 years before effects become serious.

I have to note that the present, apparent exponential rise in sea level and temperature suggest 1m and 4C by 2100, respectively. I suspect that 4C of temperature rise will be causing more havoc than 1m of sea level rise, and affecting many more people. Still, I hope for more discussion of the dam.

One might call the idea of the dam "colonial" in that developed countries of the Mediterranean would protect themselves, but impose a hardship on island nations in the Pacific, among others. If the Mediterranean Sea level does not rise, the global rise rate will increase by 0.8%. This seems a relatively small fractional increase. If even microscopic rise is forbidden, then all flood protection becomes illegal, since water is always being diverted to somewhere else. In fact, the whole climate change problem is "colonial" in that developed countries have dumped their waste carbon dioxide into the atmosphere, causing hardship to all countries, including themselves. One conclusion might be that all nations should share the cost of the Gibraltar dam, In proportion to their past carbon emissions.

3. BENEFITS OF THE DAM

The Mediterranean is the only large area of sea which could be dammed in this way, with evaporation removing the water and water level being controlled by surface sluices. There is thus little danger that similar dams would proliferate.

The dam also requires lock gates on the Suez Canal, where flow has so far been left uncontrolled. This should be relatively easy, and has at least one other benefit. The increased flow due to canal widening has resulted in the Great Bitter Lakes losing their ability to stop species migration between the Indian Ocean and the Mediterranean. Lock gates would restore the isolation.

There is clearly some benefit from the dam in power generation, but the major benefit, after sea level control, might be in providing a land link between Europe and Africa.

4. CONCLUSION

I like the idea of walking the 30km from Spain to Africa along the top of the dam, stopping occasionally at cafes and restaurants. I hope the heavy road and rail traffic will not be too distracting. The sluices for sea level control will be interesting, as will the locks for shipping. I imagine there will be wind turbines. It would be a long day's walk, but interesting, and level except for bridges. I would walk back on the other side of the dam (the top would be several hundred metres wide), with a different view, in the other direction. One would not notice that the Mediterranean level is slightly lower than that of the Atlantic. We have to wonder how security against illegal immigration will be handled, but in the long term, the dam should help reduce the development gap between Africa and Europe.

REFERENCE

Gower, J. (2015). A sea surface height control dam at the Strait of Gibraltar. Natural Hazards, 78(3), 2109-2120. Httops://doi.org/10.1007/s11069-015-1821-8

* Corresponding author. Address: 1615 McTavish Rd, North Saanich, BC, Canada. Email: Jimgower1940@gmail.com.

Space technology to quantify coastline artificialization due to sea level rise in the Mediterranean. An alternative solution : maintaining the current level by damming the Strait of Gibraltar

A. Meinesz[1] and L. Bottin

CNRS ECOSEAS University Côte d'Azur, Nice France

Abstract - Against the inevitable and increasingly rapid sea level rise, more and more defence structures are being built,, leading to the artificialization of the coastline. The coastal environment is thus gradually degraded. The biotope of the small sandy and muddy bottoms of the shallow waters is thus profoundly modified into a hard substrate. This has a negative effect on all the benthic animal species that occupy this particular coastal biotope. For the Mediterranean, another solution would make it possible to keep the marine coastline in its current state while preserving it from any future submergence: the construction of a dam at Gibraltar (Gower 2015). Satellite monitoring of the evolution of the artificialisation of the coastline of the entire Mediterranean could be the decision-making tool for the construction of the dam. Indeed, as soon as the cost of all the flood defence constructions created locally and independently exceeds that of the dam, the Mediterranean riparian countries could be convinced of the need to better analyse this project.

Keywords : sea level rise, impacts, dam strait of Gibraltar

1. INTRODUCTION

Global climate change will lead to a rise in sea level that is estimated to increase to more than one meter in 78 years – (in 2100), See Figure 1, or 2,3 m with a low confidence percentile (IPCC 2021), but we do not know the maximum amplitude that will be reached when greenhouse gas levels are under control (16 m in 2300 with the worse prediction IPCC 2021). In the Mediterranean, the consequences of rising sea level will be catastrophic for all coastal populations, heritages and infrastructures.

The coastlines most at risk of dramatic flooding for human beings are the sandy coasts with low gradients. Although the sea level has only risen by 20 cm since the beginning of the industrial era, man has already begun to defend these coasts using a number of costly techniques with a temporary effect: building dikes parallel or perpendicular to the coast (see Figure 2), filling beaches by adding sand or pebbles, and even artificially closing off lagoons as in Venice. Given the predictions of more rapid and significant sea level rise, these efforts will increase on an unprecedented scale. This will lead to a catastrophic denaturation of a large part of the coastline by means of protective dikes made of rock or concrete (Meinesz 2021).

Marine biodiversity will be moderately affected by the rise in sea level. However, the sea defences could be particularly damaging to nearshore benthic marine life. While the new artificial rocky substrate may be suitable for fixed marine species, the muddy or sandy seabed at sea level is essential for many animal species that live below the surface or require this environment for the early stages of their life cycle. The concreting of the coastline will therefore systematically reduce this particular biotope.

A solution that seemed utopian in the past could prevent the systematic concreting of the 50,000 km of Mediterranean coastline: a dam at Gibraltar (25 km long) that would maintain the current level of Mediterranean waters regardless of the rise in ocean waters (Johnson 1997, Gower 2013, 2015).
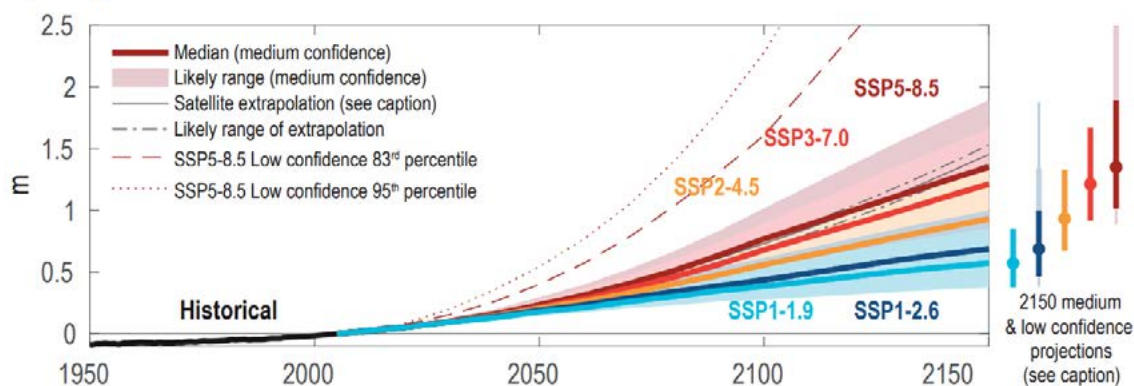

Figure 1. *Projected global mean sea level rise under different Shared Socio-economic Pathway (SSP) scenarios. (IPCC 2021)*

* Corresponding author. Address: Laboratoire CNRS UMR 7035 « ECOSEAS», University Côte d'Azur, Parc Valrose 06108 NICE Cedex 2, France. Email : meinesz@unice.fr

Figure 2 : *Examples of denaturation of the coastline of Mediterranean Sea to deal with flooding and sea level rise.*

This pharaonic project will only become a necessity when the existing flood defences are no longer effective, too expensive to build and, like the Danaides' jar, constantly need to be raised.

In this context, a precise monitoring of localized coastal defence initiatives for the whole Mediterranean coastline will be very useful to support political and economic decisions. With satellite images processed by suitable software, the structures built at sea level could be inventoried and measured (in linear meters) every year. Space technology could be useful both for recording and quantifying the efforts made to defend the coastline of the whole Mediterranean and for better predicting the tipping point where the total cost of protective structures will be higher than the construction of the dam. Gower (2015) estimated that for a one metre rise in sea level, the cost of multiple coastal defence structures will reach nearly 150 billion Euros, whereas he estimated the cost of the dam at 50 billion Euros.

In front of the French Mediterranean coasts (2100 km) a continuous surveillance of the structures built on the sea is already in place thanks to the images provided by Google Earth (www.medam.org). 1050 artificial structures (> 100 m²) have been inventoried (harbours, platforms, artificial beaches, whose exterior protections (193 km) (which will have to be raised, as well as all inland quays in ports); 432 groins perpendicular to the coast have been built to prevent beach erosion and 145 dykes (>10 m) parallel and in contact with the sea level (30 km in total) have been inventoried. The construction of these dykes will become exponential in the next few years to cope with the sea level rise.

Ecological reasons will certainly be put forward against the construction of the Gibraltar dam such as the potential variation of salinity or the need to create exchange corridors for a small number of migratory animal species (Atlantic-Mediterranean). These difficulties could be overcome. More importantly, the positive effects of the Gibraltar dam should be taken into account: no more impact of artificial hard substrate structures on the sandy-muddy ecosystems of the shallow waters and much less invasion of exotic species from the Red Sea, because with the dam, locks will have to be established in the Suez Canal. This will significantly reduce the migratory flow of exotic species to the Mediterranean. For the environment, the construction of the dam will undoubtedly avoid the concreteization of the coastline, which otherwise would certainly be denounced more and more each year by all the inhabitants

The same principle (safeguarding coastal assets and environment against future sea level rise) is planned for the northern European seas (Channel, North Sea and Baltic): the Northern European Enclosure Dam (with a dam of 161 km between Britany -France - and Cornwall (UK), a dam of 145 km between Scotland and Shetland and another of 331 km between Shetland and Norway.

2. CONCLUSION

The solution of the Gibraltar dam to keep the sea level in the Mediterranean at the same level as now was utopian until recently. But all the forecasts concerning the rapid and significant rise in sea level should prepare us to better study and consider its construction. It is also clear that the faster the political and economic decision, the less damage will be caused by defense structure on the coastline. The commitment will certainly be better accepted and validated thanks to the accurate data from space technologies that will allow, on the scale of the entire Mediterranean, year after year, to observe and quantify the vain independent and localised efforts of the cities and regions of the 23 countries bordering it to defend themselves against the rise of the sea level.

REFERENCES

Gower, J., (2013). The case for a sea-surface-height control barrage on the strait of Gibraltar. Rapp. Comm. int. Mer Médit., 40.

Gower, J. 2015. A sea surface height control dam at the Strait of Gibraltar. Nat Hazards Nat Hazards. DOI 10.1007/s11069-015-1821-8.

Groeskamp, S. and Kjellsson, J. (2020). NEED : The Northern European Enclosure Dam for if the climate Change mitigation Fails. Bulletin of the American Meteorological Society, 101(11) Doi.org/10.1175/BAMS-D-19-0145.1, pp. E1174-E1189.

IPCC (2021). Climate Change 2021: The Physical Science Basis. Sixth Assessment Report. Working Group 1, Chapter 9: Ocean, Cryosphere and Sea Level Change1-152.

Johnson, R.G., 1997. Climate Control Requires a Dam at the Strait of Gibraltar. Eos, 78 (27, 277-284.Meinesz, A. (2021) Protéger la biodiversité marine. Ed. Odile Jacob, Paris, 304 pp.

Venice and Acqua Alta in the Perspective of Climate Change

Georg Umgiesser

ISMAR-CNR, Venice, Italy

Abstract – The city of Venice will be strongly impacted by the ongoing climate change and especially by sea level rise that will endanger its survival during this century. Measures have been put in place to defend against the high water events (lime the ongoing construction of the mobile gates), but eventually sea level rise could make these works obsolete.

Keywords: Venice, storm surge, climate change.

1. Introduction

The Adriatic Sea, to the East of Italy, is an elongated basin enclosed between the Italian peninsula and the Balkan countries. Its shape, long and narrow, the bordering orography and the frequent sirocco (southeast) wind, together with the bathymetry distribution, leads to frequent storm surges in its northern part. While the whole coast of the Northern Adriatic is affected, unavoidably the international attention is focused on the consequent flooding of Venice. There are good reasons for this. Beside its unique urban structure and its historical and artistic relevance, the floor of the town is, in some parts, barely more than 0.8 m above the present mean sea level. With a spring tidal excursion of around one meter, any positive variation of the undisturbed sea level creates the conditions for a flooding.

2. Venice and Climate Change

The Venice Lagoon was in the past subjected to profound changes and environmental engineering. Rivers have been deviated, inlets have been fortified, channels have been created or existing ones have been dredged, industries have settled inside the lagoon, new islands have been constructed, and fishing farms have been isolated from the lagoon. Moreover, ground water was extracted from the underground, resulting in anthropogenic subsidence. All these interventions are signs of human pressure on the environment and have contributed to create a situation where flooding events are more and more frequent.

Granted that the possibility of a severe flooding existed also in the past (order of 100 years), the situation has worsened mainly because of two reasons. The first is the sinking of the town due to natural (3 cm) and anthropogenic (9 cm) subsidence in the 20th century, the latter due to local water extraction from the underground aquifers in the period 1930-1960 (Carbognin et al., 2004). The second reason is the sea level rise that has been estimated in the 20th century at 11-13 cm (Tsimplis et al., 2011). Estimates for the 21st century given in the last IPCC reports are much worse, with a reasonable average of 50 cm at the end of the century.

In the last years the works for the mobile barriers (MOSE) have been started that should protect the city of Venice from flooding. After the devastating high water event of November 2019 (Fig. 1) the works have accelerated and their completion is now anticipated to be in 2024. These barriers will be closed at a safeguarding level of 110 cm, a level when large parts of Venice will start to be flooded. In the last years this would have led to around 10-20 closing per year. A precise water level forecast will be crucial for the correct operation of the MOSE gates.

With the new estimates of sea level rise this closing frequency will change. Depending on the exact modality of the forecast, with a sea level rise of 50 cm the gates will have to be closed between 300 and 400 times a year (Umgiesser and Matticchio, 2006; Umgiesser, 2020). This translates to about one closure per day in the average.

Figure 1. *The day after the high water event of the 12th of Noivember, 2019.*

3. Conclusions

Other implications of this situation still have to be evaluated. It seems, however, quite impossible that both the MOSE structures and the ecosystem of the lagoon will be able to handle this closing frequency. Other solutions will have to be studied that will be more compatible with the future. A total closure of the Venice lagoon is certainly one of these options.

REFERENCES

Carbognin, L., Teatini, P., and Tosi, L. (2004). Eustacy and land subsidence in the Venice Lagoon at the beginning of the new millennium, J. Mar. Syst., 51, 345–353, 2004.

Tsimplis, M., Spada, G., Marcos, M., Flemming, N. (2011). Multi-decadal sea level trends and land movements in the Mediterranean Sea with estimates of factors perturbing tide gauge data and cumulative uncertainties. Global and Planetary Change, 76 (1). 63-76.

Umgiesser, G. and B. Matticchio (2006). Simulating the mobile barrier (MOSE) operation in the Venice Lagoon, Italy: Global sea level rise and its implication for navigation. Ocean Dynamics, Vol. 56, 320-332.

Umgiesser, G. (2020). The impact of operating the mobile barriers in Venice (MOSE) under climate change, J. Nat. Conserv., 54, 125783,

SESSION 10

CLOSING SESSION

Imaging spectroscopy for inland and coastal waters: research and applications with PRISMA

C. Giardino[1, *], M. Bresciani[1], A. Fabbretto[1], A. Pellegrino[1], S. Mangano[1], F. Braga[2], G. M. Scarpa[2], V. E. Brando[3]

1 Institute of Electromagnetic Sensing of the Environment - National Research Council of Italy (CNR-IREA) Milan , Italy
2 Institute of Marine Sciences - National Research Council (CNR-ISMAR), 30122 Venice, Italy
3 Institute of Marine Sciences, National Research Council of Italy (CNR-ISMAR), 00133 Rome, Italy

Abstract – This contribution presents research efforts developed in the last few years with PRISMA (PRecursore IperSpettrale della Missione Applicativa) funded by the Italian Space Agency, to demonstrate the benefit of spaceborne imaging spectroscopy in aquatic applications. The presented activities, which also incorporate contributions from the scientific community, embrace the satellite mission description, the evaluation of PRISMA products for their specific use in water quality applications, hence covering the challenges of atmospheric corrections and algorithms development/testing. Examples of water quality mapping for several aquatic ecosystems, encompassing from deep-clear to turbid-productive lakes, river dammed reservoirs and coal waters, distributed globally are then provided to support the use of current and future hyperspectral satellite missions, also in synergy with multi-spectral remote sensing.

Keywords: Lakes, Coastal zone, Hyperspectral, Satellite.

1. INTRODUCTION

Inland and coastal water ecosystems are environmentally essential, provide multiple eco-system services and are vital for human consumption, irrigation, sanitation, transportation, recreation and industry. In the past decades, these ecosystems have skilled high stress from various human impacts as well as climate change. Among them, the increasing eutrophication and pollution of many of these environments are major ecological threats.

There is an increasing need for regular monitoring of inland and coastal waters to support national and international directives and conventions such as the European Water Framework Directive, the US Clean Water Act & Safe Drinking Water Act and the Australian Reef Water Quality Protection Plan, requiring biological, hydro-morphological and physico-chemical parameters of water bodies to be monitored on a regular basis. Information on the state and development of water bodies is also a prerequisite to meet the United Nations Sustainable Development Goal No. 6 to "ensure availability and sustainable management of water and sanitation for all" by 2020.

Earth Observation (EO) may be used for acquiring timely, frequent synoptic information, from local to global scales, of inland and coastal waters. EO based measurements of physical and biochemical parameters in these waters mainly rely on the interpretation of the spectral reflectance, which is used to retrieve water components, water depth and bottom properties. EO data have been successfully applied for mapping inland and coastal (e.g., Odermatt et al., 2012; Palmer et al., 2015; Dekker, 2021).

To date, most of the applications developed for inland water quality monitoring and management have been based on multispectral and mid (e.g., Landsat constellation, Sentinel-2-MSI) to coarse (e.g., ENVISAT-MERIS, Sentinel-3-OLCI) spatial resolution satellites. With respect to spaceborne observations, following the launch of Hyperion which was followed a few years later by Chris-PROBA and HICO, a new generation of spaceborne hyperspectral sensors (e.g., PRISMA, GaoFen-5, DESIS, HISUI), is now available for improving water resources monitoring, while future missions are also under development (e.g., EnMap, CHIME, SBG). Accordingly, this study aims to present the exploitation of data gathered from currently orbiting spaceborne imaging spectrometer, PRecursore IperSpettrale della Missione Applicativa (PRISMA).

2. PRISMA Mission

PRISMA, a mission fully funded by the Italian Space Agency (ASI), is an EO system with innovative, electro-optical instrumentation that combines a hyperspectral sensor with a medium-resolution panchromatic camera (Coppo et al., 2020). The PRISMA orbit is characterized by a repeat cycle of approximately 29 days. The PRISMA payload is composed by an imaging spectrometer, able to take images at 30 m resolution in a continuum of spectral bands ranging from 400 to 2500 nm, and a 5 m resolution panchromatic camera. The PRISMA system provides the capability to acquire, downlink and archive images of all hyperspectral/panchromatic channels totaling 200,000 km^2 daily over the primary area of interest defined as: longitude in the range 180∘ W–180∘ E; Latitude: in the range 70∘ S–70∘ N. Although the revisit time in nadir-looking configuration is of 29 days, the system is capable of acquiring images distant 1000 km in a single pass (with a total rotation left to right side looking and vice versa) so that the temporal resolution can be significantly improved.

3. MAPPING AQUATIC SYSTEMS WITH PRISMA

For the purposes of this study, a set of PRISMA images have been explored over different inland and coastal water systems globally as shown in true-color composites in Figure 1. We have selected the case studies in order to include both coastal marine waters and lakes of different trophic status, turbidity levels, depth profiles and different hydrogeochemical and ecological processes.

According to Giardino et al. (2020) the radiometric radiances of PRISMA have adequate characteristic of water

---

analysis application. Respect to the reflectances data, according to Braga et al. (2022), for the inland and coastal waters with high magnitude reflectances signal (e.g. turbid waters) the L2D data provided by ASI is adequate to retrieve water quality parameters; for very transparency waters we have applied others atmospheric corrections (e.g. 6Sv, ATCOR) because L2D have problems to well correct the signal in the blue region.
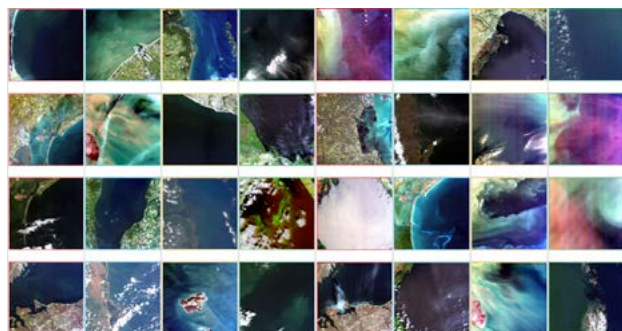

Figure 1. *True-color composites of PRISMA images of aquatic systems.*

PRISMA data corrected for the atmospheric effects were then turned into aquatic ecosystems products by inverting a bio-optical modelling to both map water quality parameters and bottom types while, vegetation indexes, were used to estimate the macrophyte biomass (Bresciani et al., 2022). In particular, the bio-optical model used in this study is similar to previously published case-2 water models, where water reflectance is depending on concentrations of water quality parameters; then, in case of shallow waters, also on bottom depths and on a fractional cover of bottom reflectances as represented in Figure 2.
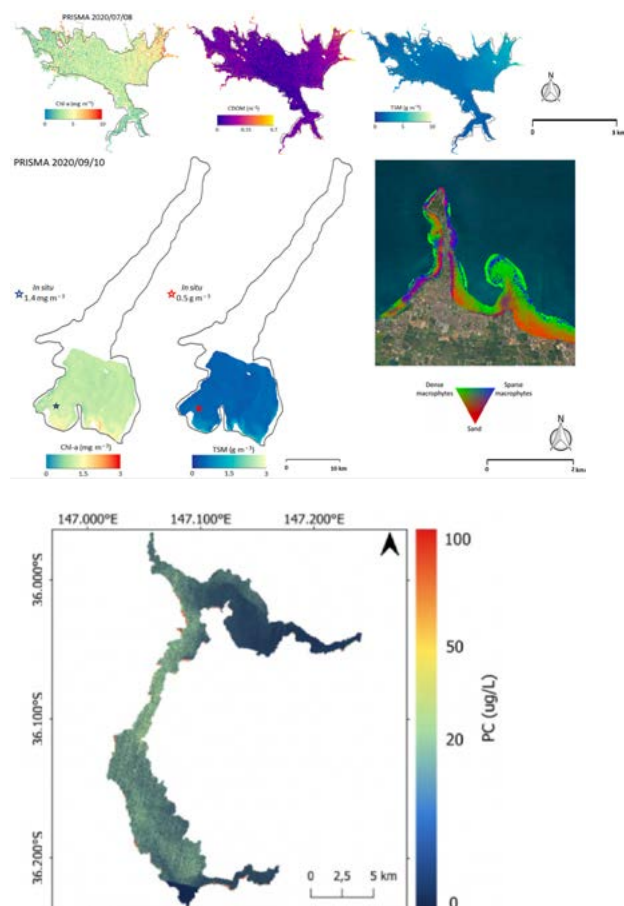
Figure 2. *Examples of PRISMA mapping for different lakes. From top: water quality parameters (Chl-a, CDOM and Total Suspended Matter) in lake Mulargia (Italy); Chl-a, TSM and bottom substrate coverage in Lake Garda (Italy); map of phycocyanin in Lake Hume (Australia).*

CONCLUSIONS

The study presented aimed to show some examples of water quality mapping based on PRISMA images of different water systems. The examples provided include the simultaneous retrieval of optical active water quality parameters, including different phytoplankton pigments, the mapping of fractional cover of bottom types and emergent macrophytes biomass.

The use of hyperspectral imagery indicating the huge scientific potential of this approach, the benefits of its use are likely to be case-specific. Spaceborne imaging spectroscopy has to be considered in synergy with all classes of sensors as cooperation among missions remains the key approach to study aquatic ecosystems, and to monitor water quality by also addressing operational needs associated with policy obligations.

ACKNOWLEDGEMENTS

REFERENCES

Palmer, S.C., T. Kutser, and P.D. Hunter, (2015). Remote sensing of inland waters: Challenges, progress and future directions. Remote Sensing of Environment. 157, pp 1–8.

Odermatt, D., A. Gitelson, V.E. Brando, and M. Schaepman, (2012). Review of constituent retrieval in optically deep and complex waters from satellite imagery. Remote Sensing of Environment. 118, pp 116–126.

Dekker, A. (2021). Committee on Earth Observation Satellites (CEOS). Feasibility Study for an Aquatic Ecosystem Earth Observing System. 2021. Available online: https://ceos.org/.

Coppo, P., F. Brandani, M. Faraci, F. Sarti, M. Dami, et al. (2020). Leonardo spaceborne infrared payloads for Earth observation: SLSTRs for Copernicus Sentinel 3 and PRISMA hyperspectral camera for PRISMA satellite. Applied Optics 59, pp 6888–6901.

Braga, F., A. Fabbretto, Q. Vanhellemont, M. Bresciani, C. Giardino, G.M. Scarpa and V.E. Brando, (2022). Assessment of PRISMA water reflectance using autonomous hyperspectral radiometry. ISPRS Journal of Photogrammetry and Remote Sensing,.192, pp 99-114.

Bresciani, M., C. Giardino, A. Fabbretto, A. Pellegrino, S. Mangano, G. Free, and M. Pinardi, (2022). Application of New Hyperspectral Sensors in the Remote Sensing of Aquatic Ecosystem Health: Exploiting PRISMA and DESIS for Four Italian Lakes. Resources, 11(2), pp 8.

Giardino, C., M. Bresciani, F. Braga, A. Fabbretto, N. Ghirardi, M. Pepe, and V.E. Brando, (2020). First evaluation of PRISMA level 1 data for water applications. Sensors, 20(16), pp 4553.

Impact of the COVID-19 lockdown on water transparency in the Venice Lagoon

Federica Braga[a]*, Gian Marco Scarpa[a], Vittorio Ernesto Brando[b], Giorgia Manfè[a], Luca Zaggia[c]

[a] Institute of Marine Sciences - National Research Council (CNR-ISMAR), Venice, Italy
[b] Institute of Marine Sciences - National Research Council (CNR-ISMAR), Rome, Italy
[c] Institute of Geosciences and Earth Resources - National Research Council (CNR-IGG), Padova, Italy

Abstract – In this study, Sentinel-2 (S2) imagery was successfully used to describe how natural and human-induced processes led to an increase in water transparency in the Venice Lagoon during the COVID-19 lockdown. Pseudo true-colour composites S2 data proved useful for qualitative visual interpretation, showing the reduction of the vessel traffic and their wakes. S2-derived turbidity, in the absence of traffic perturbations, emphasized how water transparency is affected by natural processes and the residual stress from human activities, that continued throughout the restrictions. The lockdown provided a unique opportunity to observe the lagoon without water traffic, one of the main anthropic disturbances. We conclude that the high water transparency can be considered as a transient condition determined by a combination of natural seasonal factors and the effects of COVID-19 restrictions.

Keywords: COVID-19 lockdown, water turbidity, Sentinel-2 imagery, Venice Lagoon.

1. INTRODUCTION

Since 23 February 2020, a series of restrictions, including quarantine and social distancing, were enacted in Italy after the identification of two clusters of COVID-19 in its northern regions. As of March 10th, widespread lockdown extended to the whole country and this represented a unique, unplanned experiment of drastic reduction of anthropic impacts on the environment. As a consequence of the measures to restrict mobility and the drastic reduction of the number of tourists, the ordinary urban water traffic around Venice, one of the major pressures in the lagoon, came to a halt. Public transportation, like water taxis and airport shuttles, plus tourist and leisure boats completely stopped their service, while commercial boats delivering daily supplies in the city and other public boat services reduced their runs to a minimum. An unprecedented water transparency in the city canals were widely covered by international media.

In the lagoon of Venice, several processes influence the amount of dissolved and suspended matter affecting water transparency: wind- and wave- driven resuspension and erosion (e.g. D'Alpaos et al., 2013), redistribution of suspended sediments by tidal currents (e.g. Carniello et al., 2012), freshwater runoff and associated sediment delivery from the drainage basin (e.g. Zuliani et al., 2005), and the phytoplankton growth cycle (e.g. Bianchi et al., 2003). Localized sediment mobilization is induced by ship and boat wakes (e.g. Scarpa et al., 2019), coastal engineering works and clam harvesting (e.g. Pranovi et al., 2003). Within and around the historical city, wastewater discharge is also a source of dissolved and suspended matter due to the lack of a municipal sewage system (e.g. Zaggia et al., 2007).

The environmental effect of the worldwide lockdown was reported mainly as an improvement of air quality and environmental noise due to traffic restrictions (Liu et al., 2021; Zambrano-Monserrate et al., 2020). In this work, we will summarize the Braga et al. (2020) study, where we used S2 imagery to describe the environmental effects of the lockdown on water transparency in the lagoon of Venice and to ascertain how the changes in human pressure caused temporary positive side effects on the water quality.

2. MATERIALS AND METHODS

A total of 14 cloud-free Sentinel-2 (S2) satellite images were downloaded from the Copernicus Open Access Hub, and then radiometrically calibrated according to Pahlevan et al. (2019) and atmospherically corrected with ACOLITE, applying the dark spectrum approach (Vanhellemont and Ruddick, 2018; Vanhellemont, 2019). Pseudo true-colour composites of ACOLITE-derived water leaving reflectance (ρ_w) at 665, 560, 492 nm with the same stretching were used for qualitative visual interpretation. Further, ρ_w were converted into water turbidity (expressed in FNU), following Dogliotti et al. (2015). To assess the accuracy of turbidity products derived from S2 imagery, in situ data collected at the Lido inlet were used.

Tidal levels and wave data from gauge stations in the city centre, wave and wind data from the Acqua Alta Oceanographic Tower, at 16 km off the coast of Venice, were provided by the Centro Previsione e Segnalazione Maree of the city of Venice.

3. RESULTS AND DISCUSSION

Figure 1 shows two S2 true-colour images during the Easter weekend of 2019 and 2020, a typical period of peak tourism influx. On April 19th, 2019 (Figure 1A), the density of white wakes, that trace the moving boats, is relatively high in the historic centre of Venice and around the island of Murano. Particularly evident are also the wakes of speedboats and waterbuses connecting the city to the airport, north of the image area. On April 10th 2020 (Figure 1B), during the COVID-19 lockdown period, few boat wakes are still visible around the city of Venice. The lagoon water is clearer with less suspended matter in the channels surrounding the city, particularly from Venice to Murano, towards the airport and the channel at east of Murano. The dark patches, which are visible north of the city on both dates, are the submerged vegetation over the tidal flats.

Figure 2 presents the S2-derived turbidity maps in ebb tidal phase for a portion of the northern lagoon extending from the airport to the city. On February 20th (Figure 2A), the resuspension due to the wakes of speedboats, water taxis and airport shuttles, is quite intense in the channel connecting the airport water terminal to the city and in adjacent sub-tidal flats, where the turbidity reached about 50 FNU. In the map of March 19th (Figure 2B), when the lockdown was in place and boat traffic almost stopped, the turbidity in the channel

and the airport harbour is comparable to that observed around the city (~5 FNU). On April 15th, wind- and wave-driven resuspension increases turbidity to a range of 25-50 FNU in the northern lagoon (Figure 2C). In the sub-tidal flats north of Murano, small plumes are visible in the turbidity maps (35-50 FNU). These originate within the clam harvesting concession areas where bottom sediments are mobilised by shellfishing gears.
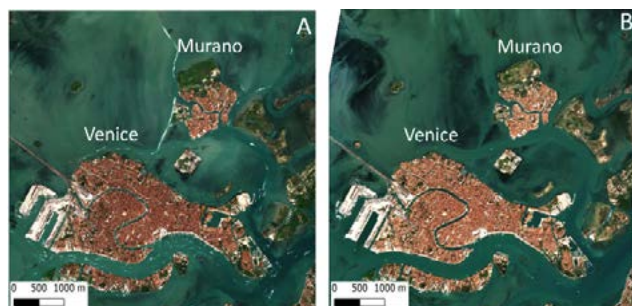

Figure 1. S2 true-colour images in the lagoon of Venice on Good Fridays of 2019 and 2020: A) April 19th 2019; B) April 10th 2020 (during lockdown).
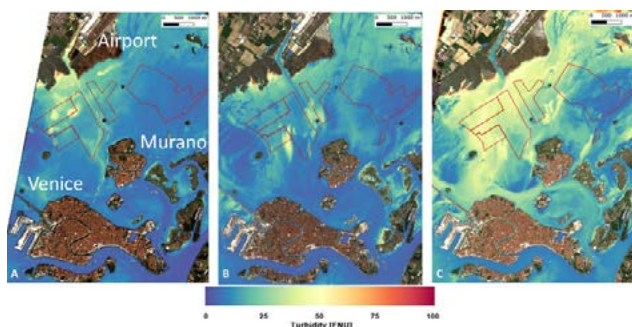
Figure 2. S2-derived turbidity maps for the northern Lagoon: A) February 20th, B) March 19th and C) April 15th 2020. Red dotted lines outline the clam harvesting concessions.

The unprecedented water transparency reported in the city canals is certainly a positive environmental consequence of the COVID-19 lockdown. However, we observed that this was an ephemeral condition due to a combination of factors: i) the minimized impact of boat and cruise ship wakes, which generate erosion and particle resuspension; ii) a decreased wastewater discharge in the canals due to the reduction in tourism; iii) a lower runoff from lagoon tributaries due to low rainfall; iv) the phytoplankton phenology, that is just at the start of the growth cycle in late winter/early spring. Moreover, the high water transparency reported by the media and evident in some of the S2 imagery corresponded to periods of low wind speed.

4. CONCLUSION

The COVID-19 lockdown had provided a unique opportunity to observe the lagoon of Venice without water traffic, one of the main anthropic disturbances. The capabilities of S2 imagery were adequate to address the investigated processes at fine spatial scale and two-to-three-day revisit time. The unprecedented water transparency was a positive environmental consequence of the COVID-19 lockdown, although it was a transient condition determined by natural seasonal factors and changes in human pressure.

REFERENCES

Bianchi, F., Acri, F., Bernardi Aubry, F., Berton, A., Boldrin, A., Camatti, E., Cassin, D., Comaschi, A., 2003. Can plankton communities be considered as bio-indicators of water quality in the Lagoon of Venice?. Mar. Pollut. Bull. 46(8), 964-971.

Braga, F., Scarpa, G. M., Brando, V. E., Manfè, G., Zaggia, L., 2020. COVID-19 lockdown measures reveal human impact on water transparency in the Venice Lagoon. Sci. Total Environ., 736, 139612.

Carniello, L., Defina, A., D'Alpaos, L., 2012. Modeling sand-mud transport induced by tidal currents and wind waves in shallow microtidal basins: Application to the Venice Lagoon (Italy). Estuar. Coast. Shelf Sci. 102, 105-115.

D'Alpaos, A., Carniello, L., Rinaldo, A., 2013. Statistical mechanics of wind wave-induced erosion in shallow tidal basins: Inferences from the Venice Lagoon. Geophys. Res. Lett. 40(13), 3402-3407.

Dogliotti, A.I., Ruddick, K.G., Nechad, B., Doxaran, D., Knaeps, E., 2015. A single algorithm to retrieve turbidity from remotely-sensed data in all coastal and estuarine waters. Remote Sens. Environ. 156, 157–168.

Liu, F., Wang, M., and Zheng, M., 2021. Effects of COVID-19 lockdown on global air quality and health. Science of the Total Environment, 755, 142533.

Pahlevan, N., Chittimalli, S.K., Balasubramanian, S.V., Vellucci, V., 2019. Sentinel-2/Landsat-8 product consistency and implications for monitoring aquatic systems. Remote Sens. Environ. 220, 19-29.

Pranovi, F., Libralato, S., Raicevich, S., Granzotto, A., Pastres, R., Giovanardi, O., 2003. Mechanical clam dredging in Venice Lagoon: Ecosystem effects evaluated with a trophic mass-balance model. Mar. Biol. 143, 393–403.

Scarpa, G.M., Zaggia, L., Manfè, G., Lorenzetti, G., Parnell, K., Soomere, T., Rapaglia, J., Molinaroli, E., 2019. The effects of ship wakes in the Venice Lagoon and implications for the sustainability of shipping in coastal waters. Sci. Rep. 9, 19014.

Vanhellemont, Q., Ruddick, K., 2018. Atmospheric correction of metre-scale optical satellite data for inland and coastal water applications. Remote Sens. Environ. 216, 586-597.

Vanhellemont, Q., 2019. Adaptation of the dark spectrum fitting atmospheric correction for aquatic applications of the Landsat and Sentinel-2 archives. Remote Sens. Environ. 225, 175-192.

Zaggia, L., Rosso, J., Zonta, R., 2007. Sulphate reduction in the sediment of the Venice canals (Italy). Mar. Pollut. Bull. 55(10-12), 415-424.

Zambrano-Monserrate, M.A., Ruano, M.A., Sanchez-Alcalde, L., 2020. Indirect effects of COVID-19 on the environment. Sci. Total Environ. 138813.

Zuliani, A., Zaggia, L., Collavini, F., Zonta, R., 2005. Freshwater discharge from the drainage basin to the Venice Lagoon (Italy). Environ. Int. 31(7), 929-938.

The use of Citizen Science for aerial monitoring of marine litter pollution

F. Alvisi[1]*, S. Merlino[2], M. Locritani[3], M. Paterni[4]

[1]Istituto di Scienze Marine – Consiglio Nazionale delle Ricerche (CNR-ISMAR), Bologna, Italy
[2]Istituto di Scienze Marine – Consiglio Nazionale delle Ricerche (CNR-ISMAR), Lerici (SP), Italy
[3]Istituto Nazionale di Geofisica e Vulcanologia - Sezione Roma 2, Roma, Italy
[4]Istituto di Fisiologia Clinica (CNR-IFC), Pisa, Italy.

Abstract – The importance of monitoring marine litter in low accessibility areas has led to the use of Unmanned Aerial Vehicles (UAVs) in recent years. Through *ad hoc* QGIS-based programmes, it is possible for "trained citizens" to analyze UAVs acquired orthophotos. This approach made it possible to achieve a significant increase in the data collected and, at the same time, to reduce the time needed to extract them. CNR-ISMAR, in collaboration with other research institutes, has launched projects to test the validity of these methodologies, also involving school pupils in the "virtual monitoring" phase. The promising results obtained have led us to involve other schools, extending these methodologies to new coastal marine areas in other countries, also considering rivers and lakes.

Keywords: Marine litter, Pollution monitoring, QGIS, UAVs, Citizen Science.

1. INTRODUCTION

Unmanned Aerial Vehicles (UAVs) are becoming increasingly accessible tools with widespread use as environmental monitoring systems. They can be used for anthropogenic marine litter (ML) survey, a growing research field. UAVs can be effective in bridging the gap by increasing the amount of data acquired to study coastal deposits, while also limiting the anthropogenic impact in protected areas. They could help to collect data on low accessibility areas, and to perform study of spatial and temporal material accumulation. In fact, post-processing system based on visual interpretation of the images allows the localization and identification of the anthropogenic ML within the scanned area, as well as an estimation of their spatial and temporal distribution in different zones of the beach thus providing an opportunity to also investigate the dynamics of their accumulation over time.
Nowadays, different image processing systems of UAV acquisitions have been tested, manually performed by human operators trough Visual Survey (VS) (Andriolo et al. 2020, Merlino et al. 2020, Merlino et al. 2021) or automated (Bao et al. 2018, Papakonstantinout al. 2021, Taddia et al. 2021). Automatic ML detection would be preferable, as it is less tedious and requires less human effort. However, current automated methodologies still lack the ability to categorizing ML items in a detailed manner (Pinto et al. 2021). On the other hand, VS is highly subjective. Thus, the quality of the ML assessment may depend on several factors such as operator experience/expertise, among others, and therefore collected data needs to be accurately validated.

The consistency of VS performed manually was previously investigated by Andriolo et al. (2021) who evaluated the different assessment quality by a group of expert operators. Their results pointed out that the number of items marked on images depended more on the knowledge of common items found on the site, and thus on the territoriality, than on the expertise of the operators. This suggests that the UAV-based ML abundance map could be produced by briefly trained personnel, such as operators recruited from emerging citizen science projects, as assessed in Merlino et al. (2021).
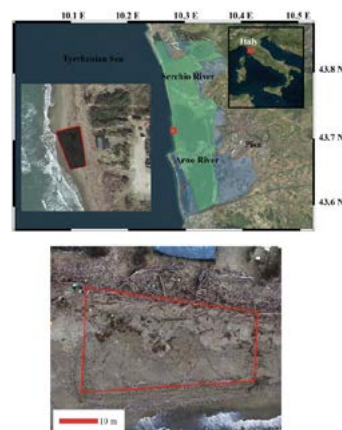

Figure 1. Above, study area location (upper green area) on the Tuscanian coast and satellite image of the study site (inset). Below, aerial image acquired by the drone (flight height 15 m) of the target area (red trapezoidal area).

Citizen science can therefore give a potential and valuable support for UAV-based ML survey. In recent years, researchers have been supported by volunteers and pupils in collecting data on stranded ML (Thiel et al. 2014, Giovacchini et al. 2018, Locritani et al. 2019). Thus, the implementation of citizen science projects with schools could exploit synergies between educational and research objectives. Training workshops are used to introduce citizen science in classrooms and improve the scientific literacy of participants (Locritani et al. 2019). Furthermore, the use of advanced software tools and data (e.g., GIS) can provide participants with new skills that are useful for their future career and social innovation.

Based on these assumptions, the CNR-ISMAR, in collaboration with other institutes, launched a project to test the validity of these methodologies, involving high school pupils in the virtual VS phase of ML monitoring. The project started during the lock-down period, when schools did not have the opportunity to carry out *in situ* activities. Ten PCTOs (Pathways for Transversal Skills and Orientation) were activated during the 2020-2021 school year, and a citizen science programme was prepared for Italian high school pupils (between 16 and 18) to perform VS on aerial photographs. Pupils were asked to mark and classify ML items on an orthophoto taken by UAV on an Italian beach. A training course was organised for the pupils, providing them with information material and a customised QGIS application (http://qgis.osgeo.org/) to mark and classify MLs. The study

---

aimed to: 1) compare our type of virtual monitoring with standard manual *in situ* monitoring; 2) assess the inherent variability of VS when performed by different operators; 3) assess the quality of VS produced by citizen science.

2. RESULTS AND DISCUSSION

The comparison of virtual VS with the standard in situ census returned a general underestimation (50%) of objects in the first case. This, together with a less-detailed identification of ML, is the main limitation of UAV-based surveys compared to the traditional manual *in situ* census. However, the categorisation of ML was in fairly good agreement with the standard in situ survey, especially for source classification. The level of agreement between the CSOs varied between 60% and 91%, depending on the properties of the objects considered (e.g., type, material, and colour). Finally, as the accuracy of the assessment was in line with previous works developed by experts (Andriolo et al. 2021), we can deduce that the remote sensing of ML on UAV images can be realized through citizen science, with an adequate training plan for participants and the provision of specific tools and materials. We specify that a preliminary screening of data evaluations was necessary, to discard low-quality MS and/or uncompleted work. The attention given during the MS by each operator is a difficult factor to weigh, as pointed out in Andriolo et al. (2021). The user-friendly application we developed helped and facilitated the CSO during the tedious marking task, limiting the time spent on and decreasing fatigue. In our specific case of "citizen-pupils", more care has to be taken in the selection of data than in the case of non-expert citizens who volunteered for this type of activity. Being a CSO group composed of pupils, a certain lack of willingness to participate was expected. Instead, most of them returned data of good quality (Merlino et al. 2021).

Starting from these results, we can attest that the use of UAVs for ML surveys, when compared to traditional ones (e.g., GESAMP Guideline, OSPAR Commission Guideline), requires much less human effort in the field and thus have the potential to increase the survey frequency. In addition, UAV-based surveys reduce the anthropogenic impact on the coast, an important aspect especially for sensitive areas such as dunes (Andriolo et al. 2020) and marine-protected areas (Merlino et al. 2020). They allow the geo-localisation of ML and thus, possibly, the identification of recurrent hotspots as well as transport/stranding dynamics (Andriolo et al. 2020), useful to improve the knowledge of ML accumulation processes on the coasts (Merlino et al. 2020). These assessments can serve to optimise dynamic ML models (Cordeiro et al. 2018) and stranded ML management with significant benefits for different types of stakeholders.
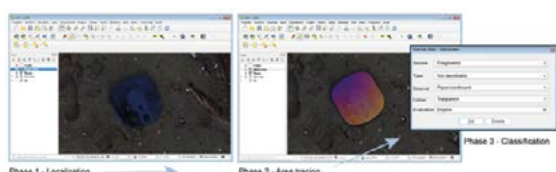
Figure 2. Screenshot of the developed software application in QGIS framework, for ML identification and classification with user-friendly combo boxes.

3. CONCLUSION

Citizen science programmes significantly increase the possibility to obtain reliable data over large areas and long-time intervals, and can be used to study the spatial and temporal ML distribution through UAV orthophoto. Future citizen science programmes could also propose the involvement of citizens in the aerial image acquisition. The current spread of low-cost drones facilitates the collection of images of stranded ML, helping to improve our knowledge of the spatial and temporal dynamics of coastal pollution.

The contribution provided by citizen science can be instrumental in further extending this type of research, while involving and raising awareness among a large number of people. The obtained promising results prompted us to involve new schools, and extending the application of these methodologies to new Italian and European coastal marine areas, considering also rivers and lakes. This will be realized in the coming months thanks to the involvement of CNR-ISMAR in the European Blue Schools Network within the BlueS_MED Project. The possibility to share these experiences with young people and the public through the EU Researchers' Nights, organized by the BlueNIGHTs project for 2022 and 2023, will further increase the potential to expand this methodological approach.

REFERENCES

Andriolo, U., G. Gonçalves, F. Bessa, P. Sobral (2020). Mapping marine litter on coastal dunes with unmanned aerial systems: A showcase on the Atlantic Coast. Science of the Total Environment, 736, 139632.

Andriolo, U., G. Gonçalves, N. Rangel-Buitrago et al. (2021). Drones for litter mapping: An inter-operator concordance test in marking beached items on aerial images. Marine Pollution Bullettin, 169, 112542.

Bao, Z., J. Sha, X. Li, T. Hanchiso, E. Shifaw (2018). Monitoring of beach litter by automatic interpretation of unmanned aerial vehicle images using the segmentation threshold method. Marine Pollution Bullettin, 137, 388–398.

Cordeiro, T.C., W. Barrella, D. Butturi-Gomes, M. Petrere Junior (2018). A modeling approach for reposition dynamics of litter composition in coastal areas of the city of Santos, Sao Paulo, Brazil. Marine Pollution Bullettin, 128, 333–339.

Giovacchini, A., S. Merlino, M. Locritani, M. Stroobant (2018). Spatial distribution of marine litter along italian coastal areas in the Pelagos sanctuary (Ligurian Sea-NW Mediterranean Sea): A focus on natural and urban beaches. Marine Pollution Bullettin, 130,140–152.

Locritani, M., S. Merlino, M. Abbate (2019). Assessing the citizen science approach as tool to increase awareness on the marine litter problem. Marine Pollution Bulletin 140, 320–329.

Merlino, S.; Paterni, M.; Berton, A.; Massetti, L. Unmanned Aerial Vehicles for Debris Survey in Coastal Areas: Long-Term Monitoring Programme to Study Spatial and Temporal Accumulation of the Dynamics of Beached Marine Litter. Remote Sens. 2020, 12, 1260.

Merlino S., Paterni M., Locritani M., Andriolo U., Gonçalves G., Massetti L. 2021. Citizen Science for Marine Litter Detection and Classification on Unmanned Aerial Vehicle Images. Water. V 13, DOI:10.3390/w13233349

Papakonstantinou, A., M. Batsaris, S. Spondylidis, K. Topouzelis (2021). A Citizen Science Unmanned Aerial System Data Acquisition Protocol and Deep Learning Techniques for the Automatic Detection and Mapping of Marine Litter Concentrations in the Coastal Zone. Drones, 5, 6.

Taddia, Y., C. Corbau, J. Buoninsegni, U. Simeoni, A. Pellegrinelli (2021). UAV Approach for Detecting Plastic Marine Debris on the Beach: A Case Study in the Po River Delta (Italy). Drones, 5, 140.

Thiel, M., M.A. Penna-Dìaz, G. Luna-Jorquera, S. Salas, J. Sellanes, W. Stotz (2014). Citizen scientists and marine research: Volunteer participants, their contributions, and projection for the future. In: Oceanography and Marine Biology: An Annual Review. CRC Press: Boca Raton, FL, USA, ISBN 9781482220667.

POSTER SESSION

Monitoring the regional heat content change over the Atlantic Ocean with the space geodetic approach: the 4DATLANTIC-OHC Project

Michaël Ablain[1], Florence Marti[1], Gilles Larnicol[1], Robin Fraudeau[1], Victor Rousseau[1], Alejandro Blazquez[2], Benoit Meyssignac[2], Matthew Hammond[3], Giuseppe Foti[3], Fransisco Calafat[3], Odilon Joël Houndegnonto[4], Damien Desbruyères[4], William Llovel[4], Pablo Ortega[5], Vladimir Lapin[5], Mar Rodrigez[5], Rachel Killick[6], Nick Rayner[6], Marie Drevillon[7], Karina von Schuckmann[7], Marco Restano[8], Jérôme Benveniste[9]

[1]Magellium, [2]LEGOS, [3]NOC, [4]LOPS , [5]BSC, [6]Met Office, [7]MOi, [8]SERCO/ESRIN, [9]ESA-ESRIN.

Abstract – Given the major role of the Atlantic Ocean in the climate system, it is essential to characterize the temporal and spatial variations of its heat content. The originality of the 4DATLANTIC-OHC Project (2021-2023) is to estimate the regional ocean heat content (OHC) change over the Atlantic Ocean from the space geodetic data (satellite altimetry and gravimetry). The 4DATLANTIC-OHC product is publicly available over the 2002-2020 period on the ODATIS/AVISO portal, after being assessed against in-situ data along the OVIDE and RAPID sections.
(DOI: 10.24400/527896/A01-2022.012)

Keywords: Ocean heat content, Space geodetic data

1. INTRODUCTION

Given the major role of the Atlantic Ocean in the climate system, it is essential to characterize the temporal and spatial variations of its heat content. The 4DATLANTIC-OHC Project (https://eo4society.esa.int/projects/4datlantic-ohc/) aims at developing and testing space geodetic approach to estimate the regional ocean heat content (OHC) changes over the Atlantic Ocean from satellite altimetry and gravimetry. The proposed approach developed in the frame of the ESA MOHeaCAN project is pursued and refined at regional scales both for the data generation and the uncertainty estimate. At two test sites, OHC derived from in situ data (RAPID and OVIDE-AR7W) are used to evaluate the accuracy and reliability of the new space geodetic based OHC change. The Atlantic OHC product will be used to better understand the complexity of the Earth's climate system. In particular, the project aims at better understanding the role played by the variability of the Meridional Heat transport in the North Atlantic and more generally the role of Atlantic Meridional Overturning Circulation (AMOC) in regional and global climate change. In addition, improving our knowledge on the Atlantic OHC change will help to better assess the global ocean heat uptake and thus estimate the Earth's energy imbalance more accurately as the oceans absorb about 90% of the excess energy stored by the Earth system.

The objectives of the 4DATLANTIC-OHC Project will be presented. The scientific requirements and data used to generate the OHC change products over the Atlantic Ocean and the results in terms of development and validation will be detailed. At a later stage, early adopters are expected to assess the OHC products strengths and limitations for the implementation of new solutions for Society. The project started in June 2021 for a 2-year duration.

2. METHOD AND DATA DESCRIPTION

OHC change time series may be inferred by different methods (Meyssignac et al., 2019). An indirect approach is the space geodetic approach which relies on the sea level budget equation. The ESA-funded project MOHeaCAN acted as a proof-of-concept, describing the application of the space geodetic approach on a global scale (Marti et al., 2022). The space geodetic approach aims at measuring the thermosteric sea level change due to seawater density change induced by temperature based on differences between the total sea level change derived from satellite altimetry measurements and the barystatic sea level change from satellite gravity measurements. Halosteric sea level changes due to saline contraction are estimated from in situ data and removed from the total sea level variations.

$$\Delta SL_{thermosteric} = \Delta S_{L total} - \Delta SL_{mass} - \Delta SL_{halosteric}$$

The data used are:
(1) Space gravimetry-based data of ocean mass variations, estimated from observations of the Gravity Recovery And Climate Experiment (GRACE) and GRACE Follow–on missions: ensemble of spherical harmonic solutions updated from Blazquez et al., 2018.
(2) Space altimetry-based data of sea level variations, delivered by the Copernicus Climate Change Service (C3S). This dataset, fully described in (Legeais et al., 2021) is dedicated to the sea level stability for climate applications. It provides daily sea-level anomalies grids based at any time on a reference altimeter mission (TopEx/Poseidon, Jason-1,2,3 and S6-MF very soon) plus complementary missions (ERS-1,2, Envisat, Cryosat, SARAL/Altika, Sentinel-3A) to increase spatial coverage.
(3) In situ-based data of halosteric sea level variations, estimated from the Argo temperature and salinity profiles: combination of ISAS20 (from 0 to 2000m depth) and EN4.2.2.l09 (below 2000m depth) products.

The OHC change can be computed at regional scales by dividing the thermosteric sea level change with the Integrated Expansion Efficiency of Heat (IEEH) coefficient. The IEEH expresses the ratio of the thermosteric sea level over the heat content and was estimated from in situ temperature and salinity measurements.

OHC change uncertainties are also rigorously estimated by propagating the error variance covariance matrices from input data until the OHC change (see Fig. 1). From the OHC error variance covariance matrix, the uncertainties on OHC trends can be estimated at any time span.

3. RESULTS AND VALIDATION

The 4DAtlantic-OHC product has been generated over all the Atlantic Ocean over the 2002-2020 period. The product

is publicly available on the ODATIS/AVISO portal (10.24400/527896/A01-2022.012). Figure 1 shows a strong signal of OHC change in the North Atlantic basin. On the western part positive trends can reach up to 10 W/m² whereas in the northeastern part trends are negative.
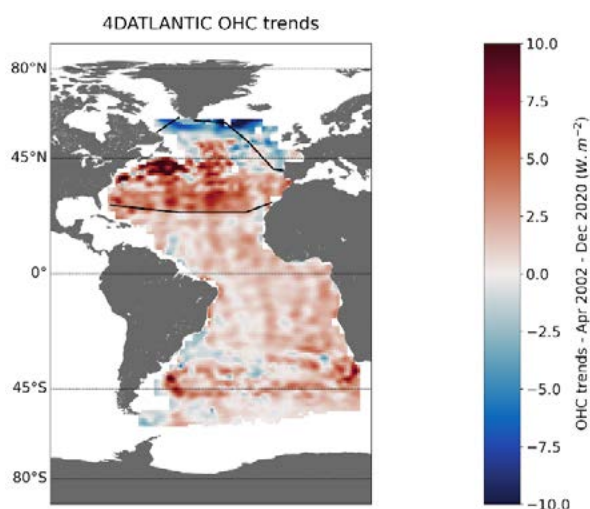

Figure 1. *OHC trend estimates over the 2002-2020 period.*

The validation activities were carried out over the Subtropical North Atlantic region. The use of the Argo dataset has revealed that patterns are very similar with an overall positive trend, strongest positive trends in the southwest, as well as areas of negative trends in the Northwest and Northeast in both datasets (Figure 2). Furthermore, correlations between the in-situ product and the geodetic product are significant over most parts of the Subtropical North Atlantic region.
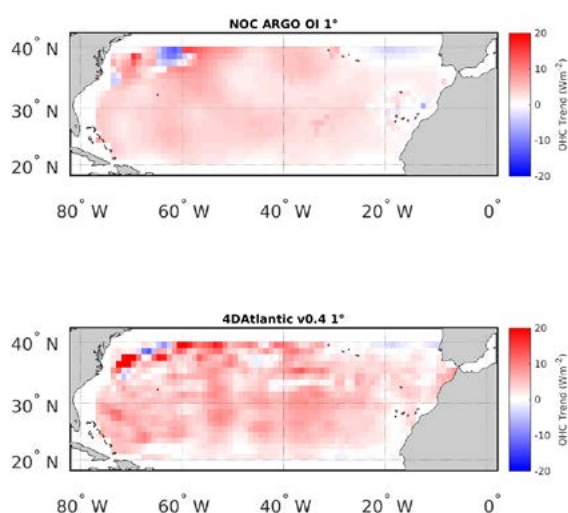
Figure 2. *OHC change trends in the Subtropical North Atlantic region for the NOC Argo product (top) and the 4DATLANTIC-OHC product (bottom).*

The use of RAPID mooring section data has also highlighted a good consistency with the trends of the geodetic product with discrepancies being less than 5-10%. Over the Western basin, trend of RAPID is 5.34 W/m² whilst trend of geodetic product is 5.82 W/m². Over the Eastern basin, the trend of RAPID is 3.75 W/m² whilst the trend of geodetic product is 3.99W/m².

The OHC geodetic product was also validated in the Subpolar North Atlantic region. The product was compared against in situ OHC estimates from A25-OVIDE (2002-2018). The comparison has shown good consistency between both products over the Irminger Sea but less over the eastern part of Reykjanes ridge.

3. CONCLUSION

The **4DATLANTIC-OHC** product based on space geodetic approach allows to capture the intense heat exchanges between ocean and atmosphere in the North Atlantic basin which is a key area for studying climate change.

The good OHC change consistency with the mooring sections (OVIDE and RAPID) validate the relevance of the geodetic approach, with in particular its ability to measure the deep ocean signal over all the ocean.

This innovative product suffers from known imitations that will be improved in the next future. For instance the product will be extended near the coast and in northern areas, and also over all the ocean. Furthermore systematic errors have been detected in oceans mass solutions derived from gravimetric data that can be corrected.

In the second part of the 4DATLANTIC-OHC project, the effort will be focused on the estimation and validation of the Meridional Heat Transport (MHT) in the North Atlantic at all latitudes with a regional ocean heat budget approach. Furthermore, several use case studies are planned by end of the project (June 2023) to assess the added value of these data in the improvement of the operational decadal predictions, in the Copernicus Marine Service ocean reporting activities, and in the Metoffice . MetOffice climate indicators dashboard.

REFERENCES

Blazquez, A. et al.: Exploring the uncertainty in GRACE estimates of the mass redistributions at the Earth surface: implications for the global water and sea level budgets, Geophys. J. Int., 215, 415–430, https://doi.org/10.1093/gji/ggy293, 2018.

Marti, F. et al.: Monitoring the ocean heat content change and the Earth energy imbalance from space altimetry and space gravimetry, Earth Syst. Sci. Data, https://doi.org/10.5194/essd-2021-220, 2022

Meyssignac, B. et al: Measuring Global Ocean Heat Content to Estimate the Earth Energy Imbalance, Front. Mar. Sci., 6, 432, https://doi.org/10.3389/fmars.2019.00432, 2019.

ESA MOHeaCAN project: https://eo4society.esa.int/projects/moheacan/

Tsunami Detection by satellite altimetry in Mediterranean Sea

G. Arena & M. Manca Zeichen[*1]

Italian National Research Institute for Environmental Protection and Research (ISPRA), Rome, Italy
Via V. Brancati 60, 00144 Rome
giovanni.arena@isprambiente.it

Abstract – **Tsunamis are routinely recorded by tidal stations located on the continental or island coastal areas in the Mediterranean Sea. Until 1999, tsunami were never recorded in the open sea. The satellite sensors used for tsunami detections are the altimeters which measure Sea Surface Height (SSH). Altimeters were used to study the 2004 Sumatra-Andaman tsunami. However, due to the difficulty of detecting a tsunami with satellite altimeter, those satellite sensors were rarely applied to the tsunami monitoring within the Mediterranean Sea.**
This study is a position paper which aims at promoting the use of altimeters to the detection and investigation of the tsunami occurring in the Mediterranean Sea.

Keywords: Tsunami, altimetry, Mediterranean Sea.

1. INTRODUCTION

Tsunamis are routinely recorded by tidal stations located on the continental or island coastal areas and until 1999 they were never recorded in the open sea. This is due to the fact that tsunamis are very difficult to detect this is mainly due to two factors, the first is that the wave amplitude is small (generally less than 1m even for exceptional events), it is only when the tsunami approaches the coast which increases and second for the extended wavelength (λ≥100 km) which makes it difficult to directly observe the deformation of the ocean surface. An effective early warning system, however, must be able to observe an impending tsunami threat away from the coast in order to provide time for coastal residents to get to safety.

The satellite measurements used for satellite tsunami detection are altimetric sensors that measure variations in the height of the sea surface or Sea Surface Height (SSH). The satellite altimetry observes the distance from the satellite to the underlying sea surface. Satellites with trace altimeters and favorable times can observe the propagating tsunami wave (Hayashi, 2008).

An ocean tsunami caused by a massive earthquake can theoretically be observed from satellite altimetry. Satellite altimeters can measure SSH with sufficient spatial resolution but they measure along the tracks on the ground and cannot provide a complete picture of an event because they generally take about ten days to obtain almost global coverage. The chances of observing a tsunami in sufficient time to alert coastal populations are therefore remote (Okal et al., 1999; Hamlington et al., 2011). However, tsunamis can be detected by the variation in SSH during oceanographic monitoring missions if you have correct traces of the satellite sensor.

In general, the likelihood of detecting a tsunami with a satellite altimeter is very low. The satellite must fly over the tsunami wave within a short time interval from the genesis of the event due to the high speed of propagation of the tsunami (about 800 km h-1 in an ocean of 5000 m depth). Furthermore, open ocean tsunami signals are generally quite weak to be able to separate oceanic wave variability (Okal et al., 1999; Hamlington et al., 2011).

The tsunami of 26 December 2004 in the Indian Ocean between the island of Sumatra and the Andaman Islands was the very first event to be clearly observed by satellite altimeters (Smith et al., 2005), largely due to its intensity and its considerable impact area. This event was the strongest to have occurred since satellite altimetry began in the 1970s. The tsunami was caused by a magnitude 9 earthquake and caused about 230,000 victims.

The satellite altimeter data were the unique measurements of the amplitude of the December 26 tsunami in the open ocean. Four satellite altimeters observed the tsunami wave that swept the entire Indian Ocean. The tsunami was detected in the first 9 hours after the earthquake by the TOPEX, Jason-1, Envisat and GEOSAT Follow On (GFO) satellite altimeters (Figure 1 and Figure 2) (Hamlington et al., 2011).
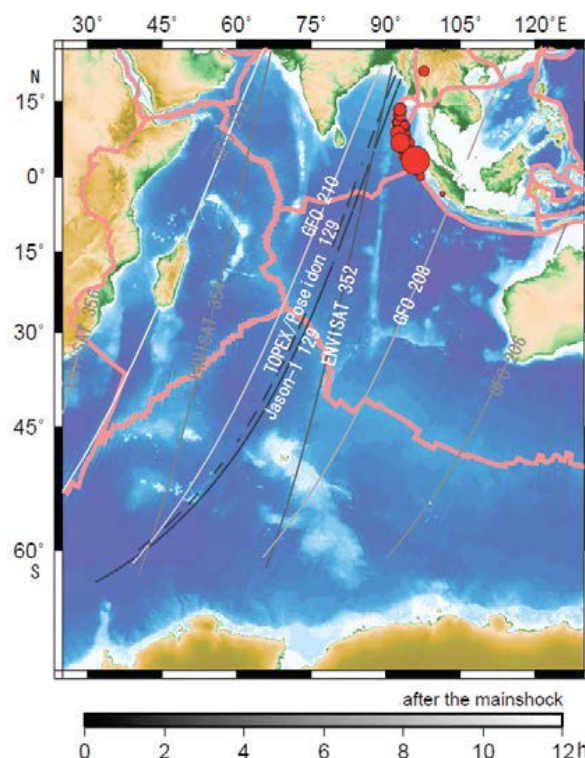

Figure 1. Satellite passages near the area of origin of the 2004 Sumatra-Andaman earthquake within 12 hours of the time of origin (December 26, 2004, 00h58m53s; UT) (Hamlington et al., 2011).

[*1] Corresponding author: via Vitaliano Brancati 60, 00144 Roma, Italia: Email: marta.mancazeichen@isprambiente.it
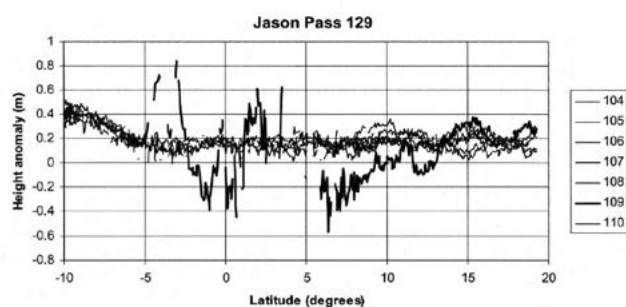
Figure 2. Plots of sea surface height anomalies on step 129 in cycles 104-110. The passage in cycle 109 (0300 UT, 26 December 2004, bold line) shows the profile of the tsunami wave (Gower, 2005).

2. POTENTIAL SYSTEM OF TSUNAMI DETECTION FOR MEDITERRANEAN SEA

Spatial coverage and temporal resolution of satellite altimeters are not suitable to form the basis of a system for early tsunami detection in the Mediterranean Sea. However, a potential tsunami detection system could be put in place by using new generation satellite altimeters such as Copernicus Sentinel 6 A Michael Freilich (Figure 3) which, since March 2022, provides the world's most precise data on sea level and monitors changes in SSH with an accuracy of a few centimeters, ensuring the continuity of the 30-year record on sea level from satellite altimeter such as TOPEX-Poseidon and Jason series. However, a major critical issue in using satellite altimeters for offshore tsunami detection are filtering techniques. Various studies have used filtering techniques to aid in extracting the tsunami signal from the ocean floor variability. Gower (2005) subtracted the leveled mean of SSH measured in the previous cycle and in the cycles following the tsunami cycle on the same pass. However, the variations in SSH observed by satellite altimetry with this technique include various oceanographic, meteorological, geodetic and seismic effects. The importance of implementing and developing filtering techniques to the tsunami detection becomes crucial, particularly in detecting weaker tsunami such as those occurring in the Mediterranean Sea.
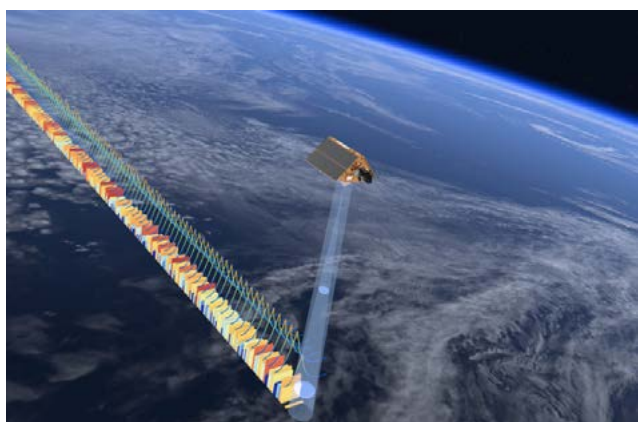
Figure 3. Sentinel 6A Michael Freilich.

In addition, the altimeter trace must be considered when trying to estimate the wavelength of the tsunami. An altimeter that travels perpendicular to the tsunami front wave gives a very different estimate of the wavelength than an altimeter that moves more tangentially to the tsunami wave front. This highlights some of the difficulties encountered in using satellite altimeters for offshore tsunami detection.

Other sensors could also be used to the tsunami detection. In fact, other tsunami manifestations such as variations in surface roughness ($\sigma 0$) are among the most promising for detecting tsunamis from space, these effects can be detected by active sensors such as scatterometers and passive sensors such as microwave radiometer on Copernicus Sentinel 1. Tsunami-induced variations in open ocean surface roughness have been called "tsunami shadows" and have the appearance of darker streaks on the ocean surface along a tsunami front. The shadow formation of the tsunami has been interpreted as a result of the air-water interaction; specifically, tsunami-induced perturbations in wind speed near the ocean surface are predicted to be much larger than currents in the tsunami wave (Godin, 2003, 2004).

3. CONCLUSION

Active satellite sensors offer the opportunity to study the effects of an offshore tsunami wave not only by providing measurements of SSH, but also through measurements of the sea surface roughness (Hamlington et al., 2011).

The spatial and temporal sampling of satellite altimeters does not allow their use as a basis for an early tsunami detection system operating in the Mediterranean Sea. However, the variation of the sea surface roughness acts as a further useful manifestation of the tsunami in the open sea, that can be detected using other satellite sensors with better spatial and temporal sampling such as scatterometers and microwave radiometers, which have a coverage of hundreds of kilometers. Analysing the tsunami in two dimensions would also allow to obtain a series of two-dimensional snapshots of the tsunami and would allow to better study the wave field and its propagation in the open ocean. In light of the above, broad-spectrum satellite observations of open ocean tsunamis consisting of an enlarged constellation of instruments, such as those supplied by Copernicus Programme, could play a crucial role in a future system and potentially improve the accuracy of tsunami detection in the Mediterranean Sea.

REFERENCES

Godin, O. A., 2003. Influence of long gravity waves on wind velocity in the near-water layer and feasibility of early tsunami detection, Dokl. Earth Sci., 391, 841–844.

Godin, O. A., 2004. Air-sea interaction and feasibility of tsunami detection in the open ocean, J. Geophys. Res., 109, C05002, doi: 10.1029/2003JC002030, 2004.

Gower J., 2005. Jason 1 Detects the 26 December 2004 Tsunami. Eos Transactions, Vol. 86, No. 4, 25.

Hayashi Y., 2008. Extracting the 2004 Indian Ocean tsunami signals from sea surface height data observed by satellite altimetry. Journal of Geophysical Research, 113, C01001, doi:10.1029/2007JC004177, 2008.

Hamlington B. D., Leben R. R., Godin O. A., Legeais J. F., Gica E., and Titov V. V., 2011. Detection of the 2010 Chilean tsunami using satellite altimetry, 2011. Nat. Hazards Earth Syst. Sci., 11, 2391–2406.

Russ. J. Earth Sci. 8, ES4004, doi:10.2205/2006ES000214.

Okal, E. A., Piatanesi, A., and Heinrich, P, 1999. Tsunami detection by satellite altimetry, J. Geophys. Res., 104, 599–615, 1999.

Smith W.H.F., Scharroo R., Titov V.V., Arcas D., Arbic B.K., 2005. Oceanography Vol.18 (2), 10- 12..

Preliminary analysis of combined Sentinel-2 and Landsat-8 remote sensing reflectance products for improved monitoring of Chlorophyll-a over the Barents Sea

M. Asim*, C. Brekke, T. Eltoft, K. Blix

Department of Physics and Technology UiT, The Arctic University of Norway (UiT), Tromsø, Norway

Abstract – The similar band design of Landsat-8 (L-8) and Sentinel-2 (S-2) sensors makes it possible to combine L-8 and S-2 imagery and acquire global observations in 2 to 3 days at a spatial resolution of 10-60 m. Within this context, the near-simultaneous L-8 and S-2 images were acquired in the years 2018 to 2020 and corrected for atmospheric effects using Acolite, C2RCC, and Polymer. Our analysis indicates that S-2 and L-8 processed via Acolite have minimum difference in their R_{rs} products. In addition, the in-situ measurements of Chl-a and the corresponding L-8 and S-2 imagery were collected over the years 2013 to 2019 and processed via Acolite. Considering L-8 derived Rrs as a reference, a novel machine learning-based bandpass adjustment (BA) model is proposed to account for the differences in the absolute radiometric responses of S-2 and L-8. Using the combined R_{rs} products and the in-situ Chl-a observation, the Ocean Color Net (OCN) model (Asim, 2021) is tuned to estimate Chl-a. Our results demonstrate that combing R_{rs} products from the two sensors using the proposed BA model achieved reduced root mean square error compared to the S-2 and L-8 alone by 47% and 28%, and simply combined Rrs products by 5.7%.

Keywords: Machine Learning, Barents Sea, Chlorophyll-a.

1. INTRODUCTION

The Barents Sea is one of the largest pan-Arctic shelves and covers about 10% of the Arctic Ocean (Fouest, 2011). It is a productive Sea in the high north and supports almost 40% of the Arctic primary production (Sakshaug, 2004).

In general, the northern Barents Sea is covered with sea ice during winter while the southern parts remain open due to the inflow of warm and salty Atlantic water. Due to its location, the northern part of the Barents Sea has been characterized by an arctic dominated ecosystem, whereas the south is dominated by subarctic communities due to an Atlantic climate. However, as a result of ongoing global warming, lately significant alterations in the ecosystem function and net primary productivity have been observed in the changing Barents Sea. The sea ice extent in the Arctic and its adjacent seas, has shown a trend of reduction. More recently, an increase in the production and seasonal growth of phytoplankton is observed in the northern Barents Sea (Dalpadado, 2020).

Phytoplankton forms the bases of aquatic food webs and is treated as a valuable indicator of marine ecosystem health condition (Pahlavan, 2021). Depending on the availability of solar radiations and nutrients or phosphorus concentration, phytoplankton can grow rapidly in a short period. Phytoplankton contain a light-harvesting pigment called Chlorophyll-a (Chl-a), which provides useful information about the aquatic biomass and numerous biophysical processes (Bailey, 2006, Pahlavan, 2021).

Considering the importance and near-daily monitoring of small-scale variations in the biogeochemical variables, the need to develop a reliable algorithm for seamless retrieval of Chl-a in the transitional Barents Sea is needed. Fortunately, the similar band design of Landsat-8 (L-8) and Sentinel-2 (S-2) sensors makes it possible to combine L-8 and S-2 imagery and acquire repeat observations in 2 to 3 days at a moderate resolution. However, the difference in sensors spatial and spectral characteristics, acquisition geometries, or different atmospheric conditions make it unreliable to use their data together.

To combine data from L-8 and S-2 into a single dataset, it is vital to minimize the difference in the remote sensing reflectance (R_{rs}) products of these sensors. In this regard, using L-8 R_{rs} as a reference, a novel ML-based model based on feedforward multilayer perceptron (MLP) is developed to account for the differences in relative spectral response functions of S-2 and L-8. The proposed model predicts S2-derived R_{rs} from those derived from L-8. The R_{rs} products derived from S-2, and the predicted R_{rs} from L-8 derived R_{rs} (S-2*) are combined to evaluate the performance of the Ocean Color Net (OCN)

2. Material and Methods

The sampling of Conductivity-Temperature-Depth (CTD) fluorescence of Chl-a was carried out in the years 2013-2019 using frequent field campaigns as part of the Ecosystem Program of the Institute of Marine Research (IMR), Norway. The Chl-a CTD data were collected from various CTD stations covering various aquatic conditions. The Chl-a content ranges from 0.014 to 10.81mg/m^3.

S-2A/2B Level1-C and L-8 Level1-T data, co-located in space with a time difference of ±8 hours with the in-situ observations for the period 2013-2019 (April-September), were acquired from https://scihub.copernicus.eu/dhus and Earth Explorer (https://earthexplorer.usgs.gov/), respectively. The S-2 and L-8 imagery was corrected for atmospheric effects using three publicly available state-of-the-art atmospheric correction (AC) processors, Acolite C2RCC and Polymer, these algorithms were also compared in (Pahlavan, 2021). To make a match-up, instead of matching surface in-situ Chl-a observation with a single nearest pixel, we consider associating depth-integrated weighted averaged Chl-a ($[Chl-a]_{Zpd}$) concentration with all valid pixels in a window of 3×3 (S2) and 6×6 (L8) pixels, centered around the in-situ location, to make it equivalent of 180×180 m for S-2 and L-8 data, respectively (Asim, 2021).

All the AC processors were applied in default settings with some slight adjustments. In the C2RCC processor, the salinity and average temperature were set to 34.5 PSU and 8°C following Climate Explorer (https://climexp.knmi.nl/). Ancillary data option was set to "True" for retrieving ozone,

* Corresponding author. Department of Physics and Technology UiT, The Arctic University of Norway (UiT), Tromsø, Norway. Email: muhammad.asim@uit.no

water vapor and atmospheric pressure for processing images through Acolite and Polymer.

Before combing the R_{rs} data, we first evaluated the spectral consistency between S-2 and L-8 derived R_{rs}. For this purpose, near simultaneous S-2 and L-8 level-1 data with a time difference less than 30 minutes were acquired over the Barents Sea in the year s2018 to 2020, and processed through Acolite, Polymer and C2RCC. Using L-8 derived R_{rs} as a reference, our results show that Acolite provides the minimum difference in the R_{rs} products amongst the three AC processors (results not shown here). Following that, the Acolite processed R_{rs} was then supplied to the OCN model in three different settings to generate Chl-a estimates, i) S-2 and L-8 derived R_{rs} individually, ii) combined S-2 and L-8 derived Rrs and iii) L-8 and band adjusted S-2 ($S2^*$) derived R_{rs}. The results of Chl-a retrieval for the three different settings are shown in Tab. 1a nd Fig.2. To band adjust S-2 data, we used the near simultaneous S-2 and L-8 R_{rs} data processed through Acolite. Considering L-8 as a reference, the proposed bandpass adjustment (BA) model is trained to perform pixel-to-pixel transformation from L-8 derived R_{rs} to S-2 derived R_{rs}. The trained model was then used to convert L-8 derived R_{rs} data into S-2 R_{rs} data. The framework of the proposed approach is shown in Fig.1.
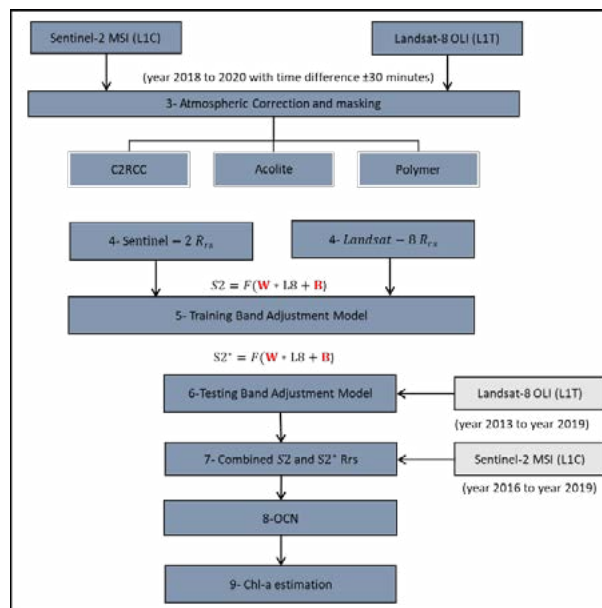
Figure 1. The framework of the proposed approach.

3. Results

The achieved results confirm the effectiveness of the combined S-2 and L-8 R_{rs} products using the proposed approach which is also supported by the regression slopes in Figs. 2. The combined R_{rs} products show the best performance in estimating Chl-a using OCN. The Pearson Score (R-score) and coefficient of determination (R^2) between in-situ and the estimated Chl-a using the proposed BA model are highest and the root mean square error (RMSE) and MSE are lowest compared to using S-2 and L-8 alone.

Table 1. Performance comparison of the OCN in retrieving ($[Chl-a]_{Zpd}$) using S-2 R_{rs} product, L-8 R_{rs} product, combined S-2 and L-8 and combined S-2 and S2* R_{rs} products, derived via Acolite.

score	S2	L8	S2 &L8	S2 &S2*
RMSLE	0.121	0.251	0.1440	0.128
RMSE	0.832	0.587	0.4703	0.443
MSE	0.692	0.345	0.2212	0.196
R-score	0.936	0.778	0.9213	0.947
R^2-score	0.874	0.588	0.848	0.889

RMSLE represents root mean square error in log scale.
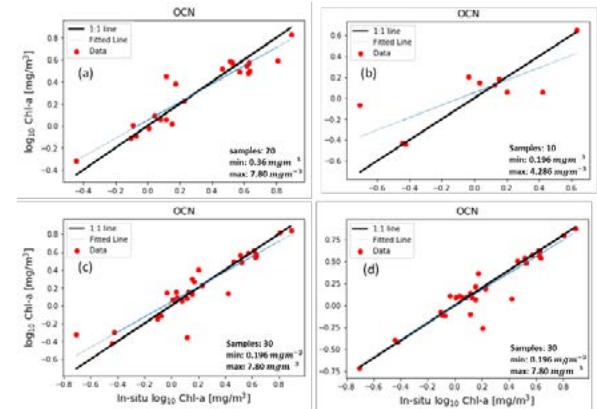
Figure 2. Comparison of regression plots using a) S-2, b) L-8, c) combined S2 and L-8, and d) combined S-2 and S-2*. The results are shown in log scale.

3. CONCLUSION

Our results demonstrate that Sentinel-2 (S2) and Landsat-8 (L-8) processed via Acolite gives the minimum difference in the Rrs products. To further minimize the difference in the Rrs products, a machine learning-based bandpass adjustment (BA) model is proposed to perform pixel-to-pixel transformation from L-8 to S-2 sensor. Our results indicate that combining data from S2- and L-8 derived products using the proposed BA approach has improved the performance of OCN in estimating Chl-a.

ACKNOWLEDGEMENTS

REFERENCES

V. Le Fouest et al., "On the role of tides and strong wind events in promoting summer primary production in the barents sea,"Continental Shelf Research, vol. 31, no. 17, pp. 1869–1879, 2011.

Sakshaug, E. (2004). Primary and secondary production in the Arctic Seas. In The organic carbon cycle in the Arctic Ocean (pp. 57-81). Springer, Berlin, Heidelberg.

Dalpadado, P. et al., (2020). Climate effects on temporal and spatial dynamics of phytoplankton and zooplankton in the Barents Sea. Progress in Oceanography, 185, 102320.

Asim, M. el al., (2021). Improving Chlorophyll-a Estimation from sentinel-2 (MSI) in the Barents Sea using Machine Learning. IEEE JSTARS.

Bailey, S. W. et al., (2006). A multi-sensor approach for the on-orbit validation of ocean color satellite data products. RSE, 102(1-2), 12-23.

Pahlevan, N. et al., (2021). ACIX-Aqua: A global assessment of atmospheric correction methods for Landsat-8 and Sentinel-2 over lakes, rivers, and coastal waters. RSE, 258, 112366.

Eddy kinetic energy as a trigger for the Azores Current intensification at depth: a perspective based on Ocean Model Analysis and Satellite Altimetry

Amorim, F.N.*, Morlet, O.[#], Bastos, L.* and Lázaro, C.*[$]

*Interdisciplinary Centre of Marine and Environmental Research, CIIMAR, University of Porto, Portugal
[#]SeaTech, École D'ingénieurs, Université de Toulon, France
[$]Faculdade de Ciências da Universidade do Porto, FCUP, Portugal

Abstract – This study investigates the occurrence of an intensification of the eastward zonal Azores Current (AzC) at depth, reaching up to 14 cm s^{-1} in the first 200 m, associated with strong eddy related energy. The energy transfer from surface eddy kinetic energy to the eastward AzC jet seems to occur with a 3-month lag, lasting for six months. The identified events occurred during the months that, seasonally, the AzC is weaker and shallower, which reinforces the assumption that such strong and deeper eastward flow is forced by changes in eddy-related energy. These findings can be of great value to evaluate the impact of deep-sea mining activities in the vicinity of the Azores ecosystem.

Keywords: Azores Current, EKE.

1. INTRODUCTION

The most prominent feature at the region of study is the Azores Current (AzC), characterized as an eastward jet-like flow (Figure 1). The region is subject of an intense eddy-related energy and the wind forcing can affect the magnitude of AzC transport and Eddy Kinetic Energy (EKE) [1]. Studies have demonstrated that large eddies passing through the open ocean can have a profound effect on the variability of near-bottom currents even at depths of 4000 m or more, likely reflecting the energy transfer of the surface EKE to the deep ocean [2]. At the Clarion-Cliperton Zone (CCZ), for instance, the current variability close to sea-floor is closely related to the passage of mesoscale eddies, when mining-related sediment plumes could spread more widely and rapidly during eddy-induced elevated bottom-water current flow periods [3].

The Mid-Atlantic Ridge (NMAR) at Azores presents relevant deposits of polymetallic sulfides (PMS) interesting for the industry, which are likely to be mined. These deposits are particularly close to the hydrothermal fields, a region with presence of fragile ecosystems. The southwestern region of NMAR is close to the AzC region of formation, where strongest eddy-related energy is found. The near-bottom and sub-surface sediment plumes produced during mining activities at this region can be influenced by eddy-related deep current variability which can drive a dispersion with the chance to impact a wider area of deep-sea communities. Based on the findings for the CCZ, this work aims to investigate the possible intensification of the AzC zonal jet as a response to events of strong eddy-related energy.

Understanding the effects of eddy-related in-depth current variability and its possible impact on sediment plume behavior, can be of great value to map environmental sensitivity regions and establish safe mining areas, giving key information to regulatory entities to standardize and approve the execution of deep-sea mining activities.

2. METHODS AND RESULTS

Sea Level Anomalies (SLA) and Geostrophic velocities (VelG) derived from Copernicus [4] and currents derived from CMEMS Global Ocean Analysis [5] were used to evaluate the impact of energetic eddies in the deep-sea circulation at the Azores Current (AzC) region (Figure 1, AzC box). The Eddy Kinetic Energy (EKE) was calculated from VelG anomalies (EKE = (u'^{2} + v'^{2})$^{0.5}$). The deep-sea circulation in the southwestern region of the North Mid-Atlantic Ridge at Azores (NMAR, Figure1) can be affected by strong eddies related to the AzC.
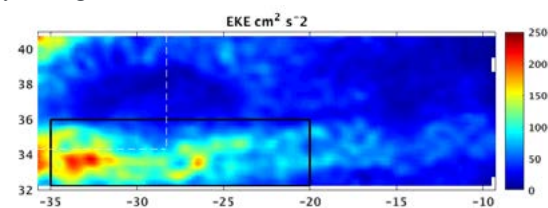
Figure 1. *Average EKE (2015-2018) for the region of study. The AzC box is delimited by the black solid lines and the Azores region by the white shaded lines.*

Our focus is on the period between 2014 and 2019. During this period, a strong EKE signal of about 180 cm^2 s^{-2} was observed in late 2014, in the entire AzC box, and lasted until the first trimester of 2015 (Figure 2). Except for 2018, a relatively similar pattern with a mean annual value of about 100 cm^2 s^{-2} is observed, with tendency to lower EKE values in the second semester, as observed for 2015. During September 2018 another strong EKE increase, of about 160 cm^2 s^{-2}, was observed.
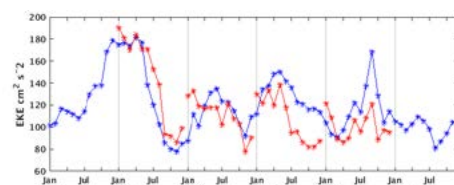

Figure 2. *Monthly mean EKE in the AzC box derived from satellite altimetry (blue) and model analysis (red).*

The VelG superimposed on the EKE maps for the winter seasons (JFM) of the study period show an intense anticyclonic circulation during 2015 close to the AzC formation (Figure 3), with intensity of the order of 40 cm s^{-1} and 200 km diameter, associated to a strong EKE of about 800 cm^2 s^{-2} and Sea Level Anomaly (SLA) of 40 cm (not shown). Centred at 25°W; 34°N there is a cyclonic circulation with approximately the same scale, but intensity up to 25 cm s^{-1} close to its border. Similar patterns can be seen in the other years, with maximum eddy intensity up to 20 cm s^{-1}. However, in September 2018, an intense anticyclonic circulation of about 40 cm s^{-1}, associated with a strong EKE, was observed, which has influenced the energy of the entire AzC box during the same month (Figure 2).
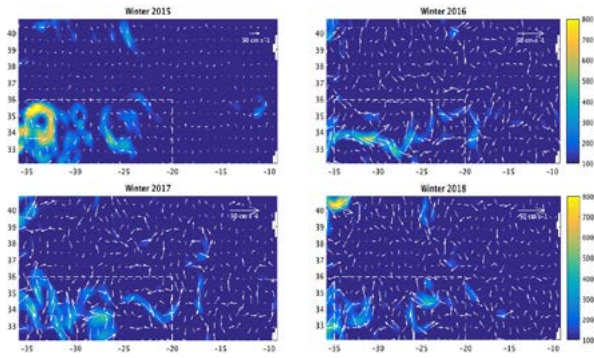
Figure 3. *Mean EKE (shaded, cm² s²) and VelG (vector, cm s⁻¹) derived from satellite altimetry during the winter seasons of 2015-2018.*

The averaged (2015-2018) zonal current structure, at depth, longitudinally averaged at the AzC box (not shown), shows a similar behaviour as the results described by [6], based on 20-years of climatic model results. According to [6], the AzC reach its maximum intensity and depth during the winter months (JFM), starting to decrease towards summer (JAS), when it is weaker and shallower. Then, the AzC increases in intensity and depth from autumn (OND) to winter. Looking at the seasonal vertical structure of the zonal current during 2015 (Figure 4), the opposite situation can be observed. There is a decrease in intensity from winter to spring, as described by [3], however, the zonal current increases in intensity and depth from summer to the autumn season, when it reaches up to 14 cm s⁻¹ in the first 200 m depth, and intensities of about 6 cm s⁻¹ can reach a depth of 800 m.
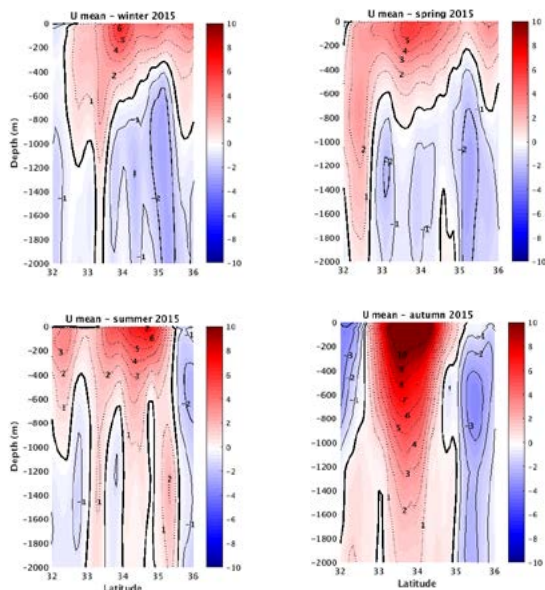
Figure 4. *Seasonal zonal current structure (cm s⁻¹), longitudinally averaged, at the AzC box during 2015. Positive (negative) values are eastwards (westwards).*

These results suggest that the adjustment of the ocean circulation to the high EKE observed in the first trimester of 2015 starts to occur with a time lag of about 3-months, lasting for a period of six months. [2] Observed that deep-sea currents at the northeast tropical Pacific Ocean took 2 weeks to adjust to an anticyclonic eddy associated to SLA values of 10 cm, and its effects lasted for almost two months.

During the late summer of 2018, a strong anticyclonic eddy was again observed at the AzC westernmost region, associated with EKE values of about 700 cm² s⁻² and SLA values of 30 cm (not shown). The zonal current reached the strongest eastward intensity in late spring, exactly nine months after the strong EKE observed in September, with intensities up to 14 cm s⁻¹ in the first 200 m (Figure 5). Seasonally, the spring/summer seasons experience a decrease of the in-depth eastward AzC flow, following to an increase from autumn to winter [3]. These results suggest that strong eddy related energy act as an important drive mechanism to the eastward AzC jet, as observed for 2015.
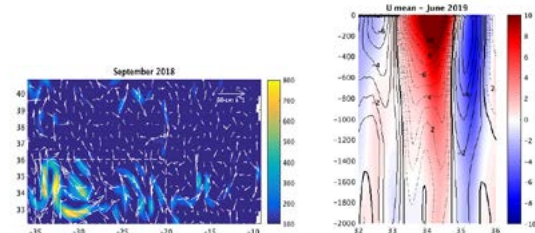
Figure 5. L*eft: mean EKE (shaded, cm² s²) and VelG (vector, cm s⁻¹) during September 2019, derived from satellite altimetry. Right: zonal current structure, longitudinally averaged, at the AzC box during March 2019.*

3. CONCLUSION

The present study aimed to investigate the response of the AzC eastward flow to events of strong surface EKE. The results suggests that the zonal current along depth starts to adjust to the strong energetic eddy field with a time lag of about three months, lasting for six months. The AzC zonal jet reached intensities if 14 cm s⁻¹ during the autumn and late spring seasons at the first 200 m depth, when, seasonally, the AzC is weaker and shallower. These findings is of great value to understand the AzC behaviour and how an EKE intensification can affect the deep-sea currents at the southwestern NMAR area. This region presents relevant deposits of PMS likely to be mined, which could harm fragile deep-sea ecosystems. Understanding the influence of EKE on deep-sea currents can be of great value to the elaboration of mitigation plans towards the adoption of environmentally friendly practices for sustainable deep-sea exploitation.

REFERENCES

[1] Volkov and Fu, 2011. doi:10.1029/2011JC007271.
[2] Purkiani et al., 2020. doi:10.5194/bg-17-6527-2020
[3] Aleynik et al., 2017. doi:10.1038/s41598-017-16912-2
[4] Copernicus Climate Change Service. https://cds.climate.copernicus.eu/
[5] Copernicus Marine Service. CMEMS Mercator. https://resources.marine.copernicus.eu/products
[6] Bettencourt et al., Seasonality of the Energy Transfers in the Azores Current. Submitted to the Journal of Geophysical Research: Oceans.

Knowledge Hub on Sea Level Rise

A. Bonaduce [1]*, Bart van den Hurk[2] (on behalf of the Knowledge Hub on Sea Level Rise)

[1]Nansen Environmental and Remote Sensing Center and Bjerknes Center for Climate Research, Norway
[2]Deltares, Delft, Netherlands

Abstract - The Knowledge Hub on Sea-level Rise (KH SLR) is a JPI Ocean and JPI Climate joint effort to provide easy access and usable knowledge on regional-local sea level change in Europe. To create an effective interface between data, knowledge, and applications the KH SLR identified the need for an assessment process including (i) scoping and (ii) survey of information needs, (ii) convening with multiple experts and application professionals, and (iv) compilation of a regional sea-level assessment report for the major European basins. The first steps of the assessment process were developed during a series of scoping workshops, focused on the Europeans Seas, setting the agenda for a sea-level conference in 2022 (Venice, Italy). The fundamental role played by sea-level remote sensing retrievals towards accurate SLR information tailored to the European basin, was acknowledged as part of main steps toward effective assessment reports.

Keywords: Sea-level rise, Knowledge Hub, European Seas, sea level regional assessments.

1. INTRODUCTION

Sea level is a key climate indicator as it represents the integrated response to changes in the atmosphere, ocean and cryosphere (Frederikse et al., 2020). Sea-level rise (SLR), together with vertical land movements and changes in sediment supply, threatens coastal population infrastructure and ecosystems worldwide. Without adaptation, the resulting damages are expected to amount up to 10% of the global gross domestic product (GDP) annually by 2100 (Hinkel et al., 2014). SLR during the 21st century is expected to be larger than during the 20th century, and is projected to continue for multiple centuries even if greenhouse gas emissions are stopped now (Hu and Bates, 2018). The latest IPCC report (Fox-Kemper et al., 2021) points to a likely global mean sea-level rise of 28–55 cm and 63-101 cm for a very low and a very high emission scenario, respectively, by the end of the 21st century. Also, for the first time it puts forward estimates for a high-end scenario (albeit with low confidence) with global SLR approaching 2 m by 2100 and exceeding 15 m by 2300. As sea level continues to rise, more regions around the world are projected to become exposed to permanent or episodic flooding (Almar et al., 2021).In this context, there is an increased need for regional sea-level assessments, based on the understanding of how global mean sea-level rise can translate locally, to provide the practitioners with the most effective information for implementing adaptation strategies (e.g. Melet et al., 2021) with high societal impact. The latter is in line with the strategic framework of the Joint Programming Initiatives (JPIs) of the European Commission on Healthy and Productive Oceans and Climate Knowledge, which are pan-European intergovernmental platforms to increase the efficiency and impact of research and innovation. A joint effort between JPI Oceans and JPI Climate led in 2020 to a networking platform promoting the generation, synthesis, exchange and integration of knowledge on local, regional and global, historic and future sea level rise: the Knowledge Hub on Sea Level Rise (KH SLR), currently supported by nine JPI member countries and composed of a network of pan-European experts on sea level rise. The ambition is to provide easy access and usable knowledge on regional-local sea level change in Europe, regularly updated as a series of periodic assessments, which calls for an effective interface between data, knowledge and application. In the next Sections we describe the KH SLR activities contributing to this interface.

2. KH SLR Activities: Assessment Process

The management committee of the KH SLR identified scoping, a survey of needs, convening with multiple experts and application professionals, and compilation of an assessment report as milestones of the assessment process required to contribute to easy access between data, knowledge, and application. The roadmap for the first phase of implementation of the KH SLR reflects those milestones, leading to a large expert scoping conference (in 2022 in Venice, Italy). The conference has been endorsed as an Ocean Decade activity under the UN Decade of Ocean Science for Sustainable Development (2021-2030). As a preparatory phase to that pan-european sea-level conference, scoping regional workshops were organized in 2022 for the major European Sea basins (see Table 1), inviting sea-level scientists and practitioners, to frame the needs for sea-level rise regional assessments. The agenda of each scoping workshop was informed by a survey, to profile the needs and knowledge gaps on regional SLR and included (i) panel discussions with practitioners from several countries facing the specific European basin, (ii) plenary sessions focused on the added value of having basin-specific assessment reports, (iii) interactive break-out sessions to inform the content of the assessments and (iv) keynote speeches on SLR physical science, impact, and adaptation. The outputs of each workshop were summarized in dedicated reports focused on basin-specific SLR information, hazards, and adaptation strategies. The main result of the workshops and conference will be an assessment report on sea level rise drivers, impacts, and policy options for each of the major European sea basins.

Table 1. Sea level *scoping workshops in the European Basins. The columns show (from the left) the relevant basins covered by each workshop, the Days when the meeting was organized. the number of registered participants (NP).*

Workshop	Days (2022)	NP
North Sea/Arctic	21-22 Mar.	101
East Atlantic	28-29 Apr.	74
Med/Black Sea	5-6 May	129
Baltic Sea	9-10 May	120

[1]* Corresponding author. Address: * Corresponding author. Address: Jahnebakken 3, 5007 Bergen, Norway. Email: antonio.bonaduce@nersc.no

3. Regional information on SLR

In all the workshops the participants highlighted the need of improved information on combined processes, e.g. due to vertical land movements, changes of wind patterns and wave climate induced by sea-ice retreat, shift of storm tracks, which can influence the magnitude of sea-level extreme events and the footprint (frequency, duration, spatial coherence) of compound events in coastal areas with cascading impacts on sensitive ecosystems (e.g. wetlands) and human activities (e.g. due to salt intrusion). The need of having reliable measurements, tailored to the sea-level variability in the open ocean and in regional and local domains, was also acknowledged emphasizing the importance of remote-sensing measurements in particular in the areas where in-situ measurements are sparse. Hence, accessing sea-level data suitable for regional sea-level assessments is a requirement for obtaining the SLR information at the right accuracy. Satellite altimetry measuring sea level at millimetric precision has made a fundamental contribution to the understanding of ocean circulation during the last three decades. Mapped sea-level anomaly (SLA) fields are typically used to assess SLR and variability at the global (Legeais et al., 2018, Horwarth et al., 2022) and regional (e.g. Raj et al., 2020) scales. Their accuracy depends on the number of satellite mission available, the mapping technique used and the-signal-to-noise ratio of the along-track measurements (Dufau et al., 2016), which can limit the observability according to the geographical area considered. As such, the error in satellite altimetry data (e.g. CMEMS, 2022a, 2022b) can be characterized both by measurement and sampling errors. It is then important to quantify how those errors propagate into the trend uncertainties (e.g. Storto et al, 2022) and affect the significance of the SLR estimates at the regional scale. Exploring the available information on the accuracy of SLR estimates will make part of the KH SLR activities addressed to the compilation of regional assessment reports.

3. CONCLUSIONS

A process to achieve effective regional sea-level rise assessments in the European Sea was developed by the KH SLR during a series of scoping workshops to inform the agenda of a pan-european sea-level conference held in 2022 in Venice. The workshops, focused on major European basins, detailed the priorities in terms of SLR information, hazards and impact, policy and adaptation needed to make regional sea-level assessment reports an effective interface between knowledge and application. In this sense, knowing the accuracy of regional SLR information and how the measurement and sampling errors affect the SLR uncertainty can represent a fundamental step where regional and coastal sea-level (Benveniste et al., 2020) retrievals from remote sensing can make a difference, in particular in areas where the lack of in-situ measurements remains an issue.

ACKNOWLEDGEMENTS

REFERENCES

Almar, R., et al. (2021). A global analysis of extreme coastal water levels with implications for potential coastal overtopping. Nat. Commun. 12, 3775. doi: 10.1038/s41467-021-24008-9.

Benveniste, J., et al. (2020). Coastal sea level anomalies and associated trends from Jason satellite altimetry over 2002–2018. Sci. Data 7, 357. doi: 10.1038/s41597-020-00694-w.

CMEMS (2022a). GLOBAL OCEAN GRIDDED L4 SEA SURFACE HEIGHTS AND DERIVED VARIABLES REPROCESSED (1993-ONGOING). Available at: https://resources.marine.copernicus.eu/product-detail/SEALEVEL_GLO_PHY_L4_MY_008_047/INFORMATION

CMEMS (2022b). EUROPEAN SEAS GRIDDED L4 SEA SURFACE HEIGHTS AND DERIVED VARIABLES REPROCESSED (1993-ONGOING). Available at: https://resources.marine.copernicus.eu/product-detail/SEALEVEL_GLO_PHY_L4_MY_008_047/INFORMATION

Dufau, C., et al. (2016). Mesoscale resolution capability of altimetry: Present and future. *J. Geophys. Res. Oceans* 121, 4910–4927. doi: 10.1002/2015JC010904.

Fox-Kemper, B., et al. (2021). Ocean, Cryosphere and Sea Level Change. In: Climate Change 2021: The Physical Science Basis. Contribution of Working Group I to the Sixth Assessment Report of the Intergovernmental Panel on Climate Change Cambridge University Press.

Frederikse, et al. (2020). The causes of sea-level rise since 1900. *Nature* 584, 393–397. doi: 10.1038/s41586-020-2591-3.

Hinkel, J., et al. (2014). Coastal flood damage and adaptation costs under 21st century sea-level rise. *Proc. Natl. Acad. Sci.* 111, 3292–3297. doi: 10.1073/pnas.1222469111.

Horwath, M., et al. (2022). Global sea-level budget and ocean-mass budget, with a focus on advanced data products and uncertainty characterisation. *Earth Syst. Sci. Data* 14, 411–447. doi: 10.5194/essd-14-411-2022.

Hu, A., and Bates, S. C. (2018). Internal climate variability and projected future regional steric and dynamic sea level rise. *Nat. Commun.* 9, 1068. doi: 10.1038/s41467-018-03474-8.

Legeais, J.-F., et al. (2018). An improved and homogeneous altimeter sea level record from the ESA Climate Change Initiative. *Earth Syst. Sci. Data* 10, 281–301. doi: 10.5194/essd-10-281-2018.

Melet, A., et al. (2021). European Copernicus Services to Inform on Sea-Level Rise Adaptation: Current Status and Perspectives. *Front. Mar. Sci.* 8. Available at: https://www.frontiersin.org/article/10.3389/fmars.2021.703425.

Storto, A., Cheng, L., and Yang, C. (2022). Revisiting the 2003–18 Deep Ocean Warming through Multiplatform Analysis of the Global Energy Budget. *J. Clim.* 35, 4701–4717. doi: 10.1175/JCLI-D-21-0726.1.

Taburet, G., et al. (2019). DUACS DT2018: 25 years of reprocessed sea level altimetry products. *Ocean Sci.* 15, 1207–1224. doi: 10.5194/os-15-1207-2019.

Mesoscale variability in the Southern Ocean: the potential of enhanced altimetry

A. Bonaduce[1*], A. Cipollone[2], A. Storto[3], R.P. Raj[1], J.A. Johannessen[4]

[1]Nansen Environmental and Remote Sensing Center and Bjerknes Center for Climate Research, Norway
[2] Centro Euro-Mediterraneo sui Cambiamenti Climatici, Italy
[3] Institute of Marine Sciences, ISMAR-CNR, Italy
[4]Nansen Environmental and Remote Sensing Center and University of Bergen, Norway

Abstract – The mesoscale field in the Southern Ocean emerging from satellite altimetry maps is investestigated by means of automated eddy detection methods and co-locating the non-linear features with Argo-profiling floats over the period 2014-2018. The results show a much larger eddy population emerging from enhanced satellite altimetry, compared to conventional maps, which also reflect also into the spatial distribution and contributions to ocean dynamics of long-living mesoscale features. The co-location with Argo profiling floats shows that the vertical profiles of temperature (salinity) trapped by cyclonic and anticyclonic features were generally colder (saltier) in the enhanced regional maps, compared to those available for the global ocean.

Keywords: Altimetry, Mesoscale Eddies, Southern Ocean

1. INTRODUCTION

Mesoscale eddies can originate nearly everywhere in the ocean, and typically exhibit different properties (e.g., heat, salt, carbon) with respect to their surroundings, which can be transported as they move around the ocean (Chelton et al., 2011; Zhao et al., 2018). At the surface, mesoscale eddies are identified from satellite altimetry data, where depression (elevation) in the sea level anomaly (SLA) field reveals a cyclonic (anticyclonic) structure. Although only the surface expression of mesoscale eddies is visible in remote sensing measurement of SLA and sea-surface temperature (SST), they are three-dimensional (3D) structures that can reach down into the pycnocline. Temperature and salinity anomalies induced by eddies tend to be opposite depending on the polarity of an eddy: cyclones (CE) versus anticyclones (ACE) (Gaube et al., 2013; Dong et al., 2014). In the Southern Ocean (SO) mesoscale eddies modulate the wind-driven overturning (Hallberg and Gnanadesikan, 2006), influence near-surface wind, clouds and rainfall (Frenger et al., 2013) and enhance the biological production (Kahru et al., 2007). Moreover, recent findings show how mesoscale eddies strongly affect atmosphere-sea ice-ocean interactions in the SO (Huot et al., 2022), as well as subsurface temperature distribution on the continental shelves surrounding Antarctica which in turn control the rate of basal melt and Antarctic ice-sheet surface mass balance with significant contribution to mean sea-level projections (van Westen et al., 2020). As such it is fundamental to monitor the changes in the SO and the mesoscale induced variability. In this sense, recent efforts were done by Auger et al., 2022 by re-tracking multimission (Cryosat-2, Sentinel-3A, and SARAL/AltiKa) along track observations in open ocean and sea-ice covered areas to obtain enhanced altimetry maps in the SO. In this study we build on those recent results to assess the mesoscale field emerging from the synergies between remote sensing retrievals and in-situ measurements. We investigate the benefits of the reprocessed altimetry dataset with augmented signal resolution in the context of ocean mesoscale dynamics. In particular, we perform a fit-for purpose assessment of this dataset investigating the contribution of eddy-induced anomalies to ocean (i) dynamics and (ii) thermodynamics, by co-locating eddies with Argo profiling floats, and (iii) compare them with those obtained from conventional altimetry maps in order to assess the added value of the enhanced altimetry reprocessing in the SO.

2. MESOSCALE CONTRIBUTIONS

In order to characterize the eddy population in the SO and disclose the mesoscale contributions to ocean dynamics and thermodynamics, an automated eddy detection algorithm (Cipollone et al., 2017; Bonaduce et al., 2021) was applied to the enhanced and conventional altimetry maps. Figure 1 shows the statistics of the eddy population detected from satellite altimetry as a function of eddy lifetime over a 5-year period (2014-2018). The results clearly show a much larger number of mesoscale features detected from enhanced satellite altimetry data, which also show a smaller size (averaged diameter of 70 km), compared to conventional altimetry maps. The overall relative eddy decay (%) from enhanced maps is affected by the richness of short-living eddies making the total eddy population decaying faster compared to conventional altimetry, while the number of long-living features (> 28 days) is higher.
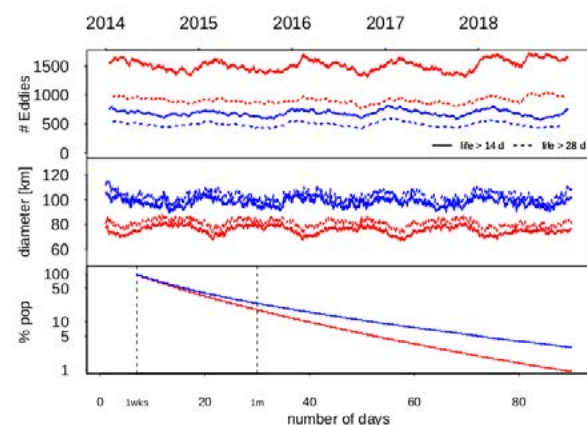

Figure 1. *Eddy statistics. The panels show the statistics of the eddy population detected from conventional (blue lines) and enhanced (red lines) satellite maps. From the top: Number of eddies and eddy diameter (km) as a function of lifetime and years. Eddy decay (% pop.) as a function of lifetime (defined as in Cipollone et al., 2017).*

The differences observed in the eddy population reflect also into the spatial distribution and contributions to ocean dynamics of long-living mesoscale features. Figure 2 shows the portion of Eddy Kinetic Energy (EKE) explained by eddy lifetime > 28 days. The results show eddy contributions larger than 50 % in both data-se, but detecting eddies from enhanced altimetry maps the ocean mesoscale field clearly emerges in the Antarctic Circumpolar Current, including sea-

---

[1*] Corresponding author. Address: Jahnebakken 3, 5007 Bergen, Norway. Email: antonio.bonaduce@nersc.no

ice covered areas such as those in the Weddell Sea, Ross Sea and Amundsen Sea.
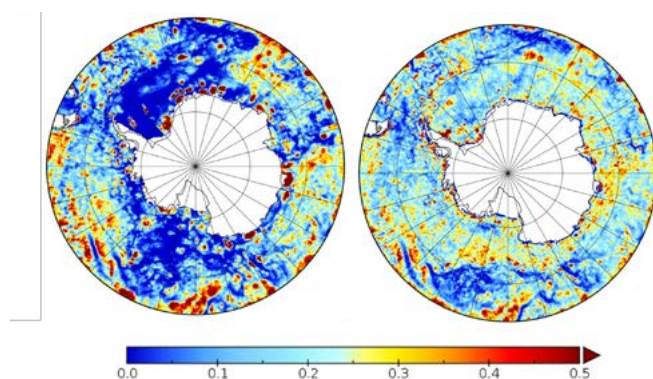

Figure 2. Figure 2. *Eddy kinetic energy explained by eddies lifetimes > 28 days expressed in percentage (%). The results are obtained considering conventional (left) and enhanced (right) satellite altimetry maps over a 5-year period, from 2014 to 2018.*

The co-location with Argo profiling floats allows for inferring the quasi-3D structure of the non-linear features by investigating the physical properties of ocean waters trapped by eddies. As expected cyclonic features tended to be colder and shallower than the anticyclones both in conventional and enhanced altimetry data. On the other hand, due to differences in the eddy populations, the number of profiling floats trapped by eddies detected from augmented signals data was significantly larger than in the reference (not shown). Figure 3 shows the differences between the vertical profiles trapped by long-living eddies detected from both data-sets. In particular, positive (negative) values means the vertical profiles of the eddies detected from augmented signal showed larger (smaller) temperatures and salinities compared to the reference altimetry maps.
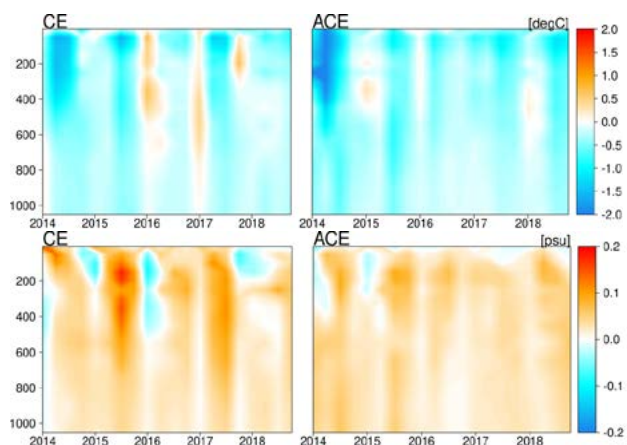
Figure 3. *Argo profiling floats trapped by eddies. The panels show the temperature (top) and salinity (bottom) seasonal profile differences obtained considering Argo profiling floats trapped by cyclonic (left) and anticyclonic (right) eddies detected from conventional and enhanced altimetry data considering eddy lifetime > 14 days.*

The results, obtained considering seasonal mean differences over the analysis considered in this study (2014-2018), clearly show the departures of the mesoscale fields emerging from the enhanced altimetry maps. The vertical profiles of temperature (salinity) trapped by cyclonic and anticyclonic features were generally colder (saltier) in the enhanced regional maps, compared to those available for the global ocean. Temperature differences larger than 2°C degrees were observed in 2014, while they ranged between 0.5°C and 1°C over other periods. Positive differences in terms of salinity, up to the order of 0.2 psu, can be noticed in almost the whole analysis period, except for negative values observed during winters, e.g. in 2016 which also reflect positive differences in terms of temperature.

3. CONCLUSIONS

The mesoscale field in the Southern Ocean emerging from satellite altimetry maps was assessed by means of automated eddy detection methods. The eddy population was significantly larger in the regional altimetry map and with a smaller size, compared to those available for the global ocean. The enhanced altimetric signals clearly show an impact to characterize the mesoscale contribution to ocean dynamics, where eddy explained a large amount of the kinetic energy associated to the ACC (> 50 %) and show their signatures also in sea-ice covered areas. The differences in the eddy populations project into different contributions to ocean thermodynamics, obtained by collocating the non-linear features with Argo profiling floats to infer their quasi-3D structures. Non-linear mesoscale features from enhanced altimetry maps tended to be significantly colder and saltier compared to those detected from conventional altimetry. The latter is expected to contribute to different heat and freshwater transports induced by eddies at the high latitudes, with high impact on ocean-cryosphere interactions.

ACKNOWLEDGEMENTS

REFERENCES

Auger, M., et al. (2022). Southern ocean sea level anomaly in the sea ice-covered sector from multimission satellite observations. *Sci. Data* 9, 70. doi: 10.1038/s41597-022-01166-z.

Bonaduce, A., et al.. (2021). Ocean Mesoscale Variability: A Case Study on the Mediterranean Sea From a Re-Analysis Perspective. *Front. Earth Sci.* 9, 816. doi: 10.3389/feart.2021.724879.

Chelton, D. et al., (2011). Global observations of nonlinear mesoscale eddies. *Prog. Oceanogr.* 91, 167–216. doi: 10.1016/j.pocean.2011.01.002.

Cipollone, A., et al. (2017). Benchmarking the mesoscale variability in global ocean eddy-permitting numerical systems. *Ocean Dyn.* 67, 1313–1333. doi: 10.1007/s10236-017-1089-5.

Dong, C., et al., (2014). Global heat and salt transports by eddy movement. *Nat. Commun.* 5, 3294. doi: 10.1038/ncomms4294.

Frenger, I., et al., (2013). Imprint of Southern Ocean eddies on winds, clouds and rainfall. *Nat. Geosci.* 6, 608–612. doi: 10.1038/ngeo1863.

Gaube, P., et al., (2013). Satellite observations of chlorophyll, phytoplankton biomass, and Ekman pumping in nonlinear mesoscale eddies. *J. Geophys. Res. Oceans* 118, 6349–6370. doi: https://doi.org/10.1002/2013JC009027.

Hallberg, R., and Gnanadesikan, A. (2006). The Role of Eddies in Determining the Structure and Response of the Wind-Driven Southern Hemisphere Overturning. *J. Phys. Oceanogr.* 36, 2232–2252. doi: 10.1175/JPO2980.1.

Kahru, M., et al., (2007). Eddies enhance biological production in the Weddell-Scotia Confluence of the Southern Ocean. *Geophys. Res. Lett.* 34. doi: 10.1029/2007GL030430.

van Westen, R. M., et al. (2020). Ocean model resolution dependence of Caribbean sea-level projections. *Sci. Rep.* 10, 14599. doi: 10.1038/s41598-020-71563-0.

Zhao, J., et al. (2018). Meridional heat transport variability induced by mesoscale processes in the subpolar North Atlantic. *Nat. Commun.* 9, 1124. doi: 10.1038/s41467-018-03134-x.

Addressing the ten UN Ocean Decade Challenges with EUMETSAT and Copernicus data

Vittorio Brando[*1], Benjamin Loveday[2,3], Christine Träger-Chatterjee[3], Hayley Evers-King[3], Vinca Rosmorduc[4], Ana Ruescas[5,6], and Aida Alvera-Azcárate[7]

1. CNR ISMAR, Rome, Italy
2. Innoflair UG, Germany
3. EUMETSAT, Eumetsat Allee 1, Darmstadt, Germany
4. CLS, Ramonville, Saint-Agne, France
5. Brockmann Consult GmbH, Hamburg, Germany
6. Universitat de València, Spain
7. GHER, University of Liege, Belgium

Abstract – The UN Decade of Ocean Science for sustainable development has proposed 10 challenges for collective impact. The challenges address marine pollution, biodiversity, sustainable food production and ocean economy, climate change, resilience to ocean hazards, ocean observation, digital representation of the ocean, capacity development, and humanity's relationship with the ocean. In a series of use case stories, we will show how data provided by EUMETSAT, and that provided by Copernicus missions and services, can support meeting these challenges. From climate scale observations of sea-level change to estimating ocean carbon pools; from providing easily accessible data visualization tools to in-depth training courses; data and activities provided by EUMETSAT are able to contribute to a more sustainable future for our oceans and thus for all of us, whether we depend on oceans directly or indirectly. Each case will include a web-based story, links to further information on data and opportunities through EUMETSAT, as well as a hosted Jupyter Notebook showing an example of the relevant data in use. In this presentation we will summarize the series of cases, released over the course of 2022, and provide a live demonstration of some example applications of these notebooks in action.

Keywords: UN Ocean Decade, EUMETSAT, Copernicus, Sentinel-3, Sentinel-6, ocean.

1. INTRODUCTION

Achieving the outcomes of the UN Ocean Decade (UNOD) requires a comprehensive strategy that employs different tools, observation methods and training approaches. Remote sensing platforms are a key part of the Global Ocean Observing System and can make an essential contribution to this strategy via activities that apply satellite-based data directly to specified challenges, or via educational platforms that seek to lower the barrier to its use.

2. UN OCEAN DECADE ACTIVITIES

EUMETSAT regularly publishes web-based case studies highlighting the use of satellite data to monitor specific ocean phenomena or events. From 2022, these will focus on addressing specific UNOD challenges (figure 1). Each case study will feature links to contextual information and a companion Jupyter Notebook showing the data in use. In support of open science, all code will be open source and freely distributed via GitLab.

In addition, EUMETSAT is engaged in a series of training events as UNOD actions. The month-long Supporting Marine Applications and Supporting Marine Educators events, run every year and every other year, respectively. These courses address the use of Earth observation data to support trainers and researchers and support the increased use of Copernicus marine data in support of challenge nine and ten.
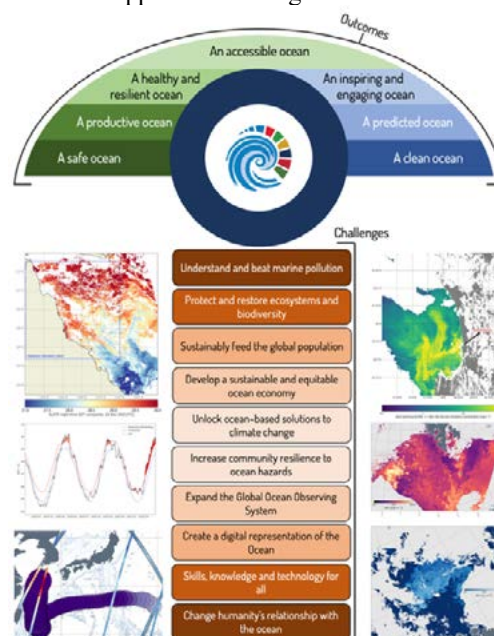
Figure 1. *Examples of Sentinel-3/6 products used in support of case studies to address UNOD outcomes and challenges.*

3. CONCLUSION

The summarised activities lower the barriers to accessing and working with marine satellite data, increasing its uptake, and provide accompanying tools and examples of its use in support of addressing UNOD challenges via case studies.

ACKNOWLEDGEMENTS

REFERENCES

UNESCO-IOC (2021). The United Nations Decade of Ocean Science for Sustainable Development (2021-2030) Implementation Plan. UNESCO, Paris (IOC Ocean Decade Series, 20.)

---

[*] Dr. Vittorio E. Brando, vittorio.brando@cnr.it, CNR – ISMAR, Roma, ITALY

ALBATROSS: Improving the bathymetry and ocean tide knowledge in the Southern Ocean with satellite observations

M. Cancet[1]*, O. Andersen[2], M. Tsamados[3], G. Moholdt[4], F. Lyard[5], T. Johnson[3], M. Restano[6], J. Benveniste[7]

[1]NOVELTIS, Labège, France, [2]DTU Space, Kongens Lyngby, Denmark, [3]UCL, London, United Kingdom, [4]Norwegian Polar Institute, Tromsø, Norway, [5]LEGOS/OMP/CNRS, Toulouse, France, [6]SERCO/ESA, Frascati, Italy, [7]ESA/ESRIN, Frascati, Italy

Abstract – The ALBATROSS (Altimery for BAthymetry and Tide Retrievals for the Southern Ocean, Sea ice and ice Shelves) project aims to revisit bathymetry information and ocean tide modelling around Antarctica by exploiting the most recent satellite datasets and bringing together international interdisciplinary expertise about bathymetry processing, physical oceanography, ocean tide modelling, and sea ice and ice shelf dynamics. The ALBATROSS project is at the crossroads of many disciplines, as the actual bathymetry and ocean tide knowledge is widely recognized as a limiting factor to the understanding of ocean and ice dynamics in the Southern Ocean, especially for climate research.

Keywords: Antarctica, Bathymetry, Ocean tides, Sea ice, Ice shelves, Satellite altimetry.

1. INTRODUCTION

The knowledge about bathymetry and ocean tides is at the crossroads of many scientific fields, especially in the Polar regions, as it has significant impact on the understanding of the coupled dynamical response of the ocean, sea ice and ice shelves system, as well as on the accuracy of ocean and ice parameters derived from satellite measurements. Tides in the Southern Ocean strongly influence the whole global ocean, and accurate and complete bathymetry information is crucial for tidal modelling, in particular under the Antarctic ice shelves.

The ALBATROSS project (ALtimetry for BAthymetry and Tide Retrievals for the Southern Ocean, Sea ice and ice Shelves), led by NOVELTIS in collaboration with DTU Space, NPI and UCL, is funded by the European Space Agency in the frame of the Polar Science Cluster in the EO4Society Programme, with the objective to foster collaborative research and interdisciplinary networking within polar Earth Observation.

ALBATROSS is a 2-year project (2021-2023) with several objectives: First, to improve the knowledge on bathymetry around Antarctica, considering decade-long reprocessed CryoSat-2 datasets, innovative information on bathymetry gradient location through the analysis of sea ice surface roughness characteristics, and the compilation of the best available bathymetry and ice draft datasets in ice-shelf regions. Second, to improve the knowledge on ocean tides in the Southern Ocean through the implementation of a high-resolution hydrodynamic model based on the most advanced developments in ocean tide modelling, including data assimilation of satellite-altimetry tidal retrievals computed from the most recent and relevant satellite altimetry products to fill the gap between the 66°S-limited coverage of the Topex-Jason suite missions and the Antarctica coast.

This paper presents the most recent results obtained within the ALBATROSS project.

2. MAIN PROJECT OUTCOMES

To improve the knowledge about the bathymetry in the Southern Ocean, different approaches are considered within the ALBATROSS project.

First, several existing bathymetry datasets have been tested to produce tidal simulations with a regional hydrodynamic model configuration in the Southern Ocean, following the same methodology as Cancet et al., 2019 and Lyard et al., 2021. A combination of the BedMachine_Antarctica-2020-v2 (Morlighem et al., 2020) and RTopo-2.0.4 (Schaffer et al., 2019) datasets provided the best tidal estimates, and has been considered as the reference bathymetry for the project.

A new open-ocean bathymetry has been produced, combining this reference bathymetry with the new DTU21 gravity field, which includes the most recently reprocessed CryoSat-2 data (including SAR and SARin modes) in the Southern Ocean. The comparison with survey observations demonstrates some improvements compared to the reference bathymetry. However, in situ bathymetry observations are scarce in the region and generally already integrated into the bathymetry models. Qualifying the bathymetry datasets through tidal hydrodynamic simulations is thus a complementary approach that enabled to highlight some regions of clear improvement thanks to the new DTU-ALBATROSS bathymetry.

As bathymetry controls ocean currents, temperature and sea ice presence, locations of steep bathymetry act as hot spots of enhanced vertical heat fluxes mediated by tides and increased turbulence, and higher lead density correlates very well with steep bathymetry. Within ALBATROSS, a novel technique developed at ES UCL (Johnson et al., 2021) is used to produce sea ice surface roughness maps from NASA MISR (Multi-angle Imaging Spectro-Radiometer) and Operation Ice-Bridge (OIB) data, with the objective to use the sea ice surface properties as proxy to assess the location of the gradients in the bathymetry dataset. The sea ice roughness characteristics based on MISR and OIB data have demonstrated the ability of such products to robustly detect a wide range of sea ice roughness features, and make it an excellent proxy for sea ice thickness. Preliminary results comparing bathymetry features, sea ice roughness and tidally driven vertical excursion maps show interesting spatially coincident patterns (Fig. 1).

Accurate information about grounding line location, bedrock topography and ice draft under the ice shelves is crucial to perform accurate tidal simulations in the Southern Ocean, but also at the global scale. A new composite grounding line (Fig. 2) has been produced by NPI within the ALBATROSS project, combining different methods based

---

* Corresponding author. Address: NOVELTIS, 153 rue du Lac, 31670 Labège, France. Email: mathilde.cancet@noveltis.fr

on satellite measurements (SAR interferometry, altimetry and optical imagery). Datasets from the NASA-MeASUREs, ESA-CCI and ESA Polar Ice Shelves projects have also been collected. The coastline has also been updated for 2022, using LandSat-8 and Sentinel-2 images, and it has been combined with the grounding line to obtain the ice-shelf mask. Recent DEMs were analysed and merged into the BedMachine_Antarctica-2020-v2 reference bathymetry dataset to improve the bathymetry under the ice shelves.
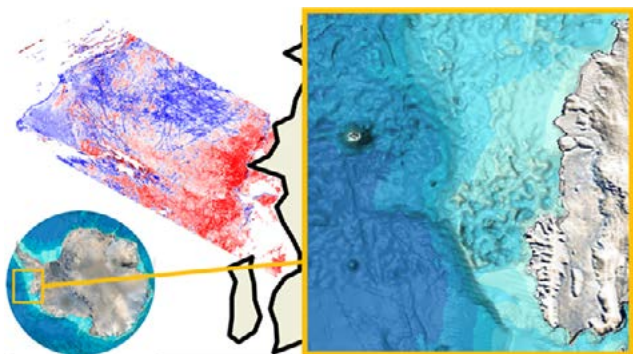

Figure 1. *Linkages between MISR sea ice surface roughness (red to blue colors, left) and bathymetry features (right) close to the Antarctic Peninsula.*
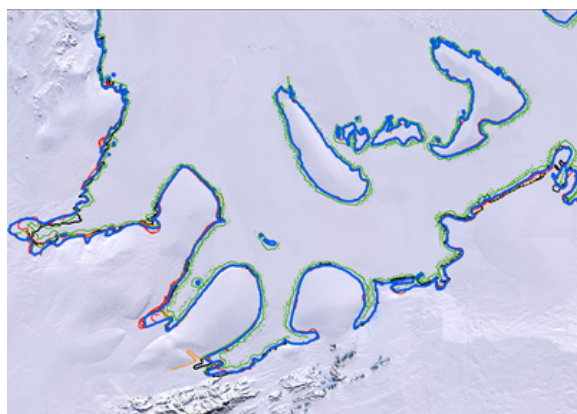
Figure 2. *Various estimates of the grounding line in the Weddell Sea. Blue line: final composite solution.*

In order to assess these new bathymetry, coastline and grounding line datasets, and to improve the knowledge about the ocean tides in the Southern Ocean, a regional hydrodynamic tidal model configuration has been implemented on a high-resolution finite-element grid. The exploration of the impact of the bathymetry, the coastline and the grounding line datasets in the tidal hydrodynamic simulations has highlighted a number of regions where the new ALBATROSS datasets clearly improve the tidal estimates.

In-situ tidal observations from tide gauge stations are scarce and scattered in the Southern Ocean, and mainly located along the Antarctic coast. Satellite-altimetry-derived tidal estimates have been computed within the ALBATROSS project, considering the most recently reprocessed CryoSat-2 data, including SAR and SARin modes, which provides invaluable information, especially in sea-ice covered areas like the Weddell Sea and the Ross Sea. This altimetry-derived tidal dataset is an outstanding validation and assimilation database for the ALBATROSS regional tidal model (Fig. 3).
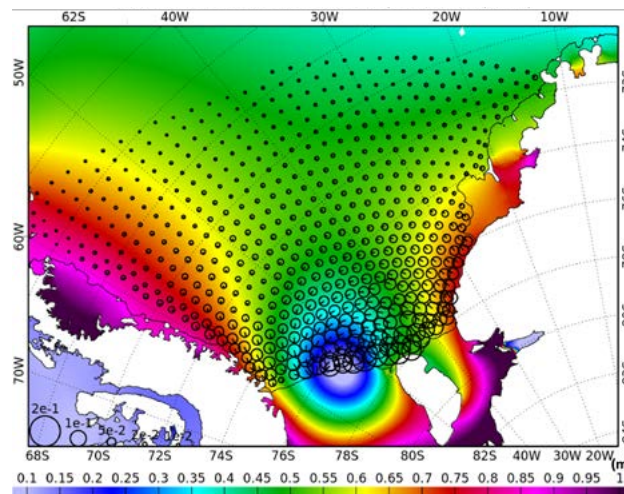
Figure 3. *High-resolution tidal model M2 estimate vs CryoSat-2 tidal harmonic retrievals in the Weddell Sea. The size of the black circles is proportional to the vector difference between the model and the observations.*

3. CONCLUSION

The analyses performed within the ALBATROSS project highlight the strong linkages between bathymetry, tides and ice (sea ice and ice shelves) in the Southern Ocean. The resulting products and model simulations show clear improvements compared to state-of-the-art datasets, and it is planned to share the project outcomes with the scientific community in the coming months.

ACKNOWLEDGEMENTS

REFERENCES

Cancet, M., Andersen, O.B., Lyard, F., Cotton, D., Benveniste, J. (2018), Arctide2017, A High Resolution Regional Tidal Model in the Arctic Ocean, Advances in Space Research, 62(6), 1324-1343, doi: https://doi.org/10.1016/j.asr.2018.01.007

Johnson, T., Tsamados, M., Muller, J.-P., and Stroeve, J.: Mapping Arctic Sea Ice Surface Roughness with Multi-angle Imaging SpectroRadiometry, EGU General Assembly 2021, online, 19–30 Apr 2021, EGU21-15897, https://doi.org/10.5194/egusphere-egu21-15897, 2021

Lyard, F. H., Allain, D. J., Cancet, M., Carrère, L., and Picot, N. (2021), FES2014 global ocean tide atlas: design and performance, Ocean Sci., 2021, 17, 615–649, https://doi.org/10.5194/os-17-615-2021

Morlighem, M., E. Rignot, T. Binder, et al., 2020. Deep glacial troughs and stabilizing ridges unveiled beneath the margins of the Antarctic ice sheet, Nature Geoscience. 13. 132-137. https://doi.org/10.1038/s41561-019-0510-8

Morlighem, M. 2020. MEaSUREs BedMachine Antarctica, Version 2. Boulder, Colorado USA. NASA National Snow and Ice Data Center Distributed Active Archive Center. https://doi.org/10.5067/E1QL9HFQ7A8M.

Schaffer, J., Timmermann, R., Arndt, J. E., et al. (2019): An update to Greenland and Antarctic ice sheet topography, cavity geometry, and global bathymetry (RTopo-2.0.4). PANGAEA, https://doi.org/10.1594/PANGAEA.905295

Role of pigment dataset uncertainties on Phytoplakton Size Class and Functional Type estimates: an inter-comparison between two laboratories

E. Canuti [1], F. Artuso [2] and A. Di Cicco [3]

[1] JRC, Joint Research Center, Ispra (VA), Italy
[2] ENEA (Italian National Agency for New Technologies, Energy and Sustainable Economic Development), Frascati (Rome), Italy
[3] CNR – ISMAR, Institute of Marine Sciences, Rome, Italy

Abstract- The analysis of phytoplankton pigments by HPLC (High Performance Liquid Chromatography) method is widely used in oceanographic studies to estimate algal biomass and to identify different Phytoplankton Functional Types (PFTs) and Size Classes (PSCs) from in-situ samples. The availability of larger amount of data provided from different laboratories allow for a better refinement of the in-situ algorithms needed for the PFT and PSC evaluation. The aim of this study is to evaluate how the uncertainties between pigment datasets obtained independently can affect the further PFT and PSC evaluation and highlight how the inter-comparison between laboratories is essential for the accuracy reliability of the final product estimates.

Keywords: Phytoplankton Pigments, Phytoplankton Functional Types, Phytoplankton Size Classes, HPLC, inter-comparison

1. INTRODUCTION

The analysis of phytoplankton pigments by HPLC (High Performance Liquid Chromatography) is widely used in oceanographic studies to estimate algal biomass and to identify different Phytoplankton Functional Types (PFTs) and Size Classes (PSCs) from in-situ samples, with the aim to evaluate the performances of the satellite products and to contribute to the development and refinement of regional algorithms. In this work, we present the results of an inter-comparison between pigment datasets of two different laboratories (Joint Research Centre, JRC and Italian National Agency for New Technologies, Energy and Sustainable Economic Development, ENEA), composed by the analysis of natural water samples collected during the campaign "Sentinel-2017". The aim of this study is to understand how the uncertainties between pigments' datasets obtained independently can affect the further PFT and PSC evaluation and to demonstrate that different analytical methods may be used for obtaining consistent pigment datasets.

2. CRUISE AND SAMPLING

The Sentinel-2017 campaign, organized by the CNR-ISMAR in the framework of OLCI-Sentinel-3 CAL/VAL activities, took place in the period May 24 – June 12, 2017 and interested the area of Sicily Channel and South Ionian Sea (Mediterranean Sea). During the cruise, JRC and ENEA laboratories collected and analyzed, independently, phytoplankton samples in 50 bio-optical stations. In addition, specific samples for a HPLC inter-comparison exercise were collected simultaneously at 4 sites in the Sicily Channel and in 5 stations along the North-East coast of Sicily as series of triplicate samples. For the inter-comparison, both laboratories collected sea water samples approximately one meter below the surface using a hand sampling bottle. Sampled water was pre-filtered with a 250 μm mesh net to remove zooplankton component and then known volumes were gently filtered through Whatman GF/F glass-fiber filters (25 mm diameter) under mild vacuum (not exceeding 150 mm Hg). Phytoplankton samples so obtained were then immediately frozen in liquid nitrogen and kept frozen in -80 °C until the analysis.

3. PIGMENTS DATASETS and METHODS

The HPLC analytical methods implemented by the laboratories were respectively Van Heukelem and Thomas (2001) [RP-C8 monomeric, extraction in 2.5 ml, acetone 100% + 150 μL MQ water, ISTD vit. E, 150 μL sample inj.] and Wright et *al.* (1991), [RP-C18 polymeric, extraction in 100% acetone, ISTD vit. E, 100 μL sample inj.]. The single pigment dataset consistency was evaluated by each laboratory, as suggested by Aiken et *al.* (2004) in terms of correlation between Total Chlorophyll a (TChl *a,* defined as the sum of mono- and divinyl Chlorophyll a and Chlorophyllide a, including allomers and epimers), Total Accessories Pigment (TAcc) and Total Pigment (TPig) concentrations (see Hooker et *al.* 2005 for the detailed list of TAcc and TPig) , based on the following criteria: *i.* TChl *a* and the TAcc correlation (variance r>0.9, slope 0.7-1.4); *ii.* difference between TChl *a* and TAcc (less than 0.3 TPig) and *iii.* 85% of the collected station satisfying the first two criteria. The uncertainties between the two laboratories for each pigment are evaluated on 4 samples collected in the Sicily Channel, on 5 series of natural samples collected and analyzed in triplicates and on a certified standard containing a mix of Primary Pigments (DHI, Denmark). The accuracy and the precision, accordingly with previous round robin exercises (Claustre et *al.* 2004, Hooker et *al.* 2005, Canuti et *al.*, 2016) are quantified in terms of Average Percent Differences and Variation Coefficient, respectively. The requirement of 25% (Hooker and McClain, 2000) for data satellite validation and of 15% for bio-optical algorithms refinement for TChl *a* is satisfied (accuracy of 11.8 % on natural samples). Fucoxanthin (Fuco) and Total Chlorophyll *b* (TChl *b*) uncertainties are lower than 15 % (see Table. 1). With regard to Peridinin (Peri) and Alloxanthin (Allo), pigments are quantified at very low concentration, thus increasing the biases between the laboratories. Due the quantification from both participants of the so called Primary Pigments (Hooker et *al.*, 2005) it is possible to derive macro-variables such as the "size equivalent pigment indices" pico- (pPF), nano- (nPF) and micro- (mPF). They are ratios between sum of pigments marker of specific size-group and the sum of all seven diagnostic pigments (DP) used (Table 1), and could be considered a first indicator of the Size Classes composition. Pigment Indices can give a first clue of the agreement of the laboratories' datasets in terms of PSCs estimation before quantifying phytoplankton biomass associated to each size group (Vidussi et *al.*, 2001 and Uitz et *al.* 2006).. In this first assessment, the macro variables uncertainties among laboratories remain within 5% for the micro- and nano-fraction (5.1% and 3.9% respectively),

while increase for the pico-fraction (13.3%) as expected (Hooker *et al.* 2005).

Table 1. Uncertainties for Primary Pigments quantified by HPLC and derived Pigment Indices as Average Percent Differences (%) between the two laboratories on natural sample replicates.

TChl *a*	TChl *b*	But	Hex	Peri	Zea	Allo	Fuco
11.8	8.3	12.5	18.9	>100	64.6	>100	10.9

mPF	nPF	pPF
5.1	3.4	13.3

4. PSC and PFT QUANTIFICATION

For each laboratory, TChl *a* fractions of the 3 PSCs were quantified independently by applying a multiple regression analysis between the concentrations of TChl *a* and the DP and providing the best estimates of the TChl *a*/DPs ratios for each datasets (Vidussi et al., 2001; Uitz et al., 2006; Di Cicco et al., 2017). Using this approach, also 4 PFT groups were considered. Three among the seven pigments (peri, but and allo) were excluded by the analysis, as they showed a negative and very low correlation with the TChl *a*. However, the RMSE values suggested that their elimination does not lead to a significant loss in explaining the variability of TChl *a*. The comparison of the TChl *a* - fractions obtained from the analysis of the two datasets shows differences in terms of APD of 4%, 10% and 13% for micro-, nano- and pico-phytoplankton, respectively. Higher values resulted for the PFTs, ranging from 18% for Diatoms to 68% for Prokaryotes, with 20% for both Haptophytes and Green algae, reflecting however the differences highlighted in the analytical evaluation of the two laboratories. At the end, the analysis of the significance of the difference between the corresponding coefficients obtained from the two regressions suggested that the coefficients associated with each population were not significantly different from each other and that the coefficients of the regression do not change when the reference population varies. Therefore, the datasets could be assessed by referring to the overall population as the sum of the two.
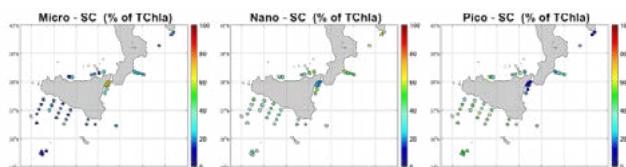
Figure 1. *Sentinel-2017 PSC distribution obtained from the regression analysis applied to JRC and ENEA pigment datasets. The TChl a values range between 0.05 and 0.92 mg m−3, confirming the oligotrophic character of the area.*

3. CONCLUSION

In the final analysis, the comparison of the two PFT and PSC datasets reveals that the differences between the two laboratories in the phytoplankton' groups quantification reflect the preliminary assessment made by comparing the individual analytical results. The results obtained by the two laboratories can be considered consistent and thus can be integrated for this and similar future work.

REFERENCES

Aiken J., Fishwick J., Moore G. and Pemberton K., 2004. The annual cycle of phytoplankton photosynthetic quantum efficiency, pigment composition and optical properties in the Western English Channel, J. of Mar. Biol. Ass. of the UK, 84, 2, 301-313.

Canuti, E., Ras, J., Grung, M., Röttgers, R., Costa Goela, P., Artuso, F., Cataldi, D., HPLC/DAD Intercomparison on Phytoplankton Pigments (HIP-1, HIP-2, HIP-3 and HIP-4), EUR 28382 EN.

Claustre, H., Hooker, S., Van Heukelem, L. Berthon, J. F., Barlow, R., Ras, J., Sessions, H., Targa, C., Thomas, C., van der Linde, D., Marty, J. C., 2004 An intercomparison of HPLC phytoplankton pigment methods using in situ samples: Application to remote sensing and database activities, Marine Chemistry 85(1):41-61

Di Cicco A., Sammarino M., Marullo S., Santoleri R., 2017. Regional empirical algorithms for an improved identification of Phytoplankton Functional Types and size classes in the Mediterranean Sea using satellite data, Front. Mar. Sci., 19 May 2017.

Hooker S. B. and C. R. McClain,2000. The calibration and validation of SeaWIFS data, Progress In Oceanography 45(3-4):427-465.

Hooker S.B., Van Heukelem L., Thomas C.S., Claustre H., Ras J., Barlow R., Sessions H., Schluter L., Perl J., Trees C., Stuart V., Head E., Clemetson L., Fishwick J., Llewellyn C., Aiken J., 2005. The second SeaWIFS HPLC Analysis Round-Robin Experiemnt /SeaHARRE-2), NASA/TM-2005-212785.

Van Heukelem, L., C.S. Thomas, 2001. Computer-assisted high-performance liquid chromatography method development with applications to the isolation and analysis of phytoplankton pigments Jour. of Chrom. **A**, 910, 31–49.

Wright S.W., Jeffrey S.W., Mantoura R.F.C., Llewellyn C.A., Bjornland T., Repeta D., Welschmeyer N., 1991. Improved HPLC method for the analysis of chlorophylls and carotenoids from marine phytoplankton. Mar. Ecol. Prog. Ser., 77, 183-96.

Uitz J, Claustre H, Morel A, Hooker S., 2006. Vertical distribution of phytoplankton communities in open ocean: an assessment based on surface chlorophyll. J Geophys Res 111:C08005.

Vidussi, F., Claustre, H., Manca, B. B., Luchetta, A., and Marty, J. C. (2001). Phytoplankton pigment distribution in relation to upper thermocline circulation in the eastern Mediterranean Sea during winter. J. Geophys. Res. 106, 19939–19956.

Validation and Comparison of the HawkEye CubeSat Sensor to Current Ocean Color Satellites over AERONET-OC Sites

V. Cross*, C. Cross*, M. McCoy, T. Moore

Florida Atlantic University; Harbor Branch Oceanographic Institute, Florida, USA

Abstract – The objective of this project is to quantify the performance of the HawkEye ocean color sensor against other current ocean color satellites over AERONET-OC sites for validation. If remote sensing reflectance from HawkEye demonstrates minimal systematic difference compared to other sensors and to the SeaPRISM instruments, the study will demonstrate the advantages of using high spatial resolution Cube Satellite (CubeSat) technology for ocean color imaging. With a 10x10x30 cm form factor and a weight of under 5 kg, CubeSats are far less expensive, have shorter timelines to build and test, have more accessible launch opportunities, have better temporal and spatial observational power, and have the capability to operate effectively in constellations. The unique capabilities of CubeSats give them unparalleled potential to be used for both outer-planetary and Earth missions in the future. The HawkEye sensor's performance over aquatic environments – both marine and freshwater – remains relatively untested. This project will advance this knowledge by assessing images over four different AERONET-OC sites.

Keywords: Ocean Color, CubeSat, HawkEye.

1. INTRODUCTION

Earth observation (EO) has evolved over the last 50 years driven by advances and sequential improvements in technologies and methodologies, and a broader increased interest and use of satellite systems world-wide (McClain et al, 2022). A recent milestone in satellite technology is the development of nano-satellites, also known as CubeSats. Although still in a nascent development phase, CubeSats are much smaller and more affordable to launch than traditional satellite systems, offering a potential paradigm shift for satellite applications. The advent of CubeSat technology in ocean color remote sensing has begun.

An experimental ocean color CubeSat – the SeaHawk - carries a high spatial resolution multispectral ocean color sensor called HawkEye. The partners on the SeaHawk mission are Cloudland Instruments, AAC Clyde Space, NASA Goddard Space Flight Center, Spaceflight, and the UGA Skidaway Institute of Oceanography (Clark 2015). The imager has eight spectral bands, a spatial resolution of 120m, and improved technology to differentiate finer coastline details and cloud edges (Smith 2021). Its high spatial resolution provides around one hundred times more information per pixel than previous ocean color satellites (Morrison 2021). This novel level of imaging will provide valuable, detailed images of coasts, estuaries, lakes, and reefs that are important for monitoring the health of our aquatic ecosystems, especially near the coast where much of the world's population lives.

Launched in 2018 and officially operational in June of 2021, data from HawkEye is relatively new to the scientific community. The leading question of this study is: how does the HawkEye perform relative to other ocean color sensors, and how accurate is the image data for generating water quality and geophysical products? This research will examine atmospherically-corrected HawkEye remote sensing reflectance performance against other current ocean color sensors with different atmospheric correction schemes. These sensors are Sentinel-2/MultiSpectral Imager (S2/MSI), Sentinel-3/Ocean Land Color Imager (S3/OLCI), the VIIRS, and MODIS-Aqua. The five selected satellites cover a broad range of spatial, temporal, and spectral resolutions, notably from 10m resolution of S2/MSI to the 1km resolution of VIIRS. The analysis will specifically examine same-day images from these sensors over four different areas where AERONET-OC stations are located to provide a ground-truth reference for all sensors.
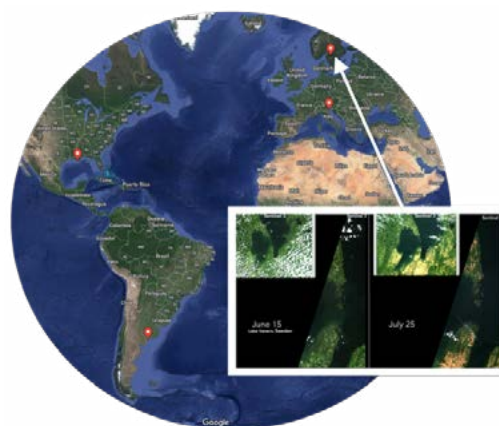
Figure 1. *AERONET-OC Sites*

The AERONET-OC (AErosol RObotic NETwork) is a global federation of identical radiometric instruments and protocols (known as SeaPRISMs) maintained by NASA. It provides the ocean color world with high quality spectral measurements of optical properties including water-leaving radiance and aerosol optical depth (AOD) at various aquatic sites around the world and generates important validation data sets for satellites. The AERONET-OC spectral bands are compatible with the bands of HawkEye, Sentinel 2 and 3, VIIRS, and MODIS-Aqua, allowing for the validation of derived remote sensing reflectance (Rrs) products across

sensor platforms. AERONET-OC sites also collect atmospheric measurements in addition to water measurements, and allows various other properties to be compared to the remote satellite sensors. In this work, the AERONET quality level 1.5 data (cloud-screened and quality controlled) will be used to validate the Rrs products of the satellite sensors.

2. METHODS

Sets of same-day level-1 images from the five different sensors over four AERONET-OC sites were collected for subsequent image processing (Figure 1). The four sites include Lake Vanern, Sweden; Bahia Blanca, Argentina; Venice, Italy; and the coast of New Orleans. These locations were selected because of their diverse water qualities and the presence of an AERONET-OC SeaPRISM instrument. Sweden's Lake Vanern, for example, contains an abundance of organic material and, therefore, appears very dark. The diversity of the water characteristics at each of the different sites is important because it allows for a holistic analysis of each sensor's performance.

The level-1 images were processed to level-2 with a select subset of currently available atmospheric correction schemes. We limited the schemes to Acolite (Vanhellemont and Ruddick, 2018), Polymer, the default SeaDAS NIR iterative scheme, and the turbid water scheme of MUMM embedded in SeaDAS. Not every scheme was applicable to every image (Figure 2). The suitability and functionality of these schemes is based in part on the turbidity of the water regions.

Ocean Color Sensor	Sentinel-2/MultiSpectral Imager (S2/MSI)	Sentinel-3/Ocean Land Color Imager (S3/OLCI)	MODIS-Aqua	VIIRS	HawkEye
Atmospheric Correction Schemes	Acolite (REF)	Acolite (REF)	Acolite (REF)		
	SeaDAS MUMM	SeaDAS MUMM	SeaDAS MUMM	SeaDAS MUMM	SeaDAS MUMM
	SeaDAS NIR	SeaDAS NIR	SeaDAS NIR	SeaDAS NIR	SeaDAS NIR
	Polymer	Polymer	Polymer	Polymer	Polymer

Figure 2. *Ocean color sensors with corresponding atmospheric correction schemes*

Time/space matchups were generated between the AERONET-OC data and each ocean color image after atmospheric correction processing. For each image, valid Rrs and AOD data (as determined from quality flag checks) were extracted and averaged from a corresponding 3x3 box of pixels centered over a given SEAPRISM location, and compared against the nearest SeaPRISM observation (in time). This analysis will provide a broad view of the performance of the HawkEye across different atmospheric correction schemes and environments relative to contemporaneous ocean color sensors and to AERONET-OC measurements.

3. PRELIMINARY RESULTS/CONCLUSIONS

Initial findings at the Palgrunden AERONET-OC site show a positive correlation and consistency in spectral shape between HawkEye, VIIRS, Sentinel-3, and the SeaPRISM,

with a negative bias apparent for both VIIRS and HawkEye and a positive bias for Sentinel-3 (Figure 3). Deriving products from HawkEye data using bio-optical algorithms and collected radiances will establish the performance of this sensor compared to those of costlier ocean color satellites. The outcomes of this study are anticipated to demonstrate the advantages of using high-resolution spatial data from the HawkEye imager for remote sensing, especially to monitor coastlines and inner-water systems, both critical areas of high biological activity. If HawkEye proves to collect accurate data comparable to that of other ocean color satellites, this will further establish the potential of CubeSats as an emerging, novel technology to better understand, monitor, and predict the future of our marine ecosystems.
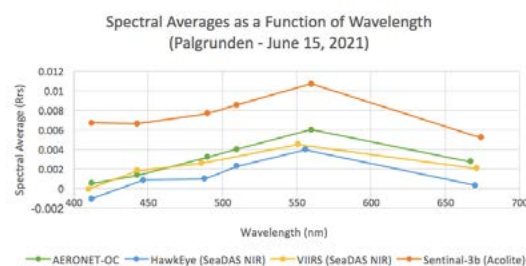
Figure 3. *Spectral Averages*

REFERENCES

Clark, C. (n.d.). SeaHawk CubeSat Satellite Bus. University of North Carolina Wilmington. Retrieved February 15, 2022, from https://uncw.edu/socon/seahawk.html

McClain, S., Kruczkiewicz, A., Ndugwa, R., Braneon, C., Bader, D., Bazo, J., & Owen, M. (2022). Building risk-informed communities: Case studies on the applications of Earth observation data. American Geophysical Union.

Morrison, J. M. (2021, June 24). Big Things Come in Very Small Packages: A New Way of Looking at the Ocean. University of North Carolina Wilmington. Retrieved February 16, 2022, from https://uncw.edu/news/2021/06/big-things-comeinvery-small-packages-a-new-wayof-lookingatthe-ocean.html

Smith, J. M. (2021, August 31). SeaHawk Mission Proves CubeSats Are a Viable Option for Collecting Credible Scientific Data. NASA (National Aeronautics and Space Administration). Retrieved February 15, 2022, from https://earthdata.nasa.gov/learn/articles/seahawk-hawkeye-ocean-color

Vanhellemont, Q., & Ruddick, K. (2018). Atmospheric correction of metre-scale optical satellite data for inland and coastal water applications. Remote Sensing of Environment, 216, https://doi.org/10.1016/j.rse.2018.07.015

Validation of ocean color satellite products in coastal lagoons and estuaries using autonomous hyperspectral sensors (the HYPERNETS and HYPERVAL projects)

D. Doxaran, A. Corizzi A., E. Leymarie, C. Penkerch, B. Elkilani, I. Salah-Salah [*]

Laboratoire d'Océanographie de Villefranche, Villefranche-sur-Mer, France

Abstract – Since 2021, two autonomous stations perform continuous above-water radiometric measurements in France, as part of the HYPERNETS network (http://www.hypernets.eu): one in the center of the Berre coastal lagoon, by the Mediterranean Sea) and one at the mouth of the Gironde Estuary (Bay of Biscay). The measurements made on these two platforms are presented so as the associated data quality control. Improved matchups protocols are then used to assess the validity of atmospheric corrections applied to multi-sensor (S2-MSI, S3-MSI, L8/9-OLI satellite data on these two optically-complex sites.

Keywords: water reflectance, validation of atmospheric corrections.

1. INTRODUCTION

A new network of autonomous stations providing above-water radiometric measurements for the validation of atmospgheric corrections applied to multi-sensor satellite data have been developed as part of the HYPERNETS EU-H2020 research project. As part of this international network, two sites are operated in France since 2021: one at the center of the Berre coastal lagoon (SE France) connected to the Mediterranean Sea; one at the mouth of the Gironde Estuary. They provide downwelling irradiance (E_d), sky radiance (L_s) and upwelling radiance (L_t) every 15 mn, following the measurement protocol recommended by Mobley (1999).

The Hypernets radiometric data are automatically transferred to a server where quality controls are applied before computing the water reflectance signal:

$$Rhow = \pi \times (L_t - \rho \times Ls) / E_d$$

Where ρ is the air-water interface reflection coefficient for radiance.

As part of the HYPERNETS project, these field water reflectance measurements are used to assess the validity of atmospheric corrections (AC) applied to multi-sensor satellite data. The sensors and AC algorithms considered in the present study are summarized in Table 1. As part of the HYPERVAL project funded by the French Space Agency, the field water reflectance measurements are related to coincident field measurements of light backscattering (or turbidity), fluorescence of chlorophyll-a (Chla), concentrations of suspnedde particulate matter and Chla).

Here we present the HYPERNETS quality-controlled data recorded since 2021 in the two French sites, redefine matchup protocols with satellite data and finally quantify the uncertainties associated with multi-sensor satellite-derived water reflectance products.

2. DATA AND METHODS

The Berre HYPERNETS station (Figure 1A) started to operate in February 2021 and provides since then field radiometric data every 30 mn. The Berre coastal lagoon waters are most of the time clear (turbidity < 2 FNU) except in winter and spring when turbid freshwater is regularly discharged from a power plant (EDF); intense and sometimes harmful algal blooms also develop at the end of summer periods if the lack of wind stress maintains a strong stratification. Consequently, he Chla (and SPM) concentrations typically vary from 0.5 to 100 mg/m^3 (mg/m^3).

New platform:
- Above-water: meteo station, HYPSTAR-VIS, rain and light sensors, 2 webcams (N & S), solar panels
- In-water: b_b, fluo_chla, T, S, O_2 ,
- Monthly maintenance and water sampling

Figure 1. *The Hypernets stations located in the center of the Berre lagoon (A) and mouth of the Gironde Estuary (B).*

The Gironde HYPERNETS station (Figure 1B) started to operate in November 2021 and provides since then field radiometric data every 15 mn at the mouth of the estuary. The BGironde is a macro-tidal estuary with a well-developed maximum turbidity zone. Within surface waters at the mouth of the estuary, SPM and Chla concentrations typically vary from 20 to 1000 g/m^3, and from 0.5 to 5 mg/m^3.according to tidal and seasonal cycles.

Quality-controls were applied to field Rhow measurements to remove suspicious ones associated to strong temporal variability, inaccurate pointing geometry, higher than expected signal in the NIR-SWIR representative of glint effects. Quality-controls were also applied to satellite products considering the spatial variability over the 5*5 pixels centred on the HYPERNETS stations, higher-than-expected satellite-derived Rhow values in the NIR-SWIR representative of glint or adjacency uncorrected effects. The result was a multi-sensor matchups database in two contrasted and optically-complex sites. This database is used hereafter to determine the validity and/or limits of up-to-date AC atmospheric correction algorithms applied to high and medium spatial resolution satellite data (see Table 1 for details).

[*] * Corresponding author. Address: LOV CNRS/SU, 06230 Villefranche-sur-Mer, France. Email: doxaran@obs-vlfr.fr

Table 1. Satellite sensors and atmospheric correction algorithms tested in the present study.

Satellite data	L8/9-OLI	S2-MSI
AC algorithms	C2RCC C2X Acolite iCOR	Sen2Cor C2RCC GRS Polymer Acolite, CMEMS-HR iCOR
Satellite data	S3-OLCI	MODIS
AC algorithms	BAC C2RCC Polymer Acolite CMEMS	MUMM NIR-SWIR

3. RESULTS

In the Berre coastal lagoon, satellite data were observed to be often affected by significant to strong glint effects, which means that the glint correction was almost as important as the atmospheric correction. Not surprisingly, the Sen2Cor, Acolite and iCOR AC algorithms underperform in such low turbid waters affected by glint. On the opposite, the GRS and C2RCC algorithms provide satisfactory results, so as Polymer but this latter clearly reaches its limits when the water becomes turbid, i.e. for water reflectance values higher than 0.01 (Figure 2).
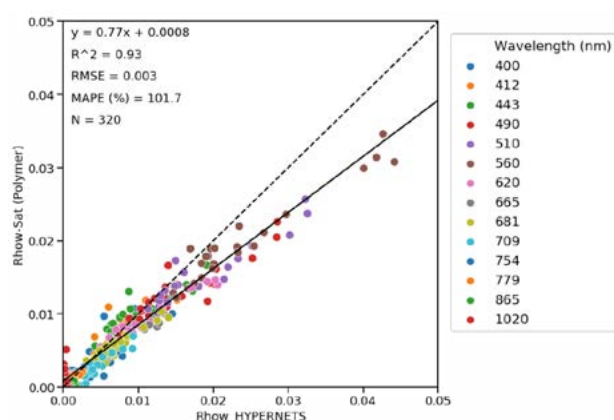
Figure 2. Scatterplots between multi-spectral Rhow values derived from S3-OLCI when applying the Polymer AC algorithm and field (HYPERNETS) Rhow values in the Berre coastal lagoon.

In the moderately to highly turbid waters of the Gironde Estuary, the best performing algorithms are clearly BAC (which underestimates by 20% actual Rhow values), GRS and Acolite.

Satisfactory results were obtained when correcting Landsat-OLI satellite data for atmospheric effects using Acolite. Results obtained using MODIS satellite data were not satisfactory, independently of the AC algorithm considered; in such enclosed water environments (lagoons and estuaries), the land surface reflectance product remains the best alternative (Doxaran et al. 2009).
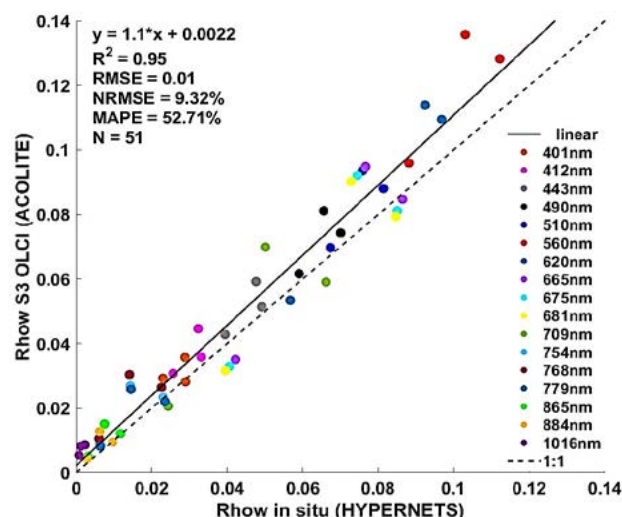
Figure 3. Scatterplots between multi-spectral Rhow values derived from S3-OLCI when applying the Acolite AC algorithm and field (HYPERNETS) Rhow values at the mouth of the Gironde Estuary.

4. CONCLUSIONS

Overall, there is no AC algorithm performing well in all the water types represented by the Berre lagoon (clear to moderately turbid, sometimes highly productive) and the Gironde estuarine waters (moderately to highly turbid). In Berre, glint effects are sometimes predominant and only AC algorithms also correcting for such effects provide satisfactory results. SWIR bands or dark targets algorithms (GRS, Acolite) provide very satisfactory results in highly turbid waters. Neural networks algorithms (C2RCC and C2X) improved their capabilities and are now performing well in moderately turbid to turbid waters.

ACKNOWLEDGEMENTS

REFERENCES

Brockmann, C.; Doerffer, R.; Peters, M.; Kerstin, S.; Embacher, S.; Ruescas, A. Evolution of the C2RCC neural network for Sentinel 2 and 3 for the retrieval of ocean colour products in normal and extreme optically complex waters. In LPS Proc., Prague, Czech Republic, 9–13 May 2016;, p. 54.

Doxaran D., J.M. Froidefond, P. Castaing and M. Babin. Dynamics of the turbidity maximum zone in a macrotidal estuary (the Gironde, France): Observations from field and MODIS satellite data. ECSS 2009, 81, 321–332.

Harmel, T., Chami, M., Tormos, T., Reynaud, N., Danis, P.-A., 2018. Sunglint correction of the multi-spectral instrument (MSI)-SENTINEL-2 imagery over inland and sea waters from SWIR bands. Remote Sens. Environ. 204, 308–321.

Mobley C.D. Estimation of the remote-sensing reflectance from above-surface measurements. Applied Optics, 1999, 38.

Steinmetz, F.; Deschamps, P.Y.; Ramon, D. Atmospheric correction in presence of sun glint: Application to MERIS. Opt. Express 2011, 19, 9783–9800.

Vanhellemont, Q.; Ruddick, K. Advantages of high quality SWIR bands for ocean colour processing:Examples from Landsat-8. Remote Sens. Environ. 2015, 161, 89–106.

Predicting Short- and Long-term Sea Level Changes Using Deep Learning

M. Ehrhorn *, O. Baltazar Andersen, C. Bjerre Ludwigsen

DTU Space, Lyngby, Denmark

Abstract – **Newly developed deep neural network architectures have started to win recent time series forecasting competitions. It is high time that these innovations are employed on the 30-year satellite altimetry observation record, hopefully allowing us to use data to see whether sea level rise is accelerating. Using JPL's MEaSUREs gridded sea level anomaly product and the state-of-the-art network architecture N-HiTS, we produce a model with an RMSE of less than 2 mm over 15 years, showing the validity of the network and a model that can forecast 30 years into the future. A model selection is also made beforehand.**

Keywords: Neural networks, sea level rise, machine learning.

1. INTRODUCTION

Much research is being done on pure deep learning solutions to time series problems (Oreshkin 2020, Lim 2021, Challu 2022). At the same time, the satellite altimetry record is now of a length where it makes sense to apply machine learning techniques to predict and analyze sea-level changes based on data. Current empirical models are typically linear- or quadratic in nature. Still, neural networks allow models to incorporate non-linearities and train on massive amounts of data in a timely fashion.

This project applies modern neural network architectures to satellite observed sea-level anomaly (SLA) data to predict global mean sea level. To do so, one must first do some data wrangling, select the best model, tune that model's hyperparameters and validate it against known data, which is the focus of this project.

2. DATASET

JPL's MEaSUREs Gridded Sea Surface Height Anomalies Version 2205 (Fournier 2022) is used for model training and validation. To ensure that the time series are similar, such that the model can learn, the dataset is broken into basins based on (Thompson 2014). The basin of interest in this project is the Northwest Pacific, as seen in figure 1, where grid points with an SLA time series are split randomly between training (60%), validation (20%), and testing (20%) set, which have all been de-seasoned and smoothed with a six-month moving average. Training proceeds by forward passes on 1500 timesteps on batches of training set time series, with a multi-step prediction of 608 timesteps. Each epoch validates the model on un-seen validation time series, and training is ended when the loss has not improved over five epochs.
The model is validated by calculating the mean sea level of both the test and prediction sets. A linear model is fitted to the first 1500 timesteps of the test set and extrapolated out; the RMSE of this fit to the last 608 timesteps is compared to the prediction set RMSE, as shown in figure 2, where the

winning model, based on the N-HiTS (Challu 2022) architecture, is shown.
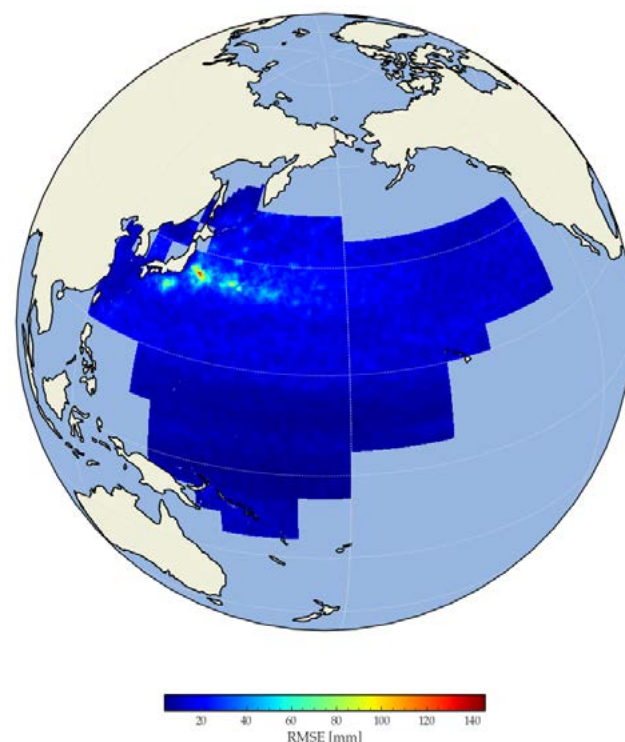
Figure 1. A map of the Northwestern Pacific region where the model is trained and tested. SLA time series in random coordinates are chosen for training, validation, and testing sets. This map shows an interpolated grid of RMSE values on the test set for one model as a general example. This model, as indeed all of them, has problems where the Japan Current dominates the sea level signal.
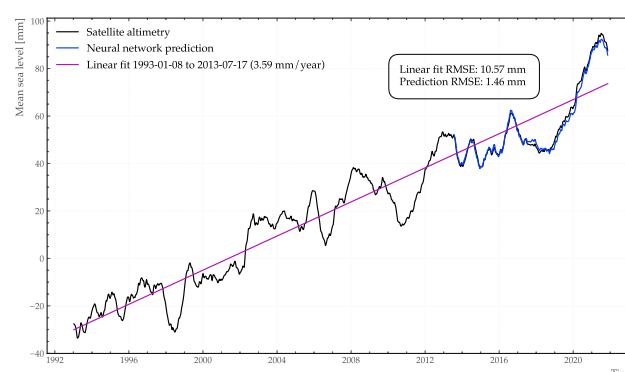
Figure 2. Two models fit the Western Pacific basin mean sea level from January 1993 to June 2007, derived from satellite altimetry and extrapolated to November 2021. One model is a linear fit, while the other is an N-HiTS neural network. The RMSE of the neural network fit is improved compared to the linear fit.

---

* Corresponding author. Address: Elektrovej 328, 2800 Kgs. Lyngby, Denmark. Email: mehkj@space.dtu.dk

3. MODEL SELECTION

Several different models were compared, and hyperparameter tuning was performed. The architectures tested were LSTMs/GRUs, Temporal Fusion Transformers (TFT) (Lim 2021), Temporal Convolutional Networks (Bai 2018), N-BEATS (Oreshkin 2020), and N-HiTS, with the two last types outperforming the rest, with GRUs coming third. N-HiTS showed a consistently low RMSE, except for areas dominated by currents, as seen in figure 1.

A transformer architecture such as TFT performs worse than N-HiTS, as shown in figure 3, while taking much longer to train.
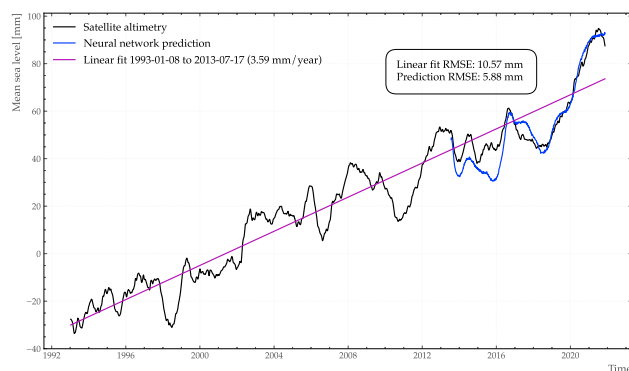
Figure 3. The Temporal Fusion Transformer architecture performs notably worse than the N-HiTS architecture.

4. RESULTS

N-HiTS can predict trends and variations in sea level rise (see figure 2). Although the model cannot recreate the sea level signals perfectly everywhere (especially where currents dominate more than climate-induced changes; see figure 4), in many places, the fit is good (figure 5). The more important metric, however, is the mean sea level in the basin of interest, and the value of the neural network solution lies in whether it can predict trend and acceleration better than current empirical models, which the evaluation hints at.
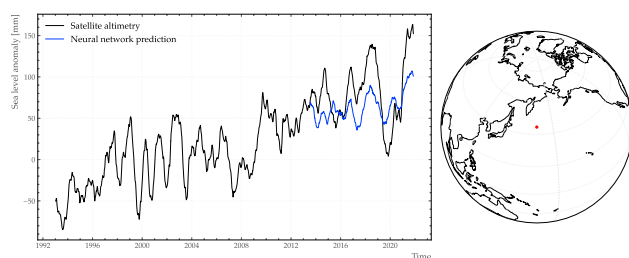
Figure 4. The worst performing prediction grid point of the N-HiTS model.
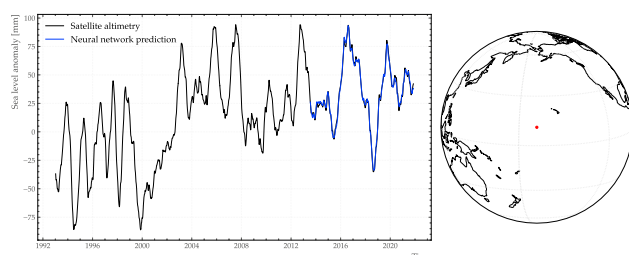
Figure 5. The best-performing prediction grid point of the N-HiTS model.

5. FUTURE WORK

Interpretability is essential, and architectures such as N-BEATS allow novel solutions that aid in that. Furthermore, most newer models allow for probabilistic predictions, outputting a distribution rather than a point estimate, allowing us to quantify the uncertainty of the network predictions.

Multivariate inputs are also obvious candidates for improvement; observational inputs such as sea surface temperature can be added to help the model learn, as well as inputs from other models.

Ensemble learning can be applied such that different model architectures, each best suited to one prediction task, can aid one another and create a meta-model that performs better than any one model alone.

Techniques such as physics-informed neural networks can be applied, which puts constraints on the network predictions, according to the differential equations governing the physics of sea level variability.

REFERENCES

Oreshkin, B., Carpov, D., Chapados, N., and Bengio, Y., 2020. N-BEATS: Neural basis expansion analysis for interpretable time series forecasting. [online] arXiv.org. Available at https://arxiv.org/abs/1905.10437 [Accessed 29 July 2022].

Lim, B., Arık, S., Loeff, N and Pfister, T, 2021. Temporal Fusion Transformers for interpretable multi-horizon time series forecasting, International Journal of Forecasting, volume 37, Issue 4, Pages 1748-1764, https://doi.org/10.1016/j.ijforecast.2021.03.012.

Challu, C., Olivares, K., Oreshkin, B., Garza, F., Mergenthaler-Canseco, M., and Dubrawski, A., 2022. N-HiTS: Neural Hierarchical Interpolation for Time Series Forecasting. [online] arXiv.org. Available at: https://arxiv.org/abs/2201.12886 [Accessed 29 July 2022].

Fournier S., Willis J., Killett E., Qu Z. and Zlotnicki V., 2022. SEA_SURFACE_HEIGHT_ALT_GRIDS_L4_2SATS_5D AY_6THDEG_V_JPL2205. Ver. 2205. PO.DAAC, CA, USA. Dataset accessed [2022-07-20] at https://doi.org/10.5067/SLREF-CDRV3

Thompson, P. R., and Merrifield, M. A. (2014), A unique asymmetry in the pattern of recent sea level change, Geophys. Res. Lett., 41, 7675– 7683, doi:10.1002/2014GL061263.

Bai, S., Kolter, J. and Koltun, V., 2018. An Empirical Evaluation of Generic Convolutional and Recurrent Networks for Sequence Modeling. [online] arXiv.org. Available at: https://arxiv.org/abs/1803.01271 [Accessed 29 July 2022].

Significant Wave Height Extremes at the Frontier of Winter Sea Ice Loss in the Bering Sea, 2002-2022

Reint Fischer[*1,2], Sinead Farrell[1,2], John M. Kuhn[2] and Kyle Duncan[1,2]

[1]University of Maryland, [2]NOAA Laboratory for Satellite Altimetry

Due to continued international effort, there are now decades worth of satellite altimetry data available to characterize interannual and spatial patterns in wave heights. Globally, many regions experienced increases in significant wave heights (Young & Ribal, 2019), with the largest increases observed at the 90th percentile of wave heights and greater. The Bering Sea stands out as a region characterized in winter by intense storms and partial sea ice cover. Pacific storms that are introduced into the Bering Sea along the northern flank of the winter cyclone tracks bring storm-force to hurricane-force winds and very high waves. The partial sea ice cover dampens waves and typically prevents significant wave heights from being measured, which can cause the Bering Sea to be omitted in annual trends (Young et al., 2011). Here we use observations from the Jason-1, -2 and -3 satellites as well as from ERS-2, Envisat, CryoSat-2, SARAL/AltiKa, Sentinel-3A and -3B to show that during the Bering Sea winters of 2002/2003 - 2021/2022, the prevalence of very rough (SWH > 9 m) and phenomenal (SWH > 14) sea state conditions have increased by an order of magnitude (Figure 1). Altimetry data are processed using RADS (Scharroo et al., 2013).
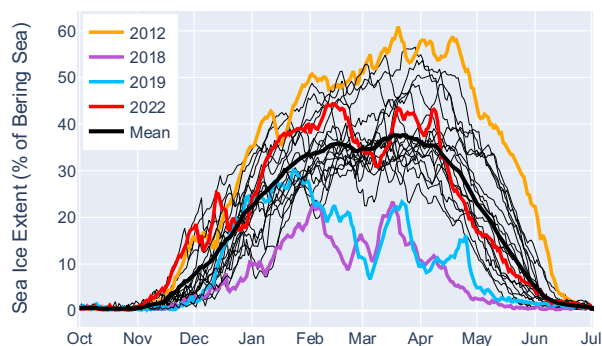
Figure 1. Daily sea ice extent as a percentage of the Bering Sea for each winter from 2002/2003 - 2021/2022. Data source: NOAA/NSIDC CDR Passive Microwave Sea Ice Concentration version 4.

Sea ice typically covers between 30% to 60% of the Bering Sea in the winter season between December and June (Figure 2). Over the past 20 years, a clear decreasing trend in the sea ice extent with record minima in 2018 and 2019 has confronted regional communities (Slats et al., 2019), ecosystems (Himmelberger, Frey & Sangermano, 2022) and fisheries (Bernton & Holmes, 2022) that all depend on the sea ice with the challenge of changing climate conditions. This decrease, which is projected to continue into the coming decades (Thoman et al., 2020), allows waves to propagate to areas where sea ice cover used to dampen the wave energy and opens up the sea surface to energy input by the wind. The trend in sea ice loss coincides with the observed increase of extreme significant wave heights. Here we analyze the evolving spatial patterns of significant wave heights during this period of sea ice loss to show the regions that are newly susceptible to high waves. To study the effect of increased input of wind energy and decreased damping by sea ice we compare significant wave heights during similar atmospheric conditions under changing sea ice conditions. Sea ice data are from NOAA/NSIDC CDR Passive Microwave Sea Ice Concentration version 4 (Meier et al., 2021) and NSIDC Multisensor Analyzed Sea Ice Extent – Northern Hemisphere (MASIE-NH) version 1 (U.S. National Ice Center and National Snow and Ice Data Center, 2010).

Figure 2. Winter storm prevalence as measured by the Jason-series and Envisat-series altimeters. Winter storm prevalence is defined as the percentage of significant wave heights larger than 9 meters.

Mean sea level pressure and 10 m wind vector data from the ERA5 reanalysis (Copernicus Climate Change Service (C3S), 2017) provide the background atmospheric conditions during the 20-year study period at 6-hour intervals. The full and regular temporal coverage of the reanalysis data allows us to assess the variable coverage of satellite altimeters over time. Over the past 20 years, the number of altimeter observations over the Bering Sea has increased significantly. How well have these altimeters captured significant wave heights associated with Bering Sea winter cyclones? Do the current altimeters have sufficient coverage to observe these storms?

After considering the effects of sea ice and satellite coverage on the observed increase in extreme significant wave heights, we should finally consider the influence of

---

[*] Corresponding Author. Address: 4254 Stadium Drive, College Park MD, 20742, United States. Email: rfische1@umd.edu

atmospheric variability. How does the trend in extreme wind speeds compare to the trend in observed extreme significant wave heights? Taking the local monthly 99th percentile highest wind speed over the period 2002/2003 – 2021/2022, we can determine for each winter how many wind speed observations exceed that 99th percentile to measure the prevalence of extreme wind speeds. Figure 3 shows how these extreme wind speeds have increased over the study period. Notable stormy winters that appear in both figure 1 and figure 3 are in 2011 (winter 2010/2011) and 2018 (winter 2017/2018) , whereas the winter of 2015 (2015/2016) shows up as a relatively calm year in both figures.
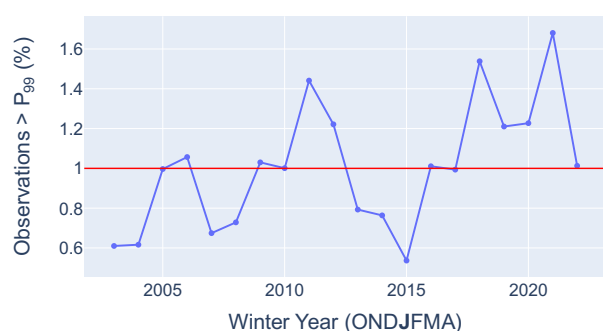
Figure 3. Percentage of wind speed observations that exceed the local monthly 99th percentile over the winters from 2002/2003 to 2021/2022. Sum of observations across the winter season from October 1st to May 1st. Data source: ERA5 Reanalysis

REFERENCES

Young, I. R., & Ribal, A. (2019). Multiplatform evaluation of global trends in wind speed and wave height. *Science*, *364*(6440), 548–552. doi:10.1126/science.aav9527

Young, I. R., Zieger, S., & Babanin, A. V. (2011). Global trends in wind speed and wave height. *Science*, *332*(6028), 451-455.

Scharroo, R., E. W. Leuliette, J. L. Lillibridge, D. Byrne, M. C. Naeije, and G. T. Mitchum, RADS: Consistent multi-mission products, in *Proc. of the Symposium on 20 Years of Progress in Radar Altimetry, Venice, 20-28 September 2012,* European Space Agency Special Publication, ESA SP-710, p. 4 pp., 2013.

Slats, R., Oliver, C., Bahnke, R., Bell, H., Miller, A., Pungowiyi, D., ... & Johnson, M. (2019). Voices from the front lines of a changing Bering Sea. *Arctic Report Card 2019*, *88*, 94.

Himmelberger, A., Frey, K. E., & Sangermano, F. (2022). Applying landscape fragmentation analysis to icescape environments: potential impacts for the Pacific walrus (Odobenus rosmarus divergens). *Polar Research*, *41*, 10-33265.

Bernton, H., & Holmes, L. (2022). A Crab Boat's Quest for Snow Crab in a Bering Sea Upended by Climate Change. *The Seattle Times*.

Thoman, R. L., Bhatt, U. S., Bieniek, P. A., Brettschneider, B. R., Brubaker, M., Danielson, S. L., Labe, Z., Lader, R., Meier, W. N., Sheffield, G., & Walsh, J. E. (2020). The Record Low Bering Sea Ice Extent in 2018: Context, Impacts, and an Assessment of the Role of Anthropogenic Climate Change, *Bulletin of the American Meteorological Society*, *101*(1), S53-S58. Retrieved Jul 29, 2022, from https://journals.ametsoc.org/view/journals/bams/101/1/bams-d-19-0175.1.xml

Meier, W. N., F. Fetterer, A. K. Windnagel, and J. S. Stewart. (2021). NOAA/NSIDC Climate Data Record of Passive Microwave Sea Ice Concentration, Version 4 [Data Set]. Boulder, Colorado USA. National Snow and Ice Data Center. https://doi.org/10.7265/efmz-2t65. Date Accessed 07-29-2022.

U.S. National Ice Center and National Snow and Ice Data Center. Compiled by F. Fetterer, M. Savoie, S. Helfrich, and P. Clemente-Colón. (2010). Multisensor Analyzed Sea Ice Extent - Northern Hemisphere (MASIE-NH), Version 1 [Data Set]. Boulder, Colorado USA. National Snow and Ice Data Center. https://doi.org/10.7265/N5GT5K3K. Date Accessed 07-29-2022.

Copernicus Climate Change Service (C3S) (2017): ERA5: Fifth generation of ECMWF atmospheric reanalyses of the global climate . Copernicus Climate Change Service Climate Data Store (CDS), *date of access*. https://cds.climate.copernicus.eu/cdsapp#!/home

Oceanographic Consoles for Ocean Literacy

E. T. Harvey*[1, 2], King A. L.[2], Sørensen K.[2], Kristiansen T.[2], Valestrand L.[2], Jaccard P. F.[2], Topland Larsen K.[3]

[1] NIVA Denmark Water Research, Copenhagen, Denmark, [2] Norwegian Institute of Water-NIVA, Oslo, Norway,
[3] Global Digital Media AS, Norway

Abstract – The increasing pressure on coastal areas caused by anthropogenic stressors leads to habitat loss and decreased biodiversity. This is acknowledged by the UN SDGs, with current focus on the Oceans by the UN Decade of Ocean Science for Sustainable Development, 2020-2030. The knowledge within society needs to better help preserve the oceans so it can continue to deliver the many ecosystem services humans depend upon. NIVA has in collaboration with Global Digital Media established Oceanographic Consoles for Ocean Literacy, under several projects. The content is constantly improving and developed. The current research project financed by the Norwegian research council have brought high resolution satellite data to the consoles.

Keywords: UN SDGs, UN Ocean Decade, Ocean Literacy, Monitoring, FerryBox, Ocean Colour

> *"The Ocean holds the keys to an equitable and sustainable planet"* [1]

1. INTRODUCTION

The knowledge within the society about the oceans needs to increase in order to have a more common ground for behavioral changes within the society to take place. The changes are necessary to better help preserve the oceans so it can continue to deliver the many ecosystem services we as human depend upon.

NIVA has developed and operates touchscreen consoles for ocean literacy in cooperation with Global Digital Media. The development has been and is still under several European Horizon-2020 projects; ResponSEAble, with several updates supported by e.g. the INTAROS, JERICO-NEXT, JERICO-S3 and the EuroSea projects. The information on the consoles aims to support the development of knowledge system for European Oceans, that contributes effectively and dynamically to an increase in ocean literacy to the public (i.e. the understanding of the ocean and our relationship with it). The consoles are currently placed on different cruise and ferry ships (e.g. in Coastal Norway; M/S Trollfjord, North Sea; M/S Color Fantasy and in the Arctic; M/S Norbjørn) that also are equipped with FerryBox systems, making it possible to display the real- time data being collected while sailing. Other platforms are placed at Science centers and museums in Hvaler and Færder National Park visitor centers,

Norwegian Museum of Science and Technology, Runde Environment Center and at NIVA offices/labs. Portable screens and tablets with HDMI+USB connection can be brought to conferences and events for flexible demonstrations.

The environmental stories on the platforms are presented by different modules e.g. time series of environmental data from the FerryBox systems, a game on for Sustainable fisheries, films on invasive species, microplastics and eutrophication, among other things. These products are available in six different languages: Norwegian, English, German, Polish, Russian and French. The platforms are developed and operated in cooperation with Global Digital Media. In 2021-2022 a new module on the platforms have been developed by the SATVIEW project, where high resolution satellite remote sensing data of water quality, are displayed.

2. APPROACH

The information on the consoles is displayed by a touch-interactive content with a targeting audience of school-aged children, tourists and the general public (Fig. 1).

Fig. 1 *Images showing the console installations onboard M/S Roald Amundsen and M/S Trollfjord, both operated by Hurtigruten. Images: Kai Sørensen/NIVA.*

Six key ocean literacy stories, including facts, games, illustrations and videos are easily accessible from the start menu, as well as selection of language preference (Fig 2).

Fig. 2 *Examples of the ocean literacy key stories.*

---

* Corresponding author. Address: Njalsgade 76, DK-2300 Copenhagen S, Denmark. Email: therese.harvey@niva-dk.dk

NIVA run several FerryBox systems for continuous measurements of marine data and regular sampling that are installed on several ferry and cargo routes along in Norway and on excursion ships. Ocean observing data from the FerryBox systems are displayed on quasi-real-time basis on the consoles (Fig. 3).

Fig. 3 Screenshot of a console page displaying quasi- real-time FerryBox temperature data. Map showing some of NIVA´s FerryBox/NorSOOP routs.

Large scale oceanographic data are also displayed including ocean modeled and satellite data layers of SST, currents, chl-a, sea ice thickness etc (Fig. 4).
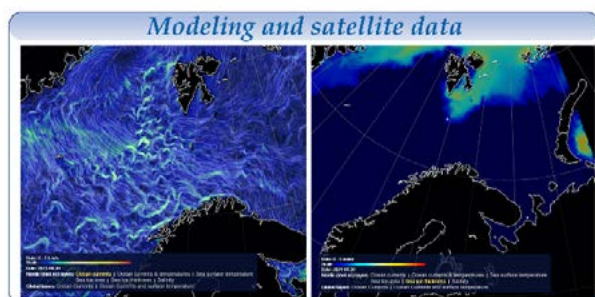
Fig. 4 Screenshots of ocean currents (left) and ice thickness (right) in the Arctic from met.no Nordic-4km data service, based on satellite and modeled data.

2. HIGH RESOLUTION SATELLITE DATA

A new module on the platforms have just been launched supported by the Norwegian Research Council funded project SATVIEW project in collaboration with Global Digital Media, where time-series of high-resolution Sentinel-2 coastal data of water quality[2] (Chlorophyll-a, Turbidity and Suspended matter) are displayed along with info texts (Fig.5).
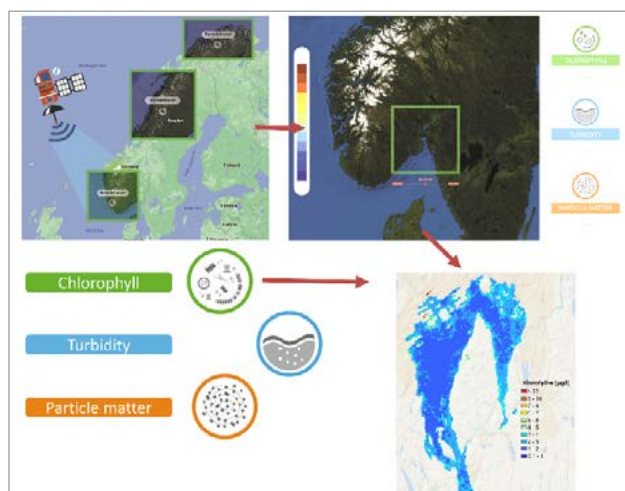
Fig.1 Example of the new module showing the entrance page for high-resolution satellite data, with and an example of monthly chlorophyll-a concentrations in Oslofjord, Norway**.*

The CMEMS marine data of the High-Resolution Ocean Colour (HR-OC) (data provided by Brockmann Consult, Royal Belgian Institute of Natural Sciences and Flemish Institute for Technological Research) will be presented on the displays. Both the daily products[3] and the montly means will be used[4]. The HR-OC service distributes data based on the Sentinel 2/MSI sensor at 100m resolution for a 20km coastal zone.

2. INSIGHTS AND EXPERIENCES

There is about 3,000 to 6,000 visitors on the consoles per month on passenger vessels (based on 4 languages) (Fig.6). User reviews indicated that they enjoyed learning about the oceans via the console - but still would like it to be more interactive and with more content targeting children. From a scientist's perspective, this is an important tool that can significantly engage the public and increase ocean literacy; which will be developed further to support the UN sustainable development goals, contribute to the UN Ocean Decade and ocean stewardship.
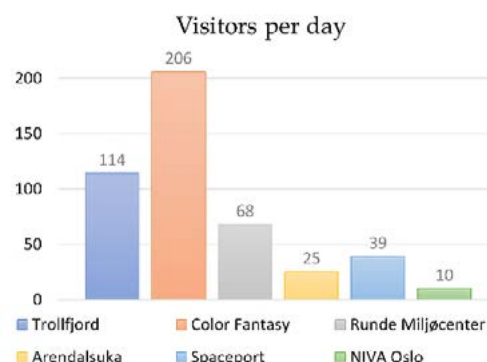
Fig. 6 Visitors per day on 6 different platforms, at museums, events and ferries.

3. CONCLUSION

With the European commission's Copernicus program, the use of remote sensing data is constantly increasing and becoming a more and more important source of information for the scientific community. By demonstrating the usefulness of satellite data and show how several water quality parameters linked to environmental problems, such as eutrophication and coastal darkening, can be monitored our understanding of the processes can increase. With SATVIEW the development and benefits of remote sensing data, especially in remote areas such as the Arctic are displayed and communicated to help enhance the Ocean Literacy.

ACKNOWLEDGEMENTS

REFERENCES

1 https://www.oceandecade.org/ **2** DCS4COP. DataCube Service for Copernicus, *DCS4COP H2020 Project, European Commission.* DCS4COP H2020 (2021). **3** CMEMS HI-CO service https://doi.org/10.48670/moi-00118- 4 CMEMS HI-CO service https://doi.org/10.48670/moi-00119-

Hydrodynamic models ensembles to improve estuarine forecasting under climate change scenarios

I. Iglesias[1,*], J.L. Pinho[2], W. Melo[2], P. Avilez-Valente[1,3], A. Bio[1], M. Cruz[4], J. Vieira[2], F. Veloso-Gomes[1,3], L. Bastos[1,5]

1 Interdisciplinary Centre of Marine and Environmental Research (CIIMAR/CIMAR), University of Porto, Portugal.
2 Centre of Territory, Environment and Construction (CTAC), Department of Civil Engineering, University of Minho, Braga, Portugal.
3 Faculty of Engineering, University of Porto, Portugal.
4 Faculty of Sciences, University of Minho, Braga, Portugal.
5 Department of Geosciences Environment and Spatial Planning, Faculty of Sciences of the University of Porto, Portugal.

Abstract – **Numerical models are essential tools for simulating the hydrodynamics of aquatic systems, making it possible to anticipate and predict the effects of anthropogenic interventions, extreme events and climatic changes, and promoting effective and integrated coastal management. However, the results of the models present uncertainties related to errors and inaccuracies in the analysis of the results and in the initial and forcing conditions. Given the need to have accurate forecasts, it is crucial to implement new solutions to avoid such errors. One of these solutions is the ensemble technique. In this research work two numerical models were chosen to predict the hydrodynamics of two Portuguese estuaries considering various sea level rise and extreme events scenarios. The models' results were combined using a weighted average, which improved the accuracy of the outcomes. Results point at an aggravation of the flood level associated with extreme events in the Douro estuary due to the configuration of the river mouth, but with little effect of the sea level rise. In the Minho estuary, on the other hand, a clear effect of the sea level rise along the estuary is estimated, with a reduction in velocities and increased flood areas.**

Keywords: Estuaries, hydrodynamics, numerical models, extreme events, climate change.

1. INTRODUCTION

Estuaries are strategically important from an environmental, economic, and social point of view. To reduce their vulnerability, it is crucial to understand their hydrodynamics. Numerical models can simulate them, providing the basis of efficient management frameworks. However, model results always present uncertainties, and there is a need to develop and implement new methodologies to increase their accuracy. In this work, the ensemble technique is proposed as a reliable tool to improve estuarine forecasting, being implemented for two Portuguese regions: Douro and Minho estuaries.

The Douro estuary is a narrow, highly dynamic, urban estuary with torrential regimes that produce strong currents and severe floods. Its dynamics are mainly forced by river flows. On the south bank of the mouth, a sand spit partially obstructs the entrance protecting the estuary (Figure 1). In 2008, some maritime works intended to stabilize this spit, including the construction of a detached breakwater and the extension of the northern breakwater. These works have interfered with local hydro-morphodynamics, causing a significant increase in the surface area and volume of the sand spit in a relatively short period (10 years). Consequently, the spit has become more robust and less likely to rupture during flood events. More severe impacts of upstream flooding can thus be expected, causing economic losses and structural damage (Bastos et al., 2012; Iglesias et al., 2019a).
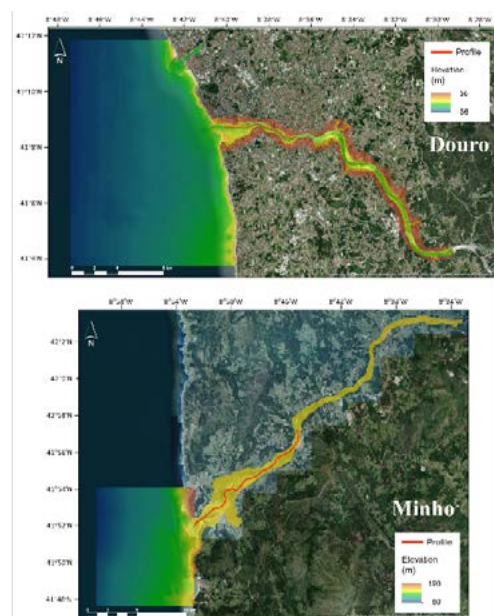
Figure 1. Douro and Minho estuaries. Topo-bathymetric data considered for grid construction and longitudinal profiles selected to extract the water elevation.

The Minho estuary presents a low level of urbanization/industrialization, and a great diversity of habitats. It is a marine dominated estuary with a strong siltation. The lower estuary presents a widening, producing a decrease in the flow velocity, favourable conditions for sedimentation and high residence times (Figure 1). The accretion patterns have caused bathymetric restrictions to navigation and the appearance of islands and sandbanks during low tide (Iglesias et al., 2019a; Melo et al., 2020). Sea level rise conditions could augment this effect, diminishing even more the velocities in the lower estuary and incrementing the sedimentation processes.

The distinct physical patterns of these two estuarine regions revealed the need for local approaches and dedicated studies to understand the dynamics of each region and support the mitigation of the risks associated with extreme events, man-made interventions and climate change effects.

---

* Corresponding author. Address: Terminal de Cruzeiros do Porto de Leixões. Avenida General Norton de Matos, S/N. 4450-208 Matosinhos, Portugal. Email: iiglesias@ciimar.up.pt

2. METHODS

The applied numerical models were openTELEMAC-MASCARET and Delft3D, already calibrated and validated for the two selected estuarine regions (Iglesias et al. 2019a, Iglesias et al. 2019b, Melo et al. 2020; Iglesias et al., 2021, Melo et al., 2021). The superensembles were constructed following previous results found by Iglesias et al. (2022), where the models were run for historical conditions to calibrate the ensemble with in situ measurements of water elevation. In this work, Iglesias et al. (2022) found that the ensembling of model outputs using the absolute error (for low river flow simulations) and the squared error (for high river flow simulations) as weighting coefficients outperformed the individual model solutions as well as other techniques of ensemble construction. This was observed for all considered scenarios, at all sampling points and in both estuaries studied. The squared error values obtained in Iglesias et al. (2022) were therefore considered here as the weights to construct the superensemble for future conditions.

The future scenarios superensembles considered extreme fluvial discharge (EFD) and extreme sea level (ESL). EFDs for 50, 100 and 1000-year return periods were calculated for each estuary considering that the river flow, provided by Portuguese hydrometric stations, follows Gumbel's law. ESL values for historical simulations as well as for RCPs 4.5 and 8.5 scenarios for 2100, for the same return periods considered in the EFD, were extracted from Vousdoukas et al. (2017), for the Douro and Minho locations (Table 1).

Table 1. Scenarios considered for the 2100 hydrodynamic conditions forecasting

	Return period (years)	River flow (m³/s)		Scenario	Water elevation (m)
		Douro	Minho		
S1	50	17357	5365	Historical	3.9
S2				RCP 4.5	4.4
S3				RCP 8.5	4.7
S4	100	19814	6038	Historical	4.0
S5				RCP 4.5	4.5
S6				RCP 8.5	4.8
S7	1000	27962	8262	Historical	4.3
S8				RCP 4.5	4.8
S9				RCP 8.5	5.0

3. RESULTS AND CONCLUSIONS

Using the obtained superensemble results for the two estuaries, the water elevation was projected along a longitudinal profile for each of the simulated scenarios (Figure 2). Results showed a clear difference between the hydrodynamic behaviours of the two estuaries. Superensemble outcomes for the Minho estuary, which is dominated by the tide and therefore by oceanographic conditions, showed a pronounced effect of rising sea levels on estuarine hydrodynamics, mainly in the lower estuarine region, but noticeable in the entire estuary. Whereas, for the Douro estuary, which is heavily dominated by the river flow, the effect of sea level rise was hardly noticeable during flood events, and the extension of the flood areas can be directly linked with the river flow imposed in the simulations.

It was demonstrated that the ensembles technique is an effective tool to improve the numerical modelling results for estuarine regions, and should be applied to provide the stakeholders and policymakers with accurate results that support their actions.
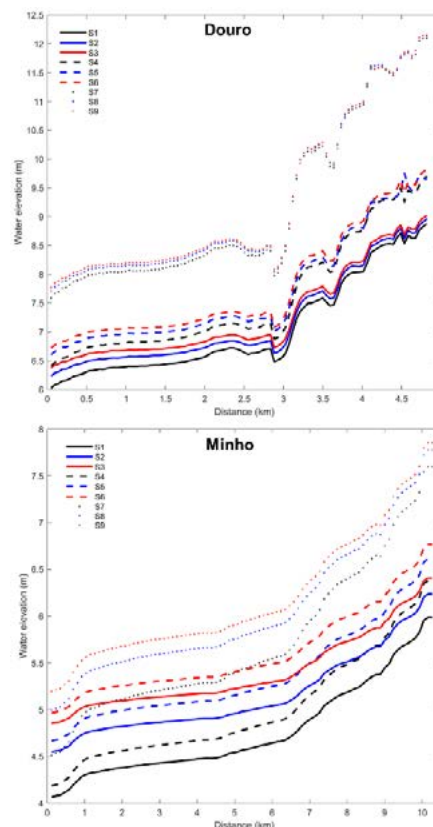
Figure 2. Longitudinal profiles of water elevation in Douro and Minho estuaries.

REFERENCES

Bastos L, Bio A, Pinho JLS, et al. Dynamics of the Douro estuary sand spit before and after breakwater construction. Estuar Coast Shelf Sci 2012;109:53–69.

Iglesias I, Venâncio S, Pinho JL,et al. Two Models Solutions for the Douro Estuary: Flood Risk Assessment and Breakwater Effects. Estuaries and Coasts 2019a;42:348–64.

Iglesias I, Avilez-Valente P, Bio A, et al. Modelling the Main Hydrodynamic Patterns in Shallow Water Estuaries: The Minho Case Study. Water 2019b;11:1040.

Iglesias I, Bio A, Bastos L, et al. Estuarine hydrodynamic patterns and hydrokinetic energy production: The Douro estuary case study. Energy 2021;222:119972.

Iglesias, I, Pinho, JL, Avilez-Valente, P, et al. Improving estuarine hydrodynamic forecasts through numerical model ensembles. Front Mar Sci 2022;9.

Melo W, Pinho J, Iglesias I, et al. Hydro- and Morphodynamic Impacts of Sea Level Rise: The Minho Estuary Case Study. J Mar Sci Eng 2020;8:441.

Melo W, Pinho J, Iglesias I, et al. Flood Risk Assessment at the Douro River Estuary. In: Kolathayar S, Mondal A, Chian SC, editors. Lect. Notes Civ. Eng. Climate Ch, Springer; 2022, p. 37–49.

Vousdoukas MI, Mentaschi L, Feyen L, et al. Earth's Future Extreme sea levels on the rise along Europe's coasts Earth's Future 2017:1–20.

'Oceans from Space' Venice 2020: Scientific and Technical Themes

C. Jamet *, C. Flamant [2], E. Lecuyer [3], J. Delanoë [2], X. Mériaux [1] and Q. Cazenave [3]

[1] Université Littoral-Côte d'Opale, Wimereux, France
[2] LATMOS, Paris, France
[3] CNRS, Wimereux, France

Abstract – Remote sensing of ocean color has changed our vision of the distribution of phytoplankton and ocean carbon for the past forty years. However, those observations have limitations that lidar techniques can overpass. Space-borne lidars already exist but they have been developed for aerosols and clouds applications. It is thus necessary to develop specific oceanic retrieval algorithms and to validate them against in-situ measurements. Here we mainly focus our work on the ESA ADM-AEOLUS space-borne lidar. A specific algorithm has been developed and a sea campaign was performed in September 2021 in Cabo Verde to collect radiometric, bio-optical and biogeochemical parameters. Preliminary retrieval algorithm and validation are presented.

Keywords: Ocean color, lidar, validation

1. INTRODUCTION

Remote sensing of ocean color has changed our vision of the distribution of phytoplankton and ocean carbon for the past forty years. These space-borne observations provide synoptic view of the concentrations of radiometric, bio-optical and biogeochemical parameters, continuously for the past twenty-+ years at high spatial (hundreds to thousand meters) and temporal (~2 days) resolutions. However, these observations are limited to clear-sky, day-light, over clouds, high Sun elevation angles and are exponentially weighted toward the ocean surface. Furthermore, they require a processing step to remove the contribution of the atmosphere and the air-sea interface.

Active remote sensing can overcome these limitations of passive space-borne ocean color observations. One of these techniques is lidar (Light Detection and Ranging). As an active remote sensing technique, it can overcome some of the above-mentioned limitations of passive observations. Despite several cases that demonstrated oceanic applications of ship-, air- and space-borne lidars, this tool has not received significant attention from the ocean color remote sensing community. Three space-borne lidars (CALIOP, ATLAS and ALADIN) are currently in space and several studies showed their interest in retrieval key oceanic optical parameters, i.e. the particulate back-scattering b_{bp} and the diffuse attenuation K_d coefficients. CALIOP and ATLAS are green lidars (532 nm) while ALADIN is a UV lidar (355nm) and using the High Spectral Resolution technique. While ocean processing algorithms were developed for CALIOP and ATLAS, there is no ocean products for ALADIN as it aims at estimating the atmospheric wind. Few validations have been made for the oceanic products from CALIOP and ATLAS.

Optical, bio-optical and biogeochemical parameters were measured during the ESA/JATAC and the CADDIWA lidar airborne campaigns dedicated to the validation of AEOLUS atmospheric products. The abstract presents the campaign and the validation of oceanic products from AEOLUS and the French airborne LNG lidar.

2. SEA AND AIRBORNE CAMPAIGNS

6 one-day at sea were performed in the south of the Sao Vicente island, Cabo Verde between September 9 and September 22, 2021 on-board the Gamboa fishing boat. These days at sea occurred during overpasses of AEOLUS or CALIOP or ATLAS (Table 1 and Figure 1). LNG flights were coordinated with AEOLUS overpasses.

LNG is a Doppler polarized airborne High Spectral Resolution Lidar operating in the UV (355nm) (Bruneau et al., 2015). It can also measure the total attenuated backscatter at 532 and 1064. Measurements were taken in nadir (same as CALIOP and ATLAS) and 37° off nadir (same as ALADIN) modes. The lidar was onboard the French Falcon 20 operated by SAFIRE (the French facility for airborne research).

Table 1. Number of co-locations

Lidar	Dates co-location	# co-locations
AEOLUS	10-15-17-22 Sept., 2021	10
CALIOP	09 Sept., 2021	2
ATLAS	18 Sept., 2021	5
LNG	10-17-18 Sept., 2021	11

Figure 1: Top: yellow pins: position of the in-situ measurements; red and purple broad lines: ADM/AEOLUS overpasses; red lines: LNG overpasses for Sept., 9, 10 and 15

* Corresponding author. Address: 32 avenue Foch 62930 Wimereux, France. Email: cedric.jamet@univ-littoral.fr

Sept. 2021. Bottom: black dots: in-situ measurements; blue line: LNG overpass on Sept. 18, 2021

16 stations were planned to acquire several optical, bio-optical and biogeochemical parameters (Table 2). Remote-sensing reflectance R_{rs} just under the surface were measured using TriOS radiometers. The diffuse attenuation coefficient were acquired continuously over the water column using TriOS radiometers. The back-scattering coefficient was measured using an ECO-VSF from WetLabs and the absorption coefficient using an AC-S from WetLabs. Water sampling were obtained using a Ninskin bottle at different depths. The particulate organic carbon (POC) is here considered as particulate carbon from organic origin retained by a Whatman GF/F filter according to the JGOFS (Joint GlobalOcean Flux Study) protocol [5]. The POC is then composed of particles with a diameter between 0.4 and 200 μm, with pre-filtration usually performed. The Colored Dissolved Organic Matter were obtained following de Matos Valerio et al. (2018).

Table 2: List of the in-situ parameters

Parameters	Depth
Remote Sensing Reflectance R_{rs}	Just under the surface
Diffuse attenuation coefficient K_d	Continuously until 30m depth
Absorption coefficient a	Continuously until 30m depth
Back-scattering coefficient b_{bp}	Continuously until 30m depth
Chlorophyll-a concentration	2, 4, 6, 8, 10, 15, 20m depths
POC	2, 4, 8m depths
CDOM	2m depth

3. PRELIMINARY RESULTS

Match-ups exercise will be performed to investigate the accuracy of the CALIOP and ATLAS oceanic products (Behrenfeld et al., 2013; Bisson et al., 2021, Liu et al., 2020) and to investigate the capabilities of AEOLUS and LNG to estimate b_{bp}. A specific algorithm will be developed for LNG. The oceanic products from AEOLUS are developed in the frame of the ESA "AOC" project.

A preliminary oceanic retrieval algorithm has specifically been developed for AEOLUS space-borne lidar. Because there is cross-talk between the Rayleigh and Mie channels, the signals in the Mie and Rayleigh channels are:

$$S_M(z) = K_{Ray}\left[\frac{A}{(nH+z)^2}\right](C_4\beta_M +$$
$$C_3\beta_P)\left[exp\left(-\int_0^z K_L(z')dz'\right)\right]^2.(T_A)^2$$

$$S_P(z) = K_{Mie}\left[\frac{A}{(nH+z)^2}\right](C_1\beta_M +$$
$$C_2\beta_P)\left[exp\left(-\int_0^z K_L(z')dz'\right)\right]^2.(T_A)^2$$

The ratio of S_M/S_P can be used to estimate β_P, considering β_M as a constant:

$$\beta_P = \beta_M \frac{(K_{Ray}C_1 - S_R K_{Mie} C_4)}{(S_R K_{Mie} C_3 - K_{Ray} C_2)}$$

If there is no cross-talk between Mie and Rayleigh channels, C_1 and C_3 are null. C_M and C_P are the instrumental calibration constant parameters and their values are impacted by the change of temperature of the M1 mirror (Weiler et al., 2021). C_1, C_2, C_3 and C_4 provide the percentage of Mie signal in the Rayleigh channel and inversely.

4. CONCLUSION

Optical, bio-optical and biogeochemical parameters were measured in Cabo Verde in September 2022 to validate oceanic observations from air- and space-borne lidars. These in-situ measurements were coordinated with the overpasses of the CALIOP (one day), ATLAS (one day) and ALADIN (four days) and the French airborne lidar LNG (five days). The objective was to validate the current oceanic products of CALIOP and ATLAS and to investigate the capabilities of AEOLUS and LNG to estimate the surface and water-column back-scattering coefficients, respectively.

REFERENCES

Behrenfeld, M.J., Y. Hu, C.A. Hostetler, G. Dall'Olmo, S. D. Rodier, J.W. Hair, and C. R. Trepte (2013). Space-based lidar measurements of global ocean carbon stocks. Geophysical Research Letters 40, pp. 4355-4360, doi:10.1002/grl.50816.

K. M. Bisson, E. Boss, P. J. Werdell, A. Ibrahim, R. Frouin, and M.J. Behrenfeld (2021). Seasonal bias in global ocean color observations. Applied Optics 60, pp. 6978-6988

Bruneau, D., J. Pelon, F. Blouzon, J. Spatazza, P. Genau, G. Buchholtz, N. Amarouche, A. Abchiche, and O. Aouji (2015). 355-nm high spectral resolution airborne lidar LNG: system description and first results. Applied Optics, 54, pp. 8776-8785.

de Matos Valerio, A., M. Kampel, V. Vantrepotte, N.D. Ward, H.O. Sawakuchi, D.F. Da Silva Less, V.Neu, A. Cunha, and J. Richey (2018). Using CDOM optical properties for estimating DOC concentrations and pCO$_2$ in the Lower Amazon River. Optics Express 26, A657-A677.

Liu, X., Y. Hu, Y. Yang, P. Bontempi, A. Omar and R. Baize (2020). Antartic spring ice-edge blooms observed from space by ICESat-2. Remote Sensing of Environment 245, s://doi.org/10.1016/j.rse.2020.111827.

Raymond, P.A., J. Hartmann, R. Lauerwald, S. Sobek, C. McDonald, M. Hoover, D. Butman, R. Striegl, E. Mayorga, C. Humborg, et al. (2013). Global carbon dioxide emissions from inland waters. Nature, 503, pp. 355–359

Weiler, F., M., Rennie, T., Kanitz, L., Isaken, E., Checa, J. de Kloe, L., Okunde and O., Reitebuch (2021). Correction of wind bias for the lidar on board Aeolus using telescope temperatures. Atmos. Meas. Tech., 14, 7167-7185.

Application of the spectrometer SWIM data for retrieval of two-dimensional field of mean square slopes of sea waves

V. Karaev[1]*, M. Panfilova[1], M. Ryabkova[1], Yu. Titchenko[1], X. Li[2]

[1]Institute of Applied Physics RAS, N.Novgorod, Russia
[2]School of Marine Sciences, Nanjing University of Information Science and Technology, Nanjing, China

Abstract – Surface Waves Investigation and Monitoring (SWIM) spectrometer installed on the Chinese-French Satellite CFOSAT opens up for the first time the possibility of reconstructing the two-dimensional field of the mean square slope (*mss*) of large-scale waves. The measurements of the backscattering radar cross section are performed at small incidence angles (<11°) at different azimuth angles. For the first time, the algorithms were developed for constructing the azimuth dependence of the *mss*, determining the direction of propagation of the dominant wave system and calculating the total *mss*s. An example of SWIM data processing confirmed the algorithms performance.

Keywords: spectrometer SWIM, mean squares slopes of sea waves, retrieval algorithms.

1. INTRODUCTION

The world ocean has a significant impact on the Earth's climate, therefore, continuous monitoring of the processes of interaction between the atmosphere and the sea surface is an important task. Orbital scatterometers (the speed and direction of the wind) and altimeters (the significant wave height (SWH) and wind speed) provide global and operational information on the state of the surface layer. Synthetic aperture radars have high spatial resolution and can also be used to estimate wind speed, SWH and dominant wavelength. However, the data are irregular, cover limited water areas and are mainly used in scientific research, for example, the study of the wind field in a cyclone, the study of internal waves.

An important characteristic of the sea surface is a variance of mean square slopes (mss). Launching the TRMM and GPM satellites made it possible to measure the mss of large-scale waves compared to the radar wavelength (hereinafter, the *mss* of large-scale waves). The backscattering radar cross section (RCS) is measured at small incidence angles, and the developed algorithms make it possible to construct global maps of the *mss* of the large-scale waves of the World Ocean (Panfilova et al., 2020). The problem of precipitation radar (PR) data is associated with the fact that measurements are performed at one azimuth angle, i.e. does not allow reconstruction of a two-dimensional *mss* field.

In October 2018, the Chinese-French Satellite (CFOSAT) was launched into orbit on board of which the SWIM spectrometer was installed, which performs measurements of the RCS at small incidence angles (<11 °), but at several azimuth angles. Thanks to such a measurement scheme, for the first time, it becomes possible to measure the *mss* of large-scale waves at different azimuth angles and to reconstruct the two-dimensional *mss* field to determine the direction along which the dominant wave system propagates.

2. SPECTROMETER SWIM

The concept of an orbiting radar capable of measuring the dependence of the RCS on the incidence angle at different azimuth angles was proposed in (Karaev et al., 2006; Karaev et al., 2010). Two approaches were considered: a rotation of the antenna system around the vertical axis and a scanning mode.

The rotation mode is implemented in the SWIM spectrometer of the CFOSAT (Hauser et al., 2017). The measurement scheme is shown in Fig. 1. Due to the rotation

of the antenna system, the dependence of the RCS on the incidence angle is measured at different azimuth angles.
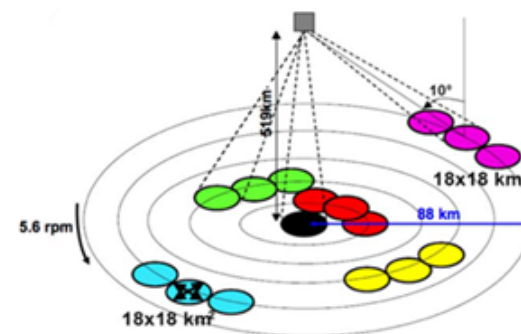
Figure 1. *Scheme of measurements of spectrometer SWIM: altitude 519 km; incidence angles: 0°, 2°, 4°, 6°, 8°, 10°; antenna aperture 2°x2°.*

3. RETRIEVAL ALGORITHMS

At small incidence angles, the backscattering mechanism is quasi-specular and reflection occurs from sections of the wave profile oriented perpendicular to the incident radiation. The Kirchhoff method is used to describe the reflected signal.

In well-known papers, for example, (Freilich, Vanhoff 2003; Tran et al., 2007; Nouguier et al., 2014; Nouguier et al., 2016), to develop an algorithm for determining the *mss* of large-scale waves, the authors used the assumption on the isotropy of sea waves with a Gaussian distribution function of heights and slopes and the formula for the RCS has the following form:

$$\sigma_0(\theta) = \frac{\left| R_{eff}(0) \right|^2}{mss \cdot \cos^4 \theta} \exp\left[-\frac{\tan^2 \theta}{mss} \right]$$

where θ is the incidence angle R_{eff} - effective reflection coefficient which introduced instead of Fresnel coefficient to take into account the influence of the short ripple on the reflected signal (Bass, Fuks, 1972).

The assumption that the sea waves are isotropic, used by the authors, does not correspond to reality and this approach can only be explained by the fact that measurements were available only at one azimuth angle and the assumption that the sea waves were isotropic was the only way to "solve" the problem and try to determine the *mss* of large-scale waves.

In the general case, taking into account the anisotropy of the sea waves, the formula for the RCS has the following kind (Bass, Fuks, 1972)

$$\sigma_0(\theta) = \frac{\left| R_{eff}(0) \right|^2}{2\cos^4 \theta \sqrt{mss_{xx} mss_{yy} - mss_{xy}^2}} \times$$

$$\times \exp\left[-\frac{\text{tg}^2 \theta}{2\left(mss_{xx} mss_{yy} - mss_{xy}^2 \right)} \cdot mss_{yy} \right]$$

* Corresponding author. Address: 46, Uljanova str., Nizhny Novgorod, 603950, Russia. Email: volody@ipfran.ru

where mss_{xx} and mss_{yy} are mss of large-scale waves along X and Y axis respectively; mss_{xy} - unnormalized correlation coefficient between the slopes along the axes X and Y (hereinafter the correlation coefficient).

Thus, 4 parameters are unknown: two mss of large-scale waves, the correlation coefficient and the direction of wave propagation φ. For the solution, it is necessary to solve the transcendental equation. If we assume that the correlation coefficient is much less than the mss ($mss_{xx}mss_{yy} \gg mss_{xy}^2$), then the solution is found in an explicit form:

$$\varphi = 0{,}5\mathrm{arctg}\left[x/y\right]$$

$$\Delta mss = \frac{2(B_2 - B_1)}{\cos(2\varphi - 2\varphi_2) - \cos(2\varphi - 2\varphi_1)}$$

$$mss_{total} = 2B_1 - \frac{2(B_2 - B_1)\cos(2\varphi - 2\varphi_1)}{\cos(2\varphi - 2\varphi_2) - \cos(2\varphi - 2\varphi_1)}$$

where $x = (B_2 - B_1)\sin(\varphi_3 - \varphi_1)\sin(\varphi_1 + \varphi_3) -$
$\qquad - (B_3 - B_1)\sin(\varphi_2 - \varphi_1)\sin(\varphi_1 + \varphi_2)$

$y = (B_2 - B_1)\sin(\varphi_3 - \varphi_1)\cos(\varphi_1 + \varphi_3) -$
$\qquad - (B_3 - B_1)\sin(\varphi_2 - \varphi_1)\cos(\varphi_1 + \varphi_2)$

where φ_n is the direction of probing; $B_n = mss(\varphi_n)$ is the mss under this azimuth angle and $mss_{total} = mss_{xx} + mss_{yy}$ -- the total mss.

4. EXAMPLE OF AZIMUTH DEPENDENCE OF *MSS*

Detail analysis and SWIM data processing is the following stage of our investigation. Example of mss retrieval is shown on the Fig. 2. Asterisks are the retrieval mss at the different azimuth angles.
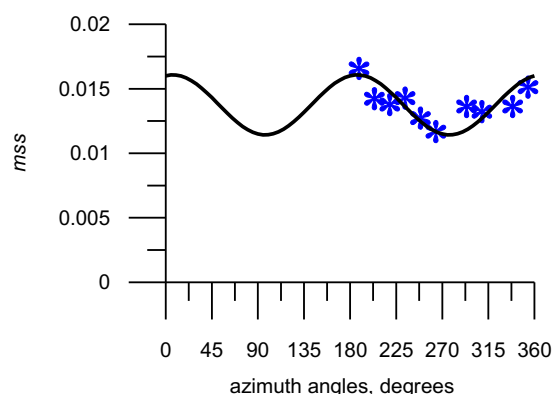
Figure 2. *Azimuth dependence of* mss_{xx}

In result of data processing were retrieved $mss_{total} = 0.0275$, $\Delta mss = 0.00465$ and $\varphi = 7°$.

Theoretical dependence of the mss (black curve) was calculated by the following formula:

$$mss_{xx}(\varphi_n) = 0.5mss_{total} + 0.5\Delta mss \ \cos(2\varphi - 2\varphi_n).$$

Evidently, that the azimuth behavior of mss will be depends from sea state: wind waves or mixed sea. Swell will influence on the mss at the low wind speed. SWIM opens new possibilities for investigation of the Word ocean.

3. CONCLUSIONS

SWIM spectrometer installed on the CFOSAT satellite opens up for the first time the possibility of reconstructing the two-dimensional field of the mss of large-scale waves. The measurements of the RCS are performed at small incidence angles (<11) at different azimuth angles, when the quasi-specular backscattering mechanism is dominant. For the first time, the algorithms were developed for calculating the azimuth dependence of the mss, determining the direction of propagation of the dominant wave system, and calculating the total mss. An example of SWIM data processing confirmed the effective of algorithms.

REFERENCES

Bass F.G., Fuks I.M. (1972) Rasseyanie voln na statisticheski nerovnoi poverkhnosti (Wave scattering on a statistically rough surface), Moscow: Nauka, 424 p.

Freilich M. H., Vanhoff B. A. (2003) The relation between winds, surface roughness, and radar backscatter at low incidence angles from TRMM Precipitation Radar measurements, Journal of Atmospheric and Oceanic Technology, Vol. 20, No. 4, pp. 549–562.

Hauser D., C. Tison, T. Amiot, L. Delaye, N. Corcoral et al, (2017) SWIM: the first spaceborne wave scatterometer, IEEE Trans. on Geosci. and Rem. Sens., Vol. 55, No. 5.

Karaev V., Kanevsky M., Balandina G., Meshkov E., Challenor P., Srokosz M., Gommenginger C. (2006) A rotating knife-beam altimeter for wide-swath remote sensing of the ocean: wind and waves, Sensors, Vol. 6, pp. 260-281.

Karaev V., Kanevsky M., Meshkov Eu., Kovalenko A. (2010) The concept of the advanced space microwave radar for remote sensing of the ocean at small incidence angles, PORSEC 2010, Taiwan, Proceedings, P. 23.

Nouguier F., Mouche A., Rascle N., Chapron B., Vandemark D. (2014), Analysis of dual-frequency ocean backscatter measurements at Ku- and Ka-band using near-nadir incidence GPM radar data, Journal of latex class files, Vol. 13, No. 9, pp. 1-5.

Nouguier F., Mouche A., Rascle N., Chapron B., Vandemark D. (2016) Analysis of Dual-Frequency Ocean Backscatter Measurements at Ku- and Ka-Bands Using Near-Nadir Incidence GPM Radar Data, IEEE Geosci. and Rem. Sens. Letters, Vol. 13, No. 9, pp. 1310-1314.

Panfilova M., Karaev V., Mitnik L., Titchenko Yu., Ryabkova M., Meshkov E., Andvanced view at the Ocean Surface (2020), Journal of Geophysical Research, Oceans, 2020, Vol. 125, No. 11, e2020JC016531,

Tran, N., Chapron, B., Vandemark, D. (2007) Effects of long waves on Ku-band ocean radar backscatter at low incidence angles using TRMM and altimeter data, IEEE Trans. on Geosci. and Rem. Sen., Vol. 4, No. 4, pp. 542–546.

Advanced concept of the orbital scatterometer

V. Karaev* M. Panfilova, M. Ryabkova, Yu. Titchenko, K. Ponur, L. Mitnik

Institute of Applied Physics RAS, N.Novgorod, Russia

Abstract – The orbital scatterometer is the main source of operational and global information about the wind field over the sea surface. The two main schemes for measuring scatterometers, when measurements are performed at middle incidence angles, are considered. To improve the precision of the wind speed retrieval along the flight track, it is proposed to additionally perform measurements at small incidence angles (+/- 12°) using a fan beam antenna. As a result, it will be possible to retrieve not only the wind speed, but also measure the mean square slopes of sea waves and determine the type of the scattering surface using the ice/water criterion in the wide swath along the track.

Keywords: scatterometer, wind speed, small incidence angles, mean square slopes of sea waves, sea ice, fan beam antenna

1. INTRODUCTION

Measurements of the wind speed over sea surface are required for a wide range of meteorological and oceanographic applications. Before scatterometer era, observations of surface wind speed were rare and were conducted by ships and sea buoys. Such measurements are important until now as instruments for verification and validation of the retrieval algorithms.

Scatterometers offer an effective way to obtain a global and operative information about wind field over World Ocean with resolution 25 km x 25 km. In addition to measuring the surface wind field, scatterometers are used to monitor the area of sea ice in Arctic and Antarctic. Currently, the measurement of the sea ice is an important task, because, a change of sea ice area is one of the key indicators of global climate change.

Despite the obvious progress in this direction, there is a number of problems that limit the capabilities of scatterometers. In this paper, a new measurement scheme is proposed that makes it possible to improve the precision of determining the wind speed and area of sea ice and obtain information about mean square slopes (*mss*) of sea waves in a wide swath along track.

2. MODERN SPECTROMETERS

The European Space Agency (ESA), Indian Space Research Organization (ISRO) and China National Space Administration (CNSA) scatterometers are currently in orbit. For measurements, two schemes are used, which are shown in Fig. 1.

A step forward was the Chinese scatterometer on the CFOSAT satellite, where instead of a pencil antenna beam, a fan beam antenna was used, which made it possible to increase the number of observations of wind vector cells (WVC). Measurements are carried out at the middle incidence angles too.

The measurement scheme of the ASCAT scatterometer (Fig.1, top) guarantees a measurement at three azimuth angles at any point in the swath, and the azimuth angles are correctly spaced, which improves the precision of the retrieval algorithm. The scatterometer uses six fixed antennas, which form two swaths with a width of more than 500 km each. The disadvantage of the measurement scheme is the fact that the scatterometer does not measure along the flight track.
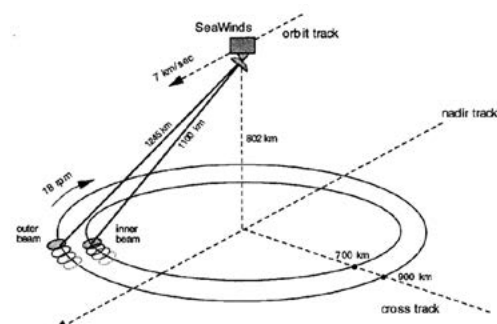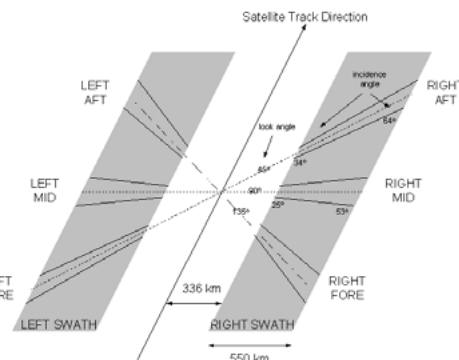
Figure 1. *Scatterometer sounding scheme: top - ASCAT (ESA), bottom - SeaWinds (NASA, ISRO, CNSA) (Portabela, 2002).*

3. CHANNEL OF NEAR NADIR SOUNDING OF THE SCATTEROMETER

Measurements at small incidence angles are performed by a Dual-frequency Precipitation Radar (DPR) installed on the GPM satellite or PR installed on the TRMM. When moving, a narrow beam is scanning in a direction perpendicular to the flight direction in the range of incidence angles +/- 18 degrees (Ku-band). As a result, a radar image of the scattering surface is formed.

An analysis was carried out and the algorithms for retrieval of wind speed, for example, (Li et al, 2004; Bao et all, 2016; Panfilova and Karaev, 2021), *mss* (Freilih and Vanhoff, 2003; Panfilova et al., 2020) and classification of the scattering surface type according to the ice / water criterion (Panfilova et al., 2020) were developed.

Thus, by supplementing the measurement scheme of the scatterometer with measurements at small incidence angles, we solve the problem of wind speed measuring along the track for ASCAT scatterometers. The problem of the precision the retrieval of wind speed and direction for SeaWinds scatterometer. Since the wind speed will be known from measurements at small incidence angles, measurements at two azimuth angles in the center of the swath will be sufficient to accurately determine the direction of the wind.

The proposed measurement scheme is shown in Fig. 2. A fan beam antenna (1° x 30°) oriented along the direction of flight is used. Scanning is performed in the direction of the perpendicular direction of flight in the range of incidence angles +/- 13°.

* Corresponding author. Address: 46, Uljanov str., Nizhny Novgorod, 603950, Russia. Email: volody@ipfran.ru
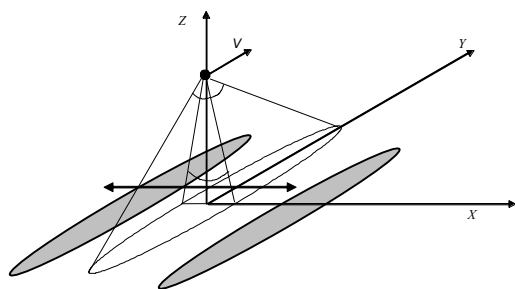
Fig. 2. *Probing scheme (a scanning fan beam antenna)*
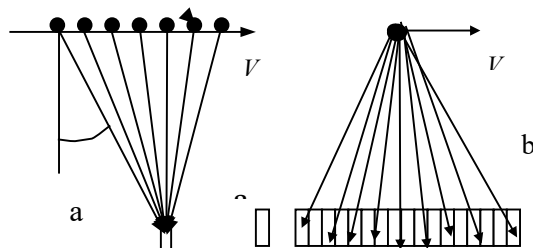
Fig. 3. *Observation of elementary scattering cell (a) and transformation of the cell into "footprint" (synthesis procedure) (b)*

The original approach for processing is used. It is possible to form for each WVC the dependence of the radar cross section (RCS) on the incidence angle (Fig. 3). It can be used to determine the *mss*.

The original approach opens up new possibilities for determining the type of scattering surface. As can be seen from Figure 4, it is easy to determine the type of the scattering surface from the dependence of RCS on incidence angle for each WVC.
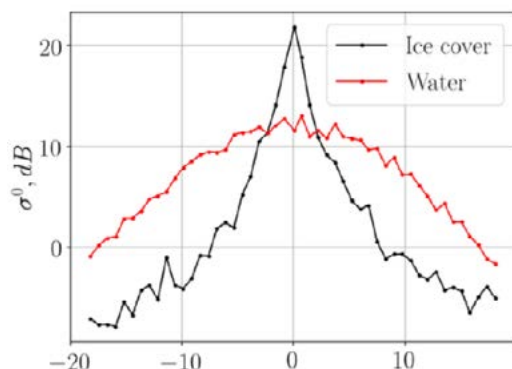
Figure 4. *Dependence RCS on the incidence angle: black curve – sea ice, red curve – sea waves.*

To automate the classification process, the kurtosis coefficient is used: for the sea surface, its value is about zero, and for the ice cover, the kurtosis coefficient can reach 20. Unlike all other methods, it does not require calibration and the stability of the radar power, which are complex technical tasks during the flight.

4. CONCLUSIONS

This investigation presents a new view on the concept of a future scatterometer. The use of a near nadir sounding channel in a scatterometer will improve the precision of wind speed retrieval, improve the measurement of the sea ice area, and provide new information about the properties of the sea surface (*mss* of sea waves).

ACKNOWLEDGEMENTS

REFERENCES

Portabella M. (2002) Wind Field Retrieval from Satellite Radar Systems, Doctoral Thesis in Physics, University of Barcelona, 2002 200 p.

Li et L. al. (2004) Retrieving ocean surface wind speed from the TRMM Precipitation Radar measurements, IEEE Transactions on Geoscience and Remote Sensing, Vol. 42, No. 6, pp. 1271−1282.

Bao Q. et al. (2016) Surface Wind Speed Inversion Using the Low Incident NRCS Measured by TRMM Precipitation Radar, IEEE Journal of Selected Topics in Applied Earth Observations and Remote Sensing, Vol. 9, No. 11. pp. 5262−5271.

Panfilova M., Karaev V. (2021) Wind Speed Retrieval Algorithm Using Ku-Band Radar Onboard GPM Satellite, Remote Sensing, Vol. 13, No. 22.

Freilich M., Vanhoff B. (2003) The relationship between winds, surface roughness, and radar backscatter at low incidence angles from TRMM precipitation radar measurements, Journal of Atmospheric and Oceanic Technology, Vol. 20, No. 4, pp. 549−562.

Panfilova M. et al. (2020) Advanced View at the Ocean Surface. Journal of Geophysical Research: Oceans, Vol. 125, No. 11, e2020JC016531.

Panfilova M. et al. (2020) Sea ice detection using Ku-band radar onboard GPM satellite. XXXIIIrd General Assembly and Scientific Symposium of the International Union of Radio Science, pp. 1−3, DOI: 10.23919/URSIGASS49373.2020.9232361.

'Variability of bio-optical properties in surface waters in northeast Greenland Shelf (Arctic Ocean) in late summer'

P. Kowalczuk[1*], A. Makarewicz[1], J. Meler[1], M. Zabłocka[1], S. Sagan[1], M. Konik[1], M. Darecki[1], C. A. Stedmon[2], M. A. Granskog[3]

[1] Institute of Oceanology Polish Academy of Sciences, Poland
[2] National Institute of Aquatic Resources, Technical University of Denmark, Lyngby, Denmark
[3] Norwegian Polar Institute, Fram Centre, Tromsø, Norway

Abstract – Fram Strait is the main gateway for water mass exchange between North Atlantic and the Arctic Ocean. The West Spitsbergen Current transports warm and saline Atlantic Water (AW) northward, while Polar Water (PW) is carried southward by the East Greenland Current. Here, we examine bio-optical relationships between the measured inherent optical properties of oceanic water and chlorophyll-*a*, *Chla*, concentration measured in collected water samples. We have derived "classic" bio-optical models between spectral values particulate and phytoplankton pigments absorption coefficients, $a_p(\lambda)$, $a_{ph}(\lambda)$ and *Chla*, and between *Chla* and pigments absorption line height, $a_{LH}(670$ proving its use as a reliable proxy for phytoplankton biomass. Vertical $a_{LH}(670)$ profiles taken across Fram Strait have revealed systematic deepening of the subsurface chlorophyll-a maximum, SCM, and lower phytoplankton biomass in PW compared to AW. In PW, the SCM is usually located at depths greater than 30 m, and overlaid with layer of PW characterized with strong CDOM absorption. CDOM absorption in PW absorbs more than 80% of available light at 443 nm. These conditions severely impaired the accuracy of *Chla* retrievals in PW with use of ocean color remote sensing global band ratio algorithms.

Keywords: Arctic Ocean, Fram Strait, inherent optical properties, particulate absorption, CDOM, absorption budget, bio-optical models.

1. INTRODUCTION

Since the launch of the Coastal Zone Color Scanners in 1979, ocean color remote sensing (OCRS) has evolved and has been used successfully for studying spatial and temporal dynamics of phytoplankton abundance, inherent and apparent optical properties (IOPs, AOPs), and oceanic primary production across a range of spatial and temporal scales (Blondeau-Patissier et al., 2014).

The concepts of ocean color algorithms to retrieve essential biogeochemical variables, IOPs, and AOPs of surface ocean waters is based on two approaches: (i) empirical band-ratio algorithms based on non-linear relationship between the retrieved variables and the ratio of the remote sensing reflectances measured in the blue and green spectral bands and (ii) semi-analytical algorithms based on the relationship between specific IOPs and biogeochemical variables in bio-optical models. Both approaches depend on available knowledge on spatial and temporal variability of IOPs, AOPs and targeted biogeochemical variables in the study area, which is necessary for calibration and validation. The first so-called "blue-green ratio" algorithms were developed for retrieval of chlorophyll a concentration (Gordon and Morel, 1983).

Satellite observations have proved that, from the mid-1970s a significant change in the Arctic Ocean system has occurred and is manifested with reduction of area and thickness of the sea ice cover at rate of -13.3% dec^{-1} (Serreze and Stroeve, 2015). The main driving force for the decline of the Arctic Sea ice was the increase in global mean temperature, which in the Arctic is two times stronger than elsewhere (Cohen et al., 2014). The exposure of dark ocean surfaces increases absorption of solar radiation and surface ocean warming, further accelerating melting of sea ice. Quantification of this effect requires detailed information on variability of IOPs and AOPs in the Arctic Ocean. In situ optical observations from various platforms are essential to develop, improve, and evaluate OCRS algorithms and provide information necessary to link surface ocean processes with those occurring at greater depths.
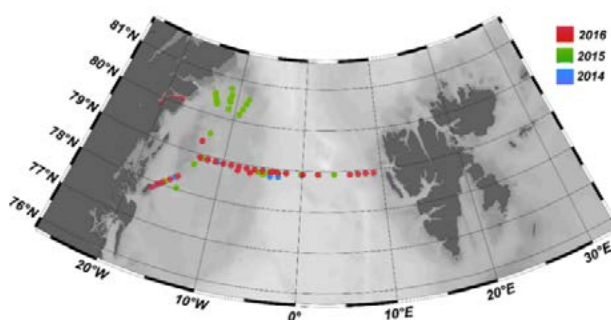
Figure 1. *Locations of sampling station in the Fram Strait, Greenland Sea, visited in summers 2014-2016.*

The main goal of this presentation, which is based on work conducted in Fram Strait, Arctic Ocean, Figure 1, in the period 2014-2016 is to understand the main drivers of variability of IOPs, establish and refine regional bio - optical relationships relevant for OCRS, and provide simple formulae for rapid quantification of *Chla* with use of in situ optical measurements and present the vertical distribution of *Chla* in water masses.

2. RESULTS

IOPs in the Atlantic influenced eastern part of Fram Strait were dominated by particulate absorption related phytoplankton biomass, while the in the western part CDOM transported with East Greenland Current was the main optically significant sea water constituent (Pavlov et al., 2015, Kowalczuk et al. 2019). The median value of $a_{CDOM}(443)$ in observed in late summer in three consecutive years 2014-2016 in AW was 0.035 m^{-1}, the median values of the $a_{CDOM}(443)$ in the same period in PW and sea ice melt water was 0.086 m^{-1} and 0.089 m^{-1}, respectively. Phytoplankton pigments absorption was ca. two to four times

Corresponding author. Address: Institute of Oceanology Polish Academy of Sciences, ul. Powstańców Warszawy 55, PL-81-712 Sopot, Poland, Email:piotr@iopan.pl

higher in AW compared to PW and melt water. Observed median values of $a_{ph}(443)$ were: 0.022 m^{-1}, 0.0054 m^{-1} and 0.092 m^{-1}, respectively. The median values of detrital absorption coefficient, $a_d(443)$, was highest in the AW: 0.061 m^{-1}, and lowest in PW: 0.0037 m^{-1}, with intermediate values observed in melt water: 0.0055 m^{-1}. The CDOM contribution to total absorption at 443 nm was on average, 64% in AW, 84% in PW and 83% in melt water. The contribution of phytoplankton pigments and detrital absorption to the total absorption increased toward red part of the spectrum regardless of the water mass. Observed averaged *Chla* concetration was 1.02, 0.65 and 0.35 mg m^{-3}, in AW, PW and sea-ice melt water respectively.
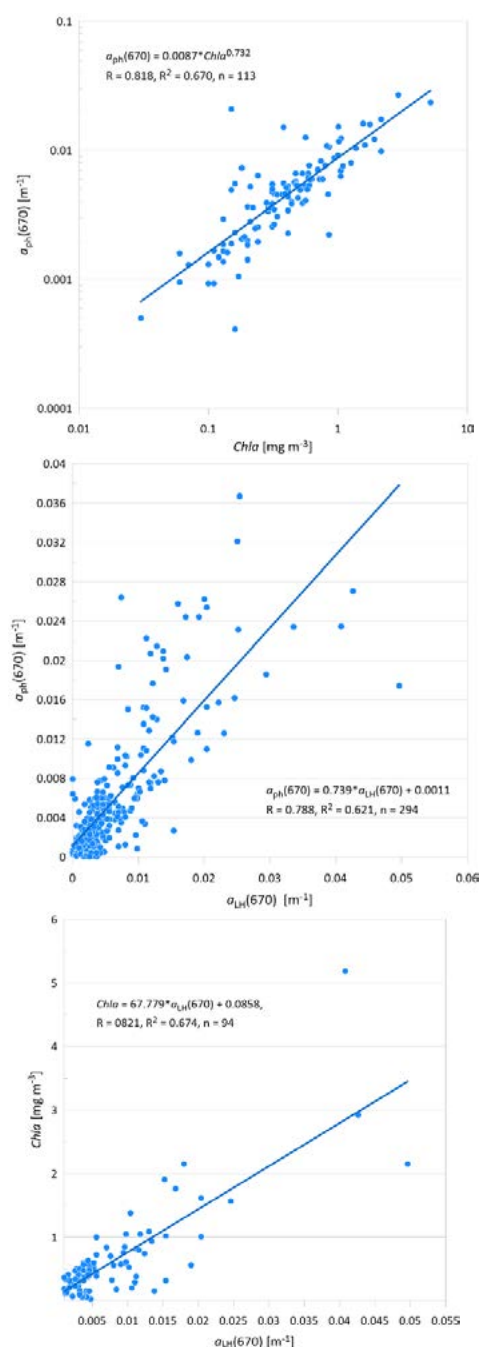
Figure 2 *Relationships between Chla and inherent optical properties and relationship between $a_{LH}(670)$ and $a_{ph}(670)$.*

Inherent optical properties were very well correlated with phytoplankton biomass, especially in the red part of the spectrum. We have derived regional relationship between

Chla and $a_{ph}(670)$ approximated by power function, that was characterized by high value of determination coefficient R^2=0.670, Figure 2 (top panel). The absorption pigments line height (Roesler and Barnard, 2013) calculated from in situ measured absorption spectrum with use of submersible spectrophotometer ac-9 (Wetlabs), correlated very well with phytoplankton pigments absorption coefficient $a_{ph}(670)$ and *Chla*, with correlation coefficients of 0.788 and 0.821, respectively (Figure 2 middle and bottom panels).

Based on $a_{LH}(670)$ l profiles we have estimated the depth on subsurface chlorophyll a maximum. SCM which was shallower in AW (on average at 20 m). In the PW the SCM was located deeper: at 26 m, with maximum SCM depth observed at 41 m in PW. Together with deepening of SCM depth we observed a significant decrease of phytoplankton biomass in PW, which was indicated by meridional distribution of $a_{ph}(670)$ in the mixed layer (Figure 3).
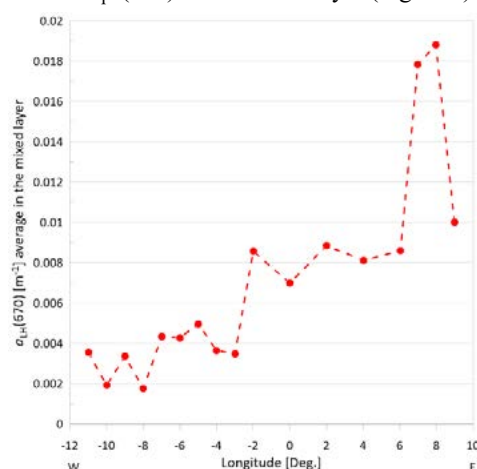
Figure 3 *Meridional distribution of $a_{LH}(670)$ in the Fram Strait in summer 2014 in the mixed layer.*

3. CONCLUSION

Ocean color remote sensing algorithms retrieval algorithms performance and accuracy in the East Greenland shelf could be significantly reduced by physical conditions, that forced reduced phytoplankton biomass deeper compared to AW. The signal due to phytoplankton pigments absorption could be further masked by overlaid layer of sea ice melt water and PW with high CDOM absorption. We postulate development of regional ocean color retrieval algorithms for east Greenland Shelf.

REFERENCES

Blondeau-Patissier, et al. (2014). Prog. Oceanogr. 123, 123–144.

Cohen, et al. (2014).. Nat. Geosci. 7, 627–637.

Gordon, H. R., and Morel, A. Y. (1983). New York, NY: Springer

Kowalczuk, et al. (2019). J. Geophys. Res. Oceans 124, 1964–1987.

Pavlov, et al. (2015. J.Mar. Syst. 143, 62–72.

Roesler, C. S., & Barnard, A. H. (2013). Methods in Oceanography, 7, 79–94

Serreze, M.C.; Stroeve, J. (2015). In Philos. Trans. R. Soc. A, 373,

Detection and attribution of manometric sea-level variations along the Norwegian coast using GRACE mascon solutions

F. Mangini[1] *, A. Bonaduce[1], L. Chafik[2,3], R. Raj[1], L. Bertino[1]

[1]Nansen Environmental and Remote Sensing Center and Bjerknes Centre for Climate Research, Bergen, Norway
[2]Department of Meteorology and Bolin Centre for Climate Research, Stockholm, Sweden
[3]National Oceanography Centre, Southampton, UK

Abstract – We provide an assessment of the manometric sea-level variability along the Norwegian coast estimated using the Gravity Recovery and Climate Experiment (GRACE) satellite gravimetry mission and a combination of satellite altimetry and hydrographic stations. The general agreement between (1) the Goddard Space Flight Center (GSFC) GRACE mascon solution, (2) the Jet Propulsion Laboratory (JPL) GRACE mascon solution and (3) the combination of satellite altimetry and hydrography gives us confidence to explore the spatio-temporal variability of the manometric sea-level along the Norwegian coast. On intra-annual time scales, both mascon's solutions reveal a large spatial-scale coherence of the manometric sea level on the shelf. On inter-annual timescales, we find that the along-slope wind stress integrated along the eastern boundary of the North Atlantic Ocean explains a large fraction of the variance of the manometric sea level averaged along the Norwegian coast. Furthermore, we reveal that the leading mode of steric height variability in the North Atlantic Ocean covaries strongly with the manometric sea level over the entire Norwegian shelf. The results give us confidence in the GRACE-derived manometric sea-level along coastal and shelf areas especially where in-situ measurements are sparse.

Keywords: GRACE, Norwegian continental shelf, Manometric sea level, Coastal trapped waves

1. INTRODUCTION

Reliable sea-level observations in coastal regions are needed to properly assess the impact of sea-level variations on coastal communities and ecosystems. By measuring the manometric component of sea level, the Gravity Recovery and Climate Experiment (GRACE) plays an important role in monitoring and understanding sea-level variations over the ocean. Despite its relevance, though, GRACE has historically been considered unreliable in coastal areas due to the signal leakage that results from GRACE's coarse spatial resolution. This is a problem since a proper understanding of coastal sea-level variations is important to assess the impact of sea level along the coastal ocean.

The mascon approach was introduced to reduce signal leakage and increase the reliability of GRACE in coastal areas (Luthcke et al., 2015; Watkins et al., 2015). It involves the pixelization of the Earth's surface into cells, with each cell characterized by its own uniform mass that is computed using known spatio-temporal constraints.

In this project, we investigate the ability of GSFC's and JPL's mascon solutions to measure the manometric sea-level variability along the Norwegian coast over a range of timescales. However, because of space limitation, this paper

only shows the results for the GSFC's mascon solution on inter-annual timescales.

We opt for the Norwegian coast for several reasons. At first, it is well covered by hydrographic stations which, together with satellite altimetry (reprocessed with the ALES-retracker), offer an independent estimate of manometric sea-level in the region. Secondly, the processes responsible for the Norwegian sea-level variability are partly known and can be used to physically evaluate GRACE. Thirdly, these processes are partly unknown. Therefore, GRACE can help understand sea-level variations in the area.

This paper is organized as follows. Section 2 compares the inter-annual manometric sea-level variability averaged along the Norwegian coast estimated using the GSFC's mascon solution and the combination of satellite altimetry and hydrography. It then analyses the contribution of wind stress on sea level to provide a physical evaluation of the two datasets. Section 3 identifies the locations where wind stress most strongly contributes to the inter-annual manometric sea level along the Norwegian coast. Section 4 summarises and lists additional results that are not included in this paper due to space constraints.

2. COMPARISON BETWEEN THE GSFC'S MASCON SOLUTION AND THE COMBINATION OF SATELLITE ALTIMETRY AND HYDROGRAPHY

When we consider the average along the Norwegian coast, we find an overall good agreement between the inter-annual manometric sea-level variability from the GSFC's mascon solution and the combination of satellite altimetry and the hydrographic stations (Figure 1).
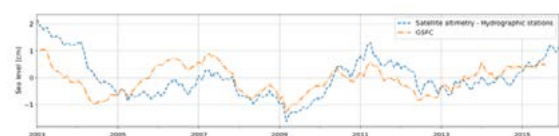
Figure 1: Manometric sea-level variability from satellite altimetry and the hydrographic stations (blue, dashed line) and from the GSFC's mascon solution (orange, dashed dotted line) on inter-annual timescales.

To understand which of the two estimates better captures the inter-annual manometric sea-level variability averaged along the Norwegian coast, we propose a physically based validation. We assess how the two estimates compare to the along-slope component of the detrended and deseasoned monthly averaged surface wind stress integrated along the continental slope from the equator up to northern Norway (at 70°N). We know from the literature that, on inter-annual and longer timescales, the sea level over the Norwegian shelf does not only respond to local winds, but also to the

* Corresponding author. Address: Jahnebakken 3, N-5007, Bergen, Norway. Email: fabman.nersc@gmail.com

winds blowing along the eastern boundary of the North Atlantic (e.g., Calafat et al., 2013). The along-slope winds set up an Ekman transport which, through upwelling and downwelling, affect the depth of the thermocline and, in turn, modify the sea level. However, the perturbation of the thermocline and of the sea level is not constrained to where the winds blow but propagates cyclonically along the ocean margin as a coastal trapped wave.

We find that both the GSFC's mascon solution and the combination of satellite altimetry and hydrographic stations well agree with the integrated along-slope wind stress, with the GSFC's mascon solution showing the best agreement (Figure 2).
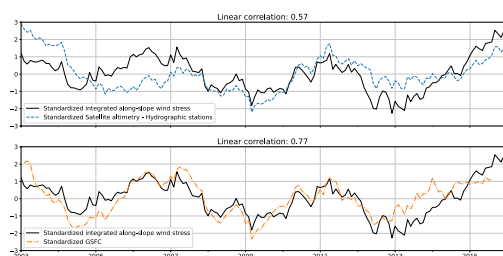
Figure 2: Manometric sea-level variability from satellite altimetry and the hydrographic stations (blue, dashed line; upper panel) and from the GSFC's mascon solution (orange, dashed dotted line; lower panel). Each estimate of the inter-annual manometric sea level is plotted together with the inter-annual integrated along-slope winds stress (black, solid line). Each time series has been standardized before the plotting.

3. INVESTIGATING THE WIND CONTRIBUTION

The manometric sea-level variability averaged along the Norwegian coast is found to be largely related to the winds blowing along the western and northern sections of the northern European continental slope (Figure 3). As we progressively integrate the along-slope component of the wind stress from the equator, we find that the linear correlation coefficient with the manometric sea level averaged along the Norwegian coast overall increases starting from the northern coast of Spain. The results support previous findings (e.g., Calafat et al., 2013) where along-shore wind forcing is shown to explain coastal sea-level variability on interannual-to-decadal time scales. This finding suggests that the coastal trapped waves generated along the coast of Spain and at southward locations might contribute minimally to the sea-level variability over the Norwegian shelf possibly because they radiate and scatter into the open-ocean due to the complex topography of the African and European continental shelf.
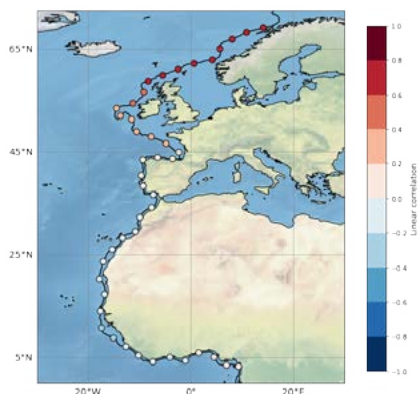
Figure 3: Each circle is located along the continental slope of the eastern boundary of the North Atlantic Ocean and is

coloured according to the linear correlation coefficient between the inter-annual manometric sea-level variability averaged along the Norwegian coast and the inter-annual along-slope wind stress integrated from the equator up to the circle in question. The black, solid line shows the location of the continental slope, depicted by the 500 m isobath.

4. CONCLUSION

In this paper, we show that the GSFC's mascon solution well captures manometric sea-level variations along the Norwegian coast on inter-annual timescales. Notably, on inter-annual timescales, the GSFC's mascon solution performs better than the combination of satellite altimetry and the hydrographic stations. This suggests that the GSFC's product can be used to investigate the sea-level variability along the Norwegian coast on inter-annual timescales (e.g., to investigate the role of the open ocean).

Even if not shown in the paper, we also find that GSFC's mascon solution well captures the intra-annual manometric sea-level variability along the Norwegian coast and that the JPL's mascon solution returns comparable results.

Overall, our results indicate that GRACE can be used to study manometric sea-level variations in coastal regions, where in-situ observations are missing.

REFERENCES

Calafat, F. M., D. P. Chambers, and M. N. Tsimplis, 2013: Inter-annual to decadal sea-level variability in the coastal zones of the Norwegian and Siberian Seas: The role of atmospheric forcing. *Journal of Geophysical Research: Oceans*, **118**, https://doi.org/10.1002/jgrc.20106.

Luthcke, S. B., D. D. Rowlands, T. J. Sabaka, B. D. Loomis, M. Horwath, and A. A. Arendt, 2015: Gravimetry measurements from space. *Remote Sensing of the Cryosphere*.

Watkins, M. M., D. N. Wiese, D. N. Yuan, C. Boening, and F. W. Landerer, 2015: Improved methods for observing Earth's time variable mass distribution with GRACE using spherical cap mascons. *Journal of Geophysical Research: Solid Earth*, **120**, https://doi.org/10.1002/2014JB011547.

Analysis of hydrographic data collected by Southern Elephant Seals in the Argentine Continental Shelf

M. M. Martinez *[1,2,3], L. A. Ruiz-Etcheverry [1,2,3], B. Picard [4], M. Saraceno [1,2,3], C. Guinet[4]

(1) Departamento de Ciencias de la Atmósfera y los Océanos. Buenos Aires, Argentina.
(2) Centro de Investigaciones del Mar y la Atmósfera (CIMA). Buenos Aires, Argentina.
(3) Instituto Franco-Argentino para el Estudio del Clima y sus Impactos. Buenos Aires, Argentina.
(4) Centre d'Etudes Biologiques de Chizé, Villiers en Bois, France.

Abstract – In situ data obtained from CTD (Conductivity, Temperature and Depth) sensors attached on 6 elephant seals (*Mirounga Leonina*) that crossed the Argentine Continental Shelf between the 17th and 31st of October 2019 are analyzed. The sub-surface (15 m depth) in situ data collected correlates very well (r=0.9) with the satellite sea surface temperature (SST), suggesting that the in situ data are of high-quality. The high spatio-temporal resolution of the in situ dataset show regions with strong gradients along the sections: T and S gradients were-up to 0.06 deg C/km and 0.03 UPS/km respectively along the trajectories, in clear association with frontal regions. Water masses typical of the region were also identified. Finally, the steric effect was estimated from potential density changes calculated from T and S vertical profiles and compared with the value estimated by a reanalysis model. The comparison between both data sets is quite good (correlation r=0.83).
Keywords: Argentina Continental Shelf, Elephant Seals, Satellite data.

1. INTRODUCTION

In recent decades, several animals have been used as autonomous platforms to collect oceanographic data, including penguins, sharks and marine mammals (Harcourt et al., 2019, Mclntyre et al., 2014). The use of diving animals allows obtaining the best spatial and temporal resolution in the Southern Hemisphere (SH) (Treasure et al., 2017). In the SH elephant seals and Weddell seals have contributed to the 98 % of the existing temperature and salinity profiles within the Southern Ocean pack ice. (Mclntyre et al., 2014).

In this study, in situ data obtained from CTD (Conductivity, Temperature and Depth) sensors attached on 6 elephant seals (*Mirounga Leonina*) during the period between the 17th and 31st of October 2019 are analyzed. SES have been instrumented in Península Valdés (PV, Figure 1) since 1992 (Campagna et al, 1995). The oceanographic data so collected have been used to study mesoscale structures in the open ocean, identify foraging places (Campagna et al., 2006) and relate the species that the SES eats to different water masses along the Patagonian shelf slope (Aubone et al., 2021). Female SES from PV forage mainly along the Patagonian shelf slope and in the Argentine Basin (Aubone et al., 2021; Campagna et al., 1995). Little has been explored about the SES transit zones. Only in Campagna (1995) it is shown that the path, speed and swimming pattern of the PV colony suggest that little feeding occurs on the continental shelf. Here we propose to use T and S data to characterize the oceanographic conditions along the trajectories of the SES

within the continental shelf, taking advantage that they crossed it very fast.

Indeed, data collected by SES provide high-resolution profiles that provide a synoptic description of the oceanographic conditions. We focus our study from the PV coast to the shelf-break (defined as the 200m isobath) from 65°W to 55°W with latitudes ranging from 41° to 44°S (Figure 1).
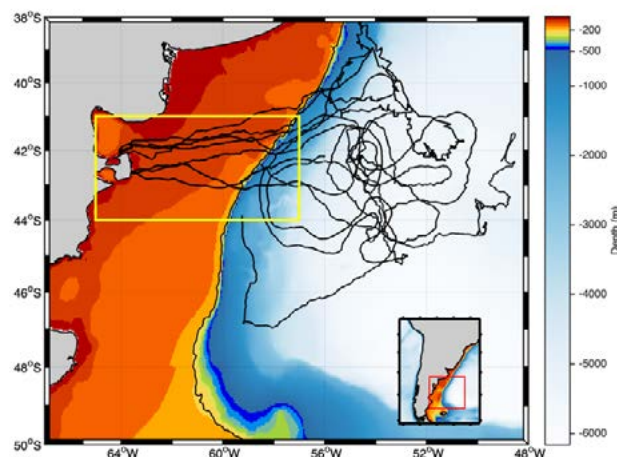
Figure 1. Trajectories of six SES instrumented in October 2019. Depth is shown in colors. The thin black line represents the 200m isobath.

2. DATA AND METHODS

The data collected by the SES used in this work are part of the international SABIO (Studying physical processes in the Southwestern Atlantic to understand BIOlogical productivity & regional ecosystems) project. One to three biologging devices were glued to each animal prior to the departure to the sea for their post-breeding foraging trip: a head-mounted sonar tag, a back-mounted Satellite Relayed Data Logger (CTD-SRDL, Sea Mammal Research Unit, St Andrews, UK), and a neck-mounted satellite tags (SPOT, Wildlife Computers, USA).

The CTD-SRDL recorded conductivity, temperature and pressure in hydrographic profiles during the ascent of the animals . The profiles are then compressed and data is sent via Advanced Research and Global Observation Satellite (ARGOS) messages. The SMRU CTD-SRDL archive data to internal memory far more frequently than they can be transmitted and, if the instruments can be recovered, additional data at higher resolution can be downloaded (Hardcour et al., 2019). The SPOT tag was included to facilitate recovery of the tags when animals returned to land,

* Adress: Intendente Güiraldes 2160, (C1428EGA) Buenos Aires, Argentina. Email: melina.martinez@cima.fcen.uba.ar

in case the CTD-SDRL had stopped transmitting. The sonar tag recorded high-resolution sonar, location, and movement data. GPS positions were obtained at each surfacing. The geolocation accuracy provided by ARGOS is ±5 km and by GPS is <1 km (Lowther et al., 2015). Only measures collected at depths larger than 15 m were considered, as the sensors stabilize at this depth.

Sea Surface Temperature (SST) from Multi-scale Ultra-high Resolution L4 product (MUR - https://mur.jpl.nasa.gov/) with daily resolution and spatial resolution of 0.011° x 0.011° is used to compare the surface temperature obtained by the SES with the satellite sea SST. The choice of this product is due to its high spatial resolution and also because it has been successfully compared with independent in situ data in the study region (Lago et al., 2019).

3. SES: RESULTS

Figure 1 shows the trajectories of the six SES considered. SES moved mainly toward the east from PV, reaching the open ocean or the continental shelf-break. They took between three to six days to cross the ACS. The average number of dives per day in the continental shelf was 90.39 ± 10.56 and the average distance parkoured per day was 109.01 ± 13.02 km. We compared the surface temperature of all SES with the satellite SST by extracting SST values along the track within the corresponding daily image. High and significant correlations were obtained ($r>0.93$ significant at 95%) in all the trajectories analyzed. A clear strip pattern is observed in some portions of the temperature and salinity in situ data (Figure 2).
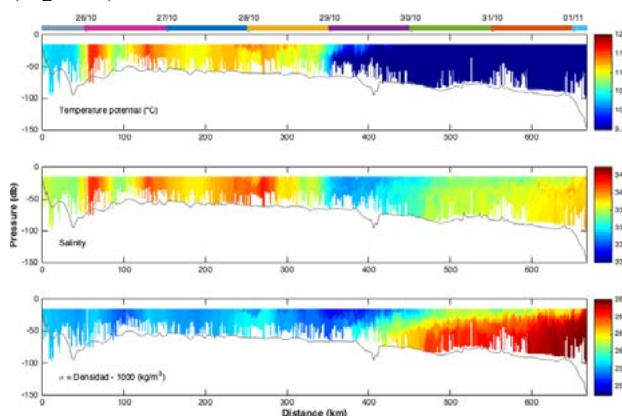
Figure 2. Temperature (top), salinity (middle), and density (bottom) profiles along the Northern elephant path. Profiles are reconstructed from SES dives from surface to bottom. The horizontal axis is the distance in km from PV. The gray line is the sea floor. The top colorbar refers to the time elapsed since the elephant left PV.

At those locations, surface (15 m depth) gradients were up to 0.06 deg C/km and 0.03 UPS/km along the trajectories. Comparison with satellite SST images clearly shows that the strip pattern is due to the fact that SES crossed frontal regions several times (not shown).

TS diagrams (not shown) show the presence of four water masses: Malvinas Water, Low Salinity Coastal Water, Middle Shelf Water and High Salinity Water from the San Matías Gulf characteristic of the region (Saraceno et al., 2021). Finally, taking advantage of the in situ T and S vertical profiles (Figure 2), the potential density change was calculated, the so-called steric effect, and compared with the value estimated by a reanalysis model (GLORYS12V1). The comparison between both data sets is quite good (correlation $r=0.83$).

4. CONCLUSION

Physical data collected by female elephant seals are useful for sampling long distances over short periods of time by providing a single high-frequency data set along trajectories. In the ACS it was possible to obtain a better resolution (approximately 90 dives per day per 100 km) than that reported by other authors (Treasure et al. 2017). The data collected in situ allow us to know the vertical and horizontal structure along the trajectories. We identified a strip pattern along some portions of the trajectories that we associated with the crossing of the SES to frontal zones. We were also able to identify the characteristic water masses of the region. Finally, preliminary results for the calculation of the steric effect from the collected data, suggest that it is possible to study the contribution to sea level through a global ocean reanalysis dataset.

ACKNOWLEDGEMENTS

REFERENCES

Aubone, N., Saraceno, M., Alberto, M. T., Campagna, J., Le Ster, L., Picard, B., ... & Guinet, C. R. (2021). Physical changes recorded by a deep diving seal on the Patagonian slope drive large ecological changes. *Journal of Marine Systems*, *223*, 103612.

Campagna, C., Boeuf, B. L., Blackwell, S. B., Crocker, D. E., & Quintana, F. (1995). Diving behaviour and foraging location of female southern elephant seals from Patagonia. *Journal of Zoology*, *236*(1), 55-71.

Campagna, C., Piola, A. R., Marin, M. R., Lewis, M., & Fernández, T. (2006). Southern elephant seal trajectories, fronts and eddies in the Brazil/Malvinas Confluence. *Deep Sea Research Part I: Oceanographic Research Papers*, *53*(12), 1907-1924. (122)

Harcourt, R., Sequeira, A. M., Zhang, X., Roquet, F., Komatsu, K., Heupel, M., ... & Fedak, M. A. (2019). Animal-borne telemetry: an integral component of the ocean observing toolkit. *Frontiers in Marine Science*, *6*, 326.

Lago, L. S., Saraceno, M., Martos, P., Guerrero, R. A., Piola, A. R., Paniagua, G. F., ... & Provost, C. (2019). On the wind contribution to the variability of ocean currents over wide continental shelves: a case study on the northern Argentine continental shelf. *Journal of Geophysical Research: Oceans*, *124*(11), 7457-7472.

McIntyre, T. (2014). Trends in tagging of marine mammals: a review of marine mammal biologging studies. *African journal of marine science*, *36*(4), 409-422.

Saraceno, M., Martín, J., Moreira, D., Pisoni, J. P., & Tonini, M. H. (2021). Physical changes in the Patagonian shelf. In *Global Change in Atlantic Coastal Patagonian Ecosystems* (pp. 43-71). Springer, Cham.

Treasure, A. M., Roquet, F., Ansorge, I. J., Bester, M. N., Boehme, L., Bornemann, H., ... & De Bruyn, P. N. (2017). Marine mammals exploring the oceans pole to pole: a review of the MEOP consortium. *Oceanography*, *30*(2), 132-138.

The Baltic Sea from Space – primary production based on ten years of *SatBałtyk System* data

M. Ostrowska[1]* D. Ficek[2], D. Stoltmann[2], J. Stoń-Egiert[1], M. Kowalewski[1], T. Zapadka[2], R. Majchrowski[2], M. Pawlik[2], M.Wichorowski[1], J. Dera[1]

[1]Institute of Oceanology of Polish Academy of Sciences, Sopot, Poland
[2]Pomeranian University in Słupsk, Poland

Abstract – Remote sensing data collected and processed by the SatBałtyk System (Satellite Monitoring of the Baltic Sea Environment), satbaltyk.iopan.gda.pl, were used to provide a comprehensive picture of productivity across the Baltic Sea over the years 2010-2019. The very broad dataset allowed to describe the characteristic features like yearly cycle, as well as spatial and time-related changes of Primary Production in the Baltic Sea using statistical descriptors. Even such a short period of observation, in the context of climate change, indicates a slight increase in the productivity of the Baltic Sea over these 10 years.

Keywords: SatBałtyk System, Baltic Sea Environment, Climate changes, Primary Production.

1. INTRODUCTION

The satellite observations, which can provide the current and relatively cheap information from a really large area are the perfect tool for studying the marine environment. The SatBałtyk System is a satellite-based platform for monitoring of the Baltic Sea at various time and spatial scales. It was developed and launched by Scientific Consortium formed by the Institute of Oceanology of the Polish Academy of Sciences (leader), the University of Gdańsk, the Pomeranian University in Słupsk and the University of Szczecin.

This system effectively combining three types of data: satellite data used for day-to-day monitoring of the whole Baltic Sea area, model data using hydrodynamic and ecohydrodynamic models describing phenomena taking place in the marine environment, and point data obtained using traditional oceanographic measurement techniques. The synergy of different data sources allows to present on the website current daily maps of the spatial distribution of values of several dozen current characteristics of the Baltic Sea environment, including the coastal zone as well as the state and optical properties of the atmosphere. Such complete information on the state of the marine environment supports advanced analyzes of complex physical, chemical and biological processes occurring in the Baltic ecosystem (Woźniak et al. 2011a,b).

In the global climate analyses, the factor of major importance is the amount of biological primary production in the sea. The already accumulated 10-year data resource makes it possible to provide a verified quantitative description of spatial and temporal changes in the primary production rate in the Baltic Sea (Ostrowska et al. 2022).

2. PRIMARY PRODUCTION OF THE BALTIC SEA

The 10 years' (2010–2019) set of daily maps from the *SatBałtyk System* was used to briefly assess the productivity of the Baltic Sea on a one- and multi-year basis. For every day of the analyzed period the mean of daily Primary Production [mgC m^{-2}day^{-1}] for the entire area of the Baltic Sea was determined with resolution 1x1 km. This allowed the characteristic features to be described using a statistical descriptor that was not influenced by any extreme Primary Production values.

Table 1. The average daily Primary Production in the water column of the entire Baltic Sea, [mgC m^{-2}day^{-1}] in the most productive months (June, July and August) for the following years 2010–2019.

Year/Month	VI	VII	VIII
2010	501	660	509
2011	526	631	507
2012	474	550	504
2013	521	637	550
2014	477	673	509
2015	487	532	556
2016	540	635	481
2017	518	545	528
2018	625	687	539
2019	528	614	537

The averaged for the entire Baltic Sea minimal and maximal values of mean daily production in subsequent months extend from 5 mgC m^{-2}day^{-1} in winter to 776 mgC m^{-2}day^{-1} in summer. The wide range of changes is mainly connected with the yearly productivity cycle. Figure 1 presents a typical yearly cycle of PP in the Baltic Sea.
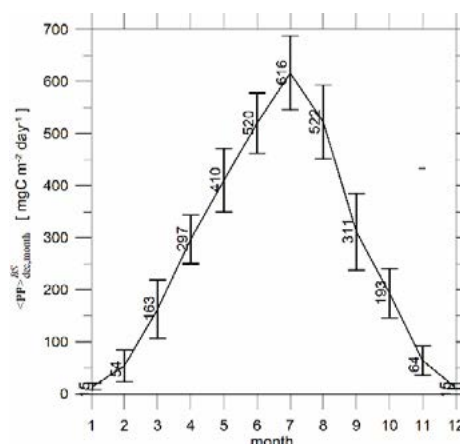
Figure 1. *Distribution and standard deviation of daily averaged primary production in the water column for each month of the year for the whole Baltic Sea area from 2010 to 2019*

* Corresponding author. Address: Powstańców Warszawy 55, 81-712 Sopot, Polska. Email: ostra@iopan.pl

Regardless of the differences in subsequent years in the mean daily values for given months the beginning of vegetative periods can be seen as a rapid increase in mean values from 54 mgC m^{-2}day^{-1} in February to 163 mgC m^{-2}day^{-1} in March. The most productive month with mean Primary Production ranged from 532 in 2014 to 687 mgC m^{-2}day^{-1} in 2018, is July (see Table1). Only in 2016, the monthly mean production in July was slightly lower than in August (532 and 556 mgC m^{-2}day^{-1}, respectively).

It is worth noticing, that the maximal daily Primary Production values in summer shown in Table 1, do not always correspond to the high values of the total yearly production [C m^{-2} year^{-1}] (see Figure 2). In 2013 in the total yearly production of the entire Baltic Sea reached one of the lowest value of the decade (93 mgC m^{-2} day^{-1}) while in the summer months are relatively high compared to other years. A similar situations can be observed for 2010, when the Primary Production values in the summer month can be considered higher ones while in the whole year the value of Primary Production does not reach a high level.
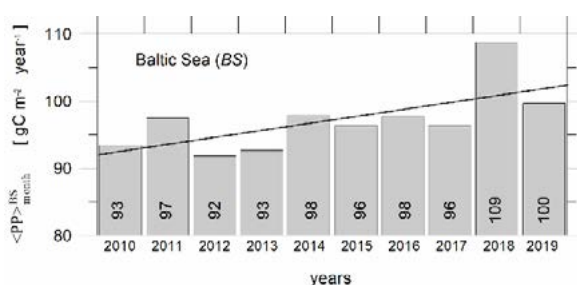
Figure 2. *The total yearly Primary Production and the trend line for the Baltic Sea determined based on the monthly means for particular years for the period 2010-2019.*

One of the main threats to the Baltic Sea ecosystem is its eutrophication, generally defined as excess Primary Production of surface water. The trend lines determined for this period (see Figure 2) indicate a slight increase in the annual production of the Baltic Sea during the decade under review. This is consistent with HELCOM's assessment that at least 97% of the Baltic Sea is below good eutrophication status between 2011 and 2016 (HELCOM, 2018).
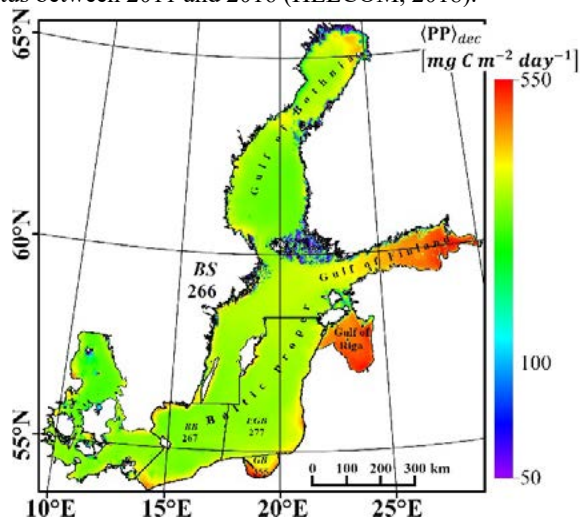
Figure 3. *Spatial distribution of mean Daily Primary Production of the Baltic Sea, the mean from the period of 2010-2019. The numbers represent mean values determined for the Bornholm Basin (BB), Eastern Gotland Basin (EGB), Gdańsk Basin(GB) and for the entire Baltic Sea (BS).*

Also, high differentiation of spatial distribution of PP values throughout the Baltic area can be observed. In Figure 3 spatial distributions of mean daily production for analyzed decade was shown together with the exemplary results of analyses of Primary Production in the three chosen basins of the Baltic Proper: the Bornholm Basin (BB), the Eastern Gotland Basin (EGB), and the Gdańsk Basin (GB).

High average values of daily Primary Production occur at all bays including the Bothnian Bay which is situated farthest North. In the south-east regions of the Baltic Sea, higher average values of the daily PP can be observed in coastal areas and in general a relatively high values of PP was recorded nearby the land.

3. CONCLUSION

Thanks to the data resources offered by the SatBaltic System, it is the first time that we have had the opportunity for a multi-year detailed analysis on such a scale, not only of the values of Primary Production, but also of other solar radiation-controlled processes in the Baltic Sea. The already accumulated 10-year data resource allows for many interesting analyses and it will be possible to present them for a longer observation period in the next years of the SatBaltic System's operation. This is of great importance in times of progressing environmental changes caused by global warming, climate change and increased human activity. The SatBałtyk System data are made available on the SatBaltyk.pl platform and will boost the Oceanographic Data and Information System, eCUDO.pl.

REFERENCES

Ostrowska M., D. Ficek, D. Stoltmann, J. Stoń-Egiert, A. Zdun, M. Kowalewski, T. Zapadka, R. Majchrowski, M. Pawlik, J. Dera, (2022). 'Ten years of remote sensing and analyses of the Baltic Sea primary production (2010-2019)', Remote Sensing Applications: Society and Environment, 26.

Woźniak B., K. Bradtke, M. Darecki, J. Dera, L. Dzierzbicka, D. Ficek, K. Furmańczyk, M. Kowalewski, A. Krężel, R. Majchrowski, M. Ostrowska, M. Paszkuta, J. Stoń-Egiert, M. Stramska, and T. Zapadka, (2011 a). 'SatBaltic – A Baltic environmental satellite remote sensing system – an ongoing Project in Poland. Part 2: Practical applicability and preliminary results', Oceanologia, 53(4), pp 897–924.

Woźniak B., K. Bradtke, M. Darecki, J. Dera, J. Dudzińska-Nowak, L. Dzierzbicka, D. Ficek, K. Furmańczyk, M. Kowalewski, A. Krężel, R. Majchrowski, M. Ostrowska, M. Paszkuta, J. Stoń-Egiert, M. Stramska, T. Zapadka, (2011 b). 'SatBaltic – A Baltic environmental satellite remote sensing system – an ongoing Project in Poland. Part 1: Assumptions, scope and operating range' Oceanologia, 53(4), pp 925–958.

HELCOM, 2018. State of the Baltic Sea – Second HELCOM holistic assessment 2011-2016, Baltic Sea Environment Proceedings 155. Available online: https://helcom.fi/media/publications/BSEP155.pdf

Multi-mission water quality products for freshwater and coastal ecosystems

Nima Pahlevan[1,2*] and Brandon Smith[1,2]

[1]Science Systems and Applications Inc., Lanham MD 20706 United States
[2]NASA Goddard Space Flight Center, Greenbelt MD 20771 United States

Abstract –This research demonstrates the extension of a recently developed machine-learning (ML) architecture, i.e., Mixture Density Networks (MDNs), to the inverse problem of simultaneously retrieving water quality (WQ) parameters, including chlorophyll-a (Chl$a$), Total Suspended Solids (TSS), and the absorption by Colored Dissolved Organic Matter at 440 nm ($a_{cdom}(440)$), from satellite measurements. We use a large in situ database to train MDN models developed for the relevant spectral measurements (400 – 800 nm) of the Operational Land Imager (OLI), MultiSpectral Instrument (MSI), and Ocean and Land Colour Instrument (OLCI) aboard the Landsat-8, Sentinel-2, and Sentinel-3 missions, respectively. Our assessments of the MDN architecture, a 50 – 50 training/validation split, suggest varying degrees of improvement with respect to second-best algorithms, depending on the sensor and WQ parameter (e.g., 68%, 75%, and 117% improvements for Chl$a$, TSS, and $a_{cdom}(440)$, respectively, for MSI-like spectra). As a second assessment, we compare between product maps of a near-concurrent OLI, MSI, and OLCI acquisition, to evaluate multi-mission product consistency across broad spatial scales. Recognizing their uncertainties, MDN models can be applied as a global algorithm to enable harmonious retrievals of WQ maps.

Keywords: Machine learning, continental waters, data product harmonization

1. INTRODUCTION

With the availability of free satellite images from multiple missions capable of making high fidelity radiometric measurements over water bodies, devising apt processing chains to produce harmonized global water quality (WQ) products is currently a crucial research topic. Global WQ products are critical for addressing the challenging questions surrounding aquatic ecosystems threatened by a changing climate and ever-increasing human exploitation of natural resources.

The optical WQ indicators considered in this study include chlorophyll-a (Chl$a$), total suspended solids (TSS), and Colored Dissolved Organic Matter (CDOM), measured as CDOM absorption at 440 nm ($a_{cdom}(440)$). Despite decades of research and developments, the potential of remote sensing for quantifying these WQ indicators across vast aquatic ecosystems has not been fully realized, and methods for generating reliable global products still deserve extensive studies.

The objective of this research is to demonstrate the validity of Mixture Density Networks (MDNs) as a robust technique for concurrent estimation of Chl$a$, TSS, and $a_{cdom}(440)$ from the Operational Land Imager (OLI), MultiSpectral Instrument (MSI), and Ocean and Land Colour Instrument (OLCI) aboard the Landsat-8, Sentinel-2, and Sentinel-3 missions, respectively. To the extent possible (owing to the differences in the spectral, spatial, and radiometric characteristics of these instruments), we aim to advance consistency among multi-mission products to deliver globally seamless WQ products. This development relies on a large *in situ* database that contains hyperspectral radiometric measurements and co-located Chl$a$, TSS, and $a_{cdom}(440)$ (Balasubramanian et al. 2020).

2. METHODS

MDNs (Bishop 1995) differ from traditional neural networks in that they produce the likelihoods of generated estimates. Succinctly, MDNs learn a probability distribution over the output space to learn multimodal target distributions. This multimodality is a fundamental characteristic of inverse problems, where a non-unique relationship exists between input and output features. In this study, several robust single-
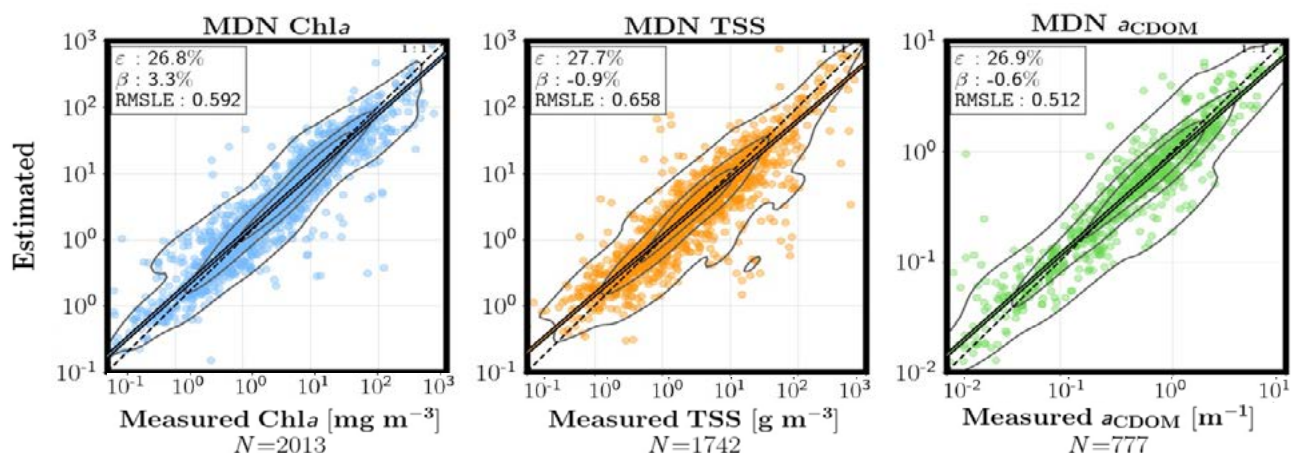
Figure 1. Performance of MDNs and best-performing state-of-the-art models demonstrated for *in situ* R$_{rs}$ spectra resampled with MSI's relative spectral responses. The number of test samples for each WQ indicator is shown on the x-axes. ε and β correspond to median error and bias, respectively.

---

* Corresponding author. 8800 Greenbelt Rd. Greenbelt MD 20771 United States. Email: nima.pahlevan@nasa.gov

parameter retrieval methods applicable to OLI, MSI, and OLCI with their original form and coefficients were considered. Their evaluations are not however elaborated on here.

To demonstrate the quality of our WQ map products, one instance of near-simultaneous images acquired by OLI, MSI, and OLCI over the San Francisco Bay region were processed via the Atmospheric Correction for OLI 'lite' (ACOLITE) (Vanhellemont and Ruddick 2021). While no ideal atmospheric correction (AC) processor for generating seamless R_{rs} from these missions has yet become available, ACOLITE is a convenient processor for inland and nearshore coastal waters and allows for retrieving R_{rs} in highly turbid or eutrophic optical regimes - thereby making it a suitable choice for demonstration purposes.

3. RESULTS

The assessments of the hold-out method (50 – 50 split) for MSI-like R_{rs} spectra are presented in Figure 1. The MDN model shows negligible biases and moderate uncertainties across the three WQ indicators. For $a_{cdom}(440)$, MDN outperforms the state-of-the-art algorithms with nearly half ε and RMSLE. Further, uncertainties in MDN estimates of $a_{cdom}(440)$ are highly uniform across the dynamic range spanning three orders of magnitude. For a detailed performance analysis, we refer readers to Pahlevan et al. (2022).

The images over the San Francisco Bay (Fig. 6) were acquired, on 7 October 2018, under clear sky conditions with OLI and OLCI imagery taken a few minutes apart, followed by MSI passing over the region $\sim$ 30 minutes later. Synoptically, there appears to be a reasonable agreement among the WQ maps, verifying the potential of MDN for producing congruous, practical multi-mission products. Although the OLI-derived Chl$a$ map resembles those of MSI and OLCI in the lower section of the bay, a closer examination of the maps suggests a higher degree of consistency in MSI and OLCI products.

A notable illustration of the advantage of the higher spatial resolution of OLI and MSI imagery is the identification of the South Bay salt ponds with very high Chl$a$ estimates. We also note more resemblance in OLI and MSI TSS maps than with OLCI. The between-sensor consistency is highest for the $a_{cdom}(440)$ products; spatial patterns show largest concentrations ($\sim$ 2 m^{-1}) in the Sacramento River outlet region and much lower magnitudes (0.2 - 0.3 m^{-1}) in the middle section of the bay. In the lower bay, the three maps agree well by predicting values on the order of $\sim$ 2 m^{-1}.

3. CONCLUSION

With the goal of producing consistent multi-mission global WQ products, to the extent possible given inherent differences in the spectral, spatial, and radiometric sampling of the sensors, we developed an MDN model using co-located *in situ* radiometry and WQ data. Our analyses suggest uncertainties ranging from 26 to 62% for Chl$a$ and TSS, and 26 to 91% for $a_{cdom}(440)$ from MSI- and OLCI-like R_{rs} spectra through MDN. For a spectral band configuration like that of OLI, 37 to 85% errors are expected for TSS and $a_{cdom}(440)$ whereas this range spans from 59 to $\sim$ 100% for Chl$a$. Our demonstration map exhibited that our model enables the generation of consistent multi-mission products within model uncertainties.

Future advancements for the MDN model will include adding band-ratio and line-height features to the input feature space to maximize its resistance to uncertainties in R_{rs}.
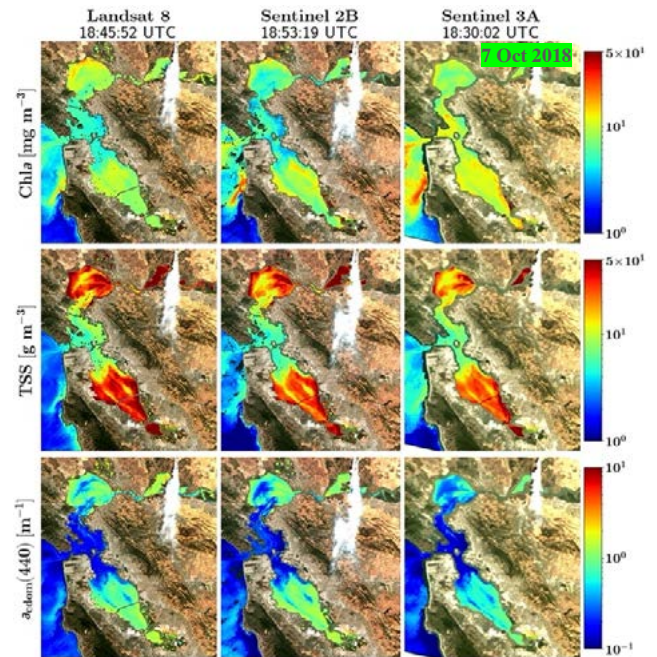
Figure 2. WQ maps produced via MDNs for near-concurrent images of OLI, MSI/B, and OLCI/A from Oct. 7th 2018. Despite uncertainties in satellite-derived R_{rs}, the products from the three sensors agree reasonably well.

Moreover, future models will provide accompanying per-pixel uncertainty estimates to allow users to choose fit-for-purpose products. The model is also planned to be extended to heritage instruments (e.g., MERIS) as well as to hyperspectral sensors to demonstrate its utility for constructing long-term WQ products from the past into the future.

REFERENCES

Balasubramanian, S.V., Pahlevan, N., Smith, B., Binding, C., Schalles, J., Loisel, H., Gurlin, D., Greb, S., Alikas, K., Randla, M., Bunkei, M., Moses, W., Nguyễn, H., Lehmann, M.K., O'Donnell, D., Ondrusek, M., Han, T.-H., Fichot, C.G., Moore, T., & Boss, E. (2020). Robust algorithm for estimating total suspended solids (TSS) in inland and nearshore coastal waters. *Remote Sensing of Environment, 246*, 111768

Bishop, C.M. (1995). *Neural networks for pattern recognition*. Oxford university press

Pahlevan, N., Smith, B., Alikas, K., Anstee, J., Barbosa, C., Binding, C., Bresciani, M., Cremella, B., Giardino, C., Gurlin, D., Fernandez, V., Jamet, C., Kangro, K., Lehmann, M.K., Loisel, H., Matsushita, B., Hà, N., Olmanson, L., Potvin, G., Simis, S.G.H., VanderWoude, A., Vantrepotte, V., & Ruiz-Verdù, A. (2022). Simultaneous retrieval of selected optical water quality indicators from Landsat-8, Sentinel-2, and Sentinel-3. *Remote Sensing of Environment, 270*, 112860

Vanhellemont, Q., & Ruddick, K. (2021). Atmospheric correction of Sentinel-3/OLCI data for mapping of suspended particulate matter and chlorophyll-a concentration in Belgian turbid coastal waters. *Remote Sensing of Environment, 256*, 112284

Wind Speed Retrieval Using Ku-band Precipitation Radar Data

M. Panfilova, V. Karaev*

Institute of Applied Physics Russian Academy of Sciences, Nizhny Novgorod, Russia

Abstract – The algorithm to retrieve wind speed in a wide swath from the normalized radar cross section (NRCS) was developed for the data of Dual Frequency Precipitation Radar (DPR) operating in scanning mode installed onboard a Global Precipitation Measurement (GPM) satellite. The data for Ku-band radar were used. Equivalent NRCS values at nadir were estimated in a wide swath under the geometrical optics approximation from off-nadir observations. Using these equivalent NRCS nadir values and the sea buoys data, the new parameterization of dependence between NRCS at nadir and the wind speed was obtained. The advantage of DPR is high resolution of 5 km, which allows us to obtain wind speed at about 10 km from the coast.

Keywords: wind speed, low incidence angles, coastal zone.

1. INTRODUCTION

Collection and analysis of the information on near-surface wind speeds are necessary for operational meteorology and the development of climate models. Most of this information is obtained on a regular basis by the instruments installed on satellites. Passive sensors used for wind speed retrieval are radiometers and active sensors are scatterometers, synthetic aperture radars (SAR) and radar altimeters. Information on wind speed can be collected only over the ocean surface and internal water bodies. This is due to the fact that the principle of work of all these instruments is based on the signal dependence on a degree of water surface roughness. Water surface in its turn becomes rougher with increasing wind speed.

In addition to the instruments listed above, there is another type of active sensors whose potential for wind speed retrieval has not been fully involved. They operate at low incidence angles. These are scanning microwave radars of Ka- and Ku-band (Dual frequency Precipitation Radar—DPR) onboard Global Precipitation Measurement (GPM) satellite launched in 2014 and Ku-band radar (Precipitation Radar—PR) onboard Tropical Rainfall Measurement Mission satellite (1997–2015). The main mission of the satellites is measurement of the spatial distribution of precipitation; but in the absence of precipitation, the information on the underlying surface can be retrieved from NRCS. The radars operate at angles ranging from 0° to 18°. Also at low incidence angles ranging from 0° to 10° SWIM (Surface Waves Investigation and Monitoring) radar onboard CFOSAT (Chinese-French Oceanography Satellite) operates.

Wind speed retrieval algorithms from PR, DPR and SWIM data were developed for example in (Li 2004, Ren 2021). The approach in this works implies the building of geophysical model functions for each incidence angle. However, correlation for NRCS at incidence angles of 8–10° with wind speed is very low and the highest correlation is observed at nadir.

The new approach was applied to DPR scanning radar data. If the off-nadir data in the swath are converted to NRCS at nadir, wind speed will be reliably obtained in a wide swath. Convertion to equivalent NRCS values at nadir can be performed within the framework of geometrical optics approximation. DPR swath will look like radar image measured at zero incidence angle as SAR image at moderate incidence angles. After that, wind speed can be retrieved from the DPR nadir swath using the approaches for altimeter data processing.

2. WIND SPEED ALGORITHM

DPR consists of Ka- and Ku-band radars which operate in scanning mode. In Ku-band it observes 245 km wide swath, incidence angle varies from −18° to 18°, antenna beam width is 0.7° and footprint size is about 5 km. In the present study, the Ku-band data for 2017–2019 was used. Within the swath, NRCS variations are caused both by changes of the underlying surface and the incidence angle. The whole radar image at one incidence angle, in this case at nadir, can be obtained under the geometrical optics approximation. Processing of the data in the swath is discussed in detail in (Panfilova 2018). Thus, the influence of incidence angle is eliminated and in the radar surface properties are manifested clearly.

The data of Ku-band radar for 2017–2019 were collocated with the data on wind speed from 157 NDBC (National Data Buoy Center) buoys located in Atlantic and Pacific oceans, and in the Great lakes. Standard meteorological wind speed product was used. It provides wind speed, wave parameters, air and water temperature every 30 min. The anemometers on buoys are installed at different heights, further wind speed was calculated at a standard height of 10 m and provided the neutral stability boundary layer. Equivalent NRCS at nadir from DPR was collocated with buoy data so that the distance between buoy and NRCS spot does not exceed 25 km, and the time gap was less than 15 min.

The regression dependence of wind speed on equivalent NRCS at nadir was obtained. The quality of the algorithm basing on comparison with buoy data is as follows. Overall bias and standard deviation of differences (SDD) were 0.26 and 1.88 m/s, the correlation coefficient was 0.84.

Comparison with ASCAT scatterometer wind speed was also performed using the data for January 2017. Overall bias and SDD between DPR and ASCAT winds were 0.28 and 1.26 m/s respectively, correlation coefficient was 0.93. For the areas corresponding to incidence angles of 8° and 10° SDD were 1.2 and 1.4 m/s respectively.

Similar comparison was performed for SWIM data in (Ren 2021), where wind speed was obtained using the approach based on geophysical model functions (GMF) for each incidence angle. Our method was compared with the GMF approach. For incidence angles 0–6°, both methods show good performance, but for θ≥8°, the GMF approach

error sufficiently exceeds the error of the present method, and for θ=10°, the GMF method can not be applied. Therefore, the proposed method allows us to obtain wind speed with good accuracy in those parts of the DPR swath, where the GMF approach would not work.

In our approach, the information on the trend of NRCS on incidence angle for a short NRCS profile was used instead of individual NRCS values. Thus, insensitivity of NRCS to wind speed at a particular incidence angle becomes less critical. However, the accuracy of the method also degrades at the parts of the swath corresponding to the footprints of beams with incidence angles 8° and 10°.

Let us assume applications of the algorithm to wind speed retrieval in the Adriatic sea. In winter, strong winds occur in this region. In Figure 1a, the distribution of wind speed in the Adriatic sea on 17 January 2017, 06:20 UTC, according to Ku-band DPR data, is shown in color, and rain rates over 0.5 mm/h are marked with black. The gaps are due to removal of noisy data. In Figure 1b, the wind speed distribution in the Adriatic sea on 17 January 2017, 08:50 UTC, according to ASCAT data is given, but the information on rain is absent. The sea state was stable and remained several hours, thus the data of both sensors are in a good agreement. Consecutive satellite data allow us to track the development of the atmospheric conditions.
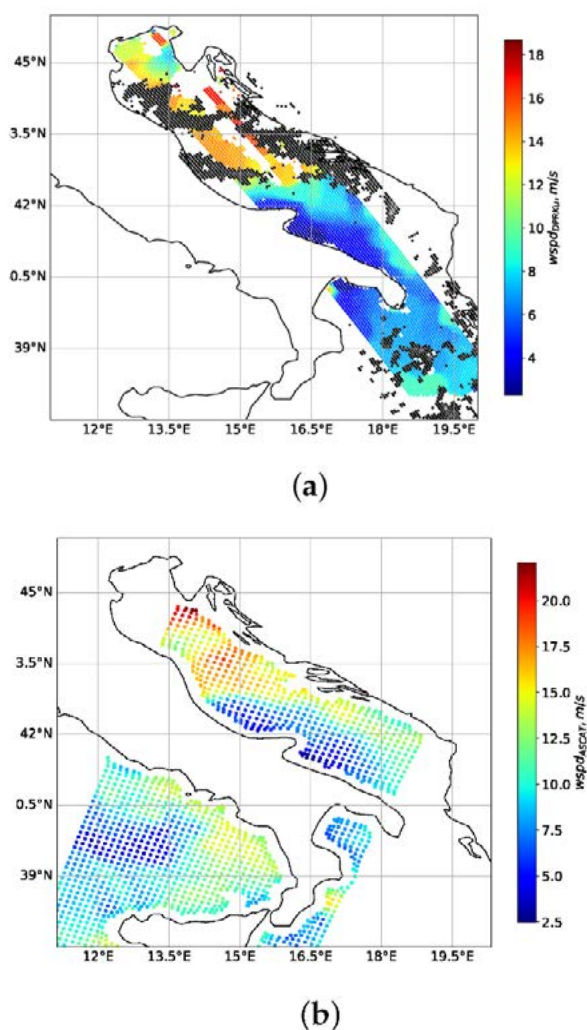
It should be noted that DPR is able to provide the data in close proximity to the shore compared to scatterometers and altimeters. The scatterometer has a wide swath, but the resolution is lower than DPR. Coastal areas are not covered by ASCAT within about 20 km. Radar altimeters have high 5 km resolution, but it can be gained in the open sea. In fact, the altimeter antenna beam is rather wide to avoid mispointing, and the area where the shore influences the signal may reach 40-50 km. The advantage of DPR is a narrow beam 0.7°, thus, its data are available at about 10 km from the coast.

3. CONCLUSION

The algorithm for wind speed retrieval from Ku-band radar onboard a GPM satellite was developed based on buoy data. The method consists of two steps: retrieval of NRCS at nadir for a wide swath, and calculation of wind speed from the regression model. The regression model suggested in our work can be applied for obtaining wind speed from altimeter NRCS with the corresponding coefficients.

The advantage of the algorithm is obtaining of wind speeds in a wide swath with high resolution, in close proximity to the shore, and taking into account simultaneous information on precipitation. The accuracy of the algorithm is good according to the comparison with ASCAT scatterometer data. In the future, it is planned to investigate the performance of the algorithm depending on the sea state.

REFERENCES

Li, L., Im, E., Connor, L., Chang, P. (2004). Retrieving ocean surface wind speed from the TRMM Precipitation Radar measurements. IEEE Trans. Geosci. Remote Sens. 42, pp 1271–1282.

Ren, L.; Yang, J.; Xu, Y.; Zhang, Y.; Zheng, G.; Wang, J.; Dai, J.; Jiang, C. (2021) Ocean Surface Wind Speed Dependence and Retrieval From Off-Nadir CFOSAT SWIM Data. Earth Space Sci., 8, e2020EA001505.

Panfilova, M.A., Karaev, V.Y., Guo, J. (2018) Oil Slick Observation at Low Incidence Angles in Ku-Band. J. Geophys. Res. Ocean., 123, pp 1924–1936.

(a)

(b)

Figure 1. *(a) Wind speed in the Adriatic sea on 17 January 2017, 06:20 UTC, according to Ku-band DPR data (color), rain contaminates cells with rain rate over 0.5 mm/h (black); (b) wind speed in the Adriatic sea on 17 January 2017, 08:50 UTC, according to ASCAT data.*

Predicting extreme waves in the French and Iberian Peninsula façade

Sonia Ponce de León[1]* and Jérôme Benveniste[1]

[1]European Space Agency (ESA-ESRIN)
Directorate of Earth Observation Programmes
EO Science, Applications, and Climate Department
Largo Galileo Galilei, 1, Frascati (Roma), I-00044, Italy

*CENTEC-Centre for Marine Technology and
Ocean Engineering-Instituto Superior Tecnico-University of Lisbon, Portugal
Visiting Scientist at ESA-ESRIN

Abstract – The study is focused on the analysis of areas that are more prone to the occurrence of extreme waves in the coastal zone of the French and Iberian Peninsula facade. The main extreme wave parameters, the BFI (Benjamin–Feir Index, Benjamin and Feir 1967) and Goda's peakedness parameter (Goda 1976), are estimated from wave spectra observations. CFOSAT-SWIM wave spectra are used from 1 December 2018 up to 1 June 2022, to estimate the composites of the Significant Wave Height, Peakedness parameter (Q_p) and BFI. The distribution of the extreme wave parameters is compiled in an average map (composites) for the period 29 July 2019 upto 31 December 2020. In the French façade the effect of tidal current (Ocean current from MERCATOR Ocean (IBIS)) on the wave field is being examined as well as its effect on the probability of occurrence of abnormal waves. The effect of strong tidal current on the spectral shape deserves to be investigated.

Keywords: Extreme waves, Benjamin-Feir index, wave spectra, CFOSAT-SWIM.

1. INTRODUCTION

Abnormal waves are defined as waves whose height exceeds the local mean significant wave height (HS) by a factor of 2.2 (Draper 1965; Dean 1990). There are several proposed mechanisms for the generation of abnormal waves. Linear focusing is one of them, due to the refraction, reflection and trapping of waves in varying bottom topography or in strong currents (Lavrenov 1998). Nonlinear focusing is another abnormal wave generation mechanism. This mechanism is considered as the most promising to understand the generation of abnormal waves due to nonlinear effects (Dysthe et al., 2008; Fedele et al.,2016) and it persists in a narrow band polychromatic wave train (Alber 1978).

This mechanism could be present in realistic wave fields, which makes it a very likely cause of real-world abnormal waves (Osborne 2010); it plays an important role on the shape of the wave spectrum and abnormal waves (Ponce de León and Osborne, 2019; Ponce de León and Guedes Soares 2022).

To improve safety in maritime operations, decision making must rely upon design and forecast criteria that required the best available knowledge of extreme wave and the related wave-structure interaction.

The CFOSAT-SWIM data (Hauser et al., 2019) wave spectra are used from 29 July 2019 up to 31 December 2020, to estimate different spectral shape parameters that allow describing the wave space-time evolution. These parameters, which characterize the energy distribution in frequency and direction, are computed in the present study from the SWIM wave spectra.

We present a brief analysis of the composites of the SWIM HS, BFI and Q_p at a regional scale.

2. DATA AND METHODS

The SWIM data distribution is shown in Fig. 1 for the period of study. We estimate the composites of the HS, Qp and *BFI2D* which are represented in Figures 2, 3 and 4, respectively.

We use the directional definition of Benjamin-Feir index called BFI_{2D} expression 1 (Le Merle et al., 2021):

$$BFI_{2D} = \frac{k_0\sqrt{m_0}Q_p\sqrt{2\pi}}{\sqrt{1+3.55*\sigma_\phi^2\pi Q_p^2}} \quad (1)$$

where $k_0\sqrt{m_0}$ is the significant slope, Q_p is Goda's peakedness parameter (Goda 1976) that gives information about how sharp the wave spectrum is around the main energy peak and σ_ϕ^2 is the directional spreading in expression (1). High values of Q_p indicate sharp spectra (Rao 1988). The spectral peakedness reads as:

$$Qp = \frac{2\sum_{f_{min}}^{f_{max}} f F^2(f)df}{\left[\sum_{f_{min}}^{f_{max}} F(f)df\right]^2} \quad (2)$$

$F(f)$ is the omnidirectional wave height spectrum. f_{min} and f_{max} the frequency domain for the frequency spread calculation: $f_{min} = 0.056$ Hz and $f_{max} = 0.28$ Hz.
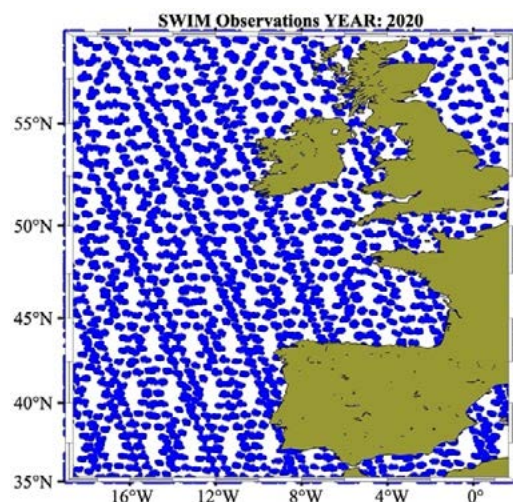
Figure 1. SWIM observations for 2020.

3. RESULTS

From the HS composite (Fig. 2) can be seen that there are some high values in the northern part of the study area with values of about 5 m associated with the North Atlantic storm tracks that result in swell. The highest HS (> 6 m) is spotted offshore of Galicia where the Prestige accident occurred associated with a rogue wave. Another HS maximum is seen offshore in front of the Lisbon port. From the BFI2D composite can be seen that the relatively high values obtained are all lower than 0.1 so during the study period no rogue waves were detected. In order to identify rogue waves using the directional concept of the BFI2D its values should be between 0.1 and 0.15.

Finally, Q_p composite estimated values from SWIM data show that the highest values are directly related with the maxima values of HS and BFI2D indicating thar those wave spectra are sharp and could become potential rogue waves at times after the observations were taken. In the French façade relatively high values of Q_p were obtained in the coastal zone perhaps associated with the wave variability that characterizes this coast where strong tidal currents modify waves.
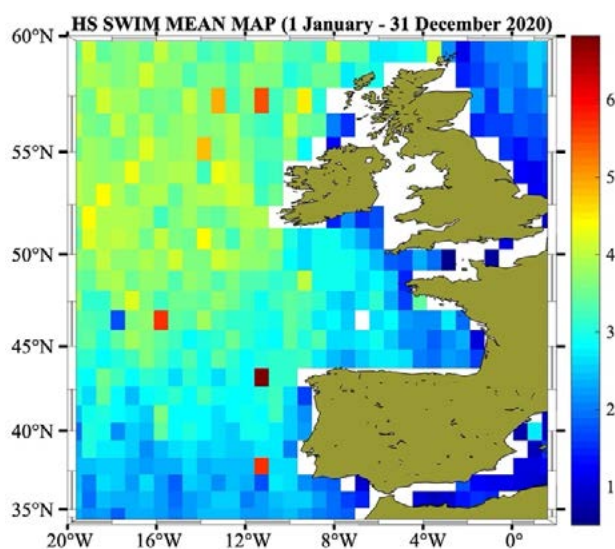
Figure 2. SWIM HS composite for 2020.
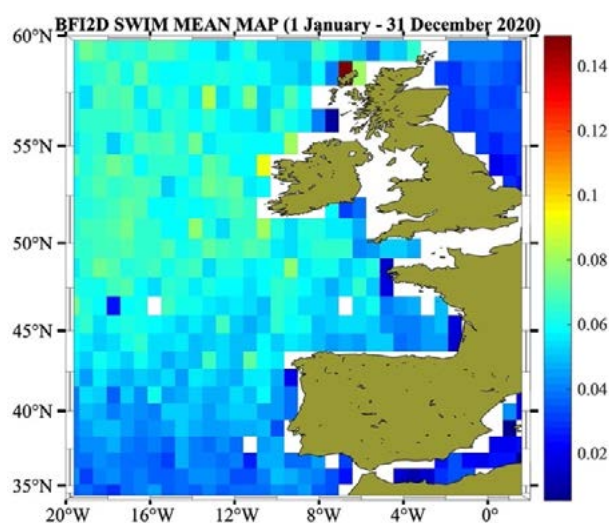
Figure 2. Directional Benjamin-Feir index estimated from SWIM wave spectra for 2020.
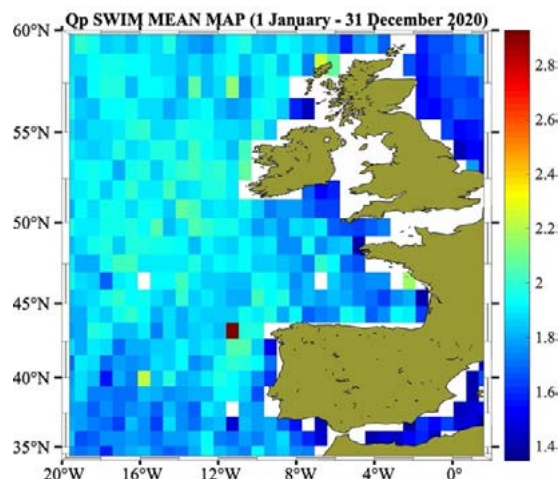
Figure 3. Goda's peakedness parameter for 2020 estimated with SWIM wave spectra.

4. CONCLUSION

The French and the Iberian Peninsula Atlantic façade was not prone to rogue waves during the period of the study. However, this conclusion must be taken with caution since the spatial coverage of the SWIM is not fully covering the coastal zone studied.

The study is ongoing using other altimetry missions such as CryoSat, Sentinel-6A Michael Freilich and Sentinel-3A/B to complement these preliminary conclusions.

ACKNOWLEDGEMENTS

REFERENCES

Alber IE, (1978). The effects of randomness on the stability of two-dimensional surface wavetrains. Proc. R. Soc. London 363,525–46.

Aouf, L., Hauser, D., Chapron, B., Toffoli, A., Tourain, C., & Peureux, C. (2021). New directional wave satellite observations: Towards improved wave forecasts and climate description in Southern Ocean. Geophysical Research Letters, 48.

Benjamin T.B., Feir J.E., (1967). The desintegration if wave train on deep water. Part 1. J. Fluid Mech. 27, 417-430.

Goda, Y. (1976). On wave groups. Proceedings of the First Behaviour of Offshore Structure Conference76.

Dysthe K, et al., (2008). Oceanic Abnormal Waves. Annual Rev. of Fluid Mech.40, 287-310.

Draper L, (1965), "Freak" ocean waves. Marine observer 35, 193-195.

Fedele F., J. Brennan, S. Ponce de León, J. Dudley, F. Dias. (2016). Real world ocean abnormal waves explained without the modulational instability Scientific Reports 6:27715.

Lavrenov I., (1998). The wave energy concentration at the Agulhas current of South Africa. Nat. Haz. 17, 117-127.

Osborne AR, 2010, Nonlinear Ocean Waves and the Inverse Scattering Transform. Academic Press, San Diego.

Ponce de León S., Guedes Soares C., (2022), Numerical study of the effect of current on waves in the Agulhas Current Retroflection, Ocean Engineering (in Edition).

Ponce de León S., Osborne A.R. (2019), Role of nonlinear Four-Wave Interactions Source Term on the Spectral Shape. J. Mar.Sci. Eng. 8, 251.

Assessing the physical effects driving the mid-shelf front in the Patagonian Sea (SW Atlantic Ocean)

L.A. Ruiz-Etcheverry*[1,2,3,4], M.C. López-Abbate[2,5], L.S. Lago[1,2,3,4], S.I. Romero[1,6,7], M. Saraceno [1,2,3,4]

(1) Universidad de Buenos Aires (UBA), Facultad de Ciencias Exactas y Naturales, Departamento de Ciencias de la Atmósfera y los Océanos, Buenos Aires, Argentina.
(2) Consejo Nacional de Investigaciones Científicas y Técnicas (CONICET), Buenos Aires, Argentina.
(3) CONICET – Universidad de Buenos Aires, Centro de Investigaciones del Mar y la Atmósfera (CIMA). Buenos Aires, Argentina.
(4) CNRS – IRD – CONICET – UBA. Instituto Franco-Argentino para el Estudio del Clima y sus Impactos (IRL 3351 IFAECI), Buenos Aires, Argentina.
(5) Instituto Argentino de Oceanografía (IADO), Bahía Blanca, Argentina.
(6) Servicio de Hidrografía Naval (SHN), Buenos Aires, Argentina.
(7) Facultad de la Armada (FaDARA, UNDEF), Buenos Aires, Argentina.

Abstract – The Mid-Shelf Front is located in the Southwestern Atlantic Continental Shelf, between 39°S and 41°S, and offshore the 50m isobath. This region is characterized by high productivity during spring and summer. However, the factors that promote this high productivity have not been fully explained. Therefore, the objective of this work is to describe the MSF using satellite sea surface temperature data and its associated biological productivity pattern with satellite chlorophyll-a (CSAT) at climatological scale. Our results show that the physical front is not the cause of the phytoplankton bloom since the front is weak in austral spring when the chlorophyll-a (chla) concentration is maximum. We discuss that the MSF and the productivity hotspot result from the joint effect of several factors.

Keywords: Mid-shelf front, Phytoplankton bloom, Patagonian sea.

1. INTRODUCTION

The Mid-Shelf Front (MSF), located in the Patagonian Sea (SW Atlantic Ocean), between 39° and 41°S and offshore the 50 m isobath, is characterized by high productivity during spring and summer. The mid-shelf area (50-70 m depth) shows a cross-shelf thermohaline front (the physical front) (Martos and Piccolo, 1988), and is characterized by northwestward low current velocities which are stronger in autumn (~8cm/sec) and weaker in spring (~3cm/sec) (e.g. Ruiz-Etcheverry et al., 2016). The area remains stratified most of the year, contributing with phytoplankton retention in upper layers as well as plankton resting stages that are ready to develop under favorable conditions. This area is within the Patagonia Large Marine Ecosystem (PLME), one of the largest marine ecosystems from the Southern Ocean and a hotspot of marine primary productivity. The PLME is east-bounded by the coastal margins and west-bounded by an Eastern Boundary Upwelling System (EBUS) embedded in the Malvinas Current (MC) and referred to as the Shelf Break Front. Although this EBUS has been intensively studied, the MSF remains poorly characterized. This productive area is partly associated with the nearby EBUS, and accordingly, both systems converge at early spring originating a cross-shelf widening of the EBUS, constituting a highly productive area of nearly 96,500 km^2 (Romero et al., 2006). While the

shelf Break Front is fueled by the constant delivery of deep, nutrient-rich waters from the MC, the factors that promote high biological productivity at MSF are less obvious. In this study, we described the climatology of the physical frontal area and its associated biological productivity pattern (estimated through CSAT) during the period 2003-2018.

There are several techniques for marine front detection based on horizontal gradients (e.g. Rivas and Pisoni, 2010). Here, we calculate the probability density function (PDF) of satellite sea surface temperature (SST) images to identify the SST front. This methodology takes into account the definition of a marine front, which is a narrow region that separates two water masses with different properties. The areas of homogeneous SST are seen in the PDF as peaks, while the front positions are seen as minimum in-between the PDF peaks. The temporal variability in PDF considers the fact that the front is a dynamic feature that varies in position and intensity. This methodology allowed us to identify the temporal patterns of the MSF and to compare them with local high CSAT events.
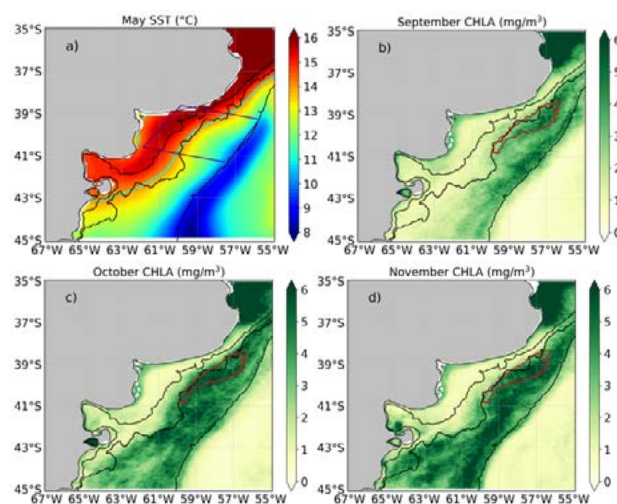
Figure 1. *a) Map of SST for mean May (2003-2018) superimposed with the SST contour that indicates the front position (cyan line) and the polygon (black box). Maps of CSAT for mean b) September, c) October and d) November superimposed with the polygon defined by Carranza (2008) (brown contour). The black contours in the four panels represent the isobaths of 50, 80 and 200 meters.*

---

* Corresponding author. Address: Intendente Güiraldes 2160 – Ciudad Universitaria Pabellón II, CABA, Argentina. Email: lruiz@cima.fcen.uba.ar

2. RESULTS

To evaluate the spatial and temporal patterns of the MSF, we analyzed the satellite SST in the northern area of the Patagonian Sea (41.3°S-38.6°S and 61.9°W-55.1°W). The daily SST product selected was Reynolds OI obtained from NCAR Climate Data Guide (https://climatedataguide.ucar.edu/). We first identified the region of maximum cross-shelf SST gradient and defined a polygon centered in this area (Fig. 1a). Then, we calculated the PDF of the daily SST within the polygon and identified two water masses: west (WWM) and east (EWM) of the front position. The spatial distribution of the climatological SST displays a cross-shelf gradient that varies according to the topography. This is confirmed with the SST contour related to minimum PDF (and front position) that is aligned within the 50 (e.g. March and April) and 80 meters isobaths (e.g. May, see Fig. 1a). The WWM is warmer than EWM during the entire period due to a shallow bathymetry (~>50m) that favors solar radiation heating and the income of warm San Matias Gulf waters (Lucas et al., 2005). The EWM is affected by relatively cold shelf waters and MC waters near the shelf-break. To assess the seasonal variability of the front, a climatological SST time series was constructed as the spatial average over the areas of WWM and EWM. Fig. 2 shows the SST difference between the water masses time series, confirming that WWM is warmer than EWM. It also shows a maximum amplitude between WWM and EWM of 3.5°C in May and a minimum amplitude of 2.4°C in September which indicates that the MSF intensifies during austral winter and weakens during austral spring.
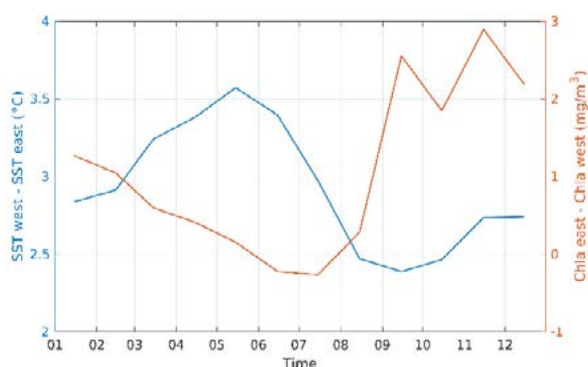
Figure 2. SST (blue line) and chla (red line) *difference between (blue line) the WWM and EWM at climatological scale.*

Over the areas of the WWM and EWM, we constructed the climatological CSAT time series based on daily MODIS Aqua L3 images (https://oceancolor.gsfc.nasa.gov/l3/). The temporal variability of CSAT in both areas shows a seasonal cycle with high concentration from September to November where the biggest difference between east and west were observed, being more productive on the eastern side (Fig. 1-2). The month of maximum discrepancy is out of phase with the SST amplitude (Fig. 2), meaning that the physical front is not a causative factor of the observed phytoplankton bloom in austral spring. The spring peak of chla in the east side of the front is also observed when the time series is constructed in the polygon defined by Carranza et al. (2008). The polygon delimits the MSF based on the annual amplitude of CSAT, selecting a threshold value of 3.5 mg/m³ (Fig. 1b-d).

One of the possible causes of the mismatch between the physical front and the phytoplankton bloom is associated with a cross-shelf transport shear. We analyzed the climatological cross-shelf geostrophic transport from satellite altimetry, observing that, on average, the transport on the east side is 1sv stronger than the transport on the west side of the 80 meter isobath. In addition, there is a weakening of the transport during spring that might favor the retention of plankton in the area.

3. DISCUSSION AND CONCLUSION

The MSF is characterized by a cross-shelf SST gradient centered between 50 and 80 meter isobaths that persists along the annual cycle. The highest SST difference (~3.5°C) between the east and west sides of the front occurs in May. This seasonal pattern is out of phase with the phenological cycle of CSAT, which shows a single spring-summer blooming event. We hypothesize that the MSF results from the joint effect of several factors, such as the heat balance (advection and surface fluxes) and cross-shelf current velocity shear. The emergence of the productivity hotspot is in turn the result of a combination of factors that retains plankton in the MSF area. The MSF described by SST may prevent plankton to be advected toward the coast and the temporal reversion of currents in spring might promote the retention of plankton in the area. The temporal persistence of the bloom may be allowed by the provision of nutrient-rich coastal waters from southern latitudes, particularly from the Valdés frontal area and the San Jorge Gulf. Additionally, the northern branch of the Malvinas current reaches the shelf area due to the relaxation of the shelf break slope produced by the presence of a topography anomaly at 41°S. The multi-causal occurrence of the spring bloom in the MSF could explain the temporal mismatch between the highest intensity of the physical front and the associated productivity hotspot. These hypotheses will be tested with numerical model simulations.

REFERENCES

Carranza, M. M.; Romero, S. I. y Piola, A. R. (2008) "Indicadores: Concentración de clorofila" en Estado de Conservación del Mar Patagónico y Áreas de Influencia. [En línea]. Puerto Madryn, publicación del Foro, disponible en: http://www.marpatagonico.org

Lucas, A. J., Guerrero, R. A., Mianzan, H. W., Acha, E. M., & Lasta, C. A. (2005). Coastal oceanographic regimes of the northern Argentine continental shelf (34–43 S). *Estuarine, Coastal and Shelf Science*, *65*(3), 405-420.

Martos, P., & Piccolo, M. C. (1988). Hydrography of the Argentine continental shelf between 38 and 42 S. *Continental Shelf Research*, *8*(9), 1043-1056.

Rivas, A. L., & Pisoni, J. P. (2010). Identification, characteristics and seasonal evolution of surface thermal fronts in the Argentinean Continental Shelf. *Journal of Marine Systems*, *79*(1-2), 134-143.

Romero, S. I., Piola, A. R., Charo, M., & Garcia, C. A. E. (2006). Chlorophyll-a variability off Patagonia based on SeaWiFS data. *Journal of Geophysical Research: Oceans*, *111*(C5).

Ruiz Etcheverry, L. A., Saraceno, M., Piola, A. R., & Strub, P. T. (2016). Sea level anomaly on the Patagonian continental shelf: Trends, annual patterns and geostrophic flows. *Journal of Geophysical Research: Oceans*, *121*(4), 2733-2754.

Spatial coherency of ocean bottom pressure variability remotely sensed by satellite gravimetry and in situ records

Jens Schröter[2], Roelof Rietbroek[1], Alexey Androsov[2], Christina Lück[3], Alisa Yakhontova[3], Sergey Danilov[2], B. Uebbing[3], Jürgen Kusche[3],

[1]University of Twente, Netherlands, [2]AWI Bremerhaven, Germany, [3]University Bonn, Germany

Abstract – Patterns of ocean bottom pressure (OBP) variability between South Africa and Antarctica are studied. Two sets of data were available: first, the GRACE analysis release RL06 and second, a four year record of an array of 14 OBP pressure gauges. The gauges were deployed along a hydrographic repeat line (WOCE SR3). Patterns of variability have been extracted from both sources of data. Patterns of variability and cross correlations of both signals as well as those of their differences are presented.
Keywords: ocean bottom pressure, satellite gravity, GRACE

1. INTRODUCTION

Ocean bottom pressure is an important observable linked to the dynamics of the ocean, and, on large scales, to sea level rise (Hsu and Velicogna 2017, Rietbroek et al. 2016). However, observing ocean bottom pressure changes and their gradients with in situ techniques is a costly endeavour. It can potentially be performed by analysing time variable gravity changes from satellite missions such as the Gravity Recovery and Climate Experiment (GRACE) and its follow on mission. Depending on the placement of the ocean bottom pressure recorders, the observations have very different spatial and temporal characteristic relative to the satellite estimates.

Short term ocean dynamics in the Southern Ocean are largely barotropic and are often associated with large scale patterns which, depending on the location, are visible in both the in situ records as well as the satellite products (e.g. Hughes et al. 2007, Rietbroek et al. 2006).

This study therefore investigates the spatial-temporal agreement between satellite-derived ocean bottom pressure and in situ time series, in order to better understand the spatial coherency of ocean bottom pressure patterns south of Africa and to see to what extent satellite gravimetry can be used to understand these dynamics.

2. OBP Data Sets

We use two sets of OBP estimates: first the release 6 version of the GRACE mission, expressed as equivalent water height (EWH) and provided by 6 different analysis centres. The analysis use data from the gridded GRACE products from various processing centres (CSR, GFZ, IGG, JPL and JPL mascon). We also use an ocean bottom pressure estimate which is derived from a joint inversion of GRACE and radar altimetry. For the comparison we take the ensemble mean of the 5 different GRACE analysis.

The second data set consists of an array of 14 in situ ocean bottom pressure recorders deployed between 2011 and 2014 in the Southern Ocean, see Figure 1. The measurements were detrended to counteract inevitable instrumental drift. Next, they were filtered to remove tidal signals and smoothed with a one day lowpass filter. A full description of the OBP data set was provided by Androsov et al., (2020).

Daily data are used for the comparison and averaged to obtain monthly mean values for the 38 valid months of GRACE RL6. Following Propat et al., (2018) we do not attempt to use the exact days used to obtain monthly values of GRACE analysis. It appears that 30 day averages of in situ OBP are an adequate equivalent to the satellite data. GRACE

analysis is detrended in the same way as in situ OBP. All data presented here are expresses in units of equivalent water height.
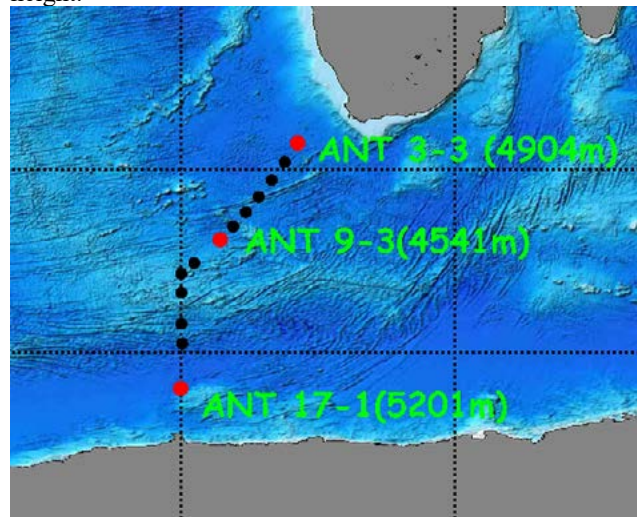
Figure 1. *Location of in situ deep ocean bottom pressure recorders between South Africa and Antarctica in 2011-2014.*

3 Analysis

Standard deviations amount up to 12cm EWH in the Agulhas retroflection area and decrease southward to about 4cm near the coast of the Antarctic Continent. More than 60% of variability occurs at periods shorter than 30 days and is not detectable by the monthly GRACE products.

We find annual and semi-annual signals of very low amplitude. Frequency spectra are slightly red. Decorrelation times (tau) are short, less than one month. However in the Agulhas retroflection area, strong intermittent motion results in tau of ca. 70 days.

Time series of in situ OBP (full lines) and GRACE (stars) for the 38 valid months are depicted in Figure 2. The two northernmost stations stick out with their strong eddy variability.
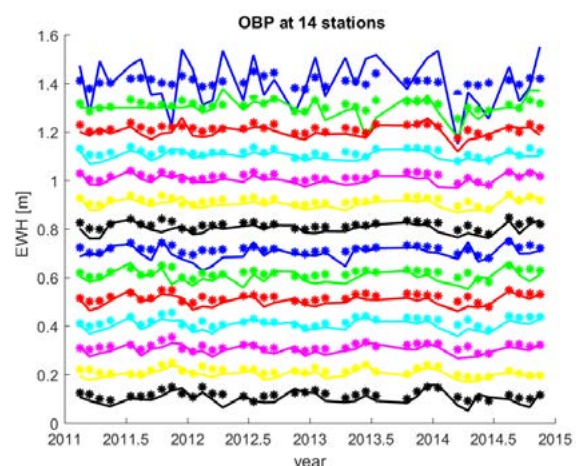
Figure 2. *Monthly mean in situ OBP (full lines) and GRACE (stars). The lines start at the top with the northernmost station(3) and continues to station(17). Values are offset vertically by 0.1m for clarity.*

Further south, we observe some similarity between the data sets as well as some large scale coherent signals. Statistical analysis is presented in Figures 3 and 4.
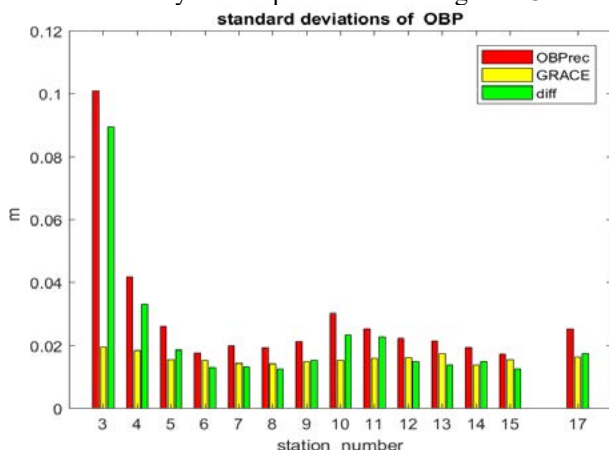
Figure 3 *Variability of OBP as measured by pressure recorders, OBPrec, GRACE, and their difference.*

On a local basis, GRACE shows less signal than OBP measurements. The difference is as large as the GRACE signal. This can be seen by the correlations which amount to around 0.7 and the skill which is between 0.4 and 0.6. All values indicate that GRACE captures roughly 50% of the variance.
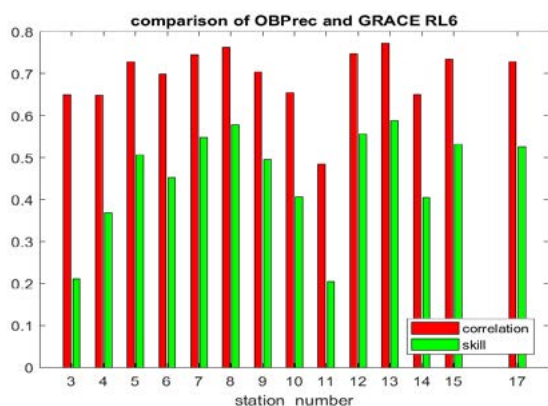
Figure 4. *Validation of GRACE RL6 on the basis of an ensemble 38 monthly mean solutions. Shown is correlation (red) and skill (green).*
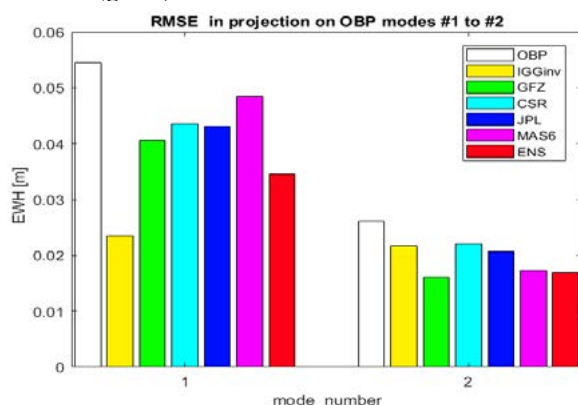
Figure 5. *Variability of OBP as measured by pressure recorders, projected on the two dominant modes of variability (white). In colour the RMS difference of the GRACE products under consideration is shown.*

Spatially coherent motion is extracted by a singular value decomposition (SVD) for the vast area south of the Sub Antarctic Front. This is done by analysing the signal covariance matrix estimated from the time series of the OBP recorders. OBP modes 1 and 2 explain 25% and 15% of the signal, respectively. Mode 1 is associated with a variation of

the mean whereas mode 2 describes independent motion at the southernmost station. Figure 5 reveals the performance of the RL6 assessment for different analysis centres.

4. Summary

For large parts of the Southern Ocean, bottom pressure variability outside the tidal band has a standard deviation of about 40 mm equivalent water height. Annual and semi-annual cycles are very small. In eddy rich areas OBP variability can exceed 100mm RMS. Their scales are small and fall below the spatial resolution of GRACE.

Roughly three quarters of the variance can be found at periods shorter than 30 days. Of the remaining variance of $(22mm)^2$ RMS GRACE detects $(15mm)^2$. On a point-wise basis correlations amount to 0.7 on average. The skill is around 0.5.

Spatial correlations of in situ OBP is on the order of the GRACE resolution, i.e. between 300km and 500km. Temporal correlations show a decay time of 1 month or less for most of the time series.

When we consider the natural models of variability as can be calculated by a singular value decomposition, we find higher correlations. Here GRACE achieves a correlation of 0.8 and 0.7 for the first two modes, respectively.

Trends of in situ OBP cannot be measured due to the design of the pressure gauges.

REFERENCES

Androsov, A. Boebel, O. Schröter, J. Danilov, S. Macrander, A. and Ivanciu, I. (2020) Ocean Bottom Pressure Variability: Can It Be Reliably Modeled?, JGR Oceans. doi:10.1029/2019JC015469 .

Böning, C. Timmermann, R., Danilov, S., Schröter, J. (2010). On the representation of transport variability of the Antarctic Circumpolar Current in GRACE gravity solutions and numerical ocean model simulations, In Flechtner F. et al (eds.) Satellite Geodesy and Earth System Science, Springer-Verlag, Berlin, Heidelberg, Part 2, 187-199, DOI: 10.1007/978-3-642-10228-8_15.

Hsu, C.-W., Velicogna, I., 2017. Detection of sea level fingerprints derived from GRACE gravity data. Geophysical Research Letters 44, 8953–8961. https://doi.org/10.1002/2017GL074070

Hughes, C.W., Stepanov, V.N., Fu, L.L., Barnier, B., Hargreaves, G.W., 2007. Three forms of variability in Argentine Basin ocean bottom pressure. J. Geophys. Res. 112. https://doi.org/10.1029/2006JC003679

Macrander, A., Böning, C., Boebel, O., Schröter, J. (2010). GRACE Validation by in-situ data of Ocean Bottom Pressure. In Flechtner F (eds.) Satellite Geodesy and Earth System Science, Springer-Verlag, Berlin, Heidelberg, Part 2, 169-185, DOI: 10.1007/978-3-642-10228-8_14.

Poropat, L., Dobslaw, H., Zhang, L., Macrander, A., Boebel, O., & Thomas, M. (2018). Time variations in ocean bottom pressure from a few hours to many years: In situ data, numerical models, and GRACE satellite gravimetry. J. Geophys. Res. *Oceans*, 123, 5612– 5623.

Rietbroek, R., Brunnabend, S.-E., Kusche, J., Schröter, J., Dahle, C., 2016. Revisiting the contemporary sea-level budget on global and regional scales. Proceedings of the National Academy of Sciences 113, 1504–1509. https://doi.org/10.1073/pnas.1519132113.

Rietbroek, R., LeGrand, P., Wouters, B., Lemoine, J.M., Ramillien, G., Hughes, C.W., 2006. Comparison of in situ bottom pressure data with GRACE gravimetry in the Crozet-Kerguelen region. Geophysical Research Letters 33. https://doi.org/10.1029/2006GL027452.

Recovery of the thermohaline structure of the Sea of Azov based on *in situ* data, regional MODIS products and 3D modeling results

T. Shulga [1*], V. Suslin, D. Shukalo

Marine Hydrophysical Institute, Sevastopol, Crimea

Abstract – This study is a continuation of the research cycle that began in 2017. The paper considered a method for salinity fields recovery of the Sea of Azov based on the established regression relationships with regional MODIS products. The implementation of the proposed method makes it possible to use the recovered data of salinity, together with remote sensing data of temperature, in assimilation procedures for a three-dimensional hydrodynamic model.

Keywords: The Sea of Azov, Regional MODIS Products, Regression Relationships, Three-dimensional Hydrodynamic Model.

1. INTRODUCTION

The importance of this study is due to the scientific and practical interest in the main hydrological components of the marine environment, the change in which is reflected in the biological resources of the water area These changes in shallow water, such as the Sea of Azov, vary significantly depending on seasonal differences in the volume of river runoff, inflow of salt water, weather conditions and anthropogenic pollution (Wolanksi et al. 2015). Despite the fact that the most reliable tool for determining the salinity of seawater is in situ measurements, but the high cost of obtaining them and the need for an operational forecast in close to real time, led to the search for alternative possibilities for determining the salinity.

Remote sensing instruments, which have a sufficiently high spatial resolution and provide daily data on any observation area, make it possible to partially solve the problem of monitoring the state and pollution of the marine environment. The presence of missing data caused by general problems of remote sensing significantly limits the amount and timeliness of information obtained from the available satellite data. One of the options for filling data (of temperature, salinity and the presence of suspended matter in seawater) is to use the results of three-dimensional hydrodynamic modeling (Shulga et al. 2018, Konik et al. 2019). The model should have a spatial resolution comparable to satellite imagery and continuously assimilate remote sensing data streams. This work is a continuation of studies (Shulga et al. 2018, Shulga et al. 2020), presenting the results of the analysis of regional satellite products in the upper layer of the Sea of Azov, supplemented by the results of assimilation modeling.

2. STUDY AREA

The Azov Sea is a continental, semi-enclosed body of water, which occupies an intermediate position between sea and fresh water bodies. Low salinity (10–12 ‰) is due to difficult water exchange with the Black Sea and the influx of river waters, which make up 12% of the volume of seawater (Hydrometeorology 1991). The study area shown in Figure 1

is completely covered by the data of MODIS satellite color scanners (https://oceancolor.gsfc.nasa.gov/cgi/browse.pl?sen=amod).
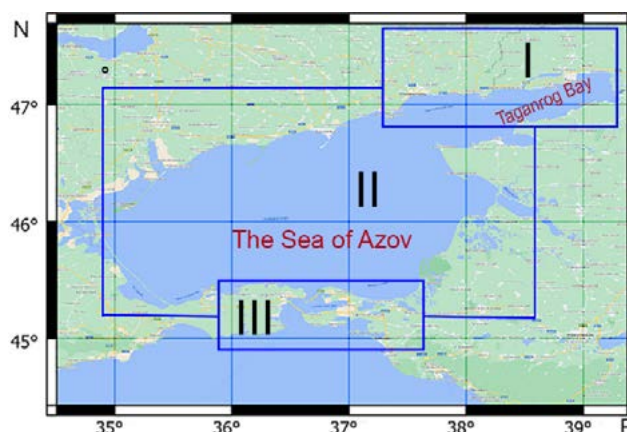
Figure 1. The map of study area the Sea of Azov. Rectangles indicate the boundaries of subregions: I — Taganrog Bay; II — the central part of the Sea of Azov ; III — the Kerch Strait and adjacent parts of the Azov and Black Seas.

3. METODOLOGY

This study was carried out in four stages. At the first stage, the archival data of in situ measurements were analyzed: from the oceanographic data base of the Southern Scientific Center of RAS for 1913–2006 (Matishov et al. 2006); from the Atlas of Climate Change in Large Marine Ecosystems of the Northern Hemisphere (atlas.ssc-ras.ru/azs/azs-invent.html); from the oceanographic data bank of the Marine Hydrophysical Institute of RAS (Bayankina et al. 2017) and sites www.seadatanet.org and www.nodc.noaa.gov. Conclusions were made based on the generalization and analysis of archival information about the long-term seasonal variability of temperature and salinity in the Sea of Azov for 1913–2018 (Shukalo et al. 2021). At the second stage, the data of the MODIS-Aqua/Terra standard satellite products for 2002–2018 were analyzed, systematized, and rejected according to the criteria described in (Suetin et al. 2002). Further, the remote sensing data are compared with the archived in situ data: according to the correspondence of the date of satellite images and in situ observations; by the deviation of coordinates of distance and in situ data not exceeding 1 km for the corresponding dates

$$\left| \sqrt{(lat_{situ} - lat_{MODIS})^2 + (long_{situ} - long_{MODIS})^2} \right| < 0.01°.$$

The formed arrays were transformed into spatio-temporal maps of five main bio-optical indicators, calculated on the basis of regional bio-optical algorithms proposed in (Kopelevich et al. 2011, Suslin et al. 2020): $a_{ph}(678)$ – the coefficients of light absorption by phytoplankton, $TChl$ – the

sum of chlorophyll a concentration and pheopigments, $a_{tot}(438)$ – light absorption rate of all optically active components, $a_{CDM}(438)$ – the coefficients of light absorption by detrital colored matter and $b_{bp}(438)$ – the light backscattering coefficient by particles (Suslin et al. 2020).

At the third stage, regression relationships between in situ data and bioptical parameters were computed. These dependencies were obtained for the II subregion of the Sea of Azov in the summer season, which has the largest amount of contact and remote sensing data for 2000–2018.

4. RESULTS AND DISCUNION

Based on the selected linear regressions satisfying the condition $R \geq 0.5$, general linear regression equations of the following form were compiled: $y = (a_{cp} \pm \sigma_1)x + (b_{cp} \pm \sigma_2)$, where a_{cp} и b_{cp} – averaged linear coefficients a и b, σ_1 и σ_2 – standard deviations, x – regional satellite products, y – salinity (‰).

Table 1. Generalized Linear Regression Equations

$a_{ph}(678)$, m^{-1}	$y=(0,046 \pm 0,025)x + (-0,375 \pm 0,256)$
$Tchl$, mg m^3	$y=(1,900\pm1,028)x + (-15,485\pm10,68)$
$a_{tot}(438)$, m^{-1}	$y=(-0,229\pm-0,062)x + (3,947 \pm 0,13)$
$a_{CDM}(438)$, m^{-1}	$y=(-0,250 \pm 0,088)x + (3,969 \pm 0,919)$
$b_{bp}(438)$, m^{-1}	$y=(-0,062 \pm 0,028)x + (0,748 \pm 0,294)$

Thus, the obtained generalized linear regression coefficients given in Table 1 are used in the procedure for salinity fields recovery in the Sea of Azov. Figure 2 shows an example of the recovered salinity fields based on the bio-optical index $a_{CDM}(438)$ for 23/06/2009 and 24/06/2009.
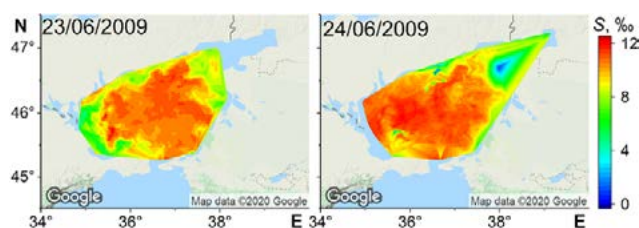
Figure 2. Results of recovering salinity fields from $a_{CDM}(438)$

At the final stage of the work, three-dimensional hydrodynamic modeling POM (Blumberg et al. 1987) was performed to obtain continuous information on temperature and salinity in the Sea of Azov. Numerical experiments were performed for the period 01.01.2009–31.12.2009, taking into account the inflow of the Don River (Kosenko et al. 2018). The bathymetry map of the Sea of Azov is interpolated to a regular grid with a resolution of 1.4 km. At the beginning of each month, archived mean annual in situ data on temperature and salinity are assimilated into the model. In addition, the model assimilates the temperature values obtained from satellite data and the reconstructed salinity fields for the corresponding date (Shulga et al. 2018, Konik et al. 2019). The fields of the SKIRON atmospheric model (*forecast.uoa.gr*) are used as input meteorological data. Modeling results represent continuous temperature and salinity fields in the Sea of Azov.

5. CONCLUSION

A new method for obtaining continuous information on temperature and salinity in the Sea of Azov on the basis of assimilation into a hydrodynamic model of both mean long-term and reconstructed salinity values from satellite sounding data is proposed. Generalized linear regression coefficients were obtained to restore salinity values. It was found that bio-optical parameters $a_{CDM}(438)$ and $b_{bp}(438)$ are the most reliable for reconstructing salinity fields in the Sea of Azov.

REFERENCES

Bayankina, T.M., E.A. Godin, E.V. Zhuk, et al., Ed. (2017). Information resources of the Marine Hydrophysical Institute of the Russian Academy of Sciences. Processes in Geomediums, Vol. 4 (13), pp. 651–659.

Blumberg, A.F. and G.L. Mellor, Ed. (1987). A description of three dimensional coastal ocean circulation model. Three-Dimensional Coastal Ocean Models, Vol.4, pp 1–16.

Hydrometeorology and hydrochemistry of the seas of the USSR, Ed. (1991). Vol. 5, pp 236.

Konik, M., M. Kowalevski, K. Bradtke, M. Darecki, Ed. (2019). The operational method of filling information gaps in satellite imagery using numerical models. International Journal of Applied Earth Observation and Geoinformation, Vol. 75, pp 66-82.

Kopelevich, O.V., V.I. Burenkov, S.V. Sheberstov, et al., Ed. (2011). Bio-optical characteristics of the Russian seas from satellite ocaen color data of 1998-2010. Proc. VI Int. Conf. Current problems in optics of natural waters, St-Petersburg, pp 181–182.

Kosenko, Yu.V., T.E. Baskakova, T.B. Kartamysheva, Ed. (2018). The role of the Don River runoff in the formation of the productivity of the Taganrog Bay. Water bioresources and habitat, Vol. 1 (3-4), pp 32–39.

Matishov, G.G., D.G. Matishov, S.V. Berdnikov, Ed. (2006) Climatic Atlas of the Sea of Azov 2006. Washington: Silver Spring.

Shukalo, D.M. and T. Ya. Shul'ga, Ed. (2021). Long-term and seasonal anomalies of the Sea of the Azov thermohaline structure for 1913 – 2018. Journal of Physics Conference Series, Vol. 2057(1):012133.

Shulga, T.Ya. and V.V. Suslin, Ed. (2018). Investigation of the evolution of passive admixture in the surface layer of the Sea of Azov based on the assimilation of the MODIS-Aqua scanner data into a hydrodynamic model. Fundamental and Applied Hydrophysics, Vol. 11 (3), pp 73–80.

Shul'ga, T.Y., V.V. Suslin, D.M. Shukalo, A.V. Ingerov, Ed. (2020). Research of the relations between the seasonal variability of salinity and bio-optical features in the Sea of Azov using the satellite data in the visible spectrum range. Fundamentalnaya i Prikladnaya Gidrofizika, Vol. 13(2), pp 68–75.

Suetin, V.S., V.V. Suslin, S.N. Korolev, A.A. Kucheryavyi, Ed. (2002). Analysis of the variability of the optical properties of water in the Black Sea in summer 1998 according to the data of a SeaWiFS satellite instrument. Physical Oceanography, Vol. 12(6), pp 331–340.

Suslin, V.V., T.Ya. Churilova, T.V. Efimova, et al., Ed. (2020). Regional bio-optical algorithm for remote estimation of the sea of Azov`s IOPS. Proceedings of SPIE. Vol. 115600R.

Wolanksi, E., M. Elliott, Ed. (2015). Estuarine Ecohydrology: An Introduction. Elsevier Science, Amsterdam, pp 322.

Detection of pigments in West Greenland shelf waters – comparison of in-situ and modeled data based on satellite observations

J. Stoń-Egiert*, K. Dragańska-Deja, A.Palacz, M. Zabłocka, M. Ostrowska, M. Wichorowski

Institute of Oceanology Polish Academy of Sciences, Sopot , Poland

Abstract - The Arctic ecosystem is highly sensitive to climate change. Monitoring these processes in the marine environment requires appropriate measurement techniques: satellite observations combined with in situ measurements. In the current work, we present the results of measurements of pigment concentrations in the West Greenland shelf collected in 2021. We also compared two different modeled estimates of chlorophyll a concentrations with in-situ results. These analyses are preliminary and will continue during the Ecitiop project.

Keywords: Pigments, Chlorophyll a, Greenland

1. INTRODUCTION

The climate changes taking place on Earth have substantially modified the physical, chemical and biological properties of the World Ocean, especially evident in polar regions. The Arctic ecosystem is highly evidute to climate warming, as manifested not only in the reduction of summer sea ice cover and volume by about 50% since last 40 years (Serreze and Meier, 2019) but also in changing thermal conditions, dissolved CO_2 concentrations in waters (acidification) and biodiversity of phytoplankton community structure (Rousseaux and Gregg, 2015; Tate et al., 2017; Häder and Gao, 2018; Martin-Garcia, 2019).

Monitoring changes in the marine environment is one of the most important issues of contemporary oceanology and requires the use of appropriate measurement techniques. The source of data, that is increasingly used for such purposes, is satellite observations providing systematic information from large areas. One of oceanographic parameters commonly used to approximate phytoplankton biomass and primary production is chlorophyll a. Other chlorophylls and carotenoids are used as indicators of presence of specific phytoplankton classes, their biomass, biodiversity, condition and developmental stage and allow to characterize the variability of phytoplankton abundance and species composition in different geographical regions (Wright and van der Enden, 2000; Roy et al., 2011, Schlüter et al., 2018; Oziel et al. 2022).
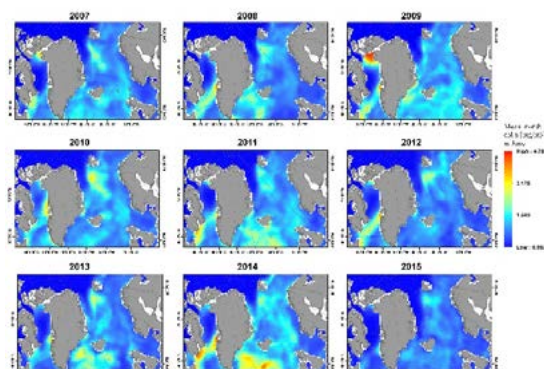
Fig.1. Mean month chlorophyll a concentration in Arctic region from Arctic Ocean Biogeochemistry analysis and Forecast model.

Information derived from a model based on satellite data is often used as a tool for mapping changes in marine environment and providing environmental background for in-situ research. They allow us to look at the phenomenon studying on a larger scale. In the Greenland shelf area and Arctic waters, a large spatial variation of the average chlorophyll a concentration during the summer period was observed in successive years from the period 2007-2015 (Fig. 1). Over the past 20 years in the West Greenland region, the values of mean chlorophyll a concentrations during the more productive period in years (June to August) ranged from 0.63 to 0.92 mg m^{-3} reaching the highest value in 2020 (Fig.2).

The purpose of the current work is to present the results of the obtained pigment concentrations in West Greenland waters during the Dana expedition in July 2021 and to compare these data with historical modeled values. This analysis is preliminary and will continue during the Ecitiop project.
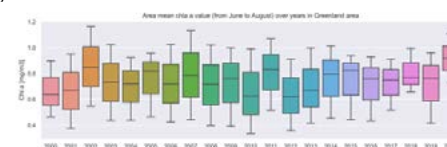
Fig.2. Area mean chlorophyll a concentration from shelf area on West Grenland presented on Fig. 3 from June to August. The box shows the quartiles of the dataset (Q1,median, Q3) while the whiskers show the rest of the distribution (min-max). Data was obtained from Gloal Biogeochemistry hindcast.

2. MATERIALS AND METHODS

In-situ data were collected in West Greenland coastal waters, covering area from north Nuuk to north of Disco island (Fig.3), during the cruise on R/V Dana conducted in late July 2021.
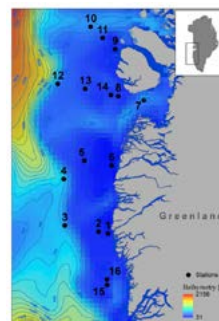
Fig.3. Localization of in-situ stations during the cruise on R/V Dana conducted in late July 2021.

Water samples were filtered through GF/F Whatman filters (pore size 0.7 μm) and immediately frozen and kept in deep freezing conditions until laboratory analysis could be carried out. The pigments were extracted in 90% acetone for 2 h in temperature 4°C. To estimate chlorophyll a concentrations as well as other carotenoids, HPLC analysis were performed. Applied methodology was based on separation and retention particular pigments on chromatographic column LichroCART™ LiChrospher™ 100 RP18e (dimension 250x4 mm, particle size 5 μm and pore size 100 Å, Merck) and detection of these compounds using absorbance and fluorescence detector displays (Stoń-Egiert and Kosakowska (2005).

Modeled chlorophyll a concentration data were acquired from Arctic Ocean Biogeochemistry Analysis and Forecast. In this model surface chlorophyll-a from satellite ocean color is assimilated every week and projected downwards using the Uitz et al. (2006) method, Global Ocean Biogeochemistry Analysis and Forecast were satellite chlorophylls data is assimilated and Global Ocean Biogeochemistry hindcast. All modeled data were

---

downloaded from https://myocean.marine.copernicus.eu/. Bathymetric data were delivered form Arctic Ocean Physics Reanalysis . The map and images were generated in ArcGIS Pro 2.9.2. The plots were generated in Python 3.7 using Matplotlib 3.1.1, seaborn 0.11.1 and Pandas 1.0.

3. CONCLUSION

Identified chlorophylls and carotenoids

In spite of the main pigment in phytoplankton cells - chlorophyll a, chlorophylls b and c, photosynthetic and photoprotectant carotenoids were also identified in different amount in samples (Fig4). The highest concentrations were noted for fucoxanthin – marker of diatoms. Also 19'hex-fucoxanthin and 19'but-fucoxanthin characteristic for Arctic small phytoplankton were identified in almost all stations.
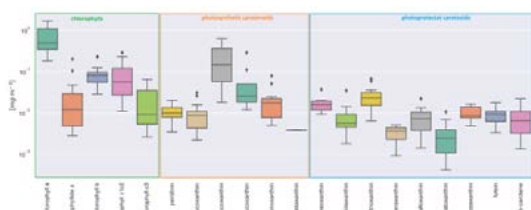
Fig.4. Ranges of concentrations of pigments identified in samples from West Greenland region in 2021.

Comparison in situ and modeled chlorophyll a data

The use of satellite data has revolutionized our ability to study the changes in Arctic region and most of the analyses presented in literature are based on data obtained from bio-hydrological models that use satellite derived data. These studies cover vast areas (e.g. the North Atlantic, the Canadian or Eurasian Arctic, the Barents Sea). An undoubted advantage of the models is the year-round prediction of marine ecosystem parameters. Despite the fact remote sensing data provide a consistent, accurate, and comprehensive record suitable for studying trends in parameters changes, they need to be validated with in situ measurements.
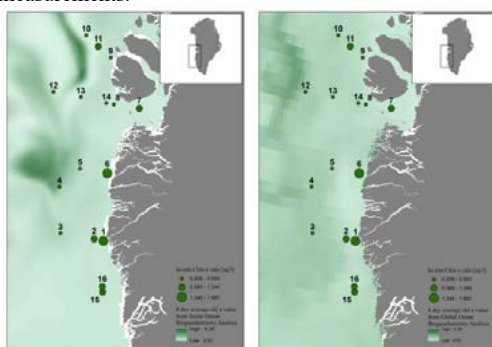
Fig.5.8-day average chlorophyll a concentration from period of Dana research cruise from Arctic Ocean Biogeochemistry Analysis and Forecast model (left) and Global Ocean Biogeochemistry Analysis and Forecast (right) and chlorophyll a in-situ data.

The comparison of modeled and in situ chlorophyll a data is displayed in Fig. 5 and 6. The trend in both models are similar, although the estimation accuracy of chlorophyll a concentration in both cases are low. Remote sensing of coastal waters is quite difficult due to the complex spectral characteristics of these waters, which are determined by the presence of various components such as phytoplankton,

dissolved organic matter and inorganic suspensions. In Greenland shelf region additionally we have a plenty of cloudy days and the influence of water from melting glaciers. This could cause a difficulties in using satellite and satellite-based modeled data to estimate chlorophyll a concentrations in Arctic water, especially in the coastal area near tidewater glaciers.
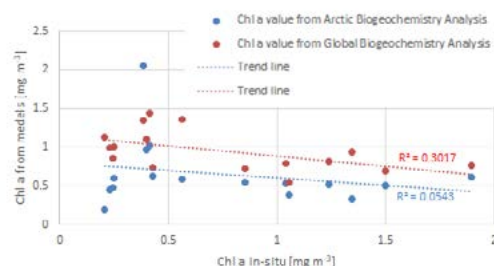
Fig.6 Scatter plot of models-estimated surface chlorophyll a concertation versus in-situ analysis data.

REFERENCES

Häder, D.P., Gao, K., 2018. Aquatic Ecosystems in a Changing Climate, CRC Press, Taylor & Francis Group, pp.318

Martin-Garcia, G.M., 2019. Oceanic impact on European climate changes during the quaternary. Geosciences. 9, 119. DOI: 10.3390/ geosciences9030119.

Oziel L., Massicotte P., Babin M., Devred E., 2022. Decadal changes in Arctic Ocean Chlorophyll a: Bridging ocean color observations from the 1980s to present time Remote Sensing of Environment 275 (2022) 113020 DOI: 10.1016/j.rse.2022.113020

Rousseaux, C.S., Gregg, W.W., 2015. Recent decadal trends in global phytoplankton composition, Glob. Biogeochemical Cycles 29, 1674–1688. DOI: 10.1002/2015GB005139.

Roy, S., Llewellyn, C.A., Egeland, E.S., Johnsen, G., 2011. Phytoplankton pigments, characterization, chemotaxonomy and applications in oceanography. Cambridge Univ. Press, pp 845.

Schlüter, L., David, G.S., Jørgensen, N.O.G., Podduturi, R., Tucci, A., Dias, A.S., da Silva, R.J., 2018. Characterization of phytoplankton by pigment analysis and the detection of toxic cyanobacteria in reservoirs with aquaculture production. *Aquaculture Environ. Interactions* 10, 35-48. DOI: 10.3354/aei00256.

Serreze, M.C., Meier, W.N., 2019. The Arctic's sea ice cover: trends, variability, predictability, and comparisons to the Antarctic. Ann. N. Y. Acad. Sci. 1436, 36–53. DOI: 10.1111/nyas.13856.

Stoń-Egiert, J., Kosakowska, A., 2005. RP-HPLC determination of phytoplankton pigments – comparison of calibration results for two columns. Mar. Biol. 147 (1), 251–260. DOI: 10.1007/s00227-004-1551-z.

Tate, R.D., Benkendorff, K., Ab Lah, R., Kelaher, B.P., 2017. Ocean acidification and warming impacts the nutritional properties of the predatory whelk, *Dicathais orbita,* J. Exp. Mar. Biol. Ecol. 493, 7-13. DOI: 10.1016/j.jembe.2017.03.006.

Uitz, J.; Claustre, H.; Morel, A.; Hooker, S.B., 2006. Vertical distribution of phytoplankton communities in open ocean: An assessment based on surface chlorophyll, J.Geophys. Res.,111,C08005, doi: 10.1029/2005JC003207

Wright, S.W., van der Enden, R.L., 2000. Phytoplankton community structure and stocks in the East Antarctic marginal ice zone (BROKE survey, January–March 1996) determined by CHEMTAX analysis of HPLC pigment signatures. Deep Sea Res. II 47(12-13), 2363-2400. DOI: 10.1016/S0967-0645(00)00029-1

Regional bio-optical algorithm for remote estimation of the Sea of Azov`s IOPs based on MODIS bands

V.V. Suslin[*1], T.Ya. Churilova[**], T.V. Efimova[**], N.V. Moiseeva[**], E.Yu. Skorokhod T.Ya. Shulga[*]

[*]Marine Hydrophysical Institute, Sevastopol, Crimea
[**]A.O. Kovalevsky Institute of Biology of the Southern Seas, Sevastopol, Crimea

Abstract – Based on the field measurements of the light absorption spectra of phytoplankton pigments, the non-algal suspended matter, the colored dissolved organic matter and ocean color product, remote sensing reflectance, reconstructed from MODIS instruments from Aqua and Terra measurements, regression equations were obtained to restore the main bio-optical characteristics (*IOP*s) in Sea of Azov: total concentration of chlorophyll–*a* and pheopigments, coefficients of light absorption by phytoplankton pigments, non-living organic matter and coefficient of light backscattered by particles suspended at 438 nm. The daily 2D *IOP*s maps were constructed in the surface layer from 2000 to 2018.

Keywords: Regional Bio-Optical Algorithm, Sea of Azov, MODIS-Aqua/Terra, 2D *IOP*s Maps, Concentration of Chlorophyll–*a* and Pheopigments, Particle Backscattering Coefficient, Colored Detrital Matter Coefficient.

1. INTRODUCTION

For the Russian Federation, which has long sea borders, actively develops the sea shelf, creates new logistics routes for transporting goods and services, and is engaged in the development of energy and bio-resources of the sea shelf, it is important, in particular, to monitor the ecological state of these areas. One of the necessary elements of such control is the availability of high-quality bio-optical algorithms that relate the spectral composition of the upwelling radiation from the water body to the concentration of optically active substances contained in the upper layer of the sea. Taking into account the use of observation technology from drones, aircraft and satellites, this makes it possible to currently assess the concentration of optically active substances for different spatial scales depending on the task, and taking into account the use of appropriate models, give their forecast in time and space. All of the above justifies the relevance of the development of regional bio-optical algorithms using satellite data from optical color scanners. Such work is being actively carried out. The main source of information on the inherent optical properties (*IOP*s) of the upper layer of water is the spectrum of the remote sensing reflectance (R_{RS}), which is the product of atmospheric correction of measurements of the spectrum of the upwelling radiation of the "water body - cloudless atmosphere" system. Given in Table 1 a classification reflects the relationship between the spectral interval with the maximum variability of the R_{RS} spectrum with the trophic status of water bodies in the scale of chlorophyll-*a* concentration and pheopigments *TChl*. The maximum R_{RS} variability of the spectral range shifts from blue to red during the move from low to high biological productivity (see Table 1). This is a consequence of the fact that: (1) for an oligotrophic water, there is an unambiguous relationship between the concentrations of optically active substances and, as a result, one R_{RS} ratio in two bands located in the blue-green region of the spectrum is sufficient to determine the chlorophyll–*a* concentration; (2) for mesotrophic waters, in terms of absorption, at least two R_{RS} ratios from the green-yellow visible domain, i.e., at least three bands, are necessary to separate the absorption associated with algal (phytoplankton) and non-algal (the sum of the colored components of the dissolved organic matter and non-living suspended matter) independently changing optically active components of sea water; (3) for eutrophic waters in the red spectral region, the main factors are scattering by particles and absorption by phytoplankton. It is well known that the standard satellite algorithm incorrectly retrieves the chlorophyll–*a* concentration in coastal areas and inland seas, for example, in the Black Sea. In this case, the Sea of Azov is no exception. According to the classification of the Table 1, the Sea of Azov is more suitable to "Inland seas, estuaries, lakes".

Table 1. Classification of the different trophic levels of water as a function of the wavelength range of the maximum variability of the R_{RS} spectrum

N	Region	Maximum variability of the R_{RS} spectrum, nm	Range of variability of *TChl*, mg·m^{-3}
1	Offshore ocean water	400–500	0.01–1.0
2	Coastal areas, inland seas	500–600	0.1–10
3	Inland seas, estuaries, lakes	600–700	1–100

The aim of this paper is to get the regional relationships between the quasi-synchronous measurements of the spectral coefficients of light absorption by the main optically active substances of sea water and the level 2 ocean color products (R_{RS}) and, based on these relationships, to retrieve the main bio-optical characteristics (*TChl*, the coefficients of light absorption by detrital colored matter (a_{CDM}) and phytoplankton (a_{ph}), and the light backscattering coefficient by particles (b_{bp})) in the upper layer of the Sea of Azov.

2. DATA

Field measurements included sampling followed by measurement of light absorption spectra by phytoplankton pigments, dissolved organic matter and non-algal suspension, and the sum concentration of chlorophyll–*a* and pheopigments. In total, over two years in the Sea of Azov, 16 measurements were taken at 4 stations. The measurements were carried out in 2016–2017 in different seasons: 2016 (winter (2), spring (3), summer (2) and autumn (3)) and 2017 (spring (3) and summer (3)). The coordinates of the stations are shown in Figure 1.

[1]Corresponding author. Address: Kapitanskaya, 2, Sevastopol, 299011, Crimea. Email: slava.suslin@mhi-ras.ru
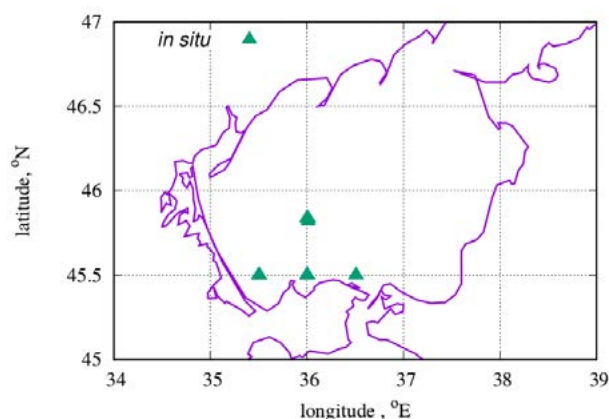
Figure 1. *The station`s location in the Sea of Azov.*

The MODIS-Aqua/Terra second-level satellite data quasi-synchronous with in situ measurements were used. Data version is R2018.0. Satellite data were selected from a neighborhood of ±0.01 degrees for measurements performed at RV stations. Satellite data were considered with a certain set of flags and masks, which removed possible errors of atmospheric correction. The time interval between the satellite product and *in situ* measurements in order of priority was as follows: on the same day, if not, then ±1 day, if not, then ±2 days.

3. METODOLOGY

For sampling, the CTD bathotometer cassettes of the Mark-3 probe were used. The concentration of chlorophyll–*a* and pheopigments was determined spectrophotometrically according to State standard 17.1.4.02-90 "Water. Method for spectrophotometric determination of chlorophyll–*a* ". Light absorption by suspended and dissolved substances was measured in accordance with the NASA current protocol. Optical measurements were carried out on a Lambda 35 double-beam spectrophotometer (Perkin Elmer) equipped with an integrating sphere. The spectral distribution of the absorption coefficient of non-algal matter (a_{NAP}) and the absorption coefficient of colored dissolved organic matter (a_{CDOM}) was described by an exponential dependence. Parameterization a_{NAP} and a_{CDOM} determination of the exponent (S_{NAP} and S_{CDOM}) were carried out in the spectral range 400–700 nm and 350–500 nm, respectively.

To determine the light absorption coefficient by phytoplankton pigments, following the established classification (Table 1), we used the spectral range 600–700 nm, as in 12–15. One of the features of this wavelength range is the absence of R_{RS} spectrum variability from the light absorption coefficient by colored detrital matter (non-algal suspended matter and colored dissolved organic matter). In addition, the light backscattering coefficient by particles is much larger than the light backscattering coefficient by clear sea water. The essence of our approach was as follows (Suslin et al. 2020): 1) to find the relationship between the *in situ* absorption coefficient by phytoplankton at 678 nm and the combination R_{RS} : $a_{ph}(678)$ vs $[R_{RS}(667)-R_{RS}(678)]/[R_{RS}(645)-R_{RS}(667)]$; 2) to determinate the relationship between *TChl* and $a_{ph}(678)$; 3) to find the relationship between *in situ* measurements of the total absorption of the colored component of the organic matter at 438 nm and remote sensing $R_{RS}(531)$: $R_{RS}(488)$ ratios; 4) using $R_{RS}(438)$ value, to obtain the b_{bp} and a_{CDM} values at 438 nm.

4. RESULTS AND DISCUNION

Examples of maps of the concentration of chlorophyll-*a* and pheopigments, the particle backscattering coefficient b_{bp}, and the light absorption coefficient of colored detrital matter a_{CDM} at 438 nm, constructed according to the algorithm described above according to MODIS-Aqua/Terra data are shown in Figure 2.
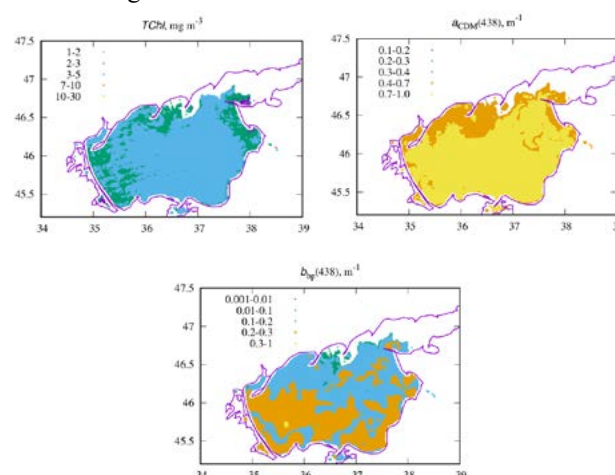
Figure 2. *A map example of TChl, $a_{CDM}(\lambda)$ and $b_{bp}(\lambda)$ at λ=438 nm on April 11, 2015 based on MODIS merge from Aqau and Terra satellites.*

5. CONCLUSION

For the Sea of Azov, a regional satellite algorithm for reconstructing the total concentration of chlorophyll–*a* and pheopigments with a range of applicability from 1 to 30 mg·m⁻³ with a standard error of 2 mg·m⁻³, coefficients of light backscattering by particles and absorption by colored detrital matter at 438 nm is proposed with correction of possible errors of standard atmospheric correction in the red visible domain. Using the MODIS-Aqua/Terra RRS standard product and the regional satellite algorithm, daily distribution (including merge) maps of the total concentration of chlorophyll–*a* and pheopigments, coefficients of light backscattering by particles and light absorption by colored detrital matter at 438 nm were constructed in the surface layer of the Sea of Azov from January 2000 to December 2018 were obtained.

REFERENCES

Suslin, V.V., T.Y. Churilova, T.V. Efimova, N.A. Moiseeva, E.Y. Skorokhod, I.E. Stepochkin, (2020). Proc. SPIE – 26th International Symposium on Atmospheric and Ocean Optics, Atmospheric Physics, 115600R.

4D IOPs structure of upper 70 m layer of the Black Sea and some applications: bio-argo float`s measurements and regional ocean color satellite products

V.V. Suslin[*1], T.Ya. Churilova[**], T.Ya. Shulga[*], A.A. Latushkin[*]

[*]Marine Hydrophysical Institute, Sevastopol, Crimea
[**]A.O. Kovalevsky Institute of Biology of the Southern Seas, Sevastopol, Crimea

Abstract – A statistical analysis of profiles from 0 to 70 m of core bio-optical characteristics of the Black Sea was performed: chlorophyll-*a* concentration, particle backscattering coefficient at 700 nm, the concentration of the colored component of dissolved organic matter, obtained as a result of long-term measurements from three bio-argo floats. The analysis made it possible to describe the profiles of the above parameters, as well as their dynamics during the year. In comparison with the obtained profiles previously used in the model, calculations showed their higher accuracy. The last made it possible in conjunction with satellite measurements more accurately restore the vertical structure of the bio-optical characteristics of the upper layer of the Black Sea from September 1997 to December 2018. Using 4D *IOPs* structure, an algorithm of assessment of photosynthetically available radiation near the bottom of the Black Sea shelf was developed and validated.

Keywords: Black Sea, Bio-Argo Float`s Data, Oceancolor Products, *IOP*s, Temperature, 4D Mapping.

1. INTRODUCTION

Currently, data assimilation of direct observations and remote sensing products are developing intensively in order to restore 4D profiles of biogeochemical characteristics of the Black Sea. Today we have the serious prerequisites for revising the profiles of the key bio-optical parameters such as: backscattering coefficient of particles, chlorophyll-*a* concentration, concentration of coloured dissolved organic matter. The aim of this work consists in restoring of 4D structure of *IOP*s in the photic zone (~0-70 m in the Black Sea) using simultaneously seasonally-depended statistics of bio-argo float`s profiles with regional oceancolor products.

2. DATA

We have the profiles of these parameters due to bio-argo float`s measurements (backscattering coefficient of particles $b_{bp}(700)$, chlorophyll-*a* concentration C_a, concentration of coloured dissolved organic matter $CDOM$) beginning from the end of 2014 (IOCCG 2011) and the developed regional oceancolor algorithms for regional oceancolor products (chlorophyll-*a* concentration C_a, absorption coefficient of coloured detrital matter at 490 nm $a_{CDM}(490)$, particles backscattering coefficient at 555 nm $b_{bp}(555)$ for SeaWiFS and MODIS scanners (Suslin and Churilova 2016).

3. METODOLOGY

Each bio-argo profile $\vec{x}$ was divided from 0 to 70 m by depth into 14 layers with a uniform step of 5 m. Separately, for each parameter, all bio-argo profiles were divided into separate

samples covering ±10 days for the next set of reference days in a year: 1, 11, .., 361. Further, a separate sample is define as *t*-sample. For each of these *t*-samples (t = 1 ... 37), the covariance matrix $\|M_t\| = \|\vec{\varepsilon}_1 \ … \ \vec{\varepsilon}_k\|_t$ is calculated, where $\vec{\varepsilon}_i$ is the variation $\vec{\varepsilon}_i = \vec{c}_i − \langle\vec{c}\rangle_t$, $\langle\vec{c}\rangle_t$ is average profile for *t*-sample, i is profile number, k is amount of profiles in *t*-sample. The next step, it has been found eigenvectors $\|\vec{v}_1, \vec{v}_2, … , \vec{v}_{14}\|$ and eigenvalues $\|\xi_1, \xi_2, … , \xi_{14}\|_t$ for each $\|M_t\| \cdot \|M_t\|^T$ from 37 matrices.

4. RESULTS AND DISCUNION

We showed that any profile $\vec{m}_t$ (in time t, where $t_k < t < t_{k+1}$) expresses as $\vec{m}_t = \frac{t_{k+1}-t}{t_{k+1}-t_k} \cdot \vec{m}_{t_k} + \frac{t-t_k}{t_{k+1}-t_k} \cdot \vec{m}_{t_{k+1}}$, where $\vec{m}_t = \langle\vec{c}\rangle_t + \alpha \cdot \vec{v}_{1,t} + \beta \cdot \vec{v}_{2,t}$, where t is number of *t*-sample, α and β are a solution of a system of two linear equations with two boundary conditions for the upper (regional oceancolor product) and lower layers (special behavior for each parameter). The accuracy of $\vec{m}_t$ are presented in Table 1.

Table 1. The averaged relative error for all 37 *t*-samples

Model	Parameter*		
	$b_{bp}(700)$	C_a	*CDOM*
old	0.912±0.041	0.604±0.012	0.311±0.009
new	0.267±0.008	0.439±0.012	0.093±0.002

*The number of profiles is 634 for $b_{bp}(700)$ and C_a, and 454 for *CDOM*.
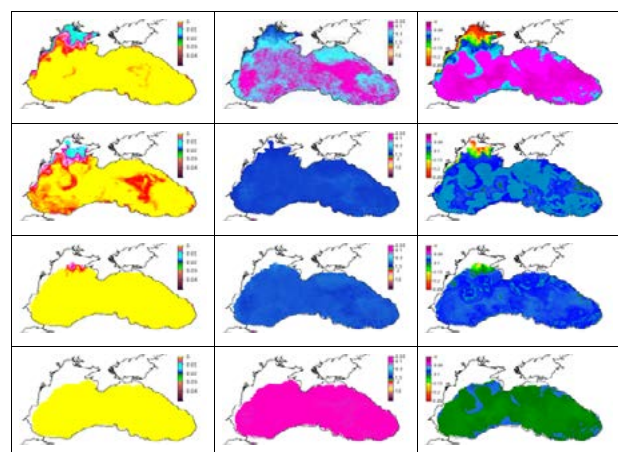
Figure 1. *Example of restored maps $b_{bp}(555)$ (m⁻¹, 1st column), C_a (mg·m⁻³, 2nd column) and $a_{CDM}(490)$ (m⁻¹, 3rd column) for some layers (0-5, 20-25, 40-45, 65-70 m, direction from surface to bottom) for the 1st half of September 2009.*

[1]Corresponding author. Address: Kapitanskaya, 2, Sevastopol, 299011, Crimea. Email: slava.suslin@mhi-ras.ru

Using 4D structure *IOP*s (see Figure 1 and Figure 2), an algorithm of assessment of photosynthetically available radiation near the bottom of the Black Sea shelf was developed (Suslin et al. 2019a) and validated (Suslin et al. 2020).
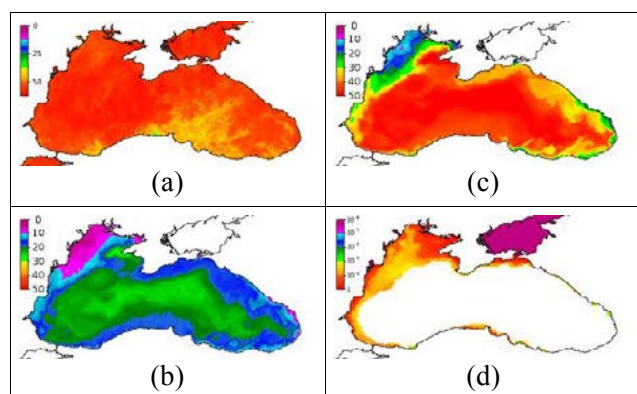
Figure 2. *Example of surface (a) and bottom (d) PAR (E m^{-2} day^{-1}) maps, depth of PAR$_{10\%}$ (b) and PAR$_{1\%}$ (m) maps in 1st half of June, 2009.*

Two-weekly, monthly, and long-term average maps of photosynthetically available radiation were obtained for the period from September 1997 to 2018. Estimates of the photosynthetically available radiation near the bottom of the Black Sea shelf are presented on two-weekly maps with a spatial resolution of 2.5 km by 2.5 km on the website at http://blackseacolor.com/browser3.html. Interannual variability of photosynthetically available radiation near the shelf bottom was analyzed for six small designated areas: Zernov's Phyllophora field, Karkinitsky Bay, in the center of the shelf slope zone, near Odessa, the mouth of the Danube River and Western Crimea (see Figure 3).
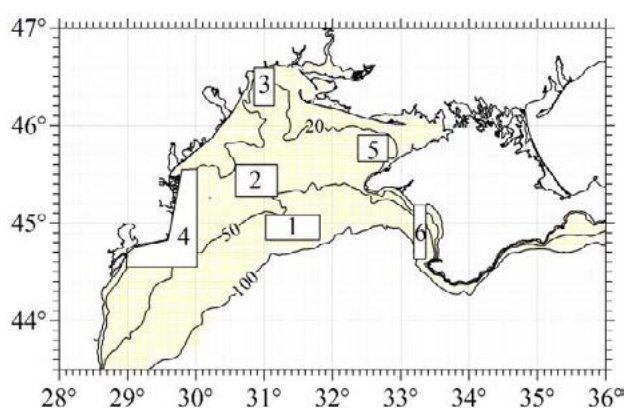
Figure 3. *A bathymetric map of the northwestern shelf of the Black Sea and the location of areas for PAR interannual variability analyses. 1 – Central region (shelf border); 2 – Zernov's Phyllophora field; 3 – Odessa; 4 – the Danube River; 5 – the Karkinitsky Bay; 6 – Western Crimea.*

The analyses for summer months revealed an increase of photosynthetically available radiation near the shelf bottom in some areas during the period from 1998 to 2018. However, it was not observed for the winter months. Restored profiles of spectral diffuse attenuation coefficient has an error of about 20–30% (Suslin et al. 2019b). The accuracy of the photosynthetically available radiation assessment is ~50%.

5. CONCLUSION

The accuracy of the profiles of the key optical parameters such as $b_{bp}(555)$, C_a and $a_{CDM}(490)$ in the Black Sea for all seasons has been significantly improved compared to what it was before. This gives the possibilities to restore their profiles, based on the satellite data for the upper layer of the sea. The 4D *IOP*s structure on a grid of 0.025^o x 0.035^o latitude and longitude in two weeks step from September 1997 to the present time with a depth resolution of 5 m from 0 to 70 m was obtained. Using 4D *IOP*s structure, an algorithm for evaluating photosynthetically available radiation reaching the bottom of the Black Sea shelf was developed and described. Extended results published in (Suslin et al. 2022).

REFERENCES

Claustre, H., Ed. (2011). 'IOCCG Bio-Optical Sensors on Argo Floats', Reports of the International Ocean-Colour Coordinating Group, No. 11, IOCCG, Dartmouth, Canada.

Suslin V., and T. Churilova, (2016). 'A regional algorithm for separating light absorption by chlorophyll-a and coloured detrital matter in the Black Sea, using 480–560 nm bands from ocean colour scanners', International Journal of Remote Sensing, Vol. 37(18), pp 4380-4400.

Suslin, V.V., M.O. Dzhamalov, V. Slabakoba, T.Y. Churilova, (2019a). '4D IOPS profiles of upper 70 m layer of the Black Sea: Bio-ARGO floats and ocean color satellite products', Proc. SPIE 25th International Symposium on Atmospheric and Ocean Optics: Atmospheric Physics. 112081K.

Suslin, V.V., T.Ya. Churilova, A.A. Latushkin, I.G. Shokurova, M.V. Shokurov, N.A. Moiseeva, T.V. Efimova, and S.F. Pryahina, (2020). 'Photosynthetically Available Radiation at the Bottom of the Northwestern Shelf of the Black Sea Based on Regional Models and Satellite Ocean Color Products and its Interannual Variability', Fundamentalnaya i Prikladnaya Gidrofizika, 13 (3), pp 68–77.

Suslin, V.V., A.A. Latushkin, O.B. Kudinov, and O.V. Martynov, (2019b). 'Pecularities of the light attenuation coefficient spectra measured in the upper layer of the Black Sea in 103rd cruise of the r/v Professor Vodyanitsky', Proc. SPIE 25th International Symposium on Atmospheric and Ocean Optics: Atmospheric Physics, 112084T.

Suslin, V., V. Slabakova, and T. Churilova, (2022). '4D structure of bio-optical characteristics of the upper 70 m layer of the Black Sea: Bio-Argo floats and ocean color scanners' Total Environment Research Themes, Vol. 3–4, pp 100006.

Harmony Scientific Workbench: Simulations of Bistatic SAR Ocean Observations and Wave-Doppler Removal

A. Theodosiou *[1], M. Kleinherenbrink[1], L. Gaultier[2], F. Collard[2], B. Chapron[3], P. López-Dekker[1]

[1] TU Delft, Delft, The Netherlands
[2] OceanDataLab, 870 Route de Deolen, 29280 Locmaria Plouzané, France
[3] Ifremer, University Brest, CNRS, IRD, Laboratoire dOcanographie Physique et Spatiale (LOPS), IUEM, Brest, France

Abstract – An ocean scientific workbench has been designed for Earth Explorer 10 candidate Harmony to study its ocean observations over large scenes with varying wind stress and ocean currents. The retrieval of ocean currents is challenging at high resolution as currents and wind affect different parts of the local wave spectrum, which affects the observed Doppler. In this study, we address strategies to separate the wave-Doppler from the ocean currents.

Keywords: Ocean currents, Air-sea interaction, wind measurements, wave-Doppler, SAR, bistatic SAR

1. INTRODUCTION

The ocean submesoscale dynamic processes are one of the gaps in our understanding of the ocean-atmosphere exchange of momentum and energy. Resolving the ocean currents and waves at submesoscale resolution is one of the missing pieces in the dynamic ocean-atmosphere processes puzzle. Harmony, an Earth Explorer 10 candidate that recently completed its phase-A studies will provide direct instantaneous estimates of the ocean surface currents, surface wind stress, and wave spectra.

Harmony consists of two satellites that will fly in a constellation with one of the Sentinel-1 satellites. Each Harmony satellite carries a passive SAR instrument that uses Sentinel-1 as an illuminator of opportunity and receives signals which are transmitted by Sentinel-1 and scattered by the surface. The full system can observe (Normalized Radar Cross Section) directional NRCS and Doppler at high-resolution, which allows for the retrieval of wind stress and surface-current vectors and ocean-wave spectra.

To estimate the performance, study the retrieved signals and develop retrieval algorithms for Harmony, a Scientific Workbench (SWB) has been developed that is able to model NRCS, Doppler and SAR spectra for large scenes. The SWB uses directional surface properties, or the local wave spectrum, to model undulations in the aforementioned parameters due to wind-stress variations, temperature changes and currents. The SWB considers both rapid responses of short waves as well as the relaxed responses of longer waves by incorporating a state-of-the-art wave model (SWAN) (Booij et al., 1996).

The varying responses of currents and wind variations at different wavelengths make it difficult to find a suitable inversion strategy that fits all level-2 products. Particularly high-resolution surface-current estimation, which requires an estimate of the wave-Doppler, is challenging. The wave-Doppler is affected by a large range of wavelengths with varying relaxation scales, which are affected differently by wind variations and currents. This work will address the issue of wave-Doppler estimation.

2. WAVE-DOPPLER ESTIMATION

Input fields for the SWB are grids of surface currents, sea-surface temperature (SST), wind stress, and interior currents from atmosphere, ocean, or air-sea-interaction models. A scene generator generates for each grid cell an ocean-wave spectrum, which provides a statistical description of the ocean surface. From the ocean model, bistatic polarimetric NRCS, Doppler and SAR spectra are computed based on bistatic versions of the Radar Imaging Model (RIM), the Doppler Radar Imaging Model (DopRIM) and the spectral SAR spectra mapping model (Kudryavtsev et al. 2003; Kudryavtsev et al. 2005; Johannessen et al. 2008; Hasselmann & Hasselmann, 1991). From the SAR spectra we derive the cut-off (Kerbaol et al. 1998), which is a proxy for the resolution loss because of the surface velocity, and the Mean Cross-Section (MACS), an integral of the SAR spectrum in the ground-range direction of the system (Li et al. 2019). All parameters are estimated for the three lines of sight of the Sentinel-1-Harmony system.

Wave-Doppler is generated by the correlation of the line of sight projected orbital velocities with tilt and hydrodynamic modulation of relatively long waves O(10 m). In scatterometry the NRCS is generally used to get an estimate of the wind stress, which is primarily generated by Bragg waves (with wavelengths O(0.1 m)). At high resolution this can be enhanced by constraining the wave age, because of omni-directional energy cascades from long to short waves, which is beyond the scope of this paper. At low resolution or uniform conditions, the wind stress vector and the wave age are sufficient to constrain a wind-wave spectrum from which the wave-Doppler can be estimated.

This does not hold for wind changes at high resolution, where short waves experience near-instant responses, but the longer Doppler-generating waves have longer relaxation rates and do not respond to local wind changes. Therefore, additionally to NRCS and cut-off, the MACS parameter is used to estimate wave-Doppler as it represents scales at the low range of the wave-Doppler generating wavelengths. Small waves still affect the intensity modulation by the longer waves as the modulation derivatives vary with wind stress. Therefore, a pyramidal system involving multiple scales of the MACS and the NRCS are used to estimate the wave-Doppler and recover the surface current in Figure 1. There is no surface current present in the scene considered in Figure 1 so a residual can directly be interpreted as an error. With the current pyramidal system, the error is suppressed to less than 0.2 m/s, but in locations with high wind-speed variations, the errors might increase to more than 0.5 m/s.

Unlike the local wind variations, the currents refract both short and long waves and redistribute the wave energy over the spectrum (Kudryavtsev et al. 2005; Kudryavtsev et al. 2012, Rascle et al. 2014; Quilfen & Chapron, 2018). Depending on the current shear and convergence, the wave-Doppler and MACS are altered in magnitude and in direction.

---

* Corresponding author. Address: Stevinweg 1, 2628 CN, Delft, The Netherlands. Email: a.theodosiou@tudelft.nl

The short waves and wave breaking are also strongly altered near shear and convergence zones, which will lead to changes in NRCS. For a scene with strong currents a different weighting is required between NRCS and MACS to obtain accurate wave-Doppler than for a scene with strong wind-speed undulations. Figure 2 shows a comparison between the input surface current and the retrieved surface currents based on a pyramidal scene with different weightings than for the scene of Figure 1. It shows that currents of a few tenths of meter per second can be observed. Weaker currents at high resolution require a more tailored retrieval strategy.

3. CONCLUSIONS

We have provided an overview of the Harmony SWB and discuss the retrieval of high-resolution surface currents for two scenes with different characteristics. Accurate estimation of wave-Doppler is challenging and requires tailored algorithms for the scene characteristics, i.e., currents and wind-speed variations. We therefore recommend a retrieval strategy, which as a first step classifies the scene. More advanced retrieval strategies based on a joint retrieval of all ocean observables are currently considered.

REFERENCES

Booij, N., Holthuijsen, L. H., and Ris, R. C. (1996). THE "SWAN" WAVE MODEL FOR SHALLOW WATER. Coastal Engineering Proceedings, (25). Number: 25.

Kudryavtsev, V., Akimov, D., Johannessen, J., and Chapron, B. (2005). On radar imaging of current features: 1. Model and comparison with observations. Journal of Geophysical Research: Oceans, 110(C7).

Kudryavtsev, V., Hauser, D., Caudal, G., and Chapron, B. (2003). A semiempirical model of the normalized radar cross-section of the sea surface 1. Background model. Journal of Geophysical Research: Oceans, 108(C3):8054.

Johannessen, J. A., Chapron, B., Collard, F., Kudryavtsev, V., Mouche, A., Akimov, D., and Dagestad, K.-F. (2008). Direct ocean surface velocity measurements from space: Improved quantitative interpretation of Envisat ASAR observations. Geophysical Research Letters, 35(22):L22608.

Hasselmann, K. and Hasselmann, S. (1991). On the nonlinear mapping of an ocean wave spectrum into a synthetic aperture radar image spectrum and its inversion. Journal of Geophysical Research: Oceans (1978–2012), 96(C6):10713-10729.

Kerbaol, V., Chapron, B., & Vachon, P. W. (1998). Analysis of ERS-1/2 synthetic aperture radar wave mode imagettes. Journal of Geophysical Research: Oceans, 103(C4), 7833-7846.

Li, H., Chapron, B., Mouche, A., & Stopa, J. E. (2019). A New Ocean SAR Cross-Spectral Parameter: Definition and Directional Property Using the Global Sentinel-1 Measurements. Journal of Geophysical Research: Oceans, 124(3), 1566–1577.

Kudryavtsev, V., Myasoedov, A., Chapron, B., Johannessen, J. A., and Collard, F. (2012). Imaging mesoscale upper ocean dynamics using synthetic aperture radar and optical data. Journal of Geophysical Research: Oceans, 117(C4).

Rascle, N., Chapron, B., Ponte, A., Ardhuin, F., & Klein, P. (2014). Surface roughness imaging of currents shows divergence and strain in the wind direction. Journal of Physical Oceanography, 44(8), 2153-2163.

Quilfen, Y., Yurovskaya, M., Chapron, B., & Ardhuin, F. (2018). Storm waves focusing and steepening in the Agulhas current: Satellite observations and modeling. Remote sensing of Environment, 216, 561-571.
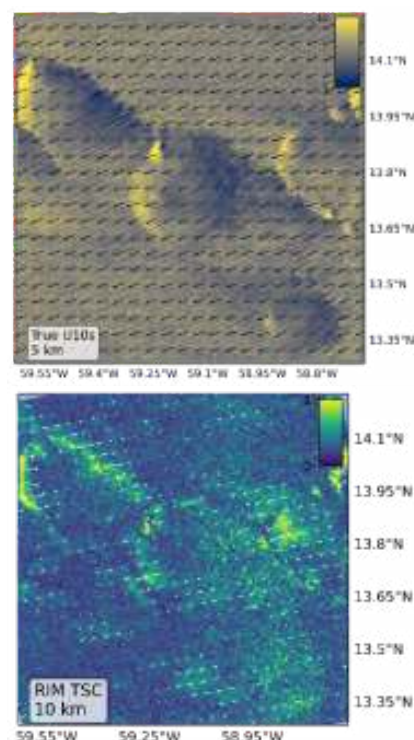
Figure 1: Input wind field (top) and estimated surface current (bottom). The input field is generated using the Dutch Atmospheric Large-Eddy Simulation (DALES). The current input field is zero over the entire region of this simulation. An underestimation of the wave-Doppler leads to a bias of the surface currents estimation
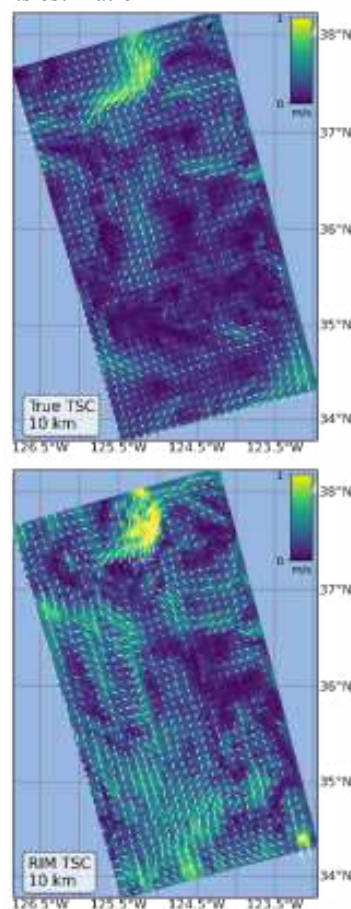
Figure 2: Input surface current (top) and estimated surface current (bottom) for the simulated acquisition over the coast of California. The arrows represent the vector direction, while the contours show the magnitude.

Evaluating the BRDF correction for the Zaneveld-Twardowski-Tonizzo semi-analytical model using field measurements

A. Tonizzo[1], M. Twardowski [1,2,*], S. Kolluru[2], A. Gleason[3], and K. Voss[3]

[1]Sunstone Scientific LLC, Vero Beach, FL, USA
[2]Harbor Branch Oceanographic Institute, Florida Atlantic University, Ft. Pierce, FL, USA
[3]University of Miami, Coral Gables, FL, USA

Abstract – Twardowski and Tonizzo [2018; TT18 herein] present a radiative transfer approximation called ZTT (Zaneveld-Twardowski-Tonizzo) based on the theoretical work of Zaneveld [1995] that relates inherent optical properties (IOPs) of the ocean to remote sensing reflectance (r_{rs}) and accounts for bidirectional reflectance distribution function (BRDF) effects. The relationships for ZTT do not have spectral resolution limitations and are generic to any natural waters, so the model is thus directly applicable to future hyperspectral satellite ocean color missions such as NASA PACE and Sentinel-10 CHIME. As a BRDF correction algorithm, IOPs are first derived through ZTT inversion at the prevailing solar-viewing geometry; the forward ZTT model is then carried out at the conceptual normalized geometry of zero solar zenith, nadir viewing. One of the few sensors available measuring the full hemispherical upwelling radiance distribution is NuRADS [Voss et al. 2005]. Herein an assessment of the ZTT BRDF model is carried out with NuRADS data for stations covering 3 field sites: the Ligurian Sea, the S. Pacific gyre, Monterey Bay. Comparisons are made with current state-of-the-art BRDF models and full radiative transfer simulations.

Keywords: Ocean optics, Radiative transfer, Inversion, Inherent Optical Properties, BRDF.

1. INTRODUCTION

The ocean color (OC) BRDF describes the translation of downwelling solar irradiance E_d into the hemispherical angular distribution of upwelling radiance, L_u. The ratio L_u / E_d is the r_{rs} distribution just below the air-sea interface. The relationship between L_u and E_d is bidirectional since L_u is a function of the direction of incident sunlight as well as viewing direction, i.e., the reflected light in the ocean is not isotropic. A BRDF model is currently applied to OC remote sensing imagery to convert water-leaving radiance L_w for any viewing angle and solar zenith geometry to a consistent geometry configuration of nadir viewing with Sun directly overhead in a non-attenuating atmosphere [Mobley et al. 2016]. This is typically carried out before empirical and semi-analytical algorithms are applied to spectral reflectance measurements to derive ocean biogeochemical properties of interest [Werdell et al. 2018]. Morel et al. [2002; M02 herein] developed the BRDF model currently used for ocean color imagers. M02 uses multi-parameter Look-Up Tables (LUTs) resolved at 7 wavelengths between 412.5 and 660 nm for open ocean waters with chlorophyll [Chl] <10 mg m^{-3}. Applicability is thus limited for coastal and inland waters and for sensors such as the future NASA Plankton, Aerosol, Cloud, and ocean Ecosystem (PACE) Ocean Color Imager (OCI; expected launch 2024) and European Union Sentinel-10 CHIME that will have hyperspectral resolution of at least 5 nm with spectral ranges extending into the UV. Another BRDF correction algorithm developed by Lee et al. [2011; L11 herein], also represented by LUTs, was designed to be more applicable to coastal and inland waters.

Recently, TT18 developed an ocean color model based on the radiative transfer approximation of Zaneveld [1995] that includes the BRDF, extends into the UV without spectral resolution restrictions, and is applicable to coastal and inland waters as well as the open ocean. This approach has several potential benefits, including 1) a single analytical expression describing the RT process for all remote sensing geometries, 2) optimal retention of native RT relationships directly linked to physically meaningful terms with more degrees of freedom than simple first order approximations of r_{rs} to b_b/a or $b_b/(a + b_b)$, 3) all parameters including the VSF are explicit in the model with readily characterized uncertainties, and 4) model can be readily enhanced by tuning one or more terms rather than developing new LUTs from complete recomputations of full RT. TT18 tested performance of the model for available in-water reflectance measurements, but only nadir viewing.

The objective of this work was to assess the ZTT BRDF model with direct measurements of upwelling radiance distributions collected by the instrument NuRADS [Gleason et al. 2012]. NuRADS is a fisheye lens camera system that measures hemispherical upwelling radiance just below the ocean surface at wavelengths centered at 412, 436, 486, 526, and 548 nm.

2. ZTT BRDF MODEL

The ZTT model is described in Twardowski and Tonizzo (2018) and briefly reviewed here. Zaneveld [1995] derived an exact restatement of the radiative transfer equation in terms of shape factors for the backscattered radiance field and forward scattering in the upwelled radiance field. His relationship demonstrated the direct link between the distribution of upwelled radiance and the shape of the volume scattering function in the backward direction. TT18 reworked the Zaneveld [1995] relationship in terms of dependencies on IOPs relating to ocean color remote sensing with associated analytical relationships so it could then be a practical tool for ocean color applications. The relationship explicitly includes the phase function, Raman scattering (Westberry et al. 2013). The backscattering ratio is also an explicit term.

TT18 made the assumption the radiance shape parameter f_L for viewing angles other than nadir would correspond to f_L computed for nadir viewing when the specific in-water single-scattering angles ψ matched, i.e., the f_L computed at nadir viewing for a specific solar zenith that results in single-scattering angle ψ may be used to approximate f_L at other viewing and solar zenith angles as long as ψ is the same. The model was recomputed without making this assumption. The

* Corresponding author. Address: HBOI/FAU, 5600 US Highway 1 N, Ft. Pierce, FL. USA. Email: mtwardowski@fau.edu

236 *POSTER SESSION*

relationship found by Sullivan and Twardowski [2009] based on VSF measurements in over 7000 diverse natural waters was used for the backward phase function.

3. RESULTS AND DISCUSSION

An example of comparisons between upwelling radiance distributions from the Ligurian Sea, S. Pacific gyre, and Monterey Bay are provided in Figs. 1-3, respectively. The 45/225 deg azimuth plane is shown to minimize the effects of NuRADS self-shadowing, strongly observed in the principal plane, although these effects are still clearly present here. No correction for self-shadowing was attempted. Positive viewing angles are toward the Sun. Only results at 436 nm are shown but results at the other NuRADS wavelengths are generally similar. Included in the comparisons are results from the M02 and L11 BRDF models.
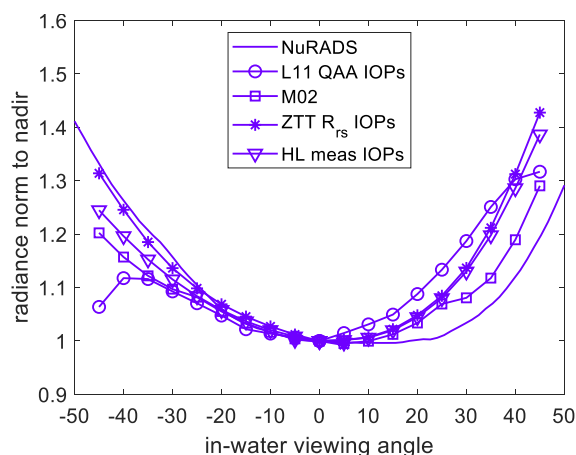
Figure 1. *Radiance distributions at 436 nm normalized to the value at nadir viewing along the 45/225 degree azimuth for a station in the Ligurian Sea, data collected in 09/2009. Solar zenith was 59°. Input for the ZTT, M02, and L11 models was measured spectral remote sensing reflectance. Inputs for the Hydrolight (HL) simulation were measured IOPs, with the phase function approximated from the backscattering ratio using the Fournier-Forand phase function.*
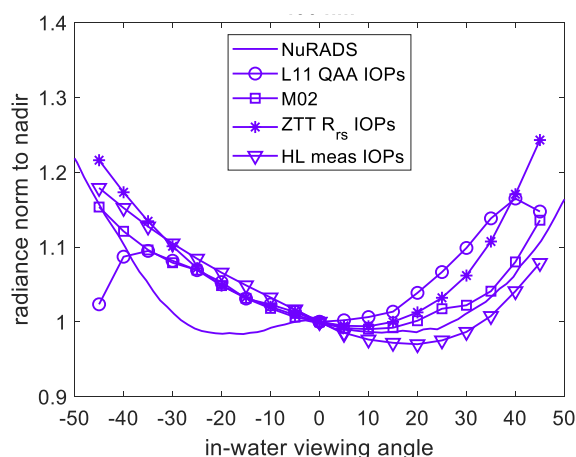
Figure 2. *Same as Fig. 1 but for a station in the South Pacific gyre, data collected in 12/2004. Solar zenith was 37°.*
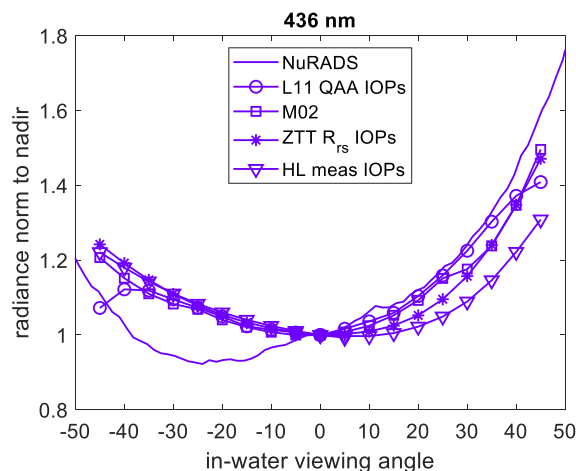
Figure 3. *Same as Fig. 1 but for a station in Monterey Bay, data collected in 10/2006. Solar zenith was 49°.*

The ZTT model typically agrees well with HL simulations, except for the viewing angles toward the Sun in the S. Pacific gyre (Fig. 2). We note the accuracy of b_b and b measurement inputs are critical in the HL simulations for these extremely clear waters, particularly in determining the relative impact of pure seawater scattering on the VSF that controls the BRDF. It is interesting to note NuRADS data often does not show strong agreement with HL simulations.

We are currently assessing several possible systematic sources of uncertainty in understanding differences between NuRADS data, HL simulations, and the models, including potential errors with NuRADS, IOP, and reflectance measurements. Potential uncertainties in HL simulations are also being considered, particularly the lack of polarization. Additional BRDF measurements and RT models will be assessed in the near future to better understand sources of uncertainty.

REFERENCES

Gleason, A. and OTHERS. Detailed validation of ocean color bidirectional effects in various Case I and Case II waters. *Opt. Express* 2012, *20*(7), 7630-7645.

Lee, Z-P, and OTHERS. An inherent optical property centered approach to correct the angular effects in water-leaving radiance. *Appl. Opt.* 2011, *50*(19), 3155-3167.

Mobley, C.D.; Werdell, J.; Franz, B.; Ahmad, Z.; Bailey, S. Atmospheric Correction for Satellite Ocean Color Radiometry. NASA Report NASA/TM–2016-217551, 2016.

Morel, A.; Antoine, D.; Gentili. B. Bidirectional reflectance of oceanic waters: accounting for Raman emission and varying particle phase function. *Appl. Opt.* 2002, *41*, 6289-6306.

Sullivan, J.M.; Twardowski, M.S. Angular shape of the volume scattering function in the backward direction. *Appl. Opt.* 2009, *48*, 6811-6819.

Twardowski, M., and A. Tonizzo. Ocean color analytical model explicitly dependent on the volume scattering function. Applied Sciences, special issue on Ocean Optics (feature publication), 2018, 8, 2684; doi:10.3390/app8122684.

Twardowski, M.; Tonizzo, A. Scattering and absorption effects on asymptotic light fields in seawater. *Opt. Express* 2017, *25*(15), 18122-18130.

Zaneveld, J.R.V. A theoretical derivation of the dependence of the remotely sensed reflectance on the inherent optical properties. *J.Geophys Res.* 1995, *100*(C7), 13,135-13,142.

The skill of measuring the Florida Current volume transport from space

D.L. Volkov [1,2]*, R.H. Smith[1], C.S. Meinen[ret], R. Garcia[1,2], M. Baringer[1], G. Goni[1]

[1]Cooperative Institute for Marine and Atmospheric Studies, University of Miami, Miami, USA
[2]NOAA Atlantic Oceanographic and Meteorological Laboratory, Miami, USA

Abstract – Florida Current (FC) provides the bulk of the northward volume transport in both the upper limb of the Atlantic meridional overturning circulation and the western boundary component of the subtropical gyre circulation. It is one of the major conduits of heat, salt, carbon, nutrients and other properties, with profound influences on regional weather, climate, sea-level, and ecosystems. Daily monitoring of the FC volume transport with a submarine cable has been carried out nearly continuously since 1982. Here, we present estimates of the FC volume transport based on along-track satellite altimetry measurements since 1993. We show that altimetry captures about 2/3 of the FC variance observed in the concurrent cable estimates, with an accuracy of 2.1 Sv. Using concurrent bottom pressure and Acoustic Doppler Current Profiler (ADCP) measurements at 27ºN, we demonstrate that the remaining unexplained variance results from the lack of the vertical coherence of the flow.

Keywords: Florida Current, satellite altimetry, volume transport, sea level.

1. INTRODUCTION

The Florida Current (FC) flows through the Straits of Florida from the southernmost Florida Keys to the northernmost Bahamas Islands (Fig. 1), and it is regarded as the beginning of the Gulf Stream. The daily FC volume transport has been monitored with submarine cable measurements supplemented with calibration/validation in situ surveys at 27ºN since 1982 as part of the NOAA Western Boundary Time Series (WBTS) project. As of today, these measurements provide the longest quasi-continuous climate record of a boundary current in existence and serve as a critical component of the trans-basin meridional overturning circulation observing array at 26.5ºN. Although the cable has been the most reliable and cost-effective FC measurement system, efforts are underway to find a suitable backup and/or replacement system that would substitute the cable during inevitable future system failures and/or future cable breaks. Some data gaps in the cable record have occurred due to instrument failures as well as logistics or operational issues.

Geostrophic balance dictates that a strong boundary current co-evolves with a perpendicular (cross-stream) sea level gradient. The FC is associated with an average sea surface height (SSH) difference between Florida and the Bahamas of about 0.7 m. The use of tide gauge measurements on either side of the Straits of Florida to monitor the FC is possible, but limited due to the lack of continuous records, especially on the Bahamas side. Recently, Meinen et al. (2020) used records from a pair of bottom pressure recorders (BPRs) deployed near the 12-m isobath on both sides of the Straits of Florida at 27ºN. They showed that the transports estimated from the pressure differences explain roughly 55% of the total variance of the FC transport measured by the cable at time scales from a few days to a year.

Along with tide gauges on land and BPRs, satellite altimetry provides periodic (~ every 10 days) sea level measurements across the Straits of Florida along predetermined ground tracks (Fig. 1). The objective of this study is to derive the satellite-based estimates of the FC volume transport and to evaluate their utility as a backup system for the cable measurements.

2. RESULTS

The altimetry-based FC volume transport, T_a, is obtained by regressing the cable transport, T_c, against the sea surface height slope (ΔSSH) measured along the track 178 (Fig. 1). The absolute correlations between T_c and SSH are notably better for track 178 than for track 243, meaning that the former better captures SSH variations. Instead of using single measurement points to the east and to the west of the FC jet, for example, the points of maximum correlations between the cable transport and SSH, better results are obtained with SSH averaged over the eastern segment 79°W–79.5°W (SSH_E) and the western segment 80°W–80.5°W (SSH_W) along the track 178 relative to the FC jet. For the linear regression, we used the period 2008–2014, similar to the period studied by Meinen et al. (2020), and, for which, the relatively high correlation between T_c and $\Delta SSH=SSH_E-SSH_W$ is estimated ($r = 0.79$). The obtained linear regression coefficients were used to estimate T_a from ΔSSH for the entire satellite altimetry record available to date (1993–2022) (cyan and green curves in Fig. 2).
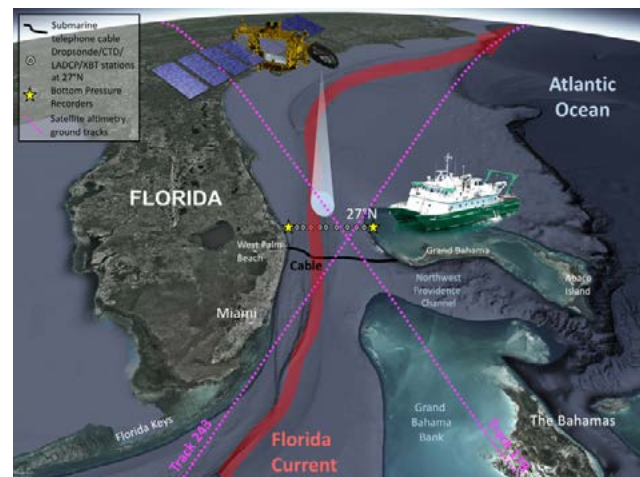
Figure 1. *Components of the Florida Current observing system. Black curve shows the approximate location of the submarine cable. The cable measurements are calibrated and validated with regular direct dropsonde and ADCP measurements at 9 stations at 27ºN (yellow dots). Bottom pressure is measured at the western and eastern ends of the 27ºN transect (yellow stars). Altimetry satellites, from Topex/Poseidon to Sentinel-6MF, have measured sea surface height along the descending track 178 and the ascending track 243 across the Florida Current since the end of 1992.*

---

* Corresponding author. Address: 4301 Rickenbacker Causeway, Miami, Florida 33149, USA. Email: denis.volkov@noaa.gov
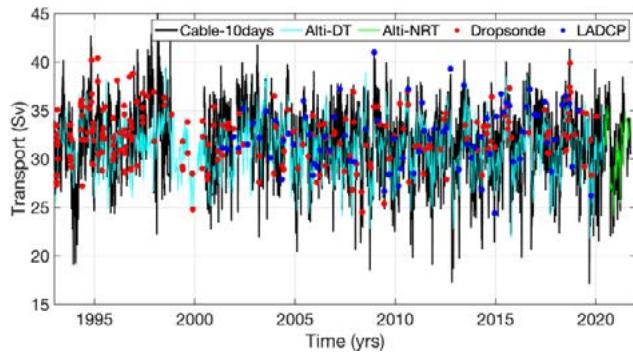
Figure 2. *The Florida Current volume transport: cable transport estimates, T_c, subsampled at 10-day intervals at the times of satellite overpasses (black), altimetry-derived transport estimates, T_a, for delayed-time (cyan) and near-real time (green) data, transports measured with dropsonde floats (red dots), and transports measured with lowered acoustic Doppler current profilers (blue dots).*

The correlation coefficient between the 10-day subsampled T_c and T_a for the entire record (1993–2022) is 0.63, which means that only about 40% of the variance is explained. This relatively small number is mostly due to a noisier cable signal in 1993–1998, during which the correlation between T_c and T_a is 0.38. The correlation increases to 0.55 and 0.75 for the periods 2000–2005 and 2006–2020, respectively. These numbers are consistent with the inhomogeneous cable data quality. Specifically, the accuracy of the cable data was low in 1993–1998 when the cable was in active use for telecommunications, and it was better but still problematic in 2000–2005 due to issues with the recording system.
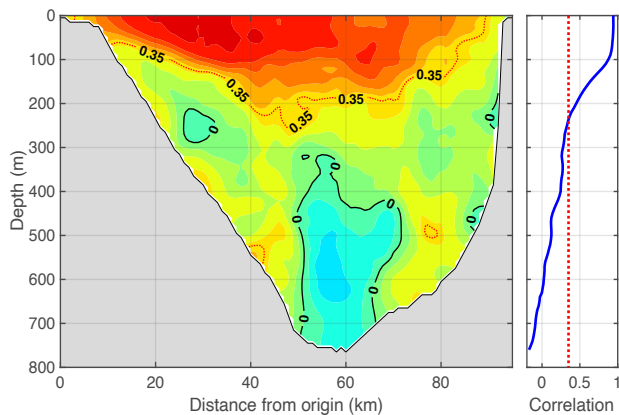
Figure 3. *Correlation between the concurrent bottom pressure differences and ADCP-based meridional velocity sections at 27°N. The 95% significance level is shown by the red dotted line.*

Excluding the period when the cable was used for telecommunications and the period used for linear regression (2008–2014), the root-mean-square (RMS) difference between T_c and T_a in 2001–2022 is 2.6 Sv. It is reasonable to assume that the transport estimates during this period are independent, so that the RMS difference between them represents the total error, ε_{tot}, determined as the square root of the sum of the individual errors squared. Therefore, the accuracy of the altimetry-derived transport estimate, ε_a, becomes $\varepsilon_a = (\varepsilon_{tot}^2 - \varepsilon_c^2)^{1/2}$, where ε_c is the error of T_c. The updated estimate of ε_c is 1.5 Sv (Volkov et al., 2020), so that ε_a becomes 2.1 Sv. The altimetry-derived transport estimates were also validated with independent quasi-instantaneous transports estimated from ship sections at 27°N, yielding the accuracy of 2.0 Sv and 1.9 Sv for dropsonde and ADCP measurements, respectively (Table 1).

Comparison between the cable and altimetry-derived transport estimates suggest that along-track SSH gradients can capture roughly 60% of the 10-day T_c variance. This is similar to the result based on daily BPR measurements (Meinen et al., 2020). Correlations between the concurrent bottom pressure differences and ADCP measurements at 27°N show that the cross-stream SSH gradients are representative for velocity fluctuations in the upper 200-m, but misrepresent the deep flow (Fig. 3). This means that about 40% of the unexplained (by SSH gradients) T_c variance results from the lack of the vertical coherence of the flow.

Table 1. Accuracies of the Florida Current Volume Transport Estimates From Different Observing Platforms

Type of the FC transport estimate	Accuracy (Sv)
T_c (*Volkov et al., 2020*)	1.5
$T_{dropsone}$ (*Garcia et al., 2014*)	0.8
T_{LADCP} (*Garcia et al., 2014*)	1.3
T_{BPR} (*Meinen et al., 2020*)	2.7
T_a compared to T_c	2.1
T_a compared to $T_{dropsonde}$	2.0
T_a compared to T_{ADCP}	1.9

3. CONCLUSION

The results presented herein demonstrate that satellite altimetry can provide a valuable resource for measuring the FC volume transport in case the cable fails and for filling in the already existing gaps in the cable time series. The altimetry-based estimates can capture roughly 60% of the T_c variance. Unlike the in-situ instrumentation, satellite altimetry is not at risk from adverse weather conditions (e.g., tropical storms and hurricanes), and its quality is homogeneous throughout the 30 years of observations. Nevertheless, due to the lack of the vertical coherence in the FC flow, altimetry alone is not sufficient for measuring the T_c. Cost-effective cable measurements supplemented with ship sections for cable calibration and validation and for measuring the vertical structure of the flow should be maintained for as long as possible.

REFERENCES

Garcia, R., & Meinen C.S. (2014). Accuracy of Florida Current volume transport measurements using multiple observational techniques, J. Atmos. Ocean. Tech., 31(5), 1169-1180, https://doi.org/10.1175/JTECH-D-13-00148.1.

Meinen, C. S., Smith, R., & Garcia, R. F. (2020). Evaluating pressure gauges as a potential future replacement for electromagnetic cable observations of the Florida Current transport at 27°N. J. Operational Oceanogr., 1–11. https://doi.org/10.1080/1755876X.2020.1780757.

Volkov, D. L., Domingues, R., Meinen, C. S., Garcia, R., Baringer, M., Goni, G., & Smith, R. H. (2020). Inferring Florida current volume transport from satellite altimetry. J. Geophys. Res.: Oceans, 125, e2020JC016763. https://doi.org/10.1029/2020JC016763.

MOBY-Refresh and MarONet: A project update

K.Voss [1]*, M. Yarbrough[2], B. C. Johnson[3], M. Feinholz[2], A. Gleason[1], D. Antoine[4], S. Flora[2]

[1]University of Miami, Coral Gables, Florida, USA
[2]Moss Landing Marine Laboratory, Moss Landing, California, USA
[3]National Institute of Standards and Technology, Gaithersburg, Maryland, USA
[4]Curtin University, Perth, Western Australia, AUS

Abstract – The Marine Optical Buoy (MOBY) has provided the primary vicarious calibration data for many ocean color satellite systems over the last 25 years. We have been working on replacing the MOBY system, with a goal of improving the operation of the system, in a process we are calling MOBY-Refresh. In addition, with the support of NASA we have developed MarONet, which takes many of the features of the MOBY-Refresh effort and adds additional components to allow deployment of the MarONet system off of Perth, Australia. We have recently deployed the first of the new systems at a location near the heritage MOBY site. We are finding that the new system agrees with the heritage MOBY system to within +-2% for simultaneous measurements of the spectral remote sensing reflectance. We are collecting data with the new system throughout calendar year 2022, in this location near the heritage site. The goal is to validate the new system performance with this cross over experiment before switching the heritage MOBY to MOBY-Refresh in 2023, and installing the MarONet system in Australia in mid-2023.

Keywords: In-situ instrumentation, calibration.

1. INTRODUCTION

Satellite instruments to measure ocean color require vicarious calibration while in orbit. The vicarious calibration process needs, as an input, high quality measurements of the spectral water leaving radiance. For over 25 years the MOBY system has been providing these data to the ocean color community. To maintain this nearly continuous data record we are updating the components of the MOBY system, with the support of the National Oceanographic and Atmospheric Agency (NOAA) in an effort called MOBY-Refresh. In addition, in anticipation of the launch of the PACE instrument by NASA, NASA has funded a program called MarONet, which is currently aimed at placing an identical system off of Perth, Australia. The first of these systems was deployed in February 2022 near the Lanai, Hawaii site of MOBY with the goal of obtaining a simultaneous data set for validation of the new instrument. This cross over experiment is expected to last through calendar year 2022. At the conclusion of this cross-over experiment, we will replace the MOBY system with the MOBY-Refresh system. The MarONet system will be deployed in mid 2023 in Perth.

At this time we have approximately 6 months of nearly simultaneous data with which we can compare the operation of the new system and the old system.

2. Discussion

We are still analyzing the data from the cross-over experiment and so these results are very preliminary, and may change before the presentation at the Oceans from Space meeting.

There are two types of data that we have from the new system: tracking of internal calibration sources and other types of stability measurements, and comparison with simultaneous measurements taken with the MOBY system. We will discuss the stability measurements first. We have measurements of the spectral stability (using Fraunhofer lines in the image), track stability on the array, and radiometric stability using the internal calibration sources.

In terms of spectral stability, examining the Fraunhofer lines in each of the data images allows us to monitor how much our spectral calibration has changed. There are two spectrometers in the system, the blue spectrograph (BSG) and the red spectrograph (RSG). For the BSG the positions of the Fraunhofer lines on the array have been constant to within 1/3 of a pixel. This indicates that the spectral shift for the BSG has been less than 0.1 nm during the first 5 months of this deployment. The RSG slit image, however, has been moving more on the array, and has moved up to 3 pixels (equivalent to 1nm) for brief periods and then relaxing back to a steady state value again. While the BSG is within the specifications, we are investigating the cause of the jumps in the RSG.

The next stability is the stability of the image of the track (which optical input) on the CCD array in the spectrographs. Once again, the image of the track is very stable for the BSG (to within tenths of a pixel). However the image on the RSG is shifting approximately 3 pixels over the 5 months of the deployment. This shift is not smooth, but there are jumps in it which occur at the same time as the shifts we see in the spectral position of the Fraunhofer lines, indicating that the image on the array is moving in both dimensions.

Finally the internal calibration lamp can be used to look at the stability of the response of a portion of the optical system. For the BSG, the stability is within 1.5% over the first 4 months of the deployment, however the two times the response to the internal lamp changed significantly were when we changed the integration time of the data collection. If these changes were ignored, the overall change in the response would be much smaller (<0.5%). The changes in the spectral position in the RSG is reflected in the lamp response data, with rapid increases during the jumps in the Fraunhofer line positions and a slow, small change over time

of the baseline response. Once again we are working to understand the cause of these changes and how they are affecting our data.

The final comparison is comparing the final product of the new system, with simultaneous data with the old system. The data with each system was taken within 30 minutes of each other, however the two systems are 12 km apart, so the water properties may vary. On average, as shown in Fig. 1, the two systems agree to each other within +-2% between 400 nm and 600 nm. The new system has not been straylight corrected, but in this spectral range, this is not important. There does seem to be a spectral variation to the agreement, and we are working on determining the reason for this. Note that at +-2% we are at the limit for the calibration of the MOBY system, which is being used as a reference, so it is not certain if the issue is in MOBY or the new system.
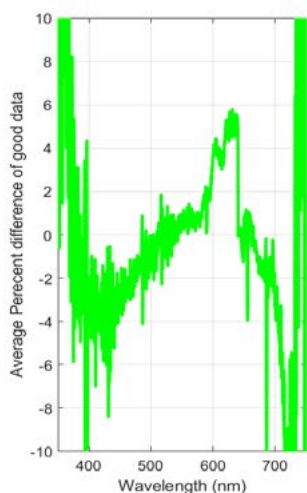
Figure 1. Average percent difference between MOBY and the new optical system

3. CONCLUSION

Progress is being made on an update to the MOBY system and in the MarONet project. The cross-over test period for the new optical system should be over near the beginning of 2023, at which time we will move the new optical system to the heritage Lanai site, and discontinue use of the old system (after more than 25 years of service). Installation of the MarONet system in its Australia location will be taking place in July of 2023.

ACKNOWLEDGEMENTS

This work has been supported by NOAA under grant NA200AR4320472 (and agreement No. STAR2017-6 and NASA with grant 80GSFC20C0100 and 80HQTR21T009. In addition we would like to thank all of the other members of the MOBY team, both past and present, that have helped us in this work.

DOM optical properties in surface waters of Kongsfjorden, Isfjorden and Hornsund (Spitsbergen) – a pilot study results of DOMinEA project.

M. Zabłocka *, P. Kowalczuk, M.Konik, K. Dragańska-Deja, K. Borzycka, A. Zdun

Institute of Oceanology Polish Academy of Sciences, Sopot, Poland

Abstract – Kongsfjorden, Isfjorden and Horsund are three main West Spitsbergen Fjords (Figure 1) which differ in hydrological regimes hence the difference between their water masses can be described by their distinct optical properties. A pilot study on DOM optical properties in surface waters of those three fjords was conducted in summer 2018 – 2019. Water samples for determination of DOM absorption coefficient and DOM fluorescence were collected. The inherent optical properties were measured with use of the Integrated Optical-Hydrological Probe. Based on 119 EEM spectra and the application of the PARAFAC , the 5 components model has been developed. The studies revealed a significant differences in both quantitative and qualitative properties of DOM optical characteristics in the West Spitsbergen Fjords. Those differences can be the outcome of a number of local scale and mesoscale processes. The goal of DOMinEA project is to investigate those findings more deeply.

Keywords: CDOM, FDOM, PARAFAC, Kongsfjorden, Isfjorden, Horsund, Spitsbergen, Arctic.

1. INTRODUCTION

Fjords, regarded as Aquatic Critical Zones, integrates terrestrial, cryospheric, oceanic and atmospheric interactions within the Earth system and are particularly sensitive to climate change, therefore processes occurring within a fjord can provide significant projection how the system may respond to environmental forces (Bianchi, et al, 2020). Fjords represent significant carbon cycle hotspots, that bury the largest amount of organic carbon per unit area in the world, which makes them a crucial ecosystem in regulating carbon cycle over time (e.g., Smith et al., 2015).

In recent decades, the Arctic Ocean and its drainage basins have experienced rapid changes. Observations confirmed that increase of mean air temperature in the Arctic is two times higher than elsewhere, which means that the Arctic is most impacted by the global warming (ACIA, 2014).Warming in the Arctic leads to a rapid sea ice reduction, glacial melting and an increase river run-off in the Arctic Ocean watershed resulting in physical and biogeochemical changes in its water masses (Meier et al., 2014), including West Spitsbergen fjords
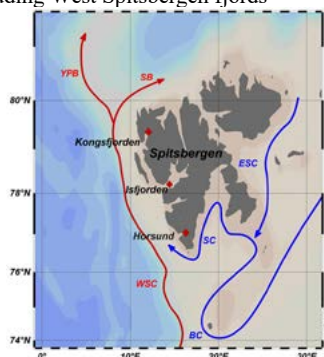
Figure 1. Map of Spitsbergen with selected West Spitsbergen fjords along with general surface circulation pattern. WSC – West Spitsbergen Current, YPB – Yermak Plateau Branch, SB – Spitsbergen Branch, SC – Sørkapp Current, BC – Bjørnøya Current, ESC – East Spitsbergen Current.

In recent years, West Spitsbergen fjords (Figure 1) have received special attention due to their importance as being "open laboratory" for observations of ongoing climate change and global warming (Pavlov et al., 2013). Those fjords are located in a critical area where warm Atlantic Water (AW; temperature > 3°C, salinity >34.9) carrying heat and salt into the Arctic Ocean interfaces the Polar Water (Aasgaard, 1987; Walczowski and Piechura, 2007).

The inherent optical properties of waters in the West Spitsbergen fjords depend strongly on the hydrodynamic conditions in these fjords. Glacier melt water discharge could impact dissolved organic matter properties in the fjords Surface Waters. The glacier rivers and leaching of organic matter from thawing permafrost could be another source of organic carbon impacting the carbon budget in West Spitsbergen fjords. Low molecular weight, *protein-like* organic matter fraction, can be produced by autotrophic protists in Atlantic Water in the West Spitsbergen Shelf (Makarewicz et al., 2018). The Arctic Water contain high concentration of organic matter that originated from Siberian rivers discharge (Stedmon et al., 2011). Therefore intrusion of Atlantic Water (AW) and Arctic Water (ArW) into fjords and their mixing with Surface Water could modify DOM properties and composition in West Spitsbergen fjords. The balance of AW and ArW influx, river run-off and glacial melt, dominates physical and optical conditions of the west Spitsbergen fjords waters (Cottier et al., 2005), however to date there is very limited information on DOM sources, transformation and fate in those Arctic fjord, with exception on some initial study on CDOM presence in Kongsfjorden (Pavlov et al., 2019).

2. METHODS

Bio-optical measurements were performed through the deployment of an integrated instrument package consisting of ctd, ac-9, CDOM fluorometer, and chlorophyll a fluorometer. Water samples were collected on sampling stations located in three west Svalbard fjords (Kongsfjorden, Isfjorden and Hornsund - Figure 1) during two summer AREX expeditions (2018 and 2019). Water samples collected for CDOM, FDOM and DOC measurements have been filtered through an Opticap XL4 Durapore flow through filter cartridge of a nominal pore size 0.2 μm. Samples collected for chlorophyll a concentration measurements were filtered through Whatman glass-fiber filters (25 mm, GF/F, nominal pore size 0.7 μm.

3. INITIAL RESULTS

Based on 119 EEM spectra and application of the Parallel Factor Analysis, the 5 components model has been developed (Figure 2). Results of pilot study have indicated that FDOM composition in three investigated Arctic fjords is dominated by *protein-like* fluorophores - mainly of *tryptophan–like* type (I_{C4}), the fluorescence of which is more than two times higher in Hornsund compared to Kongsfjorden, with intermediate values in Isfjorden. The contribution of fluorescence intensity of the identified *protein-like* components to the total fluorescence intensity varied from 59 to 75 %.

The high fluorescence intensity of the *protein-like* components in the surface waters of Hornsund may be the result of the glacier melt water discharge or the autochthonous production or (most probable) both. The primary production of organic matter in the West Spitsbergen fjords is characterized by a high spatial and temporal variability within and between fjords (Piwosz et

* Corresponding author e-mail: monika_z@iopan.pl

al., 2002). Makarewicz et al. (2018) have found that fluorescence intensity of the *protein-like* FDOM is highly correlated in West Spitsbergen shelf water with optical proxies of autotrophic protists biomass - the chlorophyll a fluorescence intensity and absorption coefficient at 676 nm, $a_{gp}(676)$. Results from pilot study suggest that observed high fluorescence intensity of the *protein-like* components in Hornsund surface water in summer 2018 and 2019 could be an effect of the biological activity in the fjords. This statement can be supported by measurements of vertical profiles of the $a_{gp}(676)$ in Kongsfjorden, Isfjorden and Hornsund, which has revealed that in water column, in the range between 0 and 30 m depth, the $a_{gp}(676)$ median values are the highest in Hornsund and the lowest in Isfjorden. The vertical distribution of the *humic-like* DOM fluorescence intensity median values measured *in situ* with the use of the Integrated Optical-Hydrological probe shows opposite pattern. The highest values of the fluorescence intensity of the *humic-like* FDOM fraction was observed in Isfjorden, intermediate in Hornsund and the lowest in Kongsfjorden.
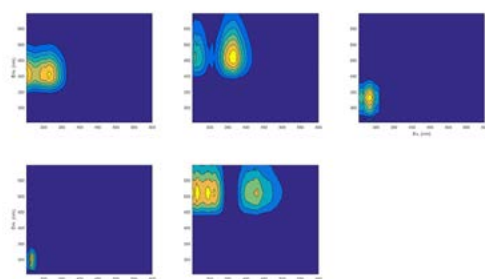
Figure 2. The spectral properties of the five components identified by parallel factor analysis (PARAFAC)(Pilot study results).

This qualitative observation needs further investigation. To support knowledge gained from use of absorption and fluorescence spectroscopy methods and supporting physical, chemical and bio-optical measurements to identify processes that are responsible for differentiation of DOM composition in Isfjorden, Hornsund and Kongsfjorden.
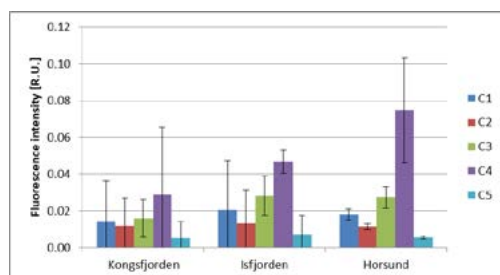
Figure 3 Distribution of fluorescence intensity of identified components C1-C5 in three West Spitsbergen fjords (Kongsfjorden, Isfjorden, Hornsund). Bar plots represent median intensity of fluorescence of given components (C1-C5). Whiskers represent the standard deviations.

3. CONCLUSION

The initial results obtained in the pilot studies of the DOMinEA project revealed a significant differences in both quantitative and qualitative properties of DOM optical characteristics in the West Spitsbergen Fjords. This initial findings suggest also that a number of local scale (autochthonous production, glacier melt, terrestrial input) and mesoscale (intensity oceanic circulation around Spitsbergen and intrusions of different water masses inside fjords and their mixing and transformation) processes could impact effective DOM composition in the study area. An intensive study on DOM qualitative and quantitative properties in Arctic fjords in West Spitsbergen is the main objective of the DOMinEA project.

REFERENCES

ACIA, 2014. Arctic climate impact assessment. Overview report. Cambridge University Press.

Bianchi, T. S., S. Arndt, W. E N. Austin, D. I. Benn, S. Bertrand, X. Cui, J. C. Faust, K. Koziorowska-Makuch, C. M. Moy, C. Savage, C. Smeaton, R. Smith, and J. Syvitski, 2020. Fjords as Aquatic Critical Zones (ACZs). Earth-Science Reviews, 203, art. no. 103145

Cottier F.R., Tverberg V., Inall M.E., Svendsen H., Nilsen F., Griffiths C., 2005. Water mass modification in an Arctic fjord through cross-shelf exchange. JGR - Oceans 110, e12005,

Makarewicz A., Kowalczuk P., Sagan S., Granskog M. A, Pavlov A. K., Zdun A., Borzycka K and M. Zabłocka (2018). Characteristics of chromophoric and fluorescent dissolved organic matter in the Nordic Seas. Ocean. Sci., 14, 543-562.

Meier, W. N., G. K. Hovelsrud, B. E. H. van Oort, J. R. Key, K. M. Kovacs, C. Michel, C. Haas, M. A. Granskog, S. Gerland, D. K. Perovich, A. Makshats, J. D. Reist, 2014. Arctic sea ice in transformation: A review of recent observed changes and impacts on biology and human activity. Rev. Geophys., 51,

Pavlov, A.K., Tverberg, V., Ivanov, B.V., Nilsen, F., Falk-Petersen, S., Granskog, M.A., 2013. Warming of Atlantic Water in two west Spitsbergen fjords over the last century (1912—2009). Polar Res. 32 (1), 11206,

Piwosz K., Walkusz W., Hapter R., Wieczorek P.,. Hop H. and J. Wiktor (2002). Comparison of productivity and phytoplankton in a warm (Kongsfjorden) and a cold (Hornsund) Spitsbergen fjord in mid-summer 2002. Polar Biol., 32 (2002), pp. 549-559

Smith P., Davis S. J., Creitzig F., Fuss S., Minx J. and Gabrielle B., (2015). Biophysical and economic limits to navigate CO_2 emissions, Nature Climate Change, 6, 42-50.

Stedmon C.A., Seredyńska-Sobecka B., Boe-Hansen R., Le Tallec N., Waul C.K., Arvin E., 2011, A potential approach for monitoring drinking water quality from groundwater systems using organic matter fluorescence as an early warning for contamination events. Water Research, 45, 6030–6038.

AUTHORS' INDEX

TITLE
Proceedings
"Oceans from Space" V
Extended Abstracts of the contributions presented at the "Oceans form Space" V Symposium
Scuola Grande di San Marco, Venice (Italy), 24-28 October 2022

EDITORS
Vittorio Barale, Jim Gower, Luigi Alberotanza

Symposium Secretariat
M. Luraschi, G. Canali, F. G. Di Bernardini, M. Runci, G. Nelli, A. Chiabotti - NSA Group srl, Rome (I)

ABSTRACT
The Extended Abstracts of the poster presentations delivered at "Oceans from Space V" – held in Venice, Italy, on 24-28 October 2022 – address every facet of space sciences and technologies applied to marine and maritime issues. Missions, satellites, sensors, passive and active techniques, all demonstrate the potential of oceanographic remote sensing to explore the dynamical and bio-geo-chemical features of the World's Oceans.